**Ausbeuten und Spektroskopie radioaktiver Isotope
bei LOHENGRIN und ISOLDE**

**Ulli Köster**

Vollständiger Abdruck der von der Fakultät für Physik der Technischen Universität München
zur Erlangung des akademischen Grades eines

Doktors der Naturwissenschaften (Dr. rer. nat.)

genehmigten Dissertation.

Vorsitzender:        Univ.-Prof. Dr. M. Kleber

Prüfer der Dissertation:
    1.  Univ.-Prof. Dr. T. von Egidy, im Ruhestand
    2.  Univ.-Prof. Dr. H.J. Körner
    3.  Univ.-Prof. Dr. F. Gönnenwein,
        Eberhard Karls Universität Tübingen (schriftliche Beurteilung)

# Summary

Yields of radioactive nuclei were measured at two facilities: the recoil separator LOHENGRIN at the Institut Laue Langevin in Grenoble and the on-line isotope separator ISOLDE at CERN in Geneva.

At LOHENGRIN the yields of light charged particles were measured from thermal neutron induced ternary fission of several actinide targets: $^{233}$U, $^{235}$U, $^{239}$Pu, $^{241}$Pu and $^{245}$Cm. Thin targets are brought into a high neutron flux. The produced nuclei leave these with the recoil obtained in the fission reaction. They are measured at different energies and ionic charge states. After corrections for the experimental acceptance, the time behaviour of the fission rate and the ionic charge fraction, the yields are integrated over the kinetic energy distribution. Comparing these yields with the predictions of various ternary fission models shows that the most abundant nuclides are well reproduced. On the other hand the models overestimate significantly the production of more "exotic" nuclides with an extreme $N/Z$ ratio. Therefore a refinement of the models is required. The collected yields provide a good database to test improved versions.

In the second part yields of various radioactive nuclei were determined at the ISOL (isotope separation on-line) facility ISOLDE. Here, high energy protons (1.0 or 1.4 GeV) hit targets from different materials and cause various nuclear reactions. The produced radioactive nuclei are stopped in the thick target, diffuse and effuse out at high temperatures, are ionized, electrostatically accelerated to 60 keV and mass separated. Subsequently they are delivered to different beam ports for various applications. The measurement of these beam intensities is less used to study the mechanism of the production reaction (fission, spallation or fragmentation), but to understand and reduce the losses occuring on the way from production to detection. In contrast to a recoil separator these losses vary strongly from isotope to isotope. To increase the final yields a careful optimization of many parameters is required: the chemical composition and the microscopic structure of the target material, the temperature of the target and ion source system, the type and operation conditions of the ion source, etc. The obtained yields and possible improvements are discussed at the example of some elements: Be, Al, Mn, Ni, Cu, Ga, Cd, In, Sn, Cs and Fr. An important contribution to the efficient and selective separation of many metallic elements gives the RILIS (resonance ionization laser ion source) technique. Its applications can be further extended to provide even isomeric selectivity or to perform atomic spectroscopy with radioactive isotopes.

With these intense and pure radioactive ion beams several new nuclear physics results were obtained. The span reaches nearly over the full periodic system, including a new determination of the lifetime and the beta-delayed neutron emission probability of $^{12}$Be ($T_{1/2} = 21.34(23)$ ms, $P_{\mathrm{n}} = 0.48^{+0.12}_{-0.10}$ %), a rough measurement of the magnetic moments of $^{70g}$Cu ($\mu = (+)1.8(3)\,\mu_{\mathrm{N}}$) and $^{70m}$Cu ($|\mu| = 1.2(3)\,\mu_{\mathrm{N}}$), the study of beta-delayed neutron emission of the neutron-rich copper isotopes $^{73-78}$Cu with the first detection of beta-delayed neutrons from $^{73}$Cu, the first measurement of the lifetimes of $^{149}$Cs ($T_{1/2} = 112(3)$ ms) and $^{150}$Cs ($T_{1/2} = 82(7)$ ms) and the observation of new gamma lines in the decay of $^{232}$Fr.

# Zusammenfassung

Ausbeuten radioaktiver Nuklide wurden an zwei verschiedenen Anlagen gemessen: dem Rückstoßseparator LOHENGRIN am Institut Laue Langevin in Grenoble und am "on-line" Isotopenseparator ISOLDE am CERN in Genf.

Am LOHENGRIN wurden die Ausbeuten leichter geladener Teilchen in der neutroneninduzierten ternären Spaltung verschiedener Aktinidentargets bestimmt: $^{233}$U, $^{235}$U, $^{239}$Pu, $^{241}$Pu und $^{245}$Cm. Dazu werden dünne Targets in einen hohen Neutronenfluß eingebracht. Die produzierten Kerne verlassen die Targets mit dem Rückstoß den sie in der Kernspaltung erhalten. Die Intensität wird bei verschiedenen Energien und Ionenladungszuständen vermessen. Nach Korrekturen für die experimentelle Akzeptanz, den zeitlichen Verlauf der Spaltrate und der Bevölkerung der Ionenladungszustände werden die Ausbeuten über die Verteilung der kinetischen Energie integriert. Ein Vergleich der so gewonnenen Ausbeuten mit den Vorhersagen verschiedener ternärer Spaltmodelle zeigt daß die Ausbeuten der häufigsten Nuklide gut vorhergesagt werden. Andererseits unterschätzen die Modelle deutlich die Produktion von "exotischen" Kernen mit einem extremen $N/Z$ Verhältnis. Daher ist eine Überarbeitung dieser Modelle notwendig. Die gesammelten Daten bieten eine gute Grundlage um verbesserte Modelle zu testen.

Im zweiten Teil der Arbeit wurden Ausbeuten von radioaktiven Nukliden an der "ISOL" (isotope separation on-line) Anlage ISOLDE bestimmt. Hier treffen hochenergetische Protonen (1.0 oder 1.4 GeV) auf Targets aus verschiedenen Materialien und verursachen diverse Kernreaktionen. Die dabei produzierten radioaktiven Kerne werden in den dicken Targets gestoppt und können bei hohen Temperaturen herausdiffundieren und freigesetzt werden. Anschließend werden sie ionisiert, elektrostatisch auf 60 keV beschleunigt und nach der Masse separiert. Nun können sie an verschiedene Experimentierplätze verteilt werden und dienen einer Vielzahl von Anwendungen. Die Messung dieser Strahlintensitäten wird weniger genutzt um den Mechanismus der Produktion (Spaltung, Spallation oder Fragmentation) zu untersuchen, sondern um die Verluste die auf dem Weg von der Produktion zur Freisetzung auftreten besser zu verstehen und zu reduzieren. Im Gegensatz zu einem Rückstoßseparator schwanken diese Verluste stark zwischen verschiedenen Isotopen. Um die nutzbare Strahlintensität zu erhöhen ist eine sorgfältige Optimierung vieler Faktoren notwendig: der chemischen Zusammensetzung und mikroskopischen Beschaffenheit des Targetmaterials, der Temperatur der Target- und Ionenquelleneinheit, des Typs und der Betriebsparameter der Ionenquelle, etc. Die erzielten Ausbeuten und mögliche Verbesserungen werden diskutiert anhand einiger Elemente: Be, Al, Mn, Ni, Cu, Ga, Cd, In, Sn, Cs and Fr. Ein wichtiger Beitrag zur effizienten und selektiven Separation vieler metallischer Elemente ist die RILIS Technik (Resonanzionisationslaserionenquelle). Ihre Anwendungen können sogar erweitert werden um selbst Isomere zu trennen oder um Atomspektroskopie mit radioaktiven Isotopen zu betreiben.

Mit diesen intensiven und "reinen" radioaktiven Ionenstrahlen wurden verschiedene neue Resultate in der Kernphysik erzielt. Diese umspannen fast die gesamte Nuklidkarte und beinhalten eine neue Bestimmung der Lebensdauer und der Emissionswahrscheinlichkeit für beta-verzögerte Neutronen von $^{12}$Be ($T_{1/2} = 21.34(23)$ ms, $P_\mathrm{n} = 0.48^{+0.12}_{-0.10}$ %), eine grobe Bestimmung der magnetischen Momente von $^{70g}$Cu ($\mu = (+)1.8(3)\,\mu_\mathrm{N}$) und $^{70m}$Cu ($|\mu| = 1.2(3)\,\mu_\mathrm{N}$), die Untersuchung der beta-verzögerten Neutronenemission der neutronenreichen Kupfer-Isotope $^{73-78}$Cu mit dem ersten Nachweis der beta-verzögerten Neutronenemission von $^{73}$Cu, der ersten Messung der Lebensdauern von $^{149}$Cs ($T_{1/2} = 112(3)$ ms) und $^{150}$Cs ($T_{1/2} = 82(7)$ ms) und dem Nachweis neuer Gammalinien im Zerfall von $^{232}$Fr.

# Contents

# Introduction

Radioactive decay of nuclei has been discovered about one hundred years ago [Bec96]. In the following years specific nuclides were isolated from the natural radioactive decay chains to study their individual decay characteristics [Skl98, Cur98]. Later nuclear reactions were used to produce artificial radio-nuclides (see e.g. ref. [Fer34b]). Most of the newly created isotopes and elements were identified and separated by chemical means. These and other traditional off-line methods, where the production happens at one place and the target or catcher is then transported elsewhere for subsequent separation of the desired isotopes, is limited to lifetimes in the minute to hour range[1]. A lot of time can be gained by coupling production and separation to a single system, a so-called on-line separator. With the use of recoil and isotope on-line separators more short-lived nuclides could be studied. This lead to a rapid growth of the number of "known" isotopes. The chart of nuclides has been extended to heavier elements and to isotopes with extreme neutron to proton ratios. Today nuclear properties like half-lives, masses, decay characteristics or even more or less complete schemes of excited levels are known for about 3000 isotopes. However, just as many exotic isotopes between the expected proton- and neutron-drip-lines are still completely unexplored. The further extension of our knowledge on these exotic isotopes is directly related to the development of efficient and selective separation methods.

The wish to study not only ground state properties of radioactive nuclei, but also reactions with them, requires facilities which provide fast beams (1 MeV $\lesssim E/A \lesssim$ 1 GeV). These so-called RIB (radioactive ion beam) facilities will provide a better insight into nuclear physics and neighboring fields like nuclear astrophysics, nuclear solid state physics, atomic physics, nuclear chemistry, the study of fundamental interactions, nuclear medicine and others, see e.g. [Cas97, Ben96, PIAFE] for an overview. There is a consensus that an important part of this physics is best addressed by post-accelerated beams from an ISOL (isotope separator on-line) facility. It is important to develop appropriate post-accelerators and efficient detector arrays, but one should not forget that the required beam has first to be produced and separated before being accelerated. Often a high potential for improving yields and selectivity by orders of magnitude is hidden in the first part of the separation process (target and ion source), exceeding any amelioration which could be achieved at high effort and cost in the later stages (accelerator and detector).

Looking at the chart of nuclides it is apparent that for some elements the chains of experimentally studied isotopes reach out much further than for neighboring ones. This is not always due to longer lifetimes or a special interest of nuclear physics in these isotopes, but also given by the technical feasibility of beams from these isotopes. Important progress of the ISOL technique in the last years allowed to provide intense beams of elements which were difficult to be produced at all before. The technological status of the separation of some typical elements will be discussed in this work.

The success of an experiment at a RIB facility is mainly determined by the *efficiency*, *rapidity* and *selectivity* of all individual steps from production to detection. Unfortunately it is not possible to optimize each point individually and then to simply join the "best" target with the "best" ion source, etc. Often these independently optimized systems are not at all compatible. It is therefore important to keep an eye on the complete system and an optimum interplay of all components.

---

[1] Seaborg describes the important contribution of a fast car to the discovery of the first mendelevium isotope [Sea90].

1

This makes the approach quite extensive and interdisciplinary, joining different fields like nuclear physics, chemistry, materials science, atomic physics, laser technology, etc.

The NuPECC[2] working group on Radioactive Beam Facilities is currently preparing a detailed comparative study of different concepts for a few key elements of high physics interest: Be, Ar, Ni, Ga, Kr, Sn and Fr. For each case over a hundred involved individual parameters have to be addressed. Even with the restriction to a single element, the answer to all open questions from production to detection would go far beyond the scope of a single thesis. Instead, only some of the properties of the stages "target" and "ion source" will be discussed here. The noble gases Ar and Kr will not be discussed in detail, but additionally a few other elements are included which have been separated recently at ISOLDE. The obtained yields are compared with the beams available at other facilities.

In the tradition of the Technische Universität München this work emphasizes the importance of the technical developments and achievements. These new and improved techniques are an important prerequisite to obtain new physics results. Thus, even a short measurement can provide new information on nuclear properties of known and new isotopes. It allowed to adorn this work with several nuclear physics "tidbits".

---

[2]Nuclear Physics European Collaboration Committee.

## Outline of the thesis

The first production method used for on-line isotope separation was thermal neutron induced fission [KH51]. It is less known that in fission not only neutron-rich medium-mass nuclides are produced, but also light elements from hydrogen to about silicon. In chapter 1 new measurements of yields and energy distributions of these light charged particles from the so-called ternary fission of $^{241}$Pu($n_{th}$,f) and $^{245}$Cm($n_{th}$,f) are presented. The most rare ternary nuclei were also studied in the thermal-neutron-induced fission of $^{233}$U and $^{235}$U. These experiments were performed with the LOHENGRIN separator at the Institut Laue Langevin (Grenoble). The experimental yields are compared with the predictions of several ternary fission models.

In chapter 2 different methods and techniques are discussed to separate beams of short-lived isotopes efficiently and selectively. Isotope separation on-line (ISOL) facilities can produce intense beams for a large variety of elements. The key part of an ISOL facility is the target-ion source unit. The design of the target determines the production rate and the release speed of the radioactive isotopes. The ion source directly affects the efficiency and the selectivity of the separation process. A review is given on some of the presently used ISOL target- and ion source types.

An ion source type which was very successful in the last years is the resonance ionization laser ion source (RILIS). It provides an element selective ionization of many elements. Using the detailed properties of the atomic spectrum, even additional applications like the separation of individual isomers become possible. The technology and applications of a RILIS are presented in chapter 3. This discussion is mainly guided by experiences with the ISOLDE RILIS.

In chapter 4 the state-of-the-art technology for ISOL production of specific elements is discussed. Yields obtained in recent experiments at ISOLDE PSB (CERN) are summarized and compared with yields from other facilities. The possibilities and limitations of the techniques are shown and an outlook is given to further improvements.

Finally the new nuclear physics results are presented in chapter 5. These include various nuclear properties like new lifetimes, magnetic moments, branching ratios for neutron emission and the assignment of new gamma lines. These results have in common that they could be achieved only by using the recently developed techniques presented in chapters 2 and 3.

This work treats problems from different disciplines. Therefore not every point can be discussed in the last detail. Instead an overview is given together with an ample number of more specific references. I experienced that the search and access of certain (less common) references can take a significant amount of time. To simplify the access to some useful values from literature (e.g. ternary fission yields and material constants) they have been summarized in the appendix.

# 1. Ternary fission yields

## 1.1. Fission

Some years after the discovery of radioactivity most natural elements were identified and arranged in the periodical system of Mendeleev. In the 1930s attempts were made to create new transuranic elements by bombarding uranium with neutrons. Indeed, new radioactive isotopes were found [Fer34a], but Hahn and Strassmann [Hah39b, Hah39a] showed that the discovered isotopes had the chemical properties of strontium, yttrium, xenon, cesium, barium, etc. That meant that new elements were not found, but a new type of nuclear reaction: the break-up of uranium into two lighter nuclei, called fission [Mei39]. Ida Noddack had already proposed this possibility in 1934 [Nod34]. Soon the large amount of energy liberated in fission (about 170 MeV kinetic energy of the fragments) was measured by Frisch [Fri39], and a theoretical explanation based on the liquid drop model (LDM) was given by Bohr and Wheeler [Boh39]. Following their arguments, a brief summary will be given here, using more recent evaluations of the parameters involved.

After reaching a maximum of about 8.8 MeV around $^{56}$Fe, the average binding energy per nucleon decreases to about 7.8 MeV for the actinides. Breaking these heavy nuclides into two lighter fragments releases a difference of about 0.8 MeV per nucleon[1]. Although being strongly exoenergetic, an immediate fission is normally prevented by a potential barrier.

Regarding the deformation of a nucleus in the liquid drop model, one finds that the surface energy $E_s$ of an ellipsoid increases with the elongation $\varepsilon$ like:

$$E_s = a_s \cdot A^{\frac{2}{3}} \cdot (1 + \frac{2}{5} \cdot \varepsilon^2 + \dots),\tag{1.1.1}$$

while the Coulomb energy $E_C$ decreases like:

$$E_C = a_C \cdot Z^2 \cdot A^{-\frac{1}{3}} \cdot (1 - \frac{1}{5} \cdot \varepsilon^2 + \dots).\tag{1.1.2}$$

The total energy change is thus positive if:

$$\frac{2}{5} a_s A^{\frac{2}{3}} \varepsilon^2 < \frac{1}{5} a_C \frac{Z^2}{A^{\frac{1}{3}}} \varepsilon^2.\tag{1.1.3}$$

Solving for $Z$ and $A$ and introducing the numerical values for the constants $a_s$ and $a_C$, obtained from fits to nuclear masses [Wei91], gives:

$$\frac{Z^2}{A} > \left(\frac{Z^2}{A}\right)_{\text{crit}} = \frac{2a_s}{a_C} = \frac{2 \cdot 17.8 \text{ MeV}}{0.71 \text{ MeV}} \approx 50.\tag{1.1.4}$$

This shows that nuclei with high $Z^2/A$ become unstable against fission. The decisive parameter $(Z^2/A)/(Z^2/A)_{\text{crit}}$ is called fissility.

---

[1]This energy release is calculated for typical asymmetrical or symmetrical mass splits respecting the conservation of the $N/Z$ ratio of the compound nucleus.

Before fissioning, the nucleus has to be strongly elongated. During the elongation the system has to overcome a potential barrier, the height and width of which decrease with increasing fissility. While very fissile nuclei can tunnel through the barrier and fission spontaneously, for most nuclides the small tunneling transmission coefficients result in extremely long half-lives for spontaneous fission. These nuclei are still fissile when the excitation energy is provided from "outside". Practically the most important case is thermal neutron induced fission where the neutron binding energy gained in neutron capture is used to excite the compound nucleus. Using more energetic projectiles, i.e. by capture of – or collisions with – fast neutrons, protons or heavy ions, fission can also be induced in isotopes which are not fissile by thermal neutrons. Another possibility is the excitation by real or virtual photons (the latter from electron scattering or Coulomb excitation) leading to gamma induced fission. The necessary energy can also be expended by capture of – or reactions with – myons, antiprotons, pions or hyperons; see e.g. ref. [Dav87, Egi93, Hic85, Pol89]. For exotic radio-isotopes far from $\beta$-stability even the Q-value of electron capture (EC), $\beta^+$ or $\beta^-$ decay can be sufficient to overcome the fission barrier. On the proton-rich side few cases of EC- and $\beta^+$-delayed fission were reported [Sko72, Hab78, Laz87, Hal92], but of the nuclides predicted to decay via $\beta^-$f up to now only $^{256m}$Es could be synthesized [Hal89].

While the liquid drop model favors a symmetrical separation[2], many experimental mass- and energy distributions show an asymmetrical fission into a light and a heavy fragment. Strutinsky introduced shape dependent shell correction energies which allow the calculation of the potential energy in dependence of elongation [Str67]. For actinides the ground state has a small prolate deformation. With increasing elongation a double humped barrier occurs in most cases, where the higher peak is called fission barrier. Between both peaks a local second minimum exists as a so-called superdeformed state with a ratio of 2:1 for the long to short axis. Due to the smaller remaining barrier this isomeric state can decay rapidly by fission. The first experimental confirmation that the fission isomer is indeed located in the second minimum was obtained at the Munich Tandem accelerator by spectroscopy of conversion electrons preceding the fission of the 4 ns fission isomer $^{240m}$Pu [Spe72]. For uranium and thorium the existence of a third minimum with hyperdeformed states (axis ratio 3:1) was also found. The first spectroscopy of hyperdeformed states in $^{236}$U and $^{234}$U was again made at the Munich Tandem accelerator [Kra98a, Kra99].

When passing the barrier the fissioning system can probe different channels. Especially with low excitation energy it will preferentially decay via energetically favorable channels, i.e. follow valleys in a multi-dimensional landscape where the energy is plotted against various multipole orders of deformations. These so-called fission modes show up in the mass and kinetic energy distribution of the fission fragments. The fission yields are therefore tightly linked to the nuclear structure of the compound system. For most light actinides an asymmetrical mass distribution with a light and a heavy fragment is found, with the maximum of the heavy fragment distribution always being centered around $A_\mathsf{H} \approx 134$, while the light fragment mass is given by: $A_\mathsf{L} = A_\mathsf{Comp} - A_\mathsf{H} - \nu$, with $A_\mathsf{Comp}$ the mass of the fissioning compound nucleus and $\nu$ the number of emitted neutrons. Only in very heavy actinides ($A \geq 258$) symmetric fission with two fragments of equal size dominates. With increasing excitation energy the shell effects are washed out and symmetrical fission is also favored in lighter systems.

Fission is a collective process including all nucleons, so most of the information on the entrance channel is lost and for a given excitation energy most gross features (mass distribution, kinetic energy distribution, etc.) are similarly regardless[3] of the excitation mechanism which led to the compound nucleus. This was confirmed in many experiments, see e.g. ref. [Dav87, Sch92, Hof94,

---

[2]Some calculations show an instability towards asymmetrical mass splits, but only at high deformation far beyond the saddle point.

[3]An important exception are the correlations of the asymmetry of fragment angular distribution and polarization of the fission inducing neutron. Thus, it becomes possible to measure parity nonconservation in fission (see e.g. [Gön94, Köt98]) and possibly even time reversal invariance [Jes98].

Eng98]. While other excitation mechanisms may create a mixture of high- and low-energy fission, thermal neutron-induced and spontaneous fission are free of high-energy contributions. Therefore they always played a leading role in the investigation of low-energy fission. The high cross-sections and the possibility to "switch" the fission on and off with the neutron beam allows the production and handling of much higher source strengths with neutron-induced fission than with spontaneous fission. Thus, very rare events which will be discussed in the following are mainly studied in thermal neutron induced fission.

## 1.2.   Ternary fission

The possibility for fission not into two, but into three fragments was already proposed in 1941 [Pre41]. Experimental evidence for emission of a third charged particle was found from fission tracks in nuclear emulsions [ST46, ST47, Far47]. Detailed investigations showed that about 90% of the ternary particles (TP) are $^4$He nuclei with a kinetic energy distribution centered around 16 MeV. They are also called long-range alphas (LRA) in order to differentiate from less energetic alphas from radioactive alpha decay. Next most abundant are all hydrogen and the heavier helium isotopes. Only about 1% of the ternary particles have a $Z > 2$, and the yields drop rapidly with increasing $Z$. For "real" ternary events with three fragments of comparable size only upper limits exist in low-energy fission[4], see [Sto66, SO87] and references therein. Also in heavy ion reactions (e.g. 12.5 MeV/nucleon Xe projectiles on Sn) fission-like three-body events were observed. However, they are interpreted as sequential fission, i.e. a subsequent fission of one of the still highly excited fission fragments occurs, thus creating three particles in a two-step process [Glä82, Har82]. For brevity I will use the expressions "ternary fission" and "tripartition" synonymously to the more correct name "light charged particle (LCP) accompanied fission".

Measured angular correlations of the TP with the fission fragments (FF) show a maximum emission of TP about perpendicular to the momenta of the FF. This fact, as well as the width of the kinetic energy distributions are consistent with an emission from the region of the stretched neck which forms between the fragments just before scission. In rare cases this neck can break more or less simultaneously[5] at two positions, thus leaving nucleons between the fragments which form a light charged particle. In the Coulomb field of both fragments it is accelerated and preferentially emitted perpendicular to the emission direction of the fragments. In fact the angle of maximum emission to the fission axis (defined by the momentum of the light fragment) is slightly smaller than 90 degrees (about 83.9 degree for helium isotopes from $^{252}$Cf(sf) [Sin96]), accounting for the stronger repulsion and "shadowing" from the heavy fragment. So-called polar emission of LCP parallel to the fragment's direction is much less abundant (only about 1% of the ternary yield comes from polar emission), and probably stems from a different mechanism. Only protons show a significant contribution of polar emission angles which can be explained by statistical evaporation models [SO91]. A detailed discussion of this polar emission of light charged particles can be found in literature, e.g. [Pia80].

## 1.3.   Ternary fission models

The models which are successful in describing binary fission are difficult to apply for ternary fission. The scission point model of Wilkens et al. [Wil76] starts with the presence of two fission fragments and has only the tip distance as free parameter. The introduction of a third particle is

---

[4]Positive results for true ternary fission can often be explained by experimental artifacts as discussed in the given references.

[5]The actual configuration in the moment of TP creation is the main difference between various models to be discussed below.

not foreseen. Also the random neck rupture model of Brosa et al. [Bro90] which uses the Lawrence parameterization [Law65] with five parameters does not have enough degrees of freedom to directly describe the development of a third particle in the neck region. Therefore, at a certain elongation a projection onto a dedicated ternary scission configuration would become necessary which is not feasible without ambiguities.

There is still no theory which can reproduce the individual yields and energy distributions of ternary fission fragments from first principles. Only in the special case of alpha accompanied fission of $^{236}U^*$ a numerical solution of the one-body Schrödinger equation describing "alpha decay during fission" was possible, and gave approximately correct values for the absolute emission probability and energy distributions of the alpha particles [Tan87, Sch95]. A similar classical approach had been used by Cârjan et al. to reproduce average energy and emission probability of LRA in the same fissioning system [Câr75, Câr76, Obe92]. For cold spontaneous $^{10}$Be accompanied fission of $^{252}$Cf the relative probabilities of the associated fragment mass splits have recently been calculated via barrier penetrabilities in a cluster model[6] [San98b]. The calculations were performed by WKB approximation of a barrier obtained from a liquid drop model including deformations $\beta_2$, $\beta_3$ and $\beta_4$, according to Möller et al. [Möl95]. The one-body densities were obtained from a spherical Hartree-Fock calculation. The inverse problem, i.e. the calculation of individual ternary particle yields with a fixed or averaged mass split for the light and heavy fragments, has not been approached yet.

A nice graphical illustration of ternary fission has been given by Mutterer and Theobald [Mut96a], who show the analogy to multifragmentation according to the Rayleigh criterion in hydrodynamical systems. However, this is a classical picture which cannot take into account quantum mechanical properties of the system (e.g. fluctuations). There are also fundamental problems if the liquid drop model (LDM) approach should be used quantitatively. If the ratio of surface to volume becomes large, which is the case in the long-stretched and thin neck, the prerequisites for a LDM approximation are no longer valid.

The statistical model of Fong [Fon71] and the first model of Pik-Pichak [PP84] only deal with the ratio of LRA to binary fission. Bouzid et al. gave a relationship between the ternary to binary ratio and the proton-odd-even-effect in binary fission [Bou98]. Other approaches gave only a qualitative discussion of ternary particle emission without treating yields or energy distributions [Hal71, Rot89, Roy92].

In the following some models will be presented which describe the relative emission probabilities of various ternary particles in different fissioning systems.

## 1.3.1.   Valskii fit formula

Valskii [Val76] gave a pure interpolation formula without assuming any specific scission configuration:

$$
\begin{aligned}
\ln y(A_{\text{TP}}, Z_{\text{TP}}) = \quad & \ln\left(\frac{g(A_{\text{TP}}, Z_{\text{TP}})A_{\text{TP}}}{2}\right) + \frac{B(A_{\text{TP}}, Z_{\text{TP}})}{T} + Z_{\text{TP}}\ln X_{\text{p}} + \\
& + (A_{\text{TP}} - Z_{\text{TP}})\ln X_{\text{n}} - (A_{\text{TP}} - 1)[\ln(\eta T^2) + K], \qquad (1.3.1)
\end{aligned}
$$

with $y(A_{\text{TP}}, Z_{\text{TP}})$ the yield of the TP relative to 10000 $^4$He, $B(A_{\text{TP}}, Z_{\text{TP}})$ the binding energy of the TP, and $K$ a normalization factor which contains the absolute emission probability of LRA and some constants. The four free parameters $\ln X_{\text{p}}$, $\ln X_{\text{n}}$, $\ln(\eta T^2)$ and $T$ were fitted to reproduce the then known ternary yields of $^{233}$U($n_{\text{th}}$,f), $^{235}$U($n_{\text{th}}$,f) and $^{239}$Pu($n_{\text{th}}$,f). The temperature parameter $T$ also determines the average initial kinetic energy of the ternary particle $E_{\text{TP}}^{\text{kin}\,0} = 2T$. It has the values 1.32 MeV, 1.17 MeV and 1.38 MeV for the systems $^{233}$U($n_{\text{th}}$,f),

---

[6]As in the case of cluster decay calculations, the influence of the preformation factor is neglected.

$^{235}$U($n_{th}$,f) and $^{239}$Pu($n_{th}$,f). For the statistical weight $g(A_{TP}, Z_{TP})$, a sum over all particle stable levels of the isotope is used:

$$g(A_{TP}, Z_{TP}) = \sum_i (2I_i + 1)\exp(-E_i/T), \tag{1.3.2}$$

with $E_i$ the excitation energies and $I_i$ the spins of the individual levels. A more detailed discussion of the contribution from excited states is given in section 1.6.5.

The formula tends to strongly overestimate the emission of heavy particles[7]. Also the parameters $\ln X_p$ and $\ln X_n$, which describe the energy necessary for separation of protons and neutrons as a kind of chemical potential, do not agree with similar separation energies from nuclear mass models.

In the next paragraphs the graphical insets show typical scission configurations of the discussed models. They are roughly drawn to scale with a fixed radius parameter of $r_0 = 1.2$ fm.

## 1.3.2.    Double-neck-rupture model

Rubchenya and Yavshits proposed a statistical model of a double neck rupture [Rub88]. A ternary proto-particle $(A_{TP}^0, Z_{TP}^0)$ with mass $A_{TP}^0 \approx 10$ is created between both fragments $(\bar{A}_H, \bar{Z}_H)$ and $(\bar{A}_L - A_{TP}^0, \bar{Z}_L - Z_{TP}^0)$ in a compact collinear configuration. $\bar{A}_H = 140$ is fixed and $\bar{Z}_H = (Z/A)\cdot\bar{A}_H$ chosen to have the same $N/Z$ ratio as the compound nucleus. Due to the compact configuration, the ternary proto-particle will stay in close contact with the light fission fragment for a while and exchange nucleons. The proton and neutron numbers are changed to that of the finally ejected particle $(A_{TP}, Z_{TP})$.
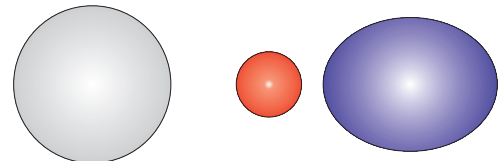
The yields are calculated according to:

$$y(A_{TP}, Z_{TP}) = C\exp\left(\frac{Q - V_{Coul}}{T}\right), \tag{1.3.3}$$

where $C$ is a normalization constant, $T$ the "effective temperature", and $Q$ the energy necessary to create the final ternary particle from the primary one:

$$Q = M(\bar{A}_L - A_{TP}^0, \bar{Z}_L - Z_{TP}^0) + M(A_{TP}^0, A_{TP}^0) - \\ -M(\bar{A}_L - A_{TP}, \bar{Z}_L - Z_{TP}) + M(A_{TP}, Z_{TP}), \tag{1.3.4}$$

with $M$ the nuclear masses of the respective isotopes. $V_{Coul}$ is the Coulomb energy between ternary and light fragment:

$$V_{Coul} = \frac{e^2 Z_{TP}(\bar{Z}_L - Z_{TP})}{r}, \tag{1.3.5}$$

$$r = r_0(\sqrt[3]{\bar{A}_L - A_{TP}} + \sqrt[3]{A_{TP}}), \tag{1.3.6}$$

where $r_0 = 1.7$ fm is chosen larger than the standard nuclear radius parameter to account for the reduced interaction energy of deformed fragments. The heavy fragment is placed at 1-2 fm distance to the ternary particle and acts only as a spectator. With $T = 2.1$, 2.3 and 2.8 MeV for the compound nuclei $^{236}$U, $^{240}$Pu and $^{252}$Cf, the experimental yields of the most abundant ternary particles can be reproduced quite well, but the odd-even effect is underestimated. For heavy ternary fragments it is difficult to understand how so many nucleons can be exchanged between the ternary proto-particle and the light fragment in the rather short time ($\mathcal{O}(10^{-21}$ s)) before separation.

---

[7]Especially for $^{233}$U($n_{th}$,f) the predictions are completely off. This can be understood from the small number of measured values used for the fit.

Imposing an even-even heavy fragment for even-even compound nuclei (i.e. $^{140}$Xe instead of $^{140}$Cs for $^{235}$U(n,f)) helps to improve the reproduction of the odd-even-effect [Bau92a]. Including explicitly momentum conservation of the three fragments leads to a better reproduction of some experimental yields [Bou94]. Trajectory calculations which can reproduce the experimental angular and energy distribution of light charged particle and fragments give additional information on the scission configuration [Ros94]. The average interfragment distance $\bar{D}$ was found to scale with [Rub94]:

$$\bar{D} = 1.2(\sqrt[3]{A_H} + \sqrt[3]{A_L} + 6.3\sqrt[3]{Z_{TP}}) \tag{1.3.7}$$

**New version**  In a more recent version of the double-neck-rupture model [Rubch], the ternary yields were averaged over the contributions of all mass splits, weighted with the pre-neutron-emission fragment yields from binary fission. Now a radius parameter of $r_0 = 1.6$ fm is used and the temperatures taken from an empirical formula are: 2.24, 2.19, 2.39, 2.31, 2.61 and 3.05 MeV for $^{233}$U(n$_{th}$,f), $^{235}$U(n$_{th}$,f), $^{239}$Pu(n$_{th}$,f), $^{241}$Pu(n$_{th}$,f), $^{245}$Cm(n$_{th}$,f) and $^{249}$Cf(n$_{th}$,f).

### 1.3.3. Modified double-neck-rupture model
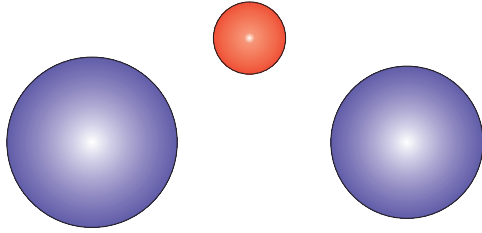


Baum et al. proposed a fundamental modification of the double neck rupture model [Bau92a, Bau92b]. They omitted the idea of a proto-particle and calculated directly the Q-value of the reaction. The mass split is chosen to obtain the highest Q-value. A triangular scission configuration is assumed where the TP is emitted off-axis about midway between both fragments. The tip distance between TP and light fragment is just half of the tip distance between both fragments. The Coulomb energy of all three fragments is calculated with the three distances[8]:

$$
\begin{aligned}
D_{L-H} &= r_L + r_H + b_0 \cdot r_{TP}, \\
D_{L-TP} &= r_L + r_{TP} + 0.5 \cdot b_0 \cdot r_{TP}, \\
D_{H-TP} &= r_H + r_{TP} + 0.5 \cdot b_0 \cdot r_{TP},
\end{aligned}
\tag{1.3.8}
$$

and the radii given by:

$$r_i = 1.2\sqrt[3]{A_i} \text{ fm.} \tag{1.3.9}$$

The scission configuration provides also the start conditions for trajectory calculations. The free parameter $b_0$ is adapted to reproduce the mean kinetic energies of the heavier ternary particles ($Z \geq 3$). $b_0 = 4.26$ is found for $^{235}$U(n$_{th}$,f) which corresponds to a rather stretched configuration. The second free parameter $T$ is fitted to reproduce the measured yields: $T = 1.7$-$2.5$ MeV is found for $^{235}$U(n$_{th}$,f) depending on the mass split[9]. For $^{235}$U(n,f) the model can approximately reproduce the experimentally observed yields, including the neutron- and proton-odd-even effect. Also the yields of rare nuclei are better reproduced than in other models. However, for the higher actinides $^{239}$Pu(n,f), $^{242}$Am(n,f) and $^{252}$Cf(sf) it also starts to overestimate the yields of rare nuclei.

### 1.3.4. "Transition energy" model

In a model proposed by Pik-Pichak [PP94] the relative emission probability of a ternary particle is related to a relative "transition energy" $\Delta\varepsilon^{TP-\alpha}$ by:

$$y(A_{TP}, Z_{TP}) = b\exp(-\Delta\varepsilon^{TP-\alpha}/\Gamma). \tag{1.3.10}$$

---

[8]In the original work [Bau92b] there is some inconsistency of the distances $D_{L-TP}$ and $D_{H-TP}$ used in figure 2.7 and equation (3.3.)

[9]For the results published in [Bau92a] a temperature $T = 1.91$ MeV was chosen [Neu92].

The transition energy is given by the difference of reaction Q-value and Coulomb energy.

$$\Delta\varepsilon^{\mathrm{TP}-\alpha} = -\Delta Q_{\mathrm{R}}^{\mathrm{TP}-\alpha} + \Delta E_{\mathrm{Coul}}^{\mathrm{TP}-\alpha}. \tag{1.3.11}$$

In principle the total excitation energy TXE, consisting of deformation energy and internal excitation energy of the fragments has also to be taken into account. However, for the chosen mass split it is assumed that TXE is roughly constant for all ternary particles and thus drops out when normalizing to the yield of LRA.

A collinear scission configuration of nearly touching fragments is used. The heavy fragment ($^{132}$Sn or a nucleus in its close vicinity) and the ternary particle are chosen to be spherical with a radius parameter $r_0 = 1.4$ fm. Only the light fragment is deformed, which is reflected in a modified radius parameter $r_0 = 2.146$ fm. The parameter $\Gamma$ is 2.1 MeV, 2.2 MeV, 2.3 MeV and 2.7 MeV respectively for the compound nuclei $^{234}$U, $^{236}$U, $^{240}$Pu and $^{252}$Cf. This parameter can be related to an effective temperature $T = 0.75\,\Gamma$. The temperature in turn determines the average initial kinetic energy of the ternary particles ($\bar{E}_0 = 2T$) which is roughly consistent with values obtained by trajectory calculations [PP84].
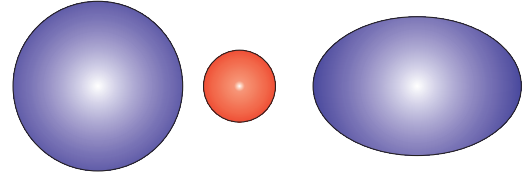
With coincident detection of ternary particles, fragments, neutrons and gammas, Singer and others could indeed measure the excitation energy of the fragments accompanied by different ternary particles [Sin96, Sin97]. He thus proposed to include the measured dependence on the total excitation energy as an additional factor in equation (1.3.10): $\exp(-\Delta\mathrm{TXE}/\Gamma)$. This method gives an independent access to the temperature parameter $\Gamma$. He finds $\Gamma = 2.35(9)$ MeV for $^{252}$Cf(sf).

## 1.3.5.   Boltzmann model

In a model proposed by Faust and Bao [Fau95b], the ternary particle yields are related by a Boltzmann ansatz to the energy necessary to create the ternary scission configuration. Normalized to the yields of $^4$He, the influence of fission modes cancel each other out, leaving:

$$y = C\exp(-\frac{\Delta E^{\mathrm{TP}-\alpha}}{T}), \tag{1.3.12}$$
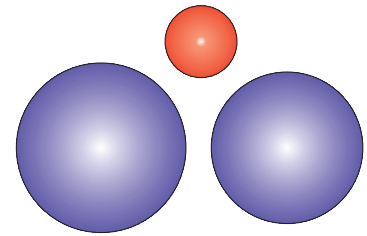
with

$$\Delta E^{\mathrm{TP}-\alpha} = E_{\mathrm{Coul}}^{\mathrm{TP}} - E_{\mathrm{Coul}}^{\alpha} - (Q_{\mathrm{R}}^{\mathrm{TP}} - Q_{\mathrm{R}}^{\alpha} + E_{\mathrm{Corr}}^{\mathrm{TP}} - E_{\mathrm{Corr}}^{\alpha}). \tag{1.3.13}$$

The Coulomb energy is calculated for a compact triangular scission configuration with three nearly touching spheres as a sum of three individual contributions:

$$E_{\mathrm{Coul}}^{\mathrm{TP}} = \sum_{i \neq j} e^2 \frac{Z_i Z_j}{r_{ij}}, \tag{1.3.14}$$

where $i, j$ stand for the three fragments L, H and TP respectively. For the distances between the spherical fragments the Bass parameterization [Bas80] is used:

$$r_{ij} = (1.12(\sqrt[3]{A_i} + \sqrt[3]{A_j}) - 0.94(\frac{1}{\sqrt[3]{A_i}} + \frac{1}{\sqrt[3]{A_j}}) + 3) \text{ fm}. \tag{1.3.15}$$

The reaction Q-value $Q_R$ is calculated from the difference of the mass excesses of the compound nucleus and all involved fragments. In case of neutron-induced fission the neutron binding energy of 6 MeV is added.

The corrections $E_{corr}^{TP}$ account for the loss of pairing energy of the ternary particles at a finite nuclear temperature $T$ [Mor72]. The values are parameterized with:

$$E_{corr}^{TP} = \begin{cases} b_1 \cdot A_{TP} + a_1 & \text{for } A_{TP} < 10, \\ b_2/A_{TP} + a_2 & \text{for } A_{TP} \geq 10. \end{cases} \quad (1.3.16)$$

The $a$ and $b$ are individually fitted for even-even, even-odd, odd-even and odd-odd ternary particles to reproduce the measured yields from $^{241}$Am(2n,f).

The temperature $T$ is assumed to be identical to the one used in a similar model for binary fission [Fau95a]. It varies between $T = 1.3$ MeV for $^{235}$U(n$_{th}$,f) and $T = 2.3$ MeV for $^{249}$Cf(n$_{th}$,f). Temperatures of other compound nuclei are interpolated. Contributions of the Boltzmann ansatz are summated over all possible fission mass splits weighted with the known binary mass yields.

Compared with all other models the scission configuration is very compact with a minimum tip distance even smaller than in compact binary fission [Gön91]. Therefore the chosen scission configuration is prohibited by energy conservation and has rather to be regarded as a "virtual" state. While initially a dozen of free parameters ($a$ and $b$ for the correction energies in all different cases) have to be fitted to reproduce the yields of one fissioning system, only the temperature parameter is changed when applying the formula to other compound nuclei.

### 1.3.6.    Extended Halpern model
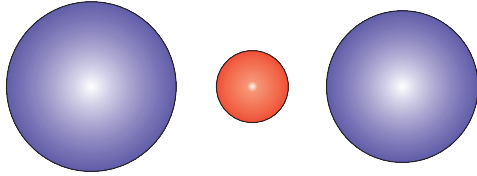


The extended Halpern model [Gön92b, Wös96] was developed at the Tübingen university following the ideas of Halpern [Hal71]. He proposed that ternary fission mainly occurs in very elongated scission configurations where the high stored deformation energy is released at the moment of scission ("sudden snapping-in of the neck") and allows the emission of a third particle. The ternary scission configuration is obtained by placing a ternary particle in between both fragments $(A_L, Z_L)$ and $(A_H - A_{TP}, Z_H - Z_{TP})$ while keeping the center-of-mass of the total system fixed. The "energy costs" for such a configuration compared with a binary configuration with $(A_L, Z_L)$ and $(A_H, Z_H)$ at a distance $2d$ (center to center) are calculated as:

$$\Delta E = \Delta Q^{bin-ter} + \Delta V_{Coul}^{ter-bin} + E_{TP}^{kin\,0}. \quad (1.3.17)$$

The initial kinetic energy of the ternary particle is neglected ($E_{TP}^{kin\,0} \approx 0$). $\Delta Q^{bin-ter}$ is given by the mass defects of all fragments involved in the binary and ternary configuration. The ternary particle is assumed to originate from the heavy fragment. The difference of the Coulomb energies in ternary and binary configurations is thus given by:

$$\Delta V_{Coul}^{ter-bin} = e^2 \frac{Z_L Z_{TP}}{d} + e^2 \frac{Z_{TP}(Z_H - Z_{TP})}{d(1 + \frac{A_{TP}}{A_H - A_{TP}})} + e^2 \frac{Z_L(Z_H - Z_{TP})}{d(2 + \frac{A_{TP}}{A_H - A_{TP}})} - e^2 \frac{Z_L Z_H}{2d}. \quad (1.3.18)$$

To obtain the average energy costs for emission of a certain ternary particle, the energy costs of all individual mass splits are averaged using the known binary yields for weighting.

The ternary particle yield is connected to the energy costs via:

$$y(A_{TP}, Z_{TP}) = C \cdot \exp(-p1 \cdot \Delta E - p2), \quad (1.3.19)$$

where $p1$ and $p2$ are fit parameters and $C$ is a constant for normalization of the yield to $10^4$ $^4$He. The tip distance in the binary configuration (and thus $d$) is calculated from the minimum kinetic energies of the fragments observed in binary fission: $E_{\text{kin}}^{\text{min}} = \bar{E}_{\text{kin}} - 3 \cdot \sigma(E_{\text{kin}})$. For $^{235}$U($n_{\text{th}}$,f) a tip distance of 9 fm is used. Thus, the ternary events are assigned to extremely stretched scission configurations[10]. The size of the fragments is parameterized with a radius constant of $r_0 = 1.29$ fm. The model can reproduce measured yields over a wide range but underestimates the proton odd-even-effect. The yields of lithium isotopes are generally overestimated by about one order of magnitude.

### 1.3.7. Summary

Different models have been proposed to describe the emission probabilities of ternary particles. It is remarkable that all models (except for the Valskii fit formula) formally have the same simple dependence:

$$y = C \exp(-\Delta E / T). \tag{1.3.20}$$

The energy parameter $\Delta E$ describes the effort of the fissioning system to emit a ternary particle. It is mainly composed of the Q-value and the Coulomb energy of the scission configuration. The main difference of the models lies in the geometry of the scission configuration which in turn strongly influences the Coulomb energy term in $\Delta E$. The second difference between the models is the interpretation of the parameter $T$ describing the ability to access energetically unfavorable scission configurations. While some models explicitly introduce it as nuclear temperature of the fissioning system, others explicitly claim it is not a temperature.
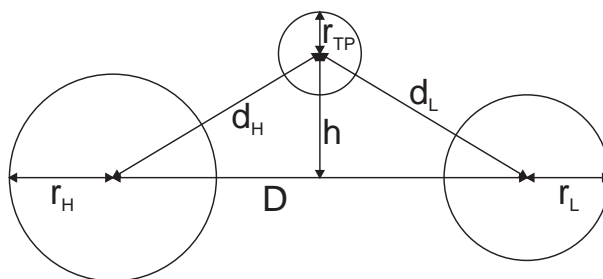


Figure 1.3.1.: Universal parameterization for the scission configuration of most ternary fission models.

Figure 1.3.1 shows a universal parameterization of the scission configuration. The parameters of the individual models are summarized in table 1.3.1. The interfragment distance of most models is in reasonable agreement with a value of 21 to 22 fm as determined by trajectory calculations for LRA accompanied fission [Gav75]. Only the Faust formula has a more compact configuration which has to be regarded as a virtual state (see above).

All models use some free parameters which are fitted to reproduce experimentally determined yield values. This procedure will always result in a more or less good reproduction of the most abundant yields, see figure 1.3.2. However, larger deviations between the models occur for rare ternary particles, i.e. very heavy ones ($A_{\text{TP}} \gg 20$) and "exotic" isotopes with an extreme $N/Z$

---

[10] This argument is also supported by the statistical model of Fong. Generally it has more compact scission shapes [Fon56], but the ternary emission preferentially proceeds via elongated shapes [Fon71]. Some trajectory calculations give even more stretched configurations [Nar69].

[11] This is the light fragment after emission of the ternary particle, i.e. $(\bar{A}_{\text{L}} - A_{\text{TP}}, \bar{Z}_{\text{L}} - Z_{\text{TP}})$ in the original notation.

[12] This is the parameter used in formula (1.3.20). $T = 0.75\Gamma$ is correspondingly 1.6 MeV.

[13] This is the heavy fragment after emission of the ternary particle, i.e. $(A_{\text{H}} - A_{\text{TP}}, Z_{\text{H}} - Z_{\text{TP}})$ in the original notation.

[14] The given value is just the inverse of parameter $p1$ in formula (1.3.19). Note that it is explicitly declared to be not a temperature.

Table 1.3.1.: Parameters as defined in figure 1.3.1 for the case of $^{10}$Be accompanied fission of $^{235}$U($n_{th}$,f). The models are listed as above. For models using an average over many mass splits only a typical example close to the peak of the fragment mass distribution is given.

| Model (ref.) | $(A_H, Z_H)$ | $(A_L, Z_L)$ | $D$ fm | $d_L$ fm | $d_H$ fm | $h$ fm | $T$ MeV |
|---|---|---|---|---|---|---|---|
| [Rub88] | $^{140}$Cs | $^{86}$As$^{(11}$ | $\approx 25$ | 11.2 | $\approx 13.8$ | 0 | 2.1 |
| [Rub94, Rubch] | $^{132}$Sn | $^{94}$Sr | 23.6 | 11.3 | 12.3 | 0 | 2.19 |
| [Bau92b] | $^{132}$Sn | $^{94}$Sr | 22.6 | 13.6 | 14.2 | 7.5 | 1.91 |
| [PP94] | $^{132}$Sn | $^{94}$Sr | 22.9 | 12.8 | 10.1 | 0 | 2.1$^{(12}$ |
| [Fau95b] | $^{132}$Sn | $^{94}$Sr | 13.4 | 9.9 | 10.5 | 7.7 | 1.3 |
| [Wös96] | $^{132}$Sn$^{(13}$ | $^{94}$Sr | 22.4 | 10.8 | 11.6 | 0 | $(3.1)^{(14}$ |
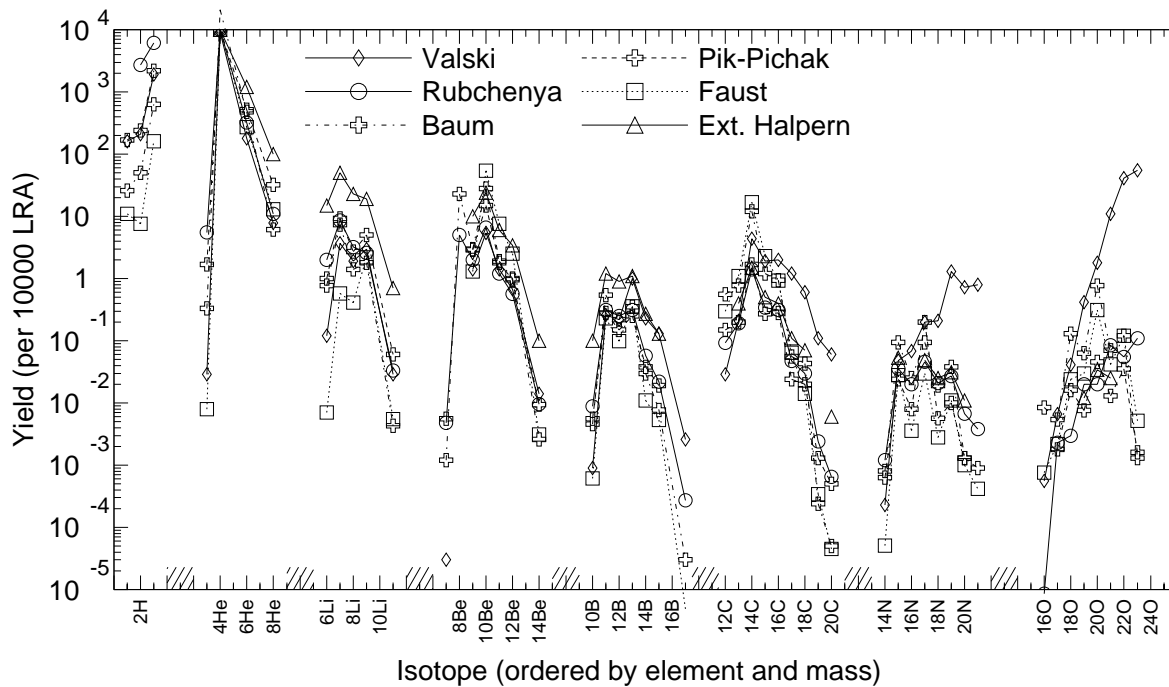


Figure 1.3.2.: Ternary fission yields for $^{235}$U($n_{th}$,f), calculated with different models. Here, and in the following yield comparisons the isotopes of each element are grouped together in a series. From left to right: $^{1-3}$H, $^{3-8}$He, $^{6-11}$Li, $^{7-14}$Be, $^{10-17}$B, $^{12-20}$C, $^{14-21}$N and $^{15-24}$O.

ratio ($^{3}$He, $^{11}$Li, etc.). The measurement of such ternary particle yields is a good way to probe the predictions of the different models.

The yield of the heavier ternary particles is affected by both the Q-value and the Coulomb energy term, while the yields of lighter exotic nuclei depend mainly on the Q-value. Exemplary this dependence is shown in figures 1.3.3 and 1.3.4. The most abundant particle-stable isotopes of the elements hydrogen to oxygen are plotted. The calculation was performed with the Boltzmann model, but all other models show qualitatively the same dependence: with slightly varying temperature the yields of less abundant nuclei change by more than one order of magnitude.
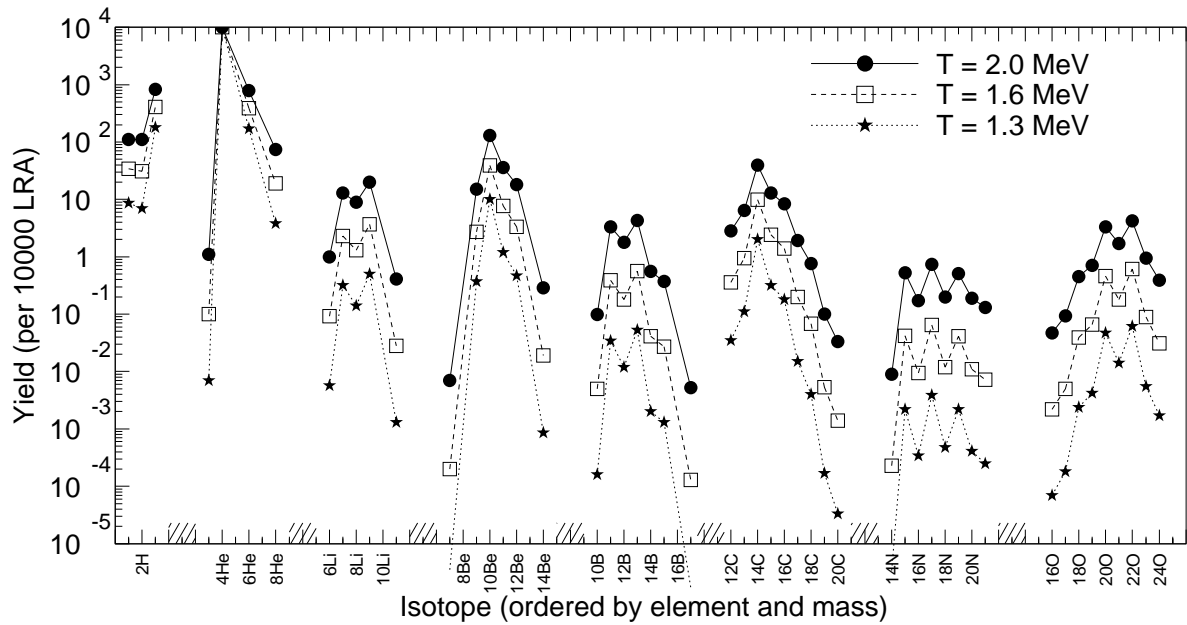
Figure 1.3.3.: Ternary fission yields for $^{241}$Pu($n_{th}$,f), calculated with different temperatures in the "Faust formula". The scale is identical to figure 1.3.2.
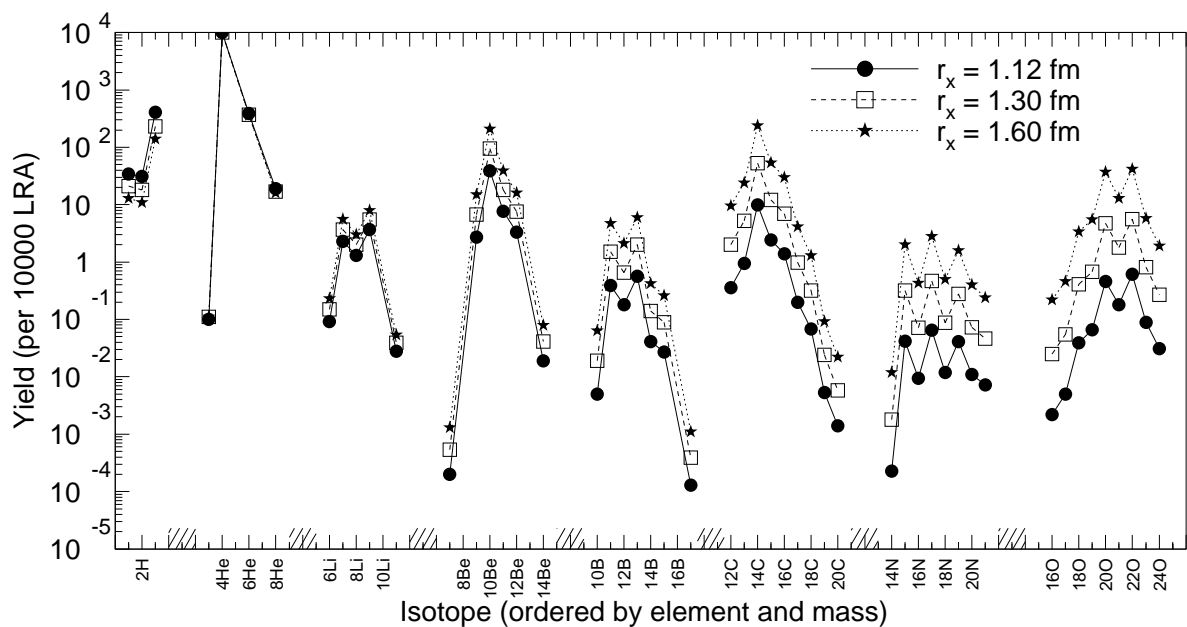


Figure 1.3.4.: Ternary fission yields for $^{241}$Pu($n_{th}$,f), calculated with different interfragment distances in the "Faust formula". $r_x$ is the main radius parameter in the Bass formula: $r_x = 1.12$ in equation (1.3.15). The scale is identical to figure 1.3.2.

When changing the shape of the scission configuration from a compact to an elongated one[15], the yields of the light rare isotopes stay practically constant, while the yields of heavier elements increase considerably. With increasing distance of the fragments, the Coulomb energy term is reduced, affecting less the "energy costs" of the heavy ternary particle production.

---

[15] Here, simply the first radius parameter in the Bass formula has been varied. Other changes of the parameterization towards a more stretched shape lead to qualitatively similar results.

Thus, yield data of both, the light exotic and the heavy ternary particles, is required to determine the two main model parameters: "temperature" and "elongation". Dedicated measurements of the heavy ternary particle yields are mainly performed by the Tübingen group [Bör93, Hes97, Wös99a], while results on light "exotic" nuclei are reported in the following.

## 1.4. LOHENGRIN separator

Coming directly from the scission point, the LCP is expected to carry valuable information on the scission configuration. Therefore yields and energy distributions of various ternary particles had been measured for several thermal neutron induced fissioning systems: $^{233}$U(n,f) [Vor69], $^{235}$U(n,f) [Vor72, Bau92b, Bau92a], $^{239}$Pu(n,f) [Vor75] and $^{241}$Am(2n,f)[16] [Vor75, Bau92a, Bau92b, Gön92b, Bör93]. However, for other fissioning systems only scarce data existed, which made a systematic study of the dependence of yields and energy distributions of ternary particles on the fissility and neutron excess of the compound system difficult.

Very low yields of fission products can be measured with a recoil separator. To date the most sensitive recoil separator for neutron-induced fission products is LOHENGRIN at the high-flux reactor of the Institut Laue Langevin (ILL) in Grenoble. Recently a series of measurements was performed at LOHENGRIN to study the ternary fission of: $^{229}$Th(n,f) [Wös99a], $^{233}$U(n,f) [Wös98], $^{239}$Pu(n,f) [Kös95, Wös99a], $^{241}$Am(2n,f) [Hes97], $^{245}$Cm(n,f) [Hes97] and $^{249}$Cf(n,f) [Dav97].

In the following I will report on new results for ternary particle yields of the systems $^{241}$Pu(n,f) and $^{245}$Cm(n,f), where practically no information was previously available. Moreover I measured new yields of exotic isotopes with an extreme $N/Z$ ratio from $^{233}$U(n,f) and $^{235}$U(n,f).

### 1.4.1. Targets

Since at LOHENGRIN only individual fission fragments are measured without coincidence, the fissioning system has to be clearly defined. Therefore targets with a high isotopic purity are used. In many cases a radiochemical separation is not sufficient, but additionally every target atom has to pass a mass separator before use. This makes the complete chain of the target production process more elaborate and expensive. The access to more "exotic" fissioning systems depends mainly on the availability of appropriate target material. All targets are produced by deposition of the actinide material as oxide within an area of $70 \cdot 5$ mm$^2$ on a platinum-coated[17] titanium backing. Targets from rare material have a smaller area (see below). All except for the "thick" $^{235}$U target (461 $\mu$g/cm$^2$) were covered with a 2500 Å thick nickel foil to reduce loss of target material by sputtering and thus guarantee a smoother "burnup". Delivery problems of Goodfellow, the former supplier of the very thin nickel foils, forced us to produce these foils ourselves. A description is found in appendix A.1. Table 1.4.1 shows a summary of all used targets.

#### $^{241}$Pu

In total four different targets of $^{241}$Pu were used. They were prepared by the IRMM (Institute for Reference Materials and Measurements) of the Joint Research Centre of the European Commission in Geel. A "thin" target with 208 $\mu$g Pu per cm$^2$ thickness was used to determine during a measurement of binary fission [Fri98a] the yield of $^{10}$Be as a reference point for further ternary fission measurements [Kös95]. Another "thin" target (100 $\mu$g/cm$^2$ Pu) was used to exactly measure the energy distribution of the helium isotopes down to 3 MeV. Two "thick" targets with 379 and

---

[16] The expression $^{241}$Am(2n,f) stands for the fissioning compound nucleus $^{243}$Am$^*$. In the high neutron flux both isomers of $^{242}$Am are breeded in-situ from the fertile $^{241}$Am target and fission after capture of a second neutron.

[17] The 400 $\mu$g per cm$^2$ thick Pt layer reduces the diffusion of target material into the Ti backing.

362 $\mu$g Pu per cm$^2$ thickness served for the measurement of ternary fission yields relative to $^{10}$Be. The first three targets in November 1990 had an isotopic composition of 87 % $^{241}$Pu, 1.6 % $^{239}$Pu and 11 % other plutonium isotopes with low fission cross-sections. At the time of the measurements about 20 %, 31 % and 28 % respectively of the $^{241}$Pu had decayed to $^{241}$Am, but as discussed in [Fri98a] during two weeks of measurement[18] the contribution of other fissioning isotopes (e.g. from bred $^{242}$Am(n,f)) will stay below 6 %. The last target was used 9 months after plutonium separation, thus limiting contributions from other fissioning systems to below 2 %.

### $^{245}$**Cm**

Three curium targets were used. The first two with 13.3 and 10.4 $\mu$g of $^{245}$Cm came from the All-Russian Scientific Research Institute of Experimental Physics in Sarov (formerly Arzamas-16) [Ves92]. The curium oxide was deposited on an area of $10 \cdot 4$ mm$^2$ corresponding to a target thickness of 33 and 26 $\mu$g/cm$^2$. Beside $^{245}$Cm (98.8 % of the curium fraction) mainly the non-fissile isotopes $^{244}$Cm and $^{246}$Cm and small traces of the radioactive decay daughters $^{241}$Pu and $^{241}$Am were present. The third target with an amount of 4 $\mu$g of $^{245}$Cm on a 3 mm diameter spot was produced in the nuclear chemistry department of Mainz University from $^{245}$Cm separated at the trans-plutonium element production facilities at Oak Ridge National Laboratory and provided by the U.S. Department of Energy (contract No. W-31-109-ENG-38).

In all three targets the contribution of impurities to the total fission rate can be neglected. Note that while the amount of $^{245}$Cm target material used for these experiments seems to be very small, it constitutes some per mil of the world resources of isotope separated curium!

### $^{233}$**U and** $^{235}$**U**

The uranium targets were also provided by the IRMM in Geel. The $^{233}$U target had a thickness of 380 $\mu$g/cm$^2$. Two $^{235}$U targets with 461 $\mu$g/cm$^2$ and 323 $\mu$g/cm$^2$ thickness were used. The area was always $70 \cdot 5$ mm$^2$. Contaminations with other fissile isotopes are negligible ($\leq$ 0.1 %).

Table 1.4.1.: Overview over all targets used for the measurement of ternary particles.

| Fissile nucleus | Total mass ($\mu$g) | Area (cm$^2$) | Cover | Measured elements |
|---|---|---|---|---|
| $^{233}$U | 1329 | $7 \cdot 0.5$ | 2500 Å Ni | He to F |
| $^{235}$U | 1614 | $7 \cdot 0.5$ | 100 Å Ta | He to O |
| $^{235}$U | 1130 | $7 \cdot 0.5$ | 2500 Å Ni | He to O |
| $^{241}$Pu | 636 | $7 \cdot 0.5$ | 2500 Å Ni | Be |
| $^{241}$Pu | 1157 | $7 \cdot 0.5$ | 2500 Å Ni | He to Si |
| $^{241}$Pu | 1268 | $7 \cdot 0.5$ | 2500 Å Ni | H to Si |
| $^{241}$Pu | 350 | $7 \cdot 0.5$ | 2500 Å Ni | He |
| $^{245}$Cm | 13.3 | $1 \cdot 0.4$ | 2500 Å Ni | He, C |
| $^{245}$Cm | 10.4 | $1 \cdot 0.4$ | 2500 Å Ni | He to O |
| $^{245}$Cm | 4 | 0.07 (round) | 2500 Å Ni | H to F |

---

[18]The second target was not even kept for 48 h in the neutron flux.

### 1.4.2. Separator

The targets are inserted in an evacuated beam tube of the ILL high-flux reactor (58 MW thermal power and $1.5 \cdot 10^{15}$ cm$^2$ s$^{-1}$ maximum unperturbed thermal flux). At the target position, about 50 cm from the reactor core, the thermal neutron flux is about $5.3 \cdot 10^{14}$ cm$^2$ s$^{-1}$. The epithermal neutron flux is more than two orders of magnitude smaller and the fast neutron flux is more than three orders of magnitude smaller. Both contributions can be neglected for our purposes. Recoiling fission products leave the target with a small energy loss and fly as highly charged ions through the beam tube. While binary fragments typically have ionic charges of 20 to 25, light ternary particles are mostly fully stripped. After 8 m the ions enter a horizontally deflecting homogeneous magnetic sector field, separating ions according to the ratio of momentum to ionic charge $p/q$. Subsequently they pass a vertically deflecting cylindrical condenser which provides a separation according to the ratio of kinetic energy to ionic charge $E/q$. Both fields are arranged to the double focusing parabola spectrometer LOHENGRIN [Mol70, Arm76, Mol77], separating ions of the same $A/q$ ratio onto a parabola on which the position is given by the kinetic energy of the ion [Neu62]. For cases where no ultimate energy resolution is needed, but rather a high beam intensity or transmission should be achieved, a second magnet was designed which focuses about 40 cm of the mass parabola to a small area (some cm$^2$), see figure 1.4.1. This so-called RED (Reverse Energy Dispersion) magnet [Fio93] was used for most measurements. Only the measurements with the "thin" plutonium targets and the measurement of the ternary to binary ratio with the curium target were made without RED magnet.
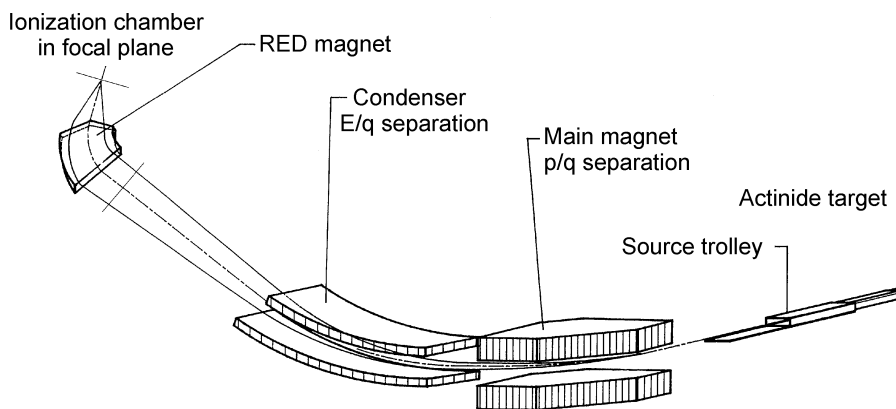


Figure 1.4.1.: Arrangement of the recoil separator LOHENGRIN.

The formulae to calculate the field settings are found in appendix A.2. While the usable range of magnetic fields (up to 0.24 T for the first magnet and 1.6 T maximum for the RED magnet) is sufficient to cover most of the required separator settings, the maximum high voltage of the condenser limits the $E/q$ ratio to about 6.5 MeV, thus excluding the measurement of high kinetic energies at low charge states.

The flight time of the fragments from the target to the detector is below 2 $\mu$s. Therefore decay losses of the studied particles with half-lives larger than milliseconds can be neglected.

### 1.4.3. Particle identification

LOHENGRIN only separates particles according to their $A/q$ and $E/q$ ratios. For an unambiguous determination of the fragment mass it is still necessary to directly measure the kinetic energy of the fragments. With the known settings for $E/q$ and $A/q$ the ionic charge $q$ and finally the mass $A$ can be determined. The kinetic energy is measured with an ionization chamber (IC) placed in

the focus of the separator. Using a split anode for the readout of the energy signal, the nuclear charge $Z$ can additionally be deduced from the specific energy loss in the first section of the ionization chamber, the so-called $\Delta E$ part. The ionization chambers used are described in detail in ref. [Boc88, Hes93]. The counting gas (isobutane) pressure was adapted in the range of 15 to 160 mbar for best $Z$ identification. The gas volume of the IC is separated from the beam tube vacuum by a thin polypropylene window. Due to energy loss and scattering of the fragments in the window, its thickness and homogeneity directly affect the $Z$ resolution of the chamber. Details on preparation and use of these windows are given in appendix A.3.

The signals from the IC are amplified by charge-sensitive preamplifiers (Ortec 142) and main amplifiers (Ortec 571). After summation of both signals to obtain the total energy they are saved both in list-mode and in a histogram of 1024 times 1024 channels.

In all cases the $Z$-resolution of the ionization chamber is by far sufficient for a clear identification of the ternary particles. The significant divergence of the ion beam behind the RED magnet (half opening angle $\Phi$ up to about $17°$ [Fio93]) causes an additional uncertainty in the $\Delta E$ signal of:

$$\frac{\delta(\Delta E)}{\Delta E} \approx \left( \frac{1}{\cos\phi} - 1 \right) \approx 5\ \% \tag{1.4.1}$$

This does not affect the clear identification of ternary particles, but has to be taken into account for accurate $Z$ identification in binary fission. A correction can be applied by reconstructing the angle of the ion path from the delay between $\Delta E$ and $E_{\text{res}}$ signals resulting from the drift time difference of the electron cloud [Hes97].

### 1.4.4.   Calibrations

**Magnet calibration**

During the measurement the magnetic fields are controlled with NMR probes and stabilized to some $10^{-5}$. However, the NMR probe measures the field only locally, whereas the particles are deflected according to the integrated field along their flight path. Hysteresis and remanence effects may change the calibration of the magnet. The optimum magnetic field settings are found by scanning the beam horizontally over the detector placed in the focus, while keeping the electrical field fixed. The so determined magnet constants, called $\chi$ (for the first magnet) and $\kappa$ (the ratio of fields of RED to first magnet), stayed constant within a range $\leq 2 \cdot 10^{-4}$ during the measurement periods of about 2 weeks.

**Energy calibration**

The absolute energy calibration of the separator can be checked with direct (n,X)-reactions producing monoenergetic particles. The electric and magnetic fields are scanned simultaneously to find the high energy edge of the energy distribution, which typically has a low energy tail due to energy loss in the target and scattered particles (see figure 1.4.2).

Three reactions were used:

1. $^6$Li(n,$\alpha$)t giving tritons with 2.73 MeV kinetic energy and alphas with 2.05 MeV. These calibrations are done "off-line" by introducing a thin $^6$Li target at the target position [Fau82].

2. $^{59}$Ni(n,$\alpha$) giving alphas with 4.78 MeV kinetic energy. The unstable $^{59}$Ni is produced "on-line" by neutron capture on $^{58}$Ni present in the nickel foil which is used to cover the target.

3. Decay alphas of $^{242}$Cm with up to 6.11 MeV energy. The $^{242}$Cm is produced in $^{241}$Pu targets by beta-decay to $^{241}$Am which is subsequently transmuted to $^{242}$Am by neutron
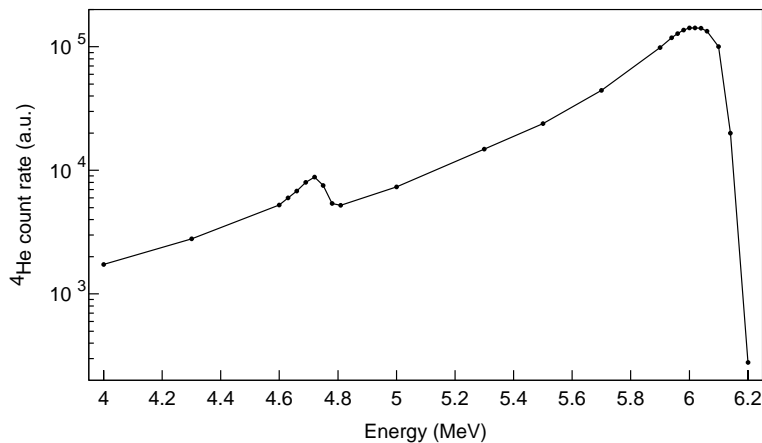
Figure 1.4.2.: Energy spectrum of $^4$He used for on-line energy calibration. The peak around 6.1 MeV is due to decay alphas from $^{242}$Cm and the peak at 4.78 MeV comes from $^{59}$Ni(n,$\alpha$). Depicted is a raw spectrum without correction for energy loss in the target and cover foil. Here and in all following figures the abbreviation "a.u." stands for arbitrary units.

capture and then decays to $^{242}$Cm. Also in the $^{245}$Cm targets enough $^{241}$Am was present to get a significant signal from $^{242}$Cm alphas after some days. This reaction is also used "on-line" without target change.

**Calibration of the ionization chamber**

The energy and nuclear charge calibration of the ionization chamber was done with reference spectra using separator settings $A/q = 3$. Here, the most abundant ternary particles ($^3$H, $^6$He, etc.) and scattered stable isotopes (e.g. $^{12}$C, $^{24}$Mg, $^{27}$Al) are easy to identify and make the calibration obvious (see figure 1.4.3).

The horizontal scale is proportional to the particle energy (and due to a fixed $A/E$ ratio also to the mass), whereas the vertical scale is roughly proportional to the nuclear charge $Z$. The spots with the same mass and higher $Z$ are slightly shifted to the left due to higher energy loss in the entrance window of the IC. The events on the diagonal are particles which are stopped in the $\Delta E$-part (therefore $\Delta E = E_{\text{total}}$). Scattered binary particles create background close to the diagonal in the upper part of the spectrum. Background in the lower part is due to pile-up (from abundant $^3$H and $^6$He) and particles scattered in the entrance window of the ionization chamber (tails going to the top and left which can be seen at $^6$He, $^9$Li and $^{12}$C). One channel approximately corresponds to 75 keV.

## 1.4.5.   Data evaluation

**Background**

Instabilities of the high voltage or sparks in the condenser can cause background in the $\Delta E$-$E$ scatter plots. Scattered binary particles especially occur with separator settings close to typical values for binary particles ($A/q = 4$ to 5, $E/A$ around 1 MeV).

High background from natural alpha decay and (n,$\alpha$) reactions is present for $^4$He below 6.1 MeV. Also for $^3$H below 2.7 MeV significant background arises from $^6$Li(n,$\alpha$) reactions. This $^6$Li is sputtered off of calibration targets (see above) and sticks to the target holder or the beam tube. For these cases only the data points with higher kinetic energy are evaluated.
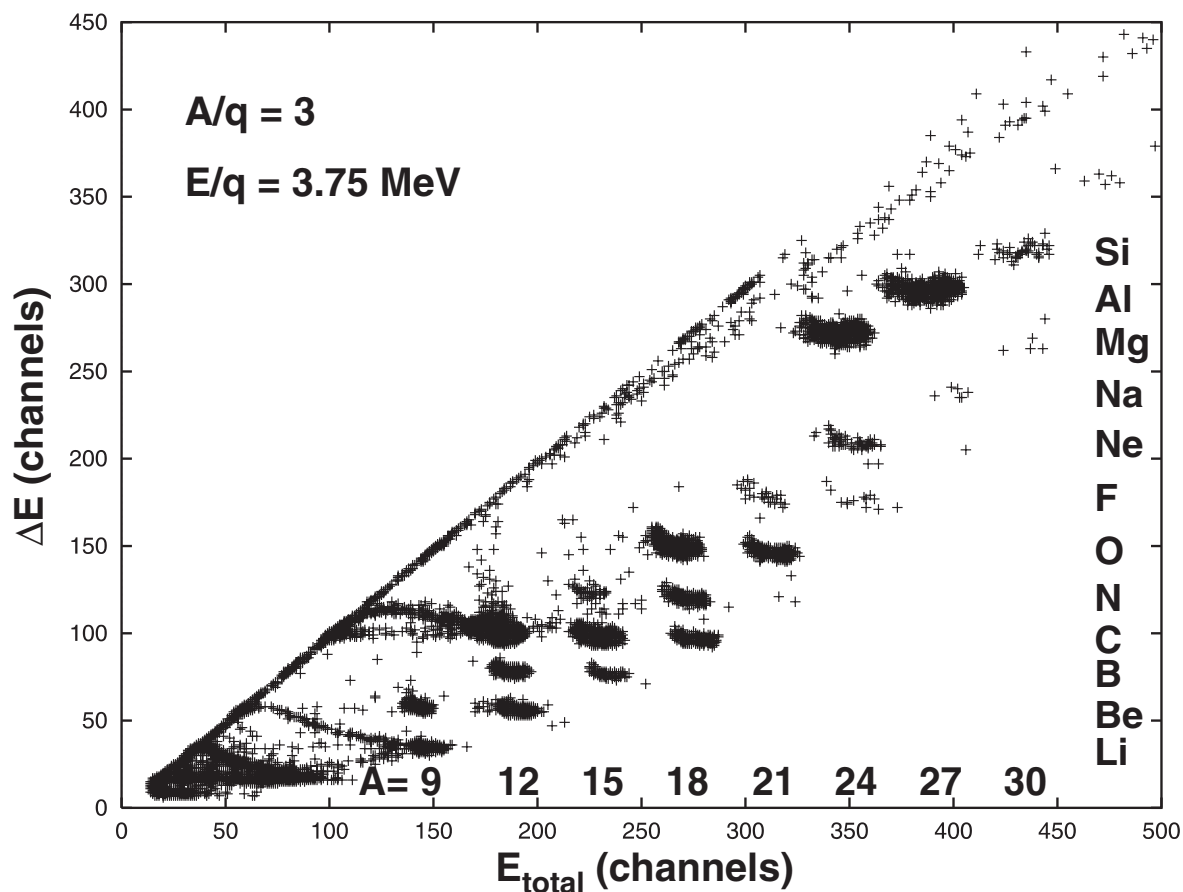
Figure 1.4.3.: $\Delta E$-$E$-scatter plot with separator setting $A/q = 3$ and $E/q = 3.75$ MeV. The measurement time for this spectrum was 6.1 h.

Some stable particles ($^{12}$C, $^{14}$N, $^{16}$O, etc.) occur very abundantly. They are knocked out of the target and its cover by fission fragments, from the residual gas in the vacuum chamber or from diaphragms in the separator. Their abundance rapidly drops towards higher kinetic energies. However, if the contribution of such background gets too high, the events stemming from fission cannot be identified and no fission yield can be determined for these stable isotopes.

Typically the background conditions are more favorable for isotopes with high neutron excess than for proton-rich isotopes. This partly explains the great differences in measured upper limits for rare ternary isotopes on the neutron-rich and the neutron-deficient side.

**Separator acceptance**

The energy dispersion coefficient[19] of the separator is 7.2 m, i.e. a 1 % large slice of the energy distribution is spread out over 7.2 cm of the mass parabola. The accepted energy range is therefore proportional to the chosen energy. To correct this effect, all count rates are divided by the set energy for normalization.

In mass direction (i.e. perpendicular to the mass parabola) the dispersion coefficient[20] is 3.24 m. Due to the different mass defects, the difference between ionic mass and atomic mass depending

---

[19]Particles with a kinetic energy $E_0 + \Delta E$ are separated in the plane of dispersion by a distance $\Delta x$ from the reference particles with energy $E_0$. For small deviations ($\Delta E \ll E_0$) the linear relation with the energy dispersion coefficient $D_E$ applies: $\Delta x = D_E \frac{\Delta E}{E_0}$.

[20]In analogy to the energy dispersion, the mass dispersion coefficient $D_m$ is defined as: $\Delta x = D_m \frac{\Delta m}{m}$.

on the charge state, and due to relativistic corrections, not all isotopes with the same $A/q$ ratio lie exactly on the mass parabola. The actual transmission is a complicated function, which could be calculated by folding the size of the target with the transmission through intermediate diaphragms and vacuum chambers, the edge focusing by the RED magnet and the acceptance of the circular entrance window of the ionization chamber. It can also be experimentally deduced from the scan curve of the main magnetic field (see figure 1.4.4). The FWHM is typically 0.2 to 0.3 % of the magnetic field. For small deviations from the ideal field the yield of a given isotope is corrected for the transmission. In case of larger deviations (e.g. for the light particles $^3$H, $^6$He, etc. in a spectrum with $A/q = 3$) two spectra with different magnetic field settings have to be taken. The scan curve of the RED magnet is much broader (FWHM some %), therefore no correction is necessary.
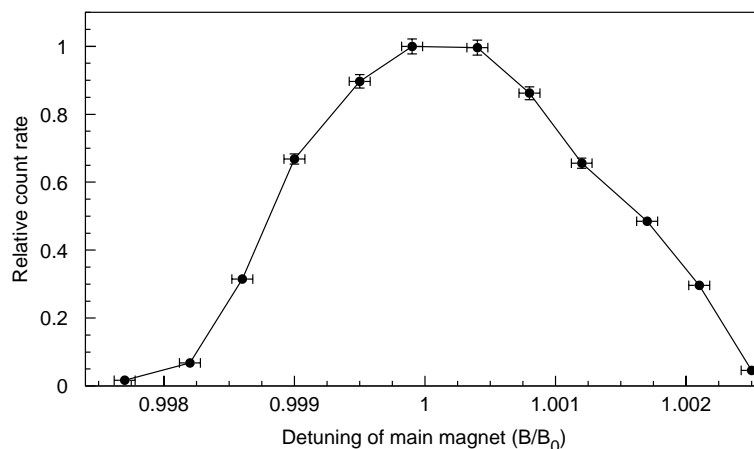


Figure 1.4.4.: Measured transmission in dependence of a detuning of the main magnetic field.

**Target burnup**

The fission rate of the target decreases with time. This is mainly due to the nuclear burnup in the high neutron flux. Additional losses of target material occur from sputtering by fission fragments, evaporation from the heated target, and diffusion and sputtering into the target backing. The slight reduction of the neutron flux (about 3 % during one reactor cycle of 52 days) can be neglected. The decrease of the fission rate is monitored with a reference spectrum taken once to twice a day and can be described with an exponential decay curve.

It should be noted that plutonium targets can show a less regular burnup characteristic than other actinide targets. This might be due to a rapid migration into the target backing or sideways out of the target area (see also [Fri98a]). The former explanation is supported by differing burnup times for heavier and lighter isotopes and a broadening of the "natural" width of the energy distribution. These effects are difficult to quantify, but contribute to the systematic errors. For very precise measurements plutonium targets cannot be "completely" used, but should be changed after some days.

The uranium targets showed a regular burnup and the curium targets were thin enough that such problems did not occur.

**Energy loss**

To deduce the original kinetic energy distribution of the fission fragments from the measured one, the energy loss in the target and in the cover foil has to be taken into account. The energy loss for

all measured isotopes and kinetic energies was calculated with the Monte-Carlo program TRIM[21] [Bie80]. Note that the energy loss in the entrance window of the ionization chamber occurs after the mass separation and therefore does not have to be considered here.

**Ionic charge distribution**

Due to the limitations of the separator fields and the available beam time it is not possible to measure the yields of a given isotope at all possible ionic charge states. Therefore a model has to be applied to inter- and extrapolate the ionic charge state fractions to other energies and isotopes. Several empiric formulae are available to predict the mean ionic charge states and the width of the charge state distribution, thus allowing the calculation of the equilibrium charge state distributions (ECSDs) [Nor63, Hec63, Bet66, Nik68, To79, BR81, BR82, Shi82, Shi92]. However, the ECSDs used for these formulae were measured under well defined experimental conditions, mostly by transmitting low charged ions from tandem accelerators through free-standing foils made from pure materials. On the other hand at LOHENGRIN the charge state before passing the foil is not well known. Moreover the target cover foils are quite fragile (0.25 $\mu$m of nickel) and coated with a protective film of acrylic or polystyrene for better handling. The nuclear heating in the reactor brings the target to above 600° C and the coating evaporates. Some atomic layers of e.g. carbon may be still left and then influence the ECSDs. Therefore the constants of such formulae have to be determined for each target by measuring in-situ the ECSDs of appropriate isotopes ($^{10}$Be, $^{14}$C, $^{20}$O).

None of the investigated formulae was able to reproduce the ECSDs of all elements with a given set of constants or with one single fit parameter. For better comparison with other LOHENGRIN measurements we finally used a modified reduced chi-square distribution with a parameterization in analogy to the data evaluation of [Bau92b, Bör93, Hes97, Wös98].

The mean charge is calculated as:

$$\bar{q} = \left( Z + \frac{1}{Z^2} \right) \cdot \left( 1 - \exp\left( -2.7284 \cdot v_{\text{ion}} \cdot \left( Z + \frac{1}{Z^2} \right)^{\frac{0.5}{\lambda} - 0.48} \right) \right), \qquad (1.4.2)$$

and the width of the charge state distribution is:

$$\sigma_q = \left( 0.426 - \mu \cdot v_{\text{ion}} \cdot \left( Z + \frac{1}{Z} \right)^{-0.475} \right) \cdot \left( Z + \frac{1}{Z} \right)^{0.447 - \frac{1}{\lambda^2}}, \qquad (1.4.3)$$

with two fit parameters $\lambda$ and $\mu$ depending on the element and target. $v_{\text{ion}}$ is given in units of cm/ns. This expression for $\bar{q}$ is, with exception of the small modifications by $\lambda$ and $1/Z$, identical to that of [To79]. $\sigma_q$ is similar to formula (6) in [BR81].

The fraction of an individual charge state can be calculated with a "reduced chi-square distribution" [BR81], modified by a factor $\exp(-a)$:

$$F(q) = \frac{c \cdot t(q)^{\frac{n}{2} - 1}}{2^{\frac{n}{2}} \cdot \Gamma(\frac{n}{2}) \cdot \exp(\frac{t(q)}{2})} \cdot \exp(-a). \qquad (1.4.4)$$

---

[21]Since TRIM does not contain trans-uranium elements as target, the calculation was performed for uranium oxide in all cases and scaled. The resulting uncertainty is negligible.

with $\Gamma$ being the gamma function and the constants:

$$
\begin{aligned}
c &= \frac{2 \cdot (Z - \bar{q} + 2)}{\sigma_q^2}, \\
t(q) &= c \cdot (Z - q + 2), \\
n &= c \cdot (Z - \bar{q} + 2), \\
a &= \left( \frac{v_{Z-q+1}}{v_{ion}} \right)^{\sqrt{1 + \frac{Z}{\lambda}}},
\end{aligned}
$$

where $\exp(-a)$ gives the stripping probability for the $(Z\text{-}q\text{+}1)$th electron. Its orbital velocity in the Bohr model $v_{Z-q+1}$ is calculated from the $q$th ionization energy given in ref. [HB].

The parameters $\lambda$ and $\mu$ have to be adapted for each element. It appears, that $\lambda$ differs strongly between some targets. This could be explained by different evaporation residues on the target cover foil. In the earlier measurements the nickel foil was covered by an acetate film (Ni foils from Goodfellow), in later ones by a polystyrene film (homemade Ni foils). On the other hand $\mu$ showed only a weak variation (ranging from 0.02 to 0.025 at maximum). It is possible to fit the constants by using the measured charge state fractions of different isotopes of one element up to about oxygen. Figure 1.4.5 shows one of the fitted ECSDs for $^{14}$C. For these light elements the ECSDs formula is mainly used for interpolation of the measured charge state fractions and simplifies a transfer of these ratios to other isotopes of the same element. The systematic errors are therefore acceptable. However, for lack of experimental data[22] the trends of the charge state distribution have to be extrapolated towards heavier elements. Here, it has to be assumed, as in [Hes97], that, compared with the big differences for light elements, the variation of the fit constants from element to element continue to decrease and the "constants" can be kept constant. The uncertainty of this extrapolation causes the main part of the systematic errors. The only target covered with a Ta layer was used to measure exotic isotopes of light elements (Li, Be). Here, the charge ratios can directly be measured with more abundant isotopes of the same element, and the ionic charge correction does not introduce a systematic error.
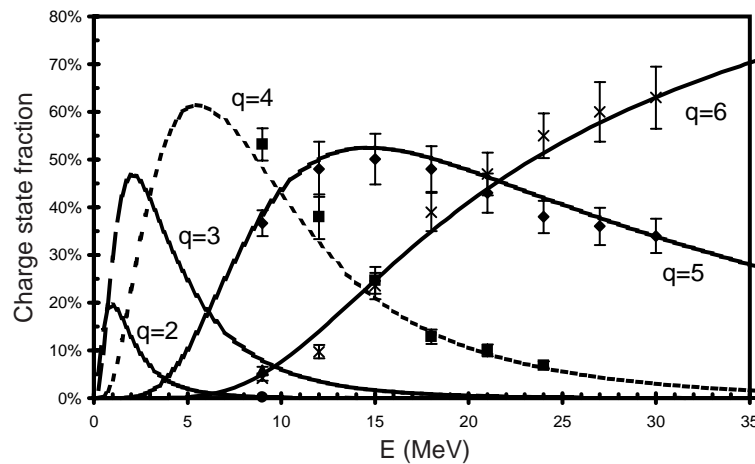


Figure 1.4.5.: Measured charge state fractions and fitted charge state distribution for $^{14}$C.

---

[22]It is in principle possible to also measure the ECSDs of elements like Mg, Si, etc. in a dedicated experiment at LOHENGRIN. Instead of ternary particles, stable isotopes of these elements would be used which are knocked out from an additional layer containing the elements in question between the actinide and the cover foil by collisions with binary fragments. In this way the constants could be determined more precisely even for heavier elements, reducing the systematic errors significantly.

Note that a model with a differing energy dependence of the charge state corrections will slightly influence the average and the width of the deduced kinetic energy distributions. In the data evaluation by Vorobyov et al. [Vor69, Vor72, Vor75] and Bouzid [Bou94] the values tabulated by Northcliffe [Nor63] were used, while Davi [Dav97] used a Gaussian distribution for the correction. In the measurement of Baum [Bau92b] a tantalum layer was sputtered onto the target and no nickel foil was used. He found a better description of the charge state distribution by suppressing the factor $\exp(-a)$ in formula (1.4.4) ("capture model" instead of "stripping model").

**Kinetic energy distribution**

The total yield of an isotope is determined by integration over its yield at different kinetic energies. In cases where, due to limitations in electric field or beam time, not enough different energies could be measured to determine the energy distribution, the mean energy and/or the width of the energy distribution have to be fixed for the fitting.

For $^4$He the mean energy and width reported in literature was used: from [Wag86] for $^{241}$Pu(n,f) and from [Wag91b] for the uranium isotopes. Note that a different energy distribution for LRA from $^{241}$Pu(n,f) had been reported in [Sol69]: $E_{mean}$=15.0(6) MeV. Only one measurement of the $^4$He energy distribution in $^{245}$Cm(n,f) is reported in literature [Koz88]. The 16.8 MeV average energy differs significantly from the reported energies of all other fissioning systems [Wag91b]. The experimental spectrum in [Koz88] showed at lower energies a significant enhancement over a Gaussian distribution, but the influence of systematic effects was not discussed. Since at LOHENGRIN only the low energy flank ($\lesssim$ 13 MeV) can be measured, an uncertainty of about 1 MeV in the average kinetic energy translates to a systematic error of about 20 % for the yield of $^4$He.

For $^3$H from $^{241}$Pu(n,f) the mean energy came from ref. [Wag86], while the width was kept as a free fit parameter. Also for $^2$H from $^{241}$Pu(n,f) the mean energy of $^3$H was used, which is justifiable regarding the systematics of other fissioning systems [Wag91b]. For $^{245}$Cm(n,f) no measurements were available for the kinetic energy parameters of $^3$H. Thus, the identical parameters to $^{241}$Pu(n,f) were used. For $^3$H from $^{235}$U(n,f) the mean energy was taken from [Vor72].

For the rare isotopes an extrapolation is used which is consistent with the systematics in other fissioning systems and the results of trajectory calculations for the fissioning systems $^{235}$U(n,f) and $^{242}$Am(n,f) [Bau92a, Bou94]. In all cases where the energy parameters were fixed for the fit, an additional systematic error was added to account for the uncertainties of these values.

Nearly all energy distributions are well reproduced by a Gaussian. An exception is $^4$He. It is well known that the low energy part of the $^4$He spectrum shows an enhancement over a symmetrical Gaussian distribution [Caï80]. This is due to contributions from the breakup residues of the particle unstable isotope $^5$He [Mut99] and possibly also $^8$Be [Mut96a]. Therefore only the data points with energies above 10 MeV were used for the integration of the yield.

A double humped structure observed in the energy distribution of $^8$He from $^{241}$Pu(n,f) [Kös98c] was probably a transmission artifact of the RED magnet. It was neither reproduced in a measurement without RED magnet nor with the RED magnet after removing a support brace in the middle of its vacuum chamber.

The measured kinetic energy distributions of prominent ternary particles are shown in appendix A.4.

## 1.5.    Results

### 1.5.1.    Yields from $^{241}$Pu(n$_{th}$,f)

Figure 1.5.1 shows an overview of the isotopes measured in $^{241}$Pu(n$_{th}$,f). The detailed data is given in tables 1.5.1 and 1.5.2. $E_{mean}$ and $E_{FWHM}$ are obtained by fitting a Gaussian distribution to the data points. Cases where these values were taken from systematics are marked by the label *"fix"* in the row of the corresponding uncertainty. For better comparison with other fissioning systems the yields are normalized to a standard of 10000 for $^4$He. Note that the reference point itself has a rather large error since the yield of $^4$He can only be determined from a small energy range (10 to 13 MeV). An additional systematic error (difficult to estimate and not included in table 1.5.1) could occur if the energy distribution showed a non-Gaussian behavior in the fit range. The given errors are the individual errors for each isotope and do not include the error of the reference point.
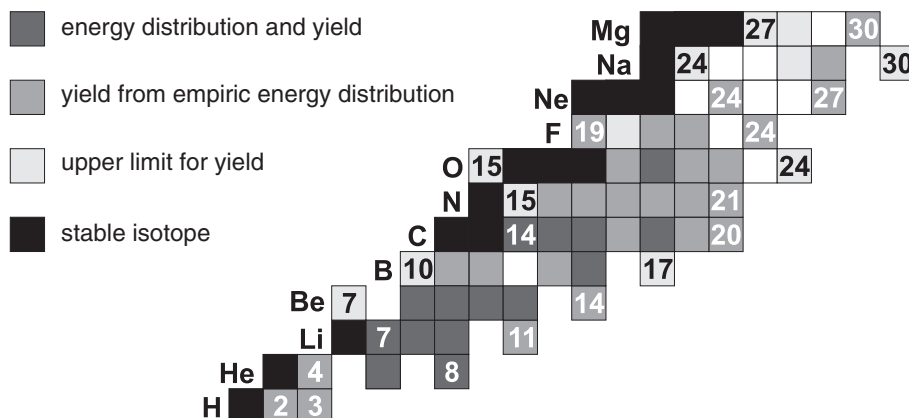


Figure 1.5.1.: Overview of the ternary particles measured with the $^{241}$Pu targets. They are arranged in form of a chart of nuclides. The numbers mark the mass of the lightest and heaviest measured isotope of each element. Black squares show stable nuclides where the background from scattered nuclei exceeds a possible contribution from ternary fission.

Figures 1.5.2 and 1.5.3 show that isotopes with large neutron excess can, despite their extremely low yield, be clearly and unambiguously identified in the $\Delta$E-E-scatter plot. Thus, from $^{241}$Pu(n$_{th}$,f) also the neutron-rich nuclides $^{11}$Li, $^{14}$Be and $^{19}$C could be identified with absolute yields of $8.4(28) \cdot 10^{-10}$, $5.0(19) \cdot 10^{-10}$ and $4.7(26) \cdot 10^{-10}$ per fission respectively.

### 1.5.2.    Yields from $^{245}$Cm(n$_{th}$,f)

The measurement of $^{245}$Cm(n$_{th}$,f) was performed in collaboration with the group from Tübingen University. We concentrated on a systematic study of the ternary particle yields up to oxygen and they studied especially the yields of heavier isotopes.

Figure 1.5.4 shows an overview of the isotopes measured by us. The detailed data is given in tables 1.5.3 and 1.5.4. Again $E_{mean}$ and $E_{FWHM}$ are obtained by fitting a Gaussian distribution to the data points. For the fluorine isotopes the energy parameters were taken identical to the ones used in [Hes97]. For the other elements our measured values were extrapolated to those nuclides for which no complete energy distribution could be taken. These energies are slightly lower than the ones used in [Hes97]. Within the error bars the yields of most isotopes measured by both groups are consistent and the remaining differences can be explained by the varying energy parameters

Table 1.5.1.: Measured yields and energy parameters for hydrogen to carbon isotopes from
           $^{241}Pu(n_{th},f)$. The label *"u.l."* marks an upper limit for isotopes where no or too
           few events were found to determine a reliable yield. See section 1.6.1 for a discussion
           of the last column ($E_{bin}$).

| Isotope | $E_{mean}$ (MeV) | $\sigma(E_{mean})$ (MeV) | $E_{FWHM}$ (MeV) | $\sigma(E_{FWHM})$ (MeV) | Yield | $\sigma$(Yield) | $E_{bin}$ (MeV) |
|---------|------------------|--------------------------|------------------|--------------------------|-------|-----------------|-----------------|
| 2H  | 8.4  | *fix* | 7.4  | 0.4   | 42     | 4      | -    |
| 3H  | 8.4  | *fix* | 7.2  | 0.4   | 786    | 42     | -    |
| 4He | 15.9 | *fix* | 10.7 | 0.5   | 10000  | 700    | 11.1 |
| 6He | 11.3 | 0.2   | 10.3 | 0.5   | 260    | 30     | 1    |
| 8He | 8.7  | 0.2   | 9.6  | 0.5   | 15     | 1      | -    |
| 7Li  | 14.7 | 0.5   | 11.6 | 1.2   | 6.7    | 0.6    | 3.7  |
| 8Li  | 15.7 | 1.1   | 13.9 | 2.2   | 4.2    | 0.6    | -    |
| 9Li  | 12.6 | 0.6   | 14.6 | 1.0   | 8.3    | 0.8    | -    |
| 11Li | 11   | *fix* | 12.9 | *fix* | 0.0045 | 0.0015 | -    |
| 7Be  | 20   | *fix* | 15.3 | *fix* | 0.2    | *u.l.* | 1    |
| 9Be  | 17.9 | 0.6   | 15.2 | 1.6   | 4.4    | 0.5    | 10.5 |
| 10Be | 18   | 0.7   | 18.8 | 2.9   | 46     | 6      | 12.4 |
| 11Be | 17.5 | 0.7   | 14.1 | 2.4   | 5.9    | 1.7    | 6.7  |
| 12Be | 14.3 | 0.8   | 15.7 | 2.2   | 2.8    | 0.3    | 4.8  |
| 14Be | 13   | *fix* | 15.3 | *fix* | 0.0027 | 0.0010 | -    |
| 10B | 22   | *fix* | 21.2 | *fix* | 0.03   | *u.l.* | 9.4  |
| 11B | 21   | *fix* | 20   | *fix* | 1.6    | 1.0    | 15.7 |
| 12B | 20   | *fix* | 18.8 | *fix* | 1.0    | 0.4    | 13.4 |
| 14B | 19   | *fix* | 17.6 | *fix* | 0.13   | 0.04   | 8    |
| 15B | 17.7 | 0.6   | 15.2 | 1.2   | 0.046  | 0.010  | 5.8  |
| 17B | 16   | *fix* | 15.3 | *fix* | 0.001  | *u.l.* | -    |
| 14C | 20.8 | 0.6   | 25.4 | 2.2   | 12.6   | 0.8    | 27.4 |
| 15C | 18.6 | 1.3   | 27.1 | 3.1   | 4.3    | 0.4    | 22.5 |
| 16C | 16.6 | 2.7   | 30   | 7     | 5.0    | 0.9    | 22.1 |
| 17C | 18   | *fix* | 23.5 | *fix* | 0.64   | 0.15   | 16.7 |
| 18C | 17.7 | 1.7   | 17.9 | 2.2   | 0.28   | 0.05   | 16   |
| 19C | 17   | *fix* | 20   | *fix* | 0.0025 | 0.0014 | 10.1 |
| 20C | 16   | *fix* | 18.8 | *fix* | 0.0036 | 0.0028 | 8.4  |

used in the evaluation. All isotopes where the energy parameters were taken from systematics are marked by the label *"fix"* in the row of the corresponding uncertainty.

Note that even for some stable isotopes a yield could be evaluated. In contrary to [Bau92b] where a correction for contributions of scattered stable particles had been applied, here only the high energy part ($> 25$ MeV) was evaluated. From the upper limit of the most abundant stable isotopes ($^{12}$C, $^{14}$N and $^{16}$O) the maximum contribution of scattered events to the evaluated isotopes ($^{13}$C, $^{15}$N and $^{18}$O) can be calculated with the ratio of natural isotopic abundances. In all cases this contribution is much smaller than the measured values and one can conclude that the observed events are indeed from ternary fission. $^{19}$F showed a large background which was clearly due to scattered stable fluorine, probably from $CF_4$ which had diffused into the beam tube (see appendix A.3).

To calculate the elemental yield of hydrogen and the total ternary yield, the sum of proton and deuteron yield was estimated to 2.0(5) % of the LRA yield. This is in agreement with the system-

Table 1.5.2.: Measured yields and energy parameters for nitrogen to silicon isotopes in $^{241}$Pu($n_{th}$,f). The label *"u.l."* marks an upper limit for isotopes where no or too few events were found to determine a reliable yield.

| Isotope | $E_{mean}$ (MeV) | $\sigma(E_{mean})$ (MeV) | $E_{FWHM}$ (MeV) | $\sigma(E_{FWHM})$ (MeV) | Yield | $\sigma$(Yield) | $E_{bin}$ (MeV) |
|---|---|---|---|---|---|---|---|
| 15N | 22 | *fix* | 21.2 | 3.5 | 0.044 | *u.l.* | 29.3 |
| 16N | 21 | *fix* | 23.5 | *fix* | 0.079 | 0.032 | 26.2 |
| 17N | 20 | *fix* | 23.5 | *fix* | 0.34 | 0.10 | 27.3 |
| 18N | 19 | *fix* | 21.9 | 2.3 | 0.16 | 0.04 | 24.3 |
| 19N | 18 | *fix* | 21.2 | *fix* | 0.26 | 0.08 | 24.7 |
| 20N | 17.5 | *fix* | 20.6 | *fix* | 0.0029 | 0.0016 | 21 |
| 21N | 17 | *fix* | 20 | *fix* | 0.0025 | 0.0014 | 20.6 |
| 15O | 24 | *fix* | 23.5 | *fix* | 0.12 | *u.l.* | 23.6 |
| 19O | 23 | *fix* | 23.5 | *fix* | 0.26 | 0.12 | 34.5 |
| 20O | 22.1 | 0.9 | 21.7 | 2.4 | 1.10 | 0.12 | 37.5 |
| 21O | 21 | *fix* | 19.9 | 4.1 | 0.23 | 0.06 | 35.1 |
| 22O | 20 | *fix* | 18.8 | *fix* | 0.12 | 0.04 | 37.4 |
| 24O | 18 | *fix* | 21.2 | *fix* | 0.08 | *u.l.* | 33.2 |
| 19F | 26 | *fix* | 25.9 | *fix* | 0.020 | 0.016 | 35.9 |
| 20F | 25 | *fix* | 27 | *fix* | 0.002 | *u.l.* | 36.9 |
| 21F | 23 | *fix* | 22.6 | 8.8 | 0.021 | 0.006 | 40.3 |
| 22F | 23 | *fix* | 27 | *fix* | 0.30 | 0.21 | 40 |
| 24F | 21 | *fix* | 26.2 | 3.8 | 0.030 | 0.016 | 40.9 |
| 24Ne | 25 | *fix* | 23.5 | 3.2 | 0.040 | 0.012 | 52.8 |
| 27Ne | 24 | *fix* | 25.9 | *fix* | 0.008 | *u.l.* | 48.4 |
| 24Na | 28 | *fix* | 28.2 | *fix* | 0.001 | *u.l.* | |
| 27Na | 26 | *fix* | 28.2 | *fix* | 0.005 | *u.l.* | 57.7 |
| 28Na | 26 | *fix* | 28.2 | *fix* | 0.006 | 0.004 | 55.9 |
| 30Na | 24 | *fix* | 28.2 | *fix* | 0.0008 | *u.l.* | 53.1 |
| 27Mg | 30 | *fix* | 30.6 | *fix* | 0.0012 | *u.l.* | |
| 28Mg | 30 | *fix* | 30.6 | *fix* | 0.018 | *u.l.* | 67.4 |
| 30Mg | 28 | *fix* | 30.6 | *fix* | 0.009 | 0.006 | 67.9 |
| 30Al | 32 | *fix* | 33 | *fix* | 0.002 | *u.l.* | |
| 34Si | 36 | *fix* | 35.3 | *fix* | 0.001 | *u.l.* | 58.3 |
| 35Si | 35 | *fix* | 35.3 | *fix* | 0.003 | *u.l.* | 78.4 |
| 36Si | 33 | *fix* | 35.3 | *fix* | 0.004 | *u.l.* | 80.4 |

atics from other fissioning systems, see appendix A.5. For the calculation of the summated mass and elemental yields the missing values ($^{16}$N, $^{21}$F and $^{22}$F) were taken from [Hes97]. The complete set of values evaluated in [Hes97] can be found in appendix A.5.

Again the yields are normalized to a standard of 10000 for $^4$He. Due to the uncertainty in the mean energy of $^4$He (see 1.4.5), the yield was evaluated under two different assumptions for the mean energy: once with the average value of all fissioning systems reported in [Wag91b] and once with the value reported in [Koz88]. Both results are given in table 1.5.3.

For the ternary to binary ratio in $^{245}$Cm($n_{th}$,f) only one measurement had been published: $2.00(45) \cdot 10^{-3}$ [Koz88]. Thus, after having finished the measurement of ternary particle yields with the second curium target, we removed the RED magnet and continued to measure a binary reference mass at the straight beam position. For mass 90 an integrated mass yield of $4.5(5) \cdot 10^4$ in the
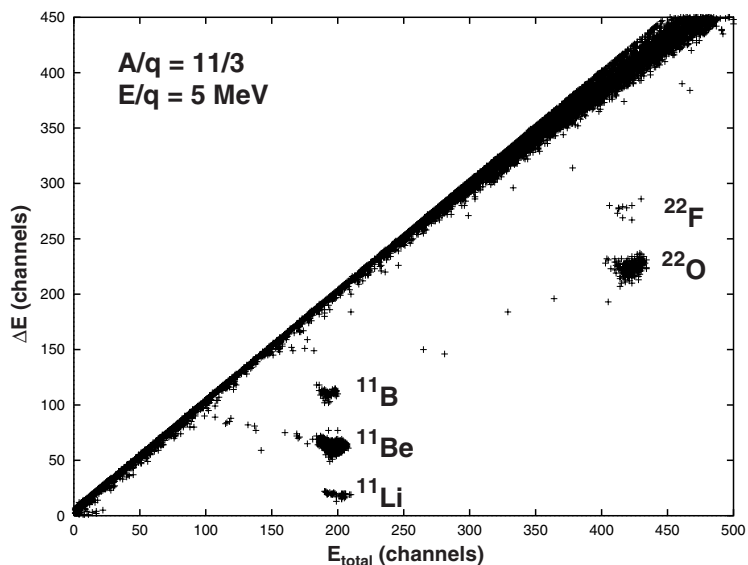
Figure 1.5.2.: $\Delta$E-E-scatter plot with separator settings $A/q = 11/3$ and $E/q = 5$ MeV. The measurement time was 18.5 h.
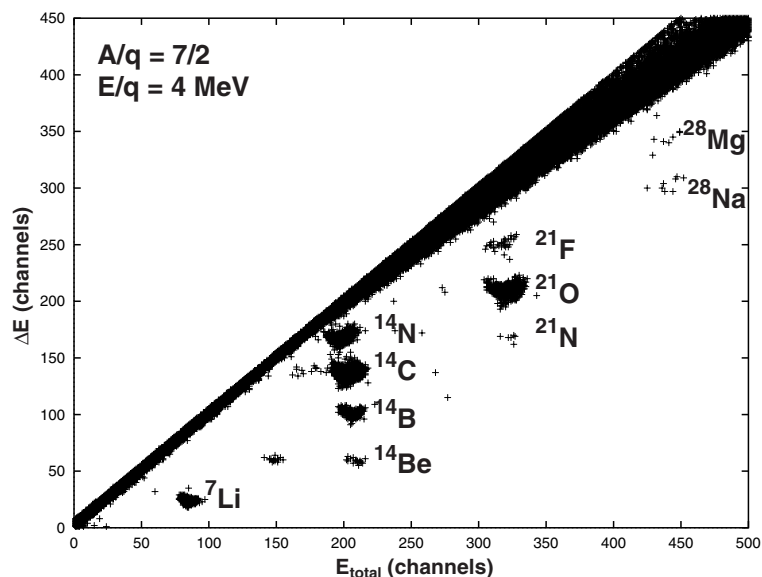


Figure 1.5.3.: $\Delta$E-E-scatter plot with separator settings $A/q = 7/2$ and $E/q = 4$ MeV. The measurement time was 19.5 h.

normalization used in tables 1.5.3 and 1.5.4 (i.e. per $10^4$ $^4$He) was obtained. The mean ionic charge at $E = 104.6$ MeV was $\bar{q} = 20.8(1)$ and the width of the charge distribution $q_{\text{FWHM}} = 5.0(2)$. These values are in good agreement with the ones obtained in [Fri98b]. Also the mean kinetic energy at ionic charge 21 is in good agreement ($E_{\text{mean}} \approx 103.5$ MeV in [Fri98b]). Only the width of the energy distribution ($E_{\text{FWHM}} \approx 15$ MeV in [Fri98b]) was broadened, probably due to migration of curium into the backing[23].

For the binary yield of mass 90 different values had been reported [Gun67, Dic81, Koz88, Fri98b]. They are shown in table 1.5.5. The derived binary to ternary ratio fluctuates depending on the chosen reference value. Note that an additional systematic error due to the unknown kinetic energy

---

[23]Between both measurements the target was removed for a while from the high-flux position. It cooled down and was heated again. This could provoke changes of the target layer.
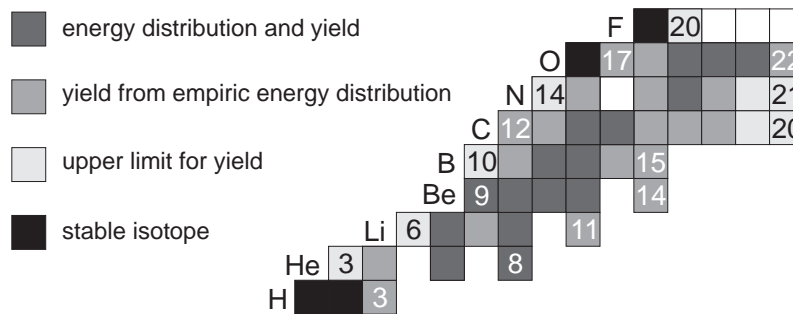
Figure 1.5.4.: Overview of the ternary particles which were measured with the $^{245}$Cm targets. The numbers mark the mass of the lightest and heaviest measured isotope of each element.

distribution of $^4$He should be added. The two reference values with the smallest errors are mutually inconsistent. Due to unknown contributions of systematic errors an unweighted average has been used. It is obvious that LOHENGRIN measurements are not ideal to derive the kinetic energy distribution of $^4$He and the ternary to binary ratio. These measurements are better performed with solid state detectors at an external neutron beam (compare e.g. the set-up of ref. [Wag86]).

### 1.5.3. Yields from $^{233}$U(n$_{th}$,f)

The measurements with the $^{233}$U target were mainly performed to find the yields of the exotic nuclei $^{11}$Li and $^{14}$Be. Also $^{21}$F was measured to complete an overview of heavy ternary particles from $^{233}$U(n$_{th}$,f) made by Wöstheinrich et al. [Wös99a].

Unfortunately $^4$He could only be measured up to a maximum energy of 11.6 MeV. An extrapolation of the low-energy values would cause a large overestimation due to the well-known deviation of the energy distribution from a Gaussian [Vor69]. Moreover the mean energy of the $^4$He distribution is not well known. Values of 15.8 MeV [Wag86] and 16.3 MeV [Vor69] have been reported. Therefore all yields were normalized to a $^{10}$Be yield of 43 per 10000 LRA which had been found in [Vor69]. The same normalization has been used in [Wös98]. The measured values are shown in table 1.5.6.

Compared with an earlier measurement of the helium, lithium and beryllium isotopes in Gatchina [Vor69], the energy distributions of this measurement are shifted towards lower energies by about 0.5 to 1 MeV. A similar tendency had been found in the comparison of light ternary particles from $^{235}$U measured in Gatchina [Vor72] and at LOHENGRIN [Bau92b]. For the helium isotopes the deviation can be explained by the difference in the measured energy range. The spectrometer in Gatchina allows to access the high energy wing of the Gaussian distribution. Any deviation from the assumed ideal Gaussian energy distribution will cause a systematic error which affects the experiments differently, depending on the measured energy range.

The yields measured in both, ref. [Wös98] and this work, are completely consistent, see table A.5.2 in appendix A.5. However, the measurement of [Wös98] gave a mean kinetic energy of 17.2 MeV for $^{10}$Be, thus confirming the result of Vorobiev (17.0 MeV [Vor69]). Also the widths of the $^{15}$C and the $^{20}$O energy distributions are larger in [Wös98]. It cannot be excluded that this difference was caused by instabilities of the high voltage of the LOHENGRIN condenser during our measurement of $^{10}$Be at the two highest energies ($E > 20$ MeV). This would lead to the observed reduction of the mean energy and the integrated yield. For the isotopes measured with the same settings ($^{15}$C and $^{20}$O), the two corresponding points are well above the mean kinetic energy. The deduced average kinetic energy is not significantly affected, while the width of the energy distribution is slightly reduced.

Table 1.5.3.:   Measured yields and energy parameters for hydrogen to carbon isotopes from $^{245}Cm(n_{th},f)$. The label *"u.l."* marks an upper limit for isotopes where no or too few events were found to determine a reliable yield.

| Isotope | $E_{mean}$ (MeV) | $\sigma(E_{mean})$ (MeV) | $E_{FWHM}$ (MeV) | $\sigma(E_{FWHM})$ (MeV) | Yield | $\sigma$(Yield) |
|---------|------|------|------|------|------|------|
| 3H | 8.4 | *fix* | 7.4 | 0.3 | 679 | 44 |
| 3He | 20 | *fix* | 10 | *fix* | 0.6 | *u.l.* |
| 4He | 15.9 | *fix* | 11.6 | 0.5 | 10000 | 600 |
| 4He | 16.8 | *fix* | 12.7 | 0.5 | 11900 | 600 |
| 6He | 11.3 | 0.4 | 11.2 | 0.7 | 286 | 16 |
| 8He | 10.4 | 0.9 | 12.8 | 2.5 | 19 | 4 |
| 6Li | 20 | *fix* | 10 | *fix* | 0.3 | *u.l.* |
| 7Li | 15.1 | 0.7 | 14.3 | 1.3 | 13.6 | 1.3 |
| 8Li | 15.8 | 1.1 | 14.1 | 2.7 | 5.6 | 0.8 |
| 9Li | 13.4 | 0.7 | 15.2 | 2.4 | 13.6 | 1.7 |
| 11Li | 12 | *fix* | 12 | *fix* | 0.010 | 0.006 |
| 9Be | 18.3 | 1.1 | 19.6 | 2.7 | 9.1 | 1.1 |
| 10Be | 19.2 | 0.6 | 17.5 | 1.6 | 66 | 5 |
| 11Be | 15.6 | 0.8 | 17.5 | 2.3 | 8.1 | 1.0 |
| 12Be | 14.2 | 0.9 | 18.0 | 2.0 | 5.5 | 0.7 |
| 14Be | 14 | *fix* | 14 | *fix* | 0.018 | 0.012 |
| 10B | 25 | *fix* | 20 | *fix* | 0.3 | *u.l.* |
| 11B | 22 | *fix* | 18 | *fix* | 2.4 | 1.3 |
| 12B | 20.6 | 1.5 | 18.1 | 2.2 | 2.3 | 0.4 |
| 13B | 20.3 | 1.3 | 16.7 | 5.8 | 2.2 | 0.6 |
| 14B | 19 | *fix* | 17 | *fix* | 0.21 | 0.06 |
| 15B | 18 | *fix* | 16 | *fix* | 0.09 | 0.05 |
| 12C | 25 | *fix* | 27 | *fix* | 4.8 | *u.l.* |
| 13C | 24 | *fix* | 26 | *fix* | 1.1 | 0.5 |
| 14C | 23.3 | 0.7 | 27.7 | 2.2 | 23.3 | 1.6 |
| 15C | 22.4 | 1.0 | 24.6 | 3.0 | 7.7 | 1.1 |
| 16C | 22.8 | 2.7 | 26 | 9.5 | 9.5 | 3.3 |
| 17C | 22 | *fix* | 24 | *fix* | 0.65 | 0.21 |
| 18C | 21.5 | *fix* | 22.9 | *fix* | 0.32 | 0.11 |
| 19C | 20 | *fix* | 21 | *fix* | 0.030 | *u.l.* |
| 20C | 19 | *fix* | 20 | *fix* | 0.053 | *u.l.* |

Note that our yield value for $^6$He (179) is significantly larger than the value 137(7) per 10000 LRA found in [Vor69]. This could be partly due to a non-Gaussian shape in the low-energy part of the spectrum. Such a deviation is already seen in figure 2 of ref. [Vor69]. On the other hand this inconsistency could also be caused by a too high value for $^{10}$Be in [Vor69]. In this case our yields and the yields from [Wös98] should be renormalized to a value of about 33 $^{10}$Be per 10000 LRA. Then also the lithium yields of [Vor69] and [Wös98] would agree completely.

From the given data it cannot be finally decided which yield values of $^6$He and $^{10}$Be are correct. Therefore both values are given in brackets in table 1.5.6. However, for the points which will be discussed in the following, i.e. the relative yields of exotic nuclei, a possible systematic error in the normalization plays no role.

Table 1.5.4.:   Measured yields and energy parameters for nitrogen to fluorine isotopes from
$^{245}$Cm(n$_{th}$,f). The label *"u.l."* marks an upper limit for isotopes where no or too
few events were found to determine a reliable yield.

| Isotope | $E_{mean}$ (MeV) | $\sigma(E_{mean})$ (MeV) | $E_{FWHM}$ (MeV) | $\sigma(E_{FWHM})$ (MeV) | Yield | $\sigma$(Yield) |
|---------|------|------|------|------|-------|-------|
| 14N | 26 | *fix* | 27 | *fix* | 4.1 | *u.l.* |
| 15N | 25 | *fix* | 26 | *fix* | 0.17 | 0.07 |
| 17N | 22 | *fix* | 24 | *fix* | 0.77 | 0.31 |
| 18N | 22 | *fix* | 24.6 | 6.5 | 0.47 | 0.21 |
| 19N | 21 | *fix* | 22 | *fix* | 0.53 | 0.19 |
| 20N | 20 | *fix* | 21 | *fix* | 0.061 | *u.l.* |
| 21N | 19 | *fix* | 20 | *fix* | 0.024 | *u.l.* |
| 16O | 28 | *fix* | 28 | *fix* | 47 | *u.l.* |
| 17O | 27 | *fix* | 27 | *fix* | 0.2 | *u.l.* |
| 18O | 26 | *fix* | 26 | *fix* | 1.0 | 0.4 |
| 19O | 21.3 | 4.9 | 24 | 14.3 | 0.77 | 0.47 |
| 20O | 23.5 | 1.3 | 22.1 | 3.8 | 2.7 | 0.4 |
| 21O | 20.6 | 4.3 | 24.8 | 5.6 | 0.71 | 0.24 |
| 22O | 22 | *fix* | 23 | *fix* | 0.39 | 0.18 |
| 20F | 32 | *fix* | 28 | *fix* | 0.08 | *u.l.* |
| $A = 90$ | 103.6 | 0.6 | 20.4 | 1.8 | 45000 | 5000 |

Table 1.5.5.: For $A = 90$ and $^4$He the absolute yields per fission of $^{245}$Cm(n$_{th}$,f) are given. Binary
to ternary ratios are calculated for different yields of the reference mass $A = 90$.
For $^4$He the average energy was assumed to be 15.9 MeV in accordance with the
normalization of tables 1.5.3 and 1.5.4.

| Reference | $A = 90$ fiss. yield (%) | $^4$He fiss. yield (%) | ternary/binary ratio | binary/ternary ratio |
|-----------|------|------|------|------|
| [Gun67] | 1.08(15) | 0.24(5) | $2.7(6) \cdot 10^{-3}$ | 370(80) |
| [Dic81] | 1.15(28) | 0.25(7) | $2.9(9) \cdot 10^{-3}$ | 350(100) |
| [Koz88] | 0.99(2) | 0.22(3) | $2.5(4) \cdot 10^{-3}$ | 410(60) |
| [Fri98b] | 1.28(5) | 0.28(4) | $3.2(5) \cdot 10^{-3}$ | 310(50) |
| Average | ≈1.13 | ≈0.25 | $\approx 2.8 \cdot 10^{-3}$ | ≈360 |

## 1.5.4.   Yields from $^{235}$U(n$_{th}$,f)

Also the experiments with the $^{235}$U targets were dedicated to determine the yields of light isotopes
with extreme $N/Z$ ratio: $^{11}$Li, $^{14}$Be, $^3$He, etc. Unfortunately these measurements were strongly
hampered by instabilities of the condenser high voltage. Only few reliable points could be taken
at higher voltages. This affects mainly the helium isotopes, causing large uncertainties in the
determination of yields and energy distributions. Therefore the helium isotopes were not evaluated
and $^{10}$Be was chosen as normalization point as in the case of $^{233}$U(n$_{th}$,f). The yield of $^{10}$Be
varies in literature between 27.6 [Bau92b] and 32 per 10000 LRA [Vor72]. To allow for a better
comparison with the yields of [Bau92b], arbitrarily the first value is taken for normalization. Note
that the yields of light isotopes ($^3$H, $^6$He, $^8$He, $^{10}$Be, ... ) from [Bau92b] are lower by 10 % to
15 % compared with ref. [Vor72], see table A.5.5 in appendix A.5. Again this could be caused by

Table 1.5.6.:  Measured yields and energy parameters for helium to fluorine isotopes from
$^{233}U(n_{th},f)$. The label *"u.l."* marks an upper limit for isotopes where no or too
few events were found to determine a reliable yield. Questionable values are shown
in parentheses, see text.

| Isotope | $E_{\mathrm{mean}}$ (MeV) | $\sigma(E_{\mathrm{mean}})$ (MeV) | $E_{\mathrm{FWHM}}$ (MeV) | $\sigma(E_{\mathrm{FWHM}})$ (MeV) | Yield | $\sigma(\mathrm{Yield})$ |
|---------|------|------|------|------|-------|--------|
| 3He  | 20     | *fix* | 10     | *fix* | 0.018   | *u.l.*   |
| 4He  |        |       |        |       | 10000   | –        |
| 6He  | 10.3   | 0.3   | 10.3   | 0.6   | (179)   | 15       |
| 9Li  | 11.2   | 0.7   | 13.2   | 2.0   | 4.3     | 0.6      |
| 11Li | 11     | *fix* | 11     | *fix* | 0.00037 | 0.00027  |
| 10Be | (16.5) | 0.5   | (14.9) | 0.8   | (43)    | 3        |
| 11Be | 15     | *fix* | 15     | *fix* | 1.9     | 1.0      |
| 14Be | 12     | *fix* | 12     | *fix* | 0.0011  | *u.l.*   |
| 14B  | 18.2   | *fix* | 18.7   | *fix* | 0.021   | 0.007    |
| 15C  | 21.6   | 0.8   | (16.7) | 1.3   | 2.2     | 0.3      |
| 15O  | 30     | *fix* | 18     | *fix* | 0.013   | *u.l.*   |
| 20O  | 22.8   | 1.5   | (21.6) | 2.1   | 0.73    | 0.09     |
| 21O  | 22     | *fix* | 21     | *fix* | 0.031   | 0.008    |
| 22O  | 21     | *fix* | 20     | *fix* | 0.0052  | 0.0024   |
| 21F  | 26.1   | 2.2   | 12.5   | 4.4   | 0.0077  | 0.0034   |

Table 1.5.7.:  Measured yields and energy parameters for hydrogen to oxygen isotopes from
$^{235}U(n_{th},f)$. The label *"u.l."* marks an upper limit for isotopes where no or too
few events were found to determine a reliable yield.

| Isotope | $E_{\mathrm{mean}}$ (MeV) | $\sigma(E_{\mathrm{mean}})$ (MeV) | $E_{\mathrm{FWHM}}$ (MeV) | $\sigma(E_{\mathrm{FWHM}})$ (MeV) | Yield | $\sigma(\mathrm{Yield})$ |
|---------|------|------|------|------|-------|--------|
| 3He  | 20   | *fix* | 10   | *fix* | 0.008   | *u.l.*   |
| 4He  |      |       |      |       | 10000   | –        |
| 6Li  | 20   | *fix* | 10   | *fix* | 0.015   | *u.l.*   |
| 9Li  | 11.8 | 0.5   | 13.2 | 1.5   | 2.9     | 0.3      |
| 11Li | 9.6  | 1.1   | 7.9  | 2.1   | 0.00090 | 0.00022  |
| 7Be  | 28   | *fix* | 14   | *fix* | 0.009   | *u.l.*   |
| 10Be | 16.8 | 0.5   | 16.5 | 0.8   | 27.6    | 2.0      |
| 14Be | 13   | *fix* | 13   | *fix* | 0.00034 | 0.00020  |
| 10B  | 25   | *fix* | 20   | *fix* | 0.008   | *u.l.*   |
| 17B  | 15   | *fix* | 15   | *fix* | 0.0004  | *u.l.*   |
| 15C  | 22.3 | 2.5   | 22.0 | 7.7   | 1.5     | 0.5      |
| 15O  | 30   | *fix* | 18   | *fix* | 0.016   | *u.l.*   |
| 20O  | 22.5 | 2.4   | 22.2 | 2.9   | 0.45    | 0.08     |
| 21O  | 21   | *fix* | 21   | *fix* | 0.053   | 0.015    |
| 22O  | 20   | *fix* | 20   | *fix* | 0.017   | 0.006    |

uncertainties in the energy distribution of the normalization point $^4$He in the measurement of ref.
[Bau92b].

With the second target even a rough energy distribution of $^{11}$Li could be measured, see figure
A.4.4 in appendix A.4. The free fit indicates that the energy distribution of $^{11}$Li seems to be

narrower than expected from trajectory calculations and systematics. This might also apply to other exotic isotopes from other fissioning systems. In this case the derived upper limits would be further reduced.

Also yields of the heavier oxygen isotopes could be evaluated. The value for $^{22}$O lies clearly above the upper limit given by Baum [Bau92b]. Probably the latter was obtained from a parasitic measurement with separator settings for $^{11}$Be. The used $\Delta E$-$E$ telescope had an acceptance of about 1 cm in mass direction while in our case the edge focusing of the RED magnet and the larger entrance window increased the acceptance considerably. Thus, uncertainties of the transmission are reduced.

## 1.6.    Discussion

### 1.6.1.    Binary contributions to ternary fission yields?

In principle the detected light charged particles could be created in an extremely asymmetrical binary fission or a cluster decay from an excited state. In LOHENGRIN measurements the light charged particle is detected without coincidence to the heavy fragments. Its origin from ternary fission[24] therefore has to be deduced from its kinetic energy distribution. Tables 1.5.1 and 1.5.2 also show the maximum kinetic energy $E_{bin}$ which the light charged particle could attain if it was produced in a binary reaction, e.g. $^{241}$Pu(n,$\alpha$)$^{238}$U. A dash indicates that the Q-value of such a direct reaction is negative, i.e. the reaction is impossible with thermal neutrons. No entry is made in cases where the mass of the potential heavy binary partner is unknown [Aud97]. Especially for the lighter isotopes it is evident from the high measured energies ($> E_{bin}$) that they are indeed produced in ternary fission. The same conclusion can be drawn for the other fissioning systems which are not explicitly shown.

Possible additional contributions of light charged particles from extremely asymmetric binary fission are hidden in a large background of ternary events. For example reactions like $^{233}$U(n,$^{14}$C)$^{220}$Rn, $^{233}$U(n,$^{20}$C)$^{214}$Po, etc. are energetically possible. To unambiguously identify such events the *heavy* partner which does not have any ternary background has to be detected. The heavy recoil nuclei (some MeV kinetic energy and low charge states $3 \lesssim q \lesssim 5$) can also be separated with the LOHENGRIN spectrometer. For a unique identification they are implanted into a silicon detector which subsequently detects the characteristic alpha decay with a delayed coincidence. Due to the low event rate, a time window of many minutes can be used even with an unsegmented silicon detector. A first experiment (ILL proposal 3-01-355) indicated evidence for such events, but more systematic studies need to be performed for proof.

### 1.6.2.    General comparison with model predictions

Figure 1.6.1 shows a plot of the individual isotopic yields of $^{241}$Pu(n$_{th}$,f). The strong proton odd-even effect which favors emission of ternary particles with even $Z$ is obvious, see also figure 1.6.3. Also the less pronounced neutron odd-even effect is clearly visible as a staggering within one element.

Only from two of the models discussed in section 1.3, predictions are available for $^{241}$Pu(n$_{th}$,f). In general the "Faust formula" (Boltzmann model) gives a slightly better agreement with the experimental values than the "Rubchenya model" (double-neck rupture model). Both overestimate

---

[24]It could also come from quaternary fission. However, such an event was never observed and should be much rarer than ternary fission. Breakup fragments from decay of excited ternary $^{7}$Li* and $^{8}$Be* which can experimentally give the impression of quaternary fission are discussed in ref. [Kat73, Fea74].
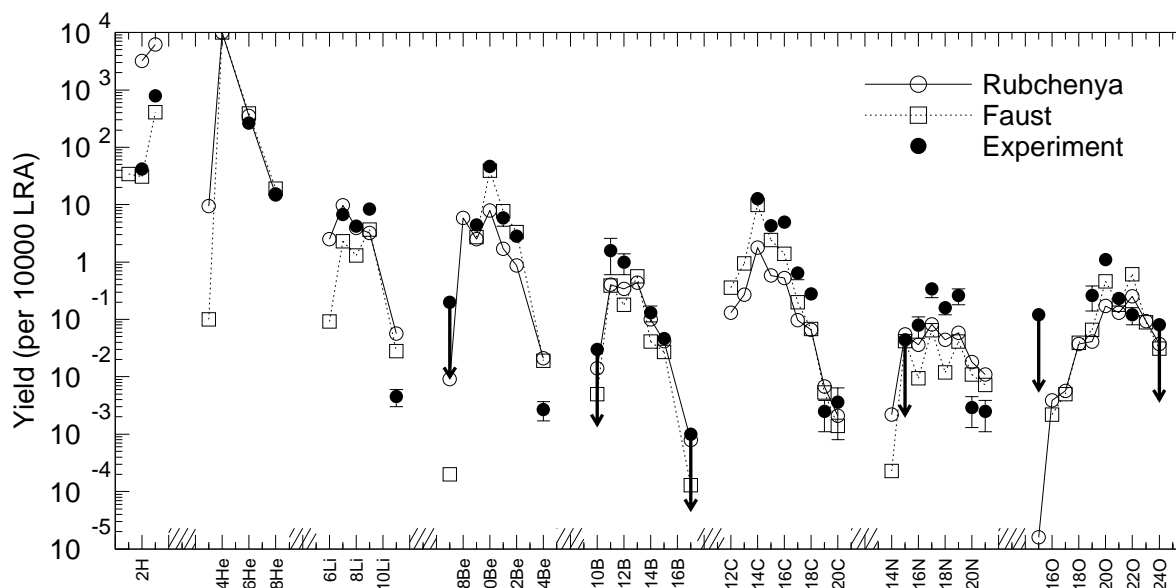
Figure 1.6.1.: Measured and predicted yields of ternary particles from $^{241}$Pu(n$_{th}$,f) normalized to $10^4$ for $^4$He. Upper limits are marked with an arrow. Some upper limits have been omitted for sake of clarity. Here, and in the following yield comparisons the isotopes of each element are grouped together in a series.

the yields of the exotic isotopes $^{11}$Li and $^{14}$Be by about one order of magnitude. Also for some nitrogen isotopes a significant deviation from the experimental values occurs.

The integrated mass and elemental yields from $^{241}$Pu(n$_{th}$,f) are shown in figures 1.6.2 and 1.6.3 respectively. For complete summing, the missing individual yields (e.g. for mass 13 nuclei from $^{241}$Pu(n$_{th}$,f)) were interpolated from neighboring yields according to the ratios predicted by the Faust formula[25]. Contributions from particle unstable nuclei are neglected. The mass yields were converted to absolute yields (per fission) with the ternary to binary ratio from [Wag86]. For comparison the binary yields of the light fragment group from [Fri98b, Sch94] are also plotted. The strong oscillation (see figure 1.6.2) of the ternary yields can be understood from the fact that most ternary mass yields are dominated by a single isotope. Thus, high yields of individual isotopes ($^{10}$Be, $^{14}$C, etc.) lead to a significant staggering of the yields.

Figure 1.6.3 shows clearly the strong proton odd-even effect[26] and the increase of heavier element yields with increasing mass of the fissioning system from $^{233}$U(n$_{th}$,f) to $^{252}$Cf(sf).

The individual isotopic yields of $^{245}$Cm(n$_{th}$,f) are plotted in figure 1.6.4. Also for this fissioning system only predictions from references [Rubch] and [Fau95b] exist. Again the agreement with the experimental values of the more abundant isotopes is quite good, but for the exotic nuclei $^{11}$Li, $^{14}$Be and some nitrogen isotopes discrepancies of one order of magnitude and more occur.

Figure 1.6.5 shows a plot of the individual isotopic yields of $^{233}$U(n$_{th}$,f). For this fissioning system most of the discussed models make a prediction. It is obvious that the Valski formula gives for heavier isotopes completely wrong results. On the other hand it is the only one which reproduces the sharp drop from $^4$He to $^3$He. All other models overestimate the $^3$He yield by two to three orders of magnitude. The extended Halpern model shows only a small proton odd-even effect and thus overestimates the yields of odd-$Z$-nuclei by up to one order of magnitude (lithium). Again

---

[25] The resulting uncertainty is negligible on the scale of the plot. In cases where higher corrections would become necessary, the resulting values are not plotted. Thus, the plotted values can be regarded as purely experimental.

[26] Due to the strong staggering of the individual isotopic yields the odd-even effect is difficult to quantify in ternary fission. Various definitions of the odd-even effect which are used in binary fission require at least locally a smoother behavior [Gön92a].
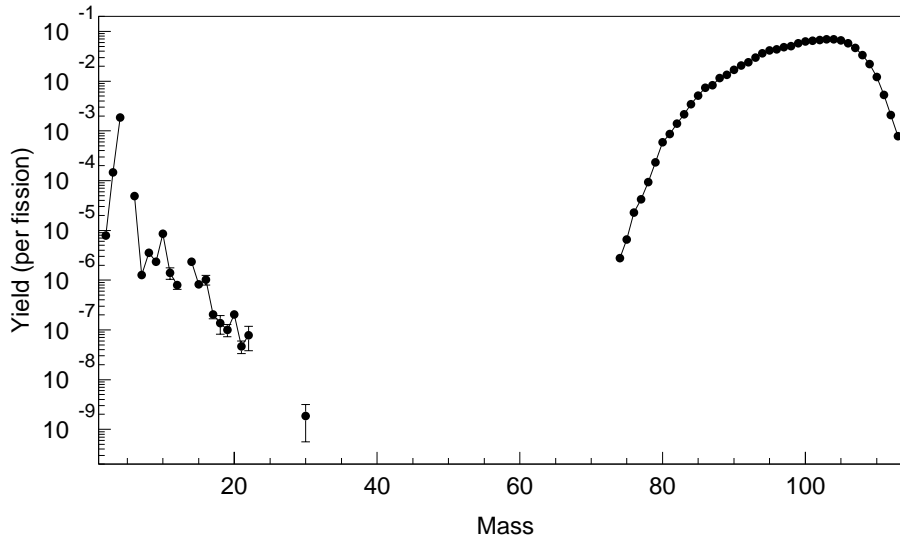
Figure 1.6.2.: Absolute mass yields from $^{241}$Pu($n_{th}$,f) in events per fission. For comparison also the binary yields of the light fragment group are shown.
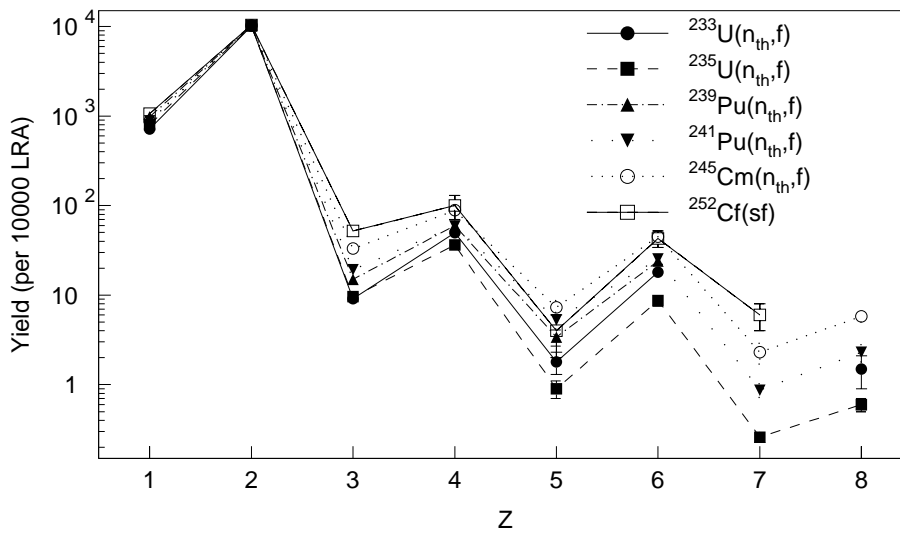


Figure 1.6.3.: Elemental yields of ternary particles from $^{233}$U($n_{th}$,f), $^{235}$U($n_{th}$,f), $^{239}$Pu($n_{th}$,f), $^{241}$Pu($n_{th}$,f), $^{245}$Cm($n_{th}$,f) and $^{252}$Cf(sf). A possible contribution of low-energy (polar) protons to the hydrogen yield was neglected.

the experimental values of light exotic nuclei are one to three orders of magnitude below all model predictions. In case the temperature parameter is slightly increased to better reproduce the yields of some heavier nuclei, the discrepancy with the light exotic nuclei would become even worse.

The individual isotopic yields of $^{235}$U($n_{th}$,f) are shown in figure 1.6.6. Predictions from all models presented in section 1.3 are plotted. Here, the Valski fit formula still deviates significantly for heavier nuclei, although less extreme than in $^{233}$U($n_{th}$,f). The overall agreement of the experimental values with most models is quite good. However, it has to be kept in mind that many models have been developed and tuned to well reproduce the yields of $^{235}$U($n_{th}$,f). Again most models strongly overestimate up to several orders of magnitude the yields of the light isotopes with extreme $N/Z$ ratio: $^{3}$He, $^{6}$Li, $^{11}$Li and $^{14}$Be.

The situation of isotopes with extreme $N/Z$ ratios is discussed in the following.
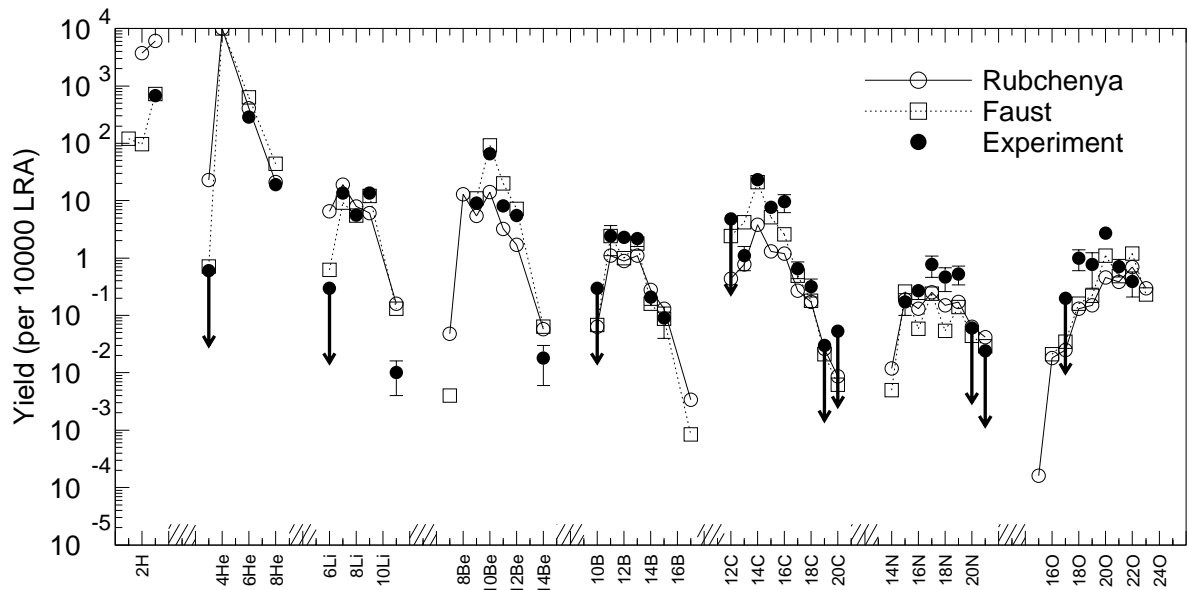
Figure 1.6.4.: Measured and predicted yields of ternary particles from $^{245}$Cm(n$_{th}$,f). All experimental values except that of $^{16}$N [Hes97] are from the present measurement. See caption of figure 1.6.1 for details.
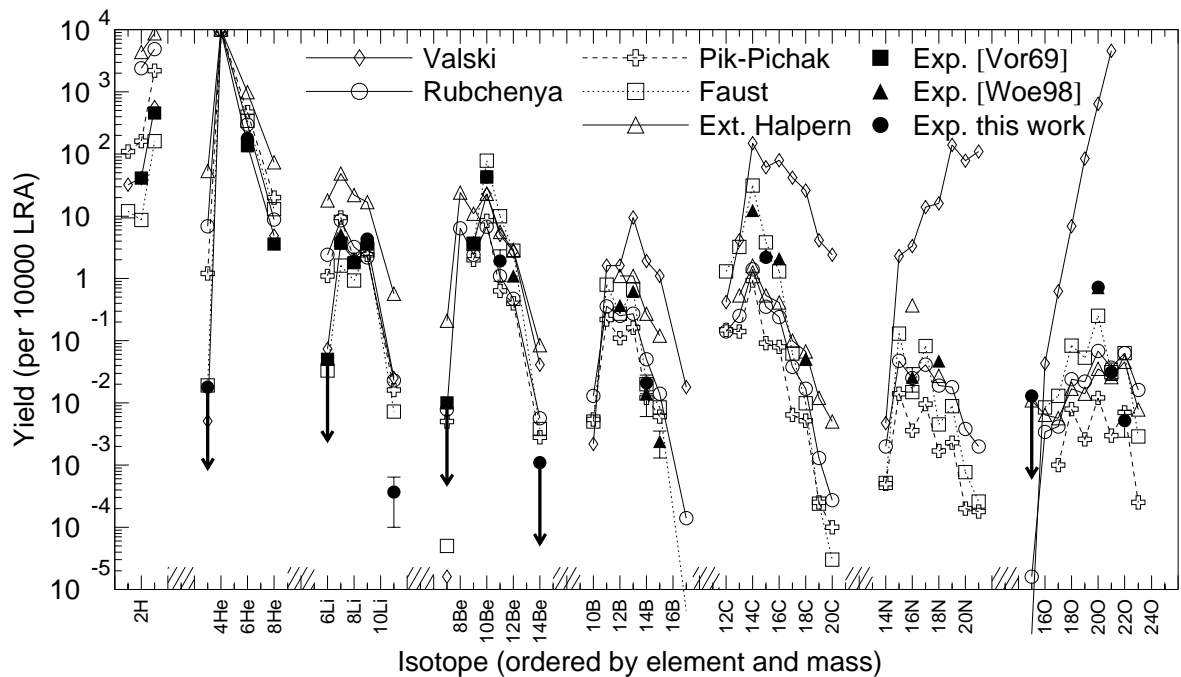


Figure 1.6.5.: Measured and predicted yields of ternary particles from $^{233}$U(n$_{th}$,f). See caption of figure 1.6.1 for details.

## 1.6.3.  Yields of neutron-deficient nuclei

Compared with neutron-rich nuclei, the measurement of rare neutron-deficient[27] nuclei is generally more difficult with the LOHENGRIN spectrometer. In spectra of fully stripped neutron-rich nuclei always isobars with the same ionic charge state but higher $Z$ are present on the $\Delta E$-$E$ plots and

---

[27]The use of the term "neutron-deficient" is here slightly extended to include also $N = Z$ nuclei. These are still "neutron-deficient" compared with the $N/Z$ ratio of the compound nucleus.
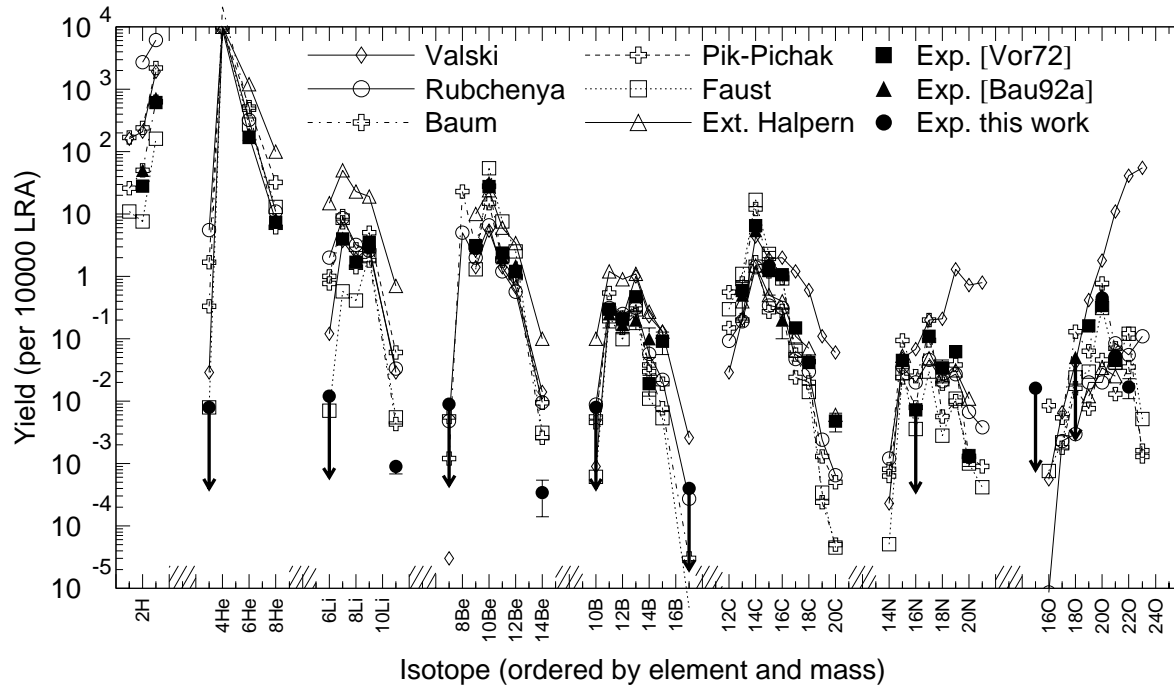
Figure 1.6.6.: Measured and predicted yields of ternary particles from $^{235}$U($n_{th}$,f). See caption of figure 1.6.1 for details.

allow a direct monitoring of the experimental conditions. Any electronic artifacts or instabilities of the separator can be easily detected. On the other hand, if the separator is set to $A/q < 2$, only fully stripped neutron-deficient isotopes can pass and no other isobars are available which would allow a monitoring of the intensity. Set to $A/q = 2$ for detection of $N = Z$ nuclei, a high background of scattered stable nuclides $^{12}$C, $^{14}$N and $^{16}$O is present, especially at lower energies. Moreover, from trajectory calculations it is expected that neutron-deficient nuclei have very high average kinetic energies which would require voltages well beyond the maximum settings of the LOHENGRIN condenser. Thus, only the low-energy tail of the energy distribution can be probed and one has to rely on the predicted energy distribution to deduce a yield. To deduce the upper limits, an unfavorably high average kinetic energy was assumed in accordance with the trajectory calculations of ref. [Bau92b, Bou94].

A dedicated set-up with a thick energy degrader foil mounted in front of the target to match the kinetic energy to the high-energy limit of the LOHENGRIN spectrometer would allow an increase of the sensitivity by at least one order of magnitude.

### $^3$He

Several older measurements gave upper limits for the fission yield of $^3$He [Weg61, Cos67, Whe67, Kug72, Vor72, Vor75], see table 1.6.1. Only in ref. [Cam69] a high yield for $^3$He from $^{233}$U(n,f) was reported: about 1.8 % of the LRA yield. However, this measurement was done with a simple $\Delta E$-$E_{res}$ telescope without additional particle separation. The alleged "$^3$He events" are clearly due to scattered alphas which show up on the $\Delta E$-$E_{res}$ plot in the "$^3$He banana" (see figure 4 in [Cam69]).

With the present work the upper limits for the yield of $^3$He from $^{235}$U($n_{th}$,f) and $^{233}$U($n_{th}$,f) could be confirmed and improved by a factor six in the latter case. Also for $^{245}$Cm($n_{th}$,f) an upper limit could be given.

Table 1.6.1.: Experimental values for $^3$He emission in ternary fission. For the spontaneous fission of $^{252}$Cf upper limits of 50 [Weg61], 7.5 [Cos67] and 9 [Whe67] per 10000 LRA were reported.

| Fissioning system | This work | [Vor69] | [Cam69] | [Vor72] | [Kug72] | [Vor75] |
|---|---|---|---|---|---|---|
| $^{233}$U($n_{th}$,f) | < 0.018 | < 0.1 | ≈ 180 | – | – | – |
| $^{235}$U($n_{th}$,f) | < 0.008 | – | – | < 0.01 | < 0.08 | – |
| $^{239}$Pu($n_{th}$,f) | – | – | – | – | – | < 0.01 |
| $^{245}$Cm($n_{th}$,f) | < 0.6 | – | – | – | – | – |

Table 1.6.2.: Experimental values for the emission of $^6$Li, $^7$Be and $^{10}$B in ternary fission.

| Fissioning system | $^6$Li | $^7$Be | $^{10}$B | Reference |
|---|---|---|---|---|
| $^{233}$U($n_{th}$,f) | < 0.05 | < 0.01 | – | [Vor69] |
| $^{235}$U($n_{th}$,f) | 0.05(2) | < 0.01 | < 0.01 | [Vor72] |
| $^{235}$U($n_{th}$,f) | 1.04(27) | – | 0.37(17) | [Bau92b] |
| $^{235}$U($n_{th}$,f) | < 0.015 | < 0.009 | < 0.008 | this work |
| $^{239}$Pu($n_{th}$,f) | < 0.05 | < 0.01 | < 0.02 | [Vor75] |
| $^{241}$Pu($n_{th}$,f) | – | < 0.2 | < 0.03 | this work |
| $^{245}$Cm($n_{th}$,f) | < 0.3 | – | < 0.3 | this work |

It should be noted that $^3$He is particularly difficult to measure with the present LOHENGRIN set-up. Its expected average kinetic energy is above that of $^4$He (≈15.9 MeV), presumably around 20 MeV. The fast $^3$He ions cannot be fully stopped in the ionization chamber with the maximum permitted gas pressure. Thus, the much more abundant tritons which could pass the condenser during a short voltage fluctuation could appear on the $\Delta E$-$E$ plot close to the position of the expected $^3$He events. Therefore the few events detected in the region of interest were only used to deduce an upper limit. A silicon detector for complete stopping and detecting of the $E_{res}$ signal would help to improve the sensitivity.

## $^6$Li, $^7$Be and $^{10}$B

For the isotopes $^6$Li, $^7$Be and $^{10}$B only upper limits were found in the studied systems (see table 1.6.2). These results are consistent with the results from Gatchina [Vor69, Vor72, Vor75], only for $^6$Li we find an upper limit below the value of ref. [Vor72]. On the contrary, relatively high yields for $^6$Li and $^{10}$B were reported in [Bau92b]. They had been corrected for contributions of scattered stable nuclei[28]. Uncertainties in this correction can lead to a relatively big systematic error which was probably underestimated in [Bau92b]. Note that $^7$Be would be an ideal candidate for a radiochemical investigation of ternary fission yields.

---

[28]Parts of the $^6$Li targets which have been introduced for on-line energy calibration of the LOHENGRIN separator, were sputtered off and deposited on the target holder. Therefore a permanent background of scattered $^6$Li as well as alphas and tritons from $^6$Li($n,\alpha$) is present at lower energies.

$^{15}$O

A significant yield for $^{15}$O from $^{235}$U($n_{th}$,f) was reported in [Bau92a]: 0.34(21) per 10000 LRA. Also in some of our measurements events showed up in the $\Delta E$-$E$ spectra which might be assigned to $^{15}$O. However, a more careful analysis showed that they are slightly shifted from the expected position on the $\Delta E$-$E$ plot. Such background could be created by $^{16}$O from the residual gas being scattered in the beam tube and passing the spectrometer with a tilted trajectory at separator settings for mass 15. This explanation is supported by several facts:

1. The energy distribution does show a non-Gaussian behavior and rises significantly towards lower energies which is typical for scattered particles (see figure 1.6.7).

2. The yield of "$^{15}$O" changes considerably between different measurements with the same fissioning system. It showed a correlation with the vacuum conditions in the beam tube (increase of the "yield" with bad vacuum).

3. Moreover, the ionic charge state distribution of "$^{15}$O" events deviates from that for ternary oxygen isotopes. The same effect occurs for other scattered stable particles. Obviously the equilibrium charge state is not reached in a single scattering process.

Using only the points above 20 MeV together with an average energy consistent with the trajectory calculations of [Bau92b, Bou94], upper limits were deduced from the present measurements: 0.013 in $^{233}$U($n_{th}$,f), 0.016 in $^{235}$U($n_{th}$,f) and 0.12 in $^{241}$Pu($n_{th}$,f) per 10000 LRA respectively.
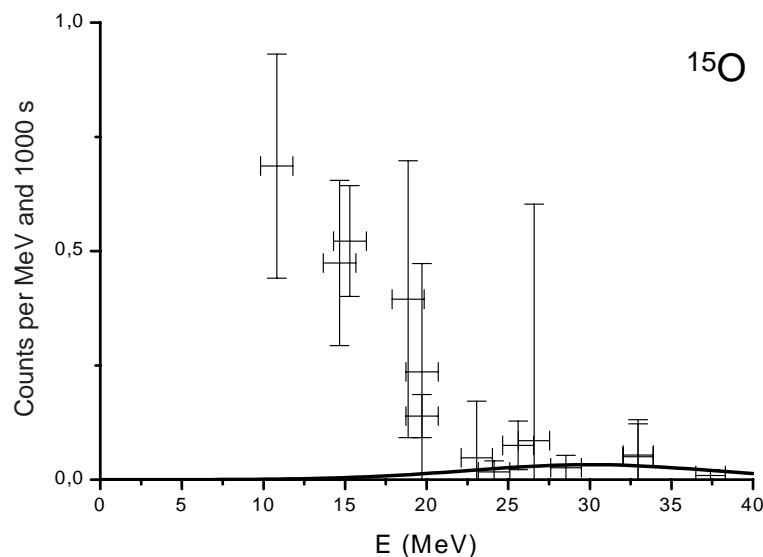


Figure 1.6.7.: Energy distribution of alleged "$^{15}$O" events in thermal neutron-induced fission of $^{233}$U. The rise towards lower energies indicates a large contribution of scattered $^{16}$O.

It can be summarized that presently in low-energy fission only upper limits exist for the experimental yields of all neutron-deficient ternary particles. Most models of ternary fission yields fail to predict the very sharp drop of the yields towards small $N/Z$ ratio.

Mutterer et al. have shown that $^5$He and $^7$He are also emitted in ternary fission and follow a smooth exponential drop towards higher masses without markable neutron odd-even effect [Mut99]. Therefore it is even more astonishing why for $^3$He such an abrupt drop occurs.

## 1.6.4.    Yield of very neutron-rich nuclei

From the experimental results it is evident that the yields of very neutron-rich light nuclei are considerably smaller than most model predictions. Before interpreting this fact as a model failure it has to be checked whether other effects could cause such a deviation. It is clear that the $N/Z$ ratios of exotic isotopes differ strongly from that of the fissioning compound nucleus. Such nuclei are intuitively expected to be created with a lower yield. However, this effect is already assumed to be included in the presented models which are generally applicable to *all* ternary particles.

**Suppression of halo nuclei?**

Another effect could occur for very neutron-rich nuclei. If the binding energy for the last neutron(s) $S_{x\text{n}}$ is very low, some nuclides show a so-called neutron halo. That means the wave function of the weakly bound valence neutrons has a tail which extends far away. Therefore the mean square matter radius and the nuclear cross-section for breakup are significantly increased. First experimental evidence for this fact was found by Tanihata et al. [Tan85].

The possibility of a halo depends on the neutron separation energy $S_{x\text{n}}$ and the angular momentum of the "halo" neutron(s). As a rule of thumb a halo can appear if $S_{x\text{n}}$ is smaller than approximately $5 - 10$ MeV fm$^2/R^2$, where $R$ is the radius of an equivalent square well potential [Rii92]. Among the studied ternary particles, $^{11}$Be and $^{19}$C are known to have a one-neutron halo, $^{6}$He, $^{11}$Li, $^{14}$Be and $^{17}$B have a two-neutron halo and $^{8}$He can be described by an alpha core with a four-neutron halo [Zhu94]. Table 1.6.3 gives a summary of the binding energies of the last neutron(s). Rms matter radii are not given in table 1.6.3. They are somehow model dependent, a recent compilation is found in [She96]. The mean square distance of the halo neutron(s) can be estimated when using a two-body approximation: core plus neutron or core plus "dineutron" [Han87]:

$$\langle r^2 \rangle = \hbar^2/(4\mu S_{x\text{n}}) \tag{1.6.1}$$

with $\mu$ the reduced mass of the system.

Table 1.6.3.: Binding energies of the halo neutrons in neutron-halo nuclei. Where no reference is given they were calculated from the atomic mass evaluation of Audi and Wapstra [Aud95].

| Isotope | $S_{1\text{n}}$ MeV | $S_{2\text{n}}$ MeV | $S_{4\text{n}}$ MeV | Reference |
|---------|---------|---------|---------|-----------|
| $^{6}$He | | 0.973(1) | | |
| $^{8}$He | | 2.139(7) | 3.112(7) | |
| $^{11}$Li | | 0.30(3) | | |
| $^{11}$Be | 0.504(6) | | | |
| $^{14}$Be | | 1.34(12) | | |
| $^{17}$B | | 1.39(15) | | |
| $^{19}$C | 0.25(9)$^{(29}$ | | | [Jon98] |

For kinetic energies far below the Coulomb barrier as in our case, Coulomb breakup of the ternary particles while passing the target can be neglected. Also, the dissociation of the halo nucleus in a scattering reaction is negligible in the thin target. The only process which could cause a significant effect is the breakup of the halo while the ternary particle is exposed to the strong nuclear and

---

[29]Recent results indicate a higher value of $S_\text{n} = 0.53(13)$ [Nak98].

Table 1.6.4.: Yield ratios of halo nuclei and well-bound isotopes. Only in two systems the ratio of $^{15}$B to $^{17}$B has been measured: $> 140$ for $^{235}$U$(n_{th},f)$ and $> 36$ for $^{241}$Pu$(n_{th},f)$.

| Fissioning system | $\dfrac{[^4He]}{[^6He]}$ | $\dfrac{[^6He]}{[^8He]}$ | $\dfrac{[^7Li]}{[^9Li]}$ | $\dfrac{[^9Li]}{[^{11}Li]}$ | $\dfrac{[^9Be]}{[^{11}Be]}$ | $\dfrac{[^{10}Be]}{[^{12}Be]}$ | $\dfrac{[^{12}Be]}{[^{14}Be]}$ |
|---|---|---|---|---|---|---|---|
| $^{233}$U$(n_{th},f)$ | 73(4) | 38(5) | 1.0(2) | 11500(9000) | 1.9(11) | 39(8) | > 840 |
| $^{235}$U$(n_{th},f)$ | 52(3) | 23(3) | 1.1(1) | 3300(900) | 1.2(3) | 23(2) | 3600(2200) |
| $^{239}$Pu$(n_{th},f)$ | 52(2) | 22(2) | 1.2(1) | 3100(1200) | 1.5(3) | 22(6) | 5600(3700) |
| $^{241}$Pu$(n_{th},f)$ | 38(4) | 17(3) | 0.81(11) | 1800(700) | 0.75(23) | 16(3) | 1000(400) |
| $^{245}$Cm$(n_{th},f)$ | 35(3) | 15(3) | 1.0(2) | 1400(900) | 1.1(2) | 12(2) | 310(210) |

Table 1.6.5.: Yield ratios of halo nuclei and well-bound isotopes.

| Fissioning system | $\dfrac{[^{14}C]}{[^{16}C]}$ | $\dfrac{[^{15}C]}{[^{17}C]}$ | $\dfrac{[^{16}C]}{[^{18}C]}$ | $\dfrac{[^{17}C]}{[^{19}C]}$ | $\dfrac{[^{18}C]}{[^{20}C]}$ | $\dfrac{[^{20}O]}{[^{22}O]}$ |
|---|---|---|---|---|---|---|
| $^{233}$U$(n_{th},f)$ | 6.0(10) | – | 40(11) | – | – | 140(70) |
| $^{235}$U$(n_{th},f)$ | 6.1(9) | 8.3(12) | 25(7) | – | 9(4) | 26(11) |
| $^{241}$Pu$(n_{th},f)$ | 2.5(5) | 6.7(17) | 18(5) | 260(160) | 78(63) | 9.2(32) |
| $^{245}$Cm$(n_{th},f)$ | 2.5(9) | 12(5) | 30(15) | >15 | >4 | 7.0(35) |

Coulomb forces when the neck is snapping and all three fragments are accelerated. The magnitude of this effect, however, is extremely dependent on all details of the scission configuration. The missing knowledge on the scission configuration already causes most of the uncertainties in the predictions of the ternary fission models discussed above. Thus, a quantitative treatment of this additional effect does not make sense. Nevertheless, it can be qualitatively checked whether a major influence on the yields could occur. For different ternary particles which are created in similar scission configurations, the breakup probability should show a strong dependence on $S_{xn}$. The effect would be more pronounced for isotopes with a weak binding of the last neutrons. The problem is to find a suitable normalization for such a comparison. To avoid biasing by proton- or neutron-odd-even effects, the ratio of the yield of the isotope $^{A-2}_{Z}X$ to the yield of $^{A}_{Z}X$ can be regarded. Thus, the influence of the proton- and neutron pairing energy should mainly cancel. Tables 1.6.4 and 1.6.5 show experimental values of the yield ratios for several pairs of nuclei.

In the case of carbon, the yields of directly neighboring nuclei can be compared. Also for the odd-$N$ isotope $^{11}$Be a different ratio is chosen for comparison. These ratios are shown in table 1.6.6. They are influenced by the neutron-pairing energy. However, the relative influence should be small since identical ratios are regarded: i.e. (o,e)- versus (e,e)- and (e,e)- versus (e,o)-nuclei.

The ratios presented in tables 1.6.4 and 1.6.5 have been calculated from the values measured in this work. Other values were taken from [Wös98, Vor69] for $^{233}$U$(n_{th},f)$, from [Bau92b] for $^{235}$U$(n_{th},f)$ and from [Vor75, Kös95] for $^{239}$Pu$(n_{th},f)$.

Table 1.6.4 shows clearly a more pronounced drop towards heavier isotopes for lithium and beryllium compared with helium, carbon and oxygen nuclei. However, from table 1.6.6 it can be seen that the other halo nuclei $^{11}$Be and $^{19}$C do not show such a significant reduction. If a suppression of halo nuclei occurs for $^{11}$Li and $^{14}$Be, it should also be present in comparable magnitude for the latter nuclei. Thus, it cannot be excluded that halo nuclei are possibly "suppressed" by a factor two or three, but this effect is not able to explain deviations of one order of magnitude and more.

To decide why the models fail to explain the yield drop for exotic lithium and beryllium nuclei, the difference in "energy costs" has to be analyzed in more detail. As explained before, the influence

Table 1.6.6.: Yield ratios of halo nuclei and well-bound isotopes.

| Fissioning system | $\dfrac{[^{15}\text{C}]}{[^{16}\text{C}]}$ | $\dfrac{[^{17}\text{C}]}{[^{18}\text{C}]}$ | $\dfrac{[^{19}\text{C}]}{[^{20}\text{C}]}$ | $\dfrac{[^{10}\text{Be}]}{[^{11}\text{Be}]}$ | $\dfrac{[^{14}\text{C}]}{[^{15}\text{C}]}$ | $\dfrac{[^{20}\text{O}]}{[^{21}\text{O}]}$ |
|---|---|---|---|---|---|---|
| $^{233}\text{U}(\text{n}_{\text{th}},\text{f})$ | 1.1(3) | – | – | 22(12) | 5.2(8) | 23(7) |
| $^{235}\text{U}(\text{n}_{\text{th}},\text{f})$ | 1.2(2) | 3.6(10) | – | 12(2) | 5.3(2) | 8.5(28) |
| $^{239}\text{Pu}(\text{n}_{\text{th}},\text{f})$ | 1.0(6) | – | – | 14(2) | 4.0(15) | – |
| $^{241}\text{Pu}(\text{n}_{\text{th}},\text{f})$ | 0.9(2) | 2.3(7) | 0.7(7) | 7.8(25) | 2.9(4) | 4.8(14) |
| $^{245}\text{Cm}(\text{n}_{\text{th}},\text{f})$ | 0.8(3) | 2.0(9) | – | 8.1(12) | 3.0(5) | 3.8(14) |

of the pairing energy is mainly removed[30] by the choice of these yield ratios. In the double-neck-rupture model and the Boltzmann model the Coulomb energy is practically constant for different isotopes of one element[31]. However, in the parameterization of the other models the fragment distance depends strongly on the ternary particle mass. Therefore, for the considered nuclei the difference in Coulomb energy $E_{\text{Coul}}^{\text{TP}}(^{A-2}_{Z}X) - E_{\text{Coul}}^{\text{TP}}(^{A}_{Z}X)$ attains about 1.5 MeV in the extended Halpern model [Wös96] and even higher values for the two other models [Bau92b, PP94]. Still the dominant contribution to the energy costs comes from the reaction Q-value. Figure 1.6.8 shows a plot of the yield ratios $[^{A-2}_{Z}X]/[^{A}_{Z}X]$ from tables 1.6.4 and 1.6.5 versus the Q-value difference $\Delta Q = Q(^{A-2}_{Z}X) - Q(^{A}_{Z}X)$. The Q-value difference was calculated with the heavy fragment fixed to $^{132}\text{Sn}$.
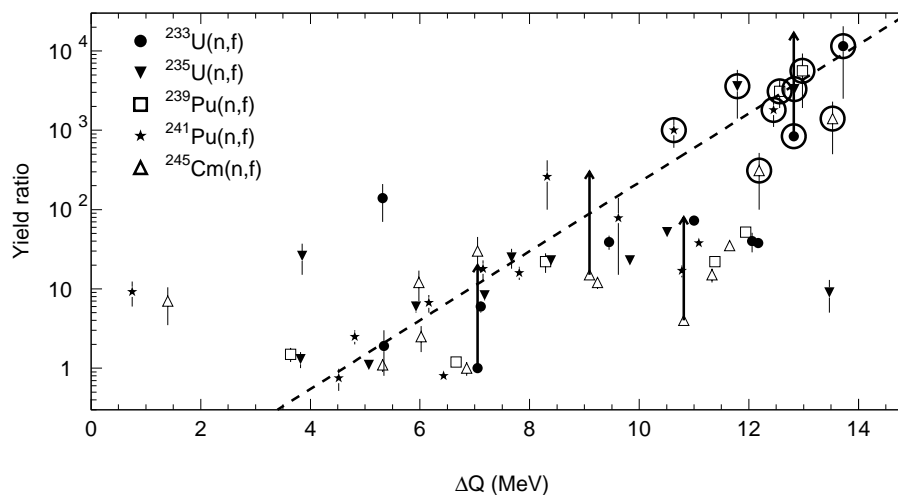


Figure 1.6.8.: Yield ratios $[^{A-2}_{Z}X]/[^{A}_{Z}X]$ versus the Q-value difference. Arrows indicate lower limits of the yield ratio. The values of $[^{9}\text{Li}]/[^{11}\text{Li}]$ and $[^{12}\text{Be}]/[^{14}\text{Be}]$ are marked with a ring around. For comparison an exponential function $y = 0.01 \cdot \exp(\Delta Q/1\text{ MeV})$ is shown as dashed line.

Despite a significant scattering of the values, the dependence of the yields on the Q-value is apparent. The dashed line shows an exponential dependence with a parameter $T = 1$ MeV in formula (1.3.20)[32]. This is significantly lower than the $T$ parameter used in all discussed ternary fission models (compare table 1.3.1). For a detailed analysis each fissioning system has to be

---

[30]Only in the Boltzmann model the pairing energy is explicitly included. For the discussed yield ratios the difference $E_{\text{corr}}^{\text{TP}}(^{A-2}_{Z}X) - E_{\text{corr}}^{\text{TP}}(^{A}_{Z}X)$ will attain up to 5 MeV, but this can be due to the somehow artificial parameterization of the pairing energy.

[31]$E_{\text{Coul}}^{\text{TP}}(^{A-2}_{Z}X) - E_{\text{Coul}}^{\text{TP}}(^{A}_{Z}X) \leq 0.3$ MeV.

[32]This is not a real fit, but just an illustration of the qualitative dependence of several fissioning systems.

studied specifically, including the features of the individual models (influence of the Coulomb and correction energies) and the yields of very heavy ternary particles.

It can be concluded that the present models of ternary fission fail to predict the strong decrease of yields for light exotic nuclei. This disagreement cannot be easily removed by "tuning" a single model parameter. Possibly the basic assumption of a direct exponential dependence of the yields on the energy costs holds no longer good for very unfavorable mass splits. A similar overestimation of the experimental yields is found for the heaviest ternary particles [Gön98, Wös99a]. From the investigation of heavy ternary particles a clear dependence between the maximum recorded mass and the mass of the compound nucleus is observed [Wös99a]. The emission of the heaviest ternary particles is interpreted as the limiting case where the system is running out of excitation energy and can no longer afford to emit still heavier ternary particles. The last detectable events are created in cold ternary fission with a remaining excitation energy of few MeV at maximum [Gön97, Gön98].

### 1.6.5.    Improvement of ternary fission models

Including these and other recent measurements, the amount of available yield data from ternary fission was more than doubled in the last years. This gives a solid basis for improving and refining the currently available ternary fission models. While developing such an improved model is beyond the scope of this work, some useful "ingredients" will be discussed in the following:

**Reproduction of hydrogen yields**

As discussed in the introduction, the yield of ternary protons contains a significant contribution of polar events which are assumed to be created in a different mechanism [Sch91]. While coincidence measurements show an equal shift of both mass peaks for most ternary particles, for tritons only the heavy fragment peak is shifted [Sin97]. This could indicate contributions from a slightly different emission mechanism. Thus, it is not unreasonable to exclude the yields of the hydrogen isotopes from a comparison with the model predictions, or to accept an underestimation of the hydrogen yields from the models.

**Scission configuration**

All experimental results point to a dominant creation of ternary particles in the neck region. More restrictions on the configuration can be obtained by trajectory calculations which have to reproduce the experimental energy- and angular distributions, see [Fon70, Obe92, Bau92b, Bou94, Ros94] and further references in [Sin89]. It has been shown that trajectory calculations often cannot determine the scission configuration unambiguously [Dak79, Gue80, Sin83]. A general problem is the definition of time zero. That means an elongated configuration may lead to similar trajectories to a compact one, if the initial kinetic energy of the LCP is changed accordingly to the initial interfragment separation. Therefore a compatible energy spectrum or angular distribution cannot prove a certain scission configuration, but on the other hand some scission configurations (e.g. too compact or too far stretched) can be falsified when they do not allow consistent trajectory calculations. In all statistical models the used temperature should also determine the average initial kinetic energy of the ternary particle, $\bar{E}_0 = 2T$. If a very different start energy is required for the trajectory calculations, the statistical approach becomes questionable.

The correlation of light charged particle emission with other observables like neutron- and gamma multiplicities, kinetic energy of the fission fragments, total excitation energy etc. is discussed e.g. in [Meh73, Mut96b].

Besides results from ternary fission, there are also several other methods to determine the elongation at scission. To achieve a compact scission configuration, a high nuclear friction is required to slow down the fission process. This in turn would lead to an enhanced emission of pre-scission neutrons which could be detected in coincidence measurements.

The approximation of the Coulomb energy as interaction of point-like charges or homogeneously charged spheres is only correct for elongated scission configurations. In compact configurations the deformation and short-range interactions have to be taken into account. This is often done in a simplified way by modifying the nuclear radius used in the Coulomb energy formula. Care has to be taken to make the trajectory calculations with a consistent shape description [Câr80].

**Contribution of individual mass splits**

Some of the ternary models weight the yields calculated for individual mass splits with their abundance in binary fission. This is not fully correct, since, especially for heavier ternary particles, the mass peaks of the fission fragments are considerably shifted due to the nucleons lost to the ternary particle. For most fissioning systems no experimental information is available on the mass splits of the fission fragments in coincidence with the TP. In a good approximation an empirically corrected mass split distribution could be used for the weighting where both peaks are shifted by half of the TP mass [Sin97], if possible with an additional correction for the reduced neutron multiplicity in ternary fission.

Only little experimental information exists on the real contribution of individual mass splits. For cold (neutronless) spontaneous fission of $^{252}$Cf accompanied by $^4$He, $^6$He, $^{10}$Be and $^{14}$C, individual yields have recently been derived with gamma coincidence measurements [Ram96, Ram97, San97, Ram98a]. For $^{10}$Be a yield of $4 \cdot 10^{-6}$ per fission has been reported in coincidence with the fission fragments $^{96}$Sr and $^{146}$Ba [Ram98b].

Table 1.6.7.: Experimentally determined yields for ternary beryllium isotopes from $^{252}$Cf(sf) relative to LRA. The experimental lower cut-off energies $E_{\text{min}}$ for both nuclei are given. Note that the errors are purely statistical and do not account for the uncertainty arising from a Gaussian extrapolation to zero energy.

| $E_{\text{min}}(^4$He$)$ | $E_{\text{min}}($Be$)$ | [all Be]/10000[$^4$He] | [$^{10}$Be]/10000[$^4$He] | Reference |
|---|---|---|---|---|
| 8.3 | 23 | 20.1(20) | | [Cos67] |
| 6 | 15 | 32 | | [And69] |
| <6 | 13 | 65(7) | | [Gaz70] |
| 8 | 22.5 | 164(9) | | [Gra88] |
| 7.8 | 23.5 | | 185(20) | [Dlo92] |
| 8 | 26 | 126(30) | | [Sin97] |

It is known that $^{252}$Cf(sf) emits $3.2(1) \cdot 10^{-3}$ LRA per fission [Rai68, Wil85]. Different values are reported for the ratio of ternary beryllium to LRA. They are summarized in table 1.6.7. While not explicitly measured for $^{252}$Cf(sf), it can safely be assumed that $^{10}$Be contributes about four fifths to the total beryllium yield, as in all other investigated fissioning systems. Roughly one ternary $^{10}$Be is emitted per 100 LRA[33]. Thus, the total $^{10}$Be yield is $\approx 3 \cdot 10^{-5}$ per fission. The single mass split measured in [Ram98b] contributes more than 10 % to the total $^{10}$Be yield. However, this mass split (96:146) is considerably more asymmetrical than the mean mass split measured in coincidence with ternary $^{10}$Be (about 103.5:138.5 before neutron emission [Sin97]). According to

---

[33]Due to the probably large contribution of systematic errors it does not make sense to take a weighted average of the values shown in table 1.6.7.

the fragment mass distributions of [Sin97] only about 3 % of the $^{10}$Be events should be found in coincidence with a light fragment of $A = 96$ or a heavy fragment of $A = 146$. This already includes a summation of all isobaric contributions and neutron evaporation channels. With typical widths for the isobaric distribution in binary fission [Wah88] and the measured neutron multiplicity in $^{10}$Be accompanied fission [Sin97], the contribution of the specific mass split $^{10}$Be-$^{96}$Sr-$^{146}$Ba to the total $^{10}$Be yield should rather be below 1 %, which is in contrast to the experimental result ($> 10$ %). It should be noted that this is not an absolute contradiction, since the results of [Sin97] are only based on ternary $^{10}$Be with high kinetic energies above the experimental energy cut-off at 26 MeV. Moreover, the biasing towards cold ternary events in the analysis of the gamma-coincidence data could enhance the contribution of energetically more favorable mass splits involving even-even-nuclides.

### "Temperature" and population of excited levels

In the statistical models a parameter of "effective temperature" is introduced which determines the probability of accessing energetically unfavorable scission configurations. It is clear that the definition of a temperature for the light ternary particles with few nucleons and a low level density is not really correct. However, if such a temperature is used to describe the production probabilities of different ternary particles, it should also allow the derivation of the occupation probabilities of excited levels in one ternary particle [Mor94]. Valskii [Val76] proposed to sum over all excited levels using statistical factors (see equation (1.3.2)). The same "temperature" parameter should be used which governs the reduction of yields for mass splits with unfavorable $Q$-value. Using a Boltzmann distribution and taking into account the statistical weights as proposed in [Val76], the fractional yield of individual levels $y_i$ should follow:

$$y_i = \frac{(2I_i + 1)\exp(-E_i/T)}{\sum\limits_{j=0}^{\infty}(2I_j + 1)\exp(-E_j/T)}, \tag{1.6.2}$$

with $I_i$ the spin of the level and $E_i$ its excitation energy. Figure 1.6.9 shows the relative yield increase $(1/y_0)$ obtained by including the population of excited levels. Contributions of the lowest states were included where known from literature [Fir96, AS88, AS90, AS91, Til93, AS87, End90]. Only levels decaying by gamma emission are considered. Particle-unstable states decay into lighter nuclei (protons, alphas or neutrons plus the residual nuclei). Since the yields drop significantly towards higher masses, these contributions to the total yield of the break-up fragments can normally be neglected. Only in few cases such events were studied experimentally (see below).

For most isotopes the contribution of the excited levels stays below 50 % of the isotopic yield. For the more exotic isotopes no excited states are known. Anyhow, the contribution of excited states decaying by gamma emission should decrease due to competition of particle emission. Isotopes for which the population of excited levels becomes dominant are: $^{12}$Be, $^{12}$B, $^{14}$B, $^{15}$C, $^{16}$C and some heavier ones. While the inclusion of the statistical weights in the yield calculation would improve the agreement for some even-even-nuclides, also the yields of odd-odd-nuclides (e.g. $^{12}$B, $^{14}$B, etc.) would be increased. Their yields already tend to be overestimated by the discussed models which underestimate the odd-even-effect. An inclusion of the excited states would further enhance the calculated yield and even worsen the agreement.

Solely from the experimental isotopic yields it is not possible to decide on the importance of the population of excited states. An independent, direct determination is necessary. While a lot of experimental data exists on isomeric ratios and the population of short-lived excited states in binary fission, only little experimental information is available on the population of excited levels of ternary particles.
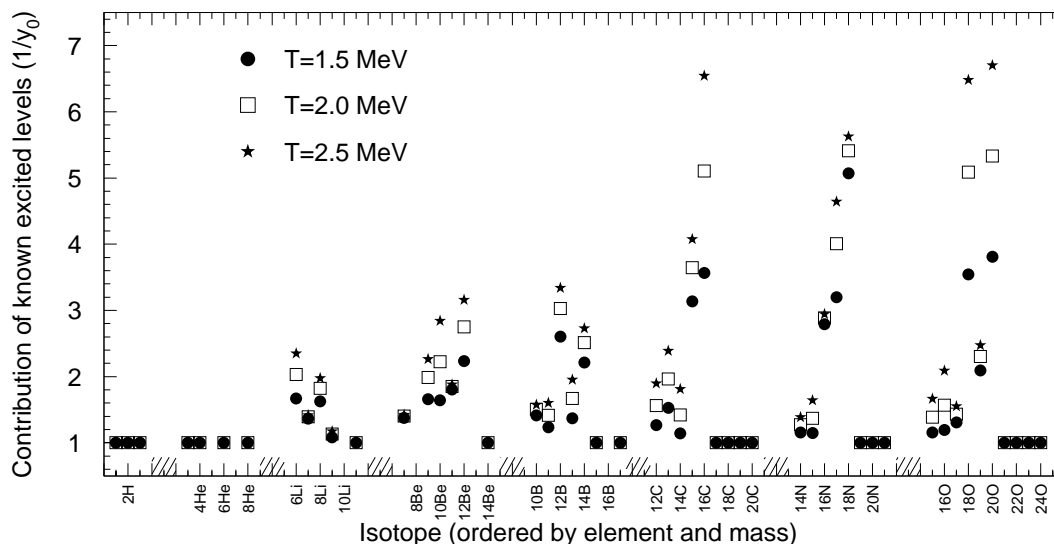
Figure 1.6.9.: Contribution of known excited levels to the statistical weight. Again the isotopes of each element are grouped together in a series. From left to right: $^{1-3}$H, $^{3-8}$He, $^{6-11}$Li, $^{7-14}$Be, $^{10-17}$B, $^{12-20}$C, $^{14-21}$N and $^{15-24}$O.

From the angular distribution of the coincident breakup fragments t and $\alpha$ measured by Kataria et al. [Kat73], Feather [Fea74] deduced a probability of $12 \pm 6$ % of finding $^{7}$Li in a triton-unstable state ($E_x \geq 4.73$ MeV [AS88]). Similarly, for $^{8}$Be he estimated from the data of ref. [Kat73], that $^{8}$Be shall be emitted in about 15 % of all emissions in its first excited state at 2.94 MeV. Mutterer et al. deduced from an enhanced neutron yield in coincidence with $^{7}$Li a population probability of neutron-unstable states ($E_x \geq 2.26$ MeV [AS88]) in $^{8}$Li of 33(20) % [Mut99]. Singer found an evidence for a gamma peak at 3.37 MeV in coincidence with $^{10}$Be, which translates into a population probability of 22(5) % for the first $2^+$ state in $^{10}$Be [Sin97].

This is in contradiction to Ramayya et al. who reported that in $^{10}$Be dominantly the first $2^+$ state at 3.368 MeV is populated, while less population goes directly to the $0^+$ ground state [Ram98b, Ham99]. However, this statement is somehow uncertain as it seems to be difficult to accurately derive low yields from this gamma coincidence data. In a previous publication [Ram96], the total $^{10}$Be yield in coincidence to $^{96}$Sr and $^{146}$Ba differed by one order of magnitude when a double gate on the light or heavy fragment was used: $8.3 \cdot 10^{-6}$ and $7.8 \cdot 10^{-5}$ per fission respectively. A yield of $4.3 \cdot 10^{-5}$ per fission had been reported for the same mass split in [San97]. This is one order of magnitude larger than the yield reported in [Ram98b]!

Assuming thermal equilibrium and using the Boltzmann ansatz (equation (1.3.2)), the temperature parameter $T$ can be estimated from the experimentally determined population of excited levels. With the value of $^{7}$Li $T$ should be in the range of 1.5 to 2 MeV, for $^{8}$Be the result is $T \approx$ 0.9 MeV. The value of 33(20) % for population of neutron-unstable states in $^{8}$Li leads to $T >$ 1.1 MeV. From the $^{10}$Be* population measured in [Sin97], $T = 1.08(9)$ MeV can be deduced while $T \geq 3.7$ MeV would be necessary to populate the excited state with at least double the ground state (corresponding to the result of Ramayya et al.). The contradictions are obvious and show that either the (few) experimental results are inconsistent or the simple description with a Boltzmann distribution is inappropriate. In any case a significant production of excited $^{10}$Be cannot be explained assuming thermal equilibrium and a reasonable nuclear temperature. Another mechanism is necessary. For example the idea of the Rubchenya model, where a nucleon exchange occurs immediately prior to scission, could explain a non-thermal population of excited levels in the light nuclei. Also the sudden snapping of the neck could increase the population of excited states.

It should be noted that the gamma line observed in [Sin96, Ram98b] is amazingly not Doppler broadened as expected from a half-life of 125 fs for the $2^+$ level [Fir96] and a flight time for the beryllium recoils larger than 1 ns. The proposed explanation [Sin97, Ram98b, Ham99] that the gamma is emitted while the beryllium sits in a potential well between the fragments is in strong contrast to typical fission time scales and would undermine the general assumption of a common emission mechanism of ternary particles. Not only the nuclides mentioned before: $^8$Be with $T_{1/2} = 6.7 \cdot 10^{-17}$ s, $^8$Be* with $T_{1/2} = 3 \cdot 10^{-22}$ s and $^7$Li* with $T_{1/2} = 5 \cdot 10^{-21}$ s are accelerated before decaying. It has also been established from $\alpha$-n-correlation measurements that even ternary $^5$He with $T_{1/2} = 7.6 \cdot 10^{-22}$ s [Che72, Mut99], $^7$He with $T_{1/2} = 2.9 \cdot 10^{-21}$ s [Mut99] and $^8$Li* with $T_{1/2} = 2.9 \cdot 10^{-21}$ s [Mut99] are emitted and decay after acceleration. It is difficult to understand why just $^{10}$Be* should not be accelerated during an up to eight orders of magnitude longer time.

In any case it would be very useful to also analyze the fission data taken with the EUROGAM and EUROBALL set-ups[34] for ternary yields.

## 1.7.   Outlook

A comparison of different ternary fission measurements from literature (see appendix A.5) shows that often the differences of the individual yields and energy parameters exceed largely the error bars. In many publications only the statistical or fit errors are given, while in such measurements normally the systematic errors dominate. For the light isotopes the main systematic error is due to the extrapolation of an only partially measured energy distribution. Often the measurements have to stay incomplete due to hardware limitations. For example the maximum high voltage of the LOHENGRIN condenser sets an upper energy limit of about 6 to 6.5 MeV per charge state. On the other hand, in cases where no spectrometer is used and the binary fission fragments are blocked by an absorber foil, only ternary particles with energies above a certain threshold can pass. For heavier isotopes additionally the uncertainty of the ionic charge distribution becomes important. Still the yields are typically reproduced with average deviations of less than 25 % and the average energies are reproduced better than 10 %. Most cases of larger deviations can be explained by clear systematic errors, e.g. an insufficient consideration of background (especially for stable isotopes) or acceptance artifacts. Where necessary, the uncertainties can be significantly reduced with the use of a dedicated set-up or method. Individual isotopes can be measured with high accuracy by measuring a maximum number of different energies and charge states of these isotopes (e.g. in [Wös99a]), but such an attempt requires considerably more beamtime per measured isotope. Presently the uncertainties of the theoretical or semi-empirical models are larger than the experimental uncertainties.

In the last years important information was obtained from multiparameter studies of spontaneously fissioning actinides, see e.g. [Sin97, Ram98a, Ram98b]. It would be very interesting to extend these studies, possibly using the same set-ups, to neutron-induced fission where more detailed information is available from complementary methods on individual yields, etc. A general problem of ternary particle detection with spontaneous fission sources is the high background of decay alphas. It can be removed by shielding the source with appropriate absorber foils, but simultaneously the detection thresholds for ternary particles are increased considerably, for lithium and heavier elements even beyond the most probable energy. With neutron-induced fission of $^{235}$U, the natural alpha background is much less and the detection thresholds could be lowered significantly.

---

[34]Presently data sets with $2.5 \cdot 10^9$ triple- and higherfold coincidence events exist for $^{248}$Cm(sf) from EUROGAM II and $9.7 \cdot 10^9$ for $^{252}$Cf(sf) from EUROBALL III. Inclusion of this data would already reduce the statistical uncertainty of the present evaluation which is based on $9.8 \cdot 10^9$ coincidences from GAMMASPHERE.

On the other hand, LOHENGRIN measurements of yields of $^{247}$Cm(n$_{th}$,f) and $^{251}$Cf(n$_{th}$,f) would enable a comparison with the yields measured in spontaneous fission of $^{248}$Cm and $^{252}$Cf. This would allow to study the relation between the excitation energy of the compound nucleus and the temperature parameter used in ternary fission models.

$^{232}$U(n,f) is another fissioning system where no information on ternary fission yields is presently available. With the study of this system, which differs from $^{233}$U(n,f) by only one neutron, a better insight into the influence of the neutron pairing on the neutron odd-even-effect of ternary particle yields could be gained.

All three proposed LOHENGRIN experiments depend mainly on the availability of suitable targets. While for the heavy actinides it is difficult to find a sufficient amount (some $10-100$ $\mu$g) of isotope-separated material, the problem of $^{232}$U is rather the high dose rate of its decay daughters[35]. Therefore the target material needs to be chemically separated shortly before production and use of the target. Else transport and handling of the target are subject to very strict regulations.

Also other detection method could give new information on ternary fission yields. The neutron-deficient nuclides $^{7}$Be and $^{22}$Na can be searched for with good sensitivity by gamma spectroscopy of chemically separated fission products. The influence of the excitation energy on the yields of heavy ternary particles could be checked by analyzing the integrated mass yields of e.g. $A = 24$. This can be done rather easily by irradiating actinide samples with neutrons or gamma rays of different energy and detecting the high-energy gammas from the decay of $^{24}$Na off-line. If the target impurities are too high, the result could be veiled by other reactions ($^{23}$Na(n,$\gamma$)$^{24}$Na, $^{25}$Mg($\gamma$,n)$^{24}$Na, ... ). In this case it is better to use a tracer nuclide further away from stability, which is less subject to such background. $^{32}$Si would be a good candidate, but its sensitive detection requires more involved techniques like accelerator mass spectroscopy. Such an experiment is analogous to the detection of $^{60}$Fe from far-asymmetric fission [Elh98].

---

[35]The high energy gamma rays of $^{212}$Po are difficult to shield.

# 2. Isotope separation

## 2.1.  Radioactive Ion Beam facilities

Before going into technical details, a rather general description shall give an overview of the fundamental aspects which have to be considered in the design of a powerful radioactive ion beam (RIB) facility[1]. The production and separation process involves several important steps. The numbers (X.) refer to the schematic overview shown in figure 2.1.1:

1. **Primary beam:** A powerful accelerator (1.) is required to provide an intense beam of primary particles. The various types of accelerators[2] differ largely in beam energy, particle flux and beam size.

2. **Target:** The production rate in the target depends on the flux of the primary beam, the production cross-section of the individual target atoms and the number of target atoms exposed to the primary beam (2.). The target size should be matched to the area covered by the primary beam.

3. **Extraction:** For the subsequent use the produced nuclei have to be extracted from the target with a high efficiency. Obviously this task gets more and more difficult with increasing target size. Note that an intense primary beam can cause a hostile environment in the target area (e.g radiation from scattered particles). An access of this area is difficult (3.) or impossible during operation.

4. **Transport:** In the next step the nuclei have to be transported to the end user (6.) who is typically situated at a remote position. In order to avoid losses in this stage the transport capacity (4.) has to be high enough to accept the complete intensity extracted from the target.

5. **Rapidity:** Since the valuable product nuclei have often a short lifetime, all steps between the target and the detection system have to be fast enough. Any delay can cause additional losses (5.).

6. **Selectivity:** Taking into account all points mentioned above will provide an intense beam. Nonetheless this may be completely useless for the end user (6.). Normally the latter requires a pure beam, containing only a particular nuclide. Therefore the discussed stages from production to "delivery" also have to provide sufficient selectivity to exclude excessive impurities of the beam. Typically the user is less interested in the most abundant species, but requests an intense and pure beam of a rather exotic species (7.). This puts even more stringent requirements on the efficiency and selectivity of all stages, including the production method.

---

[1]Often the designation "RIB facility" is used for facilities providing "fast" ion beams. However, also a 60 keV ISOLDE beam is a "radioactive ion beam" and therefore in principle such a low-energy facility also deserves the name "RIB facility".

[2]The primary accelerator can also be replaced by a nuclear reactor (see below).
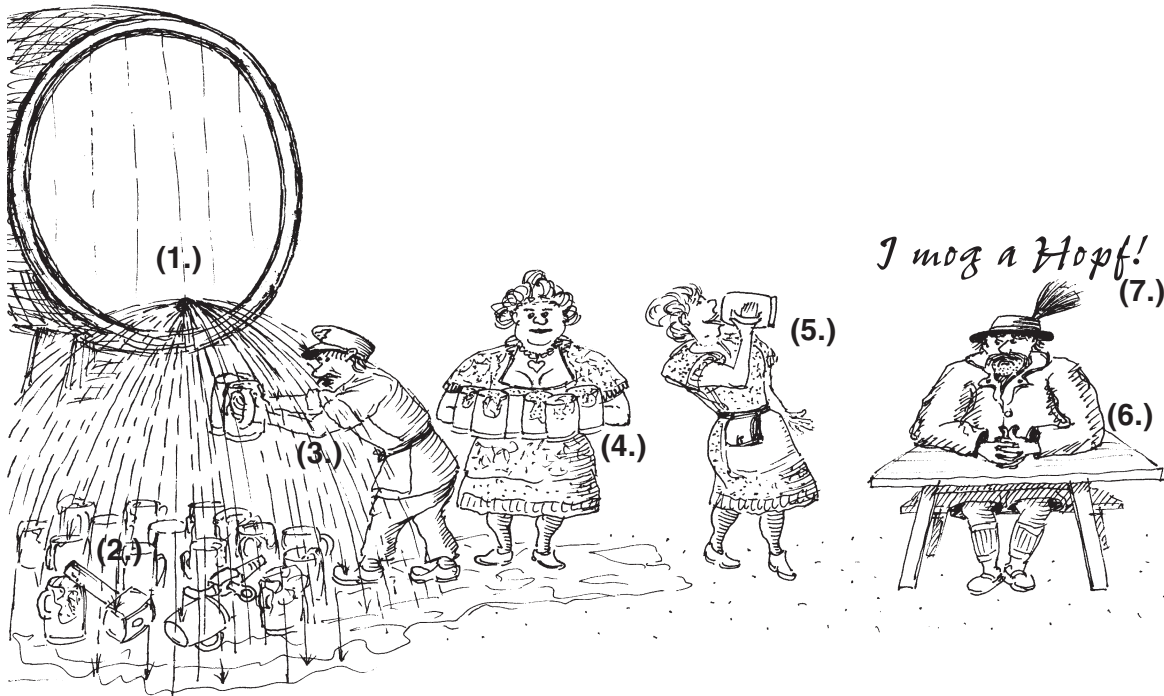
Figure 2.1.1.: Schematic representation of the stages of a radioactive beam facility.

## 2.1.1.   Efficiency of individual steps

The intensity and "quality" of the beam reaching his set-up are more decisive for a user than the technical details of the production. For example for a nuclear spectroscopy experiment the rate of particles detected with the set-up is given by:

$$r = \Phi \cdot \sigma \cdot N \cdot \varepsilon_{\text{target}} \cdot \varepsilon_{\text{source}} \cdot \varepsilon_{\text{sep}} \cdot \varepsilon_{\text{transp}} \cdot \varepsilon_{\text{det}}. \tag{2.1.1}$$

Here, $\Phi$ is the flux of primary particles provided by the accelerator, $\sigma$ the cross-section to produce the desired isotope by interaction of the primary beam with the target atoms, $N$ the number of target atoms exposed to the primary beam, $\varepsilon_{\text{target}}$ the release efficiency from the target and $\varepsilon_{\text{source}}$ the ion source efficiency which includes the ionization efficiency and the extraction efficiency. $\varepsilon_{\text{sep}}$ accounts for losses in the mass separator, $\varepsilon_{\text{transp}}$ for a possibly reduced transmission to the experimental set-up and finally $\varepsilon_{\text{det}}$ for the efficiency of the detector set-up including possible coincidence requirements. Note that the decay losses are included in the efficiencies of the single steps, i.e. the individual efficiencies $\varepsilon_{...}$ depend on the lifetime of the isotope under consideration.

For a post-accelerated beam of radioactive isotopes some more factors have to be added which account for the efficiencies of the individual parts during acceleration: the fraction of the ionic charge state to be used, the efficiencies of the individual accelerator modules, losses due to a mismatch between the time structure of the beam and the duty cycle of the accelerator, etc.

The production of exotic radioactive nuclei requires a big effort and is fundamentally limited in intensity. Therefore the produced nuclei are very "valuable" and have to be extracted with the best possible efficiency. The total efficiency is determined by the product of the efficiencies of each step. This means that the losses in the individual steps may easily accumulate to huge total losses. Equation (2.1.1) which looks like a simple product is in fact more complicated since the factors are partly correlated. Thus, the optimization of one individual part might worsen the total efficiency. For example an ion source with a good efficiency might have a bad emittance thus reducing the transmission of a following mass separator or the capture efficiency of an ion trap.

Moreover some of the factors depend not only on the element or mass of the isotope considered, but also strongly on its lifetime or other nuclear and atomic properties. Therefore, in principle the complete ISOL system has to be optimized individually for each individual isotope. In practice a compromise has to be found between this individual optimization and the universality of the used system.

In most RIB applications a high intensity of an exotic beam is of no use if it is accompanied by an overwhelming amount of other radioactive isotopes. Thus, the separation process has to have not only a good efficiency for one isotope (the desired one), but also a very small "efficiency" for others to suppress contaminating isobars.

For short-lived isotopes the decay losses in the separation process become an important factor. To limit these losses the separation has to be fast compared with the half-life of the nuclides.

The three key requirements for all individual parts of a RIB facility are thus *efficiency*, *selectivity* and *rapidity*.

## 2.1.2.    Comparison of different RIB facility concepts

It is not easy to find a suitable figure of merit for the comparison of different RIB facilities. Many individual parameters have been proposed and used, but all of them have a fundamental weakness and can be misleading if used solely. This is seen at the example of the subsystem "driver beam & target".

### Driver beam intensity

The performance of existing first generation RIB facilities often depends strongly on the capabilities of the driver accelerator. However, for the projected next generation RIB facilities using thermal neutrons or high-energy protons and light[3] ions as primary beam, the production rate in the target will no longer be limited by the intensity of the provided beam. The limitation is rather due to the associated power which has to be removed from the target and which exposes the target construction to high thermal and mechanical stress. The energy and intensity of the primary beam is "only" limited by economical considerations, but the power deposited in the target is fundamentally limited by technological and physical reasons!

### Production cross-section

Figure 2.2.2 (see page 56) shows the cross-sections for the production of rubidium isotopes with different methods. Obviously the cross-sections differ by several orders of magnitude when using different projectiles. However, not only the cross-section, but also other features of the reaction mechanism have to be considered. For example thermal neutron induced fission provides very high cross-sections, but can only be applied for neutron-rich nuclides of medium mass ($75 \lesssim A \lesssim 160$). Moreover the produced nuclei are emitted into a solid angle of $4\pi$ which badly matches the low angular acceptance of a recoil separator. Another example are fusion-evaporation reactions (not shown in figure 2.2.2). They have high cross-sections, but a small excitation width. This severely limits the effective target thickness.

It should be noted that on the one hand a sharp peaking of the production cross-sections in a certain area of the chart of nuclides makes such a production method less universal, but provides on the other a high intrinsic selectivity in the first stage of the production and separation chain.

---

[3]Accelerators for very intense beams of heavy ions are still under development.

**Luminosity**

The product of primary beam flux and number of target atoms within the effective target thickness[4], called luminosity ($L = \Phi N_{\text{eff}}$), is a useful parameter when treating reactions of comparable cross-sections or when comparing accelerators with the same or similar primary beam (e.g. in high-energy physics). However, for RIB applications it veils completely the fact that the cross-sections of different production mechanisms are not at all comparable and differ by orders of magnitude. The use of the luminosity as a classification parameter is therefore only justified in very special cases.

**Production rate**

The product of the driver beam intensity, the cross-section and the effective target thickness gives the production rate in the target. The fact that an optimization of the latter does not necessarily mean an optimum ion beam intensity is shown in the following, admittedly extreme, example: In a reactor-based facility not the neutron "current" is given, but the neutron flux. This stays relatively constant over a rather large region (tenth of cm)[5]. Thus, the production rate can be easily increased by increasing the target size and the uranium concentration in the target. The straightforward optimization of the production rate in the target would result in nothing else than a standard power reactor. There the total production rate of radioactive isotopes $r$ is roughly given by twice the ratio of the thermal power and the energy released per fission: $r \approx 2 \cdot (3200 \text{ MW})/(200 \text{ MeV}) = 2 \cdot 10^{20} \text{ s}^{-1}$. On the other hand the construction of a power reactor prevents the release of short-lived[6] fission products from the core, making it completely useless as a direct ISOL target.

At high target temperatures most of the power is emitted by radiation. Therefore the maximum tolerated primary beam current scales roughly with the target surface. With a given beam and target diameter, a surface increase is equivalent to an increase in length and volume of the target. However, with increasing target volume the path length an atom spends in random walk before "finding" the extraction hole will increase considerably. Correspondingly the decay losses for short-lived species are increased and the release efficiency decreased. A more suitable figure of merit which accounts for this fact could be e.g. the production rate per target volume. In fact the release efficiency is a more complicated function of the target geometry, therefore also this ratio is not very suitable.

One could follow this argumentation through all other steps of the separation process and will find that the only figure of merit which allows a direct comparison for practical applications is the radioactive ion beam intensity and purity delivered to the user's set-up. Even this has to be compared under the boundary condition of a certain required beam energy. Thus, when judging RIB facilities there is no other way than directly comparing the provided beam parameters. For projected facilities where these are not known, they have to be calculated from all individual steps using a *reasonable* scaling from existing facilities.

---

[4]When passing the target the primary beam will be decelerated. The range where its energy lies within the excitation function determines the effective target thickness.

[5]In the picture of figure 2.1.1, this "primary accelerator" would correspond to the legendary, inexhaustible beer lake into which the target is completely immersed.

[6]Some commercially available radio-isotopes can indeed be extracted from burned reactor fuel elements in reprocessing plants, but this method is clearly restricted to rather long-lived ($T_{1/2} \geq$ months) fission products.

## 2.2.   Production mechanisms

### 2.2.1.   Production of neutron-deficient nuclei

On the proton-rich side fusion-evaporation, transfer and direct[7] reactions are selective processes which produce only a small number of different nuclei. However, the excitation functions of these reactions are quite narrow and only allow the use of thin targets ($\lesssim 0.1$ g/cm$^2$). For thick targets ($\gg 1$ g/cm$^2$) beam energies above some 10 $A\cdot$MeV are required which are only compatible with the unselective reactions spallation and fragmentation. In spallation reactions one (heavy) fragment is created by evaporation of protons, neutrons and light ions. In (multi-)fragmentation the target nucleus is broken into several smaller fragments. The relative performance of the different methods differs from isotope to isotope. It is therefore discussed at the example of specific elements in chapter 4.

### 2.2.2.   Production of neutron-rich nuclei

The principal production method for light ($Z \lesssim 24$) and very heavy neutron-rich nuclei ($Z \gtrsim 68$) is fragmentation. With sufficient beam energy either a heavier projectile or a heavier target can be fragmented. Generally the production cross-sections for light neutron-rich fragments tend to increase with the bombarding energy. For example the heavy sodium isotopes could be studied even up to $^{35}$Na at the PS on-line separator (26 GeV protons) [Lan83]. Recently the use of 1.4 GeV protons from the PS Booster gave for different fragmentation products a yield increase by up to a factor four in comparison with 1 GeV protons [Geo99] (see also section 4.12).

Multi-nucleon transfer is another reaction mechanism, providing a good alternative for the production of neutron-rich nuclei in regions not accessible by fission (see e.g. [Ryk89]). It will be discussed in section 4.12.

#### Fission

For neutron-rich nuclei of medium mass the favorite production mechanism is fission of actinides. Due to the high $N/Z$ ratio of the latter, the products also carry a neutron excess. Fission can be induced by various projectiles. Figure 2.2.2 shows a comparison of production cross-sections for rubidium isotopes from a uranium target. The values for fission of $^{238}$U by protons were taken from [Tra72] (40 MeV), [Ama67] (150 MeV), [Bel80] (1 GeV) and [Kla68] (10.5 GeV). For thermal neutron induced fission of $^{235}$U the evaluation by Wahl [Wah88] was used up to $^{97}$Rb. The experimental values for $^{98,99}$Rb were taken from [Rud91]. For fast fission of $^{238}$U the independent yields of [Rud94] were normalized with an average cross-section of 0.3 barn for a typical reactor neutron spectrum. The cross-sections for $^{12}$C bombardment of $^{238}$U targets were taken from [SS82] and those for reactions of a 750 $A\cdot$MeV $^{238}$U beam in inverse kinematics with a beryllium or lead target were taken from [Eng98] and [Sch98b], respectively.

#### Neutron-induced fission

Thermal neutron induced fission has been used for forty years for on-line separation of radioactive isotopes [KH51]. Several actinide isotopes with high fission cross-sections could be provided in sufficient quantities for an ISOL target ($^{233}$U, $^{235}$U, $^{239}$Pu, $^{241}$Pu, $^{241}$Am, etc.). However, due to practical problems with trans-uranium targets (higher vapor pressure than uranium and very strict safety regulations) presently only the uranium isotopes (mainly $^{235}$U) are used in reactor-based RIB facilities.

---

[7]For example (p,$x$n) or ($\alpha$,$x$n) with few emitted neutrons.
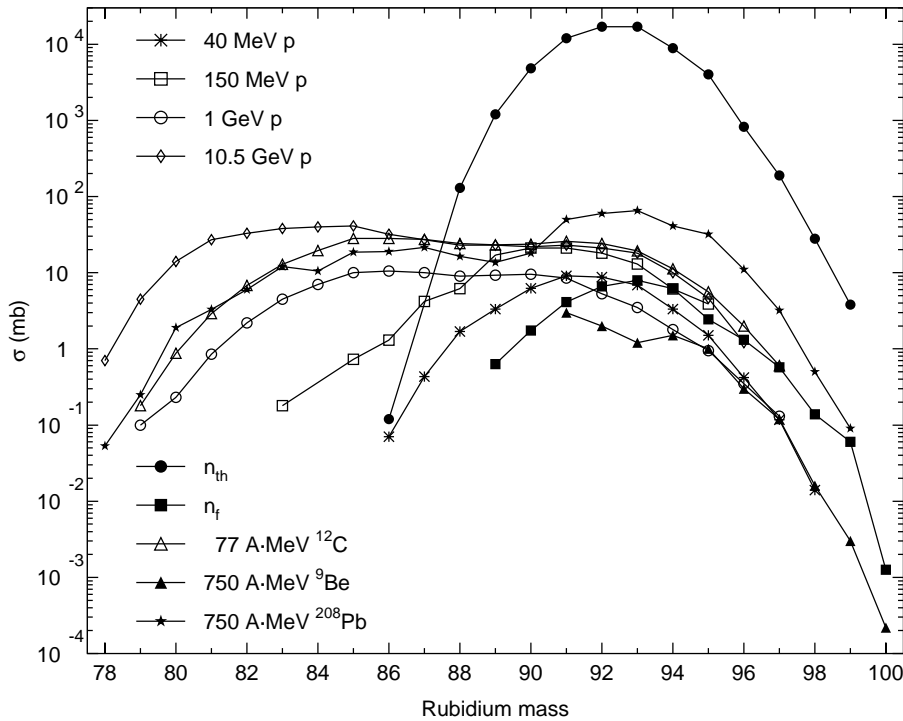
Figure 2.2.1.: Cross-sections for the production of rubidium isotopes from $^{238}$U and $^{235}$U, respectively. This is a supplemented version of the "evergreen-picture" e.g. shown as fig. 9 in ref. [Rav94]. The references are given in the text.

The ternary products from thermal neutron induced fission[8] discussed in the first chapter have relatively small yields and reactor-based facilities are not competitive with accelerator-based facilities in this region. It is, however, worthwhile to note that they can still provide e.g. $^8$Li (some $10^7$ ions per s) and $^9$Li (some $10^5$ per s) [Kös95]. With high branching ratios for $\beta\alpha$ and $\beta$n emission, respectively, these isotopes are useful for in-situ calibration of particle detectors and free of long-lived isobars which could contaminate the set-up.

Fast neutron induced fission has the advantage that $^{238}$U can be used as a target which provides three more neutrons. However, with increasing excitation energy, neutrons can be evaporated from the compound nucleus prior to fission. This reduces the probability for first-chance fission (n,f) but increases the probability for second-chance fission (n,nf), third-chance fission (n,2nf), etc. The opening of the ($x$nf) channels can be seen in the stepwise increasing total fission cross-section. Also the average number of neutrons emitted from the more excited fission fragments increases with increasing neutron energy. The dependence of the average number of evaporated neutrons on the neutron energy was summarized for several fissioning systems in ref. [Man72]. Extrapolating the given empirical relations one finds that around 20 MeV neutron energy an average of about $\bar{\nu}_p = 5.4$ prompt neutrons are emitted. Thus, the average $N/Z$ value of the fission fragments drops to 1.54 which is the value for $^{235}$U($n_{th}$,f) with $\bar{\nu}_p = 2.41$. With further increase of the neutron energy the average $N/Z$ ratio of the fragments continues to decrease (see e.g. the study of Zoeller and others [Zöl95a, Zöl95b] up to 500 MeV neutron energy).

The same is true for other projectiles, see e.g. Ledoux et al. [Led98] who measured the increase of the neutron multiplicity when raising the proton energy from 475 MeV to 2 GeV.

---

[8]It cannot be excluded that the ternary yields increase with excitation energy. Thus, they can give a certain contribution to the observed yields of light neutron-rich isotopes from high-energy proton bombardment of a uranium target, but the major part of the production cross-section will still be due to fragmentation.

However, for RIB applications individual yields of relevant neutron-rich isotopes (e.g. $^{132}$Sn) are more important than the discussed average values. It is well known that the mass distributions get broader in high-energy fission, i.e. the valley of symmetry is filled up and the wings reach further out to far asymmetric fission. Unfortunately most of the elements produced in symmetric fission are refractory ($40 \leq Z \leq 46$) and are thus practically not released from an ISOL target. An advantage remains only for few cases like lighter silver and cadmium isotopes. Also for many short-lived isotopes populated in far asymmetric fission (of the elements iron, cobalt, nickel and the lanthanides) there is no significant advantage for fast neutron induced fission until an ISOL actinide target with rapid release of these elements is found (see e.g. section 4.4).

While mass yields have been determined for many fissioning systems over wide ranges of excitation energies, much less data exist on isotopic yields of exotic isotopes. Radiochemical methods give good information on cumulative mass yields, but the determination of independent yields[9] of short-lived nuclei is more difficult. For an overview of available methods see ref. [Den86].

Data on thermal neutron induced fission have been collected over many years, e.g. at the recoil separator LOHENGRIN (for $^{235}$U(n,f) see [Lan79, Sid89]) and at the ISOL separator OSIRIS (for $^{235}$U(n,f) see [Rud90]). Wahl gave a summary of measured yields from $^{235}$U(n$_{th}$,f), $^{233}$U(n$_{th}$,f), $^{239}$Pu(n$_{th}$,f) and $^{252}$Cf(sf) together with an empirical model which allows to inter- and extrapolate the yields to other nuclei [Wah88]. Another model has been proposed for the extrapolation of yields in far asymmetric fission [Fau94]. These models give predictions with sufficient reliability for RIB applications.

On the other hand for fast neutron induced fission the used model calculations have more degrees of freedom and react sometimes sensibly on small changes of parameters [Ric99]. Also less experimental information exists. A dedicated ISOL separator had been built to measure independent yields of Rb (up to $^{97}$Rb) and Cs (up to $^{146}$Cs) isotopes[10] from fission of $^{238}$U in a reactor neutron spectrum [Bal74]. Only recently programs have been started to extend the measurements towards more exotic isotopes and other elements (e.g. Sn). At OSIRIS the yields of $^{238}$U(n$_f$,f) were measured [Rud94]. Similar measurements were also performed for $^{233}$U(n$_f$,f) [Gal99].

Also plans exist to measure the independent yields of most fast fission products simultaneously by detecting their characteristic gamma lines with a powerful Ge detector array [Joh99]. However, the analysis to extract a complete yield map is extremely tedious and the lowest detectable yields are limited by statistics and background to some $10^{-6}$ to $10^{-4}$ per fission which is still far away from the detection limit of a recoil separator or ISOL system.

A dedicated ISOL facility is very useful for the reliable determination of low yields in fast neutron induced fission. Such test facilities are presently used or in preparation to study yields of $^{238}$U(n$_f$,f) at Orsay (PARRNE), Argonne and Legnaro. The "simulation" at an existing ISOL facility, e.g. by placing a thick spallation target in front or beside of a standard UC$_x$/graphite target at ISOLDE, ISAC or IRIS is also possible. Such an experiment was recently performed at the IRIS facility by placing a tantalum rod beside a standard UC$_x$/graphite target [Nolen].

### Charged particle induced fission

Fission can also be induced with charged particles of sufficient energy. Primary beams of protons, alphas and heavy ions have been used for a long time at ISOL facilities. Compared with neutrons they have two intrinsic drawbacks:

---

[9]The independent fission yield is the number of atoms of a specific isotope produced directly per fission. The cumulative fission yield includes additional contributions from decay of precursors.

[10]Rb and Cs are good candidates for such measurements. They diffuse rapidly in graphite matrices and are easily surface ionized, giving a relatively constant and high separation efficiency. Moreover they are complementary fission fragments ($Z$(Rb)+$Z$(Cs)=92), permitting a cross check of the neutron multiplicity.

1. While in neutron-induced fission the target is only heated by the "useful" fission reaction which provides the radioactive isotopes, in charged-particle induced reactions the electronic stopping power exceeds the nuclear stopping power by three to four orders of magnitude. This means that a lot of kinetic energy of the projectiles is dissipated in the target without inducing a nuclear reaction. With a technologically given limit for the maximum target heating, the maximum fission rate per target volume will be lower in charged-particle induced fission than in neutron-induced fission.

2. The intrinsic selectivity of fission, i.e. the unique production of neutron-rich isotopes, is lost when using high-energy projectiles. There spallation and fragmentation reactions will produce simultaneously neutron-deficient nuclides which can act as beam contaminants. High effort has to be spent to remove these isobars later on.

### Other fission sources

Even the use of an intense electron beam has been proposed for an ISOL facility [Dia99]. However, of all primary beams discussed here, electrons have by far the worst ratio of target heating to production rate (only about $5 \cdot 10^{11}$ fissions per kW for 30 MeV electrons). Therefore the electron beam will not be sent directly onto the production target, but is stopped in a converter target and the produced Bremsstrahlung induces photofission in a subsequent ISOL target [Dia99].

Occasionally proposed spontaneous fission sources are absolutely no alternative as a production target for a high-intensity RIB facility. Sufficient quantities of such sources (e.g. $^{252}$Cf) are not available[11] and, even more important, could not be handled! While the activity of a production target in an ISOL facility decreases rapidly from its maximum value (up to some 10 kCi) after switching off the projectile beam, a spontaneous fission source cannot be switched off.

### Energy dependence of (p,X) cross-sections

At low proton energies ($E_\mathrm{p} \lesssim 100$ MeV) the yields of medium-mass nuclei are mainly due to fission. As in neutron-induced fission the elemental yields of medium-heavy isotopes are well described by a single Gaussian, peaking at isotopes with a slight neutron excess (e.g. $^{91}$Rb or $^{137}$Cs). Due to an enhanced neutron emission the maximum of the peak shifts towards lower $N/Z$ ratios with increasing proton energy. Above about 500 MeV proton energy a second peak on the neutron-deficient side (e.g. around $^{129}$Cs) appears [Fri63]. This causes a widening of the total peak width towards lower $N/Z$ ratios.

For the detailed behavior on the very neutron-rich side less data exist. With off-line measurements [Fri63, Ale63] the short-lived isotopes cannot be accessed. ISOL facilities allow to reach out much further (see e.g. [Bel80]), but for very short-lived nuclei ($T_{1/2} \ll \tau_\mathrm{release}$) the errors due to decay-loss-corrections become important. The cross-sections of these nuclei could be measured better with recoil separators[12], but the unfavorable kinematics will largely reduce the acceptance for light projectiles and heavy targets. Recently experiments were performed at the GSI fragment separator FRS where these cross-sections are measured in inverse kinematics, i.e. with a heavy ion beam on a light[13] target (hydrogen and deuterium). Cross-sections from H($^{197}$Au,X) [Far98, Ben99a], H($^{208}$Pb,X) [Wla00], H($^{238}$U,X) and D($^{238}$U,X) [Cas01, Ric01] were determined. Fortunately these experiments were performed at beam energies of 750-1000 $A \cdot$MeV which is just identical to the

---

[11] The annual production of $^{252}$Cf at the high-flux isotope reactor in Oak Ridge is about 500 mg [Erd98c]. 300 times this amount would be required to reach $10^{14}$ fissions per s!

[12] The cross-sections for production of light isotopes in 800 MeV induced reactions could e.g. be measured with the TOFI spectrometer (see ref. [Ree91]).

[13] Also many experiments with heavy targets were performed, but these are less suitable for a direct comparison with ISOLDE yields.

typical proton beam energy at ISOLDE PSB[14]. The derived cross-sections are thus of great value for a cross check of the measurements from ISOLDE and for an improvement of the models which are used for cross-section predictions.

Engelmann has thoroughly studied the fission yields from the interaction of a 750 $A$·MeV $^{238}$U beam with a Be target [Eng98]: he has shown that even at this high kinetic energy a significant part of the nuclei undergoes low-energy fission. In the far asymmetric region the typical features of fission like the odd-even-effect and an increase of yields at the $N = 50$ shell are found. With the increasing width of the mass distribution the yields in the far asymmetric region increase drastically compared with thermal-neutron induced fission. On the other hand the isobaric width ($\sigma_Z(A)$) found in [Eng98] and [Don98] is comparable to that of thermal-neutron induced fission. It was shown in ref. [Ben98] that e.g. the most neutron-rich nickel isotopes are mainly produced in nuclear fission. Therefore the production cross-sections are nearly identical for light (Be) and heavy (Pb) targets. For a given energy loss in the target, a beryllium target allows to reach the highest yields for very neutron-rich fission products from a relativistic $^{238}$U beam. However, the production of less neutron-rich isotopes in electromagnetic fission and of neutron-deficient nuclides by fragmentation increases with the mass of the target atoms.

It is interesting to note that not only the beam energies of ISOLDE and the GSI-FRS are comparable, but also the typical target thickness in mol/cm$^2$. A standard UC$_x$/graphite target at ISOLDE (50 g/cm$^2$) has a thickness of 0.2 mol/cm$^2$ which is identical to that of a typical fragmentation target at the FRS with 2 g/cm$^2$ Be. However, the average beam intensity is quite different: about 2 $\mu$A of protons at ISOLDE and some particle nA of $^{238}$U at the GSI (projected intensity for the end of 1999). That means the production rates in the target are higher by orders of magnitude at ISOLDE. How these production rates translate to final beam intensities for the user will be discussed in chapter 4.

## 2.2.3.   Collection of decay products

Of a certain importance is the method to "milk" radioactive decay products from a stock of long-lived mother nuclides. Compared with a complete on-line facility these experiments can be performed with a reduced effort (once a suitable source is obtained) and still allow to gain new spectroscopic information (see e.g. [Lia99]). An interesting combination is the production of a long-lived source at an isotope separator and the subsequent separation of decay daughters with a second isotope separation. In certain cases this method can give an excellent beam purity, e.g. by collection of $^{223}$Ra and $^{225}$Ra at ISOLDE and separation of daughters in the Pb and Bi region with the LISOL facility [Ver99].

## 2.2.4.   Summary

Neutrons are clearly the optimum projectiles for an efficient and selective production of medium-mass neutron-rich nuclides. The yields of most isotopes which can be separated from the present ISOL target materials behave similarly for thermal and fast neutron induced fission. Therefore this choice is rather a technical question than a matter of principle. High energy protons allow to use different targets for the production of isotopes all over the chart of nuclides, but the reactions are rather unselective. The low-energy fusion-evaporation, transfer and direct reactions are not able to produce very high beam intensities, but have a high intrinsic selectivity which makes them competitive for nuclear spectroscopy experiments on the neutron-deficient side. High-energy heavy ion beams have a significantly higher specific energy loss causing a high thermal load of the target

---

[14]This is one of the few cases where the cross-sections are comparable and it makes sense to use the concept of luminosity.

and are presently still limited in the primary beam intensity. However, in certain regions the gain in cross-section overcompensates the loss in effective target thickness compared with high-energy protons. Heavy ions are the only projectiles, which allow to access certain isotopes and give a larger flexibility in the choice of the target material in other cases.

To conclude: there is no single primary beam which offers optimum conditions for all regions of the nuclide chart. On the contrary, the particle and energy of the primary beam is the first parameter which has to be individually adapted for the production of the desired radio-isotope. Clearly a compromise has to be found between the individual optimization in this stage and the universality of the facility, but it should be kept in mind that a change in the production mechanism can easily affect the production rate and selectivity by orders of magnitude.

## 2.3.   Separation methods

The search for new isotopes goes towards more and more exotic nuclides with extreme ratios of protons to neutrons. The production cross-sections for exotic nuclei decrease considerably and more efficient and selective methods are required to separate the few exotic nuclei from the bulk of other (radioactive) nuclei. Going from the valley of beta stability to the driplines, the lifetimes decrease by many orders of magnitude and the separation method has to be fast enough to avoid excessive decay losses. To decide on the suitability of a separation method it is important to remember the main requirements: *efficiency*, *selectivity* and *rapidity*.

The presently used isotope separators can be classified into four types:

### In-flight separation

In-flight separation includes recoil and fragment separators. In a recoil separator the particles pass with the kinetic energy released in the reaction, e.g. fission. In a fragment separator the momentum of the fragments is mainly given by the center-of-mass movement of the projectile/target system (in fusion reactions) or by the projectile beam (in fragmentation). The nuclei leave the target highly ionized and are separated by means of magnetic and/or electric fields. When separating according to $A/q$, the ionic charge state distribution results in a loss of efficiency (only the ions with one charge state are separated at a time) and selectivity (due to interference with isotopes of identical or close-by $A/q$ ratios). These problems are eliminated with relativistic beam energies where practically all ions are fully stripped. The $Z$ identification can be done via the specific energy loss with $\Delta$E/E telescopes. The $Z$ identification gets easier at higher energies (larger difference in $\Delta E$) and a real $Z$ separation in space becomes possible by placing an energy degrader at an intermediate position of the spectrometer. At lower energies gas-filled magnets provide a valuable alternative. Here, the initial ionic charge is replaced by a mean ionic charge which in turn depends on $Z$. The separation follows about $A/Z^{1/3}$ [Ghi88]. Recently the competitiveness of the latter separation method was impressively confirmed with the possible discovery of element 118 at the Berkeley Gas-filled Separator (BGS) [Nin99].

All elements can be separated in-flight and the separation time is given by the flight time through the separator, typically some $0.1 - 2$ $\mu$s.

The targets have to be thin enough to prevent excessive energy loss in the target. The optimum thickness is determined by the accepted energy range of the recoil separator which varies between about 0.4 mg/cm$^2$ at LOHENGRIN (fission products with $0.5 - 1.5$ $A$·MeV) and several g/cm$^2$ at the FRS (GSI) (for 1000 $A$·MeV beams). At high beam energies the main limitation of the production rates is presently the available primary beam intensity.

The fast secondary beams can be used directly for subsequent experiments (mass spectroscopy, scattering, Coulomb excitation, breakup reactions, etc.), but if a deceleration is required, the

transversal emittance increases and large transmission losses can occur. Also the efficient focusing and stopping of the beam in a small area (e.g. for gamma spectroscopy) is difficult.

## IGISOL

In an IGISOL (Ion Guide Isotope Separator On-Line) the reaction products recoiling from the target are stopped in a gas cell filled with helium or argon. In charge-changing collisions the ionic charge decreases rapidly to $1+$ and remains constant for a while, since neutralization does not occur in collisions with the buffer gas, but requires an interaction with impurity molecules ($O_2$, $N_2$, etc.)[15]. In contrast to in-flight separators, practically all initial ionic charge states are collapsed into one ($1+$) and the initial energy distribution, often with a large spread, is replaced by a well defined beam energy, given by the extraction voltage. The total target thickness can be increased to the maximum range of the reaction products ($\approx 10$ mg/cm$^2$ for fission products) or even beyond if a stack of individual targets is used. The method has practically no chemical selectivity and can be applied to nearly[16] all elements. This makes it the presently leading method for the separation of short-lived fission products of refractory elements in the symmetric ($40 \leq Z \leq 46$, see e.g. [Wan99]) and far asymmetric fission ($26 \leq Z \leq 28$, see e.g. [Fra98a]).

The separation time is given by the time to reach charge state $1+$ and the evacuation time from the target chamber, which is of the order of some ms.

The beam emittance and energy spread is generally worse than at ISOL facilities (see below), but can be improved with sextupole (or more generally multipole) ion guides, so-called SPIGs. Thus, mass resolving powers of about 1000 can be reached which are comparable to that of a standard ISOL mass separator. Even collinear laser spectroscopy experiments requiring very good beam quality were already performed at the IGISOL facility in Jyväskylä [Bil97, Lev99].

An IGISOL variant with higher $Z$ selectivity is obtained by combination with an element specific resonance ionization laser ion source. The residence time in the gas is increased to reach full neutralization. Then the atoms of a certain isotope are selectively reionized with a laser ion source (see below) and extracted. Such an ion guide laser ion source (IGLIS) is under operation at the Leuven ISOL separator [Kud96]. To increase the element selectivity, remaining ions are removed from the extraction region by an electric field prior to the laser pulse. Here, the separation time is increased to about 100 ms. IGRIS, a similar set-up with faster extraction ($\sim 1$ ms) is used for laser spectroscopy of short-lived isotopes and isomers of transuranium elements [Bac97].

Upgrading the beam intensity of an IGISOL facility by orders of magnitude to reach that of ISOL facilities (see below) would cause major technical problems. The operation of large amounts of buffer gas in an extended pumping system would disperse the produced activity over a large area, creating huge problems for radiation protection. Further problems could arise from plasma creation in the buffer gas due to the high current of the primary beam and of the produced ions [Den97].

## ISOL

A further drastic increase of the target thickness can be obtained by stopping the reaction products not in an external gas cell, but in the target itself. Thus, no longer the range of the recoils, but the range of the primary beam determines the maximum target thickness. For most elements the target has to be heated to high temperatures to allow a rapid diffusion and effusion of the radio-isotopes. An attached ion source is used to reionize the completely neutralized atoms. This technique is

---

[15]The binding energy for the valence electron of the produced ions is much smaller than the first ionization potential of the buffer gas, but comparable to the ionization potential of the impurity molecules. In fact, already for the step from $2+$ to $1+$ the impurities play an important role, i.e. a well defined level of impurities is required for optimum operation [Den97].

[16]Obviously less efficiently for the noble gases with high ionization potential.

known as isotope separation on-line (ISOL)[17]. Presently targets with thicknesses of up to about 200 g/cm$^2$ are employed. The release time varies strongly depending on the chemical properties of target and product elements. Refractory elements are practically not released. In certain cases a high chemical selectivity can be achieved by an appropriate choice of the target material or ionization mechanism. At several occasions the status of the ISOL technique has been thoroughly reviewed by Ravn et al. (see e.g. [Rav79, Rav89, Rav98]).

A variant of the ISOL technique (e.g. at the GSI on-line separator) uses only thin targets which the product nuclei can leave with the recoil momentum. They are implanted into a catcher which is optimized for rapid release of the desired chemical species. Thus, the difficulty to find a target material which has not only optimum chemical properties for fast release, but moreover high production cross-sections, is circumvented by separating the functions of target and catcher. The same advantage is obtained by a combination of projectile fragmentation with an ISOL target. With primary heavy ion beams (e.g. at the SPIRAL facility, GANIL), the target material can be chosen nearly freely. This allows to optimize the target material for fast release even of elements which are chemically similar to the "mother element"[18], e.g. lanthanides produced in the fission of uranium.

**Chemical separator**

In chemical on-line separators the product isotopes pass a chemical separation process as atoms, ions or bound in molecules. The transport medium can be liquid or gaseous. A very good chemical selectivity is obtained, but the mass information has to come from the production mechanism[19]. As in the case of ISOL separation, thick targets can be employed and high separation efficiencies are reached. Applications where the separated isotopes are not only detected, but used for a subsequent application (implantation, post-acceleration, etc.) require them to be transformed into an easier handable form. Often this is done by reionization. Obviously chemistry plays also an important role in ISOL targets and there is no clear dividing line between a chemical separator with a subsequent ionization and an ISOL system. A review on chemical separation methods is given e.g. in ref. [Her82].

**Other methods**

The gas- or aerosol-jets do not provide a real separation, but are useful for rapid transport of reaction products and are mainly employed in combination with other separation methods. Examples are the gas-jet ISOL at JAERI for neutron-rich lanthanides [Ich98], the aerosol-jet at the Chalk River ISOL facility [Kos97a], the He-jets of the SIRIUS facility in Strasbourg [Zir74] and the HELIOS separator in Mainz [Maz81] or a mobile aerosol-jet using carnaubawax [Key94]. Thermoseparators have been used successfully to increase the chemical selectivity by combination with the OSIRIS ISOL separator [Rud81] and the JASNAPP facility in Dubna [Bey81].

Combining several of the separation methods presented above often allows to further improve the efficiency and/or the selectivity of the separation. Several projects aim at the use of an in-flight separator for pre-separation and a subsequent IGISOL set-up for the preparation of a low-energy 1+ beam with good beam quality. In the SHIPTRAP project [Sch01] the beam of product nuclei

---

[17]In fact all presented separation methods do separate isotopes on-line, but traditionally the expression ISOL technique is only used for cases where the produced isotopes are stopped in the target or a catcher.

[18]This is the element which undergoes the nuclear reaction. Normally it is the target element, but here it is the projectile.

[19]Uncertainties in this point can lead to severe problems in the interpretation as the examples of the alleged transuranium elements discovered by Fermi [Fer34b] or the lengthy disputes on the discovery of element 104 (see ref. [Gäg88] for a review) show.

will be separated with the recoil separator SHIP at GSI [Mün79] and then stopped in a gas-filled Radio-Frequency-Quadrupole (RFQ) and transported to a Penning trap, allowing among others direct mass measurements of exotic nuclei.

A similar design is planned for the separator MORRIS [Thi97] at the Munich Accelerator for Fission Fragments. It is designed for efficient and selective separation of heavy neutron-rich fusion products which are provided as $1+$ ion beam for subsequent experiments (chemistry, mass measurements, etc.).

A new proposal from Argonne National Lab even aims at building a complete next-generation RIB facility based on this concept [Sav01]. The pre-separation with a fragment separator can avoid the two main problems of the IGISOL system (missing selectivity and plasma creation) while keeping all its advantages (high efficiency and good beam quality for all elements).

Table 2.3.1.: Different methods of on-line isotope separation.

|                              | in-flight                    | IGISOL             | ISOL                          | chemical            |
|------------------------------|------------------------------|--------------------|-------------------------------|---------------------|
| separation time              | $\mathcal{O}(\mu s)$         | $\mathcal{O}(ms)$  | $\mathcal{O}(s)$              | $\mathcal{O}(min)$  |
| elements                     | all                          | all                | no refractory                 | dedicated           |
| targets                      | thin to thick                | thin               | thick                         | thick               |
| $Z$ selectivity              | increases with $E/A$         | no good with RILIS | difficult good with RILIS     | very good           |
| beam intensity limited by    | primary beam                 | activity handling  | target heating                | target heating      |
| beam quality at exp. set-up  | large size and energy spread | good               | very good                     | no real "beam"      |

Table 2.3.1 summarizes the main features of the different on-line separation methods. The typical separation times in table 2.3.1 are given only as an order of magnitude. Accepting a reduction in intensity, experiments can still be performed with isotopes of shorter half-life which has been shown in many examples: At LOHENGRIN (see section 1.4) the time of flight is about 1.4 $\mu$s, but spectroscopy experiments have already been performed with isomers of 400 ns half-life [Gen99]. At the fragment separator LISE3 (GANIL) a $0^+$ isomer in $^{74}$Kr with a half-life of 42 ns was detected [Cha97] while the flight time is about 0.4 $\mu$s[20]. Also at the IGISOL facility in Jyväskylä short-lived isomers were separated, e.g. $^{207m}$Bi ($T_{1/2} = 182$ $\mu$s) [Ärj86] and $^{204m}$Tl ($T_{1/2} = 64$ $\mu$s) [Dendo]. At ISOL facilities several isotopes with half-lives in the millisecond range could be separated. A 5 ms isomer in $^{125}$In (probably $23/2^-$) was separated at OSIRIS [Fog98] and $^{14}$Be with $T_{1/2} = 4.35$ ms was separated at ISOLDE (see section 4.2.1). Francium isotopes with half-lives down to 0.7 ms were seen at ISOLDE [Klu86] and $^{35}$Na ($T_{1/2} = 1.5$ ms) was discovered at the CERN PS on-line mass spectrometer [Lan83]. The relatively short-lived isotope $^{265}$Sg ($T_{1/2} = 7.4$ s) was recently studied at a chemical on-line separator [Tür98] and the most short-lived isotope which was studied after chemical separation is $^{92}$Br ($T_{1/2} = 0.34$ s) [Kra74, Kra75].

Chemical off-line separation is still used for identification and spectroscopy of new isotopes in regions where the on-line methods are presently less efficient. Examples are $^{185}$Hf [Shu93a] and $^{237}$Th [Shu93b].

For the production of accelerated beams in principle two methods can be used. One is the post-acceleration of a low-energy ISOL beam and the other is the direct use of an in-flight separated

---

[20]The decay proceeds normally by E0 conversion electrons and is thus suppressed during flight as a fully stripped ion.

beam. Obviously it becomes more and more expensive to build post-accelerators which bring the ISOL beam to higher and higher energies. On the other hand a necessary deceleration of high-energy fragment beams becomes less efficient and the beam quality suffers significantly for lower beam energies. Both methods have only a small overlap and are rather complementary. The dividing line depends strongly on the isotope considered and the technical advances expected in the next years. It can be roughly drawn at a beam energy of the order of 20-30 $A$·MeV. In any case it is well above the Coulomb barrier. A discussion of the different approaches is found e.g. in ref. [Gei95].

## 2.4.  ISOL targets

### 2.4.1.  Release optimization

The key part of an ISOL facility is the target and ion source unit. When using thick targets, the choice of the target material is guided by the simultaneous optimization of the production rate in the target and the release efficiency from the target. Often the same or similar target elements can be used in different chemical forms. Various materials have been tested and used as ISOL targets. An overview is given in appendix B.3.

The release efficiency from a target and ion source unit is not a fixed parameter, but depends on the rapidity of the release and the half-life of the released nuclide. The mechanisms and parameters determining the release efficiency in an ISOL system were nicely reviewed by Kirchner [Kir92a]. In appendix B.2 the main points are summarized using his terminology.

The main features of the release behavior can be summarized as follows:

- For sufficiently long times more or less everything will get released, but for ISOL applications the opposite limit, i.e. the behavior for very short times- and lifetimes, respectively, is of interest.

- The efficiency of diffusional release depends on the square root of the half-life (equation (B.2.7)). Thus, even for very short-lived nuclides a certain amount can get released.

- The effusional release shows already a linear dependence on the half-life (equation (B.2.12)), thus causing a stronger suppression of short-lived nuclei.

- The combination of both processes causes a $t^{3/2}$ dependence (equation (B.2.15)) which is even more unfavorable for the release of short-lived nuclei. Depending on $\mu_0$ and $\nu$ the release efficiency will approach the unfavorable $t^{3/2}$ dependence sooner or later.

- An additional problem occurs if the desorption time gets very long. Then the boundary condition of negligible surface concentration (equation (B.2.5)) is no longer fulfilled and the adsorbed particles can diffuse backwards into the bulk material. This will cause the release efficiency to drop with an even higher power ($\gg 3/2$) and the separation of short-lived nuclides gets practically impossible. This is often the case for refractory elements.

Obviously a change in target geometry to optimize the mean diffusion time can affect the effusion time negatively. For smallest diffusion times it is of advantage to use very thin foils, fibers or spheres. This in turn will largely increase the inner surface, thus increasing the effusion time. Such a geometry can be of advantage for elements where the release time is dominated by diffusion, e.g. noble gases, alkalis and other atoms and molecules with high volatility. This was confirmed by a release test with a special Ta target made of 2 $\mu$m thick foils. It showed to double the yield of $^{11}$Li although the target thickness was reduced by a factor of ten compared to a standard Ta target with 20 $\mu$m thick foils [Ben99c]. On the other hand for elements with a significant desorption time it can make sense to use a more coarse-grained target structure where the diffusion time is increased, but the average number of surface collisions is largely reduced.

For example in a tantalum foil the diffusion coefficients decrease in the following order: Y > As > Lanthanides > Sr > Ba > Hf > Rb > Cs > Kr [Bey77, Kir92a, HB]. This can be understood intuitively: the diffusion is related to the size of the atom. With increasing valence the volume of the atom or ion, respectively, is reduced, thus allowing a faster diffusion. However, simultaneously the element gets chemically more similar to the host (Ta) and is desorbed less easily. Noble gases and alkalis show a rather "diffusion-controlled" release while others, e.g. rare earths, are rather "desorption-controlled". Clearly this is only a very qualitative statement for intermediate times. For short times always the unfavorable $t^{3/2}$ dependence will be reached.

**Literature data**

A lot of literature data exists on the release behavior of fission products from various matrices. These were studied as possible containment materials for the fuel elements of a high-temperature reactor (see e.g. [Hil88, Kwa90, TFP83]). However, in these applications the opposite aim, i.e. the maximum retention of radio-nuclides is pursued. Therefore typically materials with a very unfavorable release characteristic were chosen. Moreover the data normally concerns the slow release behavior (hours or longer) at much lower temperatures and has large errors when extrapolated to higher temperatures.

That compound creation with other elements can significantly affect the release behavior was shown e.g. in [Bau87]. This underlines the importance of target impurities!

It has been shown that the structural changes due to a strong irradiation of the material can lead to a considerable acceleration of the release, especially at lower temperatures [Mat86]. This effect is called "radiation enhanced diffusion".

A useful compilation of diffusion data, especially in oxide matrices including $ThO_2$ is given in [Ree77]. Also included are empirical relations which allow an estimation of the diffusion behavior for elements without measured data.

## 2.4.2.    Efficiency and release time measurement

Several methods are used to measure the efficiency of a target and ion source system. Some of them can also be used to measure the release profile or an average release time. Therefore both points are discussed together in the following.

**Off-line measurement with a stable tracer:**

To determine the source efficiency of the ISOLDE ion sources, a small, well-known amount of the respective element is brought into the target container or an attached oven. While slowly evaporating this sample into the source, the current is measured with a Faraday cup (FC) and continuously logged. After complete evaporation, the source efficiency is given by the ratio of the integrated current to the inserted amount by:

$$\varepsilon_{\text{source}} = \frac{\int I_{\text{x}} dt}{n_{\text{x}} \cdot 96485 \text{ As}}, \tag{2.4.1}$$

where $n_{\text{x}}$ is the molar quantity of the inserted isotope.

As an example figure 2.4.1 shows the determination of the ion source efficiency for resonant laser ionization of copper (see below). The target heating was stepwise increased, seen in the peaking ion current. Between 21:00 and 23:00 several tests where performed with the laser set-up. Therefore the current had to be interpolated.
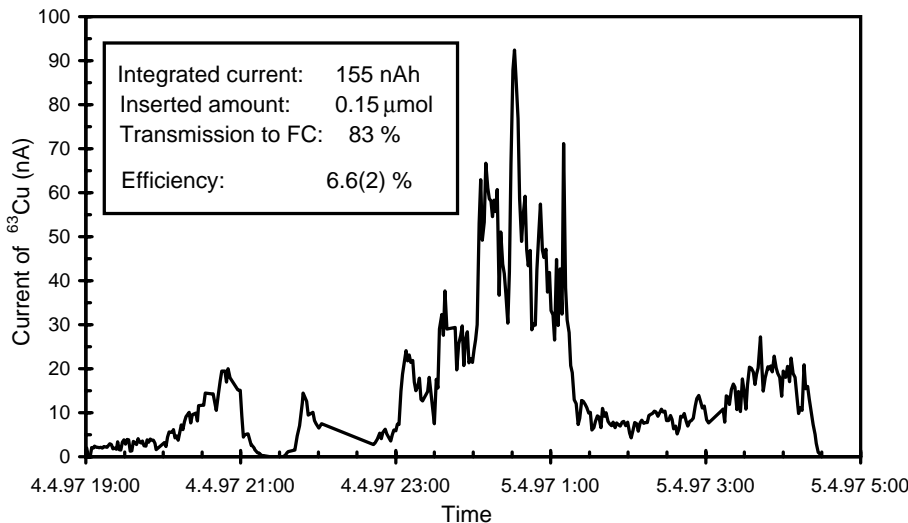
Figure 2.4.1.: Off-line determination of the laser ion source efficiency for copper.

The used samples contain typically some $\mu$g of material. They are normally prepared by dilution of aqueous solutions[21] (typically nitrates or chlorides). Some drops are deposited with a calibrated pipette onto a tantalum foil or graphite disk and dried.

Special care has to be taken to avoid systematic errors. Any contamination of the target container or source with the same element would pretend a higher source efficiency. Typical impurities are Na, Fe, Ba, etc. Contaminations with isobars can normally be identified by verifying the natural isotopic ratios of an element. On the other hand, if the sample is deposited in a "cold" part of the target-ion source system, an incomplete evaporation would lead to an underestimation of the efficiency. In any case for each efficiency determination the full sample has to be evaporated. It is not possible to determine the absolute momentary source efficiency with this method.

The response of the system to a fast temperature change can give a first indication on the rapidity of the release, but often disturbing phenomena (memory effects by condensation, etc.) render a quantitative analysis impossible.

The ionization efficiency of gases can be measured by feeding into the source a support gas with a well-known composition through a calibrated leak. The ionization efficiency of Ar and Xe in the ISOLDE plasma sources is routinely monitored in this way. Controlling the gas supply with a fast valve allows additionally to measure the delay time (mainly the effusion part) of the system [Kir81b, Wel98].

Occasionally a Knudsen cell (temperature controlled oven) is used for providing a "constant" flow of evaporated material for efficiency measurements. However, the detailed thermodynamics of the tracer and possible chemical compounds has to be studied carefully to avoid large systematic errors in the resulting efficiency values.

**Off-line measurement with radioactive tracers:**

Most of the systematic errors mentioned above can be excluded by using a radioactive tracer for the experiment. This method was e.g. used for various rare earth elements [Lat74]. No contaminations with stable isobars can occur and in case the source efficiency shows to be low, the source can even be taken apart and analyzed at which places the not released tracer was deposited. Using $^7$Be as tracer, the areas where beryllium is lost in a plasma source could be identified [Barke].

---

[21] Tin tends to precipitate in aqueous solutions easily as oxide. Therefore dry mixtures of Sn and Ta powder as well as Sn films evaporated onto a Ta foil were used as samples.

This method relies on the existence of a suitable radio-nuclide as tracer. The half-life has to be long enough ($T_{1/2} \gg$ min) and the decay should be specific and easy to detect, i.e. preferably show characteristic gamma lines.

The radioactive tracers can be produced either by reactions in the target matrix (see e.g. [Bey77, Hof84] or are implanted at ISOLDE as radioactive beams into different matrices (see e.g. [Men97]). The former method requires a dedicated system for irradiation and handling of the samples, the latter requires an available ion beam of the tracer nuclide. However, often no suitable beam exists[22]. Either the required tracer nuclide can be produced indirectly by decay of an isotope existing as on-line beam or another method has to be used.

For some elements the method can be inverted: first several identical samples are marked with a stable tracer. After individual heat treatment of each sample the remaining amount of tracer is then analysed by a sensitive trace analysis method, e.g. by (prompt) neutron activation analysis. Occasionally even a depth profile of the tracer distribution can be measured in this way [Kös94].

This off-line method allows also to study the release behavior quantitatively. From several measurements at different temperatures both Arrhenius factors, $D^0$ and $Q$ (see equation (B.2.8)), are obtained. However, very fast release components or effects of "radiation enhanced diffusion" remain unobserved.

**On-line measurement with stable tracers:**

The efficiency can also be determined by implanting a known amount of tracer atoms directly into an ISOL target and ion source system and monitor simultaneously the current which is released from the ISOL source. Heavy-ion beams with sufficient energy (some A·MeV) are required to pass a thin window in the source envelope. The GSI offers the combination of sufficiently intense and energetic ion beams from the UNILAC and a well working on-line mass separator which is routinely used for release measurements from thin targets [Kir92a, Kir96]. The release behavior can be tested over a wide range in time (fractions of a second to many minutes), temperatures (even over 2500 °C with a thermal ion source) and fractional release (down to below $10^{-4}$). The quantitative analysis of the release profiles is described in [Kir92a]. The relation $F(\mu t) \approx Y(\nu/\lambda)$ (compare appendix B.2) gives a direct conversion of the measured release profile into the release efficiency.

Of all presented methods to measure release profiles it is the most universal, allowing to test different target matrices in a short time. Due to the time correlation with the implanted beam, a constant background can be corrected in the analysis. In some target materials the beam impact can trigger the release of an additional background beam which can no longer be corrected. In these cases an isotope with a different mass has to be chosen as tracer.

This method can be used for most elements and materials, the only condition is that the beams have to be available from the UNILAC accelerator. This sets a principal limitation to elements with stable isotopes (e.g. no francium). Since these measurements take only some minutes, normally no dedicated beam is provided for them but they are performed parasitically, i.e. an available beam is used for a short time while other users do not need it.

**On-line measurement with radioactive tracers:**

If the production cross-sections for certain isotopes are well known from other measurements (recoil separator or gamma spectroscopy of irradiated samples), the on-line measurement of the isotope yield at an ISOL separator gives directly the efficiency of the complete target and ion source system. This method is used at OSIRIS [Rud90], ISOLDE and many other ISOL facilities.

---

[22]Normally the off-line tests are just made in the preparation of a new on-line beam.

It is less susceptible to systematic errors than the off-line methods, but requires a higher effort, i.e. for the test of each material a complete target and ion source unit has to be irradiated.

Just as with a stable tracer, the release profile can be measured also with the available radioactive beams. At ISOLDE the yield and release profile is normally determined with a sampling technique [Let97a]. The beam gate is opened for a short time with a well-defined delay after the proton pulse impact. The radioactive nuclides are collected on a metallised tape and transported into a $4\pi$ beta-detector. From the $\beta$-activity measured with this so-called "monitoring tape station" the ion beam intensity during the collection period is calculated. Scanning the delay time allows to measure the release time profile in a range from some milliseconds to many seconds and longer. The lower limit is given by the minimum collection period to obtain enough statistics and the upper is related to the lifetime of the sampling isotope. For example for lithium the most long-lived tracer nuclide $^8$Li limits the range to $\lesssim 10$ s. Alternatively the current of a (stable) radiogenic isotope can be followed by direct particle detection, e.g. with a Faraday cup. To deduce the total release efficiency it is important to monitor the release profile over a large range. Especially at lower temperatures the existence of a fast release component does not exclude that the bulk of the tracer is released very slowly [Bau87].

An ISOLDE target and ion source unit consists of the target, a transfer line and the ion source. The geometry of all components influences the effusion. The release profiles are typically described by a sum of two exponential decay terms multiplied by an exponential grow-in [Let97a]:

$$p(t) = C\left(1 - \exp(-t/\tau_r)\right)\left[\alpha\exp(-t/\tau_f) + (1-\alpha)\exp(-t/\tau_s)\right] \qquad (2.4.2)$$

with $\tau_r$ the characteristic rise time, $\tau_f$ the decay time of the fast component and $\tau_s$ the decay time of the slow component. $\alpha$ describes the relative contribution of the fast and slow components and $C$ gives the normalization to the observed intensity. Figure 2.4.2 shows a typical release profile of cesium.
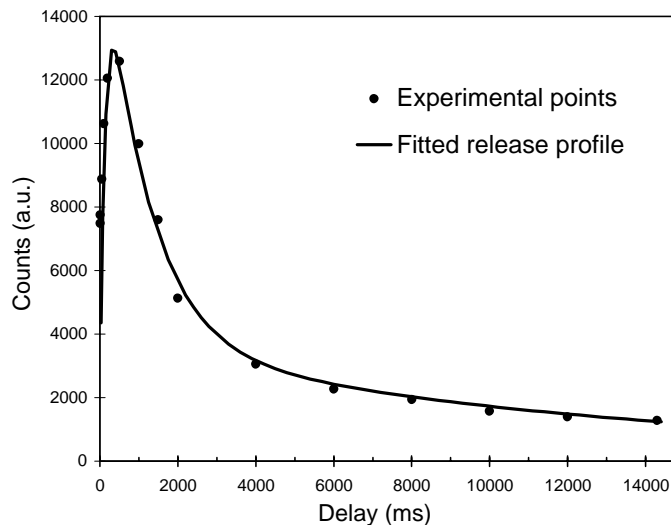


Figure 2.4.2.: Measured and fitted release profile of cesium from a $UC_x$/graphite target. The fit parameters are: $\tau_r = 0.1$ s, $\tau_f = 0.8$ s, $\tau_s = 10$ s and $\alpha = 0.85$.

Note that the form of this release function is chosen somehow arbitrarily. If no indication for a two-component release is observed, this function is reduced to a single exponential decay by setting $\alpha = 1$. The release profiles from molten metal targets are well reproduced with a single exponential decay[23] [Rav79]. On other occasions even two decay components do not allow to fully describe

---

[23]Note that also a possible oxide layer swimming on the surface of the molten metal can contribute to the diffusion time [And91].

the release characteristics, but still the two-component form is used as an approximation. This is justified since the fluctuations of the experimental points within one measurement do not allow a reasonable "fit" of a function with too many free parameters.

Note that the release function is "fitted" manually to give a good agreement with the experimental points. Therefore the resulting values for $\tau_r$, $\tau_f$, $\tau_s$ and $\alpha$ give not necessarily the minimum $\chi^2$. To perform a mathematically correct fit, it would be necessary to accumulate much more data. On the other hand the manual "fit" allows to apply an empiric weighting of the individual points. Thus, corrections for known deviations (background, beam fluctuations, etc.) can be easier taken into account. A more objective parameter which is barely affected by the detailed fit parameters is the time $t_{50}$ in which 50 % of the stable nuclides are released: $F(t_{50}) = 0.5$. However, it is not very useful if clearly two or more release components are present.

With a well-known release profile the decay losses can be calculated for most half-lives. A known or estimated half-life allows to convert an upper yield limit into a cross-section limit. On the other hand together with a cross-section systematics a limit can be set on the lifetime or binding energy of the isotope in question [Jok96].

The ISOLDE target and ion source systems have a more complicated geometry compared with the GSI ion sources with integrated catcher. Therefore the measured release profile cannot be identified easily with the diffusion and effusion contributions. Densham et al. started such an approach using Monte Carlo simulations [Den97]. Some release curves measured at ISOLDE were used to derive absolute values for the diffusion coefficient $D$ and the mean sticking time $\tau_{sorp}$. However, some of the results are in clear contradiction to other values from literature [Bey77, Kir86, Kir87a].

A combination of the GSI- and ISOLDE-method is used at GANIL. There a beam of radioactive nuclei is prepared with the fragment separator SISSI and then implanted into the ISOL target and ion source unit SIRa. The isotopes released from the ISOL separator are monitored at a tape station [Lec97]. This method allows a direct measurement of the total efficiency for a certain radio-nuclide from a given target and ion source unit. It can be applied with the given set-up at GANIL, but has no specific advantage over the far less elaborate GSI method.

### 2.4.3. Pulsed or dc driver beam?

Techniques were developed to improve the signal- to background ratio by bunching the radioactive ion beam. Variants of the FEBIAD ion source (see section 2.5.2) [Kir86, Kir87a, Kir92b] can be run in a bunched mode where the produced nuclei are continuously adsorbed on a cold spot in the source. Heating the latter rapidly releases the collected atoms as a bunch. By optimization of the adsorbent and temperature a chemical selectivity can be added to the timing effect.

With a sufficiently fast release and a pulsed driver accelerator with low repetition rate ($f_{rep} \lesssim 1/t_{50}$) an automatic beam bunching occurs. This is of great advantage for many nuclear spectroscopy studies. In all cases where the nuclides are identified by their half-life or the lifetime should be measured, a certain measurement cycle of "collection" and "decay" periods has to be used. The bunching can help in two ways:

1. It can increase the efficiency. With a dc beam the continuously produced and released radio-isotopes which are provided during the "decay" period are just lost[24]. However, if a bunched driver beam with identical average current is used, the nuclei can be collected when their ion beam intensity is at the maximum. Less nuclei are lost during the "decay" period. In fact some of the recent experiments which lead to the discovery of the most exotic isotopes

---

[24]In certain cases a more complicated set-up with a tape or wheel moving the collected nuclei alternately between several detection positions allows to make full use of a dc beam [Kir77], but with a standard set-up the nuclei are lost.

of manganese or silver would have been more difficult at a facility with a 2 $\mu$A dc proton beam!

2. The bunching can also increase the selectivity. If the beam contaminations show a significantly different release profile, they can be suppressed by an appropriate choice of the beam gate timing. Extremely high selectivities can be obtained for the suppression of a contaminant with much shorter lifetime. The beam gate is only opened after most of this contaminant has decayed. This method was applied to study the decay of the new isotope $^{217}$Bi free of background from the abundant, but short-lived isobars [Dup98].

On the other hand there are also applications where the pulsing beam structure is rather disturbing, e.g. for precision lifetime determinations if a simultaneous bunching of beam contaminants occurs (causing non-linear dead-time effects), for $\beta$-NMR experiments where the measurement cycle has to be synchronized to a multiple of the pulse repetition period, etc. Also the target is exposed to a higher thermal stress with a pulsed beam.

During impact of the proton pulses, the high voltage of the target and ion source unit at ISOLDE PSB is taken down to zero to avoid sparking by the large amount of secondary ions and electrons created in the target area [Kug92]. The beam gate remains closed for some ms till the high voltage is stabilized again at its operating value (60 kV). For extremely short-lived nuclei ($^{11}$Li, $^{14}$Be) this causes a loss in beam intensity compared with a dc facility where the nuclei are permanently extracted.

When doing nuclear spectroscopy at a pulsed RIB facility one has to keep in mind that also the background is pulsed, possibly with some delay. Besides well known background due to scattered high energy spallation neutrons or delta electrons, another source of background was identified: by impact of the pulsed proton beam onto a (heavy) target, a bunch of radioactive gas is expelled. This diffuses through the beam lines and can cause an increase in background activity some seconds after the proton pulse. This effect is more pronounced at beam ports closer to the target.

## 2.5. Ion sources

After release from the target the radioactive atoms have to be ionized and accelerated at least to some tens keV to allow for subsequent magnetic mass separation and electrostatic beam guiding. In the following, different types of ion sources are discussed which are used at ISOL facilities. Their performance has to be assessed according to the same criteria which are decisive for all steps of the ISOL process: *efficiency – selectivity – rapidity*.

### 2.5.1. Surface ionization

If an atom $X$ with low ionization potential (IP) $W_i$ hits the hot surface of a material with high work function $\Phi$ (e.g. a noble metal), it has a high probability to give its valence electron to the metal and get ionized, see figure 2.5.1. This process is called (positive) surface ionization. An analogous process of negative surface ionization exists for elements with high electron affinity $A_E$ which hit a hot surface of a material with low work function $\Phi$ (e.g. $LaB_6$) and get negatively ionized.

The efficiency of positive surface ionization can be significantly enhanced when using a hot cavity in which a thermal plasma consisting of surface ionized ions and thermionic electrons is created. The ionization efficiency of "normal" surface ion sources and of the latter, so-called "thermal ion sources", is discussed in appendix B.5.
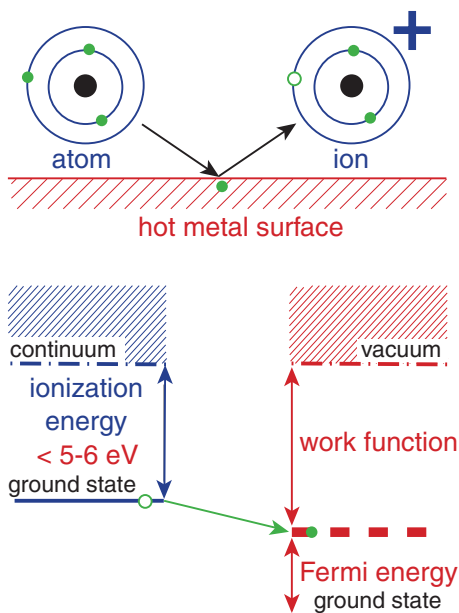
Figure 2.5.1.: Principle of positive surface ionization.

**Multicharged ions**

The second ionization potential of all elements is above 10 eV. Therefore surface ionization cannot produce multicharged ions. However, occasionally multicharged ions are observed from the ISOLDE surface ion source: $Xe^{4+}$, $Bi^{6+}$, etc. Their creation can be explained by four processes:

1. During impact of the proton beam pulse a large number of energetic particles is created. Some of them can scatter with atoms inside the ion source cavity or the transfer tube between target and ion source. In this scattering, the atoms can get highly ionized by "shake-off" effects. Being produced coincident with the beam pulse this background is largely reduced by closing the beam gate for some ms after the proton beam impact.

2. In the $\alpha$ or $\beta$ decay of radioactive nuclei the recoil velocity can be high enough that several electrons can be lost from the atomic shell. If this happens just in the ion source, the multicharged ions can be extracted directly without further wall interaction.

3. In some radioactive decays electrons are lost from an inner shell. These holes are filled by outer electrons cascading down, either in radiative transitions emitting X-rays or by the Auger effect emitting an electron. Occasionally also several Auger electrons are emitted in a cascade, thus creating multicharged ions [Nis73]. Again the multicharged ions created in the ion source region can be extracted. The magnitude of this contribution will depend strongly on the individual decay characteristics, e.g. it will be significantly enhanced if the mother decays mainly by electron capture or emission of conversion electrons. Presently not sufficient "yield" data exists on multicharged ions to draw a conclusion.

4. Secondary electrons are created by impact of surface ionized ions on the extraction electrode or on residual gas atoms in the extraction region. These are accelerated towards the extraction hole and can produce electron impact ionization (see below). Also during occasional discharges (sparks) between the extraction electrode and the hot ionizer tube atoms can get multiply ionized in the extraction region.

Normally such contaminations are not excessive, but it has to be kept in mind that they can occur and could disturb the measurement of a nuclide with very low production rate and missing specific identification like gamma-ray detection or measurement of the half-life.

It should be noted that the last mechanism is more pronounced with the single-gap extraction of the ISOLDE sources where nothing prevents the secondary electrons from flowing back to the positively charged source. For the ISAC ion sources a multi-gap extraction system was developed [Dom98] where an accel-decel structure[25] can hinder this effect. Another advantage of this system is the better adaption to a change of the extracted current. By tuning the field of the first extraction gap the curvature of the plasma sheat[26] is influenced. The overfocusing of the beam in the extraction region can be reduced to avoid an inflation of the phase space due to space charge effects. The voltage of the second electrode allows to focus the beam and match its divergence to the ion optical elements downstream. The last electrode is kept at ground potential to provide a well defined reference. With this system the source emittance was maintained below $10$ $\pi$ mm mrad (at 30 keV beam energy) even when raising the total extracted current above 10 $\mu$A [Dom98]. This is an important feature when running an ISOL facility with an intense driver beam, e.g. up to 100 $\mu$A of protons, which will create a large rate of effusing particles (radiogenic and stable).

On the other hand the electrodes of such an extraction system are spaced more closely than at ISOLDE and the higher electric field strengths could cause a sparking under bad vacuum conditions. These can occur with a bunched release of gas from the target after impact of a proton pulse. At ISAC this problem does not occur (dc beam from the cyclotron) and at ISOLDE it is cured by taking down the source potential to zero during impact of the proton beam [Kug92]. Note that the latter method is practicable at a repetition rate of $\leq 1$ Hz, but not necessarily ideal for a driver accelerator with 50 Hz repetition rate.

## 2.5.2.   Plasma ion sources
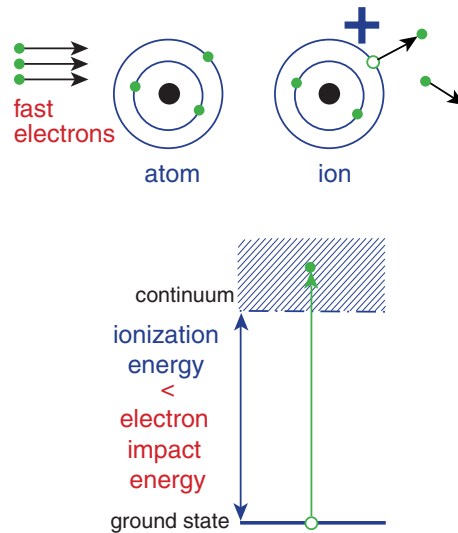


Figure 2.5.2.: Principle of ionization by electron impact.

It has been shown that elements with low IP can be ionized efficiently and selectively with a surface ion source. However, there are many interesting elements with higher IP which require another type of ion source. Plasma ion sources are such a universal tool for ionization of many different elements. If the plasma temperature $T_\mathrm{p}$ is high enough ($kT_\mathrm{p} \gtrsim W_\mathrm{i}$), practically all atoms entering the plasma can get ionized by electron impact (see figure 2.5.2) and charge changing collisions. Traditionally the plasma was created in an arc discharge. However, the electrodes are

---

[25] In an accel-decel structure the intermediate electrode is put on a positive potential compared to the first ("puller") electrode. This decelerates the ion beam.

[26] In the case of thermal ionization this is the boundary of the (thin) thermal plasma.

used up quite rapidly (some hours) and have to be exchanged frequently. This causes problems in the environment of a radioactive ion beam facility with difficult access to the target area. Several other types of plasma ion sources require less maintenance and have been applied successfully at ISOL facilities:

**FEBIAD:** The Forced Electron Beam Induced Arc Discharge (FEBIAD) source was developed by Kirchner and Roeckl for the GSI on-line separator [Kir76]. It can reach high efficiencies (around 50 % [Kir96]) for elements above argon and runs stably even at low gas pressures ($10^{-5}$ mbar). Meanwhile several types exist at GSI, optimized for high temperatures[27] or even allowing beam bunching (an adsorber area placed in the ion source is cycled in temperature to accumulate continuously produced isotopes and desorb them in bunches) [Kir87a].

Copies and variants have been applied at many ISOL facilities (see e.g. [Ver81, Gil85, Wal85, Bjø87, Sun92, Hag92a, Alt96, Ton96]). At ISOLDE the heating filament [Kir87a] was replaced by a more rugged cathode with direct ohmic heating [Sun92]. Four different types are in use at ISOLDE [Bjø86, Sun92]: MK5 is the so-called "hot plasma source" where the transfer line is maintained around 1900 °C. It permits to ionize also less volatile elements. In a medium temperature version (MK3 and MK6) the temperature of the transfer line is kept between 200 and 400 °C, mainly for the selective separation of Cd and Hg. Finally the MK7 has a water-cooled transfer line at room temperature to condense all elements except the noble gases. The MK3 has two anodes with independently controlled voltages while all others have only a single anode.

For an efficient operation of the FEBIAD it is important to keep the beam of molecular impurities at mass 28 ($CO^+$ and $N_2^+$) in a range of some $\mu$A. For elements with $W_i < W_i(CO)=14.0$ eV [Rad85] or $W_i < W_i(N_2)=15.6$ eV [Rad85], respectively, charge transfer in collisions with these molecular ions contributes considerably to the ionization efficiency. Additionally the atoms to be ionized have to stay in the ionization region long enough. Therefore the FEBIAD is very efficient for elements heavier than argon, but for lighter elements with higher ionization potential (especially He, Ne and Ar) and shorter residence time in the plasma chamber the efficiency drops considerably. For the same reason the yields of doubly charged ions are significantly reduced and for $q \geq 3$ normally negligible. Doubly-charged ions are occasionally required for special applications, e.g. to attain higher beam energies for experiments with tilted foil polarization [Lin97]. In general multicharged ions are rather considered as disturbing beam contaminants and particularly in nuclear spectroscopy experiments they can lead to misassignments (see e.g. [SO92]).

An ion source based on the same principle, but with a radial arrangement of the electrodes was developed by Nitschke [Nit85] at the OASIS facility at LBNL. It reaches an ionization efficiency of 35 % for krypton at currents up to 10 $\mu$A. It does not use a magnetic field and does not contain insulators in the high temperature region. Instead the plasma chamber is "closed" by molecular flow restriction. Thus, the internal Ta catcher can be brought to a temperature of up to 2700 °C and the cold spot temperature exceeds 2200 °C. However, this source is more sensible than the FEBIAD types.

**ECRIS:** The Electron Cyclotron Resonance Ion Source (ECRIS) [Gel96a] was developed by Geller in 1965. In an ECRIS the plasma is confined by a minimum-B-configuration, where the field lines are almost everywhere concave towards the plasma. The electrons are accelerated by resonant excitation in a microwave field (typically used frequencies range from 2.45 GHz to

---

[27]The FEBIAD-H [Kir92a] can be operated at temperatures exceeding 2000 °C and has a very small ionization chamber (1.3 cm$^3$) to minimize the intrinsic delay time.

30 GHz). High plasma temperatures[28] in the keV range can be reached which allow to ionize even elements with high IP (e.g. He) very efficiently [Gel96a].

Also higher charge states are easily obtained. Presently up to $q/A \approx 0.2$ is obtained with optimum efficiency, but even highly stripped ions were already produced (e.g. $U^{64+}$ [Xie98]), although with lower efficiency. This opens the possibility of highly charged RIBs suitable for efficient post-acceleration with a compact accelerator. For compact linear accelerators (LINACs) a charge to mass ratio of $1/9$ to $1/4$ is required. For cyclotrons high charge states are also crucial (the end energy scales with $E \sim (q/A)^2$). It has been shown that an ECRIS can be coupled directly to an on-line target for the production of n+ beams of mainly noble gases [Vil97]. However, for other elements (particularly metals) the efficiency is considerably reduced due to decay losses when the radioactive atoms stick to the relatively cold walls. On the other hand an n+ ECRIS which ionizes practically all species of atoms leaving the target can cause problems. Not only many isobars of one mass will occur, but due to the $A/q$ ambiguity also different masses get mixed. Moreover the relatively large emittance of an ECRIS ($50\pi$ mm mrad and more at typical ISOL beam energies) makes it even more difficult to perform isobar separation with a high resolution separator. Post-acceleration with a cyclotron circumvents this problem since the cyclotron can act as an efficient isobar separator [Vil97, Boy97], but the problem remains when low-energy beams are used. An additional problem arises from the radiation damage to which the permanent magnets of the source are exposed in the target area [Ler98].

For the PIAFE project a new method was developed and studied in detail to use an ECRIS as an efficient "charge state breeder" [Gel96b, Tam96, Tam97, Lam98]. Thus, standard ISOL target and ion source units can be used to provide a 1+ ion beam which is, after mass separation, injected directly into the ECRIS plasma and subsequently brought to high charge states. The advantages and disadvantages of this method compared with an alternative Electron Beam Ion Source (EBIS) charge state breeder[29] are discussed e.g. in [Kös98a]. Meanwhile it has been shown that an ECRIS can also be used for trapping [Cha98] and bunching of the RIBs [Oya98, Cha98].

Presently ECRIS sources are employed at the ISOL facilities TISOL in Vancouver [Dom90], LISOL in Louvain [Dup92], SPIRAL in Caen [Vil97] and INS in Tokyo [Oya98]. A 1+ ECRIS with quartz body was used at the SARA on-line separator in Grenoble [Gim92]. A small 1+ ECRIS (type "Picogan") fitting into an ISOLDE target unit has been proposed [Sorta] and could give an immediate gain in ISOLDE yield by one to two orders of magnitude for beams of the light elements He, C, N, O, Ne and Ar.

Besides the two performant types FEBIAD and ECRIS, other source types have some advantages for specific ISOL applications.

**Nielsen- and Nier-Bernas sources:** When running molten targets or target materials with much intrinsic impurities at very high temperatures or when using a molecular separation technique ($CF_4$ addition) which "consumes" macroscopic amounts of the target material[30], a high gas load from the target occurs. FEBIAD sources are not able to cope with such a high gas load and the ionization efficiency is quenched. For these applications a more robust ("medium current") plasma ion source has to be used. Sources of the Nielsen [Nie57, Alm57] and Nier-Bernas type have been successfully used at the separator ISOCELE with currents of

---

[28]Actually the electron energy spectrum of an ECRIS is non-Maxwellian with part of the electrons accelerated to many keV while the rest remains thermal.

[29]In an EBIS the positive ions are confined in the negative potential of a dense electron beam. An EBIS requires a very good vacuum and can thus not be coupled directly to an ISOL target.

[30]This consumption could amount up to 1 g/h [Par76]!

several mA [Put87]. The emittance remained acceptable: about $20\pi$ mm mrad at 40 kV acceleration voltage.

**Multicusp source:** Multicusp ion sources for radioactive ion beam applications are presently developed at TRIUMF [Kuo98] and LBNL [Lee96, Wut98]. A multicusp field created by alternately poled permanent magnets provides a radial confinement of the plasma which is heated by a filament or an RF (radio frequency) antenna. Multicusp sources have performances which can reach that of a 1+ ECRIS, but allow a cheaper construction. They could be used in target and ion source units which are frequently changed and thrown away after use. Typically multicusp sources reach a high efficiency for currents of some mA (1.5 mA in [Wut98], $0.2 - 1.5$ mA in [Kuo98]) which cause space-charge problems for most existing on-line separators[31].

**Electron impact source:** Electron impact ion sources are not really plasma sources, but comparable from the viewpoint of universality and nonselectivity. The ionization is done by bombardment with an electron beam, but the ions are not confined as in an EBIS and the efficiency is given by the small interception volume of atom and electron beam. Their advantage is normally restricted to few cases where the reduced decay losses due to a very high operation temperature compensate the low ionization efficiency (about 0.1 %) [Jac87].

**Other types:** Ion sources which produce multicharged ions in a plasma created by a strong laser pulse are still under development to improve efficiency and reliability of operation with stable isotopes (see e.g. ref. [Has98a]), but presently do not seem to have practical applications for RIB purposes.

The main advantage of the plasma ion sources, i.e. their universality, is simultaneously their main drawback, i.e. the missing selectivity. The selectivity has to be provided in another step of the separation process, preferably before reaching the ion source. Making use of their chemical properties, many non-metals can be brought from the target to the ion source in a rather selective way, either profiting from their low evaporation temperature or their tendency to form specific molecules. However, for metals these methods are more restricted.

Another problem occurs for elements with high adsorption enthalpy on surfaces. Nearly all[32] plasma ion sources include electrically insulating materials in the high temperature region. The FEBIAD uses insulators for mechanical separation of cathode and anode, while in an ECRIS insulators are used as windows to introduce the RF power or to hold an RF antenna. These insulating materials (mainly $Al_2O_3$, $BeO$, $BN$) limit the maximum operation temperature of the source normally to well below 2000 °C. This is considerably lower than the operation temperature of a thermal ion source. The sticking of short-lived isotopes to the insulator material can result in large decay losses for metals which form stable oxides like e.g. Be.

Thus, the problem remains to find a source type which is able to ionize efficiently and selectively high-melting elements with an IP between about 6 and 10 eV, i.e. most metals.

An alternative ionization method which provides high selectivity and a vast choice of construction materials for the ion source chamber is the resonant photo ionization. Here, the valence electron is brought to the continuum by resonant absorption of photons via several excited levels. If the photons are provided by a powerful laser, efficiencies of the order of 10 % and more become possible. The state of the art and applications of such a resonance ionization laser ion source (RILIS) are discussed in the next chapter.

---

[31]Experimentally it was observed that the extraction efficiency at ISOLDE is markedly reduced when the total current exceeds some $\mu$A.

[32]An exception is the Nitschke ion source [Nit85] using molecular flow restriction to "close" the plasma chamber and keep the insulators at a lower temperature (see above).

# 3. Resonance ionization laser ion source

## 3.1.  Laser ionization

The theory and techniques used in a resonance ionization laser ion source (RILIS) are very similar to those of standard resonance ionization spectroscopy (RIS). In fact an ISOL facility combined with a RILIS is nothing else than a comfortable resonance ionization mass spectroscopy (RIMS) facility, optimized in efficiency and rapidity for the extraction of short-lived radioactive ions. Reviews on RIS can be found in [Let77, Hur79, Bek83, Let87, Hur88]. The proceedings of the biannual symposia on RIS (see e.g. [RIS94, RIS98]) are a good source of detailed information and further references. In the following some features of RIS are discussed which are important for the use of a RILIS.

An atom exposed to a photon flux $\Phi$ of wavelength $\lambda = hc/E_{12}$ will be excited with the rate:

$$W_{12} = \Phi\sigma_{12}(\lambda) \tag{3.1.1}$$

from the ground state (1) to a level (2) with excitation energy $E_{12}$. $\sigma_{12}(\lambda)$ is the absorption cross-section for atoms in the ground state. If the absorption rate $W_{12}$ is larger than the spontaneous emission rate from the excited level, the occupation of ground state and excited state and the rates of absorption and stimulated emission will come into equilibrium[1]. The transition is then called saturated. The transition of the excited level to another excited level at higher energy can be treated analogously. If enough photons for each transition are provided simultaneously, the occupation is equilibrated among all participating levels. If the highest level is above the ionization threshold, the excited atom will emit an electron and get ionized. In a (small) electrical field the ion and the electron are separated rapidly. Thus, for the last step the upper level is always empty and stimulated emission does not occur. If the produced ions are extracted permanently, more and more atoms are shoveled upwards level by level and get ionized. Using non-resonant transitions into the continuum with a typical cross-section of $10^{-17}$ cm$^2$ and a spontaneous emission rate to metastable states[2] of $10^6$ s$^{-1}$, a photon flux of the order of $10^{23}$ cm$^{-2}$s$^{-1}$ is required. With a beam spot of some mm$^2$ area and visible light this corresponds to a power of some kW. Such a power can presently only be provided by pulsed lasers. These, however, have small duty cycles ($\sim 10^{-4}$). The interaction of a pulsed laser beam crossing a fast atomic beam has therefore intrinsically a small efficiency[3].

If the atoms can be confined for a while in the region irradiated by the laser beam, the overlap in time can be improved considerably and higher efficiencies can be reached even with low duty-cycle lasers. Three ways have been used to store the atoms:

1. collection on and desorption from a cold surface,

2. stopping in a buffer gas cell,

---

[1] Detailed features of the dynamics like Rabi oscillations, etc. are not regarded in this gross description. They are discussed thoroughly e.g. in [Hur88].

[2] "Trapping" in metastable states should be avoided since such atoms do no longer participate in the excitation and ionization process.

[3] Direct laser ionization at the outlet hole of a gas jet was proposed and estimated to reach 10 % efficiency, but off-line tests gave only about 0.1 % efficiency [Ren97].

3. diffusion through a hot cavity.

In the first method the atoms are continuously adsorbed onto a cold[4] surface. Shortly before firing the ionizing lasers, the surface is heated rapidly (e.g. by the pulsed laser desorption (PLD) method with an intense laser beam) and the atoms get desorbed. The efficiency depends strongly on the spatial and temporal overlap between ionizing laser beams and desorbed atom cloud. For not too short-lived isotopes repetition rates of $1 - 50$ Hz, which can be provided by cheap Nd-YAG lasers, are sufficient. This method has been applied for resonance ionization spectroscopy (RIS) experiments (see e.g. [Krö91, Bla97]) and was proposed as ion source at an ISOL facility [Fai87, Seb97].

In the second method the atoms are stopped in a buffer gas cell where they remain for some tens ms before being evacuated. Excimer lasers with a repetition rate of some 100 Hz are well adapted for this application [Dup97]. The set-up is comparable to that of a standard IGISOL facility. At the LISOL facility in Leuven, presently laser-ionized beams of the refractory elements Ti, Co, Ni and Rh are available [Kud96, Reu99]. In a buffer gas cell the radio-nuclides have only a small chance to interact with the walls. Therefore this method is very suitable for refractory elements which tend to stick to the walls.

In the third method the atoms are stored in a hot cavity with a small outlet hole. The cavity has to be heated to avoid excessive adsorption of the atoms to the walls. At ISOLDE normally cavities in form of a tube are used, but also other geometries are possible. With 3 mm inner diameter and 30 mm length an atom makes about 40 wall collisions while passing the tube ($A_{\mathrm{wall}}/A_{\mathrm{orifice}} = 2\pi r l/(\pi r^2) \approx 40$ )[5]. The mean free path is 3 mm and e.g. an atom of mass 33 with thermal velocity in a 2000 °C hot cavity ($\bar{v} = \sqrt{8kT/(m\pi)} \approx 1200$ m/s) will remain in the free volume of the tube for about 0.1 ms. To have at least one chance to interact with the laser beam, the latter should have a repetition rate of the order of 10 kHz. For lighter atoms the requirements are in principle even stricter while for heavier atoms they are slightly reduced. Still a higher repetition rate helps to improve the total efficiency by multiple chances of interaction.

In the following some fundamental characteristics of the "hot cavity type" ISOLDE RILIS are discussed. Comparisons to the other methods are given where appropriate.

The main "ingredients" for the efficient operation of a "hot cavity type" RILIS are:

- the ionization scheme,
- the laser system,
- the ionizer cavity,
- equipment for beam tuning and monitoring,
- additional equipment (beam chopper, etc.).

Figure 3.1.1 gives an overview of the main components of the ISOLDE RILIS.

## 3.2.  Ionization schemes

Ionization schemes including two, three or more transitions have been employed. They can be classified according to the nature of the last populated level before ionization (see also figure 3.2.1):

---

[4]The surface temperature is kept below the desorption temperature of the respective element.

[5]The face of the tube pointing towards the target is not taken into account. Atoms diffusing back into the target container will come back to the ionizer cavity sooner or later if they do not decay before.
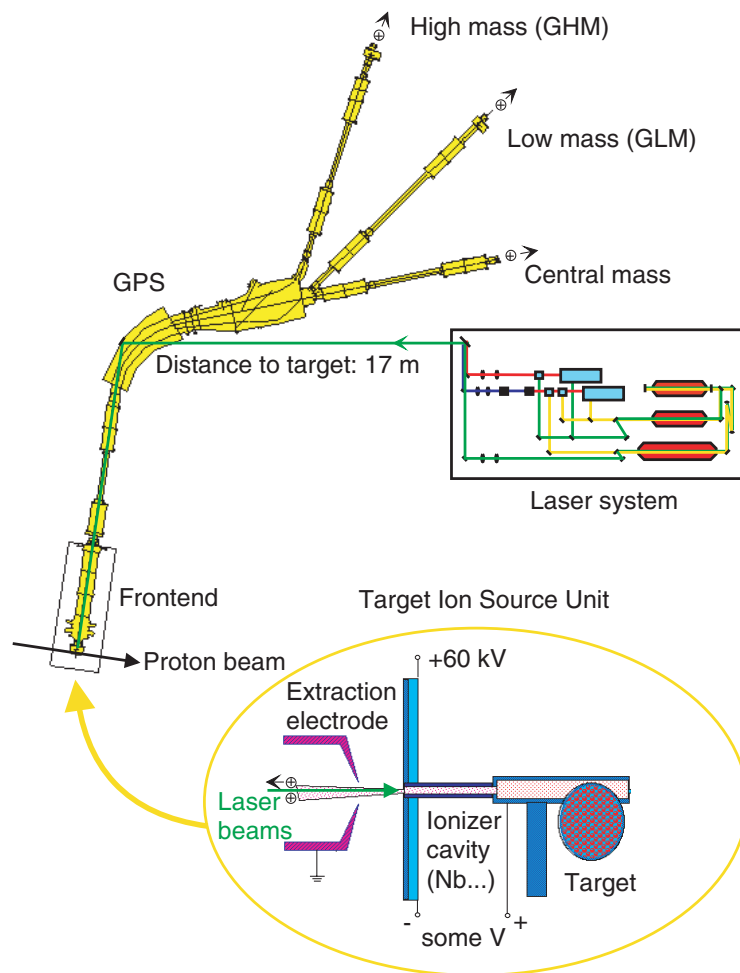
Figure 3.1.1.: Set-up of the ISOLDE RILIS at the general purpose separator (GPS).

- With a last non-resonant step to the continuum, the ionization efficiency depends strongly on the laser power for the last transition. Normally a strong non-tunable laser is used for this non-resonant step. Often it is still not sufficient to reach saturation since the non-resonant cross-sections into the continuum are relatively small ($\sigma = 10^{-19} - 10^{-17}$ cm$^2$).

- Excitation cross-sections to autoionizing states often exceed the non-resonant ones by orders of magnitude (e.g. $\sigma = 1.6 \cdot 10^{-14}$ cm$^2$ in Lu [Xu93]). An autoionizing state (AIS) is a two-electron excitation above the atomic ionization potential $W_i$ which decays in a radiationless transition into an ion and an electron. It is evident that the excitation energy for inner electrons is larger than that of the valence electron. Thus, a subsequent excitation of two electrons to individual levels below the ionization limit can lead to a total excitation energy larger than the first ionization potential. By Coulomb interaction the AIS will decay rapidly, where one electron drops to the ground state or an excited state (with energy $E_x$) of the ion and the other is emitted and gets the exceeding energy $\Delta E = E_{\mathsf{AIS}} - W_i - E_x$ as kinetic energy[6]. Typical lifetimes of AIS are from $10^{-15}$ to $10^{-10}$ s, i.e. the natural width is quite large (many GHz or even THz) and exceeds the radiative decay width (typically some ten MHz) by orders of magnitude. While all many-electron atoms have autoionizing states, only some are favorable for efficient resonance ionization.

---

[6]The atomic recoil is negligible.

- High cross-sections (of the order of $10^{-14}$ cm$^2$) can also be obtained in transitions to Rydberg states.

  The lifetime of a state with high principal quantum number increases like [Fri90]: $\tau = \tau_0(n^*)^3$ where $\tau_0$ is of the order of 1 ns for alkali atoms [Rad85] and $n^*$ is the effective quantum number corrected for the quantum defect[7]. $\tau$ can reach easily values of $\mu$s and longer. Simultaneously the binding energy of a Rydberg state decreases: $E = \mathcal{R}\frac{M}{M+m_e}\frac{Z^2}{(n^*)^2}$ where $\mathcal{R}$ is the Rydberg constant.

  This highly excited atom can be ionized with a high cross-section by absorption of an infrared photon from an additional laser or just from the thermal radiation in the hot cavity. Moreover, the atomic radius increases like $<r> = a_0(n^*)^2$. Thus, the geometric cross-section for collisions with other atoms increases like $(n^*)^4$ and reaches large values. Already a peripheral collision with an atom or an electron will remove the loosely bound electron and lead to an ionization. This ionization mode is used in buffer gas cells.

  Also a pulsed or strong static electrical field (about 10 kV/cm) can Stark shift the closely spaced Rydberg levels into the continuum and lead to ionization (see e.g. ref. [Amb75, Wor78, And86]).

- Non-resonant multiphoton ionization with high power lasers is in principle possible, but has a lower efficiency and practically no chemical selectivity. It is thus not very useful for ISOL applications.
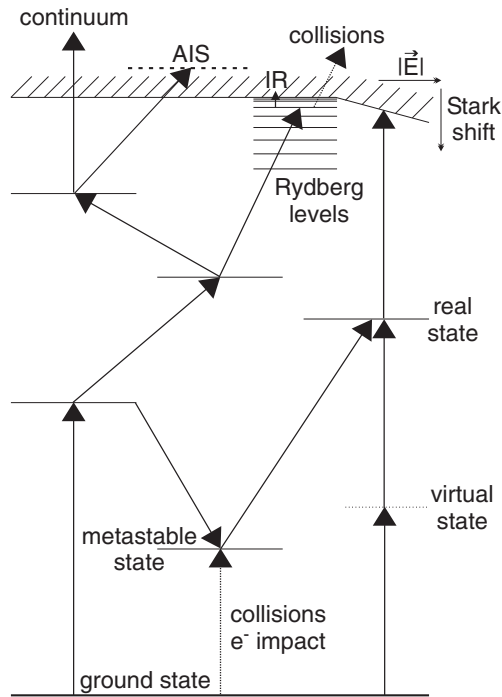


Figure 3.2.1.: Excitation schemes used for resonant laser ionization.

## 3.2.1. Applied schemes

An overview of the experimentally used resonance ionization schemes of most elements can be found in appendix B.8. In principle every element can be laser ionized. However, only if transitions

---

[7]The quantum defect accounts for the core polarization and the exchange interaction between the excited electron and the inner-shell electrons.

to low-lying states ($\lesssim 6$ eV) with a sufficient transition strength exist, appreciable yields can be obtained with the present RILIS technique. Table 3.2.1 shows the excitation schemes of elements presently ionized at the ISOLDE RILIS and figure 3.2.2 gives an overview of elements which could be ionized using dye lasers which are pumped by copper vapor lasers. Generally it can be said that the *optical* set-up of the ISOLDE RILIS can be applied for most metallic elements. Still it has to be kept in mind that first the radio-isotopes have to be released from the target. Thus, refractory elements could well be laser ionized when supplied as an atomic beam, but they are hardly released from a thick ISOL target. Such elements are better released at the buffer gas RILIS LISOL (see table 3.2.2).

Table 3.2.1.: Excitation schemes used at the ISOLDE RILIS. $\lambda_1$, $\lambda_2$ and $\lambda_3$ are the wavelengths of the first, second and possibly third excitation step. More details to the individual schemes and set-ups are given in the quoted references. A star marks the schemes where the efficiency was determined or redetermined during this work.

| Element | IP (eV) | $\lambda_1$ (nm) | $\lambda_2$ (nm) | $\lambda_3$ (nm) | Efficiency (%) | Reference |
|---------|---------|------------------|------------------|------------------|----------------|-----------|
| Li | 5.39 | 670.8 | 610.4 | 610.4, 670.8 | | [Mis93] |
| Be | 9.32 | 234.9 | 297.3 | – | $\gtrsim 7$ | *,[Fed98] |
| Mg | 7.65 | 285.2 | 552.8 | 578.2 | 9.8 | *,[Fed98] |
| Mn | 7.43 | 279.8 | 628.3 | 510.6 | 19.2 | *,[Fed97] |
| Ni | 7.64 | 305.1 | 611.1 | 748.2 | $\gtrsim 6$ | *,[Jok97] |
| Cu | 7.73 | 327.4 | 287.9 | – | $\gtrsim 7$ | *,[Kös99] |
| Zn | 9.39 | 213.9 | 636.2 | 510.6 | 4.9 | *,[Let98] |
| Ag | 7.58 | 328.1 | 546.6 | 510.6 | 14 | [Mis93, Jad97] |
| Cd | 8.99 | 228.8 | 643.8 | 510.6 | 10.4 | *,[Let98, Fed98] |
| Sn | 7.34 | 300.9 | 811.4 | 823.5 | 8.5[(8] | *,[Mis93, Fed95b] |
| Tm | 6.18 | 589.6 | 571.2 | 575.5 | | [Mis87a, Mis93] |
| Yb | 6.25 | 555.6 | 581.1 | 581.1 | 15 | [Mis93] |

Table 3.2.2.: Laser ionized elements at LISOL. The efficiency depends mainly on the efficiency of stopping the recoils in the gas cell. This explains the lower value for rhodium measured with fission products, in comparison with cobalt and nickel where fusion-evaporation products were used.

| Element | IP (eV) | $\lambda_1$ (nm) | $\lambda_2$ (nm) | Efficiency (%) | Reference |
|---------|---------|------------------|------------------|----------------|-----------|
| Ti | 6.82 | 395.8, 337.8 | 339.4, 384.1 | | [Weiss] |
| Co | 7.86 | 230.9 | 481.9 | 6.6 | [Kud96] |
| Ni | 7.64 | 232.0 | 537.8 | 4.6 | [Kud96] |
| Rh | 7.46 | 232.3 | 572.6 | 0.22 | [Kud96] |

The first excited state in the atomic spectra of non-metals is often at a relatively high energy. The ionization of such elements requires different techniques, e.g. a shorter wavelength for the first excitation step or a combination with other excitation methods (see figure 3.2.1).

There are schemes for RIS of non-metals which use selective ionization by photolysis of certain molecules with resonant laser light. This method will not be treated in the following. One has

---

[8]This efficiency was measured with a slightly different set-up at the GSI ISOL.

**elements available at ISOLDE RILIS**

**ionization scheme tested**

**ionization scheme untested**

| 1 H | | | | | | | | | | | | | | | | | 2 He |
|---|---|---|---|---|---|---|---|---|---|---|---|---|---|---|---|---|---|
| 3 Li | 4 Be | | | | | | | | | | | 5 B | 6 C | 7 N | 8 O | 9 F | 10 Ne |
| 11 Na | 12 Mg | | | | | | | | | | | 13 Al | 14 Si | 15 P | 16 S | 17 Cl | 18 Ar |
| 19 K | 20 Ca | 21 Sc | 22 Ti | 23 V | 24 Cr | 25 Mn | 26 Fe | 27 Co | 28 Ni | 29 Cu | 30 Zn | 31 Ga | 32 Ge | 33 As | 34 Se | 35 Br | 36 Kr |
| 37 Rb | 38 Sr | 39 Y | 40 Zr | 41 Nb | 42 Mo | 43 Tc | 44 Ru | 45 Rh | 46 Pd | 47 Ag | 48 Cd | 49 In | 50 Sn | 51 Sb | 52 Te | 53 I | 54 Xe |
| 55 Cs | 56 Ba | 57 La | 72 Hf | 73 Ta | 74 W | 75 Re | 76 Os | 77 Ir | 78 Pt | 79 Au | 80 Hg | 81 Tl | 82 Pb | 83 Bi | 84 Po | 85 At | 86 Rn |
| 87 Fr | 88 Ra | 89 Ac | 104 Rf | 105 Db | 106 Sg | 107 Bh | 108 Hs | 109 Mt | 110 | 111 | 112 | | | | | | |

| 58 Ce | 59 Pr | 60 Nd | 61 Pm | 62 Sm | 63 Eu | 64 Gd | 65 Tb | 66 Dy | 67 Ho | 68 Er | 69 Tm | 70 Yb | 71 Lu |
|---|---|---|---|---|---|---|---|---|---|---|---|---|---|
| 90 Th | 91 Pa | 92 U | 93 Np | 94 Pu | 95 Am | 96 Cm | 97 Bk | 98 Cf | 99 Es | 100 Fm | 101 Md | 102 No | 103 Lr |

Figure 3.2.2.: Elements ionizable with dye lasers pumped by copper vapor lasers.

to keep in mind that a dominant occupation of certain molecular states depends strongly on the chemical environment of the target and ion source system. This is not easy to control (see also section 4.1).

## 3.2.2.　Power requirements

The laser ionization efficiency depends on the saturation of all participating excitations. The power requirements to saturate these transitions can be estimated by regarding the rate equations. In the following the brief discussion from ref. [Amb76] is presented for the case of a two-step photoionization scheme. The generalization to more intermediate levels is straightforward. The density of the atoms in the ground state is $N_1$, that in the excited state is $N_2$ and the ion density is $N_i$. With $\tau_2$ the relaxation time of the excited state, $\sigma_{xy}$ the absorption cross-sections and $\Phi_{xy}$ the provided photon flux for the respective transitions, the rate equations read:

$$
\begin{aligned}
\frac{dN_1}{dt} &= -\sigma_{12}\Phi_{12}(N_1 - N_2) + \frac{N_2}{\tau_2}, & N_1(t=0) &= N_0, \\
\frac{dN_2}{dt} &= \sigma_{12}\Phi_{12}(N_1 - N_2) - \sigma_{2i}\Phi_{2i} - \frac{N_2}{\tau_2}, & N_2(t=0) &= 0, \\
\frac{dN_i}{dt} &= \sigma_{2i}\Phi_{2i}.
\end{aligned}
\tag{3.2.1}
$$

For strong enough excitation:

$$
\begin{aligned}
\sigma_{12}\Phi_{12} &\gg 1/\tau_2, \\
\sigma_{2i}\Phi_{2i} &\gg 1/\tau_2,
\end{aligned}
\tag{3.2.2}
$$

the radiative decay of the excited state $\tau_2$ can be neglected and the ionization degree depending on the time after start of the laser pulse is given by:

$$
\alpha = \frac{N_i}{N_0} = 1 - \frac{a_1 + a_2}{2a_2}\exp\left(-(a_1 - a_2)t\right) + \frac{a_1 - a_2}{2a_2}\exp\left(-(a_1 + a_2)t\right),
\tag{3.2.3}
$$

with:

$$a_1 = \sigma_{12}\Phi_{12} + \tfrac{1}{2}\sigma_{2i}\Phi_{2i},$$

$$a_2 = \sqrt{(\sigma_{12}\Phi_{12})^2 + (\tfrac{1}{2}\sigma_{2i}\Phi_{2i})^2}. \qquad (3.2.4)$$

$\alpha$ reaches its maximum for:

$$\sigma_{2i}\Phi_{2i} = 2\sigma_{12}\Phi_{12}. \qquad (3.2.5)$$

Thus, the characteristic time for ionization of all atoms is given by:

$$\tau_i = \frac{1}{a_1 - a_2} = \frac{1}{\sigma_{12}\Phi_{12}}\left[1 + \frac{\sigma_{2i}\Phi_{2i}}{2\sigma_{12}\Phi_{12}} - \sqrt{1 + \left(\frac{\sigma_{2i}\Phi_{2i}}{2\sigma_{12}\Phi_{12}}\right)}\right]^{-1} =$$

$$= \frac{1}{(2-\sqrt{2})\sigma_{12}\Phi_{12}}. \qquad (3.2.6)$$

Not only the photon flux $\Phi$ has to be high enough, but also the photon fluence integrated over the full laser pulse $\int \Phi dt$. Only then all atoms in the volume can interact with the laser beam and get ionized:

$$\int \Phi_{12}dt \gg (2\sigma_{12})^{-1},$$
$$\int \Phi_{2i}dt \gg \sigma_{2i}^{-1}. \qquad (3.2.7)$$

To achieve an optimum photo-ionization efficiency both, the flux condition (3.2.2) and the fluence condition (3.2.7) have to be fulfilled.

The discussion above assumes that the laser bandwidth $\delta\nu_{\text{laser}}$ just matches the width of the possibly broadened resonance $\delta\nu_{\text{res}}$. If the laser bandwidth is too small, only the atoms in the overlapping part of the frequency range will get excited. In case of a too broad laser bandwidth the power in the wings is lost and the effective photon flux is reduced to: $\Phi_{\text{eff}} \approx \Phi\delta\nu_{\text{res}}/\delta\nu_{\text{laser}}$.

Fulfilling the flux condition for intermediate steps is normally not very demanding. From the relation of the Einstein coefficients the stimulated emission cross-section $\sigma_{21}$ can be derived as [Hur88]:

$$\sigma_{21}(\nu_0)\delta\nu_{\text{res}} \approx \int \sigma_{21}(\nu)d\nu = \frac{\lambda^2}{4\tau_{21}}. \qquad (3.2.8)$$

Here, the integration of the cross-section over the resonance was replaced by the value at the line center $\omega_0$ times the resonance width $\delta\nu_{res}$. $\tau_{21}$ is the partial lifetime of the excited state for spontaneous emission back to the ground state. The cross-sections for absorption $\sigma_{12}$ and stimulated emission $\sigma_{21}$ are connected by:

$$\sigma_{12}g_1 = \sigma_{21}g_2 \qquad (3.2.9)$$

with the statistical factors $g_x = 2J_x + 1$ (see appendix B.6 for the ground state values). Thus:

$$\sigma_{12} = \frac{g_2}{g_1}\frac{\lambda^2}{4\delta\nu_{\text{res}}\tau_{21}}. \qquad (3.2.10)$$

That means for levels with a low $\tau_{21}$ the corresponding absorption cross-section is higher and the determining product for the saturation condition $\sigma_{12}\tau_{21}$ remains constant. However, this is only valid if the intermediate level decays mainly back to the ground state. If it has a significant transition rate to a metastable state (i.e. a short partial decay time $\tau_{2m}$), these atoms will be lost for further laser excitation. This problem occurs e.g. for lead where the intermediate level $6p7s\,^3P_1^o$ has a lifetime of 5.8 ns and only 15 % of the spontaneous decays go back to the ground state. Therefore a larger laser power is required to enhance the rate of photoionization over the spontaneous decay rate. Equation (3.2.10) shows also that a certain gain can be achieved when choosing a transition from a state with low angular momentum to one with a higher angular momentum. However, also the selection rules of the transition and the polarization of the laser light will play a role. This will be discussed at the end of this chapter.

## 3.3.   Laser system

For an efficient operation of a "hot-cavity-RILIS" the pumping lasers should meet the following requirements:

- The wavelength should be as short as possible (yellow to green or shorter).
- The repetition rate should be of the order of 10 kHz.
- For the non-resonant ionization step the number of photons should be at least some $10^{15}$ per shot. For visible light this corresponds to some mJ pulse energy. With the given repetition rate the average beam power will be some ten W.
- The pulse length should be of the order of some $10 - 30$ ns, giving a pulse power of about 100 kW at 10 kHz repetition rate.
- The laser system should allow a continuous operation for several days with minimum maintenance.

Presently mainly copper vapor lasers are used for efficient operation at such a repetition rate. The set-up of the ISOLDE RILIS consists of dye lasers pumped by copper vapor lasers. It has been described in [Sch93]. A similar system is used at Mainz university for resonance ionization spectroscopy of actinides [Rus89].

**Copper vapor laser**

Copper atoms are excited in a plasma discharge from the ground state $3d^{10}(^1S)4s\ ^2S$ to the levels $3d^{10}(^1S)4p\ ^2P^o$. The latter decay by emission of light with 510.6 and 578.2 nm to the metastable states $3d^94s^2\ ^2D$. These have to be quenched to repopulate the ground state. Their effective lifetime is some 10 to 100 $\mu$s and depends on the gas pressure in the tube. Therefore a copper vapor laser (CVL) can only run in a pulsed operation with a maximum repetition rate of some ten kHz. The yellow light is delayed by about $3 - 5$ ns with respect to the green one. CVLs can already be built with simple means [Wal90], but to obtain an efficient and reliable operation more effort is needed. Sealed tubes allow an easier set-up. A certain amount of copper is kept in the sealed glass tube which is filled with a noble gas; for the ISOLDE RILIS CVL it is Ne at 200 mbar pressure. Slowly heating the tube by plasma discharges in the noble gas will evaporate the copper. After some time (1-2 h) a thermal equilibrium (around 1500 °C[9]) with constant copper vapor pressure (about 1 mbar) is obtained and the laser is running stably and efficiently. After switching off the plasma discharge heating, the copper will condense again. These tubes have lifetimes of 1000 to 2000 h of operation. Their performance goes down gradually and eventually they have to be exchanged if too much copper was lost due to leakage or deposition in the plasma channel or on the exit windows. Compared to other lasers, CVL can reach a relatively high "plug efficiency" (total efficiency from electrical input power to emitted light) of about 1 %. A system of three tubes is used which gives a better beam quality than a single big tube. A smaller tube (about 6 W light output) runs as an oscillator with an unstable resonator and two bigger tubes (30 and 45 W light output) are used to amplify the low-divergence part of the oscillator beam. The components with higher divergence are removed with a diaphragm.

For optimum overlap in time of the three laser beams, they have to be fired within some ns. A trigger unit is used for synchronization. Thyratrons (fast triodes) are used to provide the high voltage (about 30 kV after doubling in a resonantly charged circuit) and high current (some kA peak current) with a small time jitter (some ns). For fast recovery they are filled with hydrogen. Their lifetime is also in the range of 1000 to 2000 h. An improvement could be achieved by replacing the thyratrons by fast solid state switches. These systems have lifetimes exceeding 20000 h of operation and do not show significant changes of the timing characteristics during their lifetime.

---

[9]This operation temperature can be significantly reduced by adding halides to the gas.

**Dye laser**

Dye lasers are used to provide laser light with tunable wavelength. Two or three dye lasers in Hänsch geometry [Hän72] are pumped transversely by the CVL beams. The wavelength is tuned by rotation of a diffraction grating. If necessary the light is amplified in one or two subsequent dye laser cells identical to the first one. The choice of the laser dyes and the set-up has to be optimized individually for the ionization of different elements. Beams in a spectral range of $540 - 850$ nm have been produced. As an example the set-up for ionization of copper is described in the following.

For the first step transition a narrow-band dye laser was used. Its resonator includes a holographic grating with 2400 grooves/mm and a glass etalon of 6 mm thickness. The frequency of the dye laser could be tuned by synchronous rotation of the diffraction grating and the Fabry-Perot etalon. Such rotation was provided by electronical control of both elements with a microprocessor unit. The bandwidth of this dye laser is 1.2 GHz. The light is amplified in a subsequent dye laser cell identical to the first one and then frequency doubled (see below) in an external type-I BBO crystal (6 mm long). Part of the first harmonic is guided with an optical fiber to a lambdameter (model LM-007 from ATOS [ATOS]) where the frequency is measured with a resolution of $< 300$ MHz and an accuracy of $< 90$ MHz by analysing the fringe patterns of four Fizeau interferometers. The frequency can be logged continuously.
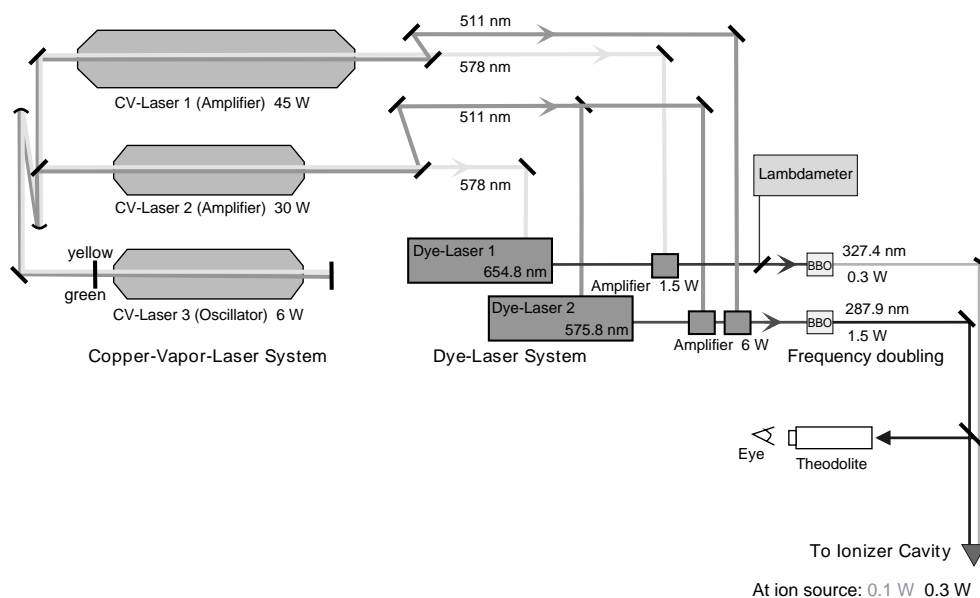


Figure 3.3.1.: Setup of the RILIS laser system for ionization of copper.

Using the laser dye Phenoxazon 9 (Lambda Physics) pumped with the yellow CVL light, a fundamental beam (654.8 nm) of 1.5 W was obtained, which then was frequency doubled producing 0.3 W at 327.4 nm. About 0.1 W of the UV beam could be focused over 17 m into the 3 mm diameter ionizer cavity. This was sufficient to saturate the first transition which has an oscillator strength of 0.22 [Rad85].

For the second step a broad-band (25 GHz bandwidth) dye laser was used. With the laser dye Rhodamine 6G pumped with the green CVL light it produced about 6 W in the fundamental beam (575.8 nm) with two dye amplifiers. With 25 % conversion efficiency for second harmonic generation about 1.5 W were available at 287.9 nm on the table and about 0.3 W were focused into the cavity. Figure 3.3.1 gives an overview of the used laser system.

**Generation of ultraviolet light**

For many elements the first excited level has an excitation energy above 3 eV. Therefore a source of intense ultraviolet light with tunable wavelength is required. Dye lasers can only produce light with wavelengths longer than that of the pumping beam and are generally restricted to wavelengths longer than about 320 nm. For shorter wavelengths a dye laser beam in the visible range can be produced and frequency doubled by Second Harmonic Generation (SHG) in a nonlinear optical crystal. While the summing of two photons of a given wavelength to one photon with half the wavelength can occur in many media, only a nonlinear medium allows to produce an intense frequency-doubled beam by a coherent superposition. For an efficient energy transfer from the electromagnetic wave with frequency $\omega$ to the wave with frequency $2\omega$, both have to remain in phase over a certain distance, i.e. their phase velocity and thus their indices of refraction have to be equal: $n(\omega) = n(2\omega)$. In non-linear crystals the birefringence (i.e. the difference between the refraction indices of extraordinary and ordinary beam $n^e - n^o$) can be used to offset the dispersion. This condition is called phase matching. It is achieved by tuning entrance angle and/or temperature of the non-linear crystal.

Beta-Barium-Borate[10] (BBO) crystals are used for frequency doubling of dye laser light with efficiencies of 20 % and above for $\lambda \gtrsim$ 210 nm. The shortest possible wavelength for SHG is 204.8 nm [Kat86, Miy86], however with low efficiency. To reach short wavelengths also Third Harmonic Generation (THG), Forth Harmonic Generation (FHG), etc. can be used. The efficiency of these nonlinear processes increases with the power density of the fundamental beam, e.g. the power of the third harmonic goes with the third power of the fundamental beam power density. With less intense dye laser beams, the third harmonic ($3\omega$) can be produced more efficiently by frequency doubling in a first crystal and then summing fundamental ($\omega$) and frequency doubled beam ($2\omega$) in a second crystal. Wavelengths down to 189 nm can be produced in this way with BBO crystals [CAS].

Production of 210 nm light with 10 mW average power has been demonstrated with dye lasers pumped by CVL [Kop94]. Using this technique beams with 2 mW average power at 229 nm were applied for resonant photo ionization of Cd [Erd98b]. Further optimizing the method for the efficient ionization of beryllium at the ISOLDE RILIS, an intense tunable UV laser beam of up to 200 mW average power at 235 nm was developed as a spin-off.

The damage threshold of BBO crystals for visible light is larger than 1 GW/cm$^2$ (for 10 ns pulse length). Although the dye laser power of the RILIS stays well below this limit, problems occurred in cases where a very intense dye laser beam (some W average power) was frequency doubled, e.g. for the second transition in Be and Cu. Heating of the nonlinear crystal changes its refraction index and thus the phase matching angle. Any power fluctuation of the copper vapor laser affects the power of the dye laser. This in turn changes the temperature of the BBO crystal, reducing the SHG efficiency. This coupling makes a stable operation of the RILIS more difficult. Moreover dust particles deposited on the surface of the crystal will absorb the dye laser light and heat the crystal. This leads locally to an enhanced absorption. Both effects are mutually amplifying and can lead eventually to a destruction of the crystal ("drilling" of a channel or cracking).

Going to wavelengths in the far UV region (below 200 nm) would require significantly higher efforts: frequency conversion with low efficiencies in gaseous media, change of quartz lenses and windows against $CaF_2$ and an evacuated or helium filled tube to guide the UV laser beam without absorption in oxygen. This and the partial loss in selectivity due to increasing direct one-step ionization of isobars make an extension of the RILIS to non-metallic elements less promising. Nevertheless, by combination with other excitation mechanisms photo-ionization could still be applied. In cases where metastable states with sufficient lifetime exist, these can be populated by electron impact, a

---

[10]$\beta$-BaB$_2$O$_4$.

plasma discharge or atomic collisions in a gas cell and then be used as initial levels for subsequent photo-ionization. The lifetime should be long enough ($\sim$ms) to remove by an electrical field isobars which were ionized in the first non-selective excitation.

### CVL and alternatives

The electromagnetic RF pulses emitted by the CVL ignition can disturb electronic devices in the environment. Especially preamplifiers of charge-collecting detectors (e.g. germanium or silicon detectors) are very sensitive to this background[11]. Despite additional shielding of the cables, an anti-gating has to be applied to close the data acquisition of nuclear spectroscopy experiments in the ISOLDE hall for some $\mu$s at each laser ignition. With about 11 kHz repetition rate this creates a constant deadtime of some percent.

Another disadvantage of the CVL is the long start-up time. A stable operation mode with thermal equilibrium of the laser tube and a constant copper vapor pressure is reached only after about two hours of heating.

### Alternative pumping lasers

Excimer lasers have the advantage that wavelengths down to the vacuum ultraviolet region (e.g. 157 nm with $F_2$ gas) can be produced. However, the repetition rates do not exceed some 100 Hz. Putting a series of multiplexed excimer lasers in parallel to reach higher repetition rates would become very expensive and the maintenance is also very cumbersome.

High-power, high repetition rate Nd-YAG lasers are under development and should become commercially available at reasonable prices in the next years. Presently available Nd-YAG lasers already match the required repetition rate and average power, but the pulse width is still quite long (200-600 ns), reducing considerably the peak power of the pumped dye laser and the frequency-doubling efficiency. Others already have the required pulse length (30 ns) and repetition rate (10 kHz), but the power is still low [Leb98].

From a Nd-YAG laser with intracavity frequency doubling a second harmonic beam of 532 nm is extracted for pumping the dye lasers. Being not too far from the 511 nm and 578 nm wavelengths of a CVL, the tested excitation schemes and optical set-ups can often be adopted with small modifications. With increasing power of the Nd-YAG laser also the efficiency for THG and FHG becomes appreciable and in individual cases these shorter wavelengths (355 and 266 nm) can be employed for direct pumping of a dye laser.

A Nd-YAG laser is ideally suitable to pump a titanium doped sapphire laser [Grü98]. The latter has an absorption band of 400 to 600 nm and the use of Q-switching allows to reduce the pulse length to the required values (about 10 to 30 ns). Moreover such a full solid-state system requires less maintenance (e.g. no change of dyes). However, only wavelengths in the red and infrared region (700 to 1000 nm) can be produced and thus additional SHG or THG steps are required. Also the commercially available Ti-sapphire lasers (e.g. INTRA-Ti from Laser Analytical Systems [LAS]) are still rather limited in power.

There is great economic interest to make uranium enrichment by resonant laser ionization competitive to the classical methods of diffusion and centrifugation. Such projects are pursued in the U.S. (AVLIS project [Har00], LLNL) and in France (SILVA project [Caz96], Cogema and CEA). First industrial application of this method is expected in 2005 and should replace the presently operating diffusion facilities within 20 years [Mot97]. The RILIS application at ISOL facilities should profit

---

[11]These pulses are even directly visible as interferences to the program on a TV screen in a building next to the ISOLDE hall (some 40 m from the laser barrack). A change of this interference pattern indicates a misfunction of the CVL. Thus, this TV is the first step towards a remote supervision system for the RILIS.

from the effort which is spent on this development of efficient and reliable laser systems which meet exactly the requirements of a hot cavity type RILIS.

## 3.4.   The RILIS cavity

### 3.4.1.   Geometry of the cavity

The role of the cavity is to keep the effusing atoms for a certain time in a volume where they can be irradiated by the laser light. The ISOLDE RILIS cavities are tubes with a diameter $d = 3$ mm (adapted to the size of the focused laser beams) and a length of 30 to 60 mm.

The flux of atoms effusing through the cavity is given by Fick's first law:

$$J_{\text{at}} = -D\frac{\partial \rho}{\partial x}. \tag{3.4.1}$$

For thin gases $D$ can be expressed as:

$$D = \frac{1}{3}\lambda\bar{v}, \tag{3.4.2}$$

with $\bar{v}$ the mean thermal velocity and $\lambda$ the mean free path. For thin tubes $(d \ll l)$ the latter is identical to $d$.

With an efficient ion extraction, the flux of photo-ions leaving the cavity is given by:

$$J_{\text{ion}} = \int_0^l \rho(x)\varepsilon_{\text{photo}}f_{\text{rep}}dx, \tag{3.4.3}$$

where $f_{\text{rep}}$ is the repetition rate of the laser system and $\varepsilon_{\text{photo}}$ the probability of photo-ionization per laser pulse. The latter is determined by the degree of saturation of all transitions and the population of the state excited in the first step. It is typically of the order of some ten percent.

Supposing a linear decrease of the atom density along the cavity $(\rho(x) = \rho_0(1 - x/l))$, the total efficiency for photo-ionization in the cavity can be estimated to:

$$\varepsilon_{\text{ion}} = \frac{J_{\text{ion}}}{J_{\text{ion}} + J_{\text{at}}} = \frac{\frac{1}{2}l\rho_0\varepsilon_{\text{photo}}f_{\text{rep}}}{\frac{1}{2}l\rho_0\varepsilon_{\text{photo}}f_{\text{rep}} + \frac{1}{3}d\bar{v}\frac{\rho_0}{l}} = \frac{\varepsilon_{\text{photo}}f_{\text{rep}}}{\varepsilon_{\text{photo}}f_{\text{rep}} + \frac{2}{3}\frac{d}{l^2}\bar{v}}. \tag{3.4.4}$$

For example with $\varepsilon_{\text{photo}} \approx 10$ %, $f_{\text{rep}} = 10$ kHz, $l = 3$ cm, $\bar{v} \approx 600$ m/s (for $A = 130$ and $\theta = 2000$ °C) a total photo-ionization efficiency of $\varepsilon_{\text{photo}} \approx 60$ % can be reached for stable isotopes $(T_{1/2} \to \infty)$. For lighter isotopes, e.g. $^7$Be in a 2400 °C hot cavity $(\bar{v} \approx 2800$ m/s), and identical $\varepsilon_{\text{photo}}$ the efficiency drops to $\varepsilon_{\text{ion}} \approx 24$ %.

For short-lived radio-nuclides additionally the radioactive decay has to be taken into account. The intrinsic delay time of the RILIS cavity $(\sim 0.1$ ms) is much shorter than that of the target and can be neglected. On the other hand the delay due to adsorption on the cavity surface can become important, especially at lower temperatures. Therefore a compromise has to be found for the geometry $(d$ and $l)$, material and temperature of the cavity.

According to equation (3.4.4) the neutral effusion losses can be reduced by increasing the length of the cavity. However, the calculated photo-ionization efficiency $\varepsilon_{\text{ion}}$ is not equal to the source efficiency $\varepsilon_{\text{source}}$ observed in practice. The latter includes also the significant losses due to imperfect ion extraction from the cavity. Obviously these losses tend to increase for long and thin cavities.

## 3.4.2.    Role of the thermal plasma potential

Without any radial potential well in the ionizer cavity, a large part of the created ions would hit the wall and recombine to neutral atoms. Due to the repelling positive space charge, the percentage of ions extracted without wall collisions would be even smaller than estimated from simple geometrical considerations. However, heating of the cavity will release electrons from the walls by thermal emission. If enough electrons are emitted into the cavity, they will not only compensate the positive space charge of the ions, but even create a negative potential which will keep most ions from touching the walls.

Compared with the current from thermionic emission, the number of electrons released by ionization of atoms in the cavity can be neglected. On the other hand the positive ions created in laser or surface ionization cannot be neglected. Due to their lower speed, they stay in the cavity much longer than the electrons. Not taking into account the electrical fields these ions would remain in the cavity for about 100 $\mu$s, giving a density of positive ions of about $n_i \approx 3 \cdot 10^7$ cm$^{-3}$. In reality a plasma potential will build up, which traps the ions in a trough and repels the electrons towards the wall. Thus, both densities become equal and in the interior of the cavity quasi-neutrality is given: $n_i = n_e = n_p$[12]. With typical ISOL targets, a significant part of the ions in the RILIS cavity still consists of easily surface ionizable species (alkalis or earth alkalis). Therefore the formalism of thermal ion sources can be applied (see appendix B.5).

Two principal differences should be noted:

1. In a thermoionization source the source efficiency increases with the work function of the cavity material. In contrast the source efficiency of a hot cavity RILIS increases when a cavity material with lower work function and thus stronger electron emission is used. The latter lowers the negative plasma potential further and thus increases the extraction efficiency of the ions ($\omega$ in equation (B.5.5)). On the other hand the single-shot laser ionization efficiency ($\beta$ in equation (B.5.5)) is only given by the ionization scheme and the laser power and is not affected by the cavity material. In this analogy the number of wall collisions ($\kappa$ in equation (B.5.5)) could be identified with the number of laser pulses which interact with the atom while the latter is stored in the cavity volume.

2. Unlike in a thermoionization source the photoionized ions are created not at the surface but mainly in the volume of the cavity, i.e. already at negative potential $U_p$. If the depth of the potential trough is larger than the radial kinetic energy of the ions ($-U_p \gg E_{kin}^{rad}$) they cannot touch the wall which is at positive potential. Thus, an increase of the neutral gas pressure will not increase $\omega$, but rather cause a loss in efficiency and selectivity due to charge-exchange collisions.

**Typical plasma parameters**

To quantify the ion trapping effect of the cavity the plasma parameters have to be derived from experimentally accessible values. The plasma potential $U_p$ depends on the cavity temperature $T$, the ion density $n_i$ and the work function $\Phi$ of the cavity wall material [Lat75]:

$$U_p = kT \ln \frac{A^* T^2}{e n_i \sqrt{\dfrac{M}{2\pi m_e}}} - \Phi, \tag{3.4.5}$$

with $A^*$ the Richardson constant (see table B.7.1). The only parameter in this equation which is not directly accessible by experiments is the density of ions in the plasma, which is in fact equal to the density of electrons and therefore just called plasma density $n_i = n_e = n_p$.

---

[12]$n_p$ is called the plasma density.

For surface ion sources the extracted current density is rather low, i.e. far below the space charge limit[13]. Thus, the extracted current is approximately related to the plasma density via [Che60]:

$$I_{\text{total}} = n_{\text{p}} S e \sqrt{\frac{kT_{\text{e}}}{M}}, \tag{3.4.6}$$

where $S = 7$ mm$^2$ is the outer plasma surface (flat boundary) at the extraction orifice. Inserting $n_{\text{p}}$ from equation (3.4.6) into equation (3.4.5) gives:

$$U_{\text{p}} = kT \ln \frac{A^* T^2}{\frac{I_{\text{total}}}{S} \sqrt{\frac{M}{2\pi m_{\text{e}}}}} - \Phi, \tag{3.4.7}$$

or in typical units:

$$
\begin{aligned}
U_{\text{p}} \approx\; & 0.22 \text{ eV} \cdot \frac{T}{2500 \text{ K}} \left( 31.1 + \ln \frac{A^*}{120 \text{ Acm}^{-2}\text{K}^{-2}} + 2 \ln \frac{T}{2500 \text{ K}} - \right. \\
& \left. - \ln \frac{I_{\text{total}}}{10 \text{ nA}} - \frac{1}{2} \ln \frac{A}{100} \right) - \Phi.
\end{aligned}
\tag{3.4.8}
$$

Often medium mass nuclei will dominate the total current, therefore $A = 100$ is arbitrarily chosen. The total current varies typically in a range of about 1 to 100 nA. With increasing temperature of the cavity the vapor pressure of impurities and the surface ionization efficiency increase and thus the total current will rise. Therefore the assumption of a constant current is surely wrong. However, due to the logarithmic dependence in formula (3.4.7) the correction remains small and can be neglected in a first approximation[14]. Figure 3.4.1 shows the dependence of the plasma potential on the temperature for various cavity materials. The values for $\Phi$ and $A^*$ were taken from table B.7.1. $A^*$ is given as multiple of the theoretical Richardson constant $A_0 = 120$ Acm$^{-2}$K$^{-2}$.
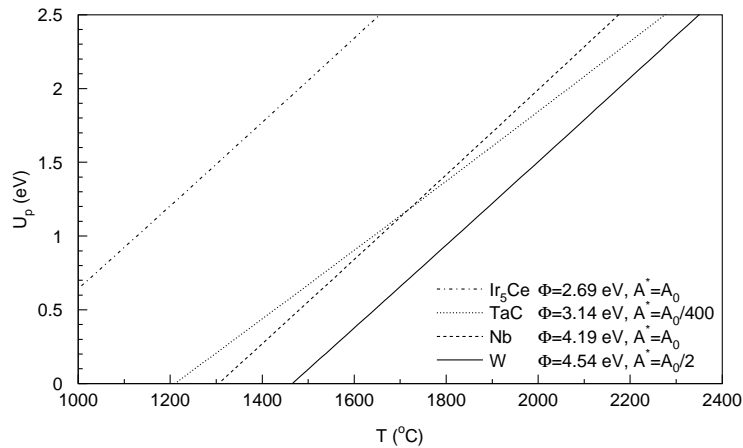


Figure 3.4.1.: Plasma potential in a RILIS cavity calculated with equation (3.4.7) with a surface ionized current of 10 nA and $A \approx 100$.

While the absolute scale of the calculated plasma potential depends to some extend on the used assumptions, the plotted curves show nicely the relative behavior of typical cavity materials. A

---

[13]The space charge limit is given by the Child-Langmuir law [Lan31]: $I = 1/(9\pi)\sqrt{2e/M}U_{\text{extr}}^{3/2}/d^2$, where $M$ is the ion mass, $U_{\text{extr}}$ the extraction voltage and $d$ the size of the extraction gap.

[14]Under on-line conditions at ISOLDE the vapor pressure of the impurities will be mainly determined by the material and temperature of the target and less by the operation conditions of the ionizer cavity. The ionization efficiency of the dominating alkalis shows only a small temperature dependence.

tungsten cavity requires the highest temperatures to provide sufficient electron emission for a trapping of the laser ionized ions. A niobium cavity will give a similar potential already at about 200 °C lower temperature. For very low temperatures a tantalum carbide cavity shows a slower drop of the plasma potential. Thus, such a cavity should better conserve a high RILIS efficiency when the cavity temperature is lowered. Indeed this was experimentally observed, see figure 9 in ref. [Mis93]. However, due to the small Richardson constant of TaC the gain is less than expected from the low work function. Finally $Ir_5Ce$ is shown as an example for a possible alternative material with very good electron emission at lower temperatures. However, it was not yet tested as RILIS cavity (see discussion below). Taking into account also the dependence of the total surface ionized current on the work function of the material would even enhance the differences between the materials presented in figure 3.4.1.

Using equation (3.4.6) the Debye length[15] can be estimated to:

$$\lambda_D = \sqrt{\frac{\varepsilon_0 kT}{n_p e^2}} = 0.8 \text{ mm} \left(\frac{I}{10 \text{ nA}}\right)^{-\frac{1}{2}} \left(\frac{T}{2500 \text{ K}}\right)^{\frac{3}{4}} \left(\frac{A}{100}\right)^{-\frac{1}{4}}. \qquad (3.4.9)$$

Thus, it is smaller than the cavity dimensions[16] (diameter $d = 3$ mm) and allows in a first approximation to neglect the influence of wall collisions on the velocity distribution of the ions. Still this plasma is quite thin and not all ions can be trapped.

The potential drop along the cavity influences the plasma potential. The ions are accelerated to a longitudinal velocity which exceeds their thermal speed considerably. Electrons are pulled towards the positive end of the line (the RILIS or surface ionizer cavity is also called "line" in the ISOLDE synoptic), therefore increasing the trapping potential there and thus the extraction probability of ions created towards this end. The front part will get depleted of electrons, thus decreasing the extraction probability. The magnitude of these effects depends on the maximum electron emission from the cavity walls (see equation (B.7.1)) and thus on the cavity material. This effect is more pronounced if the electron emission per surface area is limited, e.g. in insulator cavities.

Note that due to the pulsed laser ionization in addition $n_i$ and $n_e$ will show variations in time on a level of several 10 % (partial pressure of laser ionizable element multiplied by laser ionization efficiency per shot $\varepsilon_{ion}$). Locally $n_i(z)$ and $n_e(z)$ may vary even stronger. The time to react on this perturbation is governed by the plasma frequency $\omega_p$:

$$\omega_p = \sqrt{\frac{n_p e^2}{m_e \varepsilon_0}}. \qquad (3.4.10)$$

With the parameters derived above, the plasma frequency is of the order of $0.1 - 1$ GHz. Thus, on the time scale of a laser ion pulse (see below) the plasma immediately follows the perturbations caused during the impact of the laser beam. For a surface ionized species, a clear drop of the current is observed simultaneously to the maximum of the laser ionized peak.

**Pulse shape**

The laser ionization happens during some ten ns, but the observed ion pulse will be much longer due to the different ion extraction times depending on the position in the cavity. The ohmic heating causes a voltage drop $U$ along the length $l$ of the line and thus a constant longitudinal field $\vec{E}$ with

---

[15]The Debye length characterizes the distance over which a plasma compensates an external electrical field.

[16]The relation $\lambda_D \ll d$ is a necessary condition to obtain a "true" plasma. If the plasma is thinner, the trapping effect for the ions is significantly reduced.

$|\vec{E}| = U/l$. Created at rest in a distance $x$ from the extraction hole, the ions with mass $m = A\,\mathrm{u}$ are extracted with a delay $t_\mathrm{ex}$ of about[17]:

$$t_\mathrm{ex} = \sqrt{\frac{2mx}{e|\vec{E}|}} = 1.44\ \mu\mathrm{s}\sqrt{\frac{Ax/\mathrm{cm}}{|\vec{E}|/(\mathrm{V/cm})}} = 1.44\ \mu\mathrm{s}\sqrt{\frac{A}{U/\mathrm{V}}}\sqrt{xl/\mathrm{cm}^2}. \tag{3.4.11}$$

The spread can reach 43 $\mu$s for ions of mass $A = 100$ created in a 3 cm long cavity with a longitudinal voltage drop of 1 V.

In fact the ions are not created at rest, but during ionization they will mainly keep their initial momentum[18]. Ions with kinetic energy $E_\mathrm{kin}$ moving away from the orifice will get an additional delay $\delta t_\mathrm{ex}$ compared with ions moving with $E_\mathrm{kin}$ towards the orifice:

$$\delta t_\mathrm{ex} = \frac{\sqrt{8mE_\mathrm{kin}}}{e|\vec{E}|}. \tag{3.4.12}$$

Thus, the thermal velocity distribution translates to a Gaussian broadening of the time structure with a width:

$$\delta t_\mathrm{ex}^\mathrm{FWHM} = \frac{\sqrt{8\ln(2)mkT}}{e|\vec{E}|} = 1.06\ \mu\mathrm{s}\frac{\sqrt{AT/(2273\ \mathrm{K})}l/(\mathrm{cm})}{U/(\mathrm{V})}. \tag{3.4.13}$$

A comparison of relations (3.4.11) and (3.4.13) shows that the first contribution to the total pulse width $\tau_\mathrm{pulse}$ is dominant if the potential drop $U$ along the line is not too small:

$$U \gtrsim 0.54\ \mathrm{V}\ T/(2273\ \mathrm{K}). \tag{3.4.14}$$

From equations (3.4.11) and (3.4.13) it is obvious that a short cavity is of advantage to provide a narrow pulse width. On the other hand a short cavity will reduce the laser ionization efficiency according to equation (3.4.4). Thus a compromise has to be found for the cavity length. The detailed shape of the laser ion pulse depends on the density distribution of the neutral atoms along the line (determining the position dependent laser ionization rate), the extraction time and the position dependent extraction efficiency[19]. The latter depends in turn on the radial and longitudinal velocity components of the ion. A Monte Carlo simulation reproduces nicely most features of the experimentally observed pulse shape [Lettr]. In the following only experimentally observed pulse shapes are shown to illustrate the dependence on the cavity properties discussed above.

**Measurement of the pulse shape**

Different methods are employed to measure the shape of the laser ion pulses:

**Beam chopper:** A fast beam gate (rise and fall time about 1 $\mu$s) is opened for a given time interval after each laser pulse. Shifting the delay of this time interval relative to the laser pulse allows to scan the pulse form with a standard Faraday cup (FC) behind the beam chopper. Since the pulse form is very well reproduced from shot to shot, the FC current can be averaged over several seconds.

---

[17] Here, only the relative delay between ions created at different positions along the cavity is regarded. The additional acceleration due to the extraction field entering the front part of the cavity is neglected.

[18] The momentum of the absorbed photon and the recoil of the emitted electron are negligible.

[19] These contributions result in a reduction of the pulse width compared with the "worst-case" estimation of equation (3.4.11).

**Fast Faraday cup:** Mounting the catcher plate (5 mm diameter) of a Faraday cup as part of an integrated amplifier circuit provides a fast response. The maximum sampling frequency is 150 kHz and the amplification is 100 mV per 1 nA. Also another circuit is used which has characteristics similar to the dynode amplifier.

**Dynode amplifier:** The highest sampling rate of 1.8 MHz can be reached with a dynode amplifier at an amplification of 1 mV per 1 nA. It is just the amplification stage of a photomultiplier where the photocathode has been removed. Its dynamic range goes from 20 pA to 200 nA.

The following pulse shapes were measured with the latter two devices.

The mass dependence in formulae (3.4.11) and (3.4.13) is directly seen by comparing the pulse shapes of two different isotopes. This is shown in figure 3.4.2. The flight time of the copper ions from the source to the detector position is about 50 $\mu$s. Thus, the fluctuation of the $^{63}$Cu signal after about 38 $\mu$s is due to electronic noise from the ignition of the next laser pulse[20] after 88 $\mu$s.
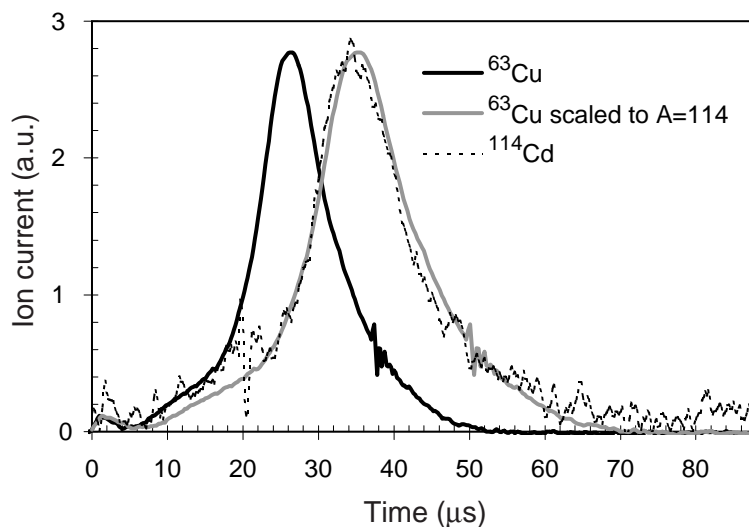


Figure 3.4.2.: The solid black line shows the measured signal of $^{63}$Cu from a thin niobium cavity (see below). The pulse shape of $^{114}$Cd (dotted black line) was measured in the same cavity under comparable conditions. Rescaling the abscissa of the copper signal with $t' = \sqrt{114/63} \cdot t$ (grey line) gives a shape practically identical to the cadmium signal.

In figure 3.4.3 the pulse shapes from a 30 mm long and a 60 mm long tungsten cavity are compared. As expected in the long cavity (black line) the maximum of the pulse is significantly delayed and the pulse is broader compared with the short cavity (grey line). The long cavity shows moreover a steeper drop towards shorter extraction times and a reduced prompt peak. Both effects could be explained by a reduced temperature in the front part of the cavity, reducing the extraction efficiency of ions created there. The small "prompt" peak consists of ions which were laser ionized in the region where the electrical field enters the ionizer cavity. They are thus extracted more rapidly, but reach a lower energy. This small peak increases the longitudinal emittance compared with a surface ion source[21]. Nevertheless it can be removed easily with the fast beam chopper.

The temperature dependence of the trapping efficiency is shown in figure 3.4.4. The extracted laser ion current rises with increasing line temperature. At about 2100 °C the plasma potential in the hot cavity is sufficiently high to trap most of the created ions and the current saturates.

---

[20]The CVL were running with a repetition rate of about 11.4 kHz.

[21]In the thermal ion source such a peak cannot occur since the atoms are ionized on the hot metal surface which is an equipotential area (except the small potential gradient along the line).
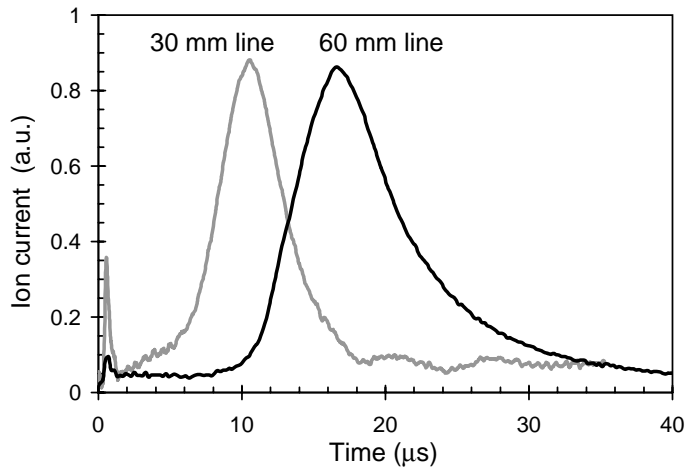
Figure 3.4.3.: Pulse shapes of $^9$Be from a 30 mm and a 60 mm long tungsten cavity (called "line") with 1 mm wall thickness.

Unfortunately such a hot tungsten line will also act as an efficient surface ionizer and cause strong isobaric background.
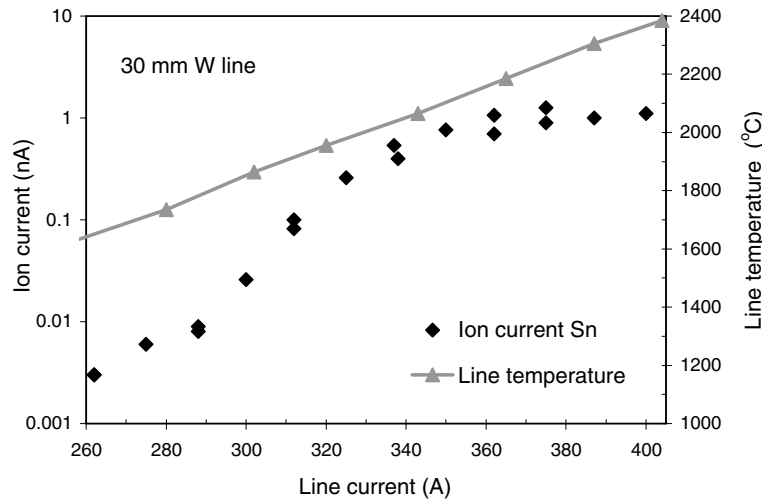


Figure 3.4.4.: Dependence of the tin beam current on the heating current of the ionizer cavity ("line"). For comparison a reference temperature calibration of the latter is shown.

A short pulse width $\tau_{pulse}$ is important to further increase the selectivity of the RILIS. The surface ionized isobars are released as a dc current (at least compared with the time between two laser pulses $\tau_{rep}$). If a fast beam gate ("beam chopper") is opened only synchronously with the main part of the laser pulse, the dc surface ionized background can be suppressed by a factor $\tau_{rep}/\tau_{pulse}$ (see also figure 3.4.8).

### 3.4.3.   Influence of the cavity material

In order to reach a high laser ion source efficiency a material with low work function is preferable which provides strong thermionic emission of electrons at a given temperature. Keeping the cavity at lower temperatures, a wall material with low work function will moreover decrease the disturbing contaminations of surface ionized elements. However, too low temperatures increase the delay time and worsen the ratio between exotic short-lived nuclei and the long-lived isobaric contaminants.

Inner cavity diameters of one, two and three mm had been tested [Mis93, Jad97, Lettr]. In principle smaller diameters should enhance the efficiency since the residence time in the cavity gets longer and the power density of the focused laser beam is increased (thus increasing $\varepsilon_{photo}$). However, in practice it is difficult to focus the laser beam over 20 m to very small diameters. Moreover with small cavity diameters the system gets more sensible to misalignments between tube and laser beam. Thus, for subsequent experiments mainly cavities with 3 mm inner diameter were used. In the following the properties of different RILIS cavities are discussed which were tested up to now.

### Standard tungsten cavity

For many RILIS runs a 30 mm long standard tungsten cavity (3 mm inner diameter, 5 mm outer diameter) was used which serves also in standard ISOLDE surface ion sources. This geometry is a good compromise to confine the atoms long enough to interact with the laser light, while the diameter still allows to focus a significant part of the laser light over about 20 m into the opening. The tungsten cavity is brought to temperatures around 2400 $^\circ$C by ohmic heating with currents up to about 400 A. Tungsten has a high work function: $\Phi_W \approx 4.54$ eV (or even above 5 eV with a surface layer of tungsten oxide). It has the advantage that the same target and ion source unit can also be used to produce surface ionized elements. Thus, the break in which the set-up of the RILIS is changed from one to another element (one to three days) can be used to continue the physics program with surface ionized elements from the same target. Since this source is optimized for high surface ionization, it shows a maximum of surface ionized isobars. It is normally used for elements where surface ionized background is less a problem (e.g. for Be or Mn) or where the higher temperature decreases the adsorption time and thus allows a faster release (e.g. for Ni).

### Long tungsten cavity

To increase the efficiency of the RILIS, tests were made with a 60 mm long version of the tungsten cavity. The first design showed an unequilibrated temperature distribution along the tube. It became much hotter in the center and thus prevented it from reaching the normal operation temperature at the ends. With an improved design this problem could be solved, but due to other parameters which were changed between the runs up to now no clear proof of a significant increase in ionization efficiency could be obtained. With a longer tube it becomes even more important to keep its axis aligned. Otherwise the laser beam cannot penetrate the full length and the possible advantage is lost. Note that the alignment has to be kept also during possible heating/cooling cycles of the target and/or ion source.

### Standard niobium cavity

To decrease the background of surface ionized isobars the cavity material was changed to niobium ($\Phi_{Nb} \approx 4.19$ eV). The standard niobium cavity is comparable the standard tungsten cavity with a length of 30 mm, an inner diameter of 3 mm and a wall thickness of 1 mm. It is operated with a lower current (up to 300 A) and at lower temperatures (up to about 2100$^\circ$C).

### Thin niobium cavity

To increase the potential drop along the tube and thus to improve the bunching of the laser ionized pulse, the wall thickness has to be reduced. Else the ohmic power gets too high. On the other hand a reduction of the wall thickness decreases the mechanical stability of the tube. Therefore, thin disks are attached radially to the tube which act as heat radiators (see figure 3.4.5). This
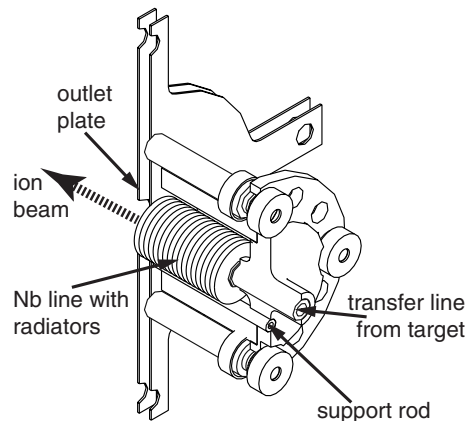
Figure 3.4.5.: Arrangement of the thin niobium line with radiator fins.

increases the power dissipation and thus allows to apply a higher voltage while keeping the same cavity temperature. Moreover the temperature along the tube is better equilibrated.

Such niobium cavities were used with 0.5 mm wall thickness and even a very thin cavity with only 60 $\mu$m wall thickness and 60 mm length has been tested successfully. The latter was produced by rolling a 20 $\mu$m thick Nb foil threefold and welding it together. Measured pulse shapes are shown in figure 3.4.6 at the example of stable copper.
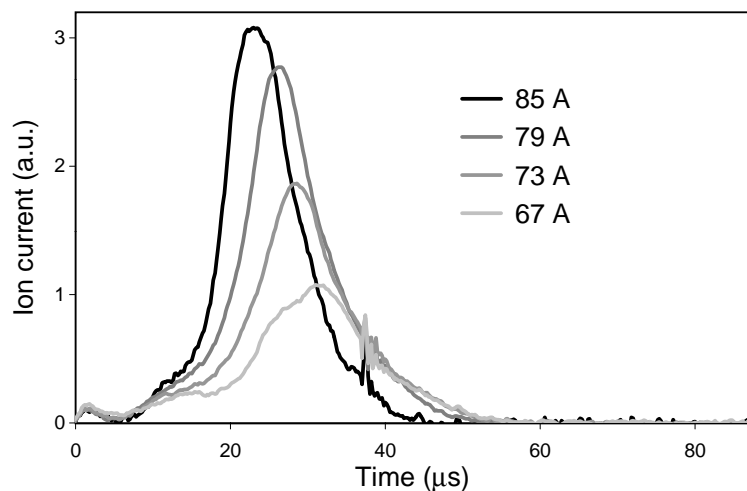


Figure 3.4.6.: Pulse shapes of a $^{63}$Cu beam from a thin (60 $\mu$m wall thickness) niobium cavity. The curves differ by the used heating current and are not normalized, i.e. the integral below the peak is proportional to the total RILIS current.

The increase of the dc heating current has two effects: the temperature increases (here from about 1600 °C at 67 A to about 2000 °C at 85 A) which favors electron emission and enhances the laser ionization efficiency. The efficiency saturates around 1850 °C. Moreover with increasing current the voltage drop along the line rises which in turn reduces the pulse width. Note that, despite the doubled length, this cavity provides already at 1850 °C a shorter pulse width in comparison to a standard tungsten cavity at 2100 °C (see figure 3.4.7).

Figure 3.4.8 shows the additional selectivity which can be achieved by using a fast beam chopper ("micro-gating" technique) in combination with the 60 $\mu$m thick Nb cavity. The black solid line shows the fraction of the total laser ionized current which is contained in the given time window around the peak maximum. It was obtained by integration of the pulse shape measured at 85 A (see figure 3.4.6). A reduction of the time window will reduce the surface ionized background
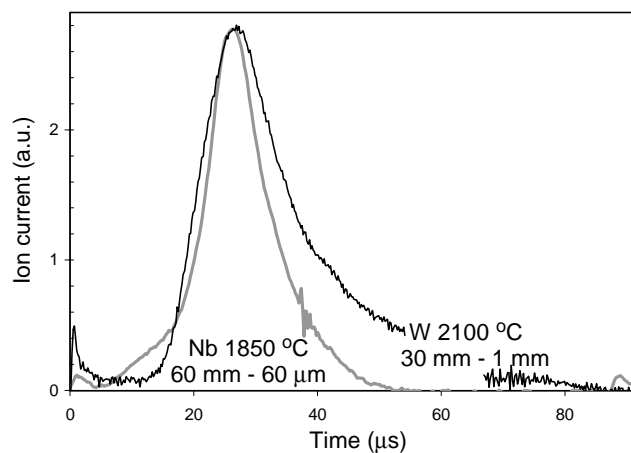
Figure 3.4.7.: Comparison of pulse widths ($^{63}$Cu) from a thin (60 $\mu$m wall thickness) niobium and a standard tungsten cavity (1 mm wall thickness). The normalization of the curves is arbitrary.

linearly (dotted line). The ratio of both gives the additional selectivity by micro-gating. Thus, the selectivity can be increased by a factor of about four to five in the case of $^{63}$Cu. Note that a very small width of the gate gives a good selectivity, but only at the expense of a rapidly dropping beam intensity! With a reduction of the cavity length a further improvement might be possible[22], but the micro-gating selectivity is principally limited to $\lesssim 10$ with self-supporting metal cavities. For heavier nuclides (e.g. silver isotopes) this factor is reduced by $\sqrt{63/A}$.
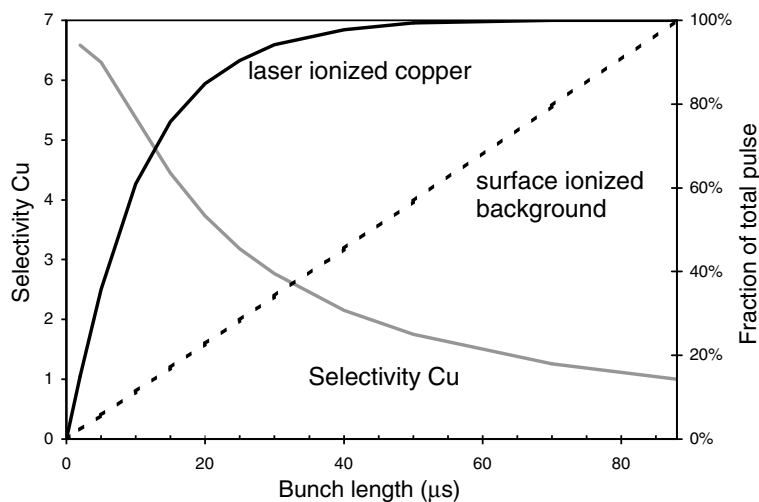


Figure 3.4.8.: Additional selectivity which can be obtained by micro-gating for $^{63}$Cu. See the text for an explanation of the curves.

**Insulator cavity**

A much higher electrical field could be applied along an insulator cavity. Indeed, earlier tests with a sapphire cavity showed a very narrow pulse shape ($\gtrsim 10$ $\mu$s for stable silver ions) [Jad97], but the ionization efficiency is reduced by a factor of three[23] compared with a niobium cavity. Sapphire

---

[22]It still needs to be tested which length gives the best compromise between efficiency and selectivity.

[23]In fact the only sapphire cavity which could be tested so far at operational temperature had only 2 mm inner diameter. Therefore it is not directly comparable to the other cavities.

(crystalline $Al_2O_3$) has a high work function ($\Phi_{Al_2O_3} \approx 4.7$ eV) and very low thermionic electron emission. Therefore the thermal plasma in the cavity cannot be sustained and the ionization efficiency drops. Moreover sapphire tubes are sensitive to thermal shocks and break easily at higher temperatures. Tubes from boron nitride were tested, but all reacted with the touching heating elements before reaching the operational temperature. A construction where the insulator tube is heated indirectly by radiation from a concentric meandering graphite heater [Jad97] could reduce these problems.

**Insulator with metal layer**

If one manages to combine the mechanically stable insulator cavity with a metal surface as thin as possible, the advantages of both systems, i.e. the short laser ion pulses and a good ionization efficiency could be combined. As in the case of pure insulator cavities, these metal layers are too thin to provide a homogeneous ohmic heating of the cavity. Therefore an extra cylindrical graphite heater is mounted around the insulator tube.

Attempts were made to coat an insulator ($Al_2O_3$ and $ZrO_2$) with layers of rhenium and niobium. The coating with Re via Chemical Vapor Deposition (CVD) (by Ultramet, California) failed completely, since the CVD process attacked heavily the insulator materials. Niobium layers were deposited onto $ZrO_2$ and $Al_2O_3$ by evaporation (LMU[24] target laboratory) and sputtering (CERN). Great difficulties arose to provide a permanent electrical contact at the front faces. Mostly the Nb layer was just too thin and lost contact at higher temperatures. Tubes with Nb layers of 0.01 to 1.6 $\mu$m were tested. However, they all "burned" before reaching a temperature of 1650 °C. To avoid a direct oxidation of niobium at higher temperatures, a rhenium layer was sputtered onto the insulator surface before deposition of the niobium. The Re did not stick well to the surface of $ZrO_2$, but a better adhesion was obtained onto $Al_2O_3$. Unfortunately also the system with the intermediate rhenium layer burned before reaching the operation temperature.

**Graphite cavity**

Graphite has a work function around 4.5 eV and a lower thermionic emission coefficient than metals. As expected from these parameters, only a low ionization efficiency was found using a cavity with a graphite surface [Lettr].

**Tantalum carbide cavity**

TaC has a low work function ($\Phi_{TaC} \approx 3.14$ eV). Indeed earlier off-line tests with a tantalum carbide cavity showed a very good suppression of surface ionization while the laser ionization efficiency stayed high even at lower temperatures [Mis93]. This tube had been prepared in Russia by sintering of hot pressed TaC powder. It showed to be extremely brittle.

Alternative production methods have been tested: TaC can also be produced by carbidisation of Ta surfaces. A tantalum tube of the desired form is heated under $CH_4$ atmosphere to a temperature between 1800 °C and 3000 °C [Swa70]. The methane is cracked on the hot surface and reacts to a golden layer of TaC. The thickness of the TaC layer increases linearly with time. We used this method, keeping a tantalum tube for some days in a graphite oven heated with a current of $\approx$750 A[25] while passing through $CH_4$. However, due to a temperature gradient the carbidisation took mainly place at the "entry" of the tube and gave no homogeneous result.

---

[24]Ludwig-Maximilians-Universität, München.

[25]The actual temperature was not determined directly, but from the calibration of other targets it should be well beyond 1800 °C.

Another way of production has been used in Russia by applying chemical vapor deposition of tantalum to a graphite tube. With these tubes we measured a laser ionization efficiency of 5.5 % for silver and a surface ionization efficiency of 0.17 % for indium. Both ionization efficiencies, for silver and indium, were a factor of two to three smaller than from a niobium cavity [Jad97]. Thus, no improvement in selectivity was obtained. In fact the ionization efficiency of these TaC cavities dropped after some hours of operation at high temperature. The color of the tubes turned from golden to grey and a surface analysis showed that a carbon layer was built up which can explain the deterioration of the performance.

Note that at the RILIS of the Institute of Modern Physics (IMP Lanzhou, China) a Nb-Zr alloy (ratio 19:1) tube coated with a TaC layer has been successfully tested off-line as cavity of a laser ion source [Zhi96].

The literature values for the work function of TaC vary significantly. This might indicate a general problem with the surface properties of heated tantalum carbide. Any deviation from the stochiometric ratio can lead to an increase of the work function: pure tantalum $\Phi_{Ta} \approx 4.25$ eV, graphite $\Phi_C \approx 4.5$ eV and tantalum oxide $\Phi_{Ta_2O_5} \approx 4.65$ eV.

## Cavity with "active surface cover"

The work function of a surface can be reduced by covering it with an electropositive element. The concentration of the latter has to be kept constant. This can be achieved by an attached oven which provides a continuous flow of the electropositive element [Pio97]. An alternative was tested at the IRIS RILIS [Bez97]: a tantalum tube is coated with a SrO layer which in turn is covered by a carbon film. The SrO molecules traversing the carbon layer are reduced to strontium and then cover the surface. The carbon layer prevents a fast evaporation of the strontium oxide, but it is not clear if the properties of such a tube can be maintained over the full length of an on-line run (several days).

## Summary and outlook

A series of different laser cavities has been tested, mainly off-line. Up to now unfortunately no breakthrough was obtained in the search for a single cavity type which provides simultaneously good laser ionization efficiency, very low surface ionization efficiency and a reliable operation over longer time (days). Several parameters (cavity material and geometry, target and line temperature, ionized element, etc.) have to be optimized and the tests proceed iteratively with small improvements. The "on-line-diagnostic" of the pulse shape is very useful for an understanding of the conditions in the cavity. Some cavity materials are particularly promising and their development will be pursued in future:

The very thin Nb foil cavity (60 $\mu$m wall thickness) gave the best off-line results for the efficiency and pulse width. It still needs to be tested on-line. However, it cannot provide ultimate suppression of surface ionizable elements due to the relatively high work function.

The principal problem of TaC tubes is the conservation of the surface properties over longer time at high temperature. The production of a TaC tube starting with tantalum should be tried again. The excess of tantalum in the bulk material could possibly hinder the creation of a surface layer from carbon. An alternative to tantalum carbide could be zirconium carbide. Literature gives a still lower work function ($\Phi_{ZrC} = 2.18$ eV), but the behavior as RILIS cavity was not yet tested.

Instead of sapphire, also an uncoated $ZrO_2$ cavity (stabilized with $Y_2O_3$) could give short bunches. The ionic conduction of $ZrO_2$ at high temperatures can help to provide a smoother potential distribution. Other possibilities are $ThO_2$ or $CeO_2$ with work functions of 2.6 eV and 2.3 eV, respectively. However, just like $Al_2O_3$ or $ZrO_2$, these materials have to be avoided for elements which are known to stick to oxide surfaces (e.g. beryllium).

The physical parameters of $Ir_5Ce$ propose it as an ideal candidate for the RILIS cavity. It has a very low work function $\Phi_{Ir_5Ce} = 2.69$ eV (at 1800 K) [Rao97] and can be operated at up to 2100 K while the vapor pressure remains very low. At 2100 K the evaporation rate is only $2 \cdot 10^{-9}$ g s$^{-1}$cm$^{-2}$ [Kuz94]. It is presently used as cathode material for electron beam ion sources and gives thermionic currents up to 230 A/cm$^2$ [Rao97]. So far only small samples in standard geometry as EBIS electrode are available and no dedicated tubes for the RILIS have been prepared yet. Ir-Ce alloys are very hard and have to be machined by spark erosion.

In all these cases a long-term test in connection with a typical target material (e.g. uranium carbide/graphite) has to show that no surface deterioration (poisoning with graphite vapor, etc.) occurs.

For short-lived isotopes the cavity temperature has to be chosen as a compromise between sensitivity and delay time. However, for long-lived nuclides the delay time is of no importance and the sensitivity could be increased further. Such an application is the implantation of a pure $^{163}$Ho beam into a cryogenic detector for the precise measurement of the electon capture decay [ISP95]. The cryogenic detector can only accept a limited count rate of some 100 Bq. Therefore any beam contaminations with radio-nuclides of $T_{1/2} \gtrsim$ months has to be suppressed by a factor of $10^4$ to $10^5$. For such an application a cavity has to be developed which provides sufficient electron emission already at low temperatures.

### 3.4.4.    Line with inverted polarity

Normally the back end of the surface ionizer or RILIS cavity is polarized positively, thus pushing positive ions out to the front orifice (see figure 3.1.1). What would happen if the polarity was inversed, i.e. the front part was charged positively?

A test was made with a surface ion source at the ISAC test stand [Dom97]. Amazingly, at equal ion source temperature the total current did not drop, but increased by about a factor two. Moreover the emittance of the extracted beam was improved when using the inverse polarity. Unfortunately the temperature of the mass marker could not be controlled independently. Therefore it could not be excluded that the phenomenon was not due to some memory effect (condensation of stable rubidium).

On-line tests were performed at ISOLDE with both, cesium as a surface ionized element and silver and tin as laser ionized elements. Figure 3.4.9 shows the effect of the polarity inversion on the release profile of cesium. The release gets slower in average and the yield is reduced by about a factor two. Since a relatively long-lived isotope ($^{140}$Cs with $T_{1/2} = 63.7$ s) was used to measure the release profile, the decay losses increase only marginally and cannot cause this clear reduction in efficiency. However, it can be explained as follows: instead of leaving the ion source, a large part of the positive ions is pushed back where they can be neutralized again on the wall. Thus, the extraction efficiency for positive ions $\omega$ is reduced while the loss rate of neutral atoms will not be affected. More of the cesium atoms will leave the source in neutral state and the source efficiency drops.

The possibility to use this phenomenon for a suppression of surface ionized elements was already observed at ISOLDE much earlier [Rav75b]! However, it has never been applied since. Especially together with a RILIS it could help to increase the sensitivity. However, just biasing the ionization cavity in inverse direction would also prevent the extraction of the laser ionized element. See figure 3.4.10 for the measured pulse shape of tin ions. Therefore the functions of the "separation tube" and the ionizer cavity have to be decoupled.

If the transfer line between target and ion source is biased in inverse direction, the atoms of the laser ionizable element (typically with a high work function) pass undisturbed while the ions of the surface ionizable isobars are pushed back. However, long-lived contaminants will be released
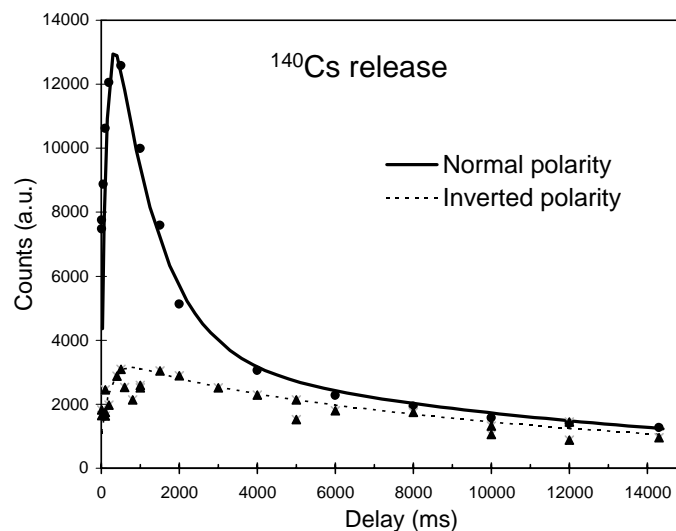
Figure 3.4.9.: Number of released cesium ions versus the delay time. With an inversion of the line polarity the fast part of the release curve is significantly suppressed and the total yield is reduced.
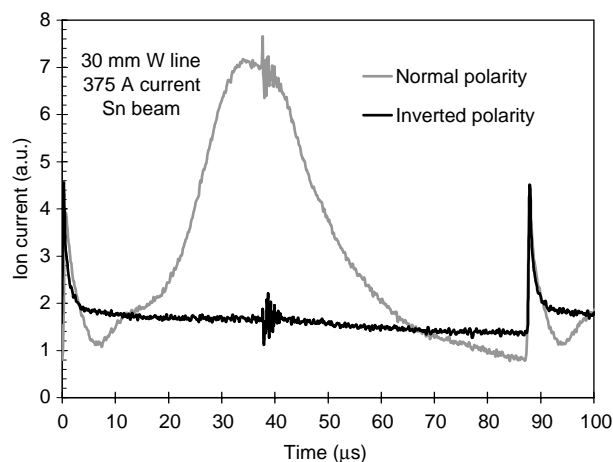


Figure 3.4.10.: Shape of the RILIS pulse. An inversion of the line polarity shows clearly the effect of the longitudinal electrical field. Most ions are no longer extracted, but pushed back. Thus, only a small part of the ions with sufficient initial kinetic energy is extracted. The peak of prompt ions is not affected.

sooner or later. A suppression of these could only be achieved by creating a second, smaller orifice in the target container. The polarity has to be chosen to push surface ionized ions towards this orifice. This could significantly reduce the number of surface ionizable atoms reaching the real ion source while causing only a small loss of the other elements, proportional to the ratio of the orifice areas of the "back exit" and the "front exit". An obstacle has to be introduced between ionizer cavity and transfer line to prevent the laser beams from entering the latter. A possible arrangement is shown in figure 3.4.11.

Also the potential gradient of the dc ohmic target heating could be used. Inside the target surface ionizable elements are pushed preferentially into one direction (i.e. perpendicular to the sectional view shown in figure 3.4.11). The transfer tube is attached at the middle of the target container. On one side the electric field will push the ions towards the transfer line, but on the other side it will push them away, towards the dead end of the container. A redesigned target unit is under preparation where both ends are put on the same (positive) potential relative to the center (close
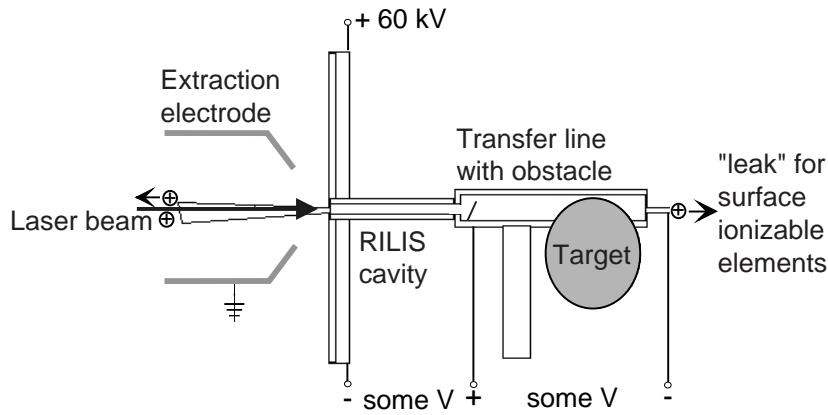
Figure 3.4.11.: Set-up with an "inversely polarized" transfer line. Atoms will mainly effuse towards
the ionizer cavity while ions created in the transfer line are pushed out through the
"back exit" on the right hand side.

to the transfer line). This should accelerate the release of surface ionizable elements and could
e.g. help to increase the release efficiency for the short-lived $^{11}$Li. Inverting the polarity could help
to deliberately suppress short-lived surface ionizable beam contaminants. Note that at the IRIS
facility the target and transfer line are heated by an ac current. This causes a fast bunching of the
extracted beam [Bar00].

## 3.5.    Atomic physics effects

The RILIS efficiency is reduced for elements with a large fine structure splitting of the ground state
(e.g. Sn) or low-lying levels in multielectron atoms (e.g. U). The thermal distribution in the hot
ionizer cavity leads to a dispersion of the population over several states of which only one can be
excited with a small bandwidth laser. Here, the residence time of the atoms in the laser field has to
be increased (to profit from the thermal reequilibration of the population) or several wavelengths
have to be provided simultaneously for excitation of more levels. The latter way further complicates
the laser system.

### 3.5.1.    Isotope shift

The atomic levels of different isotopes of the same element have not exactly equal energy, but show
a characteristic difference, the so-called isotope shift (IS). The isotope shift of a given transition is
the difference of the IS in the higher level and the IS of the lower level. A positive IS corresponds
to a shift towards higher frequencies for heavier isotopes.

The IS can be separated into three individual parts:

$$\delta\nu^{AA'} = \delta\nu_{\mathrm{NMS}}^{AA'} + \delta\nu_{\mathrm{SMS}}^{AA'} + \delta\nu_{\mathrm{FS}}^{AA'} \tag{3.5.1}$$

The normal mass shift $\delta\nu_{\mathrm{NMS}}^{AA'}$ is due to the motion of the nucleus around the atom's center of
mass and is given by the reduced electron mass in the Bohr model.

$$\delta\nu_{\mathrm{NMS}}^{AA'} = \nu_0 \frac{m_{\mathrm{e}}}{1u} \cdot \frac{M' - M}{M'M} \tag{3.5.2}$$

where $\nu_0$ is the transition frequency for infinite mass, $m_e$ is the electron mass and $M$, $M'$ are the nuclear masses of the two isotopes to be compared.

The specific mass shift $\delta\nu_{\text{SMS}}^{AA'}$ arises due to the electron exchange interaction between the valence electron and the rest of the atomic shell which makes a collective movement in reaction to the nuclear motion. The SMS has the same mass dependence as the NMS, but has a different size and can have the same or opposite sign. In the calculation of the SMS of complex atoms contributions of all electrons have to be taken into account. This is usually done with the Hartree-Fock method. Empirically it is found that for most $s$-$p$ transitions the SMS does not exceed the NMS, while in more complicated spectra involving shielded $d$ or $f$ electrons it may be one order of magnitude larger than the NMS [Ott89].

The total mass shift $\delta\nu_{\text{MS}}^{AA'} = \delta\nu_{\text{NMS}}^{AA'} + \delta\nu_{\text{SMS}}^{AA'}$ is significant for light nuclei. For beryllium the mass shift was measured at the ISOLDE RILIS for all particle-stable isotopes [Seb98]. For an optimization of individual yields (e.g. $^7$Be or $^{14}$Be) the laser frequency has to be tuned accordingly. For heavier nuclei the mass shift becomes much smaller than the Doppler width and is negligible for our applications.

The field shift $\nu_{\text{FS}}^{AA'}$ or volume shift reflects the change in the binding energy of the electrons when the radial distribution of the nuclear charge is changed. It is the product of the electronic field shift factor $F$ and a power series of nuclear radial moments [Buc87].

$$\delta\nu_{\text{FS}}^{AA'} = F(\delta\langle r^2 \rangle + C_2 \delta\langle r^4 \rangle + C_3 \delta\langle r^6 \rangle + \cdots) \approx F\delta\langle r^2 \rangle \tag{3.5.3}$$

Accurately measured it allows to derive the mean square radius of the proton density distribution in the nucleus. This can be separated into contributions from a spherical distribution and corrections due to the deformation (see e.g. [Buc87]). By investigation of long isotopic chains significant changes in the nuclear deformation could thus be found (see e.g. [Ott89]).

For RILIS applications the field shift becomes important for elements with high $Z$ where the overlap of the electron orbitals with the nucleus increases (smaller Bohr radius and larger nuclear radius). In uranium the IS is big enough to be exploited for commercial separation of $^{235}$U and $^{238}$U in a large-scale RILIS [Gil74, Jan76, Böh78, Bec82]. However, for individual transitions large differences exist in the IS and in the disturbing hyperfine splitting of $^{235}$U (see below) [Rad75] (see the two examples in table 3.5.1). A careful choice of the excitation scheme is therefore essential for an efficient separation. A compilation with 1600 assigned levels and many data on isotope shifts and $g$-factors is found in [Bla76].

Table 3.5.1.: Isotope shifts for the first transition in RILIS excitation schemes. Note the additional notation for the upper levels in uranium (given by the wavenumber in cm$^{-1}$) which has a very dense spectrum with about 300000 lines [Bec82].

| Element | Transition | $\lambda$ (nm) | Isotopes $A - A'$ | IS GHz | Reference |
|---|---|---|---|---|---|
| $_4$Be | $2s^2\ ^1S_0 - 2s2p\ ^1P_1^{\text{o}}$ | 235.0 | $9 - 10$ | 8.78 | [Chu93] |
| $_{12}$Mg | $3s^2\ ^1S_0 - 3s3p\ ^1P_1^{\text{o}}$ | 285.2 | $24 - 26$ | 1.8 | [Rad85] |
| $_{29}$Cu | $4s\ ^2S_{1/2} - 4p\ ^2P_{1/2}^{\text{o}}$ | 327.4 | $63 - 65$ | 0.6 | [Rad85] |
| $_{48}$Cd | $5s^2\ ^1S_0 - 5s5p\ ^3P_1^{\text{o}}$ | 326.1 | $102 - 114$ | 3.5 | [Buc87] |
| $_{82}$Pb | $6p^2\ ^3P_0 - 6p7s\ ^3P_1^{\text{o}}$ | 283.3 | $208 - 214$ | 11.5 | [Ans86] |
| $_{92}$U | $6d7s^2\ ^5L_6^{\text{o}} - 6d7s7p\ ^7L_6(16900_7)$ | 591.5 | 235-238 | -8.5 | [Ana92] |
| $_{92}$U | $6d7s^2\ ^5L_6^{\text{o}} - 6d^27p\ ^7N_7(27886_7)$ | 358.5 | 235-238 | -17.1 | [Ana92] |

In contrary to the mass shift, which is a common atomic property of all isotopes of an element, the field shift is a nuclear property of an individual isotope. Table 3.5.1 shows isotope shifts of some transitions relevant for RILIS. More details are found in references [Kin84, Rad85, Ott89].

On the one hand, a large isotope shift rather disturbs the RILIS operation. It requires to retune the laser frequency when switching between different isotopes and can even reduce the ionization efficiency for rare isotopes with unknown isotope shift. At an ISOL facility this mass selectivity of ionization is of no use since the following separator magnet anyhow provides a sufficient separation in mass. On the other hand the direct relation between frequency tuning and obtained ion yield allows to use the RILIS as a sensitive tool for resonance ionization spectroscopy (RIS) [Mis87a, Bar98b, Seb98].

## 3.5.2. Hyperfine splitting

The interaction of the electrons with the spin of the nucleus leads to a splitting of the atomic energy levels into a number of hyperfine components. Nuclear spin $\vec{I}$ and atomic angular momentum $J$ couple to the total angular momentum $\vec{F} = \vec{I} + \vec{J}$. In a good approximation $I$ and $J$ are good quantum numbers and the dominant contributions from the lowest order multipole moments can be written as [Ott89]:

$$E = E_0 + \frac{h}{2}AK + \frac{3h}{8}B\frac{K(K+1) - \frac{4}{3}I(I+1)J(J+1)}{I(2I-1)J(2J-1)}, \text{ for } I, J \geq 1, \tag{3.5.4}$$

with $K = F(F+1) - I(I+1) - J(J+1)$. $A$ is the magnetic dipole interaction constant:

$$A = \frac{\mu H_e(0)}{IJ} \tag{3.5.5}$$

with $\mu$ the nuclear magnetic dipole moment and $H_e(0)$ the magnetic field of the electron shell at the position of the nucleus. $B$ is the electric quadrupole interaction constant:

$$B = \frac{eQ_s}{\frac{d\Phi}{dr}\big|_0} \tag{3.5.6}$$

with $Q_s$ the spectroscopic[26] quadrupole moment of the nucleus and $\frac{d\Phi}{dr}\big|_0$ the electric field gradient of the atomic electrons at the nucleus.

Table 3.5.2.: Hyperfine splitting of some levels or transitions used in RILIS excitation schemes.

| Isotope | Nuclear Spin $I$ | Transition or atomic state | $A$ or $\Delta\nu_{HFS}$ (MHz) | $B$ (MHz) | Reference |
|---|---|---|---|---|---|
| $^{65}_{29}$Cu | 3/2 | $4s\ ^2S_{1/2}$ | 12568 | | [Rad85] |
| $^{65}_{29}$Cu | 3/2 | $4p\ ^2P^o_{1/2}$ | 540 | | [Ber89] |
| $^{103}_{48}$Cd | 5/2 | $5s^2\ ^1S_0 - 5s5p\ ^3P^o_1$ | $-1129$ | 188 | [Buc87] |
| $^{207}_{82}$Pb | 1/2 | $6p^2\ ^3P_0 - 6p7s\ ^3P^o_1$ | 8807 | $-$ | [Ans86] |
| $^{235}_{92}$U | 7/2 | $6d7s^2\ ^5L^o_6 - 6d7s7p\ ^7L_6(16900)_7$ | 250 | | [Rad75] |
| $^{235}_{92}$U | 7/2 | $6d7s^2\ ^5L^o_6 - 6d^27p\ ^7N_7(27886)_7$ | 100 | | [Rad75] |

---

[26]The spectroscopic quadrupole moment is related to the intrinsic quadrupole moment $Q_0$ via a transformation from the body-fixed frame to the laboratory frame: $Q_s = \frac{3K^2 - J(J+1)}{(J+1)(2J+3)}Q_0$ [Cas90].

Just as the isotope shift, a large hyperfine splitting complicates the normal RILIS operation but also enables additional applications like isomer separation and even the measurement of nuclear moments. Table 3.5.2 shows the hyperfine splitting of low levels relevant for RIS.

### Isomer separation

Some silver isotopes show a strong hyperfine splitting. After the suspicion that earlier attempts to find the r-process waiting-point nuclide $^{129}$Ag with the ISOLDE RILIS failed due to this reason [Jad97], this effect was studied in more detail. With the two abundant isomers of $^{107}$Ag the effect of the hyperfine splitting is clearly seen [Seb98]. The small hyperfine splitting of the stable ground-state $^{107g}$Ag with spin $1/2^-$ is not resolved with the RILIS resolution. However, the signal of the metastable state $^{107m}$Ag with spin $7/2^+$ shows a clear separation into two distinct peaks. In the even isotope $^{122}$Ag the tuning of the frequency allowed to assign individual gamma-rays to the decay of the low- and the high-spin isomer [Kau98].

Isomerically selective photo-ionization of $^{197}$Hg is discussed in [Dye85] and the separation of samarium and thulium isomers was reported in [Mis87b].

### Separation of $^{70g}$Cu and $^{70m}$Cu

The isomeric selectivity of the RILIS was also applied for the separation of the $^{70}$Cu isomers. In contrast to silver where the stable low spin isomers of mass 107 and 109 can be easily distinguished from the respective radioactive high spin isomers, in $^{70}$Cu both isomers are radioactive. A distinction has to be done via the different lifetimes and feeding of excited states after $\beta$-decay to $^{70}$Zn. The Leuven $\beta\gamma\gamma$-coincidence set-up was used for detection and identification of the radio-isotopes (see [Wei99] for technical details). The background from the surface ionized isobar $^{70}$Ga was small and did not disturb the measurement. Despite the reduction of the laser power for the scan the ion yield was high enough to determine the analysed gamma-ray intensities with statistical errors in the range of some percent.

Some gamma lines had been assigned in literature [Taf71, Rei75], but a detailed decay scheme of $^{70}$Cu based on our measurements is still under evaluation [Roosb]. The main characteristics required for the analysis of the frequency scan are known from literature and can be summarized as follows: the short-lived isomer ($T_{1/2} \approx 5$ s) is the $1^+$ ground state, while the longer-lived isomer ($T_{1/2} \approx 42$ s) is a metastable state with spin assignment $3^-$, $4^-$, $5^-$ or $6^-$ [Bha93].

For the following frequency scan the "intensity" of $^{70g}$Cu was defined by the sum of the gamma counts at 874, 1072 and 1653 keV while the lines at 902, 1108, 1252, 1782 and 2155 keV were added up for the $^{70m}$Cu intensity.

The measured ratio of gamma intensities does not reflect directly the ratio of production rates. Only gamma lines with a unique assignment were summed, but they do not represent the complete feeding. Moreover, the raw count rates are not corrected for detection efficiency or timing of the measurement cycles[27].

For the frequency scan the power of the first step laser beam was attenuated to about 20 % to reduce the saturation broadening of the resonance line. The frequency of the first step was scanned over a range of 40 GHz. Due to the huge width of the autoionizing state (FWHM more than 5 cm$^{-1}$) it was not necessary to retune the second transition when scanning the first.

Twenty measurements of two to four minutes each were done for different settings of the laser frequency (see figures 3.5.1 and 3.5.2). Unfortunately the first scan was stopped abruptly due to a technical problem of the wavelength control unit and could not be extended or repeated

---

[27]The short-lived ground state experiences more decay losses in the target than the isomeric state, on the other hand contributions from $^{70}$Ni decaying in the target will mainly feed $^{70g}$Cu [Fra99].

during this beam time. The large error on the ordinate is mainly due to power fluctuations from synchronization shifts between the three CVL.

The hyperfine splitting of the $3d^{10}4p$ $^2P^o_{1/2}$ level (excited state: es) is much smaller than the one of the $3d^{10}4s$ $^2S_{1/2}$ ground state (gs). Hence only the splitting of the ground state into two peaks is resolved. We use a fit with four Voigtian peaks of identical width, consisting of a fixed Gaussian part (3.8 GHz Doppler width) and a Lorentzian part with free width. The ratio of the upper level HFS to the lower level HFS was fixed to 0.086, given by the ratio of the $A$ factors in $^{65}$Cu: $A(^2P^o_{1/2}) = 540.1$ MHz [Ber89] and $A(^2S_{1/2}) = 6284.39$ MHz [Rad85]. The relative amplitudes of the four peaks were constrained to the theoretical ones taking into account the excitation with linearly polarized light[28] [Fedos]. They are equal for the $(F_{gs},F_{es})= (1/2,1/2)$, $(1/2,3/2)$ and $(3/2,1/2)$ transitions and twice bigger for the $(3/2,3/2)$ transition. To account for a modification of this ratio due to and a partial saturation of the transition, the intensity ratio was varied by 20 % in the fit. Finally for $^{70g}$Cu a hyperfine splitting of 10.5(14) GHz is found (see figure 3.5.1).

For $^{70m}$Cu the hyperfine splitting is not resolved (figure 3.5.2), but from the broadening of the resonance line a rough value of 5.3(10) GHz can be deduced. Here equal amplitudes were taken for the transitions since at high total angular momenta $F$ a multitude of magnetic substates contributes, leveling polarization effects nearly out (i.e. the calculated intensity ratio is close to unity).
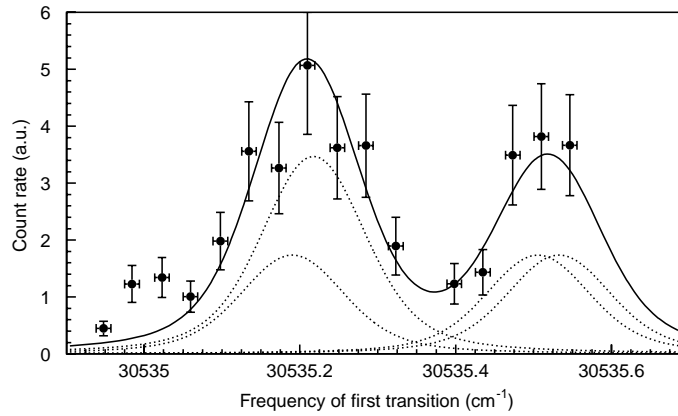


Figure 3.5.1.: Yield of $^{70g}$Cu versus laser frequency of the first transition.

**Measurement of magnetic moments**

The magnitude of the hyperfine splitting is directly determined by the nuclear spin $I$ and the magnetic moment $\mu$ via relation (3.5.5).

The hyperfine splitting of two hyperfine components with total angular momenta $F$ and $F-1$ is given by the Casimir formula [Ott89]:

$$\Delta\nu_{\text{HFS}} = AF + B\frac{3F(F^2 + \frac{1}{2})}{I(2I-1)J(2J-1)} \tag{3.5.7}$$

Due to the spherical symmetry of the charge distribution, for $J \leq 1/2$ the quadrupole interaction constant $B$ is zero. Thus, the measured hyperfine splitting follows Landé's interval rule:

$$\Delta\nu_{\text{HFS}} = A \cdot F = A \cdot (I + J) \tag{3.5.8}$$

---

[28]The ratios were calculated by summing over all allowed transitions between the magnetical sublevels of the participating states according to formula (1) in ref. [Bek81].
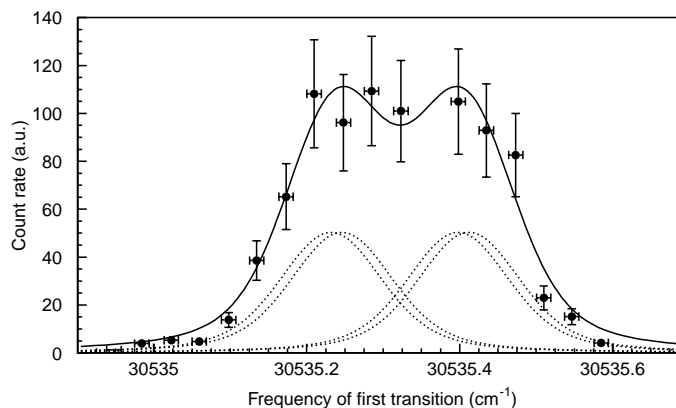
Figure 3.5.2.: Yield of $^{70m}$Cu versus laser frequency of the first transition. For the fit the line width was taken identical to the $^{70g}$Cu fit.

and the spectroscopic constant $A$ can be extracted from the measured frequency scan.

For the accuracy which can be obtained with the ISOLDE RILIS set-up, the HFS anomaly due to the finite size of the nucleus (the so-called Bohr-Weisskopf effect [Boh50]) can be neglected:

$$\frac{A_X}{A_Y} \cdot \frac{g_Y}{g_X} - 1 \overset{!}{=} 0. \qquad (3.5.9)$$

.

Therefore, the unknown magnetic moment of an isotope $Y$ follows directly from that of a calibration isotope $X$:

$$\mu_Y = \mu_X \cdot \frac{A_Y \cdot I_Y}{A_X \cdot I_X}. \qquad (3.5.10)$$

Thus, the magnetic moment of radioactive nuclei can be derived from the hyperfine splitting measured with a RILIS if the nuclear spin is determined independently (e.g. from beta-decay or transfer reactions). The results for $^{70g}$Cu and $^{70m}$Cu are discussed in section 5.2.1.


### 3.5.3.    Nuclear polarized beams

A possible further application of the RILIS is the production of nuclear polarized beams. Without external field the magnetic substates $m_F$ are degenerate and the selection rule for the angular momentum: $\Delta m_F = +1 \, (-1)$ for right (left) circularly polarized light manifests only in a general reduction of the ionization efficiency. In some cases the different magnitude of this effect allows a moderate separation of even and odd isotopes, e.g. for ytterbium [Bek81], molybdenum and tin [Fai89].

By absorption of circularly polarized light the polarization is transferred to the excited state of the atom. The coupling of electronic and nuclear spin will transfer this polarization to the nucleus. Thus, the ionized beam gets a certain degree of nuclear polarization (e.g. some 10 to 20 % for alkalis [Ney97]).


**Optical pumping**

The polarization can be increased considerably by passing several cycles of excitation with circularly polarized light and subsequent spontaneous emission. This method is called optical pumping. Figure 3.5.3 shows the principle of optical pumping at the example of alkalis (lithium). This pumping

scheme was successfully applied to an atomic $^8$Li beam at the MPI für Kernphysik in Heidelberg [Wid95]. It is also routinely used for $\beta$-NMR experiments with the collinear laser spectroscopy set-up COLLAPS at ISOLDE (see e.g. [Arn87, Arn92]).
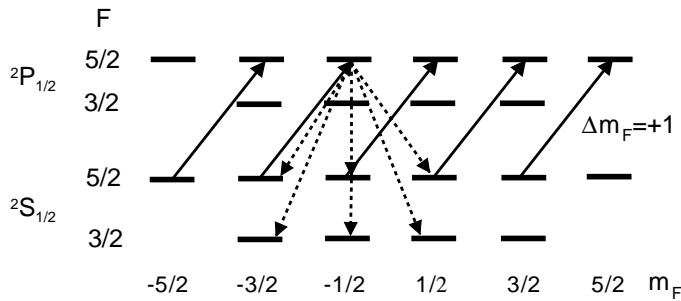


Figure 3.5.3.: In excitations of lithium atoms from the ground state $^2S_{1/2}$ to the $^2P_{1/2}$ state with right circularly polarized laser light only transitions with $\Delta m_F = +1$ are allowed according to the selection rule (solid arrows). Spontaneous emission proceeds with $\Delta m_F = -1$, 0 and $+1$ (dashed arrows). High polarization is obtained after multiple cycles of excitation and spontaneous emission, i.e. the angular momentum of the photons is transferred to the lithium atom by "pumping" the population of the latter preferentially in a well-defined Zeeman level.

Normally the optical pumping has to be done at the atom since the respective transitions of the ion are too far in the ultraviolet region. However, if one combines this optical pumping with an ionization method which preserves completely the nuclear polarization (i.e. without wall- or gas collisions as in the case of a surface ion source or a plasma source respectively), it is possible to form a highly polarized ion beam which can be guided subsequently to a remote experimental setup. The RILIS provides such an ionization. The excitation scheme for resonant photo ionization of lithium was already tested at the ISOLDE laser ion source [Mis93].

Production of the radioactive atoms, optical pumping, ionization and detection are approved techniques. However, the conservation of the polarization during beam transport from the ion source through the separator to the experimental set-up has to be checked. Loss of polarization can happen due to non-adiabatic changes of the magnetic field, e.g. when entering the strong perpendicular magnetic field of the separator magnet or in the passage close to Penning vacuum gauges or turbo pumps. To prevent such depolarization, a longitudinal guide field has to be applied during the beam transport. Such a guide field can be easily realized with permanent magnets mounted around the beamline. This technique is commonly used, e.g. when guiding polarized neutrons close to superconducting magnets with high stray fields (ILL), for the injection of polarized protons into cyclotrons (TRIUMF), etc.

## 3.6.   Implementation of the RILIS

### 3.6.1.   Beam observation and tuning

During operation of the RILIS the stability of the laser beams has to be monitored. Normally the wavelength does not fluctuate and it can be easily controlled with a lambdameter. Due to temperature changes of the laser set-up and the nonlinear crystals the spatial alignment of the laser beams can drift and they have to be retuned to the ionizer cavity. Therefore a quartz plate is installed halfway between the laser lab and the ion source. It will reflect about 6 % of the light back onto a reference screen in the laser lab. This feedback helps enormously to focus and align all laser

beams. A diaphragm with the source diameter is installed at the reference point. The laser power detected behind this diaphragm is proportional to that available at the source position. Moreover the synchronization of the three CVL can drift. Depending on the condition of the thyratrons and laser tubes it has to be retuned more or less frequently (minutes to hours). The synchronization of the oscillator and amplifier tubes is tuned to maximize the output power of the latter. Still the delay between both amplifier tubes has to be set to optimize the laser ionization efficiency. This can be controlled by optimizing the current of a stable or intense radiogenic isotope of the laser-ionized element measured with a Faraday cup (FC). The ISOLDE general purpose separator (GPS) has the nice feature that the monitor mass can be sent to the FC of another beam port (low- or high mass side, see figure 3.1.1). This allows to retune the laser with an on-line signal and facilitates the supervision considerably. For elements with low yields or very fast release a temperature controlled oven (Knudsen cell) has to be attached to the target container to provide a stable monitoring beam.

## 3.6.2.   Compatibility of RILIS and HRS

In principle a high resolution mass separator (HRS) could be applied to remove remaining contaminations from surface ionizable isobars. However, at the present ISOLDE set-up such a combination of RILIS and HRS is not ideal.

With the HRS the permanent supervision of a stable mass is not possible since only one mass passes the separator[29]. That means for each check of the laser settings the running experiment has to be stopped, a Faraday cup introduced into the beam line and the mass changed to the monitoring isotope. Without a major improvement of the RILIS stability a run at the HRS can thus become extremely tedious!

The ISOLDE HRS (see figure 3.6.1) is designed to analyze a real object defined by a slit (SL240 in ISOLDE synoptic) with a 90 degree bending magnet. After a preselection in the first focal plane (HRS.SL470) and a following 60 degree bending magnet the main separation is done with a slit in the second focal plane (SL675). The magnification from SL240 to the second focus is $M = -1.57$. while the dispersion of both magnets adds to $D_{\mathrm{m}} = 4$ m. Thus, to reach a resolving power of at least $R_{\mathrm{m}} \geq 10000$, the object size $w$ has to be restricted to about 0.25 mm in horizontal direction ($w \leq D_{\mathrm{m}}/(M \cdot R_{\mathrm{m}})$). To prevent a deterioration of the selectivity, the slit is introduced to cut the beam halo at the object position (SL240). This slit would also limit the open diameter for the laser beams which enter through a window in the HRS vacuum chamber. Since the laser beam is about 7 mm wide when passing the SL240 slit position (8 m away from the ion source) this slit cannot be used in combination with the RILIS and one has to rely on the slit in the first focal plane only.

If a RILIS cavity with a high potential drop is used, the reachable mass resolving power is limited by the energy dispersion of the beam: $R_{\mathrm{m}} = M/\Delta M \leq E/\Delta E$. To reach a mass resolving power of $R_{\mathrm{m}} > 10^4$ with 60 keV beam energy, the energy dispersion should not exceed some eV. Ceramic RILIS cavities which could provide a higher potential drop would thus require an additional energy compensation.

The problem with the energy spread can be solved in several ways:

- Including an electrostatic deflector in the high resolution separator allows to compensate the energy dispersion of any ion source, but makes the separator more elaborate.

- The given energy spread from a RILIS is not randomly distributed in the longitudinal phase space, but correlated to the phase. That means ions which are created deeper inside the

---

[29]In principle, the set-up could be modified to monitor also the current of some neighboring mass in the first focal plane. However, due to the high dispersion the mass range covers $\pm 5$ % at maximum. This is not sufficient for a monitoring of exotic isotopes (see section 3.6.3).
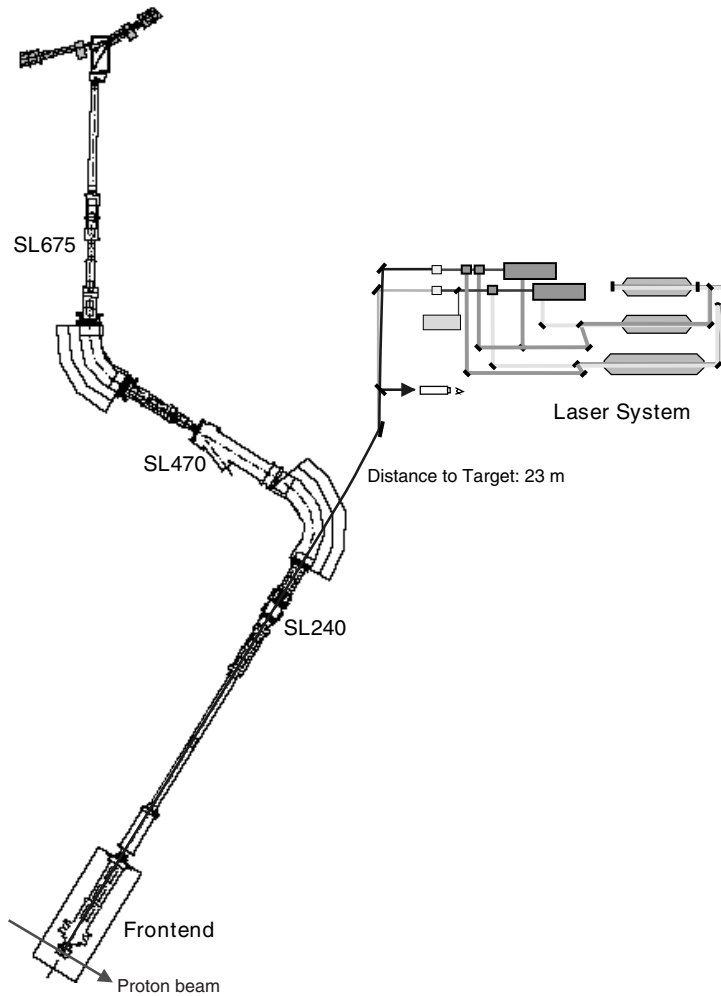
Figure 3.6.1.: Combination of the ISOLDE RILIS with the high resolution separator HRS.

cavity get a higher energy, but arrive later[30]. A debuncher which makes a transformation in the $E$-$\delta t$-phase space could be used to provide a less bunched beam with reduced energy spread. Clearly this debuncher has to be placed behind the fast beam chopper, else the possibility to gate on the well-defined laser pulses is lost.

- Another alternative is a gas-filled RFQ which can effectively reduce the phase space due to dissipation in the buffer gas [Lun99]. All these devices have to be placed behind a primary mass separator.

A beam with small energy spread is also required for other applications, e.g. collinear laser spectroscopy. Therefore the latter two methods are favorable.

### 3.6.3.   RILIS implementation at other RIB facilities

It has been shown that a RILIS can fulfill for many metallic elements the main demands to the ion source of a RIB facility: *efficiency – selectivity – rapidity*. In some cases it can even provide additional features like isomer separation or nuclear polarization. Moreover, in the standard version the front-end part of a RILIS is relatively robust compared with a plasma ion source. The

---

[30]The use of this correlation to increase the selectivity of the micro-gating technique with a "time focus" was proposed [Sch93]. However, it requires a system of adapted extraction electrodes and was not yet realized.

parts which require maintenance are far away from the target and remain easily accessible during irradiation of the target. With the rapid technical development of the laser technology it is expected that the RILIS performances will be further improved in the next years. It is important to plan already now the implementation of a RILIS at new RIB facilities. The following list gives a summary of the most important points which were already discussed above:

- The simplest RILIS ionizer cavity is identical to a typical surface ionization source, i.e. a metal tube with some mm diameter and some cm length, heated to temperatures of 2000 to 2500 °C.

- To obtain higher selectivity, a more elaborate ionizer cavity is needed. While the development of an optimum cavity is still under work, it is safe to foresee a space of about 80 mm diameter by 80 mm length to accommodate cavity and holding structures. An additional voltage supply with some ten Volts tension and low current has to be foreseen for use of insulator cavities with better beam bunching.

- A Knudsen cell should be attached to the target to provide stable beams for optimizing and retuning of the RILIS settings.

- For introduction of the laser beam, there has to be a free sight onto the ionizer cavity, not obstructed by slits, etc.

- If the options isomer separation and resonance ionization spectroscopy should be used extensively, a set-up for Doppler free two-photon absorption can be foreseen. This requires to access the ionizer cavity with two laser beams from opposite directions.

- The quartz window in the vacuum chamber through which the laser beams enter, has to be large enough (free diameter $\gtrsim 25$ mm). It has to be easily accessible for exchange when the transmission is reduced due to excessive deposition of neutral particles on the surface. Depending on the vacuum quality and the distance from the source, this happens after some weeks to years of operation.

- A shutter installed inside the vacuum chamber in front of the window protects it from pollution while the RILIS is not used.

- To reduce the diffraction limited beam size, the last focusing element has to be as close as possible to the source position ($\lesssim 20$ m). Note that it should be accessible or remote controllable for beam tuning.

- A semitransparent or removable reflector plate halfway between laser lab and ion source proved to be extremely useful for easier beam tuning.

- While not necessary for the operation, safety regulations require often to guide the laser beams in a closed envelope from the laser lab to the entrance of the vacuum chamber.

- For monitoring of the ionization efficiency it is highly desirable to control the current of a stable isotope in a Faraday cup. To not disturb separation and use of the radioactive isotope, this FC is best placed in a lateral position of the focal plane or in a parallel beam line which accepts a second mass from the separator.

- In both cases the selection of the monitor mass has to be movable along the focal plane. For separation of very neutron-rich beams, the monitor mass is up to 23 % smaller[31] (for light elements: Be, Mg) and for separation of very neutron-deficient beams the monitor mass can be up to 20 % larger than the central mass. Therefore the dispersion of the first separator magnet should not be too large to accommodate this rather large mass range in the focal

---

[31]In a reactor-based facility specialized on fission products this requirement is reduced to about 19 %.

plane. On the other hand care has to be taken that the heaviest masses are not implanted straight into the optical window. Eventually this has to be placed into a more remote position and protected by an additional magnetic or electrostatic beam deflector.

- The limitation of the dispersion clearly excludes a single stage separator with high resolution. Instead a high resolution separator should be placed behind a preseparator with resolving power $R_\mathrm{m} \leq 1000$. This configuration is anyhow better to handle safely the activity which is deposited in the focal plane (see ref. [PIAFE]).

- The size of the laser lab depends on the used laser system. A minimum area of about 4 m by 7 m is a good estimate. More equipment for additional frequency stabilization or bandwidth reduction (cw-seeded dye lasers) requires additional space. For better temperature stabilization a sufficient height and a climatisation should be foreseen. This gives an external height of $\geq 3$ m.

- For the pumping lasers a plug power of up to 20 kW is required. If CVL are used, this should be provided from a separate net to reduce the perturbations caused by the high frequency noise. In the latter case it would also help to equip the laser lab as a Faraday cage for better high frequency shielding.

### 3.6.4.   Combination with off-line use

Up to now only applications of the RILIS for on-line produced radio-nuclides were described. However, by upgrading the laser system, the RILIS at ISOLDE and generally also at other RIB facilities is mutating from a small supplement of the target-ion source system to an important set-up for its own. It would be possible to use it for off-line applications during shutdown of the RIB facility or even while running the RIB facility simultaneously with another ion source type, by sending the laser beams to a dedicated off-line separator. Besides an improvement of the RILIS capabilities by a more frequent development work, additional applications become possible. Thus, the investment into a performant laser system could be used more extensively.

- Long-lived laser-ionized isotopes could be implanted off-line for production of radioactive targets. For example "strong" implanted $^7$Be samples for a detailed measurement of the $^7$Be(p,$\gamma$) cross-section or for applications in nuclear solid state physics can be produced.

- After post-acceleration light radio-isotopes (e.g. $^7$Be) can be implanted deeper into the surface of workpieces as tracer for wear analysis in materials research [Feh97].

- With a small-bandwidth laser the hyperfine splitting could be used to separate the $11/2^-$ isomer $^{119m}$Sn (produced by $^{118}$Sn(n,$\gamma$)) from the $1/2^+$ ground state $^{119g}$Sn and implant it into semiconductors for Mößbauer spectroscopy [Weyer].

- There are many other radio-isotopes which can be efficiently produced off-line by neutron capture in a reactor or by direct reactions at a cyclotron. After separation with a RILIS and implantation in a carrier-free form they can serve for various applications in materials research or nuclear medicine (see e.g. [Bey98]).

- Also applications for trace analysis of metallic elements by RIS become possible. This method is often complementary to other ultrasensitive methods like neutron activation analysis or accelerator mass spectroscopy. An implementation at the MAFF set-up in Garching would provide an ideal supplement to the nearby existing facilities.

# 4. Yields and release of various elements

In the following the yields of isotopes from individual elements are discussed which were obtained recently at ISOLDE. ISOLDE yields are given as the beam intensity in the focal plane of the mass separator, normalized to 1 $\mu$A of primary proton beam. They do not include transmission losses in the subsequent beam transport. Traditionally always the optimum yield ever obtained is quoted [Klu86]. However, there are noticeable fluctuations of the performance from one target and ion source unit to another or even during a longer time of operation with the same target. Depending on the type of ion source the yields are generally reproducible within a factor two or three, but from certain targets they can even differ by one order of magnitude. Also the yields of very short-lived nuclei depend strongly on the individual conditions (target structure and temperature) and tend to fluctuate more. Due to the limited reproducibility it makes no sense to perform an error calculation for the presented yield values. They are therefore given without error bars. In the planning of new ISOLDE experiments an appropriate safety margin has to be considered in the count rate estimate.

Different methods are used to determine the yields:

- The ion current can be simply measured with a Faraday cup. The ISOLDE Faraday cups are reliable down to about 20 pA. With an average proton beam of 2.5 $\mu$A this is equivalent to a yield of about $5 \cdot 10^7$ per $\mu$C of primary protons. This method can be applied under the condition that no major isobaric contaminations occur and that the current does not fluctuate too much. Yields obtained in this way are marked with the label "FC".

- Lower intensities of radioactive nuclei can be determined by measuring the decay activity. A monitoring tape station attached to the main beam line is normally used to measure beta-active nuclei. A short bunch of the ion beam is implanted into a tape which is then moved into a $4\pi$ $\beta$-detector (scintillator). The integration of the release profile measured with this sampling technique [Let97a] gives the yield. This method is usable for nuclei with 0.4 s $\lesssim T_{1/2} \lesssim$ hours. More long-lived activities are not implanted to avoid a contamination of the tape, more short-lived ones decay during the tape transport (0.9 s). In some cases more short-lived nuclei can be analysed by observing the activity of the decay daughters. For nuclei decaying mainly by an isomeric transition or alpha emission the detector is less suitable and the deduced yields include the uncertainty of the detector response. A multiscaling unit allows to follow the time behaviour of the beta activity and to disentangle contributions of different isomers or isobars. However, this separation is no longer reliable if a mixture of several nuclei with similar lifetimes occurs. In these cases the sum yield was estimated by using an averaged half-life. Yields obtained with the monitoring tape station are marked with the label "$\beta$".

- Nuclei with longer lifetime ($\gtrsim$ 1 h) and a suitable gamma branching are collected by ion implantation into a metal foil and determined off-line by gamma spectroscopy. These nuclei are marked with the label "Coll".

- For the yield determination of the most short-lived nuclei a complete nuclear spectroscopy set-up has to be used. Depending on the decay pattern an efficiency calibrated alpha, beta, gamma or neutron-detector gives the count rate of the nuclei. This has to be corrected

for the transmission to and the efficiency of the detector as well as for the time structure of the collection and measurement period. For a yield estimation of unknown nuclei the branching ratio for neutron emission or certain gamma lines has to be taken from theoretical predictions. Yields obtained with these detection methods are marked with the labels "$\gamma$" or "$\beta$n", respectively.

It is a very honorable work of many ISOLDE users to perform themselves the complete yield determination of all isotopes observed with their set-up and report these. However, others do not evaluate the yields at all. They should keep in mind that this evaluation is not lost time, but the yields are useful for everyone:

- For other groups who can better plan their own experiments when having detailed information on the expected intensities of the desired beams and occuring contaminations.

- For the ISOLDE technical group to improve the target performance. Absolute yields are the most important mean to decide if a certain target is performing better or worse than another one. With the simple monitoring equipment only rough properties can be determined like yields of abundant isotopes and a release profile. Extrapolations to more exotic isotopes are possible, but a direct measurement is always better.

- For the experimental groups themselves: a rough on-line determination of the obtained yields can uncover e.g. a bad transmission of the beamline or a major misfunction of the experimental set-up (trigger settings, etc.). A detailed off-line analysis gives an additional possibility to control the evaluation. Obtained yields which differ significantly from the expected (smooth) drop towards more exotic isotopes, can give an indication of unexpected effects. Beam contaminations are easier discovered and even hints to nuclear properties can be deduced. Possibly even a limit can be given on the half-life of unobserved isotopes or on the branching ratios towards unobserved decay modes (e.g a strong beta transition to the ground state).

To allow for a better judgement of the ISOLDE yields, where available also the yields from other RIB facilities are given for comparison. Unfortunately only some facilities (e.g. the GSI ISOL) have the useful tradition to quote always the obtained yields directly in the nuclear spectroscopy publications. Otherwise the yields have to be estimated from "hints" given in the text. In the worst case this may be from the given statistical accuracy or a from figure with a gamma spectrum and an estimated measurement period[1]. Clearly these indirectly derived yields (marked with the label "est." in the corresponding tables) have a quite large uncertainty. Often also those important technical details (average beam current, transmission, etc.) are missing which would allow a scaling to meanwhile improved machine parameters (e.g. for the GSI SIS/FRS).

The used ion source types are abbreviated as follows: "$X$SI" for surface ion source with $X$ the material of the ionizer cavity and "F." for FEBIAD (complemented by the type if quoted), "MK5" for the ISOLDE "hot plasma source" and "MK3" for the ISOLDE source with medium temperature transfer line (200 to 400 °C).

Most ISOLDE SC yields were taken from ref. [Klu86, SCyie], exceptions are quoted. For the comparison with other facilities not the normalized yields (ions per $\mu$C), but the absolute yields (ions per s) are used. If not marked otherwise the ISOLDE yields are then given for a typical average proton beam current of 2.5 $\mu$A. The yields of other facilities were taken as published and not scaled to a meanwhile improved machine performance.

---

[1]If no other indications are given in the text a measurement time of one day was assumed.

## 4.1.   Separation of molecular sidebands

**Data from literature**

For elements where the release time is mainly determined by the desorption of the atoms, a separation as molecules can accelerate considerably the release. Especially many oxides and halides are stable enough at high temperatures to serve as carrier for various elements.

Ichikawa et al. made detailed off-line and on-line studies of the current ratio of monoxide to atomic ions for different lanthanides [Ich89]. Lanthanide monoxides were separated on-line at the KUR-ISOL facility [Kaw89] and are also seen as stable mass beams at ISOLDE. A barium oxide beam was found at OSIRIS [Hel92].

Also polyatomic molecular ions can be used as molecular sidebands. For example a $COSe^+$ beam from a $ZrO_2$ target was used for chemically pure separation of selenium [Hag92b].

Fluorides are preferred among the halides due to their strong binding and the existence of a single stable isotope ($^{19}F$). Chlorides cause an ambiguity in the mass assignment due to the existence of two stable isotopes ($^{35}Cl$ and $^{37}Cl$).

Occasionally impurities of the target material or the target container provide enough fluorine to cause significant molecular sidebands. $BaF^+$ was observed ten times more intense than $Ba^+$ from a molten lanthanum target without additional fluorination [Rav75b, Rav75a]. This can be explained by a 0.05 (mass)% fluorine contamination of the lanthanum [Put81]. However, in a later experiment with a controlled $CF_4$ addition, providing a $CF_4$ pressure of $5 \cdot 10^{-4}$ torr, the ratio $[BaF^+]/[Ba^+]$ dropped to 8 % [Hag92b]. Still, the use of the molecular sideband allows to suppress isobaric contaminations from alkalis[2] and gives a much higher beam purity.

Reeder et al. observed ratios of $[BaF^+]/[Ba^+] \approx 10$ and $[SrF^+]/[Sr^+] \approx 1$ from fluorine contaminations of the SOLAR $UO_2$/graphite target [Ree76].

By addition of fluoride vapors to a molten La-Th alloy at ISOLDE a ratio $[RaF^+]/[Ra^+] > 10$ was observed for radioactive radium isotopes [Rav76].

With fluorination (5 % $CF_4$ addition to the carrier gas) of the OSIRIS $UC_x$/graphite target, fluoride sidebands were observed for a series of elements [Hof80]. The following intensity ratios were reported: $[GaF^+]/[Ga^+] \approx 0.4$, $[SrF^+]/[Sr^+] \approx 15$, $[YF_2^+]/[YF^+]/[Y^+] \approx 75/25/1$, $[InF^+]/[In^+] \approx 0.1$, $[BaF^+]/[Ba^+] \approx 20$ and for various lanthanides (Ln): $[LnF_2^+]/[LnF^+]/[Ln^+] \approx 140/40/1$.

In [Hel92] a flow rate of $0.5-1.0$ nmol/s of $CF_4$ (equivalent to $(1-2)\cdot 10^{-5}$ mbar l/s) was used with the OSIRIS target, but the intensity of the fluoride sidebands was reduced to: $[SrF^+]/[Sr^+] \approx 0.2$ and $[BaF^+]/[Ba^+] \approx 2$,

Putaux et al. [Put81] report a ratio of $[LaF_2^+]/[LaF^+]/[La^+] \approx 10 : 4 : 1$ for the stable ion currents from a ISOCELE molten lanthanum target with $CF_4$ addition. For a molten cerium target without $CF_4$ addition they find $[BaF^+]/[Ba^+] \approx 1$. At ISOCELE fluorination of different targets was also used to separate new Ta, Zr and Sr isotopes as $TaF_4^+$, $ZrF_3^+$ and $SrF^+$ respectively [Lia82].

Hoff et al. reported the improved release characteristics when adding $CF_4$ to different ISOLDE target materials [Hof84]. From a $UC_x$/graphite cloth target at 1900 °C the release of lanthanum and cerium was significantly accelerated (reduction of $t_{50}$ from $> 15$ min to $< 2$ min) when adding $CF_4$ at a pressure of $1.5 \cdot 10^{-4}$ torr. For ISOLDE targets this corresponds to a leak rate of about $2 \cdot 10^{-5}$ mbar l/s $CF_4$.

With $CF_4$ addition to an ISOLDE niobium foil target practically elemental pure beams of neutron-deficient $SrF^+$ and $YF_2^+$ were separated [Ede92]. Yttrium fluorides were also separated from a tantalum foil target with an intensity ratio of $[YF_2^+]/[YF^+]/[Y^+] \approx 4/1.7/1$. A significant dependence on the operation conditions of the plasma ion source was noticed. Among the rare earths

---

[2]The alkalis do not form positive fluoride ions, probably due to immediate dissociation when a binding electron gets lost in the ionization process [Kir97].

only lutetium showed considerable fluoride sidebands (as $LuF^+$ and $LuF_2^+$). Also hafnium trifluoride ions could be separated with a remarkable yield from the tantalum target [Ede92, Hag92b]. This separation method for hafnium isotopes had already been used before at ISOCELE [Sau84]. $CaF^+$ and $ScF^+$ beams were obtained from a titanium foil target, however with yields about forty and ten times smaller than the corresponding atomic ion yields [Ede92].

Beams of $BeF^+$ and $UF^+$ were observed in a test with a $UC_x$/graphite target at ISOLDE, but in contrary to the results at OSIRIS no increase was seen for yttrium or the rare earths [Ede92]. All these experiments were done with a leak rate of about $10^{-5}$ mbar l/s.

Kirchner measured the release profiles and intensity ratios for atomic and monofluoride beams of group IIa and IIIa elements [Kir97]. In all cases the monofluoride ion beam showed a significant faster desorption and (with a FEBIAD source) a higher current. These experiments were performed with a $CF_4$-flow of only $3 \cdot 10^{-6}$ mbar l/s, but it should be kept in mind that the used target and ion source system has a total volume of only 1.3 cm$^3$ [Kir92b], about fifty times smaller than an ISOLDE target. With increasing $CF_4$ flow (from $4 \cdot 10^{-7}$ to $10^{-4}$ mbar l/s) the $[BaF^+]/[Ba^+]$ ratio increased from about 6 to 400.

A much higher $CF_4$ flow$^3$ of up to 0.15 ml/s was used by Kawase et al. to separate $BaF^+$ and $SrF^+$ beams [Kaw92]. The intensity of the latter was ten times higher than that of $Sr^+$.

## Fluorination of a $UC_x$/graphite target

A release test was made with a fluorinated standard ISOLDE $UC_x$/graphite target and tungsten surface ionizer. With a calibrated leak a constant $CF_4$ flow of $6.8 \cdot 10^{-6}$ mbar l/s is provided. For comparison yields and release curves were measured without and with fluorination.

### Aluminum

Kirchner had shown that the release of aluminum can be significantly accelerated by fluorination [Kir97]. The addition of aluminum vapor was also used for separation of radioactive fluorine isotopes from a silicon carbide target as $AlF^+$ [Hag92b]. At Oak Ridge $AlF^+$ beams were separated from an $Al_2O_3/SiO_2$ target [Car97]. $AlBr^+$ and $AlI^+$ beams were used at OSIRIS to obtain chemically pure beams of halogens as an alternative to negative surface ionization [Ale80, Hof81].

However, in our measurement no difference in the release profile of $Al^+$ was observed with and without fluorination. Note that $AlF^+$ cannot be surface ionized due to its high ionization potential (9.8 eV). Also Mg is not surface ionized. With a delay of 0.9 s between ion collection and measurement there remain no other contributions on mass 28 (sodium decays rapidly to the long-lived magnesium) and the measured beta-activity is entirely due to aluminum. The release curve can be fitted with the following parameters, see equation (2.4.2): $\tau_r = 1$ ms, $\tau_f = 0.5$ s, $\tau_s = 20$ s, $\alpha = 0.5$. At mass 30, the first part of the release curve (up to 300 ms delay) was not taken into account. It shows a contribution of $^{30}$Na which decays via magnesium and aluminum. Note that the $^{30}$Al yield was higher than reported from the ISOLDE SC [Klu86, SCyie].

The release of aluminum was fast enough to get sufficient yields of the short-lived isotopes $^{34}$Al ($T_{1/2} = 55$ ms) and $^{35}$Al ($T_{1/2} = 38$ ms) to perform new nuclear spectroscopy experiments [Han99a].

It should be noted that the heavy aluminum isotopes start to emit beta-delayed neutrons at mass 32. The contribution of these neutrons is possibly the reason for the "bump" in the measured yield curve of heavy sodium isotopes from ISOLDE SC reported in [Klu86]. These yields had been derived from the measured neutron activity with the assumption that only sodium is extracted from the surface ion source. In a measurement at the ISOLDE PSB the "bump" was not confirmed.

---

$^3$With a fixed helium flow rate of 13 ml/s.

## Strontium

The measured release curve of $^{95}$Sr$^+$ was very similar without and with fluorination. It was fitted with the parameters: $\tau_r = 20$ ms, $\tau_f = 0.6$ s, $\tau_s = 30$ s, $\alpha = 0.9$.

At mass 114 some contaminations (indium, etc.) occured. Therefore only an upper limit could be derived for the yield of $^{95}$SrF$^+$. The ratio [SrF$^+$]/[Sr$^+$] $\lesssim 0.05$ is much smaller than in all measurements reported in literature.

## Barium

Yields of radioactive barium isotopes were measured as atomic ions as well as monofluoride ions. For BaF$^+$ the release curve was fitted with a rise time of 1 s and a single fall time of about 100 s. This is in agreement with the Ba$^+$ release measured from a UC$_x$/graphite target without fluorination [Eve97]. For Ba$^+$ the first part of the release curve is veiled by a large background from Cs$^+$. Within the experimental errors the later part is identical to that of BaF$^+$. Applying the release profile of BaF$^+$ also for Ba$^+$ one finds for the latter a yield thirty times that of BaF$^+$. This is in contradiction to the ratios reported in literature where [BaF$^+$] $\gg$ [Ba$^+$].

It should be noted that these and all other fluoride yields and release curves were measured after operating the target already for three days with CF$_4$ addition. A measurement of $^{145}$Ba$^+$ and $^{145}$BaF$^+$ some hours after the first CF$_4$ addition gave a much faster rise ($\tau_r \lesssim 50$ ms) and a significantly higher yield for $^{145}$BaF$^+$ (about $7 \cdot 10^6$ $\mu$C$^{-1}$). This fact indicates a breakdown of the CF$_4$ supply during the experiment.

## Europium

$^{160}$Eu$^+$ was identified by its lifetime and thus separated from $^{141}$BaF$^+$ which is present at the same mass. The release profile can be reproduced with a fast rise ($\sim 0.1$ s) and a slow drop ($\sim 100$ s). For the monofluoride $^{160}$EuF$^+$ only an upper limit was obtained: [EuF$^+$]/[Eu$^+$] $\leq 1$ %. Note that from another unfluorinated UC$_x$/graphite target $^{160}$Eu$^+$ was observed with similar release characteristics and a yield of $2 \cdot 10^5$ per $\mu$C. Thus, there is no indication for an improvement by fluorination.

## Radium and others

The yields of $^{231}$Ra and $^{232}$Ra were estimated by disentangling from the measured beta activity the contributions of francium and radium by their half-lives. A rise time of 1 s and a single fall time of 100 s was taken for the evaluation. This arbitrary choice does not affect the yields significantly.

There was no indication of significant amounts of $^{39}$CaF$^+$, $^{46m}$ScF$^+$, $^{84g}$YF$^+$, rare earth fluorides or RaF$^+$ [4]. At masses 71, 102 and 176 some activity was observed, but from the beta-decay curves it could not be attributed unambiguously to individual isotopes.

## Fluorine partial pressure?

The low intensity of the observed fluoride sidebands, the small effect on the release times and the changing values for barium fluoride give rise to the suspect that either not enough fluorine reached the target (blocked leak) or it reacted mainly with some impurity to a non-surface-ionizable (and thus not detected molecule.

---

[4]In fact, at another occasion RaF$^+$ beams were observed from a not specially fluorinated target (see section 4.12).

Table 4.1.1.: Yields and release parameters from a standard ISOLDE uranium carbide/graphite target with $CF_4$ addition. The target was kept at about 2200 °C and the W surface ionizer at 2400 °C. All yields without reference were measured in this experiment by beta counting at the monitoring tape station.

| Isotope | Yield ($\mu C^{-1}$) | Reference |
|---------|-----------|-----------|
| $^{28}Al^+$ | $1.2 \cdot 10^6$ | |
| $^{30}Al^+$ | $2.7 \cdot 10^5$ | |
| $^{34}Al^+$ | 13 | [Num01] |
| $^{35}Al^+$ | 4 | [Num01] |
| $^{95}Sr^+$ | $3.5 \cdot 10^8$ | |
| $^{95}SrF^+$ | $\leq 1.9 \cdot 10^7$ | |
| $^{145}Ba^+$ | $3.4 \cdot 10^6$ | |
| $^{141}BaF^+$ | $6 \cdot 10^6$ | |
| $^{144}BaF^+$ | $6 \cdot 10^5$ | |
| $^{145}BaF^+$ | $1.4 \cdot 10^5$ | |
| $^{146}BaF^+$ | $\approx 1.4 \cdot 10^4$ | |
| $^{147}BaF^+$ | $\approx 2000$ | |
| $^{148}BaF^+$ | $\approx 600$ | |
| $^{160}Eu^+$ | $\approx 1.5 \cdot 10^5$ | |
| $^{231}Ra^+$ | $\approx 4 \cdot 10^5$ | |
| $^{232}Ra^+$ | $\approx 2 \cdot 10^5$ | |

The ratio of uranium fluoride ions to uranium ions could be used for a monitoring of the fluorine partial pressure in the target. The $UF^+$ current reached only 0.2 % of the $U^+$ current, although its ionization potential is slightly lower (6.0 eV instead of 6.2 eV [Lau82]). A value of $\approx 8.2$ was measured for the equilibrium constant of the reaction: $U(g) + BaF(g) \rightleftharpoons UF(g) + Ba(g)$ at 2200 °C [Lau82]. With the typical ratio of $[BaF^+]/[Ba^+] \gtrsim 10$ measured in [Rav75b, Hof80, Kir97] and comparable ratios of the ionization potentials of fluoride and atom for uranium and barium one should expect a much higher current of $UF^+$ under equilibrium conditions. $UF_2^+$ (ionization potential 6.2 eV [Lau82]) and higher fluorides[5] were not observed at all. The only markable current above $A = 238$ was at mass 262 with about 5 % of the $^{238}U^+$ intensity. $^{238}UC_2^+$ has an ionization potential of 6.4 eV while that of the other uranium carbides is above 7 eV [Gup79].

It can be concluded that the partial pressure of the fluorine was probably too low in these experiments. The obtained results give only a lower limit of the yield increase and the release acceleration which can be obtained by fluorination of a $UC_x$/graphite target.

The literature data show that the use of molecular sidebands can provide a good possibility for efficient and selective separation of certain elements. However, the considerable fluctuations in the reported ratios of molecular to atomic ion current indicate that the detailed high-temperature thermodynamics plays an important role. Thus, changes of the chemical composition or impurities can affect the intensity of molecular sidebands much stronger than that of the atomic ions. To guarantee a good reproducibility of molecular ion beam intensities special care has to be taken to avoid impurities in the target and ion source system and to provide a sufficient flow of $CF_4$, especially when using thick targets.

---

[5]These are practically not surface ionized with ionization potentials of 7.05 eV, 10.2 eV [Lau82], 11.3 eV and 14 eV [Hil77] for $UF_3$, $UF_4$, $UF_5$ and $UF_6$ respectively.

## 4.2.   Beryllium yields

Beryllium is a "difficult" element for ISOL facilities, which is often released very slowly or not at all. With a vapor pressure of $\approx 10$ mbar at 2000 K [Hon69], about equal to tin, it is less a problem of evaporation than of adsorption to surfaces.

To allow for a fast desorption the whole target-ion source assembly has to be kept at high temperatures. Off-line tests with $^7$Be in a hot plasma source gave an efficiency of $10^{-4}$ at best. About 95 % of the $^7$Be got stuck to cold spots and did not reach the ionizer [Barke]. It accumulated especially on the surface of the oxide insulators in the plasma source, forming very stable BeO.

Also by addition of $CF_4$ and separation of the monofluoride sideband no major increase was obtained. On-line tests with $^{11}$BeF$^+$ and a hot plasma source (all parts above 1800 °C) gave only an efficiency of $4 \cdot 10^{-4}$.

A recently presented ECRIS for the production of $^7$Be beams at TRIUMF [Jay98] reaching an efficiency of 2 to 3 % might be an alternative for off-line produced $^7$Be. However, the source body is too cold to allow a rapid release of short-lived beryllium isotopes. Moreover, the beam is mainly separated as BeF$^+$ and BeF$_2^+$. With a heavy target, huge contaminations of isobars like Ne$^+$, Na$^+$, Ar$^+$, K$^+$, AlF$^+$, etc. are unavoidable and will disturb nuclear spectroscopy experiments strongly due to their similar lifetimes and decay modes (e.g. $\beta$n).

The use of a hot cavity RILIS allows a major increase of the ion source temperature and the suppression of any oxide surface.

### Graphite target

Initially a "long" (40 cm length) and dense (73 g/cm$^2$) target from pure graphite was used for the production of the long-lived isotopes $^7$Be and $^{10}$Be. However, the target temperature was limited by the maximum current of the power supply and it took very long (hours) that the beam came into saturation. With this target an ion implanted $^7$Be target was produced and used for a measurement of the astrophysical $S_{17}$ factor (i.e. the cross-section for $^7$Be(p,$\gamma$)$^8$B, see ref. [Has98b]).

### UC$_x$/graphite target

A standard UC$_x$/graphite target (52 g/cm$^2$) was used to produce a $^{11}$Be beam for a collinear laser spectroscopy experiment, where the magnetic moment of $^{11}$Be was measured with $\beta$-NMR [Gei99]. In a target test also the short-lived isotopes $^{12}$Be ($T_{1/2} = 21.3$ ms) and $^{14}$Be ($T_{1/2} = 4.4$ ms) could be separated for the first time at an ISOL facility. The latter is among the most short-lived isotopes separated so far at ISOLDE.

Table 4.2.1.: Measured yields of beryllium isotopes from a standard UC$_x$/graphite target.

| Isotope | $^7$Be | $^9$Be | $^{10}$Be | $^{11}$Be | $^{12}$Be | $^{14}$Be |
|---------|--------|--------|-----------|-----------|-----------|-----------|
| $T_{1/2}$ | 53 d | stable | $1.6 \cdot 10^6$ a | 13.8 s | 21.3 ms | 4.4 ms |
| $Y$ ($\mu$C$^{-1}$) | $1.4 \cdot 10^{10}$ | $1.7 \cdot 10^{10}$ | $6 \cdot 10^9$ | $1.6 \cdot 10^7$ | 1500 | 4 |
| Method | FC | FC | FC | $\beta$ | $\beta$ | $\beta$n |

With another UC$_x$/graphite target (53 g/cm$^2$ of uranium) the yield of $^{14}$Be was confirmed and a measurement of the $\beta$ count rate allowed to redetermine the $P_n$ value [Ber99]. With this target also a higher yield of $^{11}$Be was observed, indicating some transmission loss to the monitoring tape station in the last measurement. Another measurement gave a still higher yield for $^{11}$Be but could not be confirmed. It had possibly been fooled by a misfunction of the beam gate.
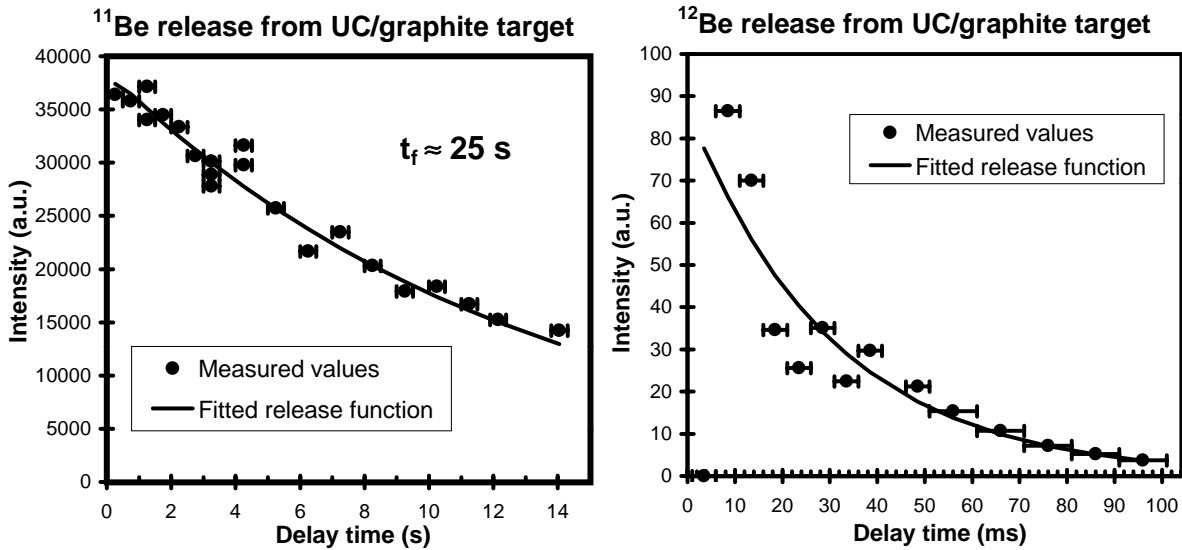
Figure 4.2.1.: Release function of beryllium measured with $^{11}$Be and $^{12}$Be.

For the simplified one-component release function (not taking into account the contribution of a possible slow component) a fall time $\tau_f$ of about 25 s can be deduced after correction for the radioactive decay of $^{11}$Be, see figure 4.2.1. The very first part of the release function (up to about 100 ms) was monitored with $^{12}$Be. Despite some fluctuations a rise time $\tau_r$ of the order of 1 ms can be deduced. This extremely fast rise might indicate a small component which is released as a bunch due to the impact of the intense proton pulse. Such a "radiation enhanced release" has already been experienced before, e.g. for noble gases from oxide targets [Rav97b]. A slower tail in the minute range can be observed in a Faraday cup from the release of the long-lived radio-nuclides $^7$Be and $^{10}$Be after switching off the proton beam. A quantitative evaluation is however difficult, since the proton beam contributes to the target heating and to the just mentioned bunched release. During the whole run the target was kept at temperatures above 2000 °C and the tungsten ionizer cavity above 2300°C.
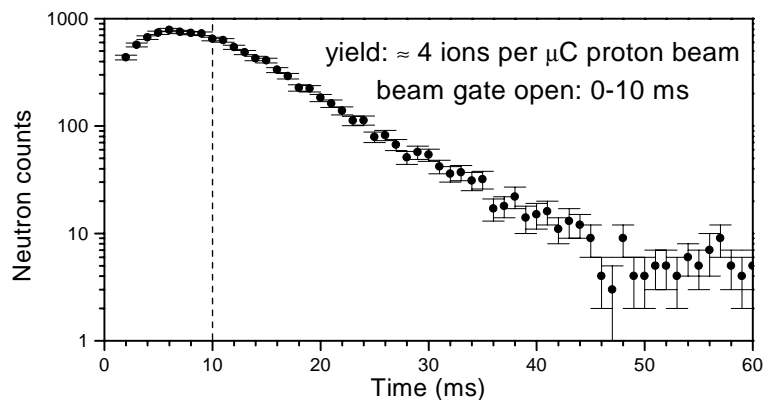


Figure 4.2.2.: Grow-in and decay curve of $^{14}$Be. The beam gate was closed after 10 ms.

$^{14}$Be was detected via its beta-delayed neutrons with a $4\pi$ neutron long counter. Figure 4.2.2 shows the release and decay curve of $^{14}$Be.

**Comparison**

ISOLDE is presently the only ISOL facility where short-lived beryllium isotopes are available. Before this has been a unique domain of fragment separators. Yields from other facilities are shown in table 4.2.2. In fact the beams are not directly comparable since the beam energy differs significantly. Depending on the application a higher or lower energy is of advantage. The low-energy ISOL beams are particularly favorable for nuclear spectroscopy experiments. This explains why new information could be gained [Ber99] despite a lower beam intensity,

Table 4.2.2.: Beam intensities of short-lived beryllium isotopes at different RIB facilities. $E/A$ gives the energy of the projectile. Note that LOHENGRIN is not a dedicated "production" facility for light elements. The given yields are for a 0.4 mg/cm$^2$ $^{241}$Pu target. The $^{14}$Be beam from the FRS was used in Cave B and had a very poor transmission [Simon].

| Intensity $(s^{-1})$ | Facility ISOLDE | Proj. | $E/A$ (MeV) | Reference |
|---|---|---|---|---|
| | | $^{11}$Be | | |
| $4 \cdot 10^7$ | ISOLDE, PSB | p | 1000 | RILIS Be |
| $1 \cdot 10^6$ | A1200, MSU | $^{13}$C | 100 | [Var98] |
| $3 \cdot 10^4$ | SISSI, GANIL | $^{15}$N | 35.3 | [For98] |
| 0.4 | LOHENGRIN | n | thermal | chapter 1 |
| | | $^{12}$Be | | |
| $4 \cdot 10^3$ | ISOLDE, PSB | p | 1000 | RILIS Be |
| $1 \cdot 10^5$ | RIPS, RIKEN | $^{18}$O | 100 | [Kor95] |
| $2 \cdot 10^4$ | LISE3, GANIL | $^{18}$O | 63 | [Fre98] |
| 0.2 | LOHENGRIN | n | thermal | chapter 1 |
| | | $^{14}$Be | | |
| 10 | ISOLDE, PSB | p | 1000 | RILIS Be |
| 350 | A1200, MSU | $^{18}$O | 80 | [Zah93] |
| 300 | RIPS, RIKEN | $^{18}$O | 100 | [Aoi97] |
| 100 | LISE3, GANIL | $^{18}$O | 63 | [Fre98] |
| 44 | U400, FLNR | $^{18}$O | | [Pen95] |
| 16 | FRS, GSI | $^{18}$O | 325 | [Simon] |
| $2 \cdot 10^{-4}$ | LOHENGRIN | n | thermal | chapter 1 |

**Prospects**

Already now new experiments with beryllium beams are scheduled at ISOLDE (detailed nuclear spectroscopy of $^{11}$Be, $^{12}$Be and $^{14}$Be [ISP99]) or planned for the future (measurement of $S_{17}$ in inverse kinematics at REX-ISOLDE [ISI20]). To perform these experiments a further increase in yield would be very useful. This could be achieved by optimizing the target geometry for fastest release (more compact design). Beryllium was also found to be released from other carbides [Hof84]. Release times below 30 s were measured for TiC-C$_3$, ZrC-C$_3$ and VC at 1900 °C each. However, for the most neutron-rich isotopes the production cross-sections are expected to be highest from fragmentation of heavier nuclei. It is not possible to predict if one of the other carbides will show a fast enough release to overcompensate this handicap.

By adding $CF_4$ the release time might be further reduced, but the beryllium-fluoride molecules have to be dissociated in the ionizer tube before laser ionization can be applied. Molecules like BeF or $BeF_2$ are not laser ionized with the wavelengths of the present scheme. They are neither surface ionized due to their high ionization potentials ($> 9$ eV). Unfortunately a first test of $CF_4$ addition to a $UC_x$/graphite target was not conclusive (see section 4.1). For beryllium no major influence of the fluorination on the release profile was observed. The yield could not be compared directly due to changed operation conditions: a four days "older" target, a retuning of the laser set-up and different target and ionizer temperatures.

A tantalum or tungsten foil target which can be heated to very high temperatures (2400 °C and above) could be a good alternative to $UC_x$/graphite. At 2400 °C the sticking time calculated from the Eichler systematics (see B.2.5) is about 2 $\mu$s for either Ta or W surfaces.

## 4.3.    Manganese yields

### $UC_x$/graphite target

A pure $^{57}$Mn beam was required for Mößbauer spectroscopy in semiconductors. Normally the Mößbauer level in $^{57}$Fe is populated by electron capture decay of the long-lived $^{57}$Co. However, at higher temperatures the cross-section for recoil free resonance absorption is reduced and a higher source strength is required to overcome the experimental noise. With the low specific activity of $^{57}$Co (1 GBq per 3 $\mu$g) this would result in an overdose of cobalt doping. Thus, no longer the intrinsic properties of the pure semiconductor material are observed, but those of a heavily cobalt doped material which is technologically irrelevant. The $\beta^-$ decay of $^{57}$Mn is an alternative to populate the 14.4 keV level in iron. Due to the shorter half-life (85.4 s) the specific activity is significantly higher: 1 GBq per $10^{11}$ atoms. Because of its short half-life the $^{57}$Mn beam has to be implanted on-line. However, the beam of a "hot plasma source" has typically a strong contamination with stable iron. This would again result in an overdoping of the sample. Therefore a more selective ionization method was required: resonant laser ionization.

For manganese a new ionization scheme was found which attains a very high efficiency ($\approx 19.2$ %) since the green CVL line just matches a resonant transition to an AIS. It was shown that a $UC_x$/graphite target can provide intense beams of heavy manganese isotopes [Fed97].

Also a tantalum target was tested, but even at a temperature of 2100 °C the release was much slower ($t_{50} > 50$ s) and the yield lower, only $2 \cdot 10^6$ $\mu C^{-1}$ for $^{57}$Mn.

In summer 1997 another manganese beam time with a $UC_x$/graphite target was scheduled and the Mainz neutron detector was set up to extend the target test towards more neutron-rich isotopes. The tuning of the RILIS took most of the night, but in the early morning the test could finally be started. The release was fast and the yields were significantly better compared with the tantalum target: till breakfast beta-delayed neutrons up to $^{68}$Mn were found. Later also $^{69}$Mn could be measured. This was surely one of the most successful "target tests" at ISOLDE with nine new or significantly improved half-lives from $^{61}$Mn to $^{69}$Mn [Han99b].

Obviously not only the fast release and the high ionization efficiency were a prerequisite for this success, but also the very good beam purity. Fortunately in this mass range there are very few isobaric contaminations. Only gallium is significantly surface ionized, but the gallium isotopes up to $^{68}$Ga are neutron-deficient and therefore less produced from an actinide target. Moreover they are long-lived and give only a flat background. Using additionally the selective detection of beta-delayed neutrons, there is absolute no isobaric contamination from surface ionized beta-delayed neutron emitters up to mass 78!

Table 4.3.1 shows the yields obtained with the 50 g/cm$^2$ $UC_x$/graphite target. The target temperature was 2100 °C, the line temperature 2400 °C. The release profile was fitted with (see equation

(2.4.2)): $\tau_r = 0.1$ s, $\tau_f = 0.6$ s, $\tau_s = 12$ s and $\alpha = 0.6$. Note that the yield of the short-lived nuclei is higher compared with the values given in [Fed97]. The latter experiment was made with the target and line at only 2000 °C giving a slightly slower release. The half-lives shown in table 4.3.2 are from [Aud97] for $^{53-60}$Mn and [Han99b] for $^{61-69}$Mn. The predicted branching ratios for neutron emission $P_n$ were taken from [Möl97].

Table 4.3.1.: Yields of manganese isotopes from a 51 g/cm$^2$ UC$_x$/graphite target and resonant laser ionization. The yield $Y$ is given in atoms per $\mu$C of primary proton beam.

| Isotope | $^{53}$Mn | $^{54}$Mn | $^{56}$Mn | $^{57}$Mn | $^{59}$Mn | $^{60g+m}$Mn | $^{61}$Mn |
|---|---|---|---|---|---|---|---|
| $T_{1/2}$ | $3.7 \cdot 10^6$ a | 312 d | 2.6 h | 85 s | 4.6 s | 1.8 s, 51 s | 625 ms |
| $Y$ ($\mu$C$^{-1}$) | $> 3 \cdot 10^7$ | $9 \cdot 10^7$ | $4 \cdot 10^8$ | $1.5 \cdot 10^8$ | $1.5 \cdot 10^8$ | $> 4 \cdot 10^7$ | $1.7 \cdot 10^6$ |
| Method | FC | Coll | Coll | $\beta$ | Coll | FC | $\beta$ |

| Isotope | $^{62}$Mn | $^{63}$Mn | $^{64}$Mn | $^{65}$Mn | $^{66}$Mn | $^{67}$Mn | $^{68}$Mn | $^{69}$Mn |
|---|---|---|---|---|---|---|---|---|
| $T_{1/2}$ | 671 ms | 275 ms | 89 ms | 88 ms | 66 ms | 42 ms | 26 ms | 14 ms |
| $Y$ ($\mu$C$^{-1}$) | $7 \cdot 10^5$ | $2 \cdot 10^5$ | 7000 | 1000 | $\approx 170$ | $\approx 100$ | $\approx 4$ | $\approx 1$ |
| Method | $\beta$ | $\beta$ | $\beta$ | $\beta$ | $\beta$ | $\beta$n | $\beta$n | $\beta$n |
| $P_n$ (%) | | | | | | $\approx 11$ | $\approx 16$ | $\approx 24$ |

The yield values of $^{63-66}$Mn determined from the decay daughters Fe and Co and those of $^{67-69}$Mn obtained with the estimated neutron branching ratios have clearly a larger uncertainty. The "bump" at mass 67 could indicate an underestimated $P_n$ value[6]. A better yield determination will become possible with completely evaluated $\beta$n- and $\beta\gamma$ branching ratios.

Also some samples of $^{53}$Mn and $^{60}$Mn (decaying to $^{60}$Fe) were collected and used as calibration standards at the AMS facilities in Munich and Zurich. The number of $^{53}$Mn atoms found in Munich was about twice as much as estimated from the Faraday cup measurement [Knie]. This indicates that the calibration of the used FC (in the collection chamber) might be too low and the transmission to the GLM beam line higher than estimated.

**Nb foil target**

The ISOLDE proposal P94 intends to study the decay of the very neutron-deficient isotope $^{47}$Mn. This is best produced in spallation of a nearby target. On the other hand it has a short half-life ($\approx 100$ ms) and requires a rapid release to limit the decay losses. A target with high production rates and a fast release of manganese is moreover useful for the production of other neutron-deficient manganese isotopes, e.g. $^{50g}$Mn which decays by a superallowed $0^+ \rightarrow 0^+$ Fermi transition and is therefore suitable for the determination of the vector coupling constant $G_V$ (see e.g. [Hag94]).

As first choice a niobium foil target was tested. However, even at nearly 2100 °C the release was too slow. The release profile was fitted with a rise time of 0.2 s and a fall time of 30 s. $^{47}$Mn was not observed, but new nuclear spectroscopy information could be obtained for other manganese isotopes, e.g. $^{59}$Mn [Oin01]. Table 4.3.2 shows the yields obtained with the 50 g/cm$^2$ Nb foil target. The shown half-lives are from [Aud97] for $^{48-60}$Mn and [Han99b] for $^{61,62}$Mn.

Interestingly at mass 60 the isomer $^{60m}$Mn was observed, while for $^{60g}$Mn only an upper limit can be given based on a possible $T_{1/2} = 51$ s component. Taking into account the correction for decay losses, the ratio of ground state to metastable state intensity is about $1 : 10$ in $^{58}$Mn, but $< 1 : 100$

---

[6]Note that other estimations propose a $P_n$ value of the order of 26 % [Pfe99].

Table 4.3.2.: Yields of manganese isotopes from a 50 g/cm$^2$ niobium foil target and resonant laser ionization. The yield $Y$ is given in atoms per $\mu$C of primary proton beam. Yields marked by $\beta\gamma$ were measured with the set-up of the IS-P94 collaboration and evaluated by Markku Oinonen [Oinon].

| Isotope | $^{48}$Mn | $^{49}$Mn | $^{50g}$Mn | $^{50m}$Mn | $^{51}$Mn | $^{52}$Mn | $^{53}$Mn | $^{54}$Mn | $^{56}$Mn |
|---|---|---|---|---|---|---|---|---|---|
| $T_{1/2}$ | 0.16 s | 0.38 s | 0.28 s | 105 s | 46 min | 5.6 d | $3.7 \cdot 10^6$ a | 312 d | 2.6 h |
| $Y$ ($\mu$C$^{-1}$) | 5 | 2800 | 400 | $6 \cdot 10^5$ | $6 \cdot 10^7$ | $3.8 \cdot 10^8$ | $9 \cdot 10^8$ | $1.1 \cdot 10^9$ | $2.7 \cdot 10^8$ |
| Method | $\beta\gamma$ | $\beta\gamma$ | $\beta\gamma$ | $\beta\gamma$ | FC | FC | FC | FC | FC |

| Isotope | $^{57}$Mn | $^{58g}$Mn | $^{58m}$Mn | $^{59}$Mn | $^{60g}$Mn | $^{60m}$Mn | $^{61}$Mn | $^{62}$Mn |
|---|---|---|---|---|---|---|---|---|
| $T_{1/2}$ | 85 s | 3 s | 65 s | 4.6 s | 51 s | 1.8 s | 625 ms | 671 ms |
| $Y$ ($\mu$C$^{-1}$) | $6 \cdot 10^7$ | $1.3 \cdot 10^5$ | $1.2 \cdot 10^7$ | $4.6 \cdot 10^5$ | < 2000 | $2 \cdot 10^4$ | 2000 | 400 |
| Method | $\beta\gamma$ | $\beta$ | $\beta$ | $\beta\gamma$ | $\beta$ | $\beta\gamma$ | $\beta$ | $\beta$ |

in $^{60}$Mn. Unfortunately with the UC$_x$/graphite target the decay curves of mass 58 and 60 were not measured and no conclusion can be drawn on the contribution of the individual isomers.

It should be noted that the $^{60g}$Mn 0$^+$ ground state with 51 s half-life was only observed once at the GSI ISOL [Bos88]. It was not found in a later search and the suspicion came up that the earlier measurement had been fooled by a beam contamination with doubly-charged $^{120}$In [SO92]. The intense and pure Mn beam from the UC$_x$/graphite target ionized by the RILIS should allow to check the half-life of $^{60g}$Mn.

The value for the ionization efficiency (19.2 %) quoted in ref. [Fed97] had been obtained by scaling an earlier off-line result (4.8 %) with the increased dye laser power. With the yields derived above it is possible to redetermine the efficiency independently. Measured spallation cross-sections are available for long-lived manganese isotopes produced by 1 GeV protons on a zirconium target [Mic97]: about 1 mbarn for $^{52}$Mn and 3 mbarn for $^{54}$Mn. The cross-sections for niobium should be very similar. The total efficiency of the target and ion source unit[7] is given by the ratio of the measured yield to the calculated production rate. For $^{52}$Mn one obtains 20 % and for $^{54}$Mn 19 %. This impressive agreement shows that the RILIS efficiency obtained off-line is fully reproducible under on-line conditions.

**Comparison**

Figure 4.3.1 shows a comparison of experimentally obtained yields of manganese isotopes at different facilities. For all isotopes from $^{50m}$Mn to $^{69}$Mn the ISOLDE yields exceed those of other facilities by orders of magnitude!

**Prospects**

On the neutron-rich side there is presently no urgent need to find an even more performant target. Already the obtained yields will allow to perform detailed nuclear spectroscopy of the iron nuclei populated in beta decay (compare [IS364]).

However, for the short-lived neutron-deficient manganese isotopes the yields are not very competitive. With a typical proton beam current of 2.5 $\mu$A the present yield of $^{50g}$Mn (1000 s$^{-1}$) is just half of that obtained at IGISOL with 1 $\mu$A protons on a $^{50}$Cr target [Ärj86] and a factor of twenty

---

[7]For long-lived isotopes it is practically equivalent to the ion source efficiency.

Table 4.3.3.: Production of manganese isotopes at different RIB facilities.

| Ref. | Facility | Proj. | $E/A$ (MeV) | $\bar{I}$ (pnA) | Target | $\zeta$ (g/cm$^2$) | Comm. |
|------|----------|-------|------|------|--------|------|-------|
| RILIS Nb | ISOLDE | p | 1000 | 2500 | Nb | 50 | RILIS |
| RILIS UC | ISOLDE | p | 1000 | 2500 | UC$_x$ | 51 | RILIS |
| [Hag92b] | ISOLDE | p | 600 | 2500 | Nb | 9.6 | MK5 |
| [Run85] | GSI-ISOL | $^{82}$Se | 11.5 | 20 | W | 0.046 | F.-E |
| [Bos88] | GSI-ISOL | $^{76}$Ge | 11.5 | 20 | W | 0.036 | F.-F |
| [Kirch] | GSI-ISOL | $^{76}$Ge | 11.5 | 10 | W | 0.023 | F.-F |
| [SO91] | GSI-ISOL | $^{50}$Ti | 13.5 | 20 | W | | |
| [Web92] | GSI-FRS | $^{86}$Kr | 500 | 0.0017 | Be | 2 | |
| [Eng98] | GSI-FRS | $^{238}$U | 750 | 0.0033 | Be | 1 | |
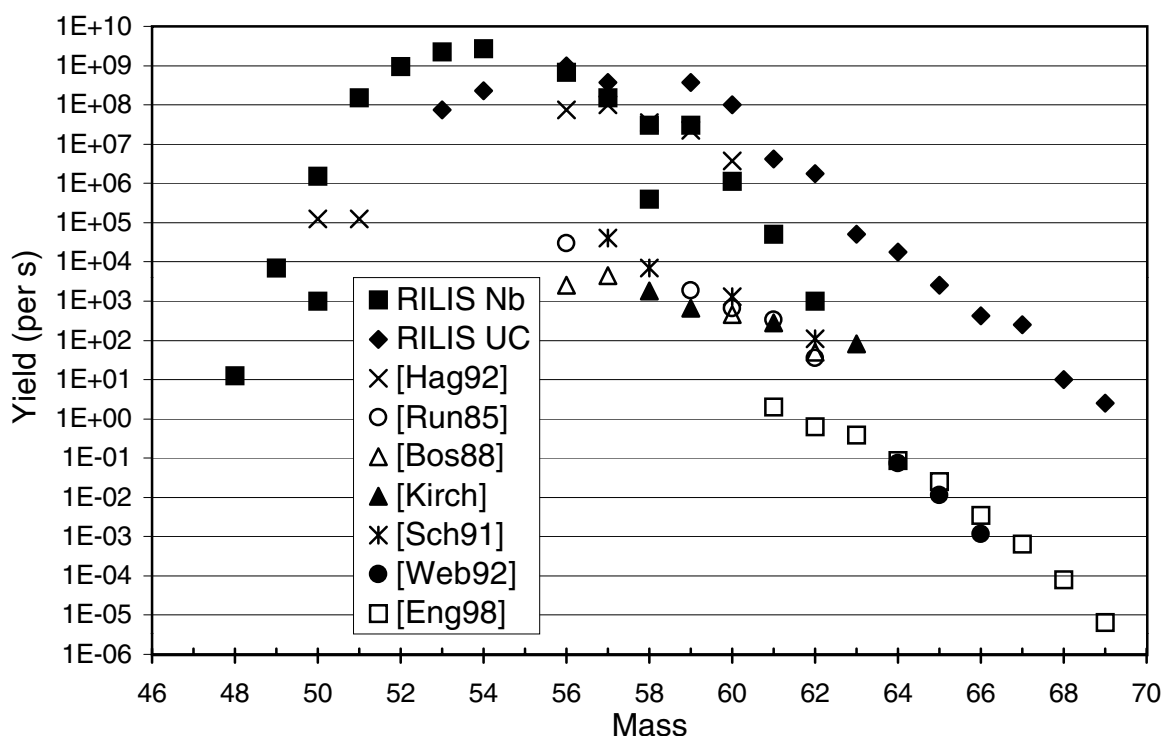


Figure 4.3.1.: Comparison of manganese yields, see table 4.3.3 for experimental details of each curve.

lower compared with the typical yields obtained at the Chalk River ISOL facility (10 $\mu$A protons on a $^{50}$Cr target) [Kos97a]. Most of the produced short-lived nuclei decayed in the ISOLDE niobium target. A target with comparable production rate and faster release has the potential to increase the yields of short-lived manganese isotopes by at least one order of magnitude.

Some release data exists on alternative materials: Hoff et al. measured in an off-line test $t_{50} \approx 1$ min for the Mn release from a $Cr_2O_3$ target at 1700 °C [Hof84]. While chromium oxide cannot be heated much more due to excessive vapor pressure, a zirconium oxide fiber target could be an alternative. Due to its fiber structure it should show intrinsically a faster release. Moreover it can be heated to significantly higher temperatures (about 2000 °C). Presently no direct data is available on the release characteristics of Mn from a $ZrO_2$ fiber target, but neutron-deficient manganese beams were already observed at the ISOLDE SC from a $ZrO_2$ target and a hot plasma source. The manganese

oxides MnO and $MnO_2$ are nearly completely dissociated at higher temperatures [Hil94] and will not hinder the resonant laser ionization of the atom.

Another possibility would be a zirconium germanide ($Zr_5Ge_3$) target which showed a rapid release of manganese at 1800 °C: $t_{50} \ll 1$ min [Hof84]. Hafnium germanide ($Hf_5Ge_3$) is less suitable. At equal temperature the release of Mn is slower [Hof84] and the hafnium spallation would cause more isobaric background on the neutron-rich side, e.g. $^{47}$K.

## 4.4.    Nickel yields

**$UC_x$/graphite target**

Neutron-rich nickel isotopes were produced from two standard $UC_x$/graphite targets (52 and 53 g/cm$^2$ of uranium respectively) and ionized with the RILIS in a tungsten cavity. The targets were kept at a temperature of about 2100 °C and the lines at about 2300 °C and 2400 °C respectively.

The current of the isotopes $^{59-66}$Ni was directly measured with a Faraday cup and corrected for the contributions of stable nickel calculated from the natural abundance ratio and the $^{58}$Ni current. The yields of $^{56,65,67}$Ni were determined by collection of a sample and subsequent off-line measurement of the gamma ray intensity.

The beta-decay of the isotopes $^{67-70}$Ni was identified by their half-life. The release curve was fitted with a rise time of 1 s and a single exponential decay of 120 s. The second target (with the line at 2400 °C) showed a faster rise time: about 0.2 s. At mass 69 only the $9/2^+$ ground state with $T_{1/2} = 11.2$ s was observed (see figure 4.4.1). A possible contribution of the $1/2^-$ metastable state with $T_{1/2} = 3.5$ s [Fra98b] is at least one order of magnitude smaller[8]. At mass 71 no significant beta-activity was visible which gives an upper limit for the $^{71}$Ni yield.
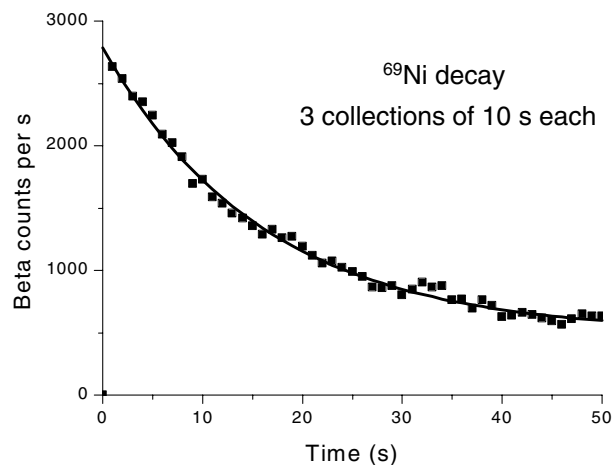


Figure 4.4.1.: Beta decay curve of $^{69}$Ni. The free fit gives a half-life of about 11.1 s. The small "bumps" at 4 s, 18 s, 33 s and 48 s are due to background from the impact of the next proton pulse.

A priori the slow average release time of nickel does not exclude that a small part of more short-lived isotopes is still released in a fast release component[9]. Therefore at the masses 74 and 76 a search was made for beta-delayed neutrons. However, no short-lived neutron activity was observed at these masses. With a calculated $P_n$ value of 4.5 % and 22 % respectively [Möl97] this corresponds

---

[8]Note that also in figure 3 of [Jok97] there is no indication for the 1298 keV line of the $^{69m}$Ni decay [Fra99].

[9]Remember that this was experienced in the case of beryllium.

to the upper limits shown in table 4.4.1. Actually the real $P_n$ values could be even higher and correspondingly the derived upper limits of the yield even lower. Franchoo et al. [Fra98a] found the strongest gamma line in the decay of $^{74}$Ni to be identical to the strongest line of the $^{73}$Ni decay. This could indicate a significant branching ratio (about 30 %) for beta-delayed neutron emission.

Table 4.4.1.: Yields of nickel isotopes from an ISOLDE UC$_x$/graphite target with resonant laser ionization. The yield $Y$ is given in atoms per $\mu$C of primary proton beam. From the second target only $^{67}$Ni was measured, giving a yield of $1.0 \cdot 10^6$ per $\mu$C.

| Isotope | $^{56}$Ni | $^{59}$Ni | $^{61}$Ni | $^{62}$Ni | $^{64}$Ni | $^{65}$Ni | $^{66}$Ni |
|---|---|---|---|---|---|---|---|
| $T_{1/2}$ | 5.9 d | $8 \cdot 10^3$ a | stable | stable | stable | 2.5 h | 55 h |
| $Y$ $(\mu C^{-1})$ | $2 \cdot 10^3$ | $6 \cdot 10^6$ | $9 \cdot 10^7$ | $1.6 \cdot 10^8$ | $1.8 \cdot 10^8$ | $7 \cdot 10^7$ | $1 \cdot 10^8$ |
| Method | Coll. | FC | FC | FC | FC | FC, Coll. | FC, Coll. |

| Isotope | $^{67}$Ni | $^{68}$Ni | $^{69g}$Ni | $^{69m}$Ni | $^{70}$Ni | $^{71}$Ni | $^{74}$Ni | $^{76}$Ni |
|---|---|---|---|---|---|---|---|---|
| $T_{1/2}$ | 21 s | 29 s | 11.2 s | 3.5 s | 6.0 s | 2.56 s | 0.9 s | 0.24 s |
| $Y$ $(\mu C^{-1})$ | $7 \cdot 10^5$ | $4 \cdot 10^5$ | $2 \cdot 10^4$ | $< 2 \cdot 10^3$ | $\approx 10^4$ | $< 2000$ | $< 200$ | $< 10$ |
| Method | Coll. | $\beta$ | $\beta$ | $\beta$ | $\beta$ | $\beta$ | $\beta$n | $\beta$n |

The half-lives shown in table 4.4.1 are from ref. [Aud97] for $^{56-67}$Ni, ref. [Fra98a, Fra98b] for $^{68-74}$Ni and ref. [Ame98] for $^{76}$Ni.

Note that the observed yields for $^{67-69}$Ni are significantly higher than those observed in a first target test at ISOLDE [Jok97]. The target and line temperature were similar, but in the first test a uranium carbide target synthesized from diphtalocyanine (see section B.4.1) had been used which contains seven times less uranium. A small isotope shift of roughly $-10$ GHz between $^{58}$Ni and $^{64}$Ni was observed in the third step transition. In the present experiment the wavelength was optimized for each isotope which could additionally give a small gain in yield.

Unfortunately no absolute cross-section measurements exist for the production of nickel isotopes from the interaction of 1 GeV protons with uranium. Interpolating the values reported in [Sil73] to 1 GeV gives a cross-section of about 1-2 mb for the cumulative production of $^{66}$Ni. Thus, the total efficiency of the target and ion source system for the release and ionization of long-lived nickel isotopes is about $6 - 12$ %. Neglecting release losses this value gives 6 % as a lower limit for the laser ionization efficiency.

**Comparison**

Figure 4.4.2 shows a comparison of experimentally obtained yields of nickel isotopes at different facilities. ISOLDE provides relatively good yields up to about $^{70}$Ni. There is a strong physics interest to extend the nickel isotopes available at ISOLDE towards the doubly magic $^{78}$Ni. However, with the thick targets tested up to now, this goal is obstructed by an extremely slow release of nickel. Presently for $^{70}$Ni and higher the signal to background ratio for nuclear spectroscopy is clearly better at LISOL. There nickel isotopes up to $^{74}$Ni have been investigated [Fra98a]. For still higher masses only yields from the GSI-FRS are reported. For the heaviest nickel isotopes the highest yields can be obtained by fragmentation of a $^{238}$U beam [Eng98]. Note that the shown values are for a relativistic fragment beam. When these fragments should be used for nuclear spectroscopy experiments, additional losses have to be taken into account: part of the nuclei will undergo nuclear reactions in the stopping process and the "beam focus" is larger than at ISOLDE or LISOL which reduces the detection efficiency due to more remote detector positions.

Table 4.4.2.: Production of nickel isotopes at different RIB facilities. At the recoil separator LOHENGRIN the 3.5 cm$^2$ large targets ($^{235}$U and $^{239}$Pu) were exposed to a neutron flux of about $5 \cdot 10^{14}$ cm$^{-2}$s$^{-1}$. With the RED magnet (see chapter 1.4) the yields could be increased by a factor of about 5. The yields of ref. [Ame98] were estimated from the number of detected particles.

| Ref. | Facility | Proj. | $E/A$ (MeV) | $\bar{I}$ (pnA) | Target | $\zeta$ (g/cm$^2$) | Comm. |
|---|---|---|---|---|---|---|---|
| RILIS UC | ISOLDE | p | 1000 | 2500 | U | 52 | RILIS |
| [Run85] | GSI-ISOL | $^{82}$Se | 11.5 | 20 | W | 0.046 | F.-E |
| [Huh97] | IGISOL | p | 25 | 3000 | U | 0.015 | |
| [Fra98a] | LISOL | p | 30 | 6000 | U | 0.03 | RILIS |
| [Ber91] | LOHENGRIN | $n_{th}$ | – | – | $^{235}$U, $^{239}$Pu | 0.00015 | |
| [Web92] | GSI-FRS | $^{86}$Kr | 500 | 0.0017 | Be | 2 | |
| [Ame98] | GSI-FRS | $^{86}$Kr | 500 | $\leq$0.05 | Be | 2 | est. |
| [Eng98] | GSI-FRS | $^{238}$U | 750 | 0.0033 | Be | 1 | |
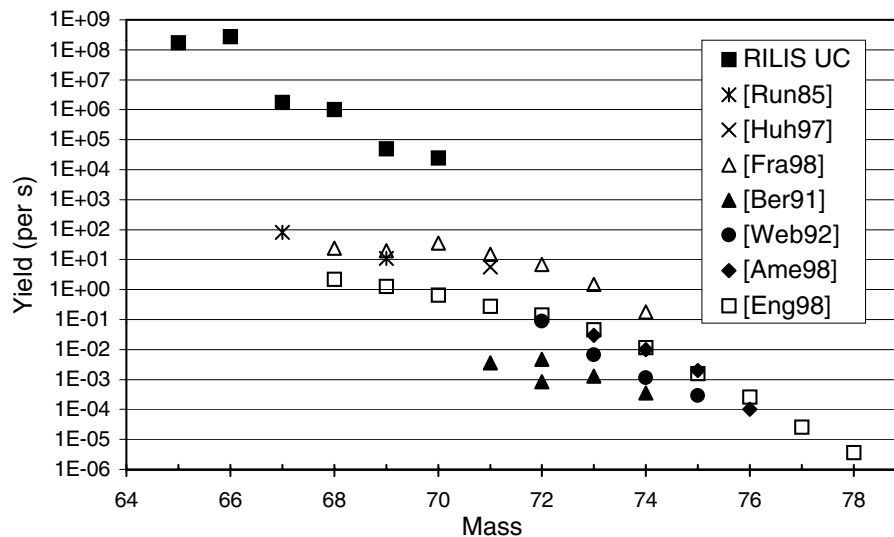


Figure 4.4.2.: Comparison of nickel yields, see table 4.4.2 for experimental details of each curve. Upper limits were omitted.

**Prospects**

It is not easy to find target materials which promise a much faster release of nickel. Kirchner measured for nickel a three orders of magnitude faster diffusion in tantalum compared with graphite [Kir92a, Kir97]. However, in a first test at ISOLDE [Jok97] also a tantalum foil target showed a very slow release and the yields were not better than from a UC$_x$/graphite target.

From the published diffusion data at lower temperatures it is not expected that nickel diffuses particularly fast in a bulk oxide matrix, but it would still be interesting to test the release from e.g. a zirconium oxide fiber target[10]. NiO dissociates around 1950 °C, thus any nickel oxide released from the target would be mostly dissociated in the hot ionizer cavity and also be available for resonant laser ionization.

---

[10]Heavy nickel isotopes are poorly produced in spallation of zirconium, but the ZrO$_2$ target can serve for a release test before building a ThO$_2$ fiber target (see section B.3).

The desorption enthalpies estimated from the Eichler systematics give for nickel a particularly long desorption time from tantalum surfaces (about 60 ms at 2200 °C). Niobium is no alternative since it cannot be heated high enough. However, for tungsten and rhenium at the same temperature the desorption time is calculated to be 50 and 100 times shorter respectively. Thus, a coating of the target container with a W or Re layer could possibly reduce the effusion time. Also the use of a small tungsten foil target in a tungsten target container should be tested for the release of nickel. This combination would moreover allow to reach the highest possible target temperatures.

## 4.5.   Copper yields

Beams of short-lived copper isotopes are of particular interest for the study of the nuclear structure close to the $Z = 28$ shell closure.

The neutron-deficient isotope $^{56}$Cu decays into the doubly-magic $^{56}$Ni. Due to the high $Q_{\mathrm{EC}}$-value (15.3 MeV) there is a large energy window for population of excited levels.

With the difficulties to separate short-lived nickel (and presumably also iron and cobalt) isotopes (see preceding section), the heavy copper isotopes allow presently the closest approach to the doubly-magic $^{78}$Ni at a thick target ISOL facility. Information on the decay properties of very neutron-rich nuclei with magic neutron number is also important to put constraints on the astrophysical r-process conditions (see e.g. ref. [Kra87, Kra99]). The heaviest copper isotopes (up to $^{79}$Cu) had been studied at ISOLDE SC with a UC$_x$/graphite cloth target [Kra91]. However, when ionized with a hot plasma source the copper beams suffer from a strong background of isobars (mainly zinc and gallium for neutron-rich copper isotopes and manganese for neutron-deficient ones). The ionization with the RILIS promises a significant amelioration of the element selectivity.

### Nb foil target

A first test for production of neutron-deficient copper isotopes was made with a standard niobium foil target. This target had given a sufficient yield for spectroscopy of the nearby nuclide $^{58}$Zn [Jok98]. However, the release of copper showed to be very slow. With the target at 2000 °C and the tungsten surface ionizer at about 2300 °C the release half-time $t_{50}$ was above 100 s. This caused a significant suppression of short-lived radio-isotopes. The obtained yields are shown in figures 4.5.1 and 4.5.2.

### Ta foil target

The next test was performed with a tantalum foil RIST target. Ta foil targets can be operated at the highest temperatures among all standard ISOLDE targets and the RIST target [Ben97] is specially designed for a fast effusion[11]. Unfortunately even at a temperature above 2200 °C the release remained slow ($t_{50} \sim 90$ s) and the yields were even lower compared with the Nb foil target (see figures 4.5.1 and 4.5.2). Note that a slow diffusion of copper in tantalum had also been measured at Oak Ridge [Alt96]: $D = 1.5 \cdot 10^{-10}$ cm$^2$/s, however at much lower temperatures ($1650 - 1700$ °C).

### ZrO$_2$ fiber target

Since the metal foil targets did not give satisfactory results, a target material with completely different structure was tested: zirconium oxide. To assure a fast effusion and to reduce sintering

---

[11]This model consisted of 100 $\mu$m thick tantalum foils, thus minimizing the effusion time at the expense of a longer diffusion time.

problems a fiber material was used (see appendix B.3). Indeed the release was much faster and the yields of short-lived isotopes were significantly improved. The release can be fitted with a single decay component: $\tau_r = 30$ ms and $\tau_f = 0.7$ s, i.e. there is no indication for a slow release component. The first test had been performed at the HRS with a vacuum chamber window from standard glass. The transmission of the UV laser beams was significantly reduced, thus reducing the RILIS efficiency. Unfortunately also the second test had to be performed at the HRS. An imperfect ion beam trajectory (with a significant tilt between both magnets) caused a strongly mass-dependent transmission to the nuclear spectroscopy set-up which changed by one order of magnitude and more when switching the mass! Thus, only lower limits could be derived from the latter measurement. Table 4.5.1 shows the yields which were measured in the first test and scaled by a factor 14 to account for the increased laser ionization efficiency in normal operation (using a quartz window). This scaling factor was confirmed by the measurement of the isotopes $^{62}$Cu and $^{66}$Cu at the monitoring tape station. In the gamma spectra taken at mass 56 only few counts were observed at 1225 keV and 2701 keV (see ref. [Ram98a] for the most intense gamma lines in the $^{56}$Cu decay). However, the peaks were not unambiguously identified and it is safer to use this intensity only as an upper limit of the $^{56}$Cu yield.

Table 4.5.1.: Yields of copper isotopes from a 6 g/cm$^2$ zirconia fiber target with resonant laser ionization in a standard tungsten cavity. The yield $Y$ is given in atoms per $\mu$C of primary proton beam.

| Isotope | $^{56}$Cu | $^{57}$Cu | $^{58}$Cu | $^{59}$Cu | $^{60}$Cu | $^{61}$Cu | $^{62}$Cu |
|---|---|---|---|---|---|---|---|
| $T_{1/2}$ | 78 ms | 199 ms | 3.2 s | 82 s | 23 min | 3.4 h | 9.7 min |
| $Y$ $(\mu C^{-1})$ | $\leq 35$ | $\approx 3000$ | $\approx 3 \cdot 10^5$ | $7 \cdot 10^6$ | $5 \cdot 10^7$ | $1.2 \cdot 10^8$ | $9 \cdot 10^8$ |
| Method | $\gamma$ | $\gamma$ | $\beta$ | $\beta$ | $\beta$ | $\beta$ | $\beta$ |

| Isotope | $^{66}$Cu | $^{68g}$Cu | $^{68m}$Cu | $^{69}$Cu | $^{70g}$Cu | $^{70m}$Cu | $^{71}$Cu |
|---|---|---|---|---|---|---|---|
| $T_{1/2}$ | 5.1 min | 30 s | 3.8 min | 3 min | 5 s | 42 s | 19.5 s |
| $Y$ $(\mu C^{-1})$ | $5 \cdot 10^7$ | $6 \cdot 10^5$ | $1.7 \cdot 10^6$ | $8 \cdot 10^5$ | $7 \cdot 10^3$ | $10^5$ | $3 \cdot 10^4$ |
| Method | $\beta$ | $\beta$ | $\beta$ | $\beta$ | $\beta$ | $\beta$ | $\beta$ |

## UC$_x$/graphite target

A standard UC$_x$/graphite target with Nb ionizer was used for the production of neutron-rich copper beams. The release is faster than from the metal foil targets, but considerably slower compared with the ZrO$_2$ target. With the target at a temperature of 2100 °C and the niobium cavity at 1900 °C the release can be described with a single decay component: $\tau_r = 1.5$ s [12] and $\tau_f = 15$ s. The neutron-rich copper isotopes were studied by $\beta\gamma$, $\gamma\gamma$ and $\beta$n spectroscopy. Even without any additional gating the gamma spectra up to mass 73 were absolutely dominated by gamma-lines from the copper decay. The impressive intensity of these neutron-rich copper beams can be demonstrated with two examples:

$^{67}$**Cu:** A sample of $^{67}$Cu was collected for an off-line measurement of the magnetic moment in Oxford (ISOLDE experiment IS358 [IS358]). The collection took less than half an hour, but the following procedure of shipping the sample and passing the customs bureaucracy took longer than expected. Additional delays occured when the experimental set-up (dilution

---

[12]Note that with another UC$_x$/graphite target at equal temperature a much faster rise was observed ($\tau_r < 50$ ms) while the fall time was identical.

Table 4.5.2.: Yields of copper isotopes from a $\approx 50$ g/cm$^2$ UC$_x$/graphite target with resonant laser ionization in a standard niobium cavity. The yield $Y$ is given in atoms per $\mu$C of primary proton beam.

| Isotope | $^{62}$Cu | $^{64}$Cu | $^{66}$Cu | $^{67}$Cu | $^{68g}$Cu | $^{68m}$Cu | $^{69}$Cu | $^{70g}$Cu | $^{70m}$Cu |
|---|---|---|---|---|---|---|---|---|---|
| $T_{1/2}$ | 9.7 min | 12.7 h | 5.1 min | 61.9 h | 30 s | 3.8 min | 3 min | 5 s | 42 s |
| $Y$ ($\mu$C$^{-1}$) | $\approx 3 \cdot 10^7$ | $\approx 2 \cdot 10^8$ | $4 \cdot 10^8$ | $3.5 \cdot 10^8$ | $8 \cdot 10^7$ | $3 \cdot 10^8$ | $1.8 \cdot 10^8$ | $7 \cdot 10^6$ | $9 \cdot 10^7$ |
| Method | $\beta$ | FC | $\beta$ | FC | $\beta$ | $\beta$ | $\beta$ | $\beta$ | $\beta$ |

| Isotope | $^{71}$Cu | $^{72}$Cu | $^{73}$Cu | $^{74}$Cu | $^{75}$Cu | $^{76}$Cu | $^{77}$Cu | $^{78}$Cu | $^{79}$Cu |
|---|---|---|---|---|---|---|---|---|---|
| $T_{1/2}$ | 19.5 s | 6.6 s | 4.2 s | (1.6 s) | 1.22 s | 0.64 s | 0.47 s | 0.34 s | 0.19 s |
| $Y$ ($\mu$C$^{-1}$) | $5 \cdot 10^7$ | $1.3 \cdot 10^7$ | $4 \cdot 10^6$ | $6 \cdot 10^5$ | $1.5 \cdot 10^5$ | $2 \cdot 10^4$ | $\approx 2000$ | $\approx 200$ | $< 1$ |
| Method | $\beta$ | $\beta$ | $\beta$ | $\beta$ | $\beta$ | $\beta$n | $\beta$n | $\beta$n | $\beta$n |

refridgerator) had to be warmed up again for repair work. The real experiment could not be started for three weeks, but finally a resonance signal was found. Even ten half-lives ($T_{1/2} = 61.9$ h) after the collection the copper activity was still high enough to determine the magnetic moment of $^{67}$Cu with good statistical accuracy [Rikov]!

$^{73}$**Cu:** Nuclear spectroscopy was recently performed with a $^{73}$Cu beam at MSU [Huh98]. After one day of data taking [Manti] about a dozen coincidences had been observed between the 450 keV and the 674 keV line (see figure 4 in [Huh98]). Even less coincidences were seen between the 450 keV and the 1559 keV line. With a similar detection set-up at ISOLDE the same coincidence windows showed about 30 times better statistics after only 20 min of data taking!

A large amount of gamma decay data was taken for the heavy copper isotopes ($A \geq 70$). It is presently under analysis [Roosb, Krugl]. Starting at $A = 74$ the isobaric gallium background gets remarkable and for $A \geq 77$ it is overwhelming. Also neutron-deficient rubidium isotopes show up as background. For instance the yield of $^{80}$Rb was about $10^8$ per $\mu$C from this target. With detection of beta-delayed neutrons a "clean" copper signal is observed till mass 78, but for higher masses the $\beta$n background from $^{79+x}$Ga overlays the copper signal (see section 4.6).

Unfortunately no target with a thin niobium cavity (compare section 3.4) was available for on-line use. Therefore a "thick" niobium cavity had to be used which gave a rather broad width of the laser ion pulses and did not allow to use the beam chopper for a major suppression of the surface ionized background. Only a slight improvement of the copper to gallium ratio was obtained by reduction of the ionizer temperature.

The yields up to $^{76}$Cu shown in table 4.5.2 were determined from beta counting with the monitoring tape station and the $\beta$n set-up. Those of the heavier copper isotopes were deduced from the detected neutron activity. For $^{77}$Cu and $^{78}$Cu an arbitrary P$_n$ value of 20 % was assumed which is in line with theoretical predictions [Pfe99]. For $^{79}$Cu no short-lived activity was observed besides the gallium background. An upper limit for the $^{79}$Cu yield was derived by using the measured values from [Kra91]: $T_{1/2} = 188$ ms and $P_n = 55$ %.

All yields given in table 4.5.2 were measured using a broad bandwidth laser for both excitation steps. For the hyperfine scan (see section 3.5.2) a small bandwidth laser (1.2 GHz) was used for the first excitation step. This reduced the yield by about a factor of three.

**Comparison**

Figure 4.5.1 shows a comparison of experimentally obtained yields of light copper isotopes at different facilities. The experimental details are given in table 4.5.3.
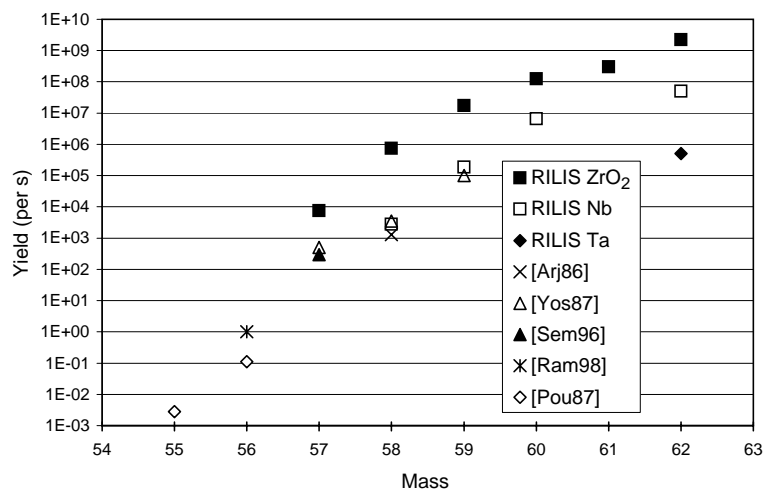


Figure 4.5.1.: Comparison of yields of neutron-deficient copper isotopes, see table 4.5.3 for experimental details of each curve. Upper limits were omitted.

Table 4.5.3.: Production of neutron-deficient copper isotopes at different RIB facilities.

| Ref. | Facility | Proj. | $E/A$ (MeV) | $\bar{I}$ (pnA) | Target | $\zeta$ (g/cm$^2$) | Comm. |
|---|---|---|---|---|---|---|---|
| RILIS ZrO$_2$ | ISOLDE PSB | p | 1000 | 2500 | ZrO$_2$ | 6 | RILIS |
| RILIS Nb | ISOLDE PSB | p | 1000 | 2500 | Nb | 48 | RILIS |
| RILIS Ta | ISOLDE PSB | p | 1000 | 2500 | Ta | 114 | RILIS |
| ZrO$_2$ SC | ISOLDE SC | p | 600 | 2500 | ZrO$_2$ | 6.3 | MK5 |
| Nb SC | ISOLDE SC | p | 600 | 2500 | Nb | 47 | MK5 |
| Ta SC | ISOLDE SC | p | 600 | 2500 | Ta | 112 | MK5 |
| [Ärj86] | Jyväskylä | p | 16 | 1000 | $^{58}$Ni | | IGISOL |
| [Yos87] | Tohoku | p, $^3$He | 16-33 | 7000 | $^{58}$Ni | 0.0027 | IGISOL |
| [Sem96] | Texas A&M | $^{58}$Ni | 30 | 0.3 | H$_2$ | 0.028 | |
| [Ram98a] | GSI-ISOL | $^{32}$S | 4.6 | 50 | Si | 0.002 | F.-B2-C |
| [Pou87] | LISE, GANIL | $^{58}$Ni | 55 | 2 | Ni | 0.05 | |

It is obvious that for light copper isotopes the ISOLDE yields (with a ZrO$_2$ target) exceed those of all other facilities down to $^{57}$Cu. It is expected that this remains valid also for $^{56}$Cu, but up to now nuclear spectroscopy with a $^{56}$Cu beam was only performed at GSI ISOL [Ram98a]. The most neutron-deficient copper isotope $^{55}$Cu was only detected at a fragment separator [Pou87]. It is probably too short-lived to be separated at an ISOL facility.

For all neutron-rich copper isotopes the ISOLDE yields exceed those of other facilities by many orders of magnitude. An extension of the nuclear spectroscopy towards the most neutron-rich copper isotopes is presently less limited by the yields than by the missing beam purity, i.e. the immense isobaric background from gallium and rubidium.

The ISOLDE SC yields were measured with a 9.6 g/cm$^2$ UC$_x$/graphite cloth target and a hot plasma source [SCyie]. The quoted $^{79}$Cu yield was roughly estimated from figure 1 in ref. [Kra91]
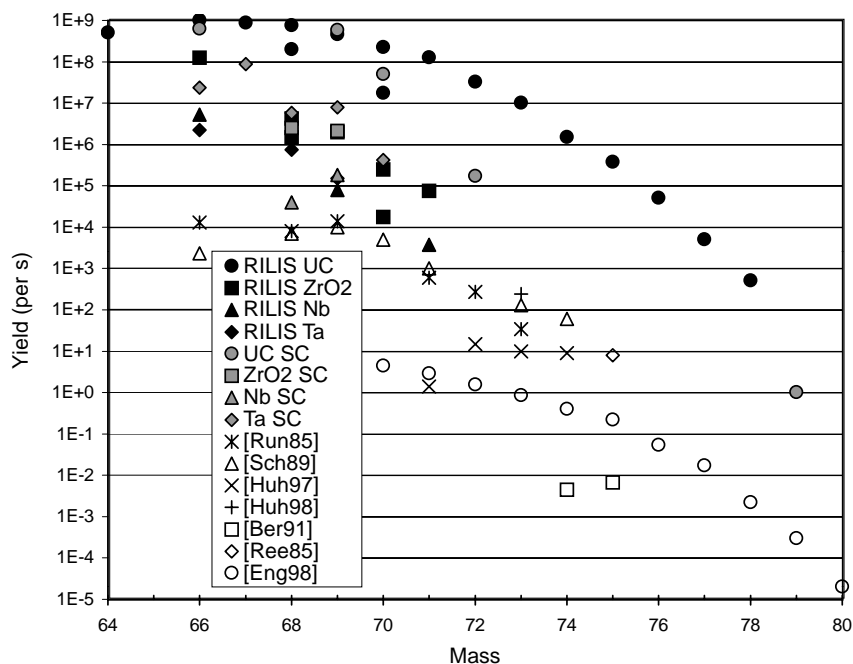
Figure 4.5.2.: Comparison of yields of neutron-rich copper isotopes, see table 4.5.4 for experimental details of each curve. Upper limits were omitted.

Table 4.5.4.: Production of neutron-rich copper isotopes at different RIB facilities. At the recoil separator LOHENGRIN the 3.5 cm$^2$ large targets were exposed to a neutron flux of about $5 \cdot 10^{14}$ cm$^{-2}$s$^{-1}$. With the RED magnet (see chapter 1.4) the yields could be increased by a factor of about 5.

| Ref. | Facility | Proj. | $E/A$ (MeV) | $\bar{I}$ (pnA) | Target | $\zeta$ (g/cm$^2$) | Comm. |
|---|---|---|---|---|---|---|---|
| RILIS UC | ISOLDE PSB | p | 1000 | 2500 | $UC_x$/graphite | 50 | RILIS |
| RILIS ZrO$_2$ | ISOLDE PSB | p | 1000 | 2500 | ZrO$_2$ | 6 | RILIS |
| RILIS Nb | ISOLDE PSB | p | 1000 | 2500 | Nb | 48 | RILIS |
| RILIS Ta | ISOLDE PSB | p | 1000 | 2500 | Ta | 114 | RILIS |
| UC SC | ISOLDE SC | p | 600 | 2500 | $UC_x$/graphite | $\approx$10 | MK5 |
| ZrO$_2$ SC | ISOLDE SC | p | 600 | 2500 | ZrO$_2$ | 6.3 | MK5 |
| Nb SC | ISOLDE SC | p | 600 | 2500 | Nb | 47 | MK5 |
| Ta SC | ISOLDE SC | p | 600 | 2500 | Ta | 112 | MK5 |
| [Run85] | GSI-ISOL | $^{82}$Se | 11.5 | 20 | W | 0.046 | F.-E |
| [SO89] | GSI-ISOL | $^{20}$Ne | 4.7-10.9 | 160 | UC/UC$_2$ | 0.02 | F.-H |
| [Huh97] | Jyväskylä | p | 25 | 3000 | $UC_x$/graphite | 0.015 | IGISOL |
| [Huh98] | A1200, MSU | $^{76}$Ge | 70 | 15 | $^9$Be | 0.2 | |
| [Ber91] | LOHENGRIN | n$_{th}$ | – | – | $^{235}$U | 0.00015 | |
| [Ree85] | TRISTAN | n$_{th}$ | – | – | $^{235}$U | 4 g | F. |
| [Eng98] | GSI-FRS | $^{238}$U | 750 | 0.0033 | Be | 1 | |

and given for a 13 g/cm$^2$ UC$_x$/graphite cloth target with a 2.2 $\mu$A beam. Note that in the present experiment many parameters had been changed: the target matrix and target thickness,

the proton beam energy, the time structure of the proton beam and finally the ion source. Therefore it is difficult to determine which parameter caused the failure to observe $^{79}$Cu in this experiment.

Neutron-rich copper isotopes were also produced at the GSI ISOL facility by multi-nucleon transfer reactions between a $^{76}$Ge beam and a tungsten target [Run83, Bos88], but the yields are similar to those obtained with a $^{82}$Se beam [Run85] which are shown in figure 4.5.2.

The yields of neutron-rich copper isotopes from thermal neutron induced fission drop only by a factor four from $^{75}$Cu to $^{77}$Cu [Sid89], but the yield of isobaric background increases considerably. Therefore no half-lives could be measured for $^{76}$Cu and $^{77}$Cu at LOHENGRIN. Nuclear spectroscopy of neutron-rich copper isotopes $^{74-78}$Cu had been performed at the reactor-based RIB facilities OSIRIS [Lun88] and TRISTAN [Win89, Win90], but no evaluated yields were given in these publications.

**Prospects**

The ZrO$_2$ target provides a fast release and offers good yields of neutron-deficient copper isotopes. This opens the way for many new experiments (nuclear spectroscopy, measurement of magnetic moments, etc.). No experimental yield can be quoted for $^{56}$Cu, but from an extrapolation of the measured yields of the heavier isotopes it could reach some ten ions per second.

The UC$_x$/graphite target gives sufficient yields on the neutron-rich side up to about $^{76}$Cu. A further extension towards more neutron-rich nuclei is presently hampered by an unfavorable ratio of copper to isobaric gallium background. This is comparable to the situation of heavy silver and cadmium isotopes which suffer from an indium background (see sections 4.7 and 4.8). The effect of this background can be seen with the following comparison: The yield of $^{77}$Cu is one order of magnitude higher than that of $^{66}$Mn (see section 4.3). While the latter was easily observed by simple beta counting with the monitoring tape station, even with a dedicated set-up no beta decay signal could be clearly attributed to the former.

The further development of a selective RILIS cavity (see section 3.4) is needed for an improvement of the signal to background ratio. Another gain can be achieved by reducing the decay losses of the short-lived copper isotopes in the target. At Oak Ridge a quite rapid diffusion of copper was observed in graphite $D = 7 \cdot 10^{-7}$ cm$^2$/s, already at $1650 - 1700$ °C. Therefore it is not obvious why the release from a 2050 °C hot UC$_x$/graphite target is not faster. Possibly the delay is caused by a slow desorption from the niobium cavity. However, the Eichler systematics (see B.2.5) gives a desorption time of about 0.1 ms for both, a Nb surface at 1800 °C and a W surface at 2150 °C.

Due to the good experiences with the ZrO$_2$ fiber target a ThO$_2$ target with comparable structure is proposed for very neutron-rich copper isotopes (see section B.3). If the release characteristic is comparable to that of the ZrO$_2$ matrix this could immediately improve the yield of $^{79}$Cu and thus the signal to background ratio by up to two orders of magnitude! Figure 4.5.3 shows the release efficiency $Y(T_{1/2})$ (see appendix B.2) which was derived from the measured release profiles of both targets.

## 4.6.    Gallium yields

Gallium is included in the NuPECC list of "key elements" for the next generation RIB facilities. On the neutron-deficient side $^{62}$Ga is one of the nuclides decaying by a superallowed $0^+ \rightarrow 0^+$ Fermi transition. A high yield of this isotope would help to extend the precision measurements of $G_V$ beyond the presently heaviest isotope of this type: $^{54g}$Co.

On the neutron-rich side gallium is one of the lightest elements which is produced with high yields at a reactor-based RIB facility. It is therefore of interest for experiments with post-accelerated beams, e.g. at the MAFF facility [MAFF].
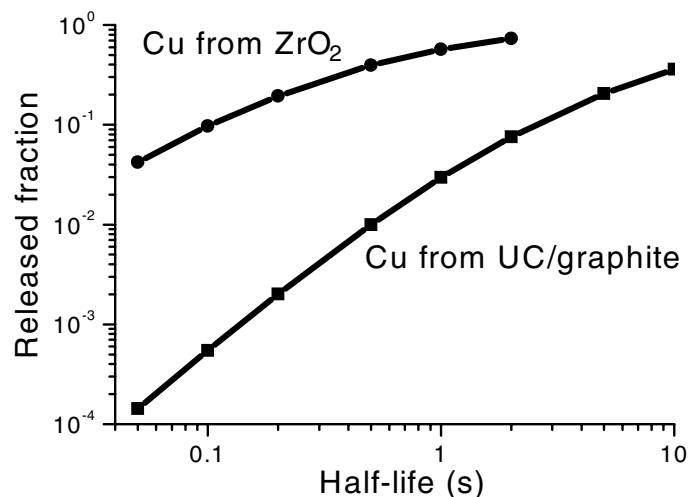
Figure 4.5.3.: For short-lived nuclei ($T_{1/2} \ll 10$ s) the $ZrO_2$ target provides a significantly higher release efficiency compared with a $UC_x$/graphite target.

**Neutron-deficient gallium isotopes**

Neutron-deficient gallium isotopes are best produced in spallation of a nearby target nucleus. However, similar to copper, also gallium is only slowly released from a niobium foil target. With the target at about 2050 °C and a tungsten ionizer at 2400 °C a release time of $t_{50} \geq 100$ s was found. With a 50 g/cm$^2$ thick target yields of $1.2 \cdot 10^7$ and $1.7 \cdot 10^7$ per $\mu$C were obtained for $^{68}$Ga and $^{70}$Ga respectively, but short-lived gallium isotopes suffer significantly from decay losses. A niobium foil target is therefore not suitable for the most short-lived gallium isotopes.

Also here the zirconium oxide target shows an improvement. The release curve was fitted with (see equation (2.4.2)) $\tau_r = 0.3$ s, $\tau_f = 1$ s. $\tau_s = 50$ s and $\alpha = 0.9$, i.e. the release is much faster compared with the niobium target. Taking into account the smaller target thickness of the $ZrO_2$ target (about 6 g/cm$^2$), already the long-lived $^{70}$Ga shows a higher yield normalized to equal target thickness. All other isotopes from $^{62}$Ga up to $^{74}$Ga show significantly higher yields from the $ZrO_2$ fiber target (see table 4.6.1). All these yields are also higher than reported from the SC for a Ta foil target or a molten Ge target [Klu86], both with a hot plasma source.

Table 4.6.1.: Yields of surface ionized gallium isotopes from a 6 g/cm$^2$ $ZrO_2$ target at about 1850 °C. The yield $Y$ is given in atoms per $\mu$C of primary proton beam.

| Isotope | $^{62}$Ga | $^{63}$Ga | $^{64}$Ga | $^{65}$Ga | $^{66}$Ga |
|---|---|---|---|---|---|
| $T_{1/2}$ | 116 ms | 31 s | 2.6 min | 15 min | 9.4 h |
| $Y$ $(\mu C^{-1})$ | 200 | $2 \cdot 10^5$ | $3.5 \cdot 10^6$ | $2 \cdot 10^7$ | $5 \cdot 10^7$ |
| Isotope | $^{67}$Ga | $^{68}$Ga | $^{70}$Ga | $^{73}$Ga | $^{74}$Ga |
| $T_{1/2}$ | 78 h | 68 min | 21 min | 4.9 h | 8 min |
| $Y$ $(\mu C^{-1})$ | $5 \cdot 10^7$ | $8 \cdot 10^7$ | $1.2 \cdot 10^7$ | $6 \cdot 10^5$ | $1 \cdot 10^5$ |

All yields were determined by beta counting with the monitoring tape station. Only the yield of $^{62}$Ga was derived from high-energy betas ($> 4$ MeV) detected in the beta telescope of the ISOLDE experiment P94 [Oinon]. In the same test no indication for $^{61}$Ga was observed.

**Neutron-rich gallium isotopes**

Neutron-rich gallium isotopes are known to be well produced and released from $UC_x$/graphite targets. The presently heaviest gallium isotope with measured half-life, [84]Ga, was discovered at the ISOLDE SC [Kra91]. On the other hand the nuclides from [72]Ga to [81]Ga play also the negative role of an omnipresent background in experiments aiming for the heaviest nickel, copper and zinc isotopes. Even when ionizing the latter with the element selective RILIS additional measures have to be taken to suppress this background.

Gallium yields were measured from a standard $UC_x$/graphite target with niobium surface ionizer, both at around 2000 °C. They are plotted in figure 4.6.1. The release can be fitted with (see formula 2.4.2): $\tau_r = 0.1$ s, $\tau_f = 1.5$ s. $\tau_s = 4.5$ s and $\alpha = 0.8$. Note that the quoted yields were neither reduced by additional measures (beam chopper, etc.) nor optimized for a maximum yield of gallium (tungsten surface ionizer). Therefore they are mainly of interest for a comparison with the yields of heavy nickel and copper isotopes presented before. A comparison with yields from other facilities was omitted. Up to mass 79 gallium is the dominating beta activity and can be measured with the monitoring tape station. The [80]Ga yield was determined from its beta-delayed neutron activity. Still heavier gallium isotopes ($A \geq 81$) were not measured to avoid a contamination of the tape station with the strong isobaric rubidium background.

**Comparison**
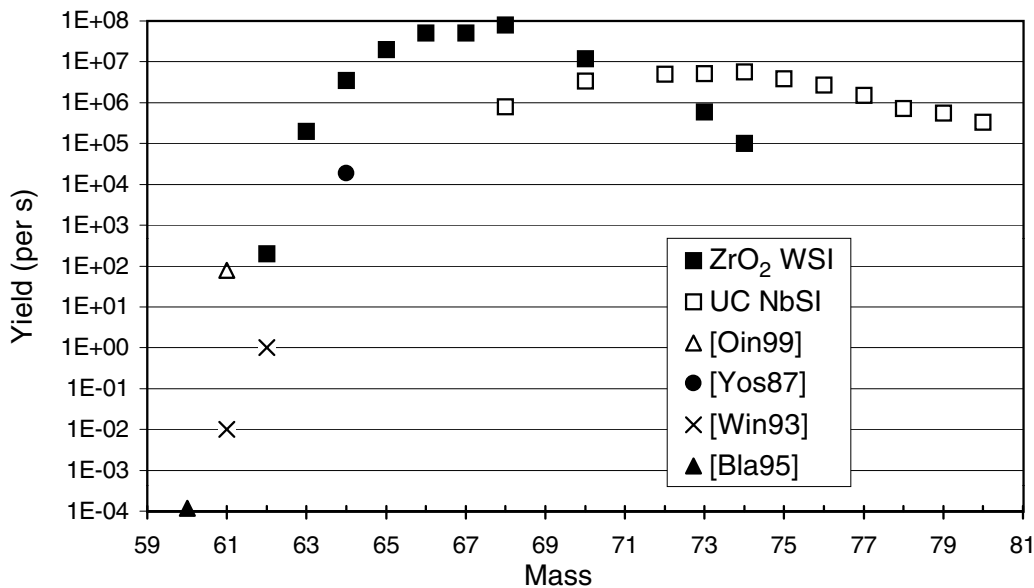


Figure 4.6.1.: Comparison of gallium yields, see table 4.6.2 for experimental details of each curve.

Figure 4.6.1 shows that the ISOLDE yields from a $ZrO_2$ target are even competitive for the short-lived [62]Ga ($T_{1/2} = 116$ ms), especially if an additional increase could be obtained by further raising the target temperature. Also the GSI ISOL can give comparable or slightly higher yields for [62]Ga, but the fragmentation facilities are still more than one order of magnitude below.

Table 4.6.2.: Production of gallium isotopes at different RIB facilities.

| Ref. | Facility | Proj. | $E/A$ (MeV) | $\bar{I}$ (pnA) | Target | $\zeta$ (g/cm$^2$) |
|---|---|---|---|---|---|---|
| ZrO$_2$ WSI | ISOLDE | p | 1000 | 2500 | ZrO$_2$ | 6 |
| UC NbSI | ISOLDE | p | 1000 | 2500 | UC | $\approx 50$ |
| [Oin99] | GSI-ISOL | $^{36}$Ar | 3.4 | 80 | Si | 0.0019 |
| [Yos87] | IGISOL, Tohoku | p | 15 | 7000 | Zn | 0.0034 |
| [Win93] | A1200, MSU | $^{78}$Kr | 75 | | Ni | 0.105 |
| [Bla95] | SISSI/LISE, GANIL | $^{78}$Kr | 73 | 30 | Ni | 0.11 |

## 4.7.   Silver yields

**UC$_x$/graphite target**

After a series of refractory elements (from Zr to Pd), which are difficult to separate at a thick target ISOL facility, silver is the first with good release characteristics. For example it is released very rapidly from a graphite matrix [Kir92a]. Neutron-rich silver isotopes are produced abundantly in high-energy-proton induced fission of uranium. However, ionization with an unselective plasma ion source will cause large beam contaminations with cadmium and many other isobars. It was just the wish to suppress this background which triggered the development of the ISOLDE RILIS [Mis93]. In the following years the silver over background ratio was continuously improved. This allowed to find new silver isotopes [Fed95a, Jad96a] and to perform detailed nuclear spectroscopy [Kau96]. Ref. [Jad97] describes the necessary developments of the RILIS in detail. Despite the use of the selective detection of beta-delayed neutrons, the strong indium background still hampered the determination of the half-life of the r-process waiting-point nucleus $^{129}$Ag. Moreover it was suspected that a strong hyperfine splitting of the latter might have reduced the laser ionization efficiency [Jad97].

Therefore in 1997 a combination of several techniques was used in another quest for $^{129}$Ag:

- A niobium cavity helped to reduce the surface ionization efficiency of indium.

- The beam chopper was set to about 25 $\mu$s width, suppressing the dc indium background and improving the Ag/In ratio by a factor of two to three.

- The tape cycle was set to transport the remaining indium activity away after every proton pulse.

- The laser frequency was tuned to the position of the expected hyperfine splitting of a $\pi g_{9/2}$ isomer. Before the frequency had been calibrated by studying the hyperfine splitting of silver isomers from $^{107}$Ag up to $^{127}$Ag [Kau98, Seb98].

Finally the long-searched isotope was found and the half-life could be determined to about 46 ms [Kra98b]. With an assumed $P_n$ value of 12 % [Möl97] the yield can be estimated to the order of some ions per $\mu$C of primary protons. Note that the number of collected indium atoms was still about 200 times larger!

Table 4.7.1 shows a selection of typical silver yields from a UC$_x$/graphite target with niobium line, both kept at 2000 °C. A typical release profile from a UC$_x$/graphite target can be fitted with (see formula (2.4.2)): $\tau_r = 40$ ms, $\tau_f = 0.4$ s, $\tau_s = 12$ s, $\alpha = 0.995$, i.e. nearly all silver is released in a single fast peak. The yield curve peaks around $^{111}$Ag and then drops towards heavier masses.

Table 4.7.1.: Yields of laser ionized silver isotopes from $\approx 50$ g/cm$^2$ UC$_x$/graphite targets with niobium line. The yield $Y$ is given in atoms per $\mu$C of primary proton beam. The yields of different isotopes were measured from different targets which introduces some additional fluctuations.

| Isotope | $^{101g+m}$Ag | $^{103g+m}$Ag | $^{105g+m}$Ag | $^{106m}$Ag | $^{109m}$Ag | $^{111g+m}$Ag | $^{112}$Ag |
|---|---|---|---|---|---|---|---|
| $T_{1/2}$ | 11 min | 1.1 h | 41 d | 8.3 d | 40 s | 7.5 d | 3.1 h |
| $Y$ $(\mu C^{-1})$ | $2 \cdot 10^5$ | $1.6 \cdot 10^6$ | $7 \cdot 10^7$ | $7 \cdot 10^7$ | $6 \cdot 10^8$ | $4 \cdot 10^9$ | $2.3 \cdot 10^9$ |
| Method | Coll. | Coll. | Coll., FC | Coll. | $\beta^{(13}$ | Coll. | Coll. |

| Isotope | $^{113g}$Ag | $^{114}$Ag | $^{115g}$Ag | $^{117g+m}$Ag | $^{121}$Ag | $^{129}$Ag |
|---|---|---|---|---|---|---|
| $T_{1/2}$ | 5.4 h | 4.5 s | 20 min | 73 s, 5.3 s | 0.78 s | 46 ms |
| $Y$ $(\mu C^{-1})$ | $2 \cdot 10^9$ | $1 \cdot 10^9$ | $1.8 \cdot 10^8$ | $7 \cdot 10^8$ | $3 \cdot 10^7$ | $\approx 1$ |
| Method | Coll. | $\beta$, FC | Coll. | Coll., FC | $\beta$ | $\beta$n |

Indium and cesium are the principal beam contaminants, but occasionally also other impurities are found. For example on mass 111 $^{92}$Sr$^{19}$F$^+$ occured with a yield of about $10^6$ per $\mu$C [Burch].

"Neutron yields" were already reported in ref. [Fed95a, Jad96b], but the complete evaluation of the $\beta$n and $\beta\gamma$ decay of the heavy silver isotopes is still in work [Kauts]. These results should also give a better overview of the yields of neutron-rich silver nuclei up to $^{129}$Ag.

### Comment on neutron-deficient silver isotopes

Yields of neutron-deficient silver isotopes down to $^{99}$Ag were reported from ISOLDE SC [SCyie]. It would also be possible to produce and separate silver beams from a LaC$_x$/graphite target (see next sections). The release characteristics should be similar to that of a UC$_x$/graphite target. Just as the heavy silver isotopes, also the neutron-deficient ones could be ionized with the RILIS. However, compared with the lightest cadmium beams (see next section) the contamination problem with rubidium will get even more serious. Going towards the most neutron-deficient silver isotopes (around $^{94}$Ag), the production rate of the isobaric rubidium will increase by about two orders of magnitude in comparison with $^{97}$Rb. Moreover, the lifetimes of the rubidium isotopes get longer and a suppression with the beam gate will be even less efficient. Therefore the very light silver nuclei will remain rather a domain of ISOL facilities using fusion-evaporation reactions and of fragment separators. However, for heavier masses (around $^{96-102}$Ag) an ISOLDE LaC$_x$/graphite target combined with the RILIS remains very interesting, in particular also for atomic spectroscopy and isomer separation.

## 4.8.   Cadmium yields

Neutron-deficient cadmium nuclides were one of the first beams separated at ISOLDE [Han69]. Concerning beam intensity and purity, these beams from a molten tin target remained always among the showpieces of ISOLDE. With a target thickness up to 130 g/cm$^2$ and practically complete condensation of non-cadmium activities in a temperature controlled transfer line the beam quality of cadmium isotopes with $T_{1/2} \gtrsim$ minutes can hardly be improved further. A drawback of the molten targets is their rather slow release behavior: $t_{50} \gtrsim 100$ s [Let97b]. Thus, considerable decay losses occur for the isotopes below $^{102}$Cd.

---

[13]Obviously $^{109m}$Ag does not emit betas. Instead the conversion electrons of the highly converted (E3) IT decay are detected.

A significant increase of the release speed can be obtained with a target providing shorter diffusion paths. A mixture of tin and graphite powder kept at 1000 °C was used to produce the neutron-deficient isotopes $^{98-105}$Cd with a $^3$He beam [Hag92b]. Due to the smaller target thickness (only 20 g/cm$^2$ tin), for the long-lived isotopes a reduced yield was observed in comparison with the standard molten tin targets. Going to more short-lived nuclei the faster release ($t_{50} \approx 30$ s) compensated this handicap [And91]. At $^{98}$Cd ($T_{1/2} \approx 9.2$ s) a small intensity gain over the molten tin target was observed. However, at ISOLDE PSB currently no helium projectiles are available and the performance of this target was not yet tested with a 1 GeV proton beam. To obtain a significant amelioration of the yield of $^{97}$Cd ($T_{1/2} \approx 3$ s) a still faster release is required.

### LaC$_x$/graphite target

The first[14] target element above cadmium which forms a refractory compound is lanthanum. A lanthanum carbide/graphite target had been tested for the production of light cesium isotopes (see section 4.11). This available LaC$_x$/graphite target was also tested together with the RILIS for the production of light cadmium isotopes (ISOLDE experiment [ISP55]).

The good yields of short-lived cadmium isotopes from the Sn/graphite target and UC/graphite targets indicated already that the release of cadmium from a graphite matrix should be relatively fast. However, the LaC$_x$/graphite has a lower target thickness (only 30 g/cm$^2$ lanthanum) and gives lower cross-sections due to a less favorable reaction mechanism, e.g. $^{139}$La(p,10p30n) instead of $^{112-124}$Sn(p,3p[10-22]n) to reach $^{100}$Cd. Therefore the production rate in the target will be reduced in comparison with a molten tin target. The efficiency of a well-tuned plasma ion source can exceed that of the RILIS ($\approx 10$ %) by a factor three to five, but with a strongly outgasing target the efficiency of the plasma ion source can also drop to well below 10 %. Therefore it is not evident to predict for which isotope the break-even will be reached where the reduced decay losses will overwhelm the smaller production rate.

The test showed that the cadmium release is indeed very fast, even that fast that the beam of stable and long-lived radiogenic cadmium oscillated rapidly with each proton pulse impact and could not be used for a monitoring of the RILIS with the Faraday cup. Therefore the RILIS had to be tuned blindly. Since stable cadmium contaminations do not remain long enough in the hot target, one should provide a continuous flow of cadmium from an attached oven. This would allow a better control of the RILIS performance.

At a target temperature of roughly[15] 1600 °C and a tungsten line temperature of about 2350 ° the release profile of cadmium could be fitted with (see equation (2.4.2)): $\tau_r = 50$ ms, $\tau_f = 250$ ms, $\tau_s = 1200$ ms and $\alpha = 0.85$. The obtained yields are shown in table 4.8.1.

The yields of the nuclei $^{98}$Cd and $^{99}$Cd were evaluated from the gamma lines observed with a set-up of two Euroball cluster detectors [LaCom]. For the lightest nucleus $^{97}$Cd no gamma lines with known branching ratios are known which could be used for a direct yield determination. In the former experiments this isotope had been identified only via beta-delayed protons. The transitions in the $^{97}$Ag daughter known from high-spin spectroscopy ($21/2^+ \rightarrow 17/2^+ \rightarrow 13/2^+ \rightarrow 9/2^+$) were not observed [LaCom]. Thus, an upper limit could be estimated for the yield of the expected $25/2^+$ isomer (see [Sch97]). This does not exclude the presence of a low-spin isomer which can decay via different levels. No yield limit can be quoted, but from an extrapolation of the neighboring nuclides a relatively low yield of the order of $0.1 - 0.5$ per $\mu$C is expected.

In fact at mass 97 immediately some short-lived gamma lines were found, but they came from $^{97}$Rb (and its daughters $^{97}$Sr and $^{96}$Sr), a beam contamination which was not expected in this

---

[14] Actually also tin forms a high-melting intermetallic compound: Hf$_5$Sn$_3$. It was tested in [Hof84] (see comments below).

[15] The temperature of this target was not calibrated individually. Instead the calibration curve of a similar UC$_x$/graphite target is used.

Table 4.8.1.: Yields of light cadmium isotopes from a 30 g/cm$^2$ LaC$_x$/graphite target and resonant laser ionization. The yield $Y$ is given in atoms per $\mu$C of primary proton beam.

| Isotope | $^{97m}$Cd | $^{98}$Cd | $^{99}$Cd | $^{100}$Cd | $^{101}$Cd |
|---------|------------|-----------|-----------|------------|------------|
| $T_{1/2}$ | 3 s | 9.2 s | 16 s | 49.1 s | 1.2 min |
| $Y$ $(\mu$C$^{-1})$ | <0.2 | $\approx$ 10 | 450 | 8500 | $1.2 \cdot 10^5$ |
| Method | $\beta\gamma$ | $\beta\gamma$ | $\beta$, $\beta\gamma$ | $\beta$ | $\beta$ |

| Isotope | $^{102}$Cd | $^{103}$Cd | $^{104}$Cd | $^{105}$Cd | $^{111m}$Cd |
|---------|------------|------------|------------|------------|-------------|
| $T_{1/2}$ | 5.5 min | 7.3 min | 57.7 min | 55.5 min | 49 min |
| $Y$ $(\mu$C$^{-1})$ | $8 \cdot 10^5$ | $6 \cdot 10^6$ | $1.5 \cdot 10^7$ | $4.5 \cdot 10^7$ | $3 \cdot 10^7$ |
| Method | $\beta$ | $\beta$ | $\beta$ | $\beta$ | $\beta$ |

amount. Therefore also the yields of other rubidium isotopes were evaluated with the monitoring tape station, see table 4.8.2. For mass 98 the rubidium contamination gets negligible, but at mass 97 it is still stronger than cadmium. The contamination can be reduced by a certain factor when opening the beam gate only later, after most of the rubidium has decayed. However, due to the fast release of cadmium this will also cut off a significant part of the cadmium intensity. With a change of the ion source temperature no significant suppression can be obtained since rubidium is also well surface ionized at lower temperatures.

On the other hand a reduced target temperature will increase the delay losses of rubidium more than those of cadmium. At 1850 °C target temperature rubidium is released about equally fast as cadmium. At lower temperatures the release of rubidium gets slower and the yields start to be reduced. At 1600 °C the rubidium yields drop by about a factor of two while the yields of cadmium remain roughly constant down to a temperature of 1400 °C. When reducing the temperature to 800 °C the cadmium yield is reduced to half its original value. Even with the target only heated by the proton beam some cadmium release was observed! Clearly the decay losses will depend on the half-life of the isotope[16]. The quoted yield/temperature relation of the cadmium yield was measured with $^{99}$Cd $(T_{1/2} = 16$ s$)$.

Table 4.8.2.: Yields of surface ionized rubidium isotopes from a 30 g/cm$^2$ LaC$_x$/graphite target at about 1850 °C. Only the yield of $^{97}$Rb was measured at 1700 °C target temperature. The yield $Y$ is given in atoms per $\mu$C of primary proton beam.

| Isotope | $^{80}$Rb | $^{88}$Rb | $^{91}$Rb | $^{92}$Rb | $^{93}$Rb | $^{94}$Rb | $^{97}$Rb |
|---------|-----------|-----------|-----------|-----------|-----------|-----------|-----------|
| $T_{1/2}$ | 30 s | 17.8 min | 58 s | 4.5 s | 5.8 s | 2.69 s | 0.17 s |
| $Y$ $(\mu$C$^{-1})$ | $7 \cdot 10^6$ | $2.4 \cdot 10^5$ | $1 \cdot 10^4$ | 6000 | 3500 | 1200 | $\approx$ 10 |
| Method | $\beta$ | $\beta$ | $\beta$ | $\beta$ | $\beta$ | $\beta$ | $\beta\gamma$ |

**UC$_x$/graphite target**

Neutron-rich cadmium isotopes had already been separated at the ISOLDE SC with a UC$_x$/graphite cloth target and a plasma source. Chemical selectivity was provided by a quartz transfer line at

---

[16]More detailed data had been taken for the release profiles of cadmium and rubidium at different temperatures, but unfortunately it was lost in a computer crash.

600 °C, suppressing a large part of the indium and cesium isobars [Kra86, SCyie]. To find the r-process waiting point nucleus $^{130}$Cd the selective detection of beta-delayed neutrons was used. Still a molecular beam of $^{40}$Ca$^{90}$Br$^+$ remained as background. The well-known lifetime of $^{90}$Br allowed to substract this background and to derive the half-life of $^{130}$Cd [Kra86]. The latter had a yield of about 50 atoms per $\mu$C [SCyie].

The heavier isotopes $^{131+x}$Cd are already beyond the $N = 82$ shell closure and are expected to have still shorter lifetimes. To minimize the decay losses, the full target and ion source unit has to be kept at a sufficiently high temperature. To assure this and to obtain a better suppression of molecular beam contaminations it was proposed to use a hotter transfer line together with ionization by the chemically selective RILIS [ISI22].

In a first experiment a standard UC$_x$/graphite target with niobium ionizer was used[17]. However, the broad width of the laser ion pulses did not allow to improve the cadmium over indium ratio by micro gating with the beam chopper.

Similarly to the LaC$_x$/graphite target a very fast release was measured. At about 2050 °C target temperature the release curve could be fitted with: $\tau_r = 50$ ms, $\tau_f = 400$ ms, $\tau_s = 1000$ ms and $\alpha = 0.7$. With the monitoring tape station the yield of $^{122}$Cd was determined (see table 4.8.3) at a reduced proton beam intensity of $10^{12}$ protons per pulse. Already here a indium background up to 30 % had to be substracted. For all other isotopes a yield determination with the monitoring tape station was not possible due to a complicated mixture of often several isomers of cadmium, indium, cesium and their decay daughters.

The yields of $^{121}$Cd to $^{128}$Cd were determined from the analysis of $\gamma$ intensities measured with the set-up described in ref. [Wei99]. It should be noted that the derived yields have a large uncertainty ($\gtrsim$ factor 3) due to a varying transmission to the end of the hall, an unknown portion of the beam which was implanted next to the tape and a high, but not constant dead time (pulsed implantation). During the measurement of mass 123 the lasers were not running properly and the yield was reduced. Still the isomeric ratio could be deduced: about 70 % of $^{123g}$Cd and 30 % of $^{123m}$Cd. The masses $A = 125$, 127 and $\geq 129$ were not studied with this set-up to avoid a contamination with long-lived isobars.

Gamma data at masses 130 and 131 were taken with the cluster detector set-up and beta-delayed neutrons were recorded at masses 130 to 132. As in the case of the heaviest silver isotopes there is a strong background from indium isobars. Still the short-lived neutron activities of the isotopes $^{130}$Cd, $^{131}$Cd and $^{132}$Cd could be identified. From the decay curves the half-lives and the $P_n$ values were extracted [Kra00, Han00], see table 4.8.3.

For comparison also yields from ISOLDE SC are given [SCyie]. There a 13.6 g/cm$^2$ UC$_x$/graphite cloth target with MK3 plasma ion source had been used. It is evident that the present yields are nearly two orders of magnitude higher. However, this cannot be attributed solely to the good efficiency of the RILIS. The target thickness at ISOLDE PSB was four times that at ISOLDE SC. Moreover the quoted SC yields close to stability are nearly a factor twenty below those of another SC target (UC$_x$/graphite cloth target with MK5 source), indicating that the source efficiency of the used ion source was particularly low.

**Comparison**

Due to the intense cadmium beams already available since long time at ISOLDE [Hag70, Rav75b] not much concurrence developed at other facilities. However, for the most neutron-deficient isotopes the facilities using fusion-evaporation reactions become competitive.

The odd cadmium isotopes $^{97}$Cd and $^{99}$Cd had been produced at the GSI ISOL facility in ($^{40}$Ca,$x$n) fusion-evaporation reactions on 3 mg/cm$^2$ nickel targets (with a beam of up to 66 pnA of 4 A·MeV

---

[17]In fact it was the same target unit which was also used for the copper run.

Table 4.8.3.: Yields of heavy cadmium isotopes from a 53 g/cm$^2$ UC$_x$/graphite target and resonant laser ionization at the PSB. The yield $Y$ is given in atoms per $\mu$C of primary proton beam and compared to a yield from ISOLDE SC (see text). Note that the yield of the isotopes determined by $\beta\gamma$ spectroscopy is quite uncertain! The half-lives and $P_n$ values of $^{130-132}$Cd were taken from [Kra00, Han00].

| Isotope | $^{121g}$Cd | $^{121m}$Cd | $^{122}$Cd | $^{124}$Cd | $^{126}$Cd | $^{128}$Cd | $^{130}$Cd | $^{131}$Cd | $^{132}$Cd |
|---|---|---|---|---|---|---|---|---|---|
| $T_{1/2}$ | 12.8 s | 8.3 s | 5.5 s | 1.3 s | 0.51 s | 0.3 s | 165 ms | 68 ms | 97 ms |
| $Y$ ($\mu$C$^{-1}$) PSB | $1.3 \cdot 10^8$ | $5 \cdot 10^8$ | $6 \cdot 10^8$ | $4 \cdot 10^7$ | $3 \cdot 10^6$ | $2 \cdot 10^5$ | $\approx 10^4$ | $\approx 10^3$ | some 10 |
| $Y$ ($\mu$C$^{-1}$) SC | $1 \cdot 10^7$ | | $9 \cdot 10^6$ | | | $3 \cdot 10^3$ | 50 | | |
| Method | $\beta\gamma$ | $\beta\gamma$ | $\beta$ | $\beta\gamma$ | $\beta\gamma$ | $\beta\gamma$ | $\beta$n | $\beta$n | $\beta$n |
| $P_n$ (%) | | | | | | | 3.6 | 3.4 | 60 |

$^{40}$Ca). They were ionized with a FEBIAD-F ion source [Kur82]. Due to an unknown branching ratio for the detected protons no yield was reported for $^{97}$Cd. However, from the number of detected events reported in ref. [Kur82, Sch97] a yield can be estimated by using the same calculated branching ratio which was used in [Elm78]: 4 %. The yield is comparable to the quoted ISOLDE SC yield, but due to the selective production mechanism contaminations like Rb and molecular ions play no role at the GSI ISOL facility.

Figure 4.8.1 shows a comparison of experimentally obtained yields of light cadmium isotopes at different facilities. The technical details are given in table 4.8.4. The yields of ref. [Ryk95] were estimated from figure 3 therein.

Table 4.8.4.: Production of light cadmium isotopes at different RIB facilities.

| Ref. | Facility | Proj. | $E/A$ (MeV) | $\bar{I}$ (pnA) | Target | $\zeta$ (g/cm$^2$) | Source |
|---|---|---|---|---|---|---|---|
| RILIS LaC | ISOLDE PSB | p | 1000 | 2500 | LaC$_x$ | 30 | RILIS |
| SC Sn | ISOLDE SC | p | 600 | 1500 | Sn | 120 | MK3 |
| [Hag92b] | ISOLDE | p | 600 | 2500 | Sn/C | 20 | MK5 |
| [Hel96] | GSI-ISOL | $^{58}$Ni | 5.9-6.7 | 40 | $^{50}$Cr | | F.-B2-C |
| [Ryk95] | LISE3, GANIL | $^{112}$Sn | 63 | 2.4 | Ni | 0.144 | |
| [Sch97] | GSI-ISOL | $^{40}$Ca | 4.2 | 50 | $^{60}$Ni | 0.003 | F.-B2 |
| [Stolz] | GSI-FRS | $^{112}$Sn | 1000 | 0.004 | Be | 4 | |

## Prospects

It has been shown that neutron-deficient cadmium beams can be produced with a LaC$_x$/graphite target and ionized by the RILIS. However, only for $^{99}$Cd a small gain in yield could be obtained compared with a tin target, but not for $^{98}$Cd and $^{100+x}$Cd. Probably this remains also true for the most short-lived isotope $^{97}$Cd. Despite the element selective ionization with a RILIS, at mass 97 the beam purity was not sufficiently improved in comparison with a molten tin target[18]. This case is a textbook example for the principle to *"suppress contaminations as early as possible"*! That means it is better to not produce them at all (e.g. by fusion-evaporation reactions) or to keep

---

[18]It should be noted that occasionally strong beam impurities were also observed with a molten tin target, e.g. $^{23}$Na$^{75}$Br$^+$ beams in [Plo92].
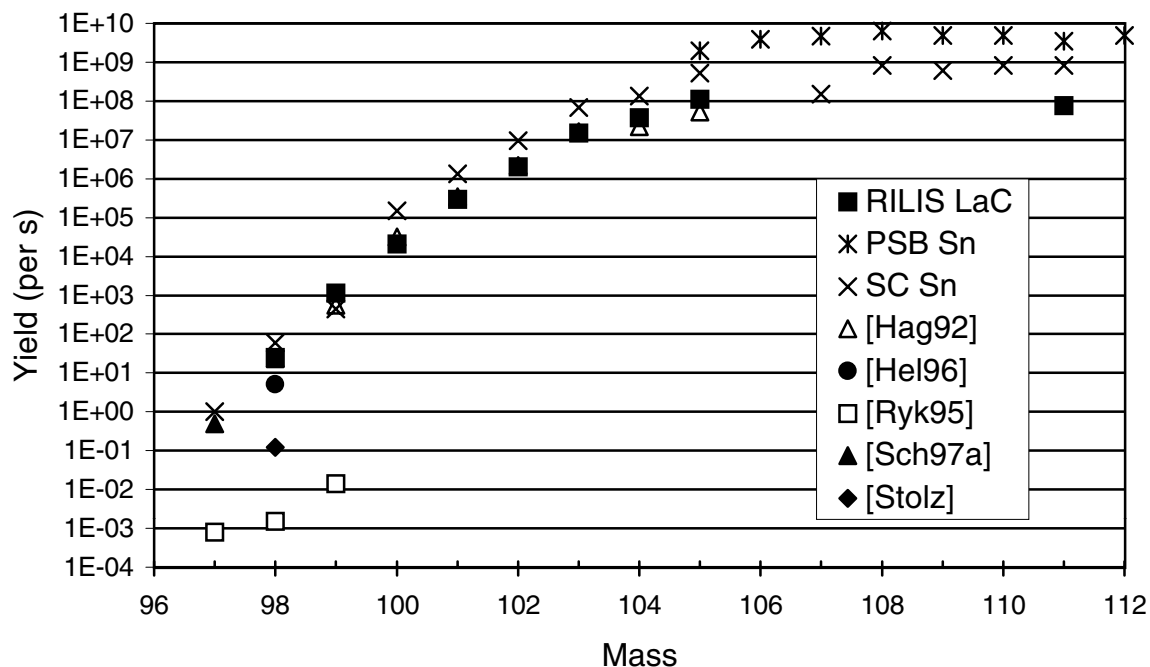
Figure 4.8.1.: Comparison of cadmium yields, see table 4.8.4 for experimental details of each curve.

them in the target or transfer line. Once alkali isobars enter the ion source, even the quite selective RILIS method cannot help. Moreover, there is no hope to separate them with a high-resolution mass separator since the mass excess of heavy rubidium and light cadmium isotopes is very similar.

An alternative solid state target could be the intermetallic compound $Hf_3Sn_5$ proposed by Hoff et al. [Hof84]. This could raise the production rates due to more favorable spallation cross-sections. However, by spallation of the hafnium component the production of rubidium would be even higher compared with a lanthanum target, thus causing more isobaric contaminations. Therefore precautions have to be taken to provide a good suppression of rubidium. The chemical selectivity could be achieved with a transfer line kept at reduced temperature, but it remains to be tested which temperature gives finally the best compromise between a rapid release of cadmium and a good suppression of rubidium.

Also the performance of a molten tin target with the improved target design [Let97b] and at maximum temperature ($\approx 1200$ °C) or that of a tin/graphite target should be tested again. The effect of bunched release should improve the yields over the SC values.

Regarding also the beam purity, at present clearly the best beams of very neutron-deficient cadmium are obtained at the GSI ISOL facility. Possibly for [97]Cd (and [96]Cd) also the GSI FRS can become competitive after the next intensity upgrade.

It should be noted that for light cadmium isotopes the atomic physics effects start to become important for the RILIS application. For example [103]Cd shows a hyperfine splitting of about 7 GHz [Buc87]. Even by excitation with a broad-band laser this can lead to a certain reduction of the ionization efficiency if the frequency is not tuned correctly.

On the other hand the ISOLDE RILIS could be used as sensitive tool for the measurement of the isotope shift and the hyperfine splitting of exotic cadmium nuclides. Presently [102]Cd is the lightest cadmium isotope studied by atomic spectroscopy, but this could certainly be extended to lighter nuclei. Using for [97]Cd the efficient and selective detection via beta-delayed protons would even allow to cross the $N = 50$ shell. A spectral resolution of about 1 GHz is already sufficient to observe a major change of the nuclear radius. As shown in section 3.5.2 for copper, the scanning of the frequency allows moreover to identify and separate isomers. In principle this could help

to identify the predicted $1/2^-$ and $25/2^+$ isomeric states in $^{97}$Cd [Sch97]. However, the latter experiment could only be performed at ISOLDE if both isomers also show a significant branching ratio for $\beta$p decay, allowing a "background-free" detection. Else a RILIS has to be set up again at the GSI ISOL facility.

On the neutron-deficient side the production cross-section is limiting an extension to more exotic isotopes. On the neutron-rich side the limiting factor is rather the beam purity. The production rates of heavy cadmium isotopes are high enough to perform interesting nuclear spectroscopy experiments, but presently the isobaric background is just overwhelming. With the help of a thin cavity and the beam chopper or with a high resolution separator this background may possibly be suppressed by about one order of magnitude, but for a larger gain the problem has to be tackled at an earlier stage, i.e. before entering the ion source.

The beam purity could be significantly improved by combining a temperature controlled transfer line with the RILIS. The former can suppress background from less volatile elements (indium and cesium) and the latter will remove molecular beams with higher ionization potential. Systematic investigations are required to find an optimum combination of material, geometry and temperature of this transfer line. The Eichler systematics indicates that e.g. a chromium surface is very promising for the Cd/In separation, but also palladium and platinum should show a significant separation effect [Rös86]. The latter could be used simultaneously for a further suppression of the surface ionizable elements by using a transfer line with "inverted polarity" (see section 3.4.4). Also non-metallic or compound surfaces could be considered for such a thermo-separator.

## 4.9.    Indium yields

**LaC$_x$/graphite target**

No yields for very neutron-deficient indium isotopes had been reported from ISOLDE SC. However, the LaC$_x$/graphite target with tungsten surface ionizer provides ideal conditions to produce them. Therefore the release and yields of indium beams were studied together with the test of the light Cd and Cs beams. With the target at about 1850 °C a fast release was found which could be fitted with (see equation (2.4.2)): $\tau_r = 60$ ms, $\tau_f = 600$ ms, $\tau_s = 6$ s and $\alpha = 0.98$.

Table 4.9.1.: Yields of light indium isotopes from a 30 g/cm$^2$ LaC$_x$/graphite target and tungsten surface ionizer. The yield $Y$ is given in atoms per $\mu$C of primary proton beam.

| Isotope | $^{101}$In | $^{102}$In | $^{103g}$In | $^{104g}$In | $^{105g}$In | $^{106g+m}$In | $^{112g}$In | $^{114g}$In |
|---|---|---|---|---|---|---|---|---|
| $T_{1/2}$ | 14.9 s | 22.1 s | 60 s | 1.8 min | 4.8 min | $\approx$ 6 min | 14.4 min | 72 s |
| $Y$ $(\mu C^{-1})$ | 30 | 900 | $1.4 \cdot 10^4$ | $4.4 \cdot 10^4$ | $1.9 \cdot 10^5$ | $3.7 \cdot 10^6$ | $1 \cdot 10^7$ | $1.2 \cdot 10^5$ |
| Method | $\beta\gamma$ | $\beta$ | $\beta$ | $\beta$ | $\beta$ | $\beta$ | $\beta$ | $\beta$ |

**Comparison**

Figure 4.9.1 shows a comparison of experimentally obtained yields of light indium isotopes at different facilities. The technical details are given in table 4.9.2. The yields of ref. [Ryk95] were estimated from figure 3 therein. The yield of $^{100}$In from ref. [Sch96] was corrected for the low transmission.

Table 4.9.2.: Production of light indium isotopes at different RIB facilities.

| Ref. | Facility | Proj. | $E/A$ (MeV) | $\bar{I}$ (pnA) | Target | $\zeta$ (g/cm$^2$) | Source |
|------|----------|-------|-------------|-----------------|--------|--------------------|--------|
| LaC | ISOLDE PSB | p | 1000 | 2500 | LaC$_x$ | 30 | WSI |
| [Bar97] | IRIS | p | 1000 | 100 | GdC$_x$ | 7 | WSI |
| [Sze95, Sze97] | GSI-ISOL | $^{58}$Ni | 5.6-5.9 | 40 | $^{50}$Cr | | F.-B2-C,-E |
| [Ebe86, Ebe87] | GSI-ISOL | $^{16}$O | 6-9 | | Mo | 0.03 | F.-B2 |
| [Ver81, Ver84] | LISOL | $^{14}$N | 5.1 | 1200 | Mo | 0.005 | Nielsen |
| [Ryk95] | LISE3, GANIL | $^{112}$Sn | 63 | 2.4 | Ni | 0.144 | |
| [Sch96] | GSI-FRS | $^{124}$Xe | 1095 | 0.0037 | Be | 6 | |
| [Wefer] | GSI-FRS | $^{112}$Sn | 1000 | 0.004 | Be | 4 | |
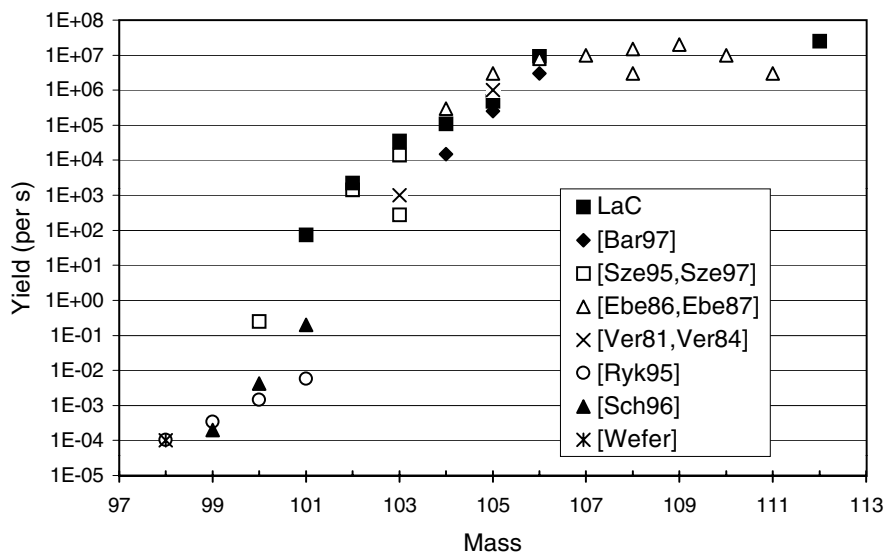


Figure 4.9.1.: Comparison of indium yields, see table 4.9.2 for experimental details of each curve.

**UC$_x$/graphite target**

Heavy indium beams are of high interest for nuclear spectroscopy, since they populate by $\beta^-$ decay excited levels of tin nuclei around the doubly magic $^{132}$Sn. The first studies of the $^{132}$In decay were performed with beams of neutron-induced fission products at the reactor-based facilities OSIRIS [Ker73] and JOSEF [Bjø80]. Later also ISOLDE beams were used for these studies [Bjø86]. These were more intense than at OSIRIS, but the production of the cesium isobar was more than seven orders of magnitude larger! At the ISOLDE PSB also the decay of the isotopes $^{133}$In and $^{134}$In could be studied [Jok95, Hof96a].

The yield of $^{132-134}$In from a UC$_x$/graphite target was measured by detecting beta-delayed neutrons. For $^{132}$In and $^{133}$In the known branching ratios were used and for $^{134}$In the predicted value from [Möl97]. To integrate the total indium yield per proton pulse the beam gate was kept open for 2 s. Therefore the half-life could not be fitted. However, folding the release profile with the known half-lives gives a satisfying agreement. That means a possible contamination with molecular ions could only contribute a minor part of the detected neutrons. The obtained yields are higher by a factor three to six compared with those obtained by Jokinen et al. [Jok95]. At another occasion another order of magnitude higher yields were observed for $^{132}$In and $^{133}$In [PSyie]. It is not clear

if this is due to a better transmission or detection efficiency[19], or just the "normal" fluctuation from target to target. The yields of $^{133}$In and $^{134}$In were not measured with other targets to avoid an excessive cesium and barium contamination of the respective tape station.

Table 4.9.3.: Yields of heavy indium isotopes from a 52 g/cm$^2$ UC$_x$/graphite target with tungsten surface ionizer. The yield $Y$ is given in atoms per $\mu$C of primary proton beam.

| Isotope | $^{132}$In | $^{133}$In | $^{134}$In |
|---|---|---|---|
| $T_{1/2}$ | 206 ms | 180 ms | 138 ms |
| $P_n$ | 5.2 % | 87 % | (100 %) |
| $Y$ ($\mu$C$^{-1}$) | $1.3 \cdot 10^5$ | 6000 | 450 |

In a recent attempt to do a more detailed gamma spectroscopy of the $^{134}$In decay the cesium background was just overwhelming. The problem of the cesium contamination is obvious when regarding the production cross-sections in high energy proton induced reactions. The width of the isobaric distribution is larger than in neutron-induced fission, causing the strong background from cesium isotopes close to stability.

To show the behavior of all isobars unaffected by experimental variations of release and ionization efficiency exceptionally no experimental yields are plotted in figure 4.9.2, but the independent cross-sections. For the proton-induced reactions the cross-sections were calculated once from the semi-empiric systematics of Silberberg and Tsao [Sil90] and once with a Monte Carlo code (abrasion-ablation model) [Farge, BenII, Ben98]. Taking into account the completely different nature of the models, the predictions agree reasonably well. For the yields from neutron-induced fission the systematics from Wahl [Wah88] was used.
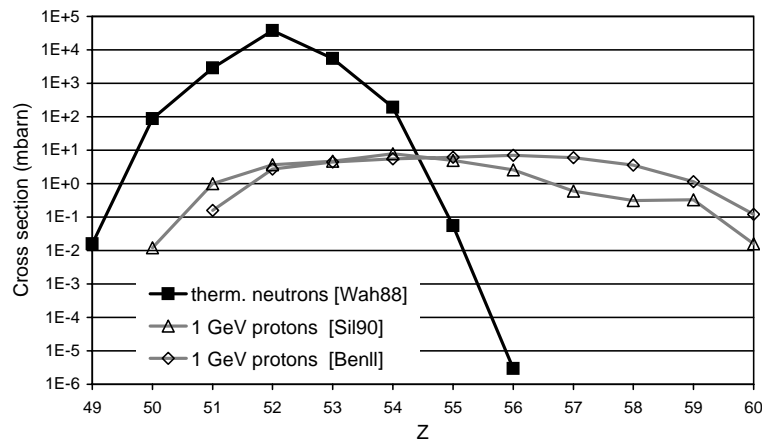


Figure 4.9.2.: Production cross-sections for the $A = 134$ isobars. The values for thermal-neutron induced fission are connected with a black line, those for 1 GeV proton induced reactions by a grey line.

Note that the ratio of the experimental yields is even more unfavorable than that of the production cross-sections: the decay losses in the target are higher for indium while the surface ionization efficiency is higher for cesium. Therefore the yield of $^{134}$Cs is about seven orders of magnitude higher than that of $^{134}$In! A major background suppression is achieved by using a tape station

---

[19]These are normally already included in the quoted yields, but occasionally the transmission varies considerably when changing the mass.

to transport the long-lived cesium contaminants periodically away. Beta gating helps to suppress the background from the $^{134m}$Cs decay. But still these experiments are done at the limit and a small fluctuation of the yields can render them impossible. Similar contamination problems can also occur for neighboring masses. The light lanthanides and metastable barium isomers can cause additional background.

To improve the indium to cesium ratio a transfer line with "inverted polarity" (see section 3.4.4) could help as well as the use of a high resolution mass separator. However, these measures might give an improvement of one order of magnitude while the production via neutron-induced fission solves the problem completely! Therefore an intense reactor-based RIB facility would be very profitable for nuclear spectroscopy in this region [Mac95].

An interesting fact which was not yet studied thoroughly is the different population of various isomers in charged particle induced fission compared with thermal- [Den86, Rud90] and fast neutron induced fission [Rud94]. Most indium isotopes have several isomers and can offer a good opportunity for a systematic study.

## 4.10.   Tin yields

Tin has the magic proton number $Z = 50$. Therefore it is highly appreciated by theorists who predict its nuclear properties from the proton- up to neutron drip line and beyond, see e.g. [Dob96] and references in [Lun97]. The experimental physics is far from keeping pace with these far-reaching predictions. However, as shown in [Lun97] e.g. the mass predictions start to differ significantly already when going only few nuclei beyond the last experimentally measured nuclei. An extension of the provided tin yields towards more exotic isotopes is particularly interesting for all RIB facilities. Therefore tin was chosen as one of the key elements to evaluate the projects of next-generation RIB facilities in Europe and North America.

### Production

On the neutron-deficient side (around $^{100}$Sn) facilities using fragmentation and fusion-evaporation are presently competing to reach the highest yields. The spallation cross-sections and the intrinsic beam purity (broad width of the isobaric production curve) of a spallation facility are not expected to be particularly favorable in this region (compare section 4.8).

However, on the neutron-rich side the heavy fission fragment distribution peaks just around the doubly-magic $^{132}$Sn. Therefore all facilities using fission reactions profit from large production cross-sections. The performance of an ISOL facility is here less limited by the production rate than by the release time and possibly by isobaric contaminations.

The heaviest tin isotopes were always produced by fission reactions, see e.g. ref. [Gre63] where $^{132}$Sn was chemically separated from irradiated $^{235}$U for the determination of its half-life, or ref. [Kaw82] where the 2 $\mu$s $8^+$ isomer of $^{132}$Sn was separated with the gas-filled recoil separator JOSEF. Presently $^{134}$Sn is the heaviest tin isotope with measured half-life and mass. It was studied already 25 years ago at OSIRIS [Sha74] and LOHENGRIN [Asg75]. The study of the neutron-rich isotopes around $^{132}$Sn remains one of the most important domains for the reactor-based RIB facilities even to this day [Fog99].

### Release

Tin isotopes ($^{107-113}$Sn) were already separated at ISOLDE 1 from a TeCl$_4$ target [Als70]. Later $^{108-111}$Sn was separated with a Ta foil target and a hot plasma source. However, for the production of neutron-rich tin isotopes by fission, an actinide target is required. The isotopes $^{125-132}$Sn were

separated from an ISOLDE $UC_x$/graphite cloth target at 1950 °C together with a hot plasma source [Hag92b].

Carraz et al. found for tin a release half-life of 2 to 3 min from both, a $UC_x$/graphite cloth material at 1600 °C and a pure $UC/UC_2$ powder at 2000 °C [Car78]. A much faster release ($\ll$ 1 min) was observed from $ThO_2$ at 2100 °C [Hof84].

Kirchner measured the release of tin from different materials: Nb, Mo, W and various types of graphite [Kir92a, Kir97]. The obtained diffusion constants are all of the same order of magnitude (some $10^{-10}$ $cm^2$/s at 2200 K), but it is noticeable that the mean effusion times are quite important: already several seconds for the small GSI target and ion source systems. Interestingly this occurs for two different types of ion sources: a FEBIAD-B2 with Ta-electrodes and BN insulators [Kir87a] and a FEBIAD-E with graphite electrodes and BeO insulators [Kir81b]. Thus, tin does not seem to stick to a particular surface of the source construction materials, but rather shows generally a larger desorption enthalpy.

On the other hand Rudstam et al. found a reasonably fast release of tin from the OSIRIS $UC_x$/graphite target with a tungsten enclosure [Rud90]. It should be noted that in another yield and release evaluation from the OSIRIS target the average release time of tin was significantly larger [Rud96]. It is not clear if this effect is an artifact from mother-daughter corrections[20] or due to a change in the target properties, e.g. a changed graphite "coating" of the tungsten surface.

Bolshakov et al. found at temperatures above 1600 °C a rapid release from $UC_x$/graphite material produced from diphtalocyanine [Bol92].

Note that the Eichler systematics predicts a 100 times longer adsorption time on tungsten at 2300 °C compared with niobium at 2000 °C. This could lead to the unexpected effect that tin is released much faster from a niobium cavity than from a tungsten cavity. According to this systematics another order of magnitude in desorption time could be gained with a molybdenum tube at 2000 °C.

### Ionization

With an ionization potential of 7.34 eV, tin is practically not surface ionized. A hot plasma ion source can give a good ionization efficiency but does not show any selectivity. The heavier isobars antimony, tellurium, iodine, etc. will cause large background in nuclear spectroscopy experiments.

The RILIS can provide a more selective ionization of tin. Several laser ionization schemes for tin have been tested successfully off-line at ISOLDE and GSI (see section B.8). However, no on-line release test with the RILIS was made yet.

With a RILIS isobaric contaminations from Sb to Xe should be significantly reduced since all these elements have ionization potentials above 8 eV. The neighboring surface ionizable isobar indium has for heavy masses a production cross-section which is about one order of magnitude lower. Moreover, due to the shell stabilization of $Z = 50$ the indium half-life is typically one order of magnitude shorter compared with the tin isobar. A suitable collection- and measurement cycle allows to exclude most indium background.

Cesium can cause a problem. With its very low ionization potential (3.89 eV) it will get surface ionized on practically all surfaces if the temperature is raised high enough to release tin. As shown in section 4.9 in high-energy proton-induced reactions the production cross-sections for heavier cesium isotopes ($A \gtrsim 128$) are many orders of magnitude larger than the corresponding cross-sections for indium and tin. Thus, even the "tricks" with the RILIS cavity discussed in section 3.4, which allow to suppress the surface ionized background by up to one order of magnitude, will not help sufficiently.

---

[20]The release of cadmium and indium was not determined in the latter evaluation.

It should be kept in mind that tin evaporates under oxidising conditions mainly as SnO [Lam87]. The latter is not ionizable by the RIS scheme for atomic tin. To avoid any loss in efficiency one has to assure that the SnO molecules are dissociated in the hot ionizer line. The same applies for possible other tin compounds. It is interesting to note that at OSIRIS tin dicarbide was observed as positive ion[21]: $SnC_2^+$ [Hel92].

### Prospects

Still, when detecting only beta-delayed neutrons, the isobaric background up to mass 141 should "only" consist of surface ionized molecules and the remaining background ionized in one of the processes discussed in section 2.5.1. Also mass measurements can be performed if the resolving power is high enough to completely exclude the cesium background. However, for detailed $\beta$- and $\gamma$-ray spectroscopy the cesium background may get too high, similar to the case of very heavy indium isotopes.

Either a high-resolution mass separator with $R_m \gg 10000$ is required[22] or an intrinsically more selective production method with a narrower isobaric distribution, i.e. neutron-induced fission.

## 4.11.   Cesium yields

Already twenty years ago 39 cesium isotopes (from $^{114}$Cs to $^{152}$Cs) with over 50 isomers were reported from ISOLDE [Rav79]. On the neutron-deficient side they are produced by spallation in a liquid lanthanum target, on the neutron-rich side by fission in a $UC_x$/graphite target. There is no other element with so many different isotopes provided by ISOLDE.

### LaC$_x$/graphite target

Cesium beams from a liquid lanthanum target have some common characteristics with cadmium beams from a liquid tin target: the high target thickness gives high yields of longer-lived species, the relative long release time is mainly responsible for the reduced yields of more short-lived nuclei and the limited target temperature provides some chemical selectivity. However, there are some quantitative differences in the latter two points. While tin targets are operated at 1000 °C maximum, the temperature of lanthanum targets goes up to 1400 °C [Let97b]. Among the nearby spallation products not "only" cadmium is released, but also xenon, cesium and even barium [Rav75b]. Thus, the elemental selectivity has to be provided by using a suitable transfer line and ion source: a cooled line coupled to a plasma ion source for xenon and a surface ion source for cesium. For very neutron-deficient nuclei the barium contaminations of a cesium beam are negligible due to the lower production cross-section, the shorter lifetime and the lower ionization efficiency. With a delay time $t_{50} \gtrsim$ 20 s [Rav75a] the decay losses become significant for $^{118}$Cs and increase rapidly towards more short-lived isotopes. A faster target is required to improve these yields.

The LaC$_x$/graphite target already presented in the sections on cadmium and indium was developed for this purpose. In practice the temperature of a LaC$_x$/graphite target is limited by oxygen impurities which will cause a strong LaO$^+$ beam quenching the ion source efficiency. Therefore the direct synthesis from lanthanum oxide and graphite described in section B.4 was modified by

---

[21]Normally tin does not form carbides, but some elements show indeed molecules which can only exist as ions in the gas phase.

[22]Note that despite the rather large mass difference between the tin and cesium isotopes ($\Delta M \geq 20$ MeV/c$^2$) a very high resolving power is necessary to suppress the wings of the cesium distribution which is more abundant by several orders of magnitude.

reducing the remaining oxides under $CH_4$ flow [Men97]. A $LaC_x$/graphite target with approximately 30 g/cm$^2$ thickness lanthanum[23] was produced.

At a target temperature of about 1850 °C the release was reasonably fast and could be fitted with (see equation (2.4.2)): $\tau_r = 20$ ms, $\tau_f = 1$ s, $\tau_s = 15$ s and $\alpha = 0.8$. Table 4.11.1 shows the obtained yields. The isotopes $^{115-138m}$Cs were detected by beta counting with the monitoring tape station. The yield for masses 117 to 121 was evaluated without separation of the isomers by using an average lifetime. At mass 116 it was not possible to separate the mixture of two cesium and three indium isomers. The yield of $^{114}$Cs was derived from the most abundant gamma lines (450, 698 and 758 keV) observed in a short measurement with the Euroball cluster detectors.

Table 4.11.1.: Yields of cesium isotopes from a 30 g/cm$^2$ $LaC_x$/graphite target and tungsten surface ionizer. The yield $Y$ is given in atoms per $\mu$C of primary proton beam. All yields but that of $^{114}$Cs were determined by beta counting.

| Isotope | $^{114}$Cs | $^{115}$Cs | $^{117g+m}$Cs | $^{118g+m}$Cs | $^{119g+m}$Cs | $^{120}$Cs | $^{121}$Cs |
|---|---|---|---|---|---|---|---|
| $T_{1/2}$ | 0.57 s | 1.4 s | $\approx 7.5$ s | $\approx 15.5$ s | $\approx 37$ s | $\approx 60$ s | $\approx 2.3$ min |
| $Y$ $(\mu C^{-1})$ | $\approx 6$ | $\approx 200$ | $1.3 \cdot 10^5$ | $2 \cdot 10^6$ | $7 \cdot 10^6$ | $4.5 \cdot 10^7$ | $1.8 \cdot 10^8$ |

| Isotope | $^{122g}$Cs | $^{123g}$Cs | $^{123m}$Cs | $^{124g}$Cs | $^{124m}$Cs | $^{125}$Cs | $^{126}$Cs |
|---|---|---|---|---|---|---|---|
| $T_{1/2}$ | 21 s | 5.9 min | 1.6 s | 30.8 s | 6.3 s | 45 min | 1.6 min |
| $Y$ $(\mu C^{-1})$ | $8 \cdot 10^8$ | $1.4 \cdot 10^9$ | $2 \cdot 10^7$ | $1 \cdot 10^9$ | $1.5 \cdot 10^7$ | $8 \cdot 10^8$ | $1.4 \cdot 10^9$ |

| Isotope | $^{128}$Cs | $^{130m}$Cs | $^{134m}$Cs | $^{135m}$Cs | $^{136m}$Cs | $^{138m}$Cs |
|---|---|---|---|---|---|---|
| $T_{1/2}$ | 3.8 min | 3.5 min | 2.9 h | 53 min | 19 s | 2.9 min |
| $Y$ $(\mu C^{-1})$ | $1.1 \cdot 10^9$ | $5 \cdot 10^8$ | $1.3 \cdot 10^8$ | $1.5 \cdot 10^7$ | $3.5 \cdot 10^6$ | $9 \cdot 10^4$ |

**Comparison**

Figure 4.11.1 shows experimentally obtained yields of light cesium isotopes at different facilities. Details are given in table 4.11.2. For better comparison the yields quoted in [Bar97] were scaled to a typical proton beam current at ISOLDE: 2.5 $\mu$A.

Table 4.11.2.: Production of light cesium isotopes at different RIB facilities. All presented ISOL facilities use a tungsten surface ion source.

| Ref. | Facility | Proj. | $E/A$ (MeV) | $\bar{I}$ (pnA) | Target | $\zeta$ (g/cm$^2$) |
|---|---|---|---|---|---|---|
| PSB LaC | ISOLDE | p | 1000 | 2500 | LaC | 30 |
| PSB La | ISOLDE | p | 1000 | 1000 | La | 123 |
| SC La | ISOLDE | p | 1000 | 1000 | La | 140 |
| SC Ta | ISOLDE | p | 1000 | 2500 | Ta | 122 |
| [Bar97] | IRIS | p | 1000 | (2500) | $GdC_x$ | 7 |
| [Roe80] | GSI-ISOL | $^{58}$Ni | 5 | 250 | $^{58}$Ni | 0.004 |
| [Bog75] | BEMS-2, JINR | $^{32}$S | 5.94 | | $^{92}$Mo | 0.002 |
| [Hof89] | SHIP, GSI | $^{58}$Ni | 3.95 | 10 | $^{58}$Ni | 0.0004 |

Note that the molten lanthanum targets are not run with the maximum available beam intensity to protect the target container from excessive thermal stress. The large difference between the yields

---

[23]Some of the material could have been lost in the production process. Therefore the thickness can only be given approximately.
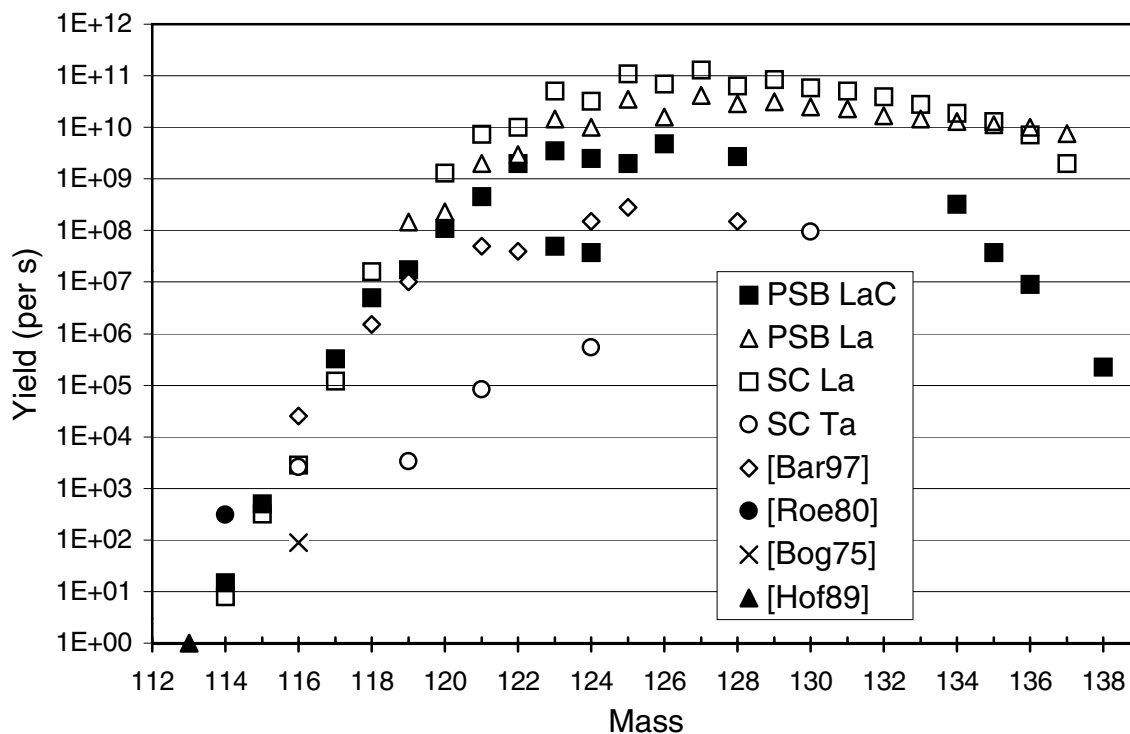
Figure 4.11.1.: Comparison of yields of light cesium isotopes, see table 4.11.2 for experimental details of each curve.

of the $LaC_x$/graphite target and the molten La target on the right-hand side of figure 4.11.1 are due to the different detection method. For the former beta counting was used and the presented yields are of the short-lived metastable state only. For the latter target the integral yields were determined with the Faraday cup. Due to the faster release the yields of short-lived cesium isotopes $A \leq 117$ from a $LaC_x$/graphite target exceed those of a molten lanthanum target. However, for the most neutron-deficient nuclides the production rates from fusion-evaporation reactions get very competitive. Thus, the beam intensity at the GSI ISOL facility is comparable around mass 116, but it is more than one order of magnitude larger than the ISOLDE yields at mass 114. Moreover the intrinsic selectivity of the production process avoids the strong indium contamination (see yields in section 4.9) which may occur at ISOLDE. Thus, the Cs beams from a $LaC_x$/graphite target might be of interest for users of ISOLDE-specific set-ups (mass measurements, collinear laser spectroscopy, etc.), but nuclear spectroscopy is better performed at the GSI ISOL.

With $^{114}$Cs the proton drip line is reached and it will always remain the most neutron-deficient cesium isotope which can be separated at an ISOL facility. A fusion-evaporation reaction ($^{58}$Ni on $^{58}$Ni) is also used to produce $^{113}$Cs and $^{112}$Cs [Fae84, Pag94], but with lifetimes well below 1 ms these isotopes have to be separated with a recoil separator[24].

### $UC_x$/graphite target

The experimental yields of heavy cesium isotopes reach further out to the neutron-rich side than for any other element. Therefore the cesium nuclei were always a favorite choice for systematic investigations, e.g. mass measurements. Moreover, by beta-decay they populate excited levels of the heavy barium isotopes. These beta-decay studies can give information on the lower part of

---

[24]Note that the first identification of $^{113}$Cs at the Munich Tandem accelerator was performed without any mass separator, but just by selecting the fusion-evaporation products with a diaphragm and an appropriate time window for the decay [Fae84]!

the barium level scheme, thus complementing the data from high-spin studies with spontaneous fission sources. Recently the latter experiments became very popular in the area of heavy barium isotopes, see e.g. [Urb97].

The yields of the heaviest Cs isotopes were monitored from different standard $UC_x$/graphite targets (50 g/cm$^2$ thickness) with niobium or tungsten ionizer. There are markable fluctuations from target to target, but they are not correlated to the type of ionizer cavity.

At a target temperature of 2100 °C a typical release profile could be fitted with (see figure 2.4.2): $\tau_r = 0.1$ s, $\tau_f = 0.8$ s, $\tau_s = 10$ s and $\alpha = 0.85$.

For the short-lived cesium nuclei the decay daughters contribute significantly to the detected beta activity. Thus the simple detection of beta counts with the monitoring tape station is less useful. Instead the beta-delayed neutron activity was detected with the Mainz neutron long counter. Table 4.11.3 shows the derived yields after correction for the beam gate settings and the $P_n$ values. The half-lives and $P_n$ values of $^{147,148}$Cs were taken from literature [Aud97], those of $^{149,150}$Cs were measured in this work (see section 5.3). The $P_n$ value of $^{149}$Cs was chosen arbitrarily to 30 % which is in line with theoretical predictions [Pfe99]. $^{151}$Cs has an unknown half-life and neutron branching ratio and was not searched for at the ISOLDE PSB.

Table 4.11.3.: Yields of cesium isotopes from a $\approx 50$ g/cm$^2$ $UC_x$/graphite target with niobium or tungsten ionizer. The yield $Y$ is given in atoms per $\mu C$ of primary proton beam.

| Isotope | $^{147}$Cs | $^{148}$Cs | $^{149}$Cs | $^{150}$Cs | $^{151}$Cs |
|---|---|---|---|---|---|
| $T_{1/2}$ (ms) | 225(5) | 158(7) | 112(3) | 82(7) | ? |
| $Y$ ($\mu C^{-1}$), this work | $1.5 \cdot 10^6$ | $9 \cdot 10^4$ | $\approx 4000$ | $\approx 100$ | |
| $P_n$ (%) | 28.5 | 25.1 | 30 | 20 | |
| $Y$ ($\mu C^{-1}$), SC ISOLDE | $1.1 \cdot 10^6$ | $2.5 \cdot 10^5$ | $7.1 \cdot 10^4$ | $1.2 \cdot 10^4$ | 1700 |

For comparison also the yields reported from the ISOLDE SC are shown [SCyie]. They were obtained with a $\approx 13$ g/cm$^2$ $UC_x$/graphite cloth target with tungsten ionizer. These yields had also been measured by detection of beta-delayed neutrons. It is evident that towards the most neutron-rich Cs isotopes the ISOLDE PSB yields drop much faster than the ISOLDE SC yields.

Several factors could explain this difference:

- A faster release from the $UC_x$/graphite cloth target could significantly reduce the decay losses of the most short-lived nuclei and overcompensate the smaller target thickness. Unfortunately no release profile exists for the graphite cloth targets which would allow to extract the fast release component and verify this assumption. A future test of a graphite cloth target at the ISOLDE PSB should therefore also include a release measurement of cesium.

- The drop could also be explained by a rapidly dropping cross-section when going from 600 MeV to 1000 MeV proton energy. Such a decrease in cross-section with increasing proton energy would also explain why at the CERN PS ISOL separator (10 GeV protons) cesium isotopes were observed only up to $^{146}$Cs [Roe74]. It would be very interesting to test this possibility directly, once a 600 MeV proton beam becomes available from the PSB.

- Finally the determination of the cesium yields at the ISOLDE SC could have been disturbed by a contamination with molecular ions or with isobaric barium or lanthanum isotopes which also emit neutrons in this mass region. Although it is not very probable that this would result in such a smoothly dropping yield curve this possibility cannot be ruled out since the half-lives were not directly verified in the ISOLDE SC yield measurement.

## 4.12.   Francium yields

Already in the earliest ISOLDE experiments the half-life of $^{224-226}$Fr had been measured for the first time [Han69]. Later the $\beta^-$ decay of heavy francium isotopes from ISOLDE was used to study the nuclear structure of the populated radium isotopes: $^{227}$Fr [Egi81], $^{228}$Fr [Ruc82], $^{229}$Fr [Bor92], $^{230}$Fr [Kur87] and $^{231}$Fr [Hil85]. The presently heaviest francium isotope $^{232}$Fr was discovered at the IRIS facility in Gatchina [Mez90] which is technically very similar to ISOLDE.

On the neutron-deficient side the isotopes $^{201}$Fr and $^{202}$Fr were discovered at ISOLDE [Ewa80]. The beams of francium nuclides close to beta stability can reach an intensity of one 1 pnA and more [Klu86].

The simple atomic structure of an alkali and the fact that francium is the heaviest element which is very efficiently separated from a thick target ISOL facility, make it the favorite choice for systematic studies of atomic physical properties of high-$Z$ elements.

Precision experiments for parity non-conservation studies in atoms are under preparation. For this purpose a sufficient amount of francium atoms has to be kept long enough in an atom trap. With the expected trapping efficiencies and storage times beam intensities of the order of $10^{10} - 10^{11}$ francium atoms per second are required [Cas97].

Therefore francium was included as the heaviest element in the list of "key beams" for the evaluation of ISOL facilities by the NuPECC study group.

### Yields

Obviously an actinide target is required for the production of francium in spallation reactions. For the lighter francium isotopes the optimum yields are obtained from a ThC/graphite target and for the heavier ones a UC$_x$/graphite target gives the best yields. Like all other alkalis francium reaches a high vapor pressure already at relatively low temperatures and the desorption from hot surfaces is uncritical. Compared with the lighter alkalis the diffusion is somewhat slower due to the larger atomic mass and volume, but the release is fast enough for an efficient separation of the beta-decaying francium isotopes with half-lives in the second to minute range. With a standard UC$_x$/graphite target at about 2100 °C and a tungsten surface ionizer[25] at 2100 °C the release can be fitted with (see equation (2.4.2)): $\tau_r = 0.1$ s, $\tau_f = 0.6$ s, $\tau_s = 6$ s and $\alpha = 0.9$.

For the more short-lived isotopes ($T_{1/2} \lesssim 1$ s) the decay losses become considerable, but even isotopes with lifetimes in the millisecond range ($^{214,218,219}$Fr) were already separated at ISOLDE [Klu86].

Table 4.12.1 shows the yields of heavy francium isotopes measured in this work at the ISOLDE PSB. All yields were measured by beta counting in the monitoring tape station. The relative yields of $^{230-232}$Fr were moreover checked by detection of gammas and high-energy betas (see section 5.4)[26]. No significant difference was found for the francium yields from a niobium or tungsten ionizer. It is evident that the yields increase when increasing the proton beam energy from 1.0 to 1.4 GeV. Since all other parameters (target, ion source, temperature, etc.) were kept constant, this difference can be attributed to an increased cross-section.

---

[25]Note that the release from a target with niobium ionizer was slower by a factor three. It is not clear if this is due to the lower line temperature (around 1850 °C) or a target aging effect (see section B.4.2). The yield of the measured isotopes was not affected significantly.

[26]No absolute yields were determined in this experiment since the transmission to the end of the hall was particularly low.

Table 4.12.1.: Yields of heavy francium isotopes from a $\approx 50$ g/cm$^2$ UC$_x$/graphite target with tungsten or niobium surface ionizer. The yield $Y$ is given in atoms per $\mu$C of primary proton beam of 1.0 and 1.4 GeV.

| Isotope | $^{223}$Fr | $^{224}$Fr | $^{225}$Fr | $^{226}$Fr | $^{228}$Fr | $^{229}$Fr | $^{230}$Fr | $^{231}$Fr | $^{232}$Fr |
|---|---|---|---|---|---|---|---|---|---|
| $T_{1/2}$ | 22 min | 3.3 min | 4 min | 49 s | 39 s | 50 s | 19 s | 18 s | 5.5 s |
| $Y$ ($\mu$C$^{-1}$) **1.0 GeV** | $4 \cdot 10^7$ | $1.7 \cdot 10^7$ | $8 \cdot 10^6$ | $4 \cdot 10^6$ | $1 \cdot 10^6$ | $4 \cdot 10^5$ | $1.1 \cdot 10^5$ | $2.8 \cdot 10^4$ | $3 \cdot 10^3$ |
| $Y$ ($\mu$C$^{-1}$) **1.4 GeV** | | $2.5 \cdot 10^7$ | | $6 \cdot 10^6$ | $1.4 \cdot 10^6$ | | $1.8 \cdot 10^5$ | $4.3 \cdot 10^4$ | $5 \cdot 10^3$ |

## Beam purity

Francium is normally ionized with a surface ion source. The ionization efficiency is good due to the low ionization potential ($W_i = 4.07$ eV).

The beam purity of the most neutron-deficient francium isotopes is limited by the resolving power of the mass separator. Due to the steep drop of the production cross-sections even a $10^{-4}$ contamination with neighboring nuclides can cause a significant background [Ewa80]. The high resolution separator (HRS) could help to solve this problem[27].

For the heaviest francium isotopes some beam contaminations with isobaric radium occur. However, due to their longer lifetimes the latter are easy to differentiate. Therefore this contamination is normally not critical. Using a niobium surface ionizer the radium background is further reduced. Thus, at mass 232 the yield of directly produced radium and actinium was lower than the francium yield. Moreover no indication was observed for directly released $^{232}$Np or $^{232}$Pa.

However, an isobaric contamination with a molecular $^{213}$RaF$^+$ beam was found. Its yield was of the order of $10^5 - 10^6$ per $\mu$C[28]. Note that the fluorine is not specially introduced (see section 4.1), but is present as an impurity in the target material or the target container. At mass 230 the contamination with $^{211}$RaF$^+$ is about one order of magnitude less (estimated from the observed $^{207}$Rn activity). A RaF$^+$ contamination had already been observed before at masses 230 and 231 [Kur87, Hil85]. For still heavier masses the RaF$^+$ contamination is less problematic for $\beta\gamma$ spectroscopy. The $^{214}$RaF$^+$ background at mass 233 decays mainly by alphas to the ground state of $^{210}$Rn. The latter again decays mainly by alphas to the ground state of $^{206}$Po. Moreover $^{210}$Rn is longlived ($T_{1/2} = 2.4$ h) and can be efficiently removed with the tape transport. From mass 234 on the RaF$^+$ beams can be easily suppressed with an appropriate beam gate setting due to the short half-lives of the corresponding radium isotopes ($^{215}$Ra and higher).

Also other molecular contaminations like e.g. BaBr$^+$ beams have been observed [Kur81]. Francium beams suffer more from isobaric contaminations with molecular beams than other neutron-rich alkalis. On one hand there are more possible combinations of atom masses to create a molecule with mass 232 than e.g. one with mass 32 isobaric to heavy sodium. On the other hand the ionization potentials of the halide molecules tend to decrease for the heavier metals, thus increasing their surface ionization efficiency. With decreasing ionizer temperature these contaminations will be reduced, but a too low temperature can cause more decay losses of short-lived francium isotopes. An individual optimization of the ionizer temperature and work function for sufficiently fast release and low contamination has to be made. To avoid excessive amounts of fluoride beams, care has to be taken to choose a tantalum container with very low fluorine contamination.

---

[27]Note that for this application there is no extreme mass resolution needed, but one can profit from the fact that two consecutive separation stages can provide a much better suppression of scattered ions and beam halos.

[28]The error is relatively large due to an unknown fraction of the beam which might have missed the tape and was not transported away after each measurement cycle.

**Comparison**

Figure 4.12.1 shows a comparison of the francium yields at different facilities. The experimental details are given in table 4.12.2.
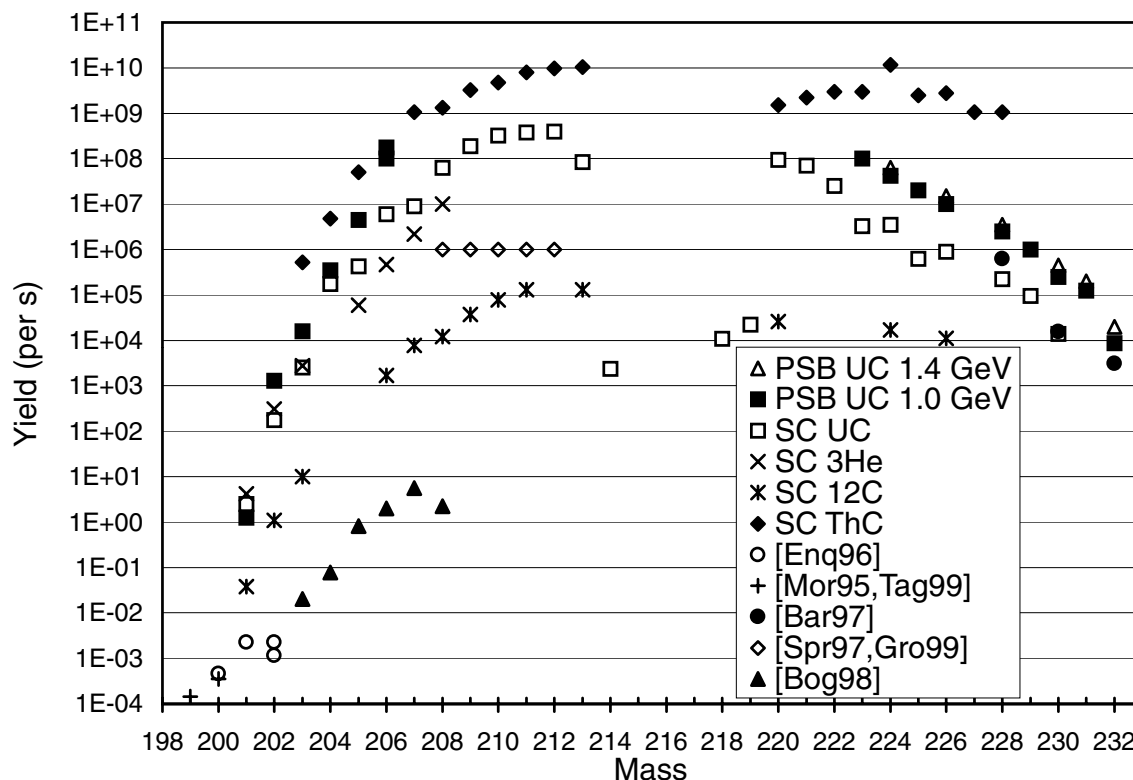


Figure 4.12.1.: Comparison of francium yields, see table 4.12.2 for experimental details of each curve.

The CERN synchro-cyclotron provided also ions heavier than protons: $^3$He, $^{12}$C, etc. [Klu86]. Thick target yield ratios for the production of different isotopes with p, $^3$He and $^{12}$C beams are reported in [Bjø81]. $^3$He beams could provide more intense beams of neutron-deficient francium isotopes, but for very neutron-rich ones no data were reported. In the studied mass range ($A \leq 229$) the use of $^{12}$C beams gave in fact lower yields for most nuclides (normalized to the same beam current), but it has to be kept in mind that the 1 GeV $^{12}$C beams were completely stopped in the front part of the target, thus reducing the effective target thickness considerably. Unfortunately no data is available for the region where an advantage for the heavy-ion projectiles is expected ($A > 230$).

The "hole" in the yield curve for masses 214 to 219 is due to the large decay losses of the short-lived nuclei (21 ms down to 90 ns). Their yields could be improved with a "faster" target, but presently there is no particular request for such beams. These isotopes are normally produced and studied as members of an alpha decay chain (see e.g. [Lia96]).

For better comparison the yields quoted in ref. [Bar97] were scaled from the typical proton current at IRIS (80 nA) to that of ISOLDE (2500 nA). Taking into account the differing target thickness and the "normal" fluctuation between different targets, the yields of IRIS and ISOLDE PSB are consistent.

For very neutron-rich francium isotopes from a UC$_x$/graphite target the ISOLDE PSB yields (filled squares in figure 4.12.1) are obviously higher than those reported from the ISOLDE SC (600 MeV protons, empty squares) [SCyie, Aud86]. Even when considering the larger target thickness, there remains an additional gain by about a factor of two which can be due to a cross-section increase

Table 4.12.2.: Production of francium isotopes at different RIB facilities.

| Ref. | Facility | Proj. | $E/A$ (MeV) | $\bar{I}$ (pnA) | Target | $\rho$ (g/cm$^2$) | Comm. |
|---|---|---|---|---|---|---|---|
| PSB UC | ISOLDE | p | 1400 | 2500 | U | 50 | NbSI |
| PSB UC | ISOLDE | p | 1000 | 2500 | U | 50 | NbSI |
| SC UC | ISOLDE | p | 600 | 2500 | U | 13 | WSI |
| SC 3He | ISOLDE | $^3$He | 910 | 500 | U | 13 | WSI |
| SC 12C | ISOLDE | $^{12}$C | 1000 | 100 | U | 4 | WSI |
| SC ThC | ISOLDE | p | 600 | 2500 | Th | 54 | WSI |
| [Bar97] | IRIS | p | 1000 | (2500) | U | 10 | scaled! |
| [Spr97, Gro99] | Stony Brook | $^{18}$O | 5.7 | 150 | Au | | |
| [Gro99] | Stony Brook | $^{19}$F | | | $^{198}$Pt | | |
| [Bog98] | VASSILISSA, JINR | $^{35}$Cl | 5.0-6.2 | 50 | $^{175}$Lu | 0.0005 | est. |
| [Bog98] | VASSILISSA, JINR | $^{31}$P | 4.8-5.1 | 50 | $^{181}$Ta | 0.0002 | est. |
| [Enq96] | RITU, JYFL | $^{35}$Cl | 4.9-5.3 | 50 | $^{170}$Yb | 0.00035 | est. |
| [Mor95] | GARIS, RIKEN | $^{36}$Ar | 5.2 | 50 | $^{169}$Tm | 0.002 | est. |
| [Tag99] | GARIS, RIKEN | $^{36}$Ar | 6 | 160 | $^{169}$Tm | 0.00044 | est. |
| [Huy92] | LISOL | $^{20}$Ne | <12 | | Ir | 0.005 | F., SI |
| [Huy92] | LISOL | $^{32}$S | <8.8 | | Ta | 0.008 | F., SI |

when going from 600 MeV to 1 GeV. This is in agreement with the trend observed for the increase from 1.0 to 1.4 GeV proton beam energy.

Note that the most neutron-deficient francium isotopes ($^{199,200}$Fr) were discovered and studied at gas-filled recoil separators. The latter provide a high transmission ($10 - 100$ %) [Lei97]. Especially in combination with the recoil decay tagging technique they are extremely powerful for in-beam spectroscopy. The yields of ref. [Bog98] were estimated from the cross-sections given therein and from the separation efficiency and primary beam current of ref. [Yer94]. The yields of the other facilities were estimated from the number of detected events. Light francium isotopes ($^{202,204,206}$Fr) were also studied in fusion-evaporation reactions at LISOL [Huy92], but no yields are quoted.

## Prospects

It would be very interesting to extend the study of the francium isotopes to higher masses $A \geq 234$ (see section 5.4 for a discussion of the physics motivation). However, the production cross-sections for proton-induced spallation drop rapidly for the heaviest francium isotopes. With 92 protons and 146 neutrons in the target nucleus it is already obvious from simple stochastic considerations[29] that it is very improbable that five protons are lost while all or most neutrons remain in the residual nucleus. Taking into account that neutrons are more easily evaporated due to the missing Coulomb barrier, the realistic ratio gets even more unfavorable.

It is not principally excluded that even nuclei with more neutrons than the target are produced at ISOLDE. In fact $^{207}$Hg has been observed at ISOLDE, produced by proton interaction with a long lead target [Jon81]. Obviously it is a thick-target effect, i.e. a spallation neutron produced in the front part of the target induces a (n,2p) reaction in the same target. However, the probability for such reactions is significantly reduced in comparison with the direct (p,$x$n$y$p) reactions[30]. Note

---

[29]Note that some models tend to overestimate the production cross-sections for very neutron-rich nuclei close to uranium (see e.g. [Sch98a]).

[30]An alternative process where a pion is emitted, i.e. a reaction like $^{208}$Pb(p,2p$\pi^+$)$^{207}$Hg occurs, would have still smaller cross-sections.

that the $^{138m}$Cs seen from the LaC$_x$/graphite target (see section 4.11) could also be created by spallation of some target impurity (higher lanthanides) or of tantalum from the target container.

To further increase the yields of heavy francium isotopes obviously the $N/Z$ ratio of the system "target+projectile" has to be increased. In principle neutron-rich isotopes of a higher actinide element (plutonium or curium) could be used as target. However, these elements are more volatile than uranium or thorium. Thus, the target could only be run at a reduced temperature which increases the delay and the decay losses. Moreover sufficient amounts of these isotopes are difficult to handle and even more difficult to obtain[31]. Only at the IRIS facility in Gatchina a test with a 0.2 mg curium (mainly $^{244}$Cm) target was made for the production of $^{220}$Fr [Bol92] and at the Brookhaven National Laboratory targets with $0.1 - 0.2$ g of $^{244}$Pu were used to produce the new neutron-rich isotope $^{242}$U by a (n,2pn) reaction [Hau79].

Since it is difficult to increase the neutron number of the target, a projectile has to be chosen which carries along some neutrons. An interesting approach would be the use of direct (n,$x$p) reactions with fast neutrons. This showed already to be successful for the production of several new isotopes (see e.g. [Hau76, Hau77, Shu93a, Shu93b]). Mirzadeh et al. [Mir83] have shown that the cross-section for $^{238}$U(n,2pn)$^{236}$Th ($E_n = 30 - 160$ MeV) is fifty times larger than for $^{238}$U(p,3p)$^{236}$Th ($E_p = 100$ MeV). At least part of this advantage is expected to persist also for more evaporated protons, e.g. for the production of $^{234}$Fr via $^{238}$U(n,5p)$^{234}$Fr. Note that the reaction Q-value is $-33$ MeV, i.e. high energy neutrons (for maximum cross-sections at least some MeV above the reaction Q-value) are required. As proposed by Nolen [Nolen] these could be obtained from the breakup of a fast deuteron beam in a light (Be) converter target. The production cross-sections of $^{228-234}$Fr from a $^{238}$U target were calculated to be up to one order of magnitude higher with 75 MeV neutrons in comparison with 1 GeV protons [Ben99b].

However, the use of neutron-induced reactions will allow to reach in the best case[32] $^{234}$Fr. To go further out a qualitatively different reaction mechanism is needed. Fusion-evaporation reactions with stable projectiles and targets produce rather neutron-deficient nuclides and are therefore not suitable. Even the use of a radioactive neutron-rich beam together with a stable target[33] does not allow to go out far enough in this region.

With heavy-ion beams as projectiles also an alternative production mechanism can be used: multi-nucleon transfer. This was successfully applied e.g. for nuclear spectroscopy experiments of heavy radium and actinium nuclei at GSI ISOL [Gip86]. Here, moreover the problem with contaminations by molecular sidebands (XO$^+$, XF$^+$, XBr$^+$, etc.) is significantly reduced by the more selective production mechanism.

Cross-sections of multi-neutron transfer reactions between different nuclei ($^{16}$O up to $^{238}$U) and $^{238}$U were mainly studied relatively close to the Coulomb barrier ($\gtrsim 8.5\,A \cdot$ MeV) [Gua84, Tōk85, Kör86, Sou88]. Gaeggeler et al. [Gäg86, Gäg88] measured production cross-sections of multi-nucleon transfer reactions with higher actinide targets. Recently Cocks et al. performed high-spin spectroscopy of radon to thorium isotopes (e.g. $^{222-230}$Ra), using multi-nucleon transfer reactions between a $^{136}$Xe beam and a $^{232}$Th target [Coc99, Coc00]. This reaction mechanism also allows an extension to more neutron-rich isotopes, but presently the identification method is the limiting factor[34].

However, for an efficient use in a thick target ISOL facility the beam energy has to be increased considerably. In contrast to fusion-evaporation reactions multi-nucleon transfer can also be performed well above the Coulomb barrier. For example 600 MeV $^{18}$O projectiles on $^{208}$Pb were

---

[31]The practical problems (high alpha activity, etc.) could be solved, but the legal restrictions virtually exclude the use of gram amounts of transuranium elements in West European RIB facilities.

[32]For additional $\pi^+$ emission even considerably higher neutron energies would be required.

[33]The "wild idea" of fusing radioactive projectiles with radioactive target nuclides is discussed in appendix B.13.

[34]The experiments are performed in-beam and at least two gamma transitions have to be known to identify the individual isotopes.

used to produce the new isotope $^{209}$Hg [Zha98b, Zha98a]. The cross-section ($\approx 4$ $\mu$barn) is two orders of magnitude higher compared with 1000 $A\cdot$MeV $^{238}$U fragmentation on a beryllium target ($\approx 30$ nbarn) [Pfü98]. Unfortunately at high beam energies $\gtrsim 30\,A\cdot$MeV no data exist on multi-nucleon transfer reactions on actinide targets.

**Experimental possibilities**

Since the move of ISOLDE from the synchrocyclotron (SC) to the proton synchrotron booster (PSB) only protons of 1 GeV were provided. In principle also a deuteron beam with 980 MeV energy and some $10^{12}$ particles per pulse could be delivered by the PSB [Schin]. This beam would be only one order of magnitude less intense than the proton beam and an increased production cross-section for very neutron-rich isotopes could compensate this drawback. On the other hand the efficiency of high-energy neutron-induced reactions could be tested at ISOLDE also by placing e.g. a tungsten block as converter in front of the target and using the "beam" from W spallation neutrons. Probably this "simulation" requires less effort than the tuning of the PSB accelerator complex to deuterons.

The PSB is also able to accelerate heavy ions. Presently only $^{208}$Pb is used to feed the PS and SPS for heavy-ion experiments, but other ions could be accelerated by the LINAC 3 for injection into the PSB if they are delivered from the ion source. As the ECR ion source runs with oxygen as support gas [Hil96], a beam of oygen ions is always present. This beam could be optimized [Scriv] and accelerated with the PSB [Schin]. Thus, a $^{16}$O beam with 490 $A\cdot$MeV energy could be sent to ISOLDE, however with an intensity ($\sim 3$ pnA) which is three orders of magnitude smaller compared with the proton beam [Hil89]. With this handicap the possible advantage of a $^{16}$O beam over protons remains restricted to very few cases. Thus, it is presently not very promising to make the effort of tuning LINAC 3 and PSB to an oxygen beam.

Much stronger light ion beams will be provided at the SPIRAL ISOL facility [Put97]. A beam intensity of up to 3 $\mu$A for $^{12}$C, $^{16}$O and $^{20}$Ne at 95 $A\cdot$MeV is the goal of the THI project (high intensity operation of the GANIL cyclotrons) [Bar99]. Even when considering the reduced effective target thickness at SPIRAL[35] the luminosity will still be two orders of magnitude larger at GANIL.

Since moreover the cross-sections for multi-nucleon transfer reactions are expected to drop towards high beam energies at present the most promising ISOL facility to produce very neutron-rich francium ($A \gtrsim 234$) isotopes is probably SPIRAL.

## 4.13.   A universal RIB facility?

From the yields shown in this chapter it is obvious that a large choice of nuclides can be provided by an ISOLDE-like facility. The availability of a universal RIB facility which can provide intense beams of all short-lived radioactive isotopes from $^{6}$He to the actinides has clear advantages for many experiments. Systematic studies can be done over a wide range of the chart of nuclides without moving expensive and complicated experimental equipment like mass spectrometers, large detector arrays, laser spectroscopy set-ups etc. from one facility to another. ISOLDE is the best example for such a multi-use and multi-user facility which allows to switch between different beams within seconds to days.

However, from the yield comparisons it is also seen that in certain mass regions the ISOLDE beams are outrun in intensity and/or purity by other, more specialized, facilities. In fact for most existing and planned RIB facilities a certain region can be identified where the given method provides

---

[35]With a standard UC$_x$/graphite target material a range of about 3.6 g/cm$^2$ is obtained with a 95 $A\cdot$MeV $^{16}$O beam at GANIL instead of 45 g/cm$^2$ with a 490 $A\cdot$MeV $^{16}$O beam at ISOLDE.

better beams than all others. It should be kept in mind that the choice of the presented nuclides was already biased to elements which are more or less suitable for separation at ISOLDE. Taking also into account the refractory elements underlines even more the importance of complementary techniques: fragment separators and IGISOL facilities. A simple look at important publications of the last years shows that it is just this diversity of smaller facilities which makes the field of radioactive ion beams so lively.

Especially when dealing with high beam intensities and thus high activities one should separate the desired nuclides from all contaminants *as early as possible*. The best way is the choice of a selective production mechanism which avoids the production of disturbing isobars. The large width of the isobaric distribution in high energy proton induced reactions can give surprising effects: e.g. when an isotope close to the proton drip-line is searched ($^{97}$Cd), but a beta-delayed neutron emitter is found ($^{97}$Rb) (see section 4.8), or when studying the very neutron-rich francium isotopes (see section 5.4) and the most intense gamma lines are from a nuclide decaying by EC.

A selective production mechanism on the neutron-deficient side is fusion-evaporation. Unfortunately it is not compatible to thick targets due to a small width of the excitation function. With the available technology of driver beams and targets it is not possible to reach with fusion-evaporation the high secondary beam intensities necessary for many experiments of post-accelerated beams.

Neutron-induced fission is a selective mechanism only populating neutron-rich nuclides in the medium mass region. However, thermal neutrons are best provided by a reactor. This type of "primary accelerator" cannot produce other beams. A reactor-based RIB facility is therefore clearly specialized for the production of neutron-rich medium-mass nuclides. Even with the most intense radioactive beams, many typical experiments on the neutron-rich side (fusion to superheavy elements, etc.) will require beam times which are rather in the range of weeks or months than days. This time scale is ideally adapted to the "macroscopic duty cycle" of a high-flux reactor ($\approx$50 days).

Again it has to be emphasized that an important part of the selectivity can and should be guaranteed already in the production step. Clearly this requires to choose a selective mechanism which is just the extreme opposite to a universal one. Thus one unique ISOL facility which relies on a single primary beam (high energy protons) can provide a large variety of beams, but will remain for some elements intrinsically limited in beam purity[36]. A facility which allows to adapt the reaction mechanism to the individual isotopes is as versatile but provides moreover the important selectivity in the first step of the ISOL process. For the same reason a division into several, specialized facilities makes sense. Moreover is can never be excluded completely that an unforeseeable problem occurs (complete failure of the target changing mechanism, vacuum leak, insulator breakdown, etc.). In the worst case a long delay (months) has to be accepted before the radiation level is sufficiently decreased and a repair becomes possible. This would severely hit the user community if it has to rely on a single RIB facility.

---

[36]The idea to have one unique ("ISOSPIN") facility which should be able to provide intense and pure beams all over the chart of nuclides sounds "typically American". It should be kept in mind that large-scale projects where the size starts to be a property for its own sake carry the risk to add another superlative to the impressive series of the world-largest particle collider (SSC), the world-strongest neutron source (ANS), the most intense proton accelerator (APT), etc.

# 5. Nuclear physics results

## 5.1. $^{12}$Be decay

The availability of a pure and relatively intense ISOL beam of $^{12}$Be gives a good opportunity to study its decay characteristics.

$^{12}$Be has a $Q_\beta$ value of 11.71 MeV. The channel for beta-delayed neutron emission can open at 3.37 MeV excitation energy, thus leaving a rather large window of 8.34 MeV for $\beta$n decay. Detecting both, the betas and the beta-delayed neutrons, allows to deduce the probability of beta-delayed neutron emission $P_n$.
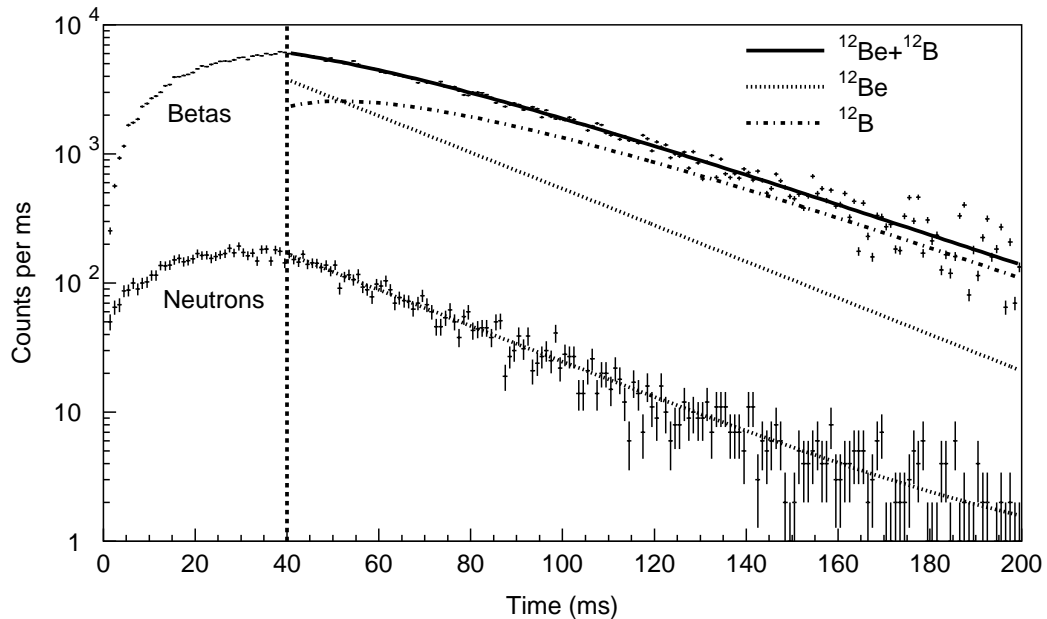


Figure 5.1.1.: Grow-in and decay curve of $^{12}$Be.

Figure 5.1.1 shows a multiscaling time spectrum of the $^{12}$Be decay which was taken within 20 min. The beam gate was closed 40 ms after each proton beam impact. The neutrons were detected with the Mainz neutron long counter. The spectrum can be fitted with a single exponential decay. Any neutron emission in the beta-decay of the daughter $^{12}$B as well as a $\beta$2n-decay of $^{12}$Be are excluded from the Q value.

The betas were detected with a thin plastic scintillator. For the fit of the beta decay curve the half-live of the daughter $^{12}$B, which is very precisely known (20.20(2) ms), was kept constant. No boron beam is released directly from the source (the surface ionization of boron is negligible with an ionization potential of 8.3 eV) but the $^{12}$B produced by $^{12}$Be decay in the grow-in phase has to be taken into account. The fits were done with the maximum likelihood method to account correctly for the Poisson distribution of the low statistics events [Jad96a].

The deduced half-lifes of the neutron and the beta-decay curves are in agreement and give in average: 21.34(23) ms. This is shorter than some older values in literature: 24.4(30) ms [Alb78], 24(1) ms [Duf84], 45(29) ms [Ree91] and 26.1(24) ms [Kel94], but in good agreement with two other literature values: 21.3(22) [Cur86] and 21.3(1) [Aud97].

The efficiency ratios of the neutron and beta counters were calibrated on-line with several neutron emitters of known $P_n$ values. Since the alignment of these weak ion beams cannot be checked directly with a scanner or Faraday cup, a systematic error arises due to differences in the effective solid angle of the detectors to a possibly shifted implantation position. While this effect is small for the neutron detector it can affect the efficiency for beta detection considerably. An error of about 25 % (relative) for the $P_n$ value was derived from the different calibration measurements including the response to various beta and neutron energies of the calibration isotopes. This is certainly a pessimistic estimate for the mainly systematic uncertainty and could still be considerably reduced with an enlarged set of calibration data and a careful study of the effective detector efficiencies by Monte Carlo simulations.

The obtained value ($P_n = 0.48^{+0.12}_{-0.10}$ %) is remarkably low compared with the large energy window available for neutron emission. It is in agreement with the upper limits 1 % from [Alb78, Duf84] and the value reported in [Aud97]: 0.52(9) %. The former value of Reeder et al. [Ree91] was higher, but is consistent within the error: 0.9(4) %. An older measurement gave a much higher value: $7.0^{+7.0}_{-3.5}$ % [Pos65], but probably the beam was contaminated with other neutron emitters[1]. Meanwhile the measurement at ISOLDE was repeated and gave a more precise[2] value of $P_n = 0.50(3)$ % [Ber99].
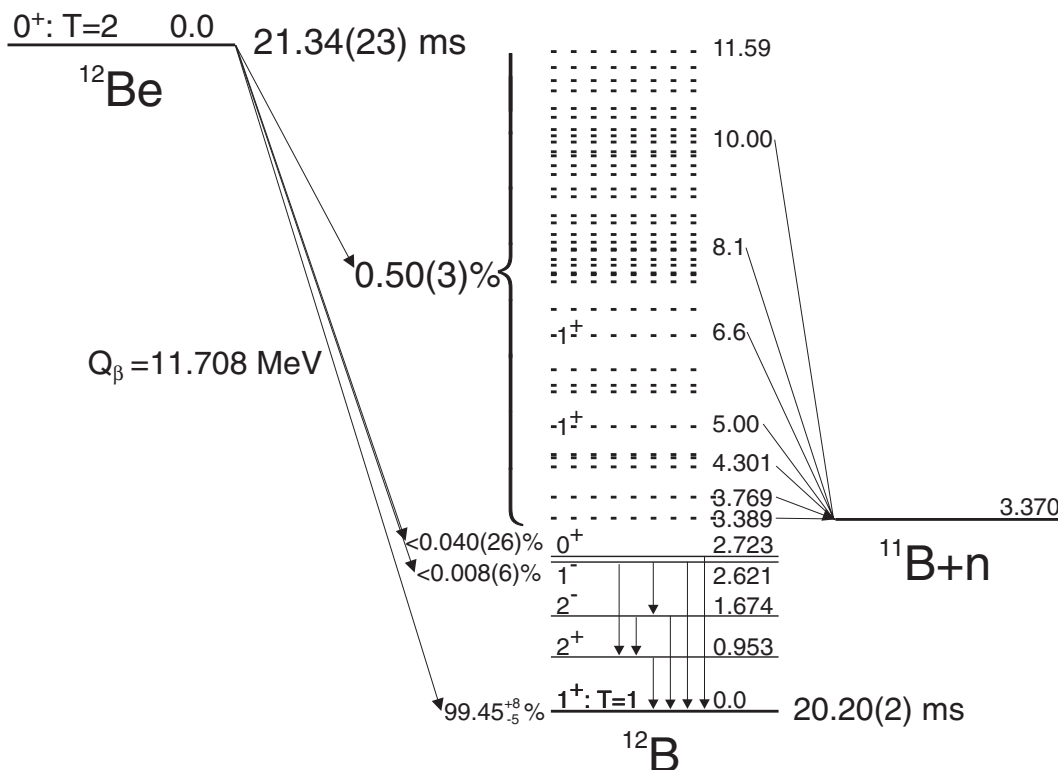


Figure 5.1.2.: Decay scheme of $^{12}Be$ from this work and ref. [AS90, Kel94, Ber99].

Combining our value for the half-life with the $P_n$ value from [Ber99] and the upper limits for transitions to gamma emitting levels [Kel94] gives for the decay to the ground state of $^{12}B$ an

---

[1]Also the quoted half-life is quite off from all other values: 11.4(5) ms.

[2]It should be noted that in the latter measurement no systematic error was included to account for possible variations of the beta detection efficiency.

improved value: $\log ft = 3.79(1)$[3]. Suzuki and Otsuka explain this relatively high value by a strong breaking (about 65 %) of the neutron $p$-shell closure [Suz97].

Figure 5.1.2 summarizes the present knowledge on the decay scheme of $^{12}$Be. The assumption that the complete branch for beta-delayed neutron emission goes to a single level moreover allows to estimate lower limits for the $\log ft$ values to other levels. For the allowed transitions to the $1^+$ levels at 5.00 MeV and at 6.6 MeV follows $\log ft > 4.9$ and $\log ft > 4.3$ respectively[4]. The corresponding upper limits for the Gamow-Teller strength $(B(GT) = 6146.6/ft)$ are 0.076 for the 5.00 MeV state and 0.27 for that at 6.6 MeV. They are in agreement with the predictions from ref. [Suz97] (see figure 9 therein).

Also the observed ring ratio (see appendix B.11.1) indicates a high kinetic energy of the neutrons: $E_n \gtrsim 1$ MeV. This would be consistent with a neutron emission from the discussed levels ($E_n = 1.5$ MeV and 3.0 MeV respectively).

### Prospects

In our set-up the neutron energy could not be measured accurately. With a different set-up ($^3$He ionization chambers or a time-of-flight arrangement) it will be possible to determine the populated neutron-emitting levels in $^{12}$B. Together with a detailed $\beta\gamma$ spectroscopy this should allow to monitor the beta strength distribution over a rather large energy range and to compare it with theoretical predictions, e.g. [Suz97, Suz98].

## 5.2.   Nuclear spectroscopy of heavy copper isotopes

### 5.2.1.   Magnetic moments of $^{70g}$Cu and $^{70m}$Cu

In section 3.5.2 it was shown that $^{70g}$Cu and $^{70m}$Cu can be separated by scanning the laser frequency over the hyperfine structure. In fact the magnetic moments of both isomers were not known before. The hyperfine splitting which was experimentally observed in our experiment can be used to derive a rough estimation of the magnetic moments.

As discussed before the linear relationship (3.5.10) can be used with $J = 1/2$:

$$\mu(^{70}\text{Cu}) = \mu(^{65}\text{Cu}) \cdot \frac{A(^{70}\text{Cu}) \cdot I(^{70}\text{Cu})}{A(^{65}\text{Cu}) \cdot I(^{65}\text{Cu})} = \mu(^{65}\text{Cu}) \cdot \frac{\Delta\nu_{\text{HFS}}(^{70}\text{Cu})}{A(^{65}\text{Cu}) \cdot I(^{65}\text{Cu})} \cdot \frac{I(^{70}\text{Cu})}{I(^{70}\text{Cu}) + \frac{1}{2}}. \quad (5.2.1)$$

With the magnetic dipole coupling constant $A(^{65}\text{Cu}) = 6284.39$ MHz [Rad85], the magnetic moment $\mu(^{65}\text{Cu}) = 2.38167(25)\,\mu_{\text{N}}$ [Fir96] and the spin $I(^{65}\text{Cu}) = 3/2$ one finds:

$$\mu(^{70g}\text{Cu}) = (+)1.8(3)\,\mu_{\text{N}}, \quad (5.2.2)$$

$$|\mu(^{70m}\text{Cu})| = 1.2(3)\,\mu_{\text{N}}. \quad (5.2.3)$$

Note that for $^{70m}$Cu the result depends slightly on the nuclear spin varying between 3 and 6 (see figure 5.2.1). The sign of the magnetic moment of $^{70g}$Cu was deduced tentatively from the intensity ratio[5] of the subpeaks in figure 3.5.1, while for $^{70m}$Cu the quality of the experimental data does not allow to deduce the sign of its magnetic moment.

---

[3]Calculated by scaling the $\log ft$ value from ref. [AS90].
[4]Calculated from a slight extrapolation of the $\log f$ values tabulated in [Gov71].
[5]In case of a negative magnetic moment the right subpeak should be more intense.

**"Theoretical" estimation**

It is known that $^{68}$Ni can be well described as a semi-double-magic nucleus with a closed proton shell ($Z = 28$) and a closed neutron subshell ($Z = 40$). Therefore one could try to describe the low-lying states of the odd-odd nucleus $^{70}$Cu as an inert core plus a single valence proton coupled to a single valence neutron.

Obviously the 29th proton will be in a $p_{3/2}$ orbital [Fir96]. The first empty neutron orbital above the $Z = 40$ subshell closure is a $g_{9/2}$. The coupling of such a neutron with the proton gives a nuclear spin of: $3 = |j_p - j_n| \leq I \leq |j_p + j_n| = 6$. This configuration is expected for the isomeric state $^{70m}$Cu. However, to create the $1^+$ ground state $^{70g}$Cu one needs to couple a $p_{1/2}$ neutron to the $p_{3/2}$ proton. This will give $I = |j_p - j_n| = 1$ according to the strong Nordheim rule [Nor51]. To have a half-empty $p_{1/2}$ orbital one pair of neutrons has to be in the $g_{9/2}$ orbitals[6].

In a first approximation one can neglect the proton-neutron interaction and use the addition theorem to estimate the g-factor[7] of the two-particle state $(j_p, j_n)I$ from the single particle g-factors of the valence proton and valence neutron [Cas90]:

$$g = \frac{1}{2}(g(p) + g(n)) + \frac{1}{2}\frac{j_p(j_p + 1) - j_n(j_n + 1)}{I(I + 1)}(g(p) - g(n)). \tag{5.2.4}$$

The g-factors of the single particle states $g(p)$ and $g(n)$ are given by:

$$g(p,n) = g_L^{eff} \pm \frac{g_S^{eff} - g_L^{eff}}{2l_{p,n} + 1}, \text{ for } j_{p,n} = l_{p,n} \pm \frac{1}{2}. \tag{5.2.5}$$

$g_L^{eff}$ and $g_S^{eff}$ are the effective g-factors of the valence nucleons in the nucleus. The orbital magnetization comes entirely from the proton, i.e.:

$$g_L^{eff}(p) = 1, \text{ and } g_L^{eff}(n) = 0. \tag{5.2.6}$$

The effective spin g-factors can be written as multiple of the free nucleon g-factors:

$$\begin{aligned} g_S^{eff}(p) &= \tilde{g}(p) \cdot g_S^{free}(p) &= \tilde{g}(p)\, 5.587\,\mu_N, \\ g_S^{eff}(n) &= \tilde{g}(n) \cdot g_S^{free}(n) &= -\tilde{g}(n)\, 3.826\,\mu_N. \end{aligned} \tag{5.2.7}$$

In a first approximation one can set the empirical quenching factors $\tilde{g}$ to unity, i.e. use directly the free nucleon g-factors. This would give $\mu(^{70g}\text{Cu}) = +2.84\,\mu_N$ and $\mu(^{70m}\text{Cu}) = -4.60$ to $+1.88$ for $I = 3$ to 6 (see figure 5.2.1). Thus, the calculated value for $^{70g}$Cu is considerably larger than the measured one while for $^{70m}$Cu no statement can be made without knowing the spin.

Clearly the magnetic moment of nucleons changes when they are bound in a heavy nucleus. Empirically it was found that a quenching of the g-factors to about $\tilde{g} \sim 60\,\%$ often gives a better description for medium-mass and heavy nuclei [Cas90]. In fact, the quenching of the g-factor depends on a series of different contributions (meson exchange currents, etc.) which have to be added up. These contributions were calculated in detail mainly for light (e.g. around $^{16}$O and $^{40}$Ca) and heavy (around $^{208}$Pb) nuclei, see e.g. [Tow87]. In between some calculated data exist e.g. around $^{90}$Zr [Hau77, Hin97b, Joh98] and $^{132}$Sn [Sto97]. However, in the area of $^{68}$Ni such calculations are still in work [Rikov].

A better approximation than above can be achieved by fitting $\tilde{g}$ to reproduce the known magnetic moments of neighboring nuclei. All odd copper isotopes from $^{57-71}$Cu have a $3/2^-$ ground state. Their magnetic moment will be dominated by the contribution of the $p_{3/2}$ proton since the contributions of the paired neutrons mainly cancel. Table 5.2.1 shows the measured magnetic moments of $^{61-67}$Cu[8]. They are well reproduced by a shell model plus RPA (random phase approximation)

---

[6]Note that in the Nilsson diagram the $p_{1/2}$ energy exceeds that of the lowest $g_{9/2}$ orbital already at low deformation ($|\beta_2| \approx 0.1$).

[7]The gyromagnetic ratio or g-factor gives the ratio of the magnetic dipole moment $\mu$ and the nuclear spin $I$ in units of the nuclear magneton: $\mu = gI\mu_N$ with $\mu_N = e\hbar/(2m_p c) = 5.0508 \cdot 10^{-17}$ J/T.

[8]The value for $^{67}$Cu was recently measured with a sample collected with the ISOLDE RILIS (see section 4.5).

calculation [Rikov]. Therefore, the same model was used for an extrapolation to $^{69,71}$Cu. The g-factor of the $p_{3/2}$ proton in $^{70}$Cu is taken from an interpolation of the neighboring copper isotopes: $g(\pi(p_{3/2})) \approx +1.87 \, \mu_N$.

Table 5.2.1.: Measured and calculated (slanted) values for the magnetic moments of odd copper isotopes with $I^\pi = 3/2^-$ and derived g-factor quenching.

| Isotope | $^{61}$Cu | $^{63}$Cu | $^{65}$Cu | $^{67}$Cu | $^{69}$Cu | $^{71}$Cu |
|---|---|---|---|---|---|---|
| $\mu \; (\mu_N)$ | +2.14 | +2.223 | +2.382 | +2.536 | *+2.77* | *+2.84* |
| $\tilde{g}$ | 0.41 | 0.44 | 0.49 | 0.55 | 0.63 | 0.66 |
| Reference | [Fir96] | [Fir96] | [Fir96] | [Rikov] | [Rikov] | [Rikov] |

The g-factor of the $p_{1/2}$ neutron can be estimated similarly. The magnetic moment of $^{67}$Ni ($I^\pi = 1/2^-$) was recently measured at the on-line nuclear orientation facility NICOLE at ISOLDE[9] to be $+0.605 \, \mu_N$. Thus, $g(\nu(p_{1/2})) \approx +1.21 \, \mu_N$.

Magnetic moments are also known for the $9/2^+$ states of the odd zinc isotopes $^{65-71}$Zn. For $^{71m}$Zn a value of $\mu = -1.035 \, \mu_N$ was reported [Her89]. Stone proposes a slight correction to $\mu = -1.052 \, \mu_N$ [Stone]. Assuming a pure $(g_{9/2})^3$ configuration allows to deduce the g-factor: $g(\nu(g_{9/2})) \approx -0.234 \, \mu_N$.

Combining these empirical single particle g-factors with the addition theorem gives $\mu(^{70g}$Cu$) = +2.04 \, \mu_N$ and $\mu(^{70m}$Cu$) = -3.07$ to $+1.75$ for $I = 3$ to $6$ (see figure 5.2.1).
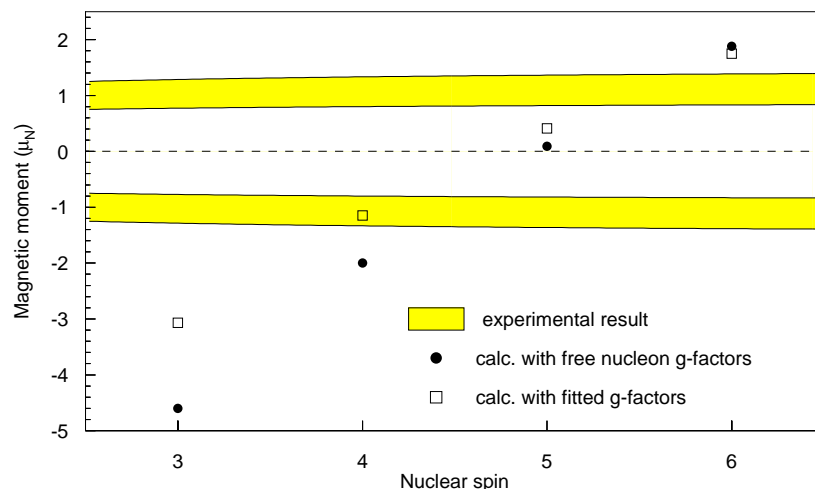


Figure 5.2.1.: Magnetic moment of $^{70m}$Cu as function of the nuclear spin. The shaded areas indicate the range consistent with our measurements. The filled circles show the values calculated with the free nucleon g-factors and the empty squares the values with the single particle g-factors fitted to the neighboring isotopes.

It is difficult to assess an empirical error for such an estimation of the magnetic moments. Around the double magic $^{16}$O and the semi-double-magic $^{90}$Zr the calculation with free nucleon g-factors can reproduce many experimental values within about 20 %. However, large deviations (up to 100 % and beyond) occur around $^{208}$Pb. The use of empirical single particle g-factors improves the results and allows to well reproduce also magnetic moments around $^{40}$Ca. However, some other cases remain which are off by more than 100 %.

---

[9]Also here the ion beam was provided from the ISOLDE RILIS.

As seen in figure 5.2.1 the magnetic moment of $^{70m}$Cu depends strongly on the nuclear spin. Thus no final conclusion can be drawn with the given accuracy of the experimental and theoretical value. Still our result supports the result from the $\beta$-decay spectroscopy [Roosb] that a nuclear spin of $3^-$ (which would be obtained with an antiparallel coupling of the proton and neutron spin) is not probable for $^{70m}$Cu. The best agreement is obtained with $I = 4$.

Although this simple model could reproduce the magnetic moment of $^{70g}$Cu within the relatively large experimental error, it should be kept in mind that several factors were not taken into account:

1. A change of the magnetic moment can occur when the core polarization gets large. For example contributions from a partial breaking of the $g_{9/2}$ neutron pair will affect the result. Results of nuclear spectroscopy experiments indicate that the $Z = 40$ subshell closure vanishes rapidly when going away from $^{68}$Ni to surrounding nuclei (see [Mue99] and references therein). Thus, also contributions of other core nucleons should be taken into account.

2. The p-n interaction is completely neglected in this independent particle model. It can also affect the magnetic moment considerably.

**Outlook**

It has been shown that a rough determination of the magnetic moment is possible by scanning the laser wavelength over the hyperfine structure of the transition. In this experiment the absolute ion yield had considerable fluctuations in time due to power fluctuations of the lasers, spatial drifts of the second harmonic beams changing the overlap area, etc. A correction for these fluctuations can be applied by simultaneously monitoring the intensity of a reference isotope (e.g. $^{65}$Cu) in a second beam-line (see figure 3.1.1). Multiple scans and a direct comparison with other known copper nuclides will allow to further increase the accuracy by about one order of magnitude. Although still far less accurate than a measurement via nuclear magnetic resonance (NMR) this method can give a valuable evidence which allows a considerable reduction of the scanning range in subsequent precise NMR experiments.

## 5.2.2.  Lifetimes and P$_n$ values of $^{73}$Cu to $^{78}$Cu

The beams of heavy copper isotopes (see section 4.5) were sent to the Mainz neutron long counter to study the emission of beta-delayed neutrons. The built-in tape transport was used to remove long-lived background after each measurement cycle. A thin plastic scintillator served for the detection of betas. Unfortunately the beta detector suffered from the electronic noise of the CVLs. Therefore the detection threshold had to be increased which lowered the detection efficiency.

Figures 5.2.2, 5.2.3 and 5.2.4 show the beta- and neutron acitivties which were registered in multiscaling mode. The neutron decay curves were fitted with a single exponential decay to determine the half-lives. The daughter nuclides (zinc) and the surface ionized isobaric background (gallium and rubidium) does not emit beta-delayed neutrons up to mass 78 [Aud97] and did not disturb these measurements. Table 5.2.2 shows the determined half-lives.

All measured lifetimes, but one, are consistent with those known from literature. The reason for the deviation in the case of $^{74}$Cu is not obvious. It could be due to a beam contamination, e.g. with molecular ions in one of the measurements. The analysis of the gamma ray decay data [Roosb] should give a final answer to this question. For $^{73}$Cu the emission of beta-delayed neutrons was observed for the first time. The deduced half-life is just between those known from literature [Aud97, Huh98]. For the heavier nuclei $^{76-78}$Cu the present data are slightly more precise than known before. As in ref. [Kra91] we did not observe any indication for beta-delayed neutron emission from $^{76m}$Cu with a reported half-life of 1.27(3) s.
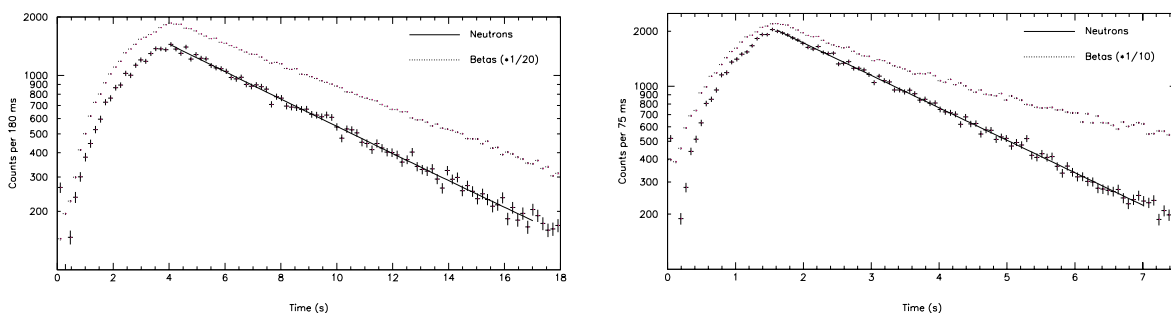
Figure 5.2.2.: Grow-in and decay curves of the beta- and neutron-activity of $^{73}$Cu (left) and $^{74}$Cu (right). The measurement time was 37 min and 25 min respectively, the beam gate was closed after 4 s ($^{73}$Cu) and 1.6 s ($^{74}$Cu).
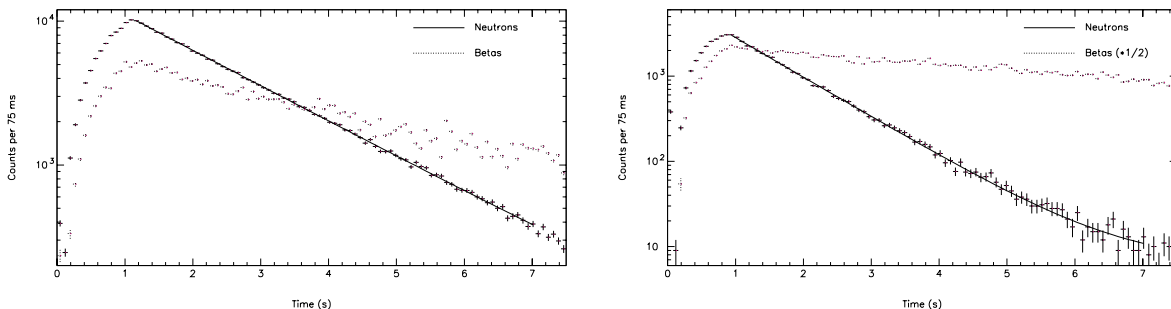


Figure 5.2.3.: Grow-in and decay curves of the beta- and neutron-activity of $^{75}$Cu (left) and $^{76}$Cu (right). The measurement time was 15 min and 20 min respectively, the beam gate was closed after 1.1 s ($^{75}$Cu) and 0.9 s ($^{76}$Cu).
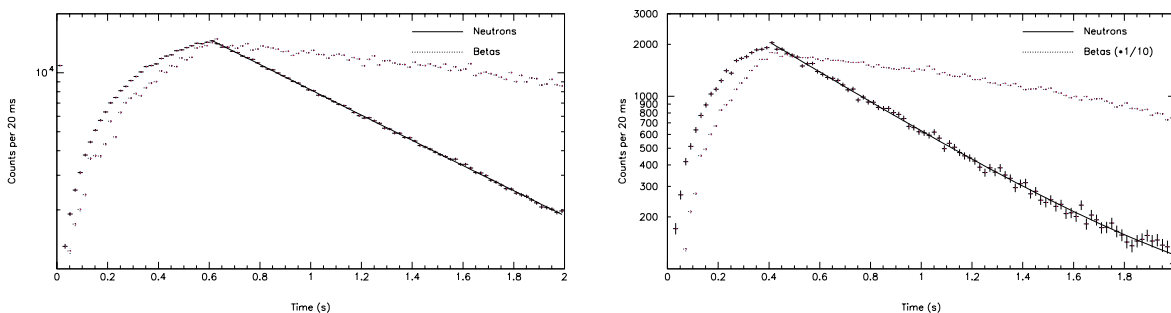


Figure 5.2.4.: Grow-in and decay curves of the beta- and neutron-activity of $^{77}$Cu (left) and $^{78}$Cu (right). The measurement time was 45 min and 67 min respectively, the beam gate was closed after 610 ms ($^{77}$Cu) and 410 ms ($^{78}$Cu).

Table 5.2.2.: Half-lives of heavy copper isotopes determined from the decay curve of the beta-delayed neutron activity.

| Isotope | $^{73}Cu$ | $^{74}Cu$ | $^{75}Cu$ | $^{76}Cu$ | $^{77}Cu$ | $^{78}Cu$ |
|---|---|---|---|---|---|---|
| $T_{1/2}$, this work | 4.22(15) s | 1.68(3) s | 1.225(7) s | 647(5) ms | 466(5) ms | 335(6) ms |
| $T_{1/2}$, literature | 3.9(3) s, 4.4(3) s | 1.594(10) s | 1.224(3) s | 641(6) ms | 469(8) ms | 342(11) ms |
| Reference | [Aud97], [Huh98] | [Kra91] | [Kra91] | [Kra91] | [Kra91] | [Kra91] |

The observed ratio of neutron- to beta-activity (see figures 5.2.2, 5.2.3 and 5.2.4) gives the relative probability for neutron emission. Note that in these figures a constant beta background was already deduced for a common representation. Beams of nuclei with known neutron branching ratio ($^{93-99}$Rb and $^{141-146}$Cs) were used for an on-line efficiency calibration of the set-up. Thus the $P_n$ values of $^{73-76}$Cu could be determined, see table 5.2.3 [10]. All given errors include a 20 % systematic error accounting for the uncertainty of the efficiency calibration and the effective solid angle of the beta detector due to possibly different positions of the beam spot when changing the settings of the mass separator.

For $^{77,78}$Cu no short-lived beta activity was observed due to the large isobaric background from gallium and long-lived contaminations on the tape. Therefore only a rough lower limit could be estimated for the $P_n$ values.

The $P_n$ values known from literature and predicted values from theory are also shown in table 5.2.3. The theoretical values calculated with the quasi-particle random phase approximation (QRPA) model (see e.g. [Möl97]), the gross theory (GT) [Tac90, Nak97] and the phenomenological Kratz-Herrmann formula (KHF) [Kra73] were taken from the compilation of Pfeiffer et al. [Pfe99]. The KHF assumes a constant beta decay strength and relates the $P_n$ value to the ratio of the energy window for neutron emission $Q_\beta - B_n$ and a "reduced energy window" $Q_\beta - E_c$ with the cut-off energy $E_c$ identical to the pairing gap: $P_n = a \left( \frac{Q_\beta - B_n}{Q_\beta - E_c} \right)^b$. The free parameters $a$ and $b$ are adapted to reproduce the known $P_n$ values for a certain range of nuclides.

Table 5.2.3.: Branching ratios for beta-delayed neutron emission of heavy copper isotopes.

| Isotope | Reference | $^{73}$Cu | $^{74}$Cu | $^{75}$Cu | $^{76}$Cu | $^{77}$Cu | $^{78}$Cu | $^{79}$Cu |
|---|---|---|---|---|---|---|---|---|
| $P_n$ (%), exp. | this work | 0.029(6) | 0.075(16) | 2.2(5) | 2.2(5) | > 10 | > 10 | |
| $P_n$ (%), exp. | [Aud97] | | | 3.5(6) | 3(2) | | | |
| $P_n$ (%), exp. | [Kra91] | | | | | | | 55(17) |
| $P_n$ (%), QRPA | [Hir92] | 0 | 0 | 0 | 0 | 0 | 0.2 | 0.2 |
| $P_n$ (%), QRPA | [Pfe99] | 0.01 | 0.2 | 3.6 | 6.7 | 30 | 45 | 43 |
| $P_n$ (%), GT | [Pfe99] | 0.03 | 0.1 | 2.5 | 2.8 | 9.5 | 12 | 23 |
| $P_n$ (%), KHF | [Pfe99] | 0.04 | 0.1 | 3.8 | 2.7 | 12 | 12 | 22 |

Our value for $^{75}$Cu is not consistent with that given in ref. [Ree85], but the deviation is within the typical "scattering range" of experimentally determined $P_n$ values, see ref. [Rud93]. Considering the precision of the experimental and theoretical values all recent theoretical predictions agree reasonably well (i.e. typically within a factor of two) with the experiments.

Of great importance for the astrophysical r-process are mainly the half-lives and $P_n$ values of the very neutron-rich isotopes $^{79}$Cu and $^{80}$Cu. Ways to improve the ISOLDE yield of the former and eventually reach also the latter were discussed in section 4.5.

## 5.3.   Decay of heavy cesium isotopes

Beta-delayed neutron activity at masses 149 to 152 had been observed already at ISOLDE SC. However, no lifetimes were measured. No information from literature is available for the lifetimes of $^{149}$Cs and $^{150}$Cs.

The yields of the heaviest cesium isotopes were monitored on several occasions by detection of beta-delayed neutrons. With the pulsed production and release and an appropriate beam gate

---

[10]The values for $^{75}$Cu and $^{76}$Cu are equal by chance.

setting moreover the lifetimes could be derived from the decay curves. However, these experiments were mainly done "parasitically" or at the end of an experimental run. Thus the experimental conditions were not always optimized. In particular the beta background accumulated on the tape was too high to allow a correct detection of the betas stemming from the $^{149}$Cs or $^{150}$Cs decays.

## 5.3.1.    Decay of $^{149}$Cs

### $\beta$n decay of $^{149}$Cs

From the decay daughter $^{149}$Ba the half-life ($T_{1/2} = 344(7)$ ms) and the branching ratio for neutron emission ($P_n = 0.43(12)$ %) are known [Fir96]. The same is true for the granddaughter $^{149}$La ($T_{1/2} = 344(7)$ ms, $P_n = 1.43(28)$ %) and the $A - 1$ daughter $^{148}$Ba ($T_{1/2} = 607(25)$ ms, $P_n = 0.4(3)$ %) and granddaughter $^{148}$La ($T_{1/2} = 1050(30)$ ms, $P_n = 1.4(3)$ %) [Rud93].

Figure 5.3.1 shows the grow-in and decay behaviour of the observed neutron activity at mass 149.



Figure 5.3.1.: Grow-in and decay behaviour of the neutron activity from the decay of $^{149}$Cs. The beam gate was closed after 100 ms. The total measurement time was 28 min.

A fit of this decay curve gives a half-life of $T_{1/2} = 112(3)$ ms. The error accounts already for possible variations of the daughter and granddaughter half-lives and neutron branching ratios within the errors quoted above[11].

Due to the low neutron branching ratios of the daughters and granddaughters the decay follows nearly a single exponential and the half-life could be determined with good precision. On the other hand these low values do not allow to determine the $P_n$ value from the ratio of filiation to the decay chains of mass 149 and 148.

Similar measurements with $^{149}$Cs beams from other targets have lower statistics, but give always a half-life of about 112 ms.

### $\beta\gamma$ decay of $^{149}$Cs

In general it cannot be excluded that the observation of a short-lived neutron activity is not due to some molecular beam contamination (see e.g. section 5.4). Therefore the decay of $^{149}$Cs was moreover studied in a $\beta\gamma$ measurement to prove the assignment of the neutron activity. The latter

---

[11]The energy window for two-neutron emission is rather small ($Q_{2\beta n} \approx 1.3$ MeV) and justifies to neglect this decay mode in the fit (i.e. $P_{2n} \equiv 0$).

was done with a 50 g/cm$^2$ UC/graphite target and niobium surface ionizer. The used detection set-up is described in [Wei99].

No gamma decay information is available for $^{149}$Cs, $^{149}$Ba and $^{149}$La. A nuclear spectroscopy experiment at the masses 149 to 152 had been performed at TRISTAN and some results were mentioned in an abstract [Mac87], but no publication is available. The $\beta$n decay can also populate excited levels in the $_{Z-1}^{A-1}$X daughter nucleus. Therefore the gamma spectrum was first analysed for known transitions in $^{148}$Ba [Hil86, Urb97]. Indeed the 141.7 keV $2^+\rightarrow0^+$ and the 281.4 keV $4^+\rightarrow2^+$ transitions are found among the strong lines of the gamma spectrum. Figure 5.3.2 shows the time behaviour of the former. A half-life of 114(16) ms can be deduced which is fully consistent with the observed half-life of the neutron activity. The 281 keV line was too weak for a reasonable fit, but shows a similar decay behaviour.
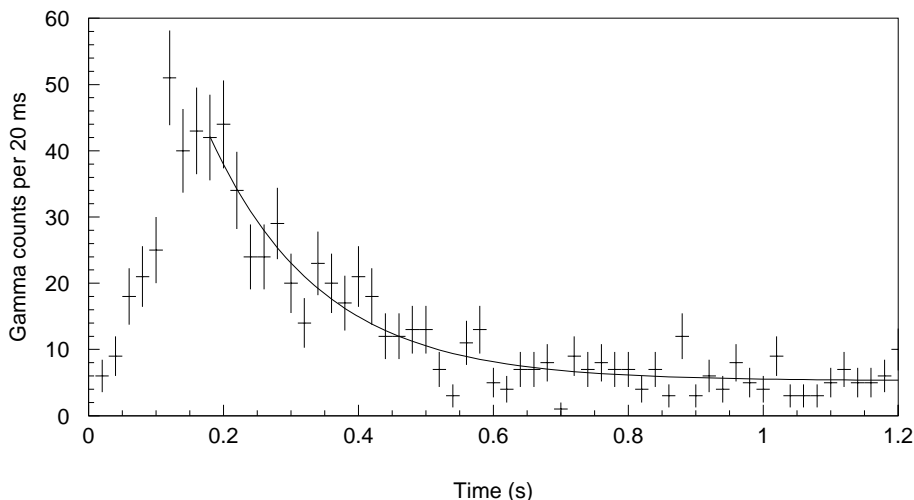


Figure 5.3.2.: Grow-in and decay behaviour of the 142 keV line from the $\beta\gamma$ decay of $^{149}$Cs. The beam gate was closed after 155 ms. The measurement time was 2 h.

Several other lines were found which could be assigned to transitions in $^{149}$Ba or the decay of the daughter nuclei $^{149}$Ba and $^{149}$La. The detailed evaluation is still under way, but the observed intensities of the transitions in $^{148}$Ba indicates a markable branching ratio for beta-delayed neutron emission. The complete evaluation of the intensities of the daughter activities should allow to deduce a value for $P_{\rm n}$.

It can be concluded that the decay of $^{149}$Cs was clearly identified from the time behaviour of the neutrons and gamma rays. At least the major part of the neutron activity consists indeed of $^{149}$Cs. Therefore the half-life of 112(3) ms is adopted for the latter.

## 5.3.2.   Decay of $^{150}$Cs

The decay of $^{150}$Cs was also studied with the Mainz neutron long counter set-up. Obviously the statistics is worse than in the case of $^{149}$Cs. Moreover the daughter $^{150}$Ba has an unknown branching ratio for beta-delayed neutron emission and an only roughly known half-life ($T_{1/2} \approx 0.3$ s).

Figure 5.3.3 shows the grow-in and decay behaviour of the observed neutron activity at mass 150.

The statistics of this decay data is not sufficient for a completely free fit (i.e. free lifetimes and neutron branching ratios for $^{150}$Cs and $^{150}$Ba). Therefore the data of the latter had to be fixed. However, the results of the fit depend strongly on the used parameters[12]. Varying $T_{1/2}(^{150}$Ba)

---

[12]Again the branching ratio for $\beta$2n was arbitrarily set to zero. This assumption is justified by the relatively low $Q_{2\beta{\rm n}}$ of about 2.8 MeV and the fact that a small $\beta$2n branch (some %) would not affect the fitted half-life.
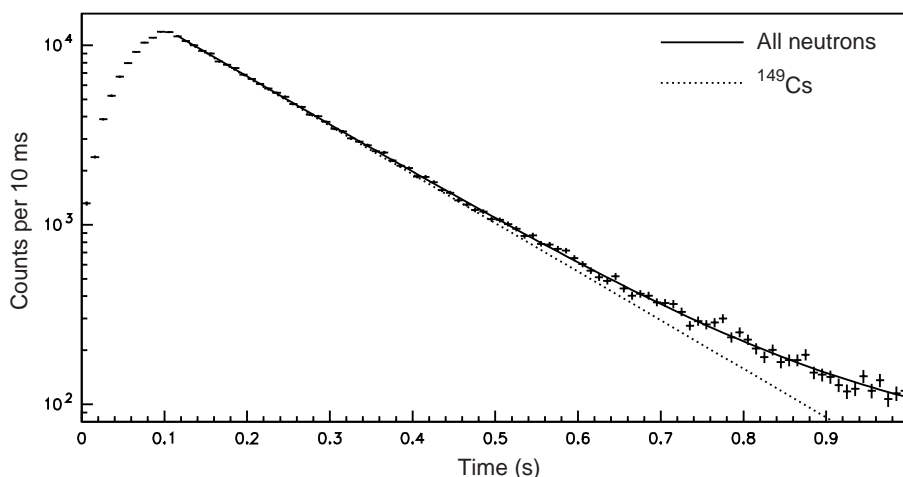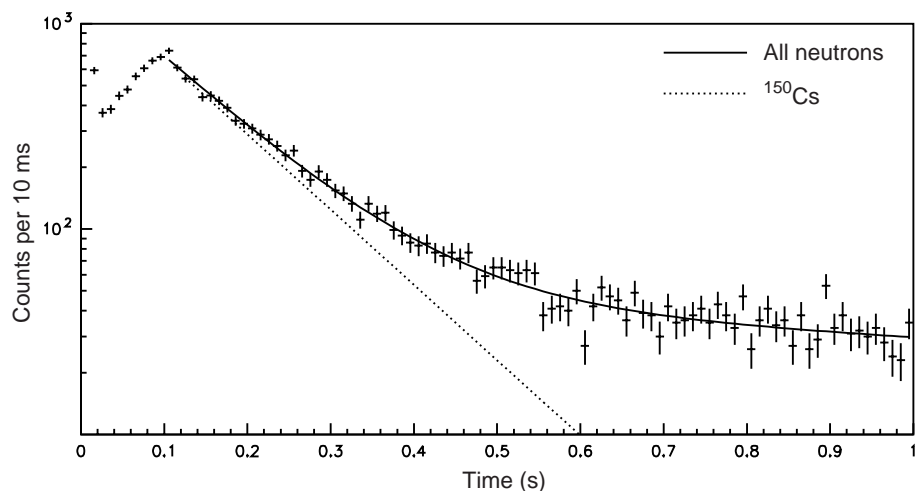
Figure 5.3.3.: Grow-in and decay behaviour of the neutron activity from the decay of $^{150}$Cs. The beam gate was closed after 100 ms. The measurement time was 65 min.

from 250 ms to 350 ms and $P_n(^{150}$Ba) from 0.1 % to 10 % gives $T_{1/2}(^{150}$Cs)=82(7) ms, but the resulting $P_n$ value is quite uncertain. Most theoretical predictions for $P_n(^{150}$Ba) are around 1 % [Pfe99]. Fixing $P_n(^{150}$Ba) to this ratio one can deduce a rough value of $P_n(^{150}$Cs) $\approx$ 20(10) %.

Note that the obtained yield for $^{150}$Cs would be sufficient to perform also $\beta\gamma$ spectroscopy. Within few shifts of beam time it should be possible to identify at least the most intense lines (e.g. the $2^+ \rightarrow 0^+$ and $4^+ \rightarrow 2^+$ transitions). Thus, with a gating on two or three known gamma lines, the available high-spin spectroscopy data (e.g. from spontaneous fission of $^{248}$Cm [Urb97]) could also be analysed for $^{150}$Ba. Moreover, such a gamma ray measurement would allow to separate the $^{150}$Cs activity from $^{150}$Ba and other daughters. Thus the lifetimes and neutron branching ratios could be determined with better precision.

## 5.3.3.   Comparison

Table 5.3.1 shows for the heavy cesium isotopes a comparison of measured half-lives and theoretical predictions. For a better overview also the known values for $^{145-148}$Cs were included. The different models were already explained in section 5.2.2.

Table 5.3.1.: Comparison of measured half-lives of heavy cesium isotopes with theoretical predictions.

| Isotope | Model | Reference | $^{145}$Cs | $^{146}$Cs | $^{147}$Cs | $^{148}$Cs | $^{149}$Cs | $^{150}$Cs |
|---------|-------|-----------|------------|------------|------------|------------|------------|------------|
| $T_{1/2}$ (ms) | exp. | this work |        |        |        |        | 112(3) | 82(7) |
| $T_{1/2}$ (ms) | exp. | [Aud97] | 582(6) | 323(6) | 225(5) | 158(7) |        |        |
| $T_{1/2}$ (ms) | micr. | [Kla84] |        |        |        |        | 127 | 85 |
| $T_{1/2}$ (ms) | QRPA | [Pfe99] | 382 | 656 | 193 | 157 | 200 | 169 |
| $T_{1/2}$ (ms) | GT | [Pfe99] | 1079 | 1075 | 457 | 545 | 363 | 295 |
| $T_{1/2}$ (ms) | KHF | [Pfe99] | 436 | 381 | 206 | 207 | 172 | 123 |

It is evident from the table that the older microscopic theory of Klapdor et al. is able to reproduce the experimental half-lives of the heaviest cesium isotopes astonishingly well while the modern

theories overestimate them systematically. To explain the reason for this failure more experimental data has to be collected: a directly measured mass will reduce the uncertainties in the $Q_\beta$ value and a measured $P_n$ value plus possibly observed gamma rays can give an indication on the Gamow Teller strength distribution. With this additional information the mentioned models could be refined.

The cesium isotopes are not as predestined for a direct test of individual model parameters as the nuclei close to filled proton shells (cobalt, nickel, indium, tin, etc.). However, the experimental conditions allow to reach very far out and provide a good testing ground for the general model behaviour far from stability.


## 5.4.   Beta-decay of heavy francium isotopes

### 5.4.1.   Decay of $^{232}$Fr

$^{232}$Fr was first identified at the IRIS facility in Gatchina [Mez90]. Only one gamma ray with 125 keV was reported. The half-life was measured to be 5(1) s. The $Q_\beta$-value of $^{232}$Fr is estimated to be 5.55(74) MeV [Aud97], thus opening a rather large window for population of higher levels in $^{232}$Ra. The ground state spin of $^{232}$Fr is unknown.

During the change of the RILIS from copper to cadmium (see above) we used the available nuclear spectroscopy set-ups to look for the heaviest francium isotopes. This test was performed with a standard UC$_x$/graphite target and niobium surface ionizer. For $^{232}$Fr a 1 h measurement was made at the Leuven $\beta\gamma\gamma$ set-up described in ref. [Wei99]. Five consecutive pulses with $3.1 \cdot 10^{13}$ protons each were used per 19.2 s supercycle. 15 ms after each pulse the beam gate was opened for 1.15 s to collect the activity. It followed an undisturbed decay period of 11 s, then the tape was transported to remove the remaining activity and the next cycle started. In a second experiment the set-up was complemented by a small beta telescope made from plastic scintillators. A 20 min measurement was done with four consecutive proton pulses per supercycle.

The obtained gamma spectrum shows a contamination with $^{209}$Rn, $^{209}$At and $^{205}$Po. This are decay daughters of $^{213}$Ra being separated as RaF$^+$ ion. The significant amount of the long-lived daughters indicates that part of the $^{213}$Ra $\alpha$ decay recoils left the tape and were implanted in the front part of the tape station. Also gamma lines of $^{232}$Ra and $^{232}$Ac decay were observed, but their intensity was small as expected from the timing of the tape cycle. However, the spectrum was dominated by a series of gamma lines with unknown assignment. Many of them are mutually coincident. In the beta gated spectrum this background is significantly reduced. Gating with the beta telescope on high energy betas it is further suppressed with increasing electron energy threshold. This indicates that the nucleus showing the background lines is populated by electron capture with a small $\beta^+$ branch. Therefore the contamination is from the neutron-deficient side.

Figure 5.4.1 shows the gamma spectrum gated with the beta telescope. The threshold was chosen high enough to eliminate most contaminations[13]. One can identify the radium K$_\alpha$ X-rays and several gamma lines.

The three strongest gamma lines are also clearly visible in the gamma single spectra and the energy can be fitted with good statistics: 124.6(1) keV, 188.4(1) keV and 720.5(2) keV. They are moreover coincident with the radium X-rays and can be assigned unambiguously to the $^{232}$Fr decay. A fit of their half-lives gives a value of 5.8(8) s, 5.3(10) s and 5.4(12) s respectively (see figure 5.4.2). The weighted mean of the three values is 5.5(6) s. Note that in the gamma single spectra these lines were "sitting" on a mixed background of small other peaks and a Compton continuum. Most of the error in the half-life determination is due to the subtraction of this background. The decay behavior gives an additional indication that the three gamma lines are to be attributed to

---

[13]The telescope was not calibrated, but the threshold energy is estimated to 2−2.5 MeV.
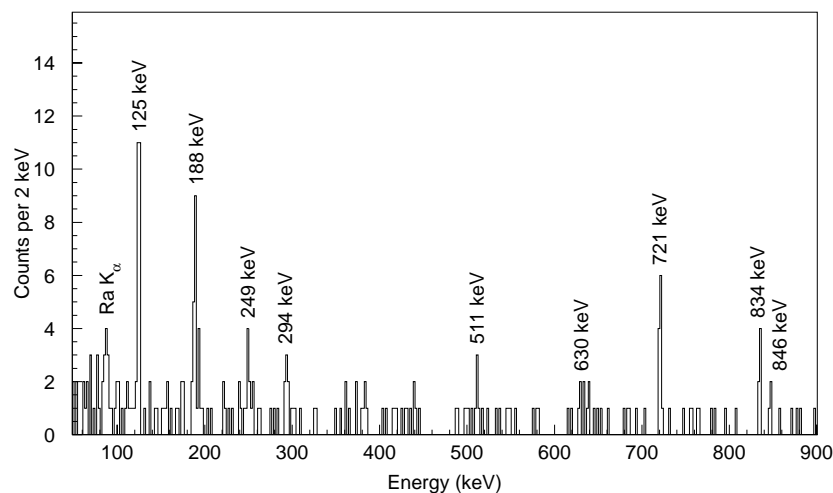
Figure 5.4.1.: Gamma spectrum of mass 232 gated with high energy betas.

the same isotope, but for a more precise determination of the half-life the tape cycle should be extended to follow the decay over several lifetimes.
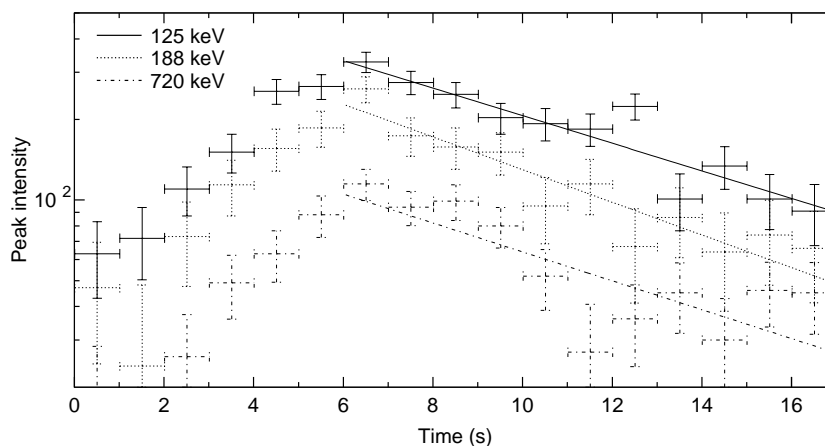


Figure 5.4.2.: Time behavior of the three strongest gamma lines of the $^{232}$Fr decay.

The 511 keV line in figure 5.4.1 is obviously due to high-energy positrons which annihilate after stopping in the nearby beta telescope. The 630 and 834 keV lines are background from $^{72}$Ga decay. Before this experiment $^{72}$Cu had been studied at the same set-up. The isobaric beam contamination $^{72}$Ga was implanted into the tape and remained there.

Other very weak lines are only visible with a gate on high-energy betas, (see figure 5.4.1): 249(1) keV, 294(1) keV, and 846(1) keV. In the gamma single spectra they are burried under background and no lifetime could be measured. Thus no assignment can be made.

From the $\gamma\gamma$ coincidence spectra it is found that the 125 keV line is coincident to both, the 188 and the 721 keV line. However, there is no coincidence between the latter two. There are also traces of a coincidence between the 125 keV and other lines but due to the presence of beam contaminations with high gamma multiplicity it cannot be excluded that the observed coincidences are not just randomly.

**Level assignment**

Figure 5.4.3 shows the development of the lowest levels in the even radium isotopes. The energies were taken from ref. [Fir96, Coc99]. When moving away from the $N = 126$ shell closure the positive parity states of the ground state band show the typical transition from a shell model structure via a vibrator to a rotator structure. Their energy is continuously decreasing towards midshell ($N = 139$ at $^{225}$Ra). Due to increasing deformation $\beta_2$, this tendency continues beyond midshell and for the heaviest radium isotopes the typical values of rotational bands in the actinide region are approached. Extrapolating this systematics to $^{232}$Ra, the first $2^+$ level should be around 55 keV. Due to the high $Z$ this $2^+ \rightarrow 0^+$ E2 transition will be highly converted[14]. Conversion electrons cannot be detected with our experimental set-up and the efficiency for gamma ray detection with the standard HP-Ge detectors is already significantly reduced at this energy. Therefore this transition was not observable with the given statistics.
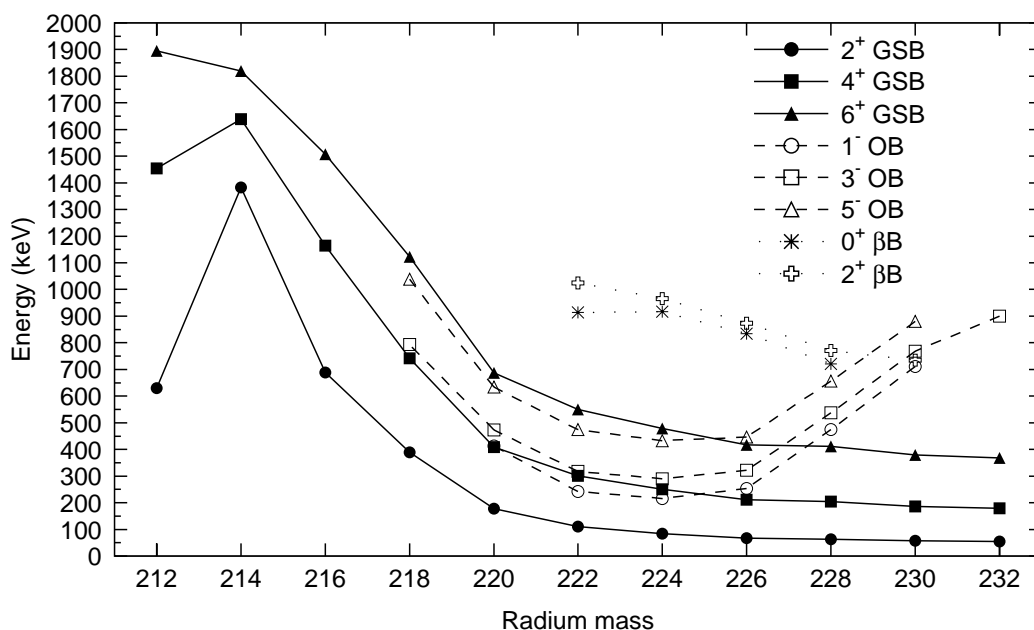


Figure 5.4.3.: Systematics of the lowest levels in even radium isotopes. Shown are levels of the ground state band (GSB), the octupole vibration band (OB) and the $\beta$-vibration band ($\beta$B). For a presentation of the present results for $^{232}$Ra the $2^+$ GSB level was placed arbitrarily at 54.5 keV. The $\approx 900$ keV level is tentatively assigned to a $3^-$ OB state.

For an even-even nucleus it is not expected that usually high-lying states are found below 1 MeV excitation energy. Therefore the two strongest gamma lines detected in the $^{232}$Fr beta decay to $^{232}$Ra (125 and 188 keV) can safely be assigned to the E2 transitions $4^+ \rightarrow 2^+$ and $6^+ \rightarrow 4^+$. The 721 keV line is coincident to 125 keV, but not to 188 keV. Therefore it should feed the $4^+$ level directly, possibly from the $3^-$ or $5^-$ level of the octupole vibration band. In case the 721 keV transition comes from the $5^-$ level, the 532.2 keV $5^- \rightarrow 6^+$ should show up in the single spectra as well as in coincidence to the 125 and 188 keV lines. This was not observed. If, however, it comes from the $3^-$ level one should also see the 845.1 keV $3^- \rightarrow 2^+$ transition in the gamma single spectra. In fact, a slight indication for such a line is seen in figure 5.4.1. Therefore the 721 keV line is tentatively[15] assigned to the $3^- \rightarrow 2^+$ transition. As seen in figure 5.4.3 the deduced $3^-$

---

[14]The total conversion coefficient is $\alpha \approx 160$ [Fir96].

[15]It should be noted that the transition strength expected from a Weisskopf estimation is 20 % higher for $3^- \rightarrow 2^+$ compared with $3^- \rightarrow 4^+$. This is not observed in figure 5.4.1, but the trigger efficiency of the data acquisition is

position fits well in the systematics. The energy of the collective octupole excitation increases after midshell due to the reduced number of valence neutrons.

The feeding of the $4^+$ level by the 188 keV line is slightly stronger than by the 721 keV line[16]. Both lines together give about half of the $4^+\rightarrow2^+$ intensity. Thus the $4^+$ level is also populated by other sources: either gamma transitions which are not detected or directly from the beta decay. From a comparison with the detected intensity of high-energy betas it is found that roughly half of all $^{232}$Fr decays go via the $4^+\rightarrow2^+$ transitions to the ground state. Conversion coefficients of 3.5 for the 125 keV line and 0.7 for the 188 keV line were used for these comparisons.

Due to an unknown direct population of the $0^+$ ground state and the $2^+$ state no useful log $ft$ values could be derived and no statement can be made on the ground state spin of $^{232}$Fr. Figure 5.4.4 summarizes the observed gamma lines in a tentative level scheme of $^{232}$Ra.
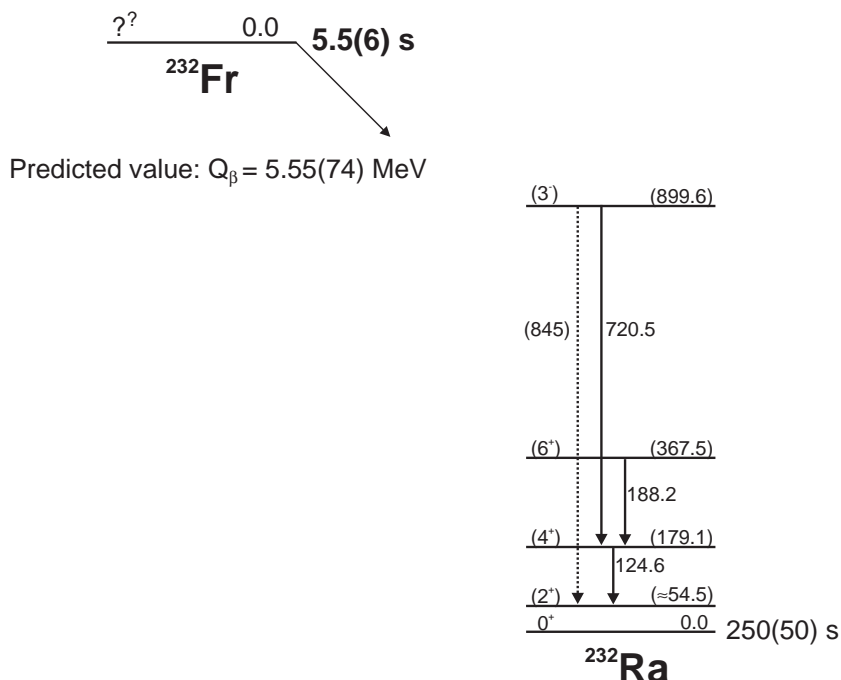


Figure 5.4.4.: Placement of the observed gamma lines in a tentative level scheme of $^{232}$Ra. For the 845 keV line only a weak hint was observed. The energy of the $2^+$ state was derived from systematics. The $Q_\beta$ value was taken from [Aud97] and the half-life of $^{232}$Ra from [Gip86].

The ratio of the energies $E(6^+\rightarrow4^+)/E(4^+\rightarrow2^+) = 1.51$ comes close to that of an ideal rotator. Its energy eigenvalues for a total angular momentum $I$ are:

$$E = I(I+1)\hbar^2/(2\theta). \tag{5.4.1}$$

Thus: $E(6^+\rightarrow4^+)/E(4^+\rightarrow2^+) = (6\cdot7-4\cdot5)/(4\cdot5-2\cdot3) = 11/7 \approx 1.57$. The kinetic momentum of inertia is obtained as:

$$\theta = \frac{\hbar^2(2I-1)}{E_I - E_{I-2}}. \tag{5.4.2}$$

---

not necessarily equal for both lines (see below). Else the intensity ratio would rather indicate an assignment to e.g. a $2^+$, $K = 2$ state.

[16]A more precise intensity evaluation is still to be done by taking into account the total trigger efficiency (beta and gamma-gamma events). Due to the very close geometry it depends noticeably on the gamma multiplicity of the decay and on random gamma-gamma coincidences. This effect is reproduced with GEANT simulations [Wei99].

Thus: $\theta(4^+\rightarrow2^+) = 56.2\ \hbar^2/\text{MeV}$ and $\theta(6^+\rightarrow4^+) = 58.4\ \hbar^2/\text{MeV}$.

A more precise reproduction of the rotator energies is obtained with an additional quadratic term in equation (5.4.1) [Cas90]:

$$E = AI(I+1) + BI^2(I+1)^2 \tag{5.4.3}$$

with $A = \hbar^2/(2\theta)$ and $B \ll A$ a small correction term. With the two given transition energies $\theta = 54.7\ \hbar^2/\text{MeV}$ and $B = -0.0093$ keV are found. Thus the $2^+$ level is expected to be at about 54.5 keV. The extrapolated energy of the $8^+$ and $10^+$ levels is 610 and 893 keV, respectively.

The rigid rotator momentum of inertia of a solid sphere is $\theta = 2/5Mr^2$, that of an ellipsoid with quadrupole deformation $\beta_2$:

$$\theta_{\text{rigid}} \approx \frac{2}{5}Am_N r_0^2(1 + 0.31\beta_2). \tag{5.4.4}$$

The radius and the deformation of even-even nuclei were recently calculated by the relativistic mean-field theory [Lal99]. For $^{232}$Ra the mean proton radius $r_p = 5.75$ fm and the mean neutron radius $r_n = 6.07$ fm can be combined to the mean matter radius: $r_{\text{mat}} = \sqrt{r_p^2\, Z/A + r_n^2\, N/A} = 5.95$ fm. Using also $\beta_2 = 0.202$ from ref. [Lal99] gives $\theta_{\text{rigid}} = 83.5$ keV. The experimental value is just two third of the calculated one, showing that the description with a rigid rotator is less suitable than e.g. for neutron-rich lanthanides.

Actually the nuclear charge distribution up to $^{232}$Ra was already measured by collinear laser spectroscopy at ISOLDE [17] [Ahm83, Wen87]. A comparison of the calculated and experimental values shows for the heaviest radium nuclei ($A \geq 228$) a slight overestimation of $\delta\langle r^2\rangle^{A,214}$ by theory (14 % in $^{232}$Ra). However, this affects $\theta_{\text{rigid}}$ only marginally.

## Outlook

To increase the efficiency for detection of the low-energy transitions ($2^+\rightarrow0^+$, $4^+\rightarrow2^+$, $3^-\rightarrow1^-$, etc.) it would be very profitable to use a conversion electron detector. An X-ray detector is necessary to see the L-X-rays[18]. A set-up dedicated for the detailed decay study of $^{232}$Fr should moreover contain a calibrated beta telescope[19]. This could give additional information on a direct beta feeding of the low levels. It would also allow a rough determination of the nuclear mass. Presently the uncertainty of the experimental masses is still quite high in this region [Aud97].

Setting a double gate on the gamma lines 124.6 keV and 188.4 keV or 124.6 keV and 720.5 keV, respectively, can help to extract higher levels of $^{232}$Ra from the coincidence data taken with GAMMASPHERE in multi-nucleon transfer reactions of $^{136}$Xe on $^{232}$Th [Coc99].

## "The contamination"

Finally also the strong contamination could be identified. The gamma lines are coincident with francium X-rays. They can be assigned to the EC/$\beta^+$ decay of the $1/2^-$ ground state of $^{213}$Ra (20 % branching ratio for EC and $\beta^+$). This decay will mainly populate low spin states in $^{213}$Fr. Indeed the strongest observed line is the $7/2^-\rightarrow9/2^-$ transition: 498.3(2) keV. The intensity of this line was used (with an assumed branching ratio of 80 %) to determine the yield of $^{213}$RaF$^+$ (see section 4.12). Up to now $^{213}$Fr was mainly studied by high spin spectroscopy, and except the

---

[17] In fact, $^{232}$Ra was first discovered in this experiment. Even the half-life was not known at this time. This is a good example for the sensitivity of on-line laser spectroscopy.

[18] The conversion of the E2 transitions mainly creates vacancies in the L shell.

[19] The one used was very small, just to fit between both Ge detectors in close geometry. It was not optimized for linearity etc.

$7/2^-$ no other low spin state was reported. Thus, an evaluation of the collected data (more than a dozen strong lines) will allow to complement the existing level scheme of the neutron-magic ($N = 126$) nucleus $^{213}$Fr.

## 5.4.2.   Search for $^{233}$Fr

$^{233}$Fr was searched for about 80 min with the same set-up. Unfortunately the beta telescope was not operational. Only few gamma lines were observed where the intensity decreased during some seconds. They were too weak for a half-life determination or a detection of coincident lines. Moreover the odd francium isotopes show a very rich decay scheme (see e.g. [Egi81, Bor92]) which does not allow an obvious assignment as in the case of the even francium isotopes. Since the spectrum was taken immediately after the measurement of $^{232}$Fr, the remaining contaminations of the tape station ($^{209}$Rn, $^{209}$At and $^{205}$Po) gave the strongest gamma lines. Their K$_\beta$ X-rays mask possible radium K$_\alpha$ lines from the $^{233}$Fr decay. Due to the low K-X-ray yield in this decay no radium K$_\beta$ lines could be found.

A more selective detection method would simplify the identification of $^{233}$Fr and the measurement of its half-life. In fact, just for $^{233}$Fr the onset of beta-delayed neutron emission is predicted [Möl97, Pfe99]. Therefore at another occasion an $A = 233$ beam from a UC$_x$/graphite target with tungsten surface ionizer was sent to the Mainz neutron detector.
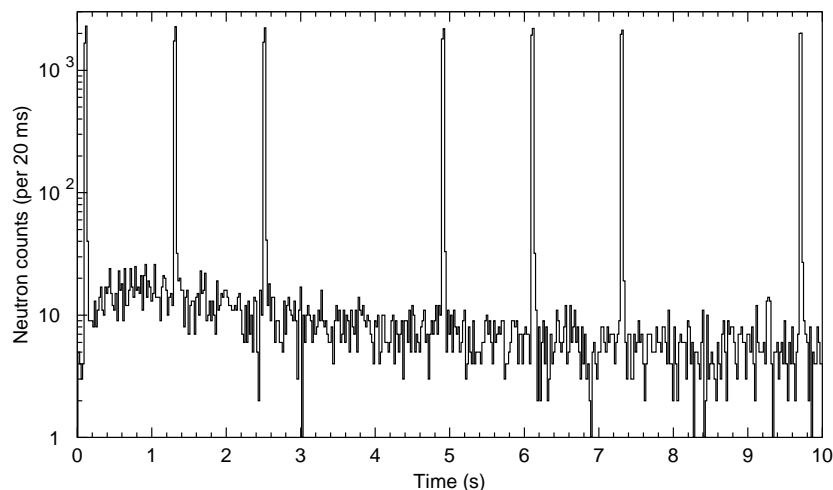


Figure 5.4.5.: Neutron multiscaling spectrum of the "$A = 233$" decay. The spikes are due to spallation neutrons of the proton pulse impact.

In this measurement the beam gate was opened once per 14.4 s super cycle for 1 s. Figure 5.4.5 shows the observed time spectrum of the neutrons taken in a 45 min measurement. The sharp peaks at 0.1, 1.3, 2.5, 4.9, 6.1, 7.3 and 9.7 s are from spallation neutrons when the proton pulse hits the ISOLDE target and beam stop. Note that this spectrum was taken "parasitically" during a collection of $^{225}$Fr/$^{225}$Ra at another beam port. Seven proton pulses per super cycle were used for a maximum production of the latter. Below the spikes a small component of (beta-delayed) neutrons is visible. It shows clearly a grow-in and decay behavior. When removing the spikes from the spectrum and summing the remaining counts in bins of 1.1 s the time behavior can be fitted. It gives a half-life of $1.8^{+0.6}_{-0.4}$ s and a value of 8 per $\mu$C for the "neutron yield", i.e. the product of yield and $P_n$ value. The time behavior and the ring ratios show that these neutrons are indeed

beta-delayed and related to the ion beam of mass 233 and not due to any source of external background[20].

Also the beta activity was investigated. However, the tape station was still heavily contaminated with $^{132}$Cs[(21] and a huge constant background had to be deduced. On top of it still some short-lived activity is visible. A free fit with a single exponential decay gives a half-life of 10(2) s, but probably several sources contribute to this activity ($^{233}$Ra, $^{233}$Ac, molecular ions, etc.). For a $\approx$1.8 s activity an upper limit of 1600 per $\mu$C can be deduced. Thus the lower limit for the $P_n$ value of the beta-delayed neutron activity is about 0.5 %, i.e. well above the predicted $P_n$ value of $^{233}$Fr (0.01 to 0.05 % [Möl97, Pfe99]).
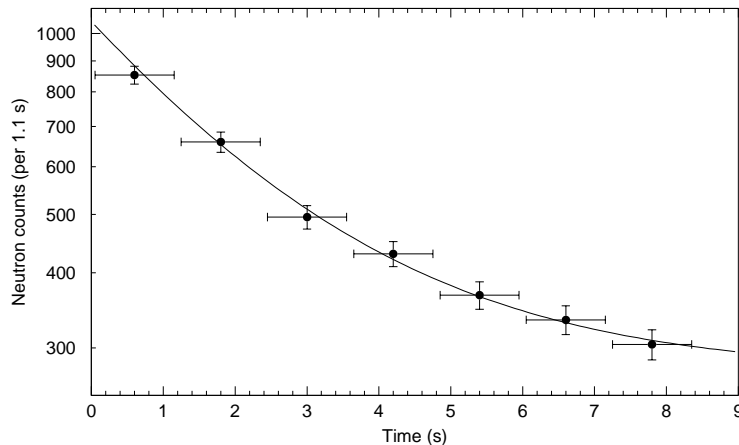


Figure 5.4.6.: Neutron multiscaling spectrum of "$A = 233$" decay. The decay can be fitted with a half-life of $1.8^{+0.6}_{-0.4}$ s.

Before assigning these neutrons to the decay of $^{233}$Fr the possibility of beam contaminations has to be checked. None of the surface ionizable isobars or $A = 214$ monofluorides is expected to emit neutrons. However, contaminations could come from other molecular ions, e.g. metal halides. A molecular ion which could cause such a background of beta-delayed neutrons is e.g. $^{143}X^{90}$Br$^+$, with $^{90}$Br ($T_{1/2} = 1.91$ s and $P_n = 25.2$ %) the beta-delayed neutron emitter and $X$ a rare earth element (Nd, Pm, Pr or Ce) or a polyatomic radical. Such a combination was not observed before, but cannot be excluded.

Beta-delayed neutrons from the $^{233}$Fr decay were also searched at two other occasions with standard UC$_x$/graphite targets and a W surface ionizer. The short measurements (30 min) gave only an upper limit of about 3 per $\mu$C for the neutron yield at mass 233 and 234. Therefore one can conclude that a beam contamination in the first measurement is rather probable and presently there is no evidence for the detection of $^{233}$Fr.

Clearly the disturbing molecular background could be reduced by lowering the ionizer temperature or using a material with lower work function (Ta or Nb). However, in the given experiment a tungsten surface ionizer at about 2350 °C was used to optimize the yield of the $^{225}$Ra collection.

As shown before the detection of beta-delayed neutrons is a very selective method, but for its own it does not allow a unique assignment[22]. The integration of a gamma detector into the neutron detector set-up could give useful information on the kind and the amount of possible beam contaminations, even if it not used in coincidence but independently. Still the best way to

---

[20]Note that the bunched release of radioactive noble gases discussed in section B.9 should show up with every proton pulse, not only when the beam gate is opened!

[21]As discussed before, this occurs as intense isobaric background when measuring $^{132}$In.

[22]The combination with the RILIS allows to "switch" a certain element on and off, but francium is always surface ionized.

identify $^{233}$Fr unambiguously remains the detection of X-rays and high-energy betas. Therefore a spectroscopy set-up as proposed above for a further study of the $^{232}$Fr decay will also be very suitable for the detection of heavier francium isotopes.

## 5.4.3.   Outlook to $^{234+x}$Fr

For very heavy francium isotopes ($A \gtrsim 234$) a new decay mode could occur: beta-delayed fission (see section 1.1). Its study is not only of principal interest to improve the knowledge of the development of the fission barriers towards very neutron-rich isotopes, but has also implications on the astrophysical r-process.

All naturally occuring actinide isotopes were created in the r-process. See Burbidge et al. (BBFH) [Bur57] for a general description and e.g. ref. [Cow99] for a recent review. Neutron-induced and spontaneous fission of very heavy neutron-rich r-process nuclei can occur already during the r-process. It sets an upper limit to the produced masses and causes some recycling of the r-process nuclei: the fission products act again as seed material for further neutron capture.

As in the case of lighter r-process nuclei the observed abundances of actinides are related to the mass yields at the end of the neutron burst. For lighter masses the final abundances are slightly modified by beta-delayed neutron emission occuring on the way from the primary r-process nuclei to the beta stable daughters. For the heaviest nuclei additionally spontaneous and beta-delayed fission can occur. This can cause some enhancement in the fission product region and, even more important, a depletion of the actinide yields. The long-lived actinides $^{232}$Th, $^{235}$U and $^{238}$U are normally used as cosmochronometers to determine the age of the solar system. A significant suppression of one of these nuclei by beta-delayed fission of a progenitor would change the primary abundance ratio and thus affect the derived age of the Galaxy. Clearly the yields of these nuclei do not reflect directly the mass yields of the respective isobaric progenitors. Instead they represent an integration over all mass yields of the (alpha) decay chains ending there. For example the yield of $^{238}$U is a collection of the mass yields $A =$238, 242, 246 and 250[23]. Still, due to the odd-even staggering of the $Q_\beta$ values and fission barriers the three cosmochronometers will be affected differently by beta-delayed fission. Therefore a good understanding of the latter process is very important.

The theoretical predictions for beta-delayed fission probabilities differ significantly. Thielemann et al. predicted a beta-delayed fission probability of 3 to 20 % for $^{234}$Fr, depending on the used mass formula [Thi83]. This is in contrast to other calculations [Ber69, Lyu86, Mey89, Sta92] which predict the on-set of beta-delayed fission much further out (around $^{244}$Fr or even beyond). A general difficulty in the calculation of delayed fission probabilities is the need to find a consistent description of the nuclear masses and the fission barrier heights. This was recently achieved with the microscopic ETFSI method [Mam98] and fission barriers of many neutron-rich heavy isotopes have been calculated [Ray99]. Consistent fission barriers and Q values could also be deduced from relativistic mean field calculations [Lal99, Lalaz].

As in the case of most medium-mass r-process nuclei, there is no hope to study experimentally all heavy isotopes between beta stability and the end of the r-process path in the near future. On the other hand already nuclear spectroscopy information on few prominent isotopes in this area helps to improve the theoretical predictions for the full region. The branching ratio for beta-delayed fission is determined by the beta-strength function, the $Q_\beta$ value and the fission barrier. However, any experimentally accessible property (e.g. the lifetime, the mass, the beta-strength distribution or the ground state deformation) is a valuable input parameter to test and improve the model calculations.

---

[23]Contributions from higher masses will mainly undergo spontaneous fission.

**Experimental information on $\beta^-$-delayed fission**

Gangrskii et al. reported beta-delayed fission of heavy protactinium isotopes ($^{236,238}$Pa) [Gan78], but a later study could not confirm the results [BM85]. Thus, $^{256m}$Es remains the only case of experimentally observed $\beta^-$f activity [Hal92].

An experimental search for $\beta^-$-delayed fission in the sub-actinide region was performed at the IRIS facility [Mez90]. No fission event was detected in the decay of $^{232}$Fr. Estimating the number of observed $^{232}$Fr decays with the assumption of one $L_\beta$ Ra X-ray per decay gave an upper limit of $2 \cdot 10^{-6}$ for the delayed fission probability $P_{\mathrm{DF}}$ [Mez90]. Using this value Izosimov estimated the height of the fission barrier in $^{232}$Ra [Izo92].

Very neutron-rich actinide nuclei were produced by multiple neutron capture on $^{238}$U and $^{242}$Pu targets [Dor65, Ing69]. Information on the fission barrier heights was deduced from the production yields of higher actinides. However, such experiments give only an integral information and do not allow to study individual short-lived nuclei. Moreover the experimental set-up to produce the required neutron flux is rather involved (nuclear explosions). Note that in the given references beta-delayed fission was not yet included in the evaluation. See ref. [Hof86] for a discussion of the corrections.

Several methods can be used to find an experimental indication of beta-delayed fission:

- The fission fragments could be detected directly. Their high kinetic energy ($\gtrsim 130$ MeV in total[24]) gives an unambiguous signal. Implanting the beam into a silicon detector allows to reach a detection efficiency of nearly 100 %. However, if very abundant beam contaminations with alpha activity are present, pile-up could cause a problem.

- Another feature of fission is the high gamma multiplicity. Also here a good detection efficiency can be obtained with a segmented array of gamma detectors covering a large solid angle (e.g. over 90 % in [Sin97]), but the experimental effort is much higher.

- Finally the fission neutrons could be detected. For example with the Mainz neutron detector and an expected neutron multiplicity $\nu_{\mathrm{p}} \gtrsim 3$ a detection efficiency above 65 % can be reached. However, an ambiguity occurs if the isotope in question has also a decay branch for beta-delayed neutron emission. This is the case for all nuclei in this region with a sufficiently high Q value for $\beta^-$f. Then a time-correlation technique [Ber99] has to be used to find events with higher neutron multiplicity.

Thus, the search for beta-delayed fission does not necessarily require particular set-ups, but can be performed in parallel to the standard nuclear spectroscopy. The heavy francium isotopes would provide a good opportunity for such a study.

---

[24] Compared to fission of e.g. $^{236}$U$^*$ the Q value is somehow reduced due to a higher neutron excess of the fission fragments.

# Epilog

Many yields of radioactive isotopes have been measured in this work[25].

They were obtained with two completely different set-ups: the recoil separator LOHENGRIN at the Institut Laue Langevin in Grenoble and the on-line isotope separator ISOLDE at CERN in Geneva. Not only the separation method is very different, but also the production process (the kinetic energy of the "primary beam" varies by more than ten orders of magnitude) and the aim of the measurement. However, there are several important parallels between the first and second part of this thesis and in particular one "red line": *fission*. First it was shown that even light exotic isotopes are created in a variation of the well-known process of thermal neutron induced fission of actinides. Later fission occured again as a powerful production method for many neutron-rich isotopes at ISOLDE. There fission is induced by high-energy protons[26]. In some regions of the nuclide chart thermal neutron induced fission would be an even better, i.e. more efficient and more selective, production method for ISOL facilities. And finally it was discussed that the availability of ISOL beams could possibly be extended towards the region where beta-delayed fission sets in.

Another parallel is the quest for very exotic isotopes. Why should one take the high effort to produce and study "exotic" nuclides far from beta-stability if there are still many unsolved problems in the experimental and theoretical study of "standard" nuclides?

The systematic study of nuclear parameters (masses, lifetimes, excitation energies, decay modes, beta-strength functions, spins, magnetic moments, nuclear density distributions, etc.) along long isotopic chains allows to find qualitative changes in the proton-neutron-interaction and other model parameters. Often many models based on completely different assumptions give predictions for observables which differ only marginally for nuclei around the valley of beta stability, but going towards the drip-lines they start to deviate significantly, see e.g. [Lun97]. Thus, an even rough study of exotic nuclides can often provide more information to prove or falsify certain models or to fix free model parameters than a detailed study of nuclides close to stability. The situation is just identical in the case of ternary fission: as discussed in chapter 1 the yields of very rare ternary particles provide a good test of the various ternary fission models.

The experimental methods and difficulties to provide appropriate beams of these exotic nuclei were discussed in detail in chapters 2, 3 and 4. One should always recall the basic principles which have to be followed: *efficiency*, *selectivity* and *rapidity*.

Finally the most "exotic" isotope separated in this work coincides at LOHENGRIN and ISOLDE: $^{14}$Be. It is the rarest nuclide detected from ternary fission of $^{235}$U (only one per twenty billion fissions and the most short-lived isotope ($T_{1/2} = 4.35$ ms) which was separated up to now at the ISOLDE PSB. A last example shall put the frequently used designation "exotic nuclide" into a different perspective: While you, dear reader, might have spent two hours under a 60 W desk lamp for reading parts of this thesis, about one million $^{14}$Be nuclei were produced in the nuclear reactors providing the electrical power for it. However, already before this page is completely turned, all of them have decayed inside the fuel elements. This illustrates the central problem of an ISOL facility: an abundant production is often easier realized than an efficient extraction. Improvements of the latter point offer still a huge potential to increase the yields.

---

[25]Still the number falls short of justifying the more poetic thesis title "Mille et un rendements en mille et une nuits de manip" [Lettr].

[26]It should be noted that even ISOLDE could hardly operate without neutron-induced fission: French nuclear reactors provide affordable electricity to run the CERN accelerators.

# A. Appendix to LOHENGRIN measurements

## A.1. Preparation of thin, self-supporting nickel films

The foils are produced by evaporation or sputtering of nickel onto a flat surface. The substrate has to be impregnated with a parting agent to allow the removal of the foil. To stabilize the foil during removal and subsequent handling, one side is covered by a thin protective film. It follows a recipe with the fundamental production steps:

- Prepare a saturated solution from betain ($C_5H_{11}NO_2 \cdot H_2O$) and saccharose ($C_{12}H_{22}O_{11}$) with a mass ratio of about 7 to 1 [MK72].

- Keep it at least over night, that the oversaturated part can settle.

- Clean glass plates (in our case $100 \cdot 100$ mm$^2$) with detergent and rinse well with water. Let them dry.

- Distribute a little of the sugar solution with a damp cloth on the glass.

- When the film starts to dry, grind it with a dry cloth that it gets milky. The plates should look homogeneously like frosted glass. Store these glass plates in dry atmosphere, they are hygroscopic.

- Evaporate or sputter the metal in the requested thickness (here 2500 Å) onto the substrates.

- Dissolve polystyrene in chloroform, about 10 to 20 g per liter for a thin film; 50 g per liter gives a thicker film [Richa].

- Coat the plate by dipping it briefly into the polystyrene solution. Let it dry.

- Cut the coated foil with a scalpel into pieces of the desired size.

- Place the plate slightly inclined in a bowl.

- Fill the bowl slowly with water. This will dissolve the sugar film and make the metal foil swim on the water. If the water rises faster than the sugar layer dissolves, the buoyancy will break the foil.

- Carefully fish the swimming foil out with a suitable frame. When the foil is wet, it will be relatively stable and stay on the frame, but after drying (less than half an hour) it gets extremely brittle. To prevent that it comes off the frame, the rim of the foil should be clamped as soon as possible with another frame.

- If it did not come off already in the water, the protective layer of polystyrene can be removed without detectable residues by heating the foil under vacuum for a while to about 500 °C.

The evaporated foils are more brittle than the sputtered ones, resulting in more loss due to cracks when removing them from the substrate.

The betain parting agent also could be replaced by a salt layer deposited onto the substrate with an appropriate evaporation facility. With both methods a small agglomeration of betain or salt can form a needle which in turn causes a pinhole in the foil when the parting agent is removed. While for the use as target cover foil such pinholes are absolutely uncritical, other applications have more severe requirements. Simultaneously to our foils we prepared a batch of foils for "subbarrier penetration" experiments with ultracold neutrons [Var97]. To stay below the requested limit of pinhole area (less than $10^{-7}$ surface of open holes on a freestanding area of up to 70 cm$^2$ [Nesvi]) we tried also other parting agents, however with inferior results. A thin layer painted with a waterproof marker ("Edding") onto the glass substrate was dissolved in acetone, but the foil cracked completely. The evaporation of nickel onto a thin aluminum foil and a subsequent dissolving of the aluminum in a diluted sodium hydroxide solution did only allow to produce foils of small size (about 1 cm$^2$). Foils with larger area were broken from the pressure of gas bubbles produced in: $2 \text{ Al} + 6 \text{ H}_2\text{O} \rightarrow 2 \text{ Al}^{3+} + 6 \text{ OH}^- + 3 \text{ H}_2 \uparrow$.

## A.2.   Field settings of the LOHENGRIN separator

In the LOHENGRIN spectrometer the ions are separated according to their mass, ionic charge and kinetic energy. The trajectory is given by the identity of the centrifugal force $F_z$ and the Lorentz force $F_L$. First they traverse a homogeneous magnetic sector field $B$ and are deflected horizontally according to their momentum over ionic charge ratio $p/q$:

$$F_z = \frac{mv^2}{\rho_{\text{magn}}} = qvB = F_L,$$

$$\frac{p}{q} = \frac{mv}{q} = B\rho_{\text{magn}}. \tag{A.2.1}$$

Next they are deflected by a cylindrical condenser in vertical direction and separated according to the ratio of kinetic energy to ionic charge $E/q$:

$$\frac{mv^2}{\rho_{\text{el}}} = q\mathcal{E},$$

$$\frac{E}{q} = \frac{mv^2}{2q} = \frac{1}{2}\mathcal{E}\rho_{\text{el}}, \tag{A.2.2}$$

where $\mathcal{E}$ is the electrical field strength in the condenser. The field of a cylindrical condenser is given by:

$$\mathcal{E}(r) = \frac{U}{r \cdot \ln\left(\frac{\rho_{\text{el}}+d/2}{\rho_{\text{el}}-d/2}\right)} \approx \frac{U}{r}. \tag{A.2.3}$$

With $r = \rho_{\text{el}} = 5.6$ m and $d = 0.3$ m the full denominator only deviates by 70 $\mu$m from $d = 0.3$ m. This is much less than the positioning accuracy of the electrodes and can be neglected.

Solving equations A.2.1 and A.2.2 for the experimental parameters $U$ and $B$ gives:

$$U = \frac{mv^2}{q} \cdot d\rho_{\text{el}} = \frac{E}{q} \cdot \frac{1}{\Phi}, \tag{A.2.4}$$

$$B = \sqrt{\frac{m}{q} \cdot U \cdot \frac{\rho_{\text{el}}}{d\rho_{\text{magn}}^2}} = \sqrt{\frac{m}{q} \cdot U \cdot \chi}. \tag{A.2.5}$$

Here, the separator constants $\Phi = \frac{\rho_{el}}{2d}$ and $\chi = \frac{\rho_{el}}{d\rho_{magn}^2}$ were introduced. For the RED magnet a higher field has to be applied, which is given by the ratio of the mean radii of the main magnet $\rho_{magn}$ and the RED magnet $\rho_{RED}$:

$$\kappa = \frac{B_{RED}}{B} = \frac{\rho_{magn}}{\rho_{RED}} \approx \frac{4 \text{ m}}{0.6 \text{ m}} = 6.67. \tag{A.2.6}$$

For binary fission fragments these equations are normally accurate enough. However, for fast ternary particles the small relativistic correction (some per mil) has to be taken into account. Using a power series in $\beta = v/c$, they can be expressed as [Hes97]:

$$U = \frac{E}{q} \cdot \frac{1}{\Phi} \cdot \frac{1}{1 + \dfrac{\beta^2}{4} - \dfrac{\beta^4}{2} - \dfrac{3\beta^6}{32}}, \tag{A.2.7}$$

$$B = \sqrt{\frac{m}{q} \cdot U \cdot \chi} \cdot \left(1 + \frac{\beta^2}{2} + \frac{3\beta^4}{8}\right). \tag{A.2.8}$$

It should be kept in mind that $m$ is the ionic mass of $_Z^A X^{q+}$. The nuclear mass defect and the $q$ missing electron masses have to be taken into account.

## A.3.   Entrance window of the ionization chamber

The window of the ionization chamber has to separate the counting gas (normally isobutane) from the vacuum in the separator beam tube. The counting gas pressure is typically around 50 mbar for binary fission product measurements, but has to be increased up to 150 mbar and more for light charged particles. The window has to be thin and homogeneous to avoid excessive energy loss and scattering of the fragments. Plastic foils show a good compromise between tensile strength and energy loss of the fragments. The thin foils are supported with a metal mesh of about 90 % transmission.

Originally the foils were produced at ILL with a special foil stretching apparatus, following the recipe of ref. [Bar77, Het86]. A commercial polypropylene foil (about 35 $\mu$m thickness) is clamped onto a ring frame. A mushroom structure heated to 100-120 °C is moved at a constant speed of some mm/s through the frame and stretches the foil. The approximate thickness of the foil is observed by regarding the interference colors under neon light. When the desired thickness is reached, the mushroom is stopped and a smaller ring is glued around a homogeneous looking area. The foil is then removed and glued onto the window holder. To allow a smooth stretching, the mushroom is covered with a teflon layer which has to be cleaned and polished before use. Foils with thicknesses down to some 40 $\mu$g/cm$^2$ can be produced, but the thinner the foil gets, the higher is the probability that it breaks before being taken off. Thus, the yield of successful attempts drops significantly. Any dust particle on the mushroom can provoke a local rupture of the foil. After an unprofessional building operation, the ILL room with the stretching machine was even further from reaching clean room conditions. Thin IC windows were then prepared with a similar machine at Tübingen University.

Alternatively the polypropylene foil can also be stretched cold by slowly inflating it to a bubble with compressed air [Kat72]. Other production methods are discussed in ref. [Hui81].

Originally the maximum pressure for isobutane (potentially inflammable gas) in the ionization chamber was limited to 100 mbar for safety reasons. This is not sufficient to stop energetic ternary particles. Therefore the counting gas was changed to carbon tetrafluoride where no pressure

limitation applies. Also in binary fission measurements where the entrance angle of the ions is reconstructed from the time difference of the $\Delta E$ and $E_{\text{res}}$ signal, $CF_4$ is preferable due to the faster drift and better time resolution. However, the molecular diameter of $CF_4$ is smaller than that of $C_4H_{10}$ and it tends to diffuse faster through the IC window. Leak rates up to some 10 Pa l/s through the 20 cm² big window were measured. This had dramatic consequences!

The $CF_4$ diffused into the LOHENGRIN condenser and deposited on the electrodes. In discharges of the condenser, the $CF_4$ was cracked and the radicals attacked the surface of the electrodes and the insulators of the holding structure. This in turn caused even more frequent sparking. Consequently the maximum voltage of the condenser dropped drastically. Therefore the carbon tetrafluoride was replaced again by isobutane, most insulators had to exchanged and the surface of the electrodes was cleaned in a long conditioning period. That $CF_4$ had indeed diffused far into the beam tube could also be seen from the increase of the "yield" of $^{19}F$ atoms, scattered by fission fragments between target and magnet and detected in the ionization chamber after separation.

## A.4.   Kinetic energy distributions of ternary particles

In the following some experimental energy distributions are shown. The measured points include already all corrections discussed in section 1.4.5.

### A.4.1.   $^{233}$U($n_{th}$,f)
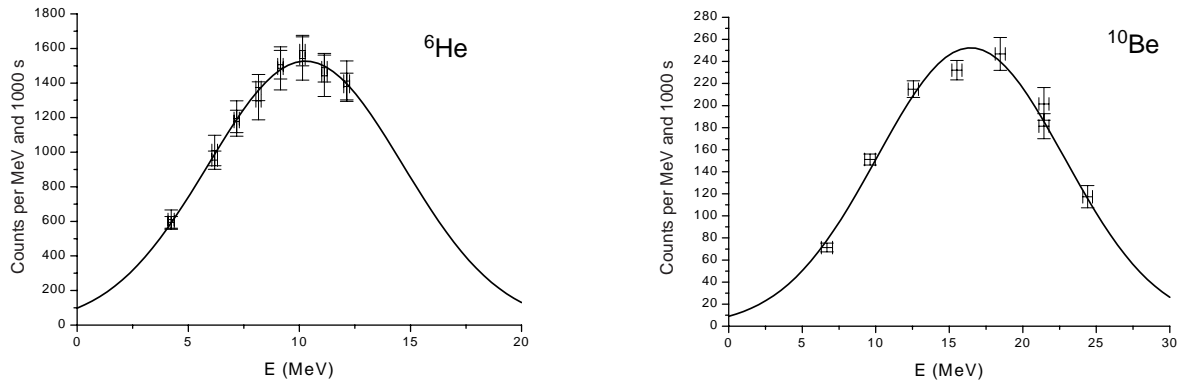


Figure A.4.1.: Kinetic energy distributions of $^6$He and $^{10}$Be from $^{233}$U($n_{th}$,f).
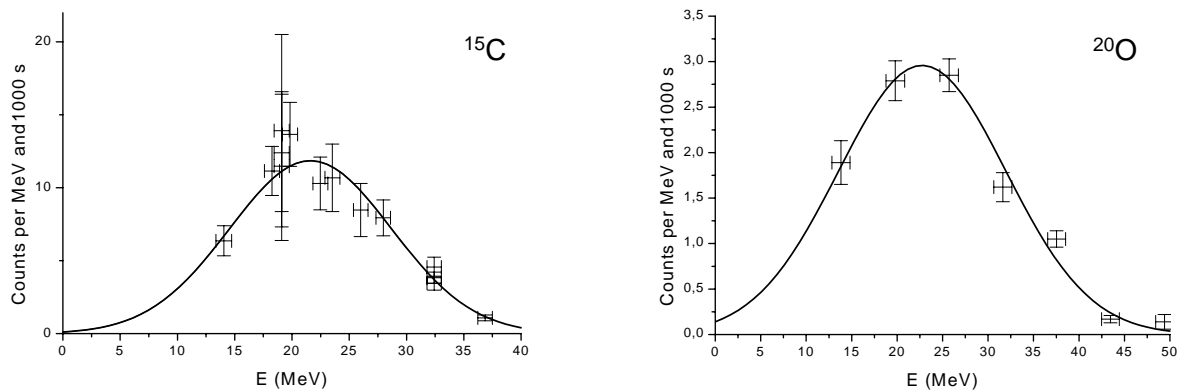


Figure A.4.2.: Kinetic energy distributions of $^{15}$C and $^{20}$O from $^{233}$U($n_{th}$,f).
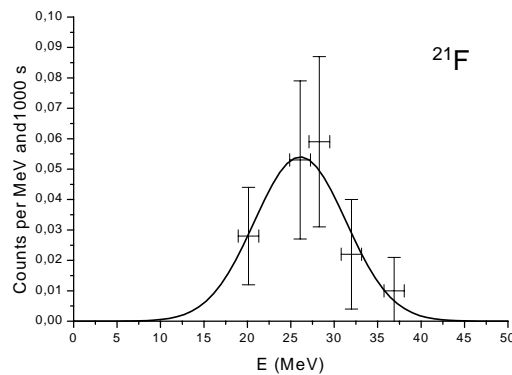


Figure A.4.3.: Kinetic energy distribution of $^{21}$F from $^{233}$U($n_{th}$,f).

## A.4.2.    $^{235}$U(n$_{th}$,f)
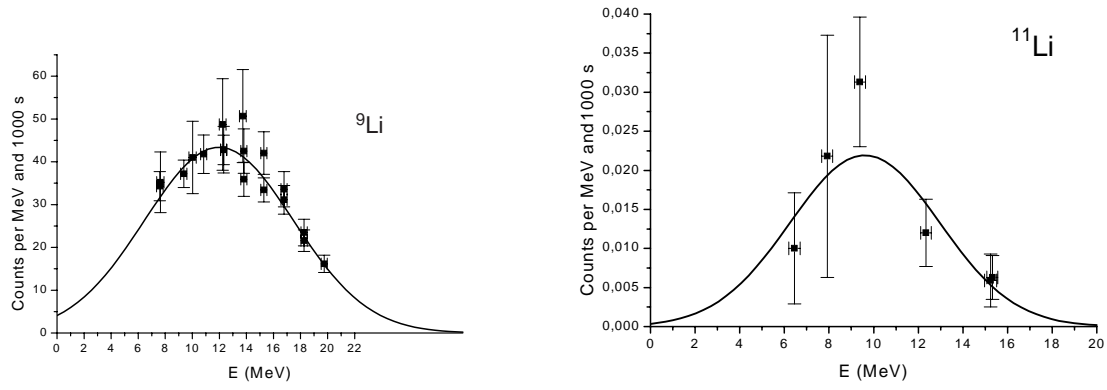


Figure A.4.4.: Kinetic energy distributions of $^9$Li and $^{11}$Li from $^{235}$U(n$_{th}$,f).
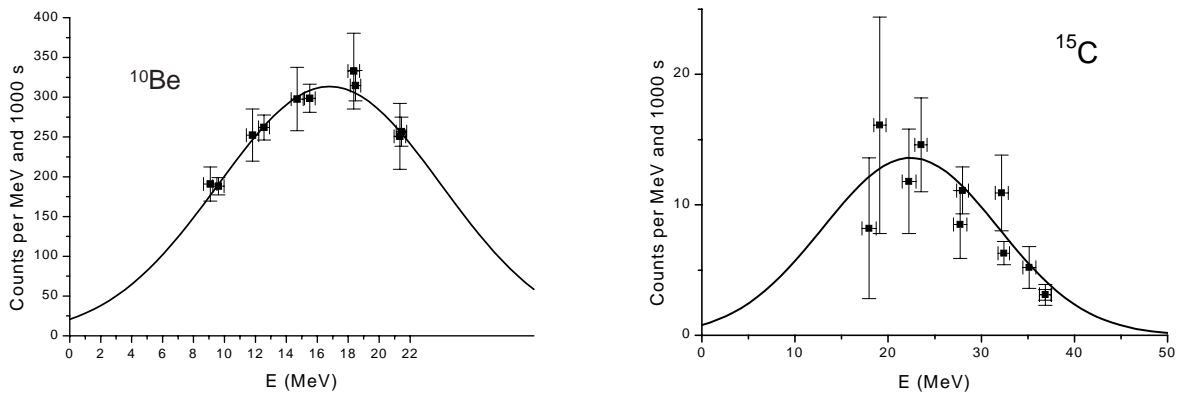


Figure A.4.5.: Kinetic energy distributions of $^{10}$Be and $^{15}$C from $^{235}$U(n$_{th}$,f).
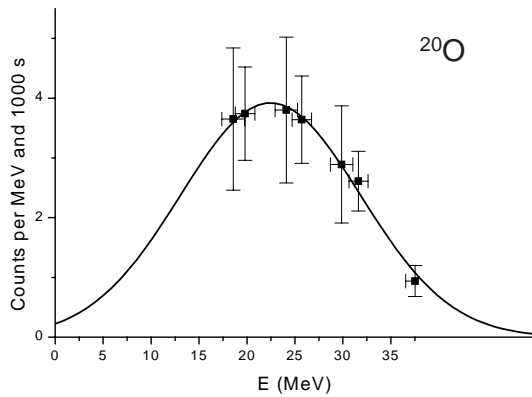


Figure A.4.6.: Kinetic energy distributions of $^{20}$O from $^{235}$U(n$_{th}$,f).

## A.4.3.    $^{241}$Pu($n_{th}$,f)
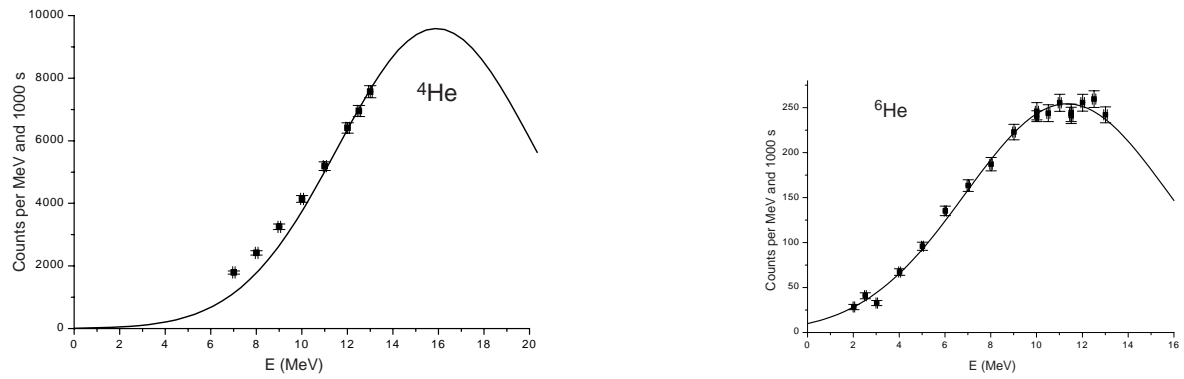


Figure A.4.7.: Kinetic energy distributions of $^4$He and $^6$He from $^{241}$Pu($n_{th}$,f).
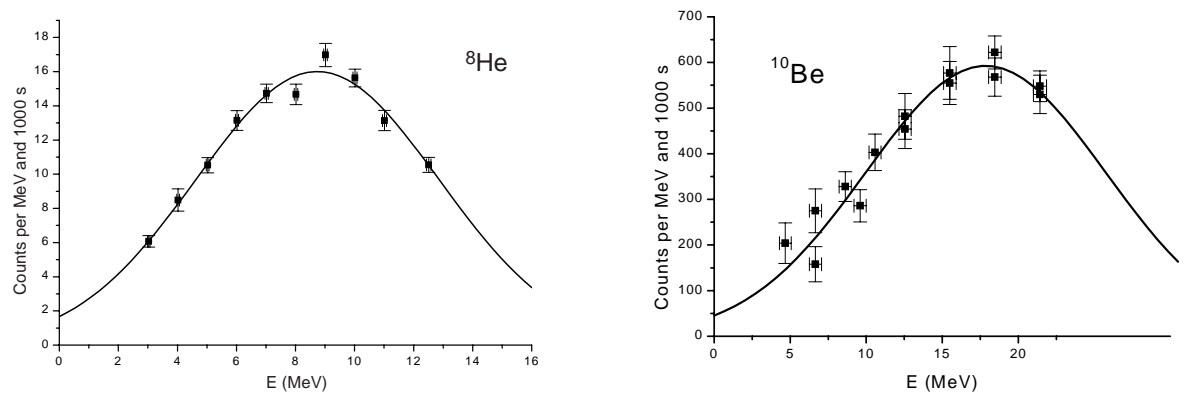


Figure A.4.8.: Kinetic energy distributions of $^8$He and $^{10}$Be from $^{241}$Pu($n_{th}$,f).
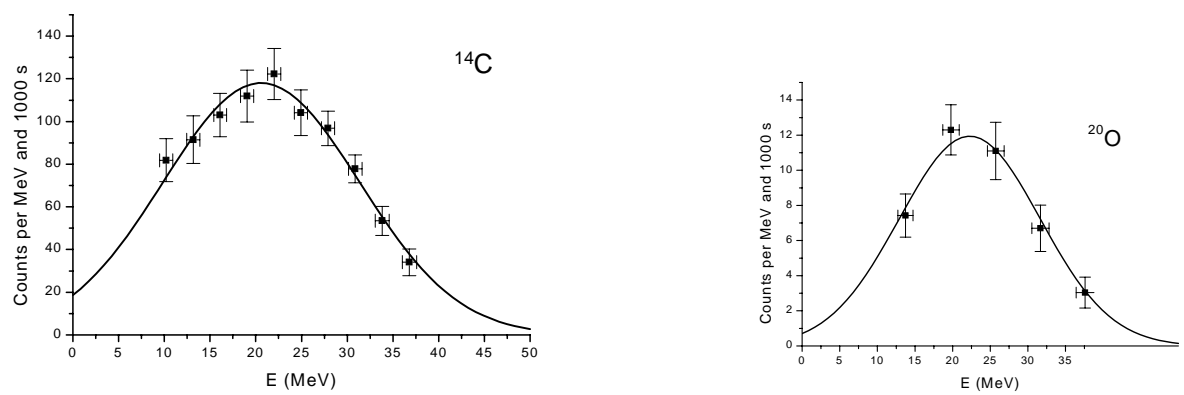


Figure A.4.9.: Kinetic energy distributions of $^{14}$C and $^{20}$O from $^{241}$Pu($n_{th}$,f).

## A.4.4.  $^{245}$Cm(n$_{th}$,f)
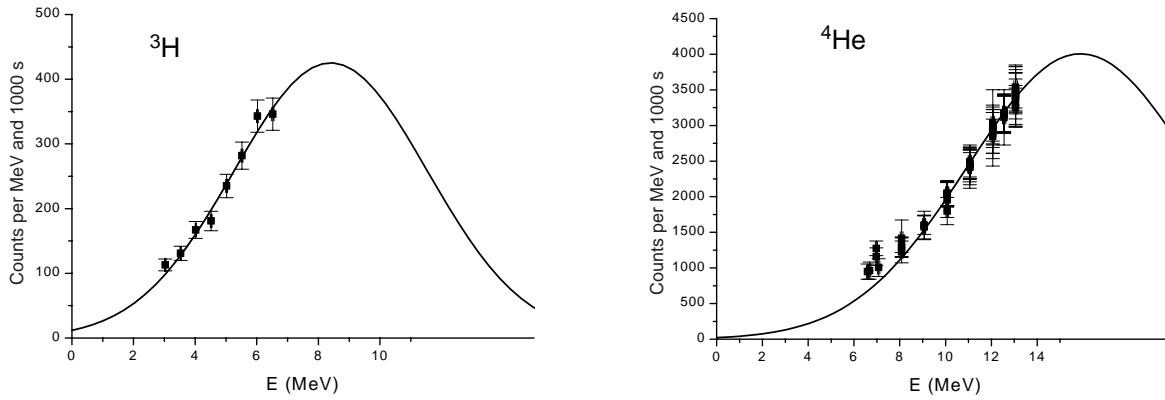


Figure A.4.10.: Kinetic energy distributions of $^3$H and $^4$He from $^{245}$Cm(n$_{th}$,f).
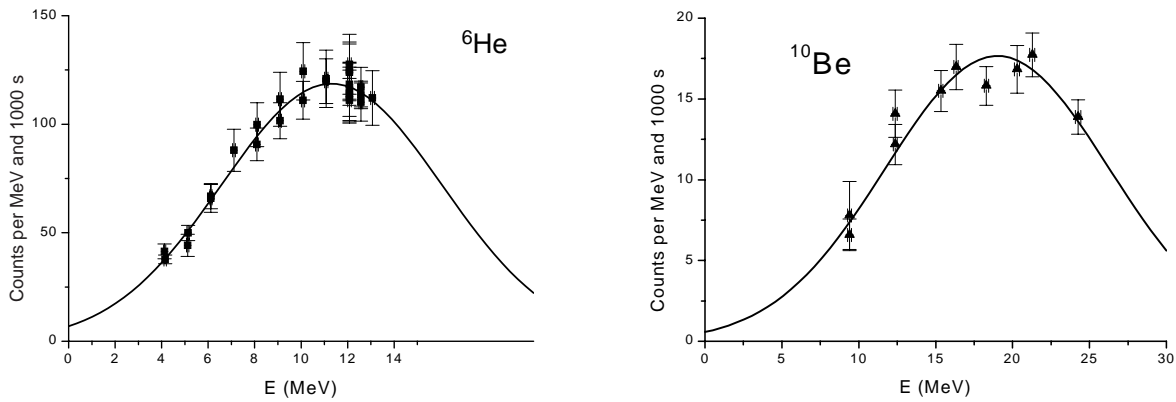


Figure A.4.11.: Kinetic energy distributions of $^6$He and $^{10}$Be from $^{245}$Cm(n$_{th}$,f).
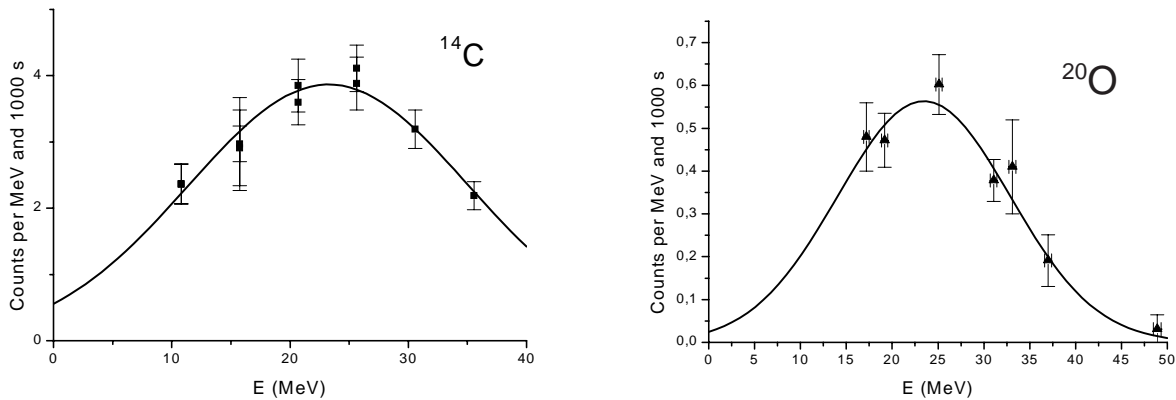


Figure A.4.12.: Kinetic energy distributions of $^{14}$C and $^{20}$O from $^{245}$Cm(n$_{th}$,f).

## A.5.   Ternary particle yields

To allow for an easier comparison of the different fissioning systems, experimental data on relative ternary fission yields has been collected from literature. The tables show the measured yields normalized to $10^4$ LRA with the error where available. The values and errors from the original publications are shown. Note that not in all cases the systematic errors are included. Moreover a renormalization of the $^4$He yield has been recommended for some measurements [Wag89]. References which give only partial yields over a limited energy range (e.g. [Rai68]) are not reported here.

### A.5.1.   $^{229}$Th(n$_{th}$,f)

Table A.5.1.: Measured ternary fission yields from $^{229}$Th(n$_{th}$,f). Note that for the target material used for the measurements of ref. [Wös99a] a contamination with higher actinides cannot be excluded. Thus all quoted values should be taken as upper limits only [Wös99b].

| Isotope | [Wag92] Yield | [Wös99a] Yield |
|---------|---------------|----------------|
| 3H      | 392(71)       |                |
| 4He     | 10000(−)      | 10000(−)       |
| 7Li     |               | 10.4(17)       |
| 9Be     |               | 3.8(23)        |
| 10Be    |               | 75.7(71)       |
| 12Be    |               | 1.1(5)         |
| 14C     |               | 20.9(24)       |
| 15C     |               | 4.3(4)         |
| 18N     |               | 0.12(9)        |
| 20O     |               | 1.8(5)         |
| 21O     |               | 0.14(6)        |
| 21F     |               | 0.025(20)      |
| 24Ne    |               | 0.029(24)      |

## A.5.2.    $^{233}$U($n_{th}$,f)

Table A.5.2.: Measured ternary fission yields from $^{233}$U($n_{th}$,f).

| Isotope | [Vor69] Yield | [Cam69] Yield | [Wag86] Yield | [Wös98] Yield | This work Yield |
|---------|---------------|---------------|---------------|---------------|-----------------|
| d | 41(2) | | | | |
| t | 460(20) | 280 | 527(14) | | |
| 3He | ≤0.1 | 180 | | | ≤0.018 |
| 4He | 10000(−) | 10000(−) | 10000(−) | | |
| 6He | 137(7) | 73(5) | | | (179(15)) |
| 8He | 3.6(4) | | | | |
| 6Li | ≤0.05 | | | | |
| 7Li | 3.7(2) | | | 5.1(13) | |
| 8Li | 1.8(2) | | | 2.0(3) | |
| 9Li | 3.6(5) | | | | 4.3(6) |
| 11Li | | | | | 0.00037(27) |
| 7Be | ≤0.01 | | | | |
| 9Be | 3.7(8) | | | | |
| 10Be | 43(3) | | | 43(3) | (43(3)) |
| 11Be | ≤0.3 | | | | 1.9(10) |
| 12Be | | | | 1.1(2) | |
| 14Be | | | | | ≤ 0.0011 |
| 12B | | | | 0.37(6) | |
| 13B | | | | 0.62(13) | |
| 14B | | | | 0.014(8) | 0.021(7) |
| 15B | | | | 0.0024(11) | |
| 14C | | | | 11.4(4) | |
| 15C | | | | 2.4(3) | 2.2(3) |
| 16C | | | | 2.1(3) | |
| 18C | | | | 0.052(12) | |
| 16N | | | | 0.026(11) | |
| 18N | | | | 0.047(9) | |
| 20O | | | | 0.71(8) | 0.73(9) |
| 21O | | | | 0.034(10) | 0.031(8) |
| 22O | | | | | 0.0052(24) |
| 21F | | | | | 0.0077(34) |
| 24Ne | | | | 0.0040(21) | |
| 27Na | | | | ≤0.00064 | |

## A.5.3.     $^{235}$U(n$_{\text{th}}$,f)

Table A.5.3.: Measured ternary fission yields from $^{235}$U(n$_{\text{th}}$,f).

| Isotope | [Chw67] Yield | [Dak67] Yield | [And69] Yield | [Blo69] Yield | [Kug72] Yield | [D'H80] Yield |
|---------|---------|---------|---------|---------|---------|---------|
| p | 200 | 115(15) | | | | 96(1) |
| d | 60 | 50(10) | | | | 56(2) |
| t | 550 | 620(50) | | | 310(80) | 627(3) |
| 3He | | | | | ≤0.08 | |
| 4He | 10000(−) | 10000(−) | 10000(−) | 10000(−) | 10000(−) | 10000(−) |
| 6He | 80 | 110(20) | | | | 170(2) |
| 8He | | | | | | 8 |
| all Li | | | 90 | 12(2) | | 10 |
| all Be | | | 32 | 37(4) | | 39 |
| all B | | | 1 | | | |
| all C | | | 50 | | | |
| all N | | | 2 | | | |
| all O | | | 50 | | | |
| all F | | | 24 | | | |

Table A.5.4.: Measured ternary fission yields from $^{235}$U(n$_{\text{th}}$,f).

| Isotope | [Vor72] Yield | [Doa86] Yield | [Bau92b] Yield | [Bou94] Yield | This work Yield |
|---------|---------|---------|---------|---------|---------|
| d | 50(2) | | 28.15(16) | | |
| t | 720(30) | | 610(2) | | |
| 3He | ≤0.01 | | | | ≤0.008 |
| 4He | 10000(−) | | 10000(−) | 10000(−) | |
| 6He | 191(8) | 169(2) | 169(2) | | |
| 8He | 8.2(6) | | 7.4(8) | | |
| 6Li | 0.05(2) | | 1.04(27) | | ≤0.012 |
| 7Li | 4.1(3) | | 3.99(15) | 4.2(3) | |
| 8Li | 1.8(3) | | 1.68(6) | 2.0(2) | |
| 9Li | 3.0(4) | 2.19(11) | 3.54(12) | 2.3(3) | 2.9(3) |
| 11Li | | | ≤0.0019 | | 0.00090(22) |

Table A.5.5.: Measured ternary fission yields from $^{235}$U($n_{th}$,f).

| Isotope | [Vor72] Yield | [Doa86] Yield | [Sic89] Yield | [Bau92b] Yield | [Bou94] Yield | This work Yield |
|---|---|---|---|---|---|---|
| 7Be | ≤0.01 | | | | | ≤0.009 |
| 8Be | | | | | | |
| 9Be | 2.9(3) | 1.67(8) | 4.2(4) | 3.12(10) | | |
| 10Be | 32(2) | 32(7) | 32(7) | 27.6(11) | | 27.6(20) |
| 11Be | 2.0(3) | | 2.96(35) | 2.36(36) | | |
| 12Be | 1.5(3) | 0.7(13) | 1.45(2) | 1.2(8) | | |
| 14Be | | | ≤0.003 | ≤0.0027 | | 0.00034(20) |
| 10B | ≤0.02 | | | 0.37(17) | | ≤0.008 |
| 11B | 0.25(10) | | | 0.30(2) | 0.31(4) | |
| 12B | 0.17(5) | 0.22(2) | | 0.21(3) | | |
| 13B | 0.20(6) | | | 0.47(4) | 0.44(3) | |
| 14B | 0.10(5) | | | 0.019(7) | | |
| 15B | | ≤0.01 | | 0.092(36) | | |
| 17B | | | | ≤0.0037 | | ≤0.0004 |
| 12C | | | | | | |
| 13C | 0.5(3) | | 0.4(15) | 0.59(8) | | |
| 14C | 5.4(6) | | 9.8(7) | 6.55(10) | | |
| 15C | 1.5(10) | 1.28(1) | 1.85(16) | 1.24(4) | | 1.5(5) |
| 16C | 0.2(1) | | 1.55(2) | 1.07(15) | | |
| 17C | | | 0.14(4) | 0.15(2) | | |
| 18C | | 0.057(15) | 0.05(2) | 0.042(9) | | |
| 19C | | | | | | |
| 20C | | | ≤0.0036 | 0.0048(16) | | |
| 15N | | | | 0.045(12) | | |
| 16N | ≤0.05 | | | ≤0.0072 | | |
| 17N | | | | 0.11(1) | | |
| 18N | | | | 0.034(12) | | |
| 19N | | | | 0.062(4) | | |
| 20N | | | | 0.0013(4) | | |
| 15O | | | | 0.34(21) | | ≤0.016 |
| 18O | ≤0.05 | 2.7(55) | | | | |
| 19O | | | | 0.16(1) | | |
| 20O | 0.5(2) | | 0.18(4) | 0.34(2) | 0.18(4) | 0.45(8) |
| 21O | | ≤0.12 | ≤0.12 | 0.045(13) | | 0.053(15) |
| 22O | | | | ≤0.0002 | | 0.017(6) |
| 21Ne | | 12.63(23) | | | | |

## A.5.4.    $^{239}$Pu(n$_{th}$,f)

Table A.5.6.: Measured ternary fission yields from $^{239}$Pu(n$_{th}$,f).

| Isotope | [Kro69] Yield | [Cam72] Yield | [Vor75] Yield | [Wag86] Yield | [Kös95] Yield | [Wös98] Yield |
|---------|---------------|---------------|---------------|---------------|---------------|---------------|
| p | 190(10) | | | | | |
| d | 50(10) | | 69(2) | | | |
| t | 680(30) | 570 | 720(30) | 641(19) | | |
| 3He | | | ≤0.01 | | | |
| 4He | 10000(−) | 10000(−) | 10000(−) | 10000(−) | 10000(−) | 10000(−) |
| 6He | 190(20) | 196 | 192(5) | | 186(10) | |
| 8He | 8(2) | | 8.8(4) | | | |
| 6Li | | | ≤0.05 | | | |
| 7Li | | | 6.5(2) | | | |
| 8Li | | | 3.2(3) | | | |
| 9Li | | | 5.3(3) | | | |
| 11Li | | | | | 0.0016(6) | |
| 7Be | | | ≤0.01 | | | |
| 9Be | | | 5.1(6) | | | |
| 10Be | | | 49(1) | | 49(−) | 49(1) |
| 11Be | | | 3.5(3) | | | |
| 12Be | | | 2.2(5) | | | |
| 14Be | | | | | 0.00037(23) | |
| 10B | | | ≤0.02 | | | |
| 11B | | | 0.9(3) | | | |
| 12B | | | 1.0(4) | | | |
| 13B | | | 1.3(4) | | | |
| 14B | | | 0.2(1) | | | |
| 13C | | | ≤1 | | | |
| 14C | | | 14.0(6) | | | |
| 15C | | | 3.5(13) | | | |
| 16C | | | 3.5(16) | | | |
| 16N | | | ≤0.02 | | | |
| 17N | | | | | | 0.19(1) |
| 20O | | | 0.8(4) | | | 0.68(3) |
| 21F | | | | | | 0.025(4) |
| 24Ne | | | | | | 0.025(3) |
| 27Na | | | | | | 0.0020(5) |
| 30Mg | | | | | | 0.0028(15) |
| 32Al | | | | | | ≤0.00032 |
| 34Si | | | | | | ≤0.00035 |
| F to Mg | | | ≤0.00002 | | | |
| Si to Ar | | | ≤0.000004 | | | |
| K to Fe | | | ≤0.00002 | | | |

## A.5.5.    $^{241}$Pu(n$_{th}$,f)

Table A.5.7.: Measured ternary fission yields from $^{241}$Pu(n$_{th}$,f).

| Isotope | [Wag86] Yield | This work Yield |
|---------|---------------|-----------------|
| d       |               | 42(4)           |
| t       | 761(19)       | 786(42)         |
| 4He     | 10000(−)      | 10000(700)      |
| 6He     |               | 263(18)         |
| 8He     |               | 15(1)           |
| 7Li     |               | 6.7(6)          |
| 8Li     |               | 4.2(6)          |
| 9Li     |               | 8.3(8)          |
| 11Li    |               | 0.0045(15)      |
| 7Be     |               | ≤0.2            |
| 9Be     |               | 4.4(5)          |
| 10Be    |               | 46(6)           |
| 11Be    |               | 5.9(17)         |
| 12Be    |               | 2.8(3)          |
| 14Be    |               | 0.0027(10)      |
| 10B     |               | ≤0.03           |
| 11B     |               | 1.6(10)         |
| 12B     |               | 1.0(4)          |
| 14B     |               | 0.13(4)         |
| 15B     |               | 0.046(10)       |
| 17B     |               | ≤0.001          |
| 14C     |               | 12.6(8)         |
| 15C     |               | 4.3(4)          |
| 16C     |               | 5.0(9)          |
| 17C     |               | 0.64(15)        |
| 18C     |               | 0.28(5)         |
| 19C     |               | 0.0025(14)      |
| 20C     |               | 0.0036(28)      |

| Isotope | [Wag86] Yield | This work Yield |
|---------|---------------|-----------------|
| 15N     |               | ≤0.044          |
| 16N     |               | 0.079(32)       |
| 17N     |               | 0.34(10)        |
| 18N     |               | 0.16(4)         |
| 19N     |               | 0.26(8)         |
| 20N     |               | 0.0029(16)      |
| 21N     |               | 0.0025(14)      |
| 15O     |               | ≤0.12           |
| 19O     |               | 0.26(12)        |
| 20O     |               | 1.10(12)        |
| 21O     |               | 0.23(6)         |
| 22O     |               | 0.12(4)         |
| 24O     |               | ≤0.08           |
| 19F     |               | 0.020(16)       |
| 20F     |               | 0.002           |
| 21F     |               | 0.021(6)        |
| 22F     |               | 0.30(21)        |
| 24F     |               | 0.030(16)       |
| 24Ne    |               | 0.040(12)       |
| 27Ne    |               | ≤0.008          |
| 24Na    |               | ≤0.001          |
| 27Na    |               | ≤0.005          |
| 28Na    |               | 0.006(4)        |
| 30Na    |               | ≤0.0008         |
| 27Mg    |               | ≤0.0012         |
| 28Mg    |               | ≤0.018          |
| 30Mg    |               | 0.009(6)        |
| 30Al    |               | ≤0.002          |
| 34Si    |               | ≤0.001          |
| 35Si    |               | ≤0.003          |
| 36Si    |               | ≤0.004          |

## A.5.6. $^{241}$**Am(2n$_{th}$,f)**

Table A.5.8.: Measured ternary fission yields from $^{241}$Am(2n$_{th}$,f). The values in ref. [Hes97] are only given relative to $^{14}$C. For better comparison they were normalized to a value of [$^{14}$C]=15.8(7) which is the weighted mean of ref. [Vor75, NL92, Neu92, Bör93, Bou94].

| Isotope | [Vor75] Yield | [NL92] Yield | [Neu92] Yield | [Bör93] Yield | [Bou94] Yield | [Hes97] Yield |
|---|---|---|---|---|---|---|
| t | 620(60) | | | | | |
| 4He | 10000(−) | 10000(−) | 10000(−) | | 10000(−) | |
| 6He | 214(6) | 243(33) | | | 165(17) | |
| 8He | | 10.2(26) | | | 6.7(6) | |
| 7Li | 8.2(26) | 7.2(12) | | | 7.1(7) | |
| 8Li | 3.6(4) | 4.1(7) | | | 4.4(4) | |
| 9Li | 6.4(13) | 6.9(1) | | | 7.5(9) | |
| 9Be | 7.5(15) | 6.8(8) | | | 7.1(3) | |
| 10Be | 57(6) | 52.8(53) | | 54 | 54.2(41) | |
| 11Be | | 6(7) | | | 5.4(16) | |
| 12Be | | 3.4(4) | | 3 | 2.8(3) | |
| 11B | | | 1.11(15) | | | |
| 12B | | | 1.59(24) | 0.8 | | |
| 13B | | | 2.55(31) | | | |
| 14B | | | 0.13(13) | 0.1 | | |
| 15B | | | 0.09(3) | 0.07 | | |
| 13C | | | 3.41(54) | | | |
| 14C | 14.5(15) | 16.5(17) | 16.7(13) | 17 | 15.1(13) | 15.8(7) |
| 15C | | 6.2(1) | 4.97(45) | 5.7 | | 6.4(7) |
| 16C | | | 4.6(4) | 3.1 | | 5.6(7) |
| 17C | | | 1.29(13) | 0.47 | | 0.57(8) |
| 18C | | | 0.3(3) | 0.14 | | 0.17(6) |
| 16N | | | 0.05(2) | 0.062 | | 0.20(5) |
| 17N | | | 0.6(1) | 0.56 | | 0.53(8) |
| 18N | | | 0.32(5) | 0.2 | | 0.25(7) |
| 19N | | | 0.61(11) | | | |
| 20N | | | 0.13(6) | 0.01 | | 0.014(8) |
| 21N | | | | | | 0.0035(15) |
| 17O | | | 0.16(6) | | | |
| 18O | | | 0.85(14) | | | |
| 19O | | | 0.65(9) | | | |
| 20O | | | 1.5(2) | 0.75 | | 1.8(3) |
| 21O | | | 0.25(4) | 0.34 | | 0.29(4) |
| 22O | | | | | | 0.19(3) |
| 23O | | | | | | 0.044(15) |
| 24O | | | | | | 0.018(8) |

---

[0]Since no errors were given in ref. [Bör93], a value of 17(2) with estimated uncertainty was taken for the average.

Table A.5.9.: Measured ternary fission yields from $^{241}$Am(2n$_{th}$,f). Continuation of table A.5.8.

| Isotope | [Bör93] Yield | [Hes97] Yield |
|---------|---------------|---------------|
| 20F | ≤ 0.01 | 0.015(9) |
| 21F | 0.055 | 0.11(3) |
| 22F | | 0.056(20) |
| 23F | | 0.086(21) |
| 24F | 0.0266 | 0.084(34) |
| 25F | ≤ 0.01 | |
| 21Ne | ≤ 0.005 | |
| 23Ne | | 0.024(11) |
| 24Ne | 0.091 | 0.13(40) |
| 25Ne | 0.05 | |
| 27Ne | ≤ 0.005 | |
| 28Ne | | 0.0060(20) |
| 24Na | ≤ 0.01 | |
| 25Na | ≤ 0.01 | |
| 27Na | 0.03 | |
| 28Na | ≤ 0.01 | 0.024(6) |
| 30Na | ≤ 0.01 | 0.0036(27) |
| 27Mg | ≤ 0.005 | |
| 28Mg | 0.01 | 0.014(5) |
| 30Mg | 0.01 | 0.030(7) |
| 31Mg | | 0.051(36) |
| 32Mg | 0.01 | 0.050(45) |
| 28Al | ≤ 0.005 | 0.11(3) |
| 30Al | ≤ 0.005 | |
| 32Al | ≤ 0.005 | 0.034(25) |
| 33Al | | 0.0048(43) |
| 32Si | 0.01 | 0.084(41) |
| 33Si | | 0.0078(53) |
| 34Si | 0.01 | 0.018(16) |
| 35Si | | 0.0089(64) |
| 33P | | ≤0.0035 |
| 40S | | ≤0.0019 |
| 42S | | ≤0.0012 |
| 42Cl | | ≤0.0010 |
| 44Ar | | ≤0.0011 |
| 50Ca | | ≤0.0009 |
| 50Sc | | ≤0.0009 |

## A.5.7.   $^{245}$Cm(n$_{th}$,f)

Table A.5.10.: Measured ternary fission yields from $^{245}$Cm(n$_{th}$,f). The values in [Hes97] are only given relative to $^{14}$C. For better comparison they were renormalized to a value of [$^{14}$C]=23.3(16) which was obtained from our measurement, see section 1.5.

| Isotope | This work Yield | [Hes97] Yield | Isotope | This work Yield | [Hes97] Yield |
|---------|-----------------|----------------|---------|-----------------|----------------|
| t    | 679(44)     |          | 14N  | ≤4.1      |           |
| 3He  | ≤0.6        |          | 15N  | 0.17(7)   |           |
| 4He  | 10000(600)  |          | 16N  |           | 0.27(8)   |
| 6He  | 286(16)     |          | 17N  | 0.77(31)  |           |
| 8He  | 19(4)       |          | 18N  | 0.47(21)  | 0.77(21)  |
| 6Li  | ≤0.3        |          | 19N  | 0.53(19)  |           |
| 7Li  | 13.6(13)    |          | 20N  | ≤0.061    |           |
| 8Li  | 5.6(8)      |          | 21N  | ≤0.024    |           |
| 9Li  | 13.6(17)    |          | 16O  | ≤47       |           |
| 11Li | 0.010(6)    |          | 17O  | ≤0.2      |           |
| 9Be  | 9.1(11)     |          | 18O  | 1.0(4)    |           |
| 10Be | 66(5)       |          | 19O  | 0.77(47)  |           |
| 11Be | 8.1(10)     |          | 20O  | 2.7(4)    |           |
| 12Be | 5.5(7)      |          | 21O  | 0.71(24)  | 0.75(19)  |
| 14Be | 0.018(12)   |          | 22O  | 0.39(18)  | 0.53(11)  |
| 10B  | ≤0.3        |          | 20F  | ≤0.08     |           |
| 11B  | 2.4(13)     |          | 21F  |           | 0.17(5)   |
| 12B  | 2.3(4)      |          | 22F  |           | 0.21(5)   |
| 13B  | 2.2(6)      |          | 24F  |           | 0.082(28) |
| 14B  | 0.21(6)     |          | 24Ne |           | 0.23(6)   |
| 15B  | 0.09(5)     |          | 27Na |           | 0.12(6)   |
| 12C  | ≤4.8        |          | 27Mg |           | 0.062(32) |
| 13C  | 1.1(5)      |          | 28Mg |           | 0.026(18) |
| 14C  | 23.3(16)    | 23.3(16) | 30Mg |           | 0.060(27) |
| 15C  | 7.7(11)     | 9.6(12)  | 32Mg |           | 0.021(17) |
| 16C  | 9.5(33)     | 9.2(11)  | 28Al |           | 0.47(11)  |
| 17C  | 0.65(21)    |          | 33Si |           | ≤0.03     |
| 18C  | 0.32(11)    | 0.51(10) | 44Ar |           | ≤0.016    |
| 19C  | ≤0.030      |          | 44K  |           | ≤0.011    |
| 20C  | ≤0.053      |          | 48K  |           | ≤0.05     |

## A.5.8.    $^{249}$Cf(n$_{th}$,f)

Table A.5.11.: Measured ternary fission yields from $^{249}$Cf(n$_{th}$,f). Exceptionally absolute yields (per fission) are given since no data for the $^4$He yield is known. Lower limits are for cases where some events were observed, but not enough data could be taken to deduce an energy distribution or a yield.

| Isotope | [Dav97] Yield |
|---------|---------------|
| 6He | $\geq 5.9 \cdot 10^{-5}$ |
| 8Li | $\geq 2.3 \cdot 10^{-6}$ |
| 9Li | $\geq 3.4 \cdot 10^{-6}$ |
| 10Be | $4.1(9) \cdot 10^{-6}$ |
| 11Be | $3.6(12) \cdot 10^{-6}$ |
| 12Be | $\geq 1.6 \cdot 10^{-6}$ |
| 12B | $1.3(3) \cdot 10^{-7}$ |
| 13B | $2.4(7) \cdot 10^{-7}$ |
| 14B | $1.8(12) \cdot 10^{-7}$ |
| 15B | $4.2(13) \cdot 10^{-8}$ |
| 14C | $1.3(3) \cdot 10^{-6}$ |
| 15C | $5.3(10) \cdot 10^{-6}$ |
| 16C | $4.7(13) \cdot 10^{-6}$ |
| 17C | $6.0(32) \cdot 10^{-7}$ |
| 18C | $1.5(4) \cdot 10^{-8}$ |
| 16N | $1.3(11) \cdot 10^{-7}$ |
| 18N | $4.4(24) \cdot 10^{-7}$ |
| 20O | $1.5(3) \cdot 10^{-7}$ |
| 21O | $9.8(59) \cdot 10^{-7}$ |
| 22O | $\geq 9.4 \cdot 10^{-8}$ |
| 21F | $1.3(5) \cdot 10^{-8}$ |
| 24F | $\geq 1.7 \cdot 10^{-8}$ |
| 24Ne | $\geq 1.0 \cdot 10^{-7}$ |
| 27Na | $\geq 1.1 \cdot 10^{-8}$ |
| 28Na | $\geq 3.2 \cdot 10^{-9}$ |
| 30Mg | $8.4(31) \cdot 10^{-8}$ |
| 33Al | $\geq 4.1 \cdot 10^{-10}$ |

## A.5.9.    $^{252}$**Cf(sf)**

Table A.5.12.: Measured ternary fission yields from $^{252}$Cf(sf).

| Isotope | [Weg61] Yield | [Bay81] Yield | [Wil85] Yield | [Gra88] Yield | [Bud90] Yield | [Iva96] Yield |
|---|---|---|---|---|---|---|
| p | 220(50) | | 156(39) | | | 180(60) |
| d | ≤50 | | | | 68(3) | |
| t | 600(50) | | 779(192) | 836(12) | | 700(40) |
| 3He | ≤50 | | | | | |
| $^4$He | 10000(−) | 10000(−) | 10000(−) | 10000(−) | 10000(−) | 10000(−) |
| $^6$He | | 306(15) | | 386(12) | | |
| 7Li | | 12.7(21) | | | | |
| 8Li | | 8.5(14) | | | | |
| all Li | | | | 55(4) | | |
| all Be | | | | 164(9) | | |

Additionally a yield of 200(70) per 10000 LRA is quoted for $^6$He in ref. [Cum81].

Table A.5.13.: Measured ternary fission yields from $^{252}$Cf(sf).

| Isotope | [Whe67] Yield | [Cos67] Yield | [And69] Yield | [Gaz70] Yield | [Dlo92] Yield | [Sin97] Yield |
|---|---|---|---|---|---|---|
| p | 160(20) | 175(30) | | | | |
| d | 63(3) | 68(3) | | | | |
| t | 590(20) | 846(28) | | | | |
| 3He | ≤9 | ≤7.5 | | | | |
| 4He | 10000(−) | 10000(−) | 10000(−) | 10000(−) | 10000(−) | 10000(−) |
| 6He | 240(50) | 263(18) | | | 403(26) | 315(60) |
| 8He | 18(5) | 9.0(12) | | | 25(4) | 25(5) |
| 7Li | | | | | 17(4) | |
| 8Li | | | | | 10(5) | |
| 9Li | | | | | 25(11) | |
| all Li | 12(6) | 13.2(16) | 9 | 29(5) | | 52(5) |
| 8Be | 0.48 | | | | | |
| 10Be | | | | | 185(20) | |
| all Be | ≥1 | 20.1(20) | 32 | 65(7) | | 126(30) |
| all B | | | 0.95 | 3.5(10) | | 6.3(4) |
| all C | | | 48 | 43(9) | | |
| all N | | | 2.4 | 6.6(15) | | |
| all O | | | 48 | 0.5(1) | | |
| all F | | | 24 | | | |

## A.5.10.  Other fissioning systems

Table A.5.14.: Measured ternary fission yields from $^{248}$Cm(sf), $^{250}$Cf(sf) and $^{256}$Fm(sf).

| Isotope | $^{248}$Cm(sf) [Iva96] Yield | $^{248}$Cm(sf) [Iva97] Yield | $^{250}$Cf(sf) [Wil85] Yield | $^{256}$Fm(sf) [Wil85] Yield |
|---------|------------------------------|------------------------------|------------------------------|------------------------------|
| p       | 150(70)                      | 160(20)                      | 226(53)                      | 152(47)                      |
| d       |                              | 50(5)                        |                              |                              |
| t       | 860(40)                      | 922(18)                      | 678(134)                     | 844(153)                     |
| 4He     | 10000(−)                     | 10000(−)                     | 10000(−)                     | 10000(−)                     |
| 6He     |                              | 354(31)                      |                              |                              |
| 8He     |                              | 24(4)                        |                              |                              |
| all Li  |                              | 26(9)                        |                              |                              |
| all Be  |                              | 49(24)                       |                              |                              |

# B. Appendix to ISOL technique

## B.1. Useful conversion factors and formulae

### Thermodynamics

In chemistry the energies and enthalpies are often given in kJ/mol or kcal/mol. The following conversion (given by the Faraday constant) applies for the reaction energy of a single atom or molecule:

| (eV) | (kJ/mol) | (kcal/mol) |
|---|---|---|
| 1 | 96.48 | 404.0 |
| 0.01036 | 1 | 4.187 |
| $2.475 \cdot 10^{-3}$ | 0.2388 | 1 |

### Evaporation

The maximum unhindered[1] evaporation rate per unit surface of a material with molar mass $M$ and vapor pressure $p_{\text{vap}}$ is given by the Hertz-Knudsen equation:

$$
\begin{aligned}
J_0 &= \alpha\, p_{\text{vap}} \frac{M}{\sqrt{2\pi R T}} \\
J_0/(\text{kg m}^{-2}\text{s}^{-1}) &= 0.438\,\alpha\, \frac{p_{\text{vap}}}{\text{mbar}} \sqrt{\frac{M}{\text{g mol}^{-1}} \frac{T}{\text{K}}}
\end{aligned}
\tag{B.1.1}
$$

$R$ is the gas constant, $T$ the temperature and $\alpha$ the accommodation or Langmuir coefficient. This empirical coefficient was taken to be unity by Langmuir [Lan13]. Meanwhile several studies indicated that it may differ by many orders of magnitude [Nes63]. Therefore the values derived with $\alpha = 1$ should be taken as an upper limit.

### Laser spectroscopy

In laser spectroscopy different units are employed, the following compilation gives some handy conversion factors:

| Energy $E$ (eV) | Frequency $\nu$ (GHz) | Vac. wavelength $\lambda$ (nm) | Wave number $k$ (cm$^{-1}$) |
|---|---|---|---|
| 1 | $2.418 \cdot 10^5$ | 1239.85 | 8065.54 |
| $1.2399 \cdot 10^{-4}$ | 29.979 | $10^7$ | 1 |

The unit cm$^{-1}$ is also called kayser in older publications.

---

[1]Unhindered means that all evaporated particles are pumped away immediately and are not redeposited onto the surface.

## B.2.    Release from ISOL targets

The efficiency for release from an ISOL target and ion source system $Y(T_{1/2})$ is obtained by folding $p(t)$, the probability for release in the interval $[t; t + dt]$, with the probability for survival of the radioactive decay $\exp(-\lambda t)$, where $\lambda = \ln 2/T_{1/2}$:

$$Y(T_{1/2}) = \int_0^\infty p(t)\exp(-\lambda t)dt. \tag{B.2.1}$$

The fractional release $F(t)$ quantifies the fraction of stable nuclei which is released up to the time $t$:

$$F(t) = \int_0^t p(t')dt'. \tag{B.2.2}$$

The total release time is composed of the diffusion time in the bulk material and the effusion time through target container, transfer line and ion source.

### B.2.1.    Diffusion

Diffusion in solid state matrices is driven by a concentration gradient as described by Fick's second law:

$$\frac{\partial}{\partial t}\rho(\vec{x}, t) = D\Delta\rho(\vec{x}, t) \tag{B.2.3}$$

with $\rho(\vec{x}, t)$ the local density of the diffusing species, $D$ the diffusion coefficient and $\Delta$ the Laplace operator.

In many ISOL applications[2] the spread of the stopped reaction products will be uniform compared with the size of the microscopic structure of the target matrix. Thus, the starting condition is:

$$\rho(\vec{x}, 0) = \rho_0. \tag{B.2.4}$$

Under the assumption that the nuclei desorb and effuse rapidly away from the surface, the concentration above the surface remains negligible and the boundary condition becomes:

$$D\left(\frac{\partial\rho(\vec{x}, t)}{\partial n}\right)_{\vec{x}=\vec{x}_{\text{surface}}} = C\rho(\vec{x}, t)_{\vec{x}=\vec{x}_{\text{surface}}}, \tag{B.2.5}$$

where $\partial/\partial n$ denotes the differentiation normal to the surface and $C$ is a constant.

This set of equations can be solved for the three practical cases of one-dimensional diffusion ($n = 1$: a flat foil), two-dimensional diffusion ($n = 2$: a long fiber) and three-dimensional diffusion ($n = 3$: a sphere) giving the diffusional delay $p_\mu(t)$ (see e.g. references [Cra70, Fuj81, Kir92a] for the exact solutions). For one-dimensional diffusion ($n = 1$) in a foil with thickness $d$ the fractional release is given by:

$$F_\mu(t) \overset{\text{for } \mu_0 t \lesssim 0.5}{\approx} 0.72\sqrt{\mu_0 t}. \tag{B.2.6}$$

with $\mu_0 = \pi^2 D/d^2$ the delay parameter. For short times it increases with the square root of the delay parameter and for longer times it goes into saturation: $\lim_{t\to\infty} F_\mu(t) = 1$. For the detailed behavior in intermediate times see e.g. ref. [Fuj81, Kir92a].

---

[2]This is surely valid for high-energy proton induced reactions. However, it is not necessarily true for a catcher of fusion-evaporation products [Kir92a].

The behavior of the release efficiency $Y_\mu(T_{1/2})$ is similar for all discussed geometries:

$$Y_\mu(T_{1/2}) \overset{\text{for } \mu_0 T_{1/2} \lesssim 0.3}{\approx} 0.76n\sqrt{\mu_0 T_{1/2}}, \tag{B.2.7}$$

where $n$ gives the dimension of the Laplace operator as defined above.

It is intuitively clear that the diffusion out of a sphere with diameter $d$ is faster compared with a fiber with diameter $d$, which in turn is faster than from a foil with thickness $d$. However, in a practical target material it is difficult to realize these ideal geometries. Metal foil targets come close to the ideal description if the touching area between neighboring foils is not too big. In practice this is achieved by denting the foils. On the other hand the close packing of small spheres (e.g. in a powder target) can result in a denser structure with more touching surfaces. Therefore the difference between the actual material density and the theoretical bulk density does not necessarily show up as open porosity, but caverns are created in which the diffusing particles can get trapped. This was experienced in the diffusion of xenon in graphite [Kir97]. The closing of the pores which increases the release time gets even worse if the spheres start to "bake" together, i.e. if the target sinters. This was e.g. observed with powder targets from metal oxides [Han73]. Fibers on the other hand support themselves and can provide a stable structure with large open porosity. Therefore a fiber target can show in practice a faster release compared to a powder target.

The temperature dependence of the diffusion coefficient $D$ is normally represented by an Arrhenius equation of the form:

$$D(T) = D_0 \exp\left(-\frac{Q}{RT}\right), \tag{B.2.8}$$

where $D(T)$ is the diffusion coefficient at the temperature $T$, $D_0$ is the extrapolated diffusion coefficient at infinite temperature, $Q$ is the activation energy (in kJ/mol) and $R$ the gas constant. There are cases where one has to use more than one exponential term in the Arrhenius equation to take into account components with different diffusion mechanisms or different activation energies [Flü39, Cow58].

In principle the diffusion constant $D$ is also influenced by the atomic mass $A$ of the diffusing isotope. The isotope effect parameter describing this fact is defined as:

$$E_{A1,A2} = \frac{D^{A1}/D^{A2} - 1}{\sqrt{A2/A1} - 1}. \tag{B.2.9}$$

It takes values between 1 (maximum mass effect) and 0. Generally $E_{A1,A2}$ tends to decrease for higher temperatures. Only few values have been measured for typical ISOL elements and targets: e.g. 0.025 for Fe in Nb at 1900 °C [Bak90] or 0.11 for Cr in W at 2400 °C. The isotope effect is generally neglected when discussing ISOL applications.

## B.2.2.   Effusion

The total effusion time $\tau_\nu$ is given by the number of wall collisions $\chi$ times the average time between two wall collisions. The latter is the sum of the average flight time $\tau_{\text{free}}$ between two collisions and the average surface sticking time $\tau_{\text{sorp}}$. Neglecting surface sticking (e.g. for noble gas atoms) the effusion time is just given by the total flight time inside the target. This is called intrinsic delay time.

The delay function is given by:

$$p_\nu(t) = \nu \exp(-\nu t) \tag{B.2.10}$$

with the delay parameter $\nu = 1/\tau_\nu = (\chi(\tau_{\text{free}} + \tau_{\text{sorp}}))^{-1}$. The fractional release becomes:

$$F_\nu(t) = 1 - \exp(-\nu t) \overset{\text{for } \nu t \lesssim 0.2}{\approx} \nu t \tag{B.2.11}$$

and the release efficiency is:

$$Y_\nu(T_{1/2}) = \frac{\nu}{\nu + \lambda} \overset{\text{for } \nu T_{1/2} \lesssim 0.2}{\approx} 1.44 \nu T_{1/2}. \tag{B.2.12}$$

The number of wall collisions is very approximately given by the ratio of the inner surface to the size of the extraction opening[3]. In a typical ISOLDE metal foil target the inner surface can reach 1 m$^2$ or more. In other materials similar or even bigger surfaces occur, e.g. about 10 m$^2$ in a graphite cloth target. Thus, the atoms will make in average some hundred thousand[4] wall collisions before being released through the 7 mm$^2$ orifice. Consequently even a surface sticking time of some $\mu$s can lead to delays in the range of seconds.

## B.2.3.   Desorption

The average desorption time of an adsorbate atom from an adsorbent surface $\tau_{\text{sorp}}$ is governed by a Frenkel equation [Kir86]:

$$\tau_{\text{sorp}} = \tau_0 \exp\left(-\frac{E_d}{RT}\right) \tag{B.2.13}$$

with $1/\tau_0$ a frequency factor, $E_d$ the interaction energy of the adsorbed atom with the surface, $R$ the gas constant and $T$ the surface temperature. With the assumption of negligible activation energy and low surface coverage, $E_d$ is approximately equal to the partial molar absorption enthalpy $\Delta \bar{H}_a$. For many adsorbate/adsorbent pairs no literature values exist for $\Delta \bar{H}_a$. However, the empirical "Eichler systematics" [Roß84, Eic85a, Eic85b] can allow a rough estimation of the desorption enthalpy from metal surfaces. Tables B.2.1 and B.2.2 in appendix B.2.5 give an overview of derived desorption times. Note that these *calculated* times should only be taken as an estimate of the order of magnitude in the cases where no measured values are available!

It is obvious that some elements are practically not desorbed in elemental form. Here, the separation as molecules can decrease the desorption enthalpy and thus drastically accelerate the release (see section 4.1).

## B.2.4.   Real situation

For a real target and ion source unit the total release time is given by a combination of the diffusion time and the effusion time. The fractional release and the release efficiency become:

$$F(t) \overset{\text{for } \nu > 0.1 \mu_0 \text{ and } \nu t \lesssim 0.2}{\approx} 0.48 n \nu \sqrt{\mu_0} t^{3/2} = \frac{2}{3} F_\mu(t) F_\nu(t). \tag{B.2.14}$$

$$Y(T_{1/2}) = Y_\mu(T_{1/2}) \cdot Y_\nu(T_{1/2}). \tag{B.2.15}$$

---

[3]This assumes 100 % diffuse scattering and a geometry with high conductance. A small part of reflecting collisions could accelerate the effusion while a complicated geometry with low conductance can hinder it strongly.

[4]For the RIST target still higher values of $(0.7 - 5.2) \cdot 10^6$ [Den97] or even $2 \cdot 10^7$ [Ben97] were calculated.

## B.2.5.    Wall sticking times from the Eichler systematics

Eichler et al. developed an empirical model for the calculation of the desorption enthalpy of different adsorbates $A$ on metallic surfaces $M$ [Roß84, Eic85a, Eic85b].

First the partial molar solution enthalpy $\Delta \bar{H}_\text{s}$ is calculated:

$$\Delta \bar{H}_\text{s} = \frac{2 \cdot \bar{V}_\text{A}^{2/3} \cdot P}{n_\text{WSA}^{-1/3} + n_\text{WSM}^{-1/3}} \cdot \left( 9.4 \cdot (n_\text{WSA}^{1/3} - n_\text{WSM}^{1/3})^2 - (e\Phi_\text{A}^* - e\Phi_\text{M}^*)^2 - \frac{R_\text{m}}{P} \right), \qquad \text{(B.2.16)}$$

with $n_\text{WS}$ the electron density at the border of the Wigner-Seitz-cell, $P$ and $R_\text{m}/P$ constants specific for the chemical group, $\Phi^*$ the electro-negativity parameter and $\bar{V}_\text{A}$ the effective atom volume of the adsorbate:

$$\bar{V}_\text{A} = V_\text{A} \cdot (1 + a \cdot (\Phi_\text{A}^* - \Phi_\text{M}^*))^{3/2} \qquad \text{(B.2.17)}$$

which accounts for the change of the original atom volume $V_\text{A}$ due to charge transfer.

With $\Delta \bar{H}_\text{s} \geq 50$ kJ/mol the adsorbate is practically insoluble in the metal and only adsorbed to the surface. Then $\Delta \bar{H}_\text{a}$ is given by:

$$\Delta \bar{H}_\text{a} = \Delta H_\text{DA}^0 + 0.6 \cdot \left( \Delta \bar{H}_\text{s} - \frac{V_\text{A}^*}{V_\text{M}} \cdot \Delta \bar{H}_\text{VM} \right), \qquad \text{(B.2.18)}$$

with $\Delta H_\text{DA}^0$ the de-sublimation enthalpy of the adsorbate, $V_\text{M}$ the atom volume of the metal and $\Delta \bar{H}_\text{VM}$ the enthalpy for creation of volume vacancies in the metal.

With $\Delta \bar{H}_\text{s} < 50$ kJ/mol the adsorbate is partially or totally soluble in the metal and can even create compounds. In these cases the adsorbate can substitute a surface atom of the metal and the absorption enthalpy becomes:

$$\Delta \bar{H}_\text{a} = \Delta H_\text{DA}^0 + 0.9 \cdot (\Delta \bar{H}_\text{s} - \frac{V_\text{A}^*}{V_\text{M}} \cdot \Delta \bar{H}_\text{VM}) + \frac{V_\text{A}^*}{V_\text{M}} \cdot \Delta \bar{H}_\text{SM}, \qquad \text{(B.2.19)}$$

with $\Delta \bar{H}_\text{SM}$ the enthalpy for creation of surface vacancies in the metal.

All required values are listed in references [Roß84, Eic85a, Eic85b]. A large uncertainty arises from the unknown frequency factor $C$ in equation (B.2.13) which varies between $10^8$ and $10^{13}$ s$^{-1}$ [Rös86]. In the following $C = 10^{13}$ s$^{-1}$ will be used which allows to give an estimate on the lower limit of the desorption time. Thus, a rough comparison between different materials becomes possible.

Tables B.2.1 and B.2.2 give an overview of calculated desorption times of different elements from typical metal surfaces. These calculated values can give a first hint in cases where no measured data are available.

Table B.2.1.: Mean wall sticking times calculated with the Eichler systematics. The calculated
times should only be taken as a relative estimate for the order of magnitude!

| Metal | | Ti | Zr | Nb | Mo | Ta | W | Re | Ir | Pt |
|---|---|---|---|---|---|---|---|---|---|---|
| $\theta$ (°C) | | 1600 | 1800 | 2000 | 2000 | 2400 | 2400 | 2400 | 2200 | 1700 |
| Z | El. | $\log(t)$ | $\log(t)$ | $\log(t)$ | $\log(t)$ | $\log(t)$ | $\log(t)$ | $\log(t)$ | $\log(t)$ | $\log(t)$ |
| | | (s) | (s) | (s) | (s) | (s) | (s) | (s) | (s) | (s) |
| 3 | Li | -7.9 | -8.3 | -9.3 | -8.8 | -9.0 | -8.9 | -9.9 | -9.3 | -6.6 |
| 4 | Be | -2.7 | -3.7 | -4.8 | -4.6 | -5.6 | -5.7 | -5.0 | -4.3 | -1.6 |
| 5 | B | 7.0 | 5.5 | 2.7 | 1.9 | 0.7 | -0.4 | -0.4 | 0.7 | 4.6 |
| 6 | C | 14.1 | 11.9 | 9.0 | 7.6 | 5.8 | 4.4 | 3.3 | 4.5 | 8.5 |
| 7 | N | 16.3 | 14.7 | 9.5 | 6.1 | 6.2 | 2.6 | 0.3 | 1.4 | 4.6 |
| 11 | Na | -10.7 | -10.6 | -11.9 | -11.2 | -10.5 | -10.5 | -9.4 | -9.4 | -10.5 |
| 12 | Mg | -8.9 | -8.6 | -7.9 | -7.5 | -7.6 | -7.6 | -9.4 | -8.7 | -5.7 |
| 13 | Al | 1.3 | 0.6 | -2.5 | -3.2 | -3.4 | -4.6 | -3.8 | -2.9 | 0.8 |
| 14 | Si | 7.2 | 5.9 | 2.4 | 1.2 | 0.7 | -0.9 | -0.9 | 0.2 | 4.2 |
| 19 | K | -11.0 | -11.1 | -12.2 | -10.6 | -9.7 | -9.4 | -8.1 | -8.3 | -6.9 |
| 20 | Ca | -6.0 | -6.8 | -7.7 | -6.2 | -6.7 | -6.0 | -8.4 | -7.4 | -2.9 |
| 21 | Sc | -2.1 | -2.9 | -1.8 | -3.9 | -2.2 | -4.7 | -1.6 | -0.3 | 5.3 |
| 22 | Ti | 0.9 | -0.5 | -1.9 | -0.8 | -2.7 | -2.1 | 0.3 | 1.5 | 6.8 |
| 23 | V | 2.1 | 0.7 | -0.7 | -0.3 | -1.9 | -1.9 | -0.6 | 0.4 | 4.6 |
| 24 | Cr | -0.6 | -1.7 | -3.0 | -3.2 | -4.0 | -4.4 | -3.8 | -3.1 | -0.2 |
| 25 | Mn | -3.7 | -4.3 | -5.9 | -6.2 | -6.4 | -7.0 | -6.3 | -5.7 | -3.1 |
| 26 | Fe | 1.0 | -0.1 | -1.8 | -2.5 | -3.0 | -3.9 | -3.8 | -3.2 | -0.5 |
| 27 | Co | 2.2 | 1.2 | -1.0 | -2.1 | -2.4 | -3.7 | -4.0 | -3.3 | -0.8 |
| 28 | Ni | 2.8 | 1.9 | -0.6 | -2.0 | -2.1 | -3.7 | -4.1 | -3.4 | -1.0 |
| 29 | Cu | -1.3 | -1.7 | -4.7 | -3.7 | -5.5 | -4.8 | -4.7 | -5.9 | -3.3 |
| 30 | Zn | -5.9 | -5.9 | -8.7 | -9.4 | -8.7 | -9.9 | -9.2 | -8.6 | -6.4 |
| 31 | Ga | -0.4 | -0.8 | -4.3 | -5.2 | -4.8 | -6.2 | -5.3 | -4.3 | -0.7 |
| 32 | Ge | 4.3 | 3.6 | -0.5 | -2.1 | -1.7 | -3.7 | -3.6 | -2.6 | 1.0 |
| 33 | As | 4.9 | 4.2 | -0.3 | -2.3 | -1.4 | -4.0 | -4.2 | -3.4 | -0.1 |
| 37 | Rb | -11.0 | -11.2 | -12.2 | -10.3 | -9.3 | -8.9 | -7.5 | -7.9 | -6.6 |
| 38 | Sr | -6.4 | -7.1 | -8.1 | -6.2 | -6.6 | -5.7 | -3.8 | -8.0 | -3.2 |
| 39 | Y | 2.3 | -2.1 | -0.5 | 1.0 | -0.8 | 0.1 | -1.1 | 0.4 | 6.9 |
| 40 | Zr | 4.9 | 3.1 | 1.2 | 2.9 | 0.2 | 1.2 | 4.3 | 6.0 | 13.1 |
| 41 | Nb | 7.7 | 5.5 | 4.0 | 5.2 | 2.4 | 3.0 | 5.1 | 6.6 | 12.7 |
| 42 | Mo | 6.5 | 4.6 | 3.0 | 3.1 | 1.3 | 1.1 | 1.8 | 2.9 | 7.3 |
| 43 | Tc | 11.3 | 9.5 | 6.4 | 4.8 | 4.0 | 2.2 | 1.5 | 2.5 | 6.3 |
| 44 | Ru | 9.1 | 7.6 | 4.6 | 2.9 | 2.5 | 0.5 | -0.3 | 0.5 | 3.7 |
| 45 | Rh | 8.9 | 7.5 | 4.0 | 1.9 | 2.0 | -0.4 | -1.4 | -0.5 | 2.5 |
| 46 | Pd | 5.7 | 5.0 | 0.8 | -2.0 | -0.8 | -3.9 | -5.2 | -4.5 | -2.4 |
| 47 | Ag | -2.7 | -2.6 | -6.6 | -4.8 | -6.8 | -5.5 | -5.3 | -5.1 | -5.1 |
| 48 | Cd | -6.4 | -5.9 | -9.8 | -7.5 | -9.4 | -7.7 | -10.2 | -9.7 | -7.3 |

Table B.2.2.: Continuation of table B.2.1.

| Metal | | Ti | Zr | Nb | Mo | Ta | W | Re | Ir | Pt |
|---|---|---|---|---|---|---|---|---|---|---|
| θ (°C) | | 1600 | 1800 | 2000 | 2000 | 2400 | 2400 | 2400 | 2200 | 1700 |
| Z | El. | log(t) (s) | log(t) (s) | log(t) (s) | log(t) (s) | log(t) (s) | log(t) (s) | log(t) (s) | log(t) (s) | log(t) (s) |
| 49 | In | -2.2 | -2.1 | -6.7 | -3.5 | -6.5 | -4.1 | -7.2 | -6.3 | -2.5 |
| 50 | Sn | 1.6 | 1.4 | -3.6 | -5.1 | -3.9 | -2.0 | -5.3 | -4.3 | -0.3 |
| 51 | Sb | 2.6 | 2.6 | -3.2 | -5.4 | -3.5 | -6.6 | -6.2 | -5.3 | -1.7 |
| 55 | Cs | -10.7 | -11.0 | -11.8 | -9.5 | -8.4 | -7.9 | -6.7 | -7.1 | -5.9 |
| 56 | Ba | -5.2 | -6.1 | -7.1 | -5.0 | -5.4 | -4.4 | -2.3 | -7.3 | -2.0 |
| 57 | La | 1.8 | 0.4 | -1.3 | 0.1 | -1.3 | -0.5 | -2.7 | -1.2 | 5.3 |
| 58 | Ce | 1.3 | -2.6 | -1.5 | -0.2 | -1.8 | -1.1 | -2.1 | -0.7 | 5.2 |
| 59 | Pr | -0.4 | -1.6 | -3.0 | -1.7 | -2.9 | -2.1 | -4.0 | -2.7 | 3.3 |
| 60 | Nd | -0.6 | -1.9 | -3.1 | -1.6 | -2.9 | -2.0 | -3.5 | -2.1 | 3.8 |
| 61 | Pm | -0.6 | -2.0 | -3.0 | -1.5 | -2.9 | -1.9 | -3.1 | -1.7 | 4.4 |
| 62 | Sm | -4.2 | -5.2 | -6.1 | -4.7 | -5.5 | -4.7 | -6.2 | -5.1 | 0.1 |
| 63 | Eu | -5.4 | -6.2 | -7.4 | -5.4 | -6.0 | -4.9 | -7.7 | -6.4 | -0.4 |
| 64 | Gd | 1.8 | -2.6 | -0.9 | 0.7 | -1.1 | -0.1 | -1.2 | 0.3 | 6.7 |
| 65 | Tb | 1.3 | -3.0 | -1.4 | 0.1 | -1.6 | -0.6 | -1.7 | -0.3 | 5.9 |
| 66 | Dy | -1.5 | -5.4 | -3.6 | -2.2 | -3.5 | -2.6 | -3.6 | -2.3 | 3.3 |
| 67 | Ho | -4.5 | -5.0 | -3.3 | -1.8 | -3.2 | -2.2 | -3.1 | -1.8 | 3.9 |
| 68 | Er | -3.7 | -4.4 | -2.6 | -1.1 | -2.7 | -1.6 | -2.4 | -1.0 | 4.8 |
| 69 | Tm | -6.4 | -6.8 | -5.0 | -3.5 | -4.7 | -3.8 | -4.6 | -3.5 | 1.8 |
| 70 | Yb | -6.1 | -6.7 | -7.8 | -6.3 | -6.7 | -5.8 | -8.4 | -7.3 | -2.0 |
| 71 | Lu | -0.6 | -1.6 | -0.2 | 1.3 | -0.6 | 0.4 | -0.3 | 1.2 | 7.5 |
| 72 | Hf | 5.2 | 3.4 | 1.5 | 2.9 | 0.4 | 1.1 | 4.0 | 5.6 | 12.3 |
| 73 | Ta | 9.5 | 7.1 | 5.5 | 6.6 | 3.6 | 4.2 | 6.2 | 7.7 | 14.1 |
| 74 | W | 12.2 | 9.8 | 7.7 | 7.7 | 5.4 | 4.9 | 5.4 | 6.7 | 11.9 |
| 75 | Re | 13.7 | 11.7 | 8.5 | 7.0 | 5.9 | 4.0 | 3.2 | 4.3 | 8.2 |
| 76 | Os | 14.2 | 12.1 | 8.8 | 7.3 | 6.1 | 4.3 | 3.4 | 4.5 | 8.6 |
| 77 | Ir | 12.5 | 10.8 | 7.2 | 5.0 | 4.7 | 2.3 | 1.0 | 2.0 | 5.3 |
| 78 | Pt | 11.9 | 10.6 | 6.2 | 3.4 | 3.9 | 0.7 | -0.9 | 0.0 | 2.8 |
| 79 | Au | 3.9 | 3.7 | -1.2 | -4.0 | -2.3 | -5.6 | -3.3 | -3.0 | -3.4 |
| 80 | Hg | -7.1 | -6.4 | -10.8 | -8.5 | -10.1 | -8.5 | -8.4 | -11.3 | -9.3 |
| 81 | Tl | -4.6 | -4.0 | -9.1 | -5.6 | -5.1 | -5.9 | -5.4 | -5.3 | -5.7 |
| 82 | Pb | -2.5 | -1.9 | -7.7 | -4.4 | -7.2 | -4.7 | -4.4 | -4.3 | -5.1 |
| 83 | Bi | -1.2 | -0.7 | -6.8 | -3.6 | -6.4 | -4.0 | -3.7 | -7.8 | -4.4 |
| 84 | Po | -3.7 | -1.7 | -5.2 | -7.1 | -4.6 | -7.1 | -7.6 | -7.9 | -7.1 |
| 89 | Ac | 1.9 | 0.5 | -1.2 | 0.2 | -1.2 | -0.5 | -2.8 | -1.3 | 5.2 |
| 90 | Th | 4.3 | 2.7 | 4.3 | 1.8 | 3.4 | 0.4 | 4.5 | 6.4 | 14.5 |
| 91 | Pa | 4.2 | 2.6 | 3.5 | 1.6 | 2.3 | 0.1 | 3.4 | 5.1 | 12.3 |
| 92 | U | 2.8 | 1.3 | -0.5 | 0.5 | -1.4 | -1.0 | 1.5 | 2.9 | 8.7 |
| 93 | Np | 0.7 | -0.6 | -2.2 | -1.3 | -2.9 | -2.6 | -0.4 | 0.8 | 5.9 |
| 94 | Pu | -2.5 | -3.5 | -5.0 | -3.9 | -5.3 | -4.8 | -2.2 | -1.0 | 4.0 |

## B.3.   Target materials

In ISOL facilities using thick targets, the choice of the target material is guided by the simultaneous optimization of the production rate in the target and the release efficiency from the target. Often the same or similar target elements can be used in different chemical forms.

### B.3.1.   Molten metal targets

The highest target density can be obtained with bulk material. The target thickness is just given by the product of target length and natural density of the material. To allow the release of the produced nuclei despite of the close packing, the target has to be kept in a molten state.

Normally elements melting at relatively low temperatures are used: tin, lanthanum and lead. Also liquid germanium, bismuth, gold and several other elements and alloys have been employed.

Table B.3.1.: Overview of molten metal targets used at ISOLDE. The molten uranium target was not yet used on-line at ISOLDE, but is given as an outlook. $\vartheta_m$ is the melting point of the target material and $\vartheta_{max}$ the maximum operation temperature. $p_{vap}$ is the vapor pressure (from [Hon69, Bal94, Mey88]) and $\rho$ the bulk density at $\vartheta_{max}$. $\zeta$ is the calculated target thickness at 20 cm length and $\vartheta_{max}$.

| Elem. | $\vartheta_m$ °C | $\vartheta_{max}$ °C | $p_{vap}$ mbar | $\rho$ g/cm$^3$ | $\zeta$ g/cm$^2$ | Typical isotopes | Ref. |
|---|---|---|---|---|---|---|---|
| Ge | 937 | 1100 | $6 \cdot 10^{-5}$ | 5.5 | 110 | $^{60-74}$Zn, $^{64-75}$Ga | [Rav75b, Bjø86] |
| Sn | 232 | 1200 | $7 \cdot 10^{-3}$ | 6.4 | 128 | $^{97-122}$Cd | [Elm78] |
| La | 920 | 1400 | $10^{-4}$ | 6.2 | 124 | $^{115\text{-}133}$Xe, $^{114\text{-}137}$Cs $^{122\text{-}138}$Ba | [Rav75b, D'A78] |
| Pb | 328 | 800 | $10^{-1}$ | 10.1 | 200 | $^{177-207}$Hg | [Let97b] |
| Bi | 271 | 600 | $2 \cdot 10^{-3}$ | 9.6 | 190 | $^{177-207}$Hg | [Let97b] |
| U | 1132 | 1400 | $8 \cdot 10^{-7}$ | 17.9 | (350) | Kr, Xe, Br, I, Te, etc. | [KR00] |

Table B.3.1 gives an overview of typical ISOLDE molten metal targets. It should be noted that the quoted vapor pressures are inside the target. Condensation in the chimney and transfer line will reduce it sufficiently to avoid a quenching of the ion source efficiency.

Experiences with other liquid targets (various La-X alloys, a U-Cr alloy and a ThF$_4$-LiF mixture) are discussed in [Rav75b]. Yields from a molten La-Th target are given in [Rav76]. A molten gold target was tested at ISOLDE for the production of mercury beams via Au($^3$He,p$xn$) reactions as an alternative to the Pb(p,3p$xn$) reactions [Klu86]. At the ISOCELE facility also molten targets of other elements or compounds were used: Ag, Ce, Pr, Nd, Tb, Gd-Cu, Er-Cu, Pt-B and ThF$_4$-NaF [Par76, Put81]. Molten Ce$_3$S$_4$ was proposed for the production of tellurium isotopes [Car78]. A liquid germanium target at temperatures up to 1570 °C is presently used at the HRIBF facility (Oak Ridge) for the production of arsenic beams [Car97]. An eutectic mixture of TeO$_2$, KCl and LiCl was used for production of elementally pure beams of antimony [Hof84].

There is high interest to use also liquid uranium targets. However, liquid uranium is very aggressive, attacking practically all possible container materials [Rav75b]. Recent experiments at Orsay showed that Y$_2$O$_3$ can be used as wall material up to 1400 °C [KR00]. The relation between higher target temperatures and target lifetime is still under study.

Normally only elements with a low boiling point ($\lesssim$ target temperature) are released. The average release times are typically of the order of minutes [Let97b]. They decrease at higher target tem-

peratures. In general the vapor pressure of the target material sets an upper limit for the usable target temperatures. For higher-melting materials the target is not run to this limit to avoid a reduction of the target lifetime by cavitation damage of the container [Let97b].

Due to the high target density molten metal targets can provide the highest intensities for not too short-lived isotopes of certain elements: Cd from a Sn target, Hg from a Pb target, Xe and Cs from a La target.

The pulsed structure of the PSB (proton synchrotron booster) beam gave some changes compared with the continuous beam from the SC (synchrocyclotron). Due to the impact of the beam pulse a shock wave "shakes" the liquid metal. Drops splashing into the transfer line or ion source can provoke an immediate failure (blocking of the transfer line or destruction of the ion source). A special chimney construction with baffle plates was developed to prevent this [Let97b]. Moreover the spacing of the sub-pulses from the four individual PSB rings was increased up to 500 $\mu$s ("staggered beam"), reducing the shock waves and the damage to the target container. The ends of the target container were reinforced. The slightly reduced intensity of the staggered beam (about 3.5 $\mu$C per pulse instead of 5 $\mu$C) is not really a drawback since normally the proton beam intensity is even further reduced to assure a longer target lifetime. On the other hand the shock waves accelerate the release, rising the yields of short-lived isotopes [Let97b].

## B.3.2.   Solid metal targets

Elements with high boiling point and high desorption enthalpy require higher target temperatures for an efficient release. Liquid metal targets can no longer be used due to their excessive vapor pressure and the rapid attack of the container materials. Instead high-melting metals in solid form are used. To keep the diffusion path short[5], powders or thin foils (typically 20 $\mu$m thick) are used. The foil targets are made from a single strip of foil which is rolled and kept together with a tantalum wire. The foil is embossed to keep some distance between the layers and hinder thermal contact. The round package is inserted along the length of a tantalum target container. Typical packing fractions are 30-40 %, i.e. the average target density is about one third of the bulk density. Table B.3.2 shows an overview of typical ISOLDE metal foil targets.

Table B.3.2.: Overview of metal foil targets presently used at ISOLDE. Note that the Ti foil targets are run close to the melting point and can even start to melt locally. For the symbols used see the caption of table B.3.1. Here, $\rho$ is the bulk density at room temperature.

| Elem. | $\vartheta_m$ °C | $\vartheta_{max}$ °C | $p_{vap}$ mbar | $\rho$ g/cm$^3$ | $\zeta$ g/cm$^2$ | Typical isotopes |
|---|---|---|---|---|---|---|
| Ti | 1675 | 1600 | $2 \cdot 10^{-3}$ | 4.5 | 25 | $^{37-46}$Ca |
| Nb | 2470 | 2050 | $3 \cdot 10^{-6}$ | 8.6 | 50 | many |
| Ta | 2996 | 2200 | $5 \cdot 10^{-7}$ | 16.7 | 110 | many |
| W | 3410 | 2200 | $5 \cdot 10^{-8}$ | 19.3 | 7[(6] | test: $^{11}$Li |

A tantalum target optimized for minimum effusion time was proposed for the RIST (Radioactive Ion Source Test) project in the UK. It consists of 6000 disks with 25 $\mu$m thickness arranged alternately with washers and radiator fins [Ben97]. Tests at ISOLDE showed improvements for the release of certain species [Dru97], but the production is significantly more labor-intensive than that of a standard ISOLDE metal foil target.

---

[5]The diffusion coefficient in solid metals is typically some orders of magnitude smaller than in liquid metals. However, the smaller dimensions ($\sim \mu$m instead of cm) normally overcompensate this drawback.
[6]This target has a very compact geometry: 7 mm in diameter and 50 mm long.

While the production cross-sections with high-energy protons are similar from Zr, Nb and Mo, normally only niobium foil targets are used at ISOLDE since niobium has a lower vapor pressure than zirconium or molybdenum at a given temperature. Moreover the diffusion of rubidium was found to be twenty times faster in Nb compared with Mo [Car78]. Also Beyer et al. [Bey78] found at equal temperature the release of Rb, Sr and Y to be fastest in Zr, followed by Nb and then Mo[7]. Note that at TISOL a zirconium foil target gave higher yields than a niobium foil target for most isotopes [Dom90].

Metal powder targets (Nb, Mo, Ir, V, Hf, Ta, W) [Car78] were studied off-line and partly used on-line at ISOLDE [Bjø86, Bjø87] and deposited metal layers from Si, V, Mo, Ta, Ir, Th and U were used at the PS on-line separator [Kla68, TP71]. Bjørnstad et al. report on the use of a mixed Th/Nb powder target [Bjø86]. The release from other metals (Ru, Re, Os), such as pure powder or mixed with graphite powder, was studied off-line [Hof84].

Sn- and Pt/graphite powder mixtures were heated above the melting point of the metal, thus giving a target structure which is something in between a solid and a liquid target. The target element is kept in a liquid phase, but the admixture of graphite powder assures a reduced diffusion length in the bulk material. With this method beams of short-lived cadmium isotopes were separated from the Sn/graphite target at 1000 °C and gold beams from the Pt/graphite target at up to 1900 °C [Hag92b].

There are target elements which are difficult to keep in metallic state at high temperatures. They tend to react with the container material or the metal foils fuse together, increasing the diffusion path. Also some elements show a very slow diffusion in solid metals. In these cases refractory compounds like carbides, oxides, etc. have to be used as target material.

### B.3.3.    Carbides

Some metals form very stable carbides: actinides, lanthanides, titanium, chromium, etc. Here, it is not the melting point of the target material which limits the operation temperature, but the vapor pressure of impurities and of the metal component.

Table B.3.3.: Overview of carbide targets used at ISOLDE. For the symbols used see the caption of table B.3.1. $p_{vap}(LaC_2)$ is the sum of all evaporated compounds, taken from [Ste71]. $\rho$ is the bulk density of the pure carbide, but in fact most materials are mixed with additional graphite. $\zeta$ gives the effective thickness of the metal content. A "melting point" in parentheses indicates the decomposition temperature of the compound.

| Elem. | $\vartheta_m$ °C | $\vartheta_{max}$ °C | $p_{vap}$ mbar | $\rho$ g/cm³ | $\zeta$ g/cm² | Typical isotopes | Ref. |
|---|---|---|---|---|---|---|---|
| C | 3600 | 1800 [8] | $2 \cdot 10^{-7}$ | 2.5 | 37 [9] | [7,10,11]Be | [Seb99] |
| $Al_4C_3$ | (1400) | 1200 | $4 \cdot 10^{-4}$ | 2.4 | 21 | [20−24]Na | |
| SiC | ≈2700 | 1200 | $(< 10^{-6})$ [10] | 3.2 | 21 | [20−24]Na | |
| $LaC_2$ | ? | ≈ 1750 | $2 \cdot 10^{-3}$ | 5.0 | ≈ 30 | Cd, In, Cs | |
| $ThC_2$ | ≈ 2450 | ≈ 2200 [11] | $2 \cdot 10^{-5}$ | 9.0 | ≈ 50 | many | |
| $UC_2$ | ≈ 2450 | ≈ 2200 [11] | $2 \cdot 10^{-4}$ | 11.3 | ≈ 50 | many | |

[7]However, at ISOCELE a molybdenum foil target was used to separate by fluorine addition $YF_2^+$ and $ZrF_3^+$ [Sau84].

For the production of neutron-deficient potassium isotopes a $Sc_4C_3$-graphite target was used at ISOLDE [Bjø86] and a $CaC_2$ target at INS [Ike92]. VC was used to produce argon isotopes [Bjø81]. Moreover off-line release studies were performed with TiC/graphite and ZrC/graphite [Hof84]. At TISOL ZrC targets are in use for the production of various alkaline isotopes [Dom90]. At IRIS a $GdC_x$ target was used for production of In, Cs and Eu [Bar97] and even a $CmC_x$ target was tested [Bol92].

Due to the usefulness of uranium carbide/graphite targets for the production of most of the neutron-rich isotopes and its importance for reactor-based RIB facilities, a separate subsection (B.4) is devoted to a more detailed discussion of the production and the properties of this material.

## B.3.4.    Oxides

Table B.3.4 shows an overview of oxide targets currently used at ISOLDE[12]. To avoid a reaction with the tantalum target container often a thin foil from platinum or rhenium is inserted.

Table B.3.4.: Overview of oxide targets used at ISOLDE. For the symbols used see the caption of table B.3.1. $\vartheta_m$ was taken from [Mai70]. $\rho$ is the density of the bulk material without porosity.

| Elem. | $\vartheta_m$ $^\circ$C | $\vartheta_{max}$ $^\circ$C | $p_{vap}$ mbar | $\rho$ g/cm$^3$ | $\zeta$ g/cm$^2$ | Typical isotopes | Ref. |
|---|---|---|---|---|---|---|---|
| $Al_2O_3$ | 2054 | 1550 | $4 \cdot 10^{-4}$ | 4 | 9 | $^{20-25}$Na | |
| MgO | 2800 | $\approx$1500 | $\approx 5 \cdot 10^{-3}$ | 3.6 | 2.9 | $^{17-24}$Ne | [Rav97b] |
| CaO | $\approx$2600 | 1400 | $< 10^{-4}$ | 3.3 | 5 | He, C, N, Ne, Ar | [Rav97b] |
| $ZrO_2$ | 2700 | 1850 | $\approx 10^{-4}$ | 5.9 | 6 | Se, Br, As, Cu | [Hof84] |
| $ThO_2$ | 3050 | 2100 | $2 \cdot 10^{-4}$ | 9.9 | $\gtrsim 30$ | many | [Hof84] |

A particularly interesting material is yttria-stabilized zirconia ($ZrO_2 \cdot Y_2O_3$) which is available in form of felt or wool. It contains no binders and can be heated to high temperatures without excessive outgassing. It has a melting point near 2600 $^\circ$C and should retain its fibrous nature up to 2480 $^\circ$C. Such zirconia felt is sold under the brand name ZYF100 in sheets of 45x60 cm and 2.5 mm thickness by Zircar Fibrous Ceramics[13]. $WO_3$ and $Ta_2O_5$ are available in a similar form, see [Hof84] for release tests from $Cr_2O_3$ and $Ta_2O_5$ material. Figure B.3.1 shows the cross-section of a $ZrO_2$ fiber. The fiber diameter varies between 5 and 8 $\mu$m.

In a release measurement at the GSI on-line separator this material showed a relatively rapid release for xenon [Kirch]. At about 2300 K the release was faster than from a sintergraphite [Kir97]. A diffusion constant of about $D(2300 \text{ K}) \approx 4 \cdot 10^{-10}$ cm$^{-2}$ s$^{-1}$ can be derived (depending on the average fiber diameter). Also zinc was released reasonably fast, but due to isobaric background no diffusion constant can be quoted. For the release of other elements see chapter 4.

Obviously oxide matrices like $ZrO_2$ will release elements which form volatile oxides particularly rapidly, but delay elements which form refractory oxides. This was already observed in [Cow58]. Unfortunately in spallation of zirconium only rather neutron-deficient isotopes of elements up

---

[8]The temperature was not limited by the target, but by the maximum current of the target power supply.

[9]In fact a 400 mm long target was used with a thickness of 73 g/cm$^2$.

[10]The temperature is limited by the vapor pressure of impurities.

[11]See subsection B.4 for a discussion of the maximum target temperature.

[12]Initially at ISOLDE also hydrated oxide targets at low temperature (only heated by the proton beam) were used [Han69, Pat70].

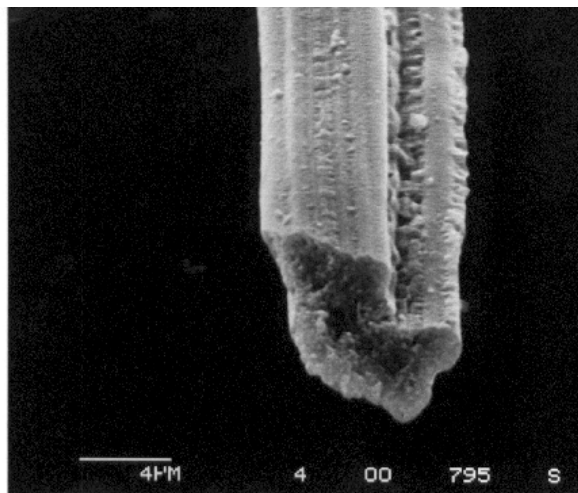[13]Zircar Fibrous Ceramics, Florida, NY Tel. (914) 651-4481.

Figure B.3.1.: Cross-section through a single fiber from the $ZrO_2$ felt material. The picture was taken with a Scanning Electron Microscope (SEM) at a magnification of about 3000.

to $Z = 40$ can be produced. It would be very useful to find a material with similar release characteristics but significantly higher $Z$, if possible in the actinide range. Due to the chemical similarity the actinide oxides could allow to produce and separate more neutron-rich isotopes of those elements which proved to be well released from $ZrO_2$.

Among the actinides especially uranium and thorium form stable oxides. Thoria ($ThO_2$) is more stable at higher temperatures[14] and therefore preferable. Thorium oxide powder targets have already been used at ISOLDE and showed a rapid release of noble gases [Rav87], but had the tendency to sinter within some hours at operational temperature[15].

The process of sintering could be slowed down by admixture of an oxide which is more stable at high temperatures, e.g. zirconium oxide. A good target could consist of a mixture of $ZrO_2$ and $ThO_2$ fibers.

In the production process of thoria natural radon ($^{220}Rn$) will emanate. Due to this fact very severe safety regulations apply for the treatment of thoria. Therefore the commercial producers of the $ZrO_2$ felt or of rock wool are not able to provide thoria in a similar form. However, thoria fiber cloth is commonly used as so-called Welsbach mantle for gas lights. It remains to be checked if commercially available material fulfills the requirements towards purity for vacuum application at high temperatures. Else these fibers can also be synthesized with limited effort. Either cotton or rayon are soaked with a solution of a thorium salt (e.g. chloride). When burning the supporting tissue pure thoria fibers will remain [Div77]. Alternatively zirconia cloth material could be impregnated with a thorium salt solution and sintered. Similarly also felt materials of other refractory oxides can be produced.

## B.3.5.    Other materials

Off-line release tests of many other refractory compounds ($Hf_3Si_2$, $Ta_5Si_3$, $Zr_5Ge_3$, $Hf_5Ge_3$, $Hf_5Sn_3$) are reported in [Hof84]. Other tested samples include $CeB_6$, $CeS$, $BaB_6$ and $BaZrO_3$ [Car78]. $CaB_6$ was tested on-line for the release of argon [Bjø81]. At Oak Ridge the release of various elements from BN, CeS, $Zr_5Si_3$ and $Zr_5Ge_3$ was measured [Alt96].

---

[14]Urania has at 2100 °C already a vapor pressure of $6 \cdot 10^{-2}$ mbar.

[15]It is also possible that the observed slower delay arises due to radiation induced structural changes which cause more "trapping" (compare [Kir97]) of the noble gas. This has been observed for a fission fluence $> 10^{16}$ cm$^{-3}$ [Mat80].

At TISOL targets from AlN and from Na-, Ca- and Tl-zeolites were successfully used for the release of C, N, O and noble gases [Dom96, Dombs].

LuF$_3$ and SrF$_2$ powder targets were successfully used at ISOCELE for the separation of new Ta, Zr and Sr isotopes as TaF$_4^+$, ZrF$_3^+$ and SrF$^+$ respectively [Lia82]. However, these materials are quite volatile and can only be handled with the robust ISOCELE ion sources. The large gas amount would immediately quench the efficiency of the low-current ion sources used at ISOLDE.

## B.4.   Uranium carbide targets

Especially for uranium and thorium different chemical compounds have been tested as target material. In the very first ISOL facility a mixture of uranium oxide and ammonium carbonate (baking powder) kept at room temperature had been used [KH51]. Later uranium stearates were used at room temperature for the release of noble gases [Wah62, Bor65, Hag67, Boc70, Ehr72, Bur74]. Other materials were used off- and on-line: uranyl ions on hydrated ZrO$_2$, UO$_2$, U$_3$O$_8$ (pure or mixed with B$_2$O$_3$) and UF$_4$ at temperatures up to 650 °C [Bor71, Bur74, McC75, Tal76].

Mixtures of uranium oxide and graphite at higher temperatures have shown a particulary favorable release characteristic for many elements. However, a large amount of carbon monoxide is released from the reaction of uranium oxide and graphite. An excessive amount of gas decreases the efficiency of most ion sources. Thus, it is favorable if this reaction proceeds previously off-line where the carbon monoxide can be pumped off more easily. The produced uranium carbide/graphite mixtures have been used as targets at many ISOL facilities.

### B.4.1.   Production

Many different methods can be used for the production of uranium[16] carbide/graphite targets [Kat86]. In most cases the uranium carbide is diluted in graphite to obtain a faster release. It has been observed qualitatively that an increasing uranium concentration causes a slower release[17] [Ort61, Fog92].

Natural graphite contains too much impurities and would outgas strongly at high target temperatures. Therefore "artificial" graphite has to be used. This is produced at high temperatures ($\gg 2000$ °C) by pyrolysis of hydrocarbon compounds or thermal decomposition of carbides (e.g. SiC) or other compounds [Man68]. Depending on the production process a multitude[18] of structures is obtained, varying in density, open porosity, size of the microscopic units (particles and pores), etc. All these details can influence the release characteristics of the target material considerably.

#### Standard ISOLDE UC$_x$/graphite

The standard ISOLDE ThC/graphite[19] and UC$_x$/graphite targets [Bjø81, Rav87] are prepared by mixing uranium oxide and graphite (from Johnson Matthey, Nr. 00641, graphite powder < 325 mesh size, purity 99.5 %) in a molar ratio 1:6. After careful mixing of the powder in a ball mill, it is statically (cold) pressed into 1 mm thick pills of 14 mm diameter. These pills are

---

[16]Thorium behaves very similar and is not discussed separately. Also lanthanide carbides can be produced in a similar way.

[17]It should be noted that in ref. [Ort61] the samples of varying concentrations had been prepared by different methods.

[18]Hundreds of different types are commercially available.

[19]More precisely these materials will consist mainly of dicarbides, e.g. UC$_2$, which are solved in the graphite matrix. However, in the following the short notation "XC/graphite" will be used to indicate a composition with a large carbon excess over the stochiometric ratio.

heated under vacuum in a graphite container for several hours to about 1900 °C [Hof84]. The graphite will react with the uranium oxide to uranium carbide, thereby releasing carbon monoxide: $UO_2 + 6\ C \longrightarrow UC_2 + 2\ CO\uparrow + 2\ C$. Finally one obtains uranium carbide dispersed in excess graphite with a molar ratio U:C $\approx$ 1:4. The release of the gaseous carbon monoxide automatically creates some open porosity. The pills are finally crushed and then filled in the target container. An inserted graphite cylinder with 2 mm wall thickness is used to prevent a reaction between uranium carbide and the tantalum target container.

Lacking a uranium carbide sample, figure B.4.1 shows instead the surface of an ISOLDE lanthanum carbide pill which was prepared in a similar way from lanthanum oxide and graphite[20]. Note that the lanthanum carbide started to hydrolyze rapidly (within minutes) while being removed from the protective argon atmosphere and inserted into the microscope. This rapid reaction had been observed also in ref. [Car79]. The picture looks a bit fuzzy due to loose crumbs which are swept away and due to surface charges which built up during the exposure.
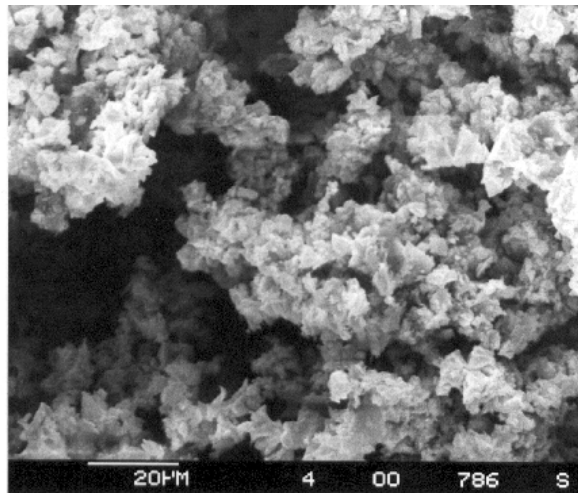


Figure B.4.1.: Scanning Electron Microscope (SEM) picture of the microscopic $LaC_2$-$C_x$ structure with about 600fold magnification. The smallest units of the cauliflower structure have a size of about 10 $\mu$m.

**Impregnated graphite cloth**

A less dense graphite cloth material was mainly used at the ISOLDE SC. Graphite cloth material from Union Carbide (grade WCA, X2014, fiber density 1.5 g/cm$^2$) is impregnated with a uranyl nitrate $(UO_2(NO_3)_2)$ solution. Heating to 2000 °C for several hours again causes a reaction to uranium carbide [Car79]. The filling of an ISOLDE target container gives an effective target thickness of 9-17 g/cm$^2$ uranium. For historical reasons at the ISOLDE SC mainly graphite cloth targets were used, while at the ISOLDE PSB only $UC_x$/graphite targets from pressed pills were used up to now. This makes a systematic comparison of yields and release times from $UC_x$/graphite targets at the SC and PSB more difficult.

**Impregnated porous graphite**

The $UC_x$/graphite targets at OSIRIS [Rud76, Jac87] and many other facilities (see e.g. [Ami76, Wün78, Rei80]) are produced similarly to the ISOLDE graphite cloth targets. Instead of graphite cloth a porous graphite cylinder (e.g. at OSIRIS from Le Carbone Lorraine, grade 60, apparent

---

[20]$La_2O_3 + 11\ C \longrightarrow 2\ LaC_2 + 3\ CO\uparrow + 4\ C$.
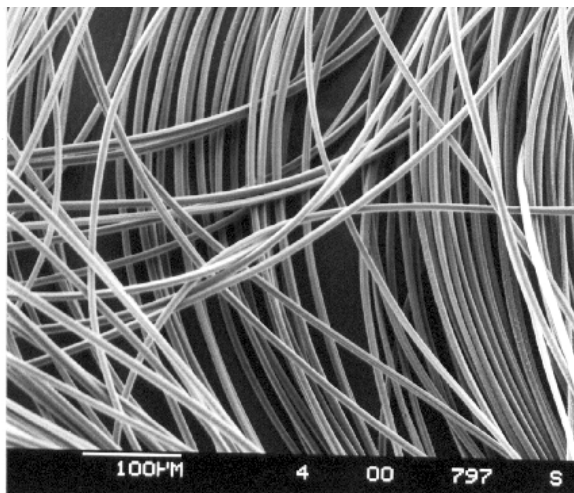
Figure B.4.2.: SEM picture of the untreated graphite cloth material. The single fibers are loosely bundled to a plait without fixed connections. The magnification is about 120fold, the diameter of single fibers is 8-10 $\mu$m.

density 1.05 g/cm$^3$, porosity 50 %, ashcontent 1.2 %) is used as base material. Following the recipe from Studsvik [Fogel], some test samples have been prepared in the target laboratory of the Ludwig-Maximilians-Universität. After saturating the graphite samples with uranyl nitrate solution it was heated under vacuum to 600 °C. The uranyl nitrate will decompose to uranium oxide. A molar ratio (U/C) of about 1:100 is obtained[21]. The samples were further outgassed for one hour at 2000°C. An additional mass loss of 2-4 % was observed, probably due to ongoing emission of carbon monoxide.
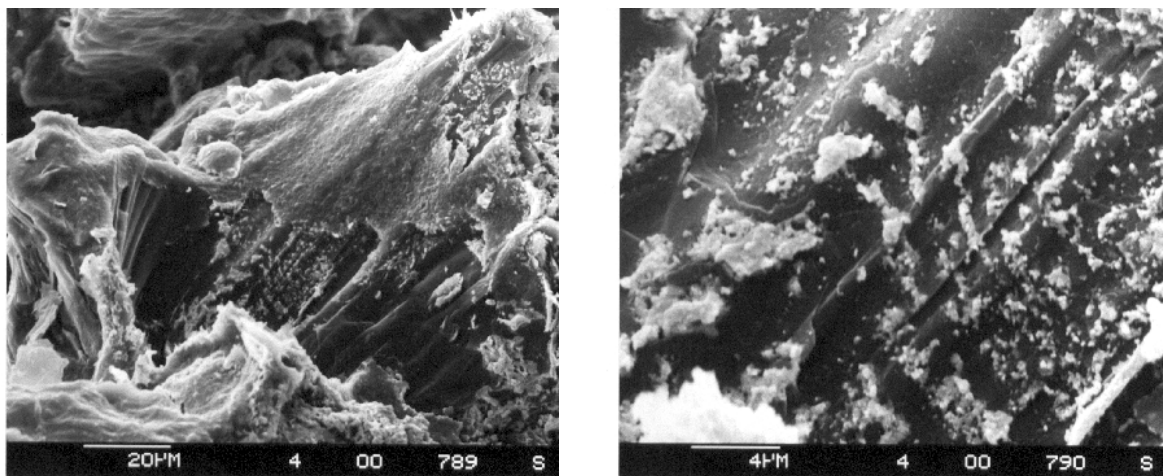


Figure B.4.3.: SEM picture of the "Studsvik graphite" with deposited uranium oxide. The magnification is about 600fold for the general view (left) and about 3000fold for the detail (right).

The scanning electron microscope picture showed that the uranium oxide did not react completely to uranium carbide immersed in graphite but was rather deposited on the surface in well defined spots of about 1 $\mu$m diameter. See the left part of figure B.4.3 for the general structure and the

---

[21]The uranium content could be enhanced by repeating the impregnation/heating cycle several times.

right part for the magnified uranium oxide spots. An elemental analysis of these spots by EDXRF (Energy Dispersive X-Ray Fluorescence) analysis[22] showed still a significant content of oxide.

A TRISTAN graphite cloth target produced in a similar way showed a gradual increase of the lanthanide yields during operation for several days [Shm83]. This could be explained by a reduction of the oxygen content in the target and consequently an improvement of the release for elements which tend to form very stable oxides.

**Pyrolysis of uranium diphtalocyanine**

Tikhonov et al. developed a technique to synthesize carbides of different metals ($M$) by pyrolysis of diphtalocyanine compounds ($C_{64}H_{32}N_{16}M$) [Bar97]. These targets are typically used at the IRIS facility at Gatchina. In case of uranium carbide the molar ratio U:C is about 1:13. The filling of an ISOLDE standard target container with powder produced from uranium diphtalocyanine gives a target thickness of 7.5 g/cm$^2$. For some elements a faster release was measured from this material compared with a standard ISOLDE UC$_x$/graphite target [Eve97, Bar97], but there is practically no case where the faster release could compensate for the target thickness reduced by a factor of seven. A practical drawback of the method is the high effort to produce the material and the large amount of iodine contamination which comes in from an intermediate production step and produces a strong outgassing[23].

**Oak Ridge porous graphite**

For the use at the HFRIB facility at Oak Ridge various types of highly "porous" graphite have been proposed as target material [Alt96]. A carbon-bonded-carbon-fiber material is comparable to the ISOLDE graphite cloth material, but has a smaller fiber diameter of 6 $\mu$m. Also a reticulated carbon material is investigated. The uranium should be deposited by chemical vapor deposition either directly onto the graphite or onto a thin intermediate layer of rhenium.

Another target material from Oak Ridge looks macroscopically like a porous foam. Under the microscope it is seen that the material consists of "twisted bars" of about 100 to 200 $\mu$m diameter which in turn have some fissures probably caused by shrinking when the hot sample was cooled in the production process. The effective diffusion paths vary largely between about 2 and 50 $\mu$m.

## B.4.2.   Target aging effects

A significant yield decrease is observed after longer operation (several days) of ISOLDE UC$_x$/graphite targets [Rav97a]. Several mechanisms could be responsible for this effect:

**Poisoning of the surface ionizer:** At ISOLDE the UC$_x$/graphite targets are mainly used together with a tungsten surface ionizer ion source. It is known that a surface layer of oxide increases the work function of tungsten and thus improves the efficiency of surface ionization. If a significant amount of carbon is evaporated from the target, it could react with adsorbed oxygen by creation of carbon monoxide or even react to tungsten carbide which has an even lower work function. In this case the intensity drop should show a dependence on the ionization potential of the element under consideration. The effect should be larger for the lighter alkalis and the earth alkalis than for the heavier alkalis.

---

[22]The energetic electron beam of the SEM creates vacancies in the inner electron shells of sample atoms. Characteristic X-rays are emitted when the vacancies are filled in radiative transitions by outer electrons. An energy dispersive X-ray detector allows to identify the elemental distribution.

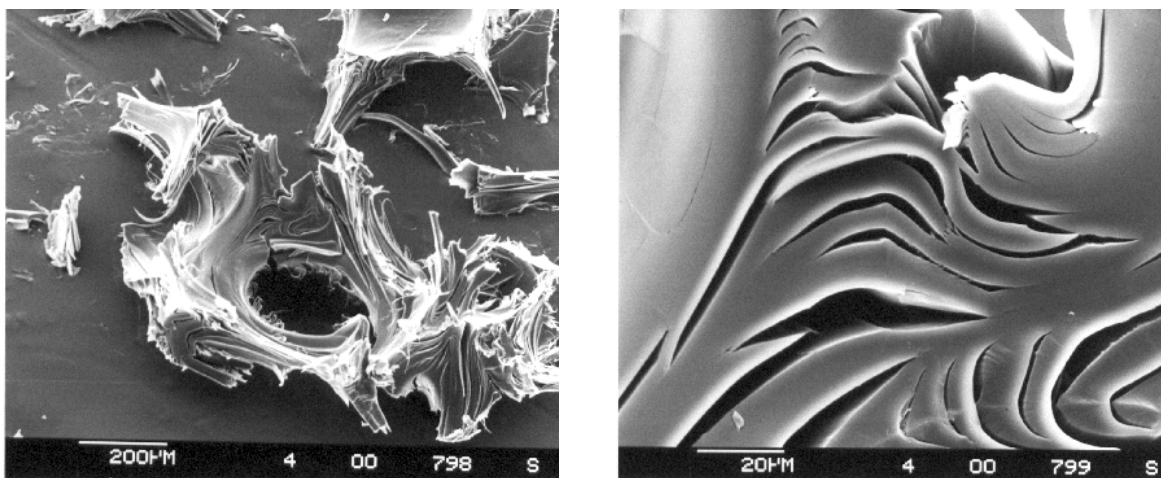[23]This in turn can cause a large "consumption" of turbo pumps.

Figure B.4.4.: SEM picture of the porous "graphite foam" material from Oak Ridge. The left side shows an about 50fold magnification, the right side a detail from the center with about 500fold magnification.

**Loss of uranium:** Loss of target material could be one explanation for a continuous drop of the intensity which is equal for all produced isotopes. Clearly the nuclear burnup of the uranium content by fission and spallation reactions is negligible in the ISOLDE target[24]. Still uranium could get lost by diffusing out of the target. A self-diffusion coefficient of $10^{-10}$ cm$^2$/s was measured for U in pure $UC_{2.00}$ at 2000 °C, rising to about $10^{-8}$ cm$^2$/s at 2400 ° [Mat73]. In $UC_{1.00}$ the diffusion coefficients are two to three orders of magnitude lower [Mat73, Mat86], while in pure pyrolytic graphite the diffusion coefficients are at 2200 °C: $1.5 \cdot 10^{-9}$ cm$^2$/s for diffusion orthogonal to the crystal planes and $4.5 \cdot 10^{-7}$ cm$^2$/s [Ask70, Bor88] parallel to the planes. At 2400 °C these values are one order of magnitude larger. Obviously the uranium is not lost in significant amounts by evaporation through the ion source orifice. The U$^+$ current which is always observed from a surface ion source lies in the range of some tens to hundred nA. Even assuming a particularly low ionization efficiency for U (the ionization potential is 6.2 eV) of $\sim 0.1$ % and taking into account the evaporation of other $UC_x$ compounds, the loss will never exceed 1 % of the uranium content in several weeks of permanent operation. The hypothesis that uranium diffuses slowly into the surrounding graphite cylinder and subsequently into the tantalum container [Rav97a] was checked by scanning the proton beam across the cross-section of target and container. No change of the profile was observed after two weeks of operation. Still this is rather an indication than a proof since fission products produced in the bulk graphite or tantalum cylinder would be released much slower and are not necessarily detected by a rapid scan over the target. A clear answer to this question could be given by a quantitative analysis of the uranium content in the irradiated target.

**Losses through the target container:** During operation the tantalum target container will re-crystallize to large domains (some cm$^2$) with visible grain boundaries traversing the complete wall. Uranium on the one hand and the produced radio-nuclides on the other could escape by grain boundary diffusion [Rav97a], thus reducing the portion which reaches the ion source. A test of this hypothesis could be made by an analysis of the heat screens around the target container. If uranium and radio-nuclides escaped in significant amounts (i.e. about 90 % of the target inventory to explain the observed yield decrease), a certain part should have condensed on the colder heat screens.

---

[24]On the contrary in a high-flux reactor there is a significant nuclear burnup of fission targets, see e.g. section 1.4.5 and references [Kös97b, Gro97] for a more detailed discussion.

**Sintering of the target:** It is also possible that the radio-nuclides are still created with the same rate in the target, but the diffusion losses are increased due to a change in the microscopic structure of the target material. If such a structural change is confirmed, the question remains if it arises from purely thermal equilibrium effects, i.e. by vaporization and redeposition of graphite, or if it is mainly caused by the impact of the intense proton pulses[25]. In the first case it would set a limit to the target lifetime just depending on the target temperature. In the latter case it would seriously affect the operation of $UC_x$/graphite targets at a high-current proton beam facility. If the target degradation is roughly proportional to the proton beam dose, the scaling from the 2 $\mu$A average current at ISOLDE to a 100 $\mu$A facility would result in a lifetime of only some hours!

Due to changes in the operation conditions (target and source temperature) the first dedicated measurements at ISOLDE do not yet allow to decide which of the discussed effects causes the loss in yield. A measurement with a plasma ion source would allow to exclude the first point and a more detailed examination of a larger part of the release curve ("slow contribution") would allow to probe the last effect.

## B.4.3.    Operation temperature of $UC_x$/graphite targets

There have been contradictory reports on the maximum temperature at which $UC_x$/graphite targets can be operated over longer time, see e.g. [Fog97, Rav97a, Put97, Kirch]. A part of these contradictions can be explained by differing definitions of the "target temperature". At ISOLDE the relation between heating current and target temperature is individually calibrated off-line for each target container. The temperature at the outside of the target cylinder is measured by pyrometry. The reproducibility is difficult to estimate (changing effect of the heat screens, only estimated contribution of the proton beam heating, etc.) but should be in the range of $\pm 50 - 100$ K. The same applies for the temperature measurements of the OSIRIS target which are also performed off-line. However, at OSIRIS the temperature is measured in the central part of the target [Fog92]. This is the *hottest* point of the target. At GSI the temperature of the source with integrated catcher is normally given for the *coldest* point which is determining for the delay losses. Under on-line conditions the average temperature of the ISOLDE $UC_x$/graphite target is kept at maximum 2150 or even 2200 °C, but locally it can be heated to much higher temperatures during the impact of the intense proton beam pulses! Taking all these factors into account, the data from Studsvik, GSI and ISOLDE do not differ as extremely as sometimes quoted.

Considering only thermal effects, the effective target lifetime is mainly determined by two factors: the loss of graphite and uranium carbide through the extraction orifice and the lifetime of the target container.

### Evaporation of graphite

Figure B.4.5 shows the total vapor pressure over graphite taken from literature[26] [Hul73]. In this range the vapor pressure can be fitted with:

$$\log(p_{\mathsf{vap}}/\mathsf{mbar}) = 12.70 - 39840/(T/\text{ K}). \tag{B.4.1}$$

Also the maximum unhindered evaporation rate per unit surface $J_0$ (in kg m$^{-2}$s$^{-1}$), calculated with equation (B.1.1) and $\alpha = 1$ is shown in figure B.4.5. This maximum value is only valid in the case

---

[25]It should be noted that no change in yields was observed when operating standard $UC_x$/graphite targets at the reactor-based ISOL facilities TRISTAN [Shm83] and OSIRIS [Fogel] for several weeks. On the other hand a graphite cloth target at TRISTAN showed a significant yield decrease for most elements [Shm83].

[26]The literature values for the vapor pressure of graphite differ up to a factor three. The cited reference is at the upper end of the range of values.

of free evaporation, i.e. if the evaporated particles are pumped away and are not redeposited on the surface and with a Langmuir coefficient of $\alpha = 1$. Experimentally lower values have been observed [Put97] rather suggesting $\alpha \sim 0.1$. Clearly the evaporation rate in a nearly closed system is much lower, being determined by the equilibrium between evaporation and redeposition. Note that the calculated maximum unhindered regress rate $dx/dt = J_0/\rho$ would attain 0.1 $\mu$m/s at 2400 °C, i.e. under vacuum a single fiber of the graphite cloth material should completely evaporate within seconds to minutes. However, practically it was observed that graphite cloth material can be used at 2500 °C over an extended period [Man68].
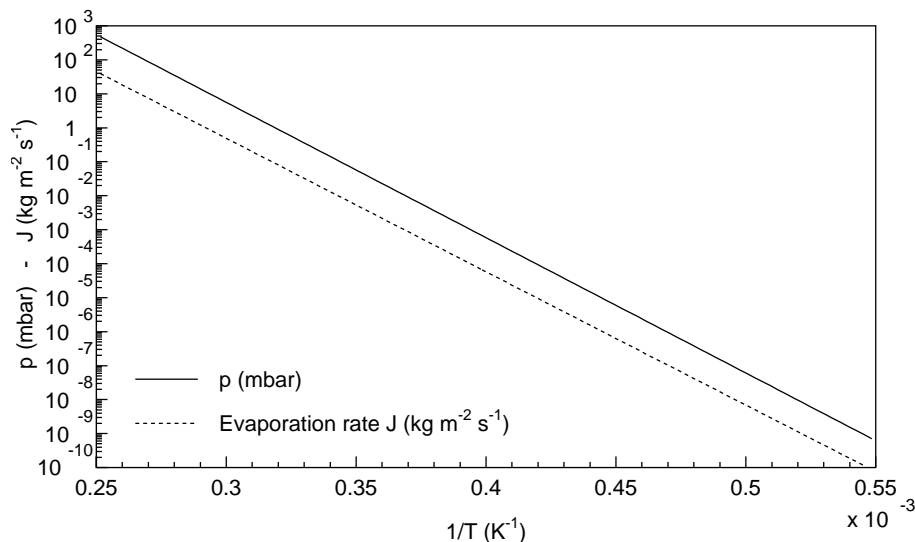


Figure B.4.5.: Vapor pressure and maximum evaporation rate for graphite at temperatures between 1800 and 4000 K. Note that the slope of the two curves is slightly different due to a different contribution of the carbon clusters C, C$_2$, C$_3$, etc.

The amount of graphite leaving the target container is determined by the vapor pressure in the target container and by the orifice area. With a small outlet hole most of the evaporated graphite will redeposit inside the target. Only a small part (given by the ratio of orifice area to inner surface) will leave the target. For a container with an orifice of 2 mm diameter the graphite loss can be estimated to about 4 mg per day at a temperature of 2200 °C and 70 mg per day at 2400°C respectively. Thus, even when operating the MAFF target for 50 days at 2400 °C, not more than 10 % of the original target content may get lost. This amount will not harm the integrity of the target.

Excessive amounts of graphite leaving the target can cause a coating of ion source insulators and result in a short circuit. This problem had occured at TRISTAN, but was cured with a modified design of the ion source [Gil85].

Even if the loss through the target orifice is kept under control, the evaporation and redeposition in the target container can change the microscopic structure of the target material. It is difficult to predict the structural change quantitatively[27], since it will depend on many factors like thermal gradients, the content of impurities, etc. A clear answer can only be given by an experimental investigation for each individual target design.

As discussed before, the antagonism of diffusion and effusion can affect the release behaviour of different elements in quite different way, i.e. due to the structural change the target may become slower for some elements but even faster for others!

---

[27] The structure created in the equilibrium of evaporation and redeposition has not necessarily maximum density. Note that occasionally even dendritic structures are created in vapor deposition [Gue87].

**Self-diffusion of target material**

Changes can also occur in the bulk target material due to self-diffusion. Normally this diffusion, if significant at all, has the rather positive effect to equilibrate concentration differences.

The thermodiffusion or Soret effect could play a role in a target which is heated inhomogeneously. This can happen in an ISOL facility driven by a high-current-accelerator where the target heating is dominated by the energy loss of the beam. It could also occur in the target of a high-flux-reactor based ISOL facility where the main heating is due to the fission power of the uranium content. Any major irregularities in the uranium concentration can cause thermal gradients, which in turn could increase the concentration inhomogeneity by thermodiffusion. No thermodiffusion of uranium has been observed in $UC_2$ [Mat86]. However, the carbon content has the tendency to diffuse towards the colder parts, i.e. it has a positive heat of transport [Mat86]. The flux of carbon atoms $J_C$ is described by:

$$J_C = -D_C \left( \frac{\partial c_C}{\partial x} + \frac{Q_C^* c_C}{RT^2} \frac{\partial T}{\partial x} \right), \tag{B.4.2}$$

where $D_c$ is the diffusion constant and $c_C$ is the concentration of carbon. The first term describes the normal diffusion which will level out inhomogeneities and the second term describes the thermodiffusion. The heat of transport for carbon in $UC_2$ was measured at 1600 °C to $Q_C^* = 385(113)$ kJ/mol [Gul72]. The concentration of the carbon content will remain close to unity, even if a major migration occurs. Therefore the first term can be neglected and the migration rate $dx/dt$ (in cm/s) can be expressed by:

$$\frac{dx}{dt} \approx \frac{C^*}{T^2} \frac{dT}{dx} \exp\left( -\frac{\Delta H}{RT} \right) \tag{B.4.3}$$

with an activation energy of $\Delta H = 320(38)$ kJ/mol and an experimental migration rate coefficient $C^* \approx 1.1 \cdot 10^5$ K cm$^2$/s deduced from figure 5 of ref. [Gul72]. Extrapolation gives a migration rate of 0.27 mm per day at 2200 °C and 0.74 mm per day at 2400 °C. Clearly there are large uncertainties due to the extrapolation from the measured temperature range (up to 1700 °C), but the magnitude of the effect shows that it is worthwile to study it in more detail.

However, even if a major transport of carbon occurs, it will only slightly affect the distribution of uranium. With an initial molar ratio of C:U $\approx$ 1000:1 these changes play no role, since the critical stochiometric ratio $UC_{1.00}$, where uranium would start to migrate considerably, is three orders of magnitude smaller.

**Lifetime of the target container**

The ISOLDE target containers made from tantalum show a significant recrystallization after about one week of operation at 2200 °C [Rav97a]. A tungsten container is used for the OSIRIS target. It shows similar recrystallization grains after 50 days of operation at 2400 °C [Fog97]. The container for the MAFF target will be made from rhenium. Rhenium forms much smaller grains during recrystallization (37 $\mu$m grain diameter at 2400 °C [Sav62]), not causing cracks of the container[28]. Moreover it does not form carbides [Sim62] as tantalum and tungsten do and is therefore chemically more stable in contact with graphite. At OSIRIS a graphite liner has to be used to protect the inner part of the target against reaction with tungsten to WC. It is consumed at a rate of 1 mm per 1000 h at 2300 °C and 1 mm per 300 h at 2500 °C [Jac87]. Therefore the thickness of this graphite liner (2 mm) sets an upper limit for the useful lifetime of the target.

---

[28]Re and W/Re alloys are even considered for the containment of high-temperature reactors driving spacecrafts.

To study all the points discussed above experimentally, an oven was installed at the target laboratory of the LMU where rhenium containers loaded with various graphite and uranium carbide samples can be heated over several weeks to a temperature of 2400 °C [Maier].

## B.5.   Surface ionization efficiency

### B.5.1.   Positive surface ionization

The degree of ionization $\alpha = [X^+]/[X^0]$ is described by:

$$\alpha_\mathrm{s} = \frac{[X^+]}{[X^0]} = \frac{g_+}{g_0} \exp \left( \frac{\Phi - W_\mathrm{i}}{kT} \right) , \tag{B.5.1}$$

with $\Phi$ the work function and $T$ the temperature of the source material, $W_\mathrm{i}$ the ionization potential of the element to be ionized, $g_+ = 2J_+ + 1$ and $g_0 = 2J_0 + 1$ the statistical weights of the ionic and atomic ground state of $X$. For example $g_0 = 2$ and $g_+ = 1$ for alkalis ($^2S_{1/2}$ atomic ground state and $^1S_0$ ionic ground state). Equation (B.5.1) is called Langmuir equation or Saha-Langmuir equation. It can be derived from the chemical equilibrium constant of the reaction $X^+ + e^- \rightleftharpoons X$ with the law of mass action, see ref. [Lan25, Zan71]. Several other ways to derive the same equation are shown in [Zan71]. The surface ionization efficiency is:

$$\beta_\mathrm{s} = \frac{[X^+]}{[X^+] + [X^0]} = \frac{\alpha_\mathrm{s}}{1 + \alpha_\mathrm{s}} \tag{B.5.2}$$

Tables B.6.1 and B.6.2 in appendix B.6 give an overview of the ionization potentials of the elements. Table B.7.1 summarizes the work function and maximum operation temperature of materials typically used in ion sources. Note that the work function depends significantly on the surface properties, i.e. on the orientation of a single crystal structure or the use of a polycrystalline surface, and on the adsorption of impurities[29] (see e.g. [Alt86]). The temperature dependent vapor pressure and adsorption time of these impurities can lead to a stronger temperature dependence of the effective work function. A strong electric field will also cause a modification of equation (B.5.1) [Zan71].

Even with very noble metal ionizers, the numerator in the exponent of equation (B.5.1) ($\Phi - W_\mathrm{i}$) is negative for most elements. To reach higher ionization efficiencies "the hotter - the better" applies. The upper temperature limit is normally given by the vapor pressure of the ionizer material or impurities. On the other hand for alkalis with $W_\mathrm{i} < \Phi$ the efficiency will decrease with higher temperatures. Here, it can be favorable to use lower temperatures or a material with lower $\Phi$. Both will also reduce the isobaric background of elements with larger ionization potential.

### B.5.2.   Negative surface ionization

In the case of negative surface ionization the ionization degree is given by:

$$\alpha = \frac{[X^-]}{[X^0]} = \frac{g_-}{g_0} \exp \left( \frac{A_\mathrm{E} - \Phi}{kT} \right) , \tag{B.5.3}$$

with $A_\mathrm{E}$ the electron affinity of the element to be ionized. The ionization efficiency is again given by equation (B.5.2). The electron affinities are also shown in tables B.6.1 and B.6.2 of appendix B.6.

---

[29]Adsorbed electronegative layers like oxygen enhance the work function while adsorbed electropositive layers (particularly alkali and earth alkali elements) lower it.

Negative surface ionization is used for the efficient (up to about 50 % efficiency) and selective ionization of halogens[30] and some other non-metallic elements. For more details see references [Ven70, Vos81, Shm81, Rab87, Pio97]. Negative ions are also required for the RIB facilities using a Tandem post-accelerator: HFRIB in Oak Ridge [Alt96] and the EXCYT project in Catania [Cia97]. There the adaption of the physics program to negative surface ionizable elements and molecules will avoid an additional efficiency loss in a charge exchange cell.

In most cases $LaB_6$ is used as ionizer with a low work function of about 2.6 eV. However, it cannot be combined with all target materials. For example the carbon emanation from carbide/graphite targets leads to a rapid poisoning of the surface [Vos81]. Negative surface ionization is not practicable either for in-pile sources in a high neutron flux. The rapid transmutation of $LaB_6$ by the $^{10}B(n,\alpha)^7Li$ reaction and the excessive electron emission from a negatively biased hot ion source are prohibitive. An alternative selective ionization method for halogens is discussed in section 4.1.

## B.5.3.    Ionization in a hot cavity

Experimentally it was found that the efficiency of positive surface ionization can reach high values in hot cavities where the area of the extraction orifice is small compared with the inner cavity surface [Bey71, Joh73]. The observed ionization efficiency can exceed the predictions of the Saha-Langmuir equation (B.5.1) by many orders of magnitude. This effect was studied in detail experimentally and theoretically [Lat75, Kal76, Afa77, Kir78, Kir81a, Huy83, Kir90].

It was shown that the ionization efficiency is strongly influenced by the space charge potential in the ionizer cavity. The latter is determined by an equilibrium between the flow of surface ionized particles and thermionic electrons from the wall into the cavity volume. A thermal plasma is created with a plasma potential which assures quasi-neutrality in the cavity volume. Assuming thermal equilibrium the ionization efficiency in the volume $\beta_v$ becomes:

$$\begin{aligned}
\beta_v &= \frac{\gamma}{1+\gamma}, \\
\gamma &= \frac{2g_+}{g_0}\left(\frac{2\pi m}{h^2}\right)^{\frac{3}{2}}\frac{1}{p}(kT)^{\frac{5}{2}}\exp\left(-\frac{W_i}{kT}\right).
\end{aligned}$$ (B.5.4)

$p$ is the total pressure in the cavity, involving neutrals, ions and electrons: $p = (n_0 + n_+ + n_e)kT$. Equation (B.5.4) is called the Saha equation. It was derived by Saha to describe the ionization degree in the solar chromosphere [Sah20]. It is interesting that equation (B.5.4) does no longer contain $\Phi$, i.e. in thermal equilibrium the ionization efficiency of a hot cavity becomes independent of the work function of the wall material. A material with lower work function has a lower surface ionization efficiency, but will emit more electrons into the cavity volume[31]. Thus, the negative plasma potential is further decreased and the positive ions are better trapped in the plasma protecting them against neutralization at the wall. The neutrals have still a finite chance to get surface ionized at each wall collision. In thermal equilibrium the better trapping just compensates the lower ionization efficiency.

To assure the necessary condition, i.e. complete thermalization, the atoms and ions have to remain "infinitely long" in the cavity. However, a cavity without extraction hole is not very useful for ISOL applications. Therefore a compromise has to be found, combining a slightly reduced ionization efficiency with a finite extraction efficiency. This situation was described by Kirchner [Kir90] with the following equation:

$$\eta = \frac{\beta_s\omega\kappa}{1 - \beta_s\omega\kappa}.$$ (B.5.5)

---

[30]However, fluorine shows a low efficiency in negative surface ion sources. This is caused by strong adsorption of the very reactive fluorine atoms to surfaces in the source [Ewa84].

[31]Therefore at the SOLIS thermal ion source a ZrC disk was inserted into the cavity to act as an additional efficient electron emitter [Pil87].

$\eta$ is the ionization efficiency for particles which are extracted from the cavity, $\omega$ the probability that a surface ionized particle leaves the cavity as ion, $\kappa$ the mean number of wall collisions and $\beta_s$ the surface ionization efficiency according to equations (B.5.1) and (B.5.2).

To increase $\omega$ towards unity, one has to assure that the created ions lose their excess energy in the cavity volume before hitting the opposite wall. This can be achieved by increasing the neutral gas pressure to reduce the mean free path below cavity dimensions. Kirchner could increase the ionization efficiency by up to a factor of five when introducing xenon with a flow rate of about $10^{-3}$ mbar l/s [Kir90].

$\kappa$ is given by the ratio of the orifice area to the total inner cavity surface. With decreasing orifice diameter the mean number of wall collisions increases, but simultaneously the penetration of the extraction field and thus the extraction efficiency decrease. Moreover, the mean residence time in the cavity is increased, which can cause additional decay losses for very short-lived isotopes. With an orifice diameter of 0.8 mm for the GSI thermal ion source $\kappa$ is around 700, but for a standard ISOLDE surface ionizer with a tube diameter of 3 mm it is only 40.

$\omega$ can be determined by measuring a set of ionization efficiencies with the same ion source and fitting the product $N = \omega\kappa$ to reproduce the measured efficiencies. For the GSI thermal ion source $N$ was found to be around 150, but at ISOLDE the ionization efficiency of surface ionizable elements is measured only occasionally and under varying conditions. Therefore no exact value can be given, but $N$ is estimated to be between 5 and 20.

Figures B.5.1 and B.5.2 show typical ionization efficiencies derived with equation (B.5.5). The ratio $g_+/g_0$ was taken as unity. The efficiency with a Nb cavity should be similar to that of a Ta cavity.
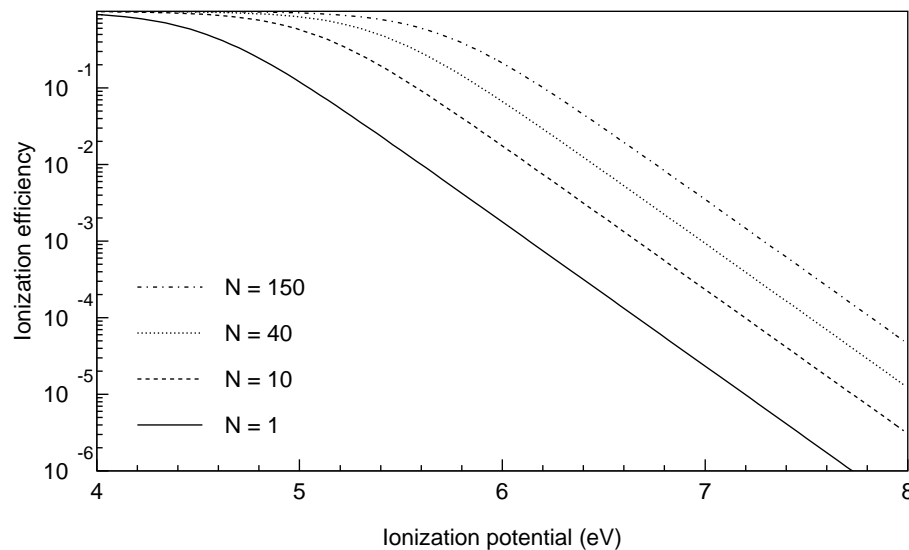


Figure B.5.1.: Influence of the parameter $N = \omega\kappa$ on the calculated surface ionization efficiency for a tungsten ionizer cavity ($\Phi_W = 4.54$ eV) at 2400 °C. The case $N = 1$ is equal to pure surface ionization without cavity effect.

To emphasize the difference to standard surface ionization which is only governed by the Langmuir equation, the hot cavity surface ion sources are also called thermal ion sources or thermoionization sources. Note that in the following, according to the ISOLDE synoptics, also the expression "line" will be used for the hot cavity.

Also negative ions can be exctracted from a hot tungsten cavity, see [Pio97] for experimental results.
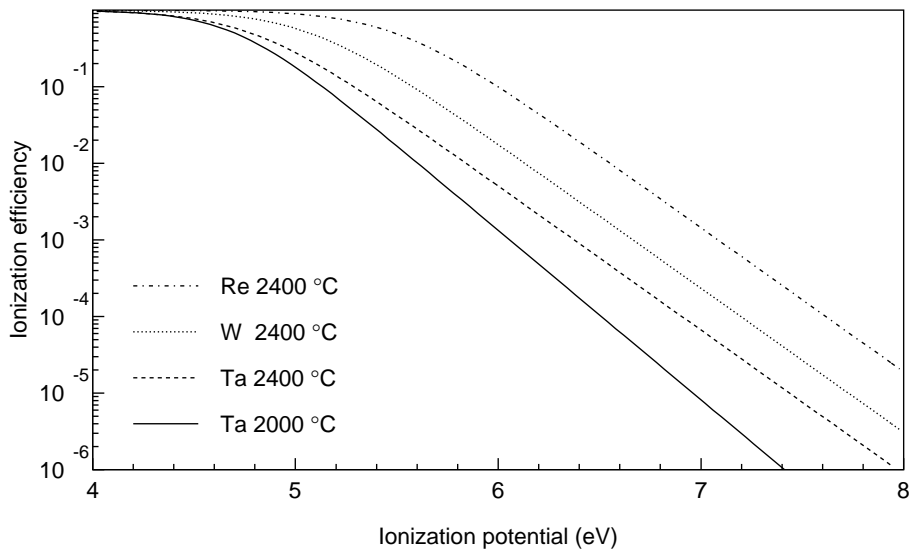
Figure B.5.2.: Influence of the ion source parameters on the calculated ionization efficiency. The four curves show Ta ($\Phi_{Ta} = 4.25$ eV) at 2000 °C and 2400 °C respectively, W ($\Phi_W = 4.54$ eV) at 2400 °C and Re ($\Phi_{Re} = 4.96$ eV) at 2400 °C.

# B.6.   Ionization potentials and electron affinities

Table B.6.1.: Ionization potentials $W_i$ (from [NISTA, Erd98a]), electron affinities $A_E$ (from [Moi76, Hot85, Rad85, HB, Ber95, And99] and references therein) and statistical weights of the elements: $g_0$ for the atomic ground state (from [NISTA]), $g_+$ for the positive ion (from [Rad85]) and $g_-$ for the negative ion (from [Moi76, Hot85] where known). The label "–" in the column of $A_E$ indicates that the negative ion is unstable or was not observed. Estimated values are given in parentheses.

| $Z$ | El. | $W_i$ (eV) | $A_E$ (eV) | $g_0$ | $g_+$ | $g_-$ | $Z$ | El. | $W_i$ (eV) | $A_E$ (eV) | $g_0$ | $g_+$ | $g_-$ |
|---|---|---|---|---|---|---|---|---|---|---|---|---|---|
| 1 | H | 13.6 | 0.75 | 2 | 1 | 1 | 37 | Rb | 4.18 | 0.49 | 2 | 1 | 1 |
| 2 | He | 24.59 | – | 1 | 2 | | 38 | Sr | 5.69 | 0.05 | 1 | 2 | |
| 3 | Li | 5.39 | 0.62 | 2 | 1 | 1 | 39 | Y | 6.22 | 0.31 | 4 | 1 | 5 |
| 4 | Be | 9.32 | – | 1 | 2 | | 40 | Zr | 6.63 | 0.43 | 5 | 4 | 4 |
| 5 | B | 8.3 | 0.28 | 2 | 1 | 1 | 41 | Nb | 6.76 | 0.89 | 2 | 1 | 1 |
| 6 | C | 11.26 | 1.26 | 1 | 2 | 4 | 42 | Mo | 7.09 | 0.75 | 7 | 6 | 6 |
| 7 | N | 14.53 | – | 4 | 1 | | 43 | Tc | 7.28 | 0.55 | 6 | 7 | 9 |
| 8 | O | 13.62 | 1.46 | 5 | 4 | 4 | 44 | Ru | 7.36 | 1.05 | 11 | 10 | 10 |
| 9 | F | 17.42 | 3.40 | 4 | 5 | 1 | 45 | Rh | 7.46 | 1.14 | 10 | 9 | 10 |
| 10 | Ne | 21.56 | – | 1 | 4 | | 46 | Pd | 8.34 | 0.56 | 1 | 6 | 6 |
| 11 | Na | 5.14 | 0.55 | 2 | 1 | 1 | 47 | Ag | 7.58 | 1.30 | 2 | 1 | 1 |
| 12 | Mg | 7.65 | – | 1 | 2 | | 48 | Cd | 8.99 | – | 1 | 2 | |
| 13 | Al | 5.99 | 0.43 | 2 | 1 | 1 | 49 | In | 5.79 | 0.40 | 2 | 1 | 1 |
| 14 | Si | 8.15 | 1.39 | 1 | 2 | 4 | 50 | Sn | 7.34 | 1.11 | 1 | 2 | 4 |
| 15 | P | 10.49 | 0.75 | 4 | 1 | 5 | 51 | Sb | 8.61 | 1.05 | 4 | 1 | 5 |
| 16 | S | 10.36 | 2.08 | 5 | 4 | 4 | 52 | Te | 9.01 | 1.97 | 5 | 4 | 4 |
| 17 | Cl | 12.97 | 3.61 | 4 | 5 | 1 | 53 | I | 10.45 | 3.06 | 4 | 5 | 1 |
| 18 | Ar | 15.76 | – | 1 | 4 | | 54 | Xe | 12.13 | – | 1 | 4 | |
| 19 | K | 4.34 | 0.50 | 2 | 1 | 1 | 55 | Cs | 3.89 | 0.47 | 2 | 1 | 1 |
| 20 | Ca | 6.11 | 0.02 | 1 | 2 | | 56 | Ba | 5.21 | 0.14 | 1 | 2 | |
| 21 | Sc | 6.56 | 0.19 | 4 | 3 | 5 | 57 | La | 5.58 | 0.47 | 4 | 5 | 5 |
| 22 | Ti | 6.83 | 0.08 | 5 | 4 | 4 | 58 | Ce | 5.54 | 0.26 | 9 | 8 | |
| 23 | V | 6.75 | 0.53 | 4 | 1 | 1 | 59 | Pr | 5.47 | 0.11 | 10 | 9 | |
| 24 | Cr | 6.77 | 0.678 | 7 | 6 | 6 | 60 | Nd | 5.53 | 0.1 | 9 | 8 | |
| 25 | Mn | 7.43 | – | 6 | 7 | | 61 | Pm | 5.58 | – | 6 | 5 | |
| 26 | Fe | 7.9 | 0.15 | 9 | 10 | 10 | 62 | Sm | 5.64 | 0.3 | 1 | 2 | |
| 27 | Co | 7.88 | 0.66 | 10 | 9 | 9 | 63 | Eu | 5.67 | – | 8 | 9 | |
| 28 | Ni | 7.64 | 1.16 | 9 | 11 | 6 | 64 | Gd | 6.15 | 0.34 | 5 | 6 | |
| 29 | Cu | 7.73 | 1.24 | 2 | 1 | 1 | 65 | Tb | 5.86 | 0.5 | 16 | 17 | |
| 30 | Zn | 9.39 | – | 1 | 2 | | 66 | Dy | 5.94 | 0.16 | 17 | 18 | |
| 31 | Ga | 6.00 | 0.41 | 2 | 1 | 1 | 67 | Ho | 6.02 | – | 16 | 17 | |
| 32 | Ge | 7.9 | 1.23 | 1 | 2 | 4 | 68 | Er | 6.11 | – | 13 | 14 | |
| 33 | As | 9.82 | 0.81 | 4 | 1 | 5 | 69 | Tm | 6.18 | 0.03 | 8 | 9 | |
| 34 | Se | 9.75 | 2.02 | 5 | 4 | 4 | 70 | Yb | 6.25 | 0.01 | 1 | 2 | 2 |
| 35 | Br | 11.81 | 3.36 | 4 | 5 | 1 | 71 | Lu | 5.43 | 0.26 | 4 | 1 | |
| 36 | Kr | 14 | – | 1 | 4 | | 72 | Hf | 6.83 | – | 5 | 4 | |

Table B.6.2.: Continuation of table B.6.1.

| $Z$ | El. | $W_i$ (eV) | $A_E$ (eV) | $g_0$ | $g_+$ | $g_-$ |
|---|---|---|---|---|---|---|
| 73 | Ta | 7.55 | 0.32 | 4 | 3 | 1 |
| 74 | W | 7.86 | 0.82 | 1 | 2 | 6 |
| 75 | Re | 7.83 | 0.15 | 6 | 7 | 9 |
| 76 | Os | 8.44 | 1.08 | 9 | 10 | |
| 77 | Ir | 8.97 | 1.56 | 10 | 11 | 9 |
| 78 | Pt | 8.96 | 2.13 | 7 | 6 | 6 |
| 79 | Au | 9.23 | 2.31 | 2 | 1 | 1 |
| 80 | Hg | 10.44 | – | 1 | 2 | |
| 81 | Tl | 6.11 | 0.38 | 2 | 1 | 1 |
| 82 | Pb | 7.42 | 0.36 | 1 | 2 | 4 |
| 83 | Bi | 7.29 | 0.94 | 4 | 1 | 5 |
| 84 | Po | 8.42 | 1.9 | 5 | | 4 |
| 85 | At | | 2.8 | 4 | | 1 |
| 86 | Rn | 10.75 | – | 1 | | |
| 87 | Fr | 4.07 | 0.50 | 2 | 1 | |
| 88 | Ra | 5.28 | 0.15 | 1 | 2 | |
| 89 | Ac | 5.17 | 0.35 | 4 | 1 | |
| 90 | Th | 6.31 | 0.37 | 5 | 4 | |
| 91 | Pa | 5.89 | (0.3) | 12 | 9 | |
| 92 | U | 6.19 | 0.3 | 13 | 10 | |
| 93 | Np | 6.27 | (0.3) | 12 | 13 | |
| 94 | Pu | 6.03 | – | 1 | 2 | |
| 95 | Am | 5.97 | – | 8 | 9 | |
| 96 | Cm | 5.99 | (0.3) | 5 | 8 | |
| 97 | Bk | 6.2 | – | 16 | 17 | |
| 98 | Cf | 6.28 | – | 17 | 18 | |
| 99 | Es | 6.37 | – | 16 | 17 | |
| 100 | Fm | 6.5 | – | 13 | | |
| 101 | Md | 6.58 | (1.0) | 8 | | |
| 102 | No | 6.65 | – | 1 | 2 | |

## B.7. Work function and Richardson parameter

The cavity material plays an important role for the efficiency of surface ionization sources and resonance ionization laser ion sources. The saturated emission current per unit area $J$ is described by the Richardson-Dushman equation:

$$J = A^* T^2 \exp\left(-\frac{\Phi}{kT}\right). \tag{B.7.1}$$

The theoretical value[32] for the Richardson constant of most metals is $A_0 = 120 \ \mathrm{Acm^{-2}K^{-2}}$. Including a possible temperature dependence of $\Phi$ gives an effective constant $A^*$ which may be different. The work function is considerably affected by the surface properties. Here, the values for clean polycrystalline surfaces are given. As example for surface modifications the value for an oxygen covered tungsten surface (W-O) is also given. The values were taken from [HB, Fom70, Sam71, Mic77, Smi92, Rao97]. The second column of table B.7.1 shows the range of reported values measured with the thermionic emission method; extreme values were omitted. The last two columns give the "recommended" values, mainly from [Smi92].

Table B.7.1.: Work function $\Phi$ and effective Richardson constant $A^*$.

| Mat. | $\Phi_{\mathrm{exp}}$ (eV) | $\Phi_{\mathrm{rec}}$ (eV) | $A^*$ $(\mathrm{Acm^{-2}K^{-2}})$ |
|------|------|------|------|
| C | 3.9-5.0 | 4.5 | 15 |
| Ti | 3.7-4.2 | 3.9 | |
| Zr | 3.5-4.5 | 4.12 | 330 |
| Nb | 4.0-4.3 | 4.19 | 120 |
| Mo | 4.1-4.5 | 4.15 | 55 |
| Hf | 3.5-3.9 | 3.6 | 22 |
| Ta | 4.0-4.4 | 4.25 | 120 |
| W | 4.4-5.0 | 4.54 | 60 |
| Re | 4.7-5.1 | 4.96 | 120 |
| Ir | 5.0-5.4 | 5.27 | 120 |
| Pt | 4.1-6.3 | 5.32 | 32 |
| Th | 3.3-3.5 | 3.38 | 70 |
| TiB$_2$ | 3.8-4.0 | | |
| LaB$_6$ | 2.6-3.2 | 2.7 | 29 |

| Mat. | $\Phi_{\mathrm{exp}}$ (eV) | $\Phi_{\mathrm{rec}}$ (eV) | $A^*$ $(\mathrm{Acm^{-2}K^{-2}})$ |
|------|------|------|------|
| TiC | 2.4-4.2 | 3.35 | 25 |
| ZrC | 2.1-4.1 | 2.18 | 0.3 |
| HfC | 3.0-4.0 | | |
| TaC | 3.1-4.4 | 3.14 | 0.3 |
| WC | 3.6 | | |
| ThC$_2$ | 3.2-3.5 | 3.5 | 550 |
| Al$_2$O$_3$ | 4.7 | 4.7 | |
| ZrO$_2$ | 4.0-4.6 | 3.96 | |
| CeO$_2$ | 2.3-3.2 | 2.3 | 1 |
| Ta$_2$O$_5$ | 4.65 | | |
| WO$_2$ | 4.96 | | |
| W-O | 5.3-9.2 | | |
| ThO$_2$ | 2.5-3.1 | 2.6 | 5 |
| Ir$_5$Ce | | 2.69 | 120 |

---

[32] $A_0 = G \cdot \frac{2\pi e m_e k^2}{h^3}$ with $G$ the number of electrons in the conduction band, i.e. typically 2 for metals.

# B.8. Resonance ionization schemes

In principle resonance ionization can be applied for all elements. However, there are large differences in the required set-up and the ionization efficiency which can be obtained.

The following tables B.8.1, B.8.2, B.8.3 and B.8.4 give an overview of experimentally used resonance ionization schemes for various elements. In cases where no application of RIS has been reported in literature, a promising "theoretical" scheme is included. The proposed schemes are marked with a label 'prop.' in the column 'Pumping laser'. The wavelengths marked with an 'A' or a 'R' indicate a transition to an autoionizing state or a Rydberg state respectively. In some cases a static or pulsed electrical field is used for the final ionization step - marked with '$\vec{E}$' in the table.

The shown wavelengths may give an idea of the difficulty of a technical realization. Often a multitude of alternative schemes exist and only some representative ones are shown. Extensive compilations can be found in [Let87] and [Hur79].

Useful data for resonance ionization spectroscopy has been collected at NIST, Gaithersburg and was published as a series of data sheets: [Sal90] contains As, B, Cd, C, Ge, Au, Fe, Pb, Si and Zn, [Sal91] contains Al, Ca, Cs, Cr, Co, Cu, Kr, Mg, Hg and Ni, [Sal92] contains Sb, Bi, P, Na and Sn, [Sal93] contains Be, In, Li, K, Rb, Ag, Ti, V and an update for Ni and [Sal95] contains Ga, Mn, Sc and Tl. They also include information on transition strengths, lifetimes, isotope shifts and hyperfine splitting constants. Many other references can be found in the proceedings of the biannual conference series "Resonance Ionization Spectroscopy".

Table B.8.1.: Excitation schemes used for resonance ionization. The label '*ms*' stands for a scheme starting from a metastable state. This has to be populated by collisions in a gas cell or by a plasma discharge.

| El. | IP (eV) | $\lambda_1$ (nm) | $\lambda_2$ (nm) | $\lambda_3$ (nm) | Pumping laser | Reference |
|-----|---------|------------------|------------------|------------------|---------------|-----------|
| H  | 13.60 | 266 & 223.9 | 266 | – | Nd-YAG | [Bjo78] |
| He | 24.59 | *ms* | 389 | $796^R$ & $\vec{E}$ | CVL | [Ase91a, Kud92] |
| He | 24.59 | 58.4 | 292 | – | Nd-YAG | [Eik96] |
| Li | 5.39 | 670.8 | 610.4 | 610.4, 670.8 | CVL | [Kra79, Mis93] |
| Be | 9.32 | 234.9 | $297.3^A$ | – | CVL | [Fed98] |
| B  | 8.30 | 249.7 | 378.4 | $\vec{E}$ | | [Bek84a] |
| B  | 8.30 | 249.7 | 563.3 | 1064 | Nd-YAG | [Arl93] |
| C  | 11.26 | $2 \cdot 286.9$ | 286.9 | – | Nd-YAG | [Moo85] |
| F  | 17.42 | $3 \cdot 286.4$ | $2 \cdot 286.4$ | | Nd-YAG | [Bis85a, Bis85b] |
| Ne | 21.56 | 74.4 | 223.1 | – | Nd-YAG | [Eik94] |
| Na | 5.14 | 589.6 | 416.6 | $\vec{E}$ | $N_2$ | [Amb75] |
| Na | 5.14 | 589.0 | 616.0 | 589, 616 | Nd-YAG | [Ren97] |
| Mg | 7.65 | 285.2 | 552.8 | 578 | CVL | [Fed98] |
| Al | 5.99 | 396.2 | 447.4 | $\vec{E}$ | $N_2$ | [Bek83] |
| Al | 5.99 | 308.2 | $630\text{-}670^R$ | $\vec{E}$ | $N_2$ | [Zhe84a] |
| Si | 8.15 | 251.4 | 564.6 | 1064 | prop. | [Sal90] |
| P  | 10.49 | $2 \cdot 299.2$ | 299.2 | – | Nd-YAG | [Gel89] |
| Ar | 15.76 | 106.7 | 365.9 | 1064 | Nd-YAG | [Leh83, Hur85] |
| K  | 4.34 | 766.5 | $460.5^R$ | $\vec{E}$ | XeCl | [Kud85] |
| Ca | 6.11 | 422.7 | 732.8 | 514.5 | Dio. & Ar$^+$ | [Mül98] |
| Sc | 6.56 | 621.1 | 461.0 | $647.7^A$ | prop. | [Sal95] |
| Ti | 6.83 | 554.8 | 266 | – | Nd-YAG | [Mar87] |
| Ti | 6.83 | 504.1 | 266 | – | Nd-YAG | [Mar87] |
| Ti | 6.83 | 395.8 | 339.4 | – | XeCl | [Weiss] |
| Ti | 6.83 | 337.8 | 384.1 | – | XeCl | [Weiss] |
| V  | 6.75 | 294.3 | 294.3 | – | Nd-YAG | [Fai89] |
| V  | 6.75 | 297.8 | 297.8 | – | Nd-YAG | [May90] |
| Cr | 6.77 | 297.0 | 297.0 | – | Nd-YAG | [May90] |
| Cr | 6.77 | 425.4 | 308 | – | XeCl | [Wil84] |
| Mn | 7.43 | 279.8 | 628.3 | $510.6^A$ | CVL | [Fed97] |
| Fe | 7.90 | 283.6 | 283.6 | – | Nd-YAG | [Fas84] |
| Co | 7.88 | 230.9 | $481.9^A$ | – | XeCl | [Kud96] |
| Ni | 7.64 | 305.1 | 611.1 | $748.2^A$ | CVL | [Jok97] |
| Ni | 7.64 | 232.0 | $537.8^A$ | – | XeCl | [Kud96] |

Table B.8.2.: Continuation of table B.8.1. Further schemes for the lanthanides from cerium to erbium can be found in [Wor78].

| El. | IP (eV) | $\lambda_1$ (nm) | $\lambda_2$ (nm) | $\lambda_3$ (nm) | Pumping laser | Reference |
|-----|---------|----------|----------|----------|---------|-----------|
| Cu | 7.73 | 327.4 | $287.9^A$ | – | CVL | [Kös00] |
| Zn | 9.39 | 213.9 | 636.2 | 510.6 | CVL | [Let98] |
| Ga | 6.00 | 294.4 | 578.2 | – | CVL | [Zhe83] |
| Ge | 7.90 | 265.2 | 569.2 | 1064 | prop. | [Sal90] |
| As | 9.82 | $2 \cdot 318.0$ | $540.9^A$ | – | prop. | [Sal90] |
| Kr | 14.00 | 116.5 | 558.1 | 1064 | Nd-YAG | [Leh83, Kra86] |
| Kr | 14.00 | $ms$ | 557.0 | $676.0^R$ & $\vec{E}$ | CVL | [Ase91b] |
| Kr | 14.00 | $ms$ | 760.2 | $510.6^R$ & $\vec{E}$ | CVL | [Kud92] |
| Rb | 4.18 | 794.8 | 347.1 | – | Ruby | [Amb71] |
| Rb | 4.18 | 420.2 | 694.3 | – | Ruby | [Amb76] |
| Sr | 5.69 | 689.3 | 687.8 | 602.7 | CVL | [And86] |
| Y | 6.22 | $2 \cdot 548$ | 548 | – | Exc. | [Est91] |
| Zr | 6.63 | 451.6 | $319^R$ | $\vec{E}$ | Exc.&Nd-Y. | [Hac86] |
| Nb | 6.76 | 566.5 | 524.0 | 523.0 | Excimer | [Lau90] |
| Mo | 7.09 | 313.3 | 313.3 | – | Nd-YAG | [Fas83, Fai89] |
| Mo | 7.09 | 386.5 | $2 \cdot 386.5$ | – | XeCl | [Min92] |
| Tc | 7.28 | 318.2 | 787.9 | $670.7^A$ | CVL | [Rus89] |
| Tc | 7.28 | 313.2 | 821.1 | 670.7 | CVL | [Ame90] |
| Ru | 7.36 | 392.6 | 633.1 | $567.3^R$ & $\vec{E}$ | | [Bek84b, Bek85] |
| Ru | 7.36 | 330.2 | $344\text{–}346^R$ | $\vec{E}$ | XeCl | [Xu90] |
| Ru | 7.36 | 273.6 | $435.1^A$ | – | | [Xu95] |
| Rh | 7.46 | 232.3 | $572.6^A$ | – | XeCl | [Kud96] |
| Pd | 8.34 | 244.9 | $344.6^A$ | – | | [Cal88b] |
| Ag | 7.58 | 328.1 | 546.6 | 510.6 | CVL | [Mis93, Jad97] |
| Cd | 8.99 | 228.8 | 643.8 | 510.6 | CVL | [Erd98b, Let98] |
| In | 5.79 | $2 \cdot 423.7^A$ | – | – | N$_2$ | [Mir78] |
| In | 5.79 | 303.9 | 578.2 | – | CVL | [Muc83] |
| Sn | 7.34 | 286 | 617 | 617 | Nd-YAG | [Fai89] |
| Sn | 7.34 | 303.6 | 606.9 | 606.9 | CVL | [Mis93] |
| Sn | 7.34 | 317.5 | 811.4 | $823.5^A$ | CVL | [Mis93] |
| Sb | 8.61 | 231.1 | 563.2 | $< 1186$ | prop. | [Sal92] |
| Xe | 12.13 | 125.0 | 532 | – | Nd-YAG | [Leh83, Hur85] |
| Xe | 12.13 | $94.2^A$ | – | – | Nd-YAG | [Bon85] |

Table B.8.3.: Continuation of table B.8.1.

| El. | IP (eV) | $\lambda_1$ (nm) | $\lambda_2$ (nm) | $\lambda_3$ (nm) | Pumping laser | Reference |
|-----|---------|------------------|------------------|------------------|---------------|-----------|
| Cs | 3.89 | 455.5 | 455.5 | – | Flashlamp | [Hur77] |
| Cs | 3.89 | 852.1 | 603.5 | 503 | Nd-YAG | [Tem98] |
| Ba | 5.21 | 350.1 | 532 | – | Nd-YAG | [Koi97] |
| La | 5.58 | 593.0 | 820.5 | 532 | Nd-YAG | [Koi97] |
| Ce | 5.54 | 458.3 | $437.1^R$ | $\vec{E}$ | $N_2$ | [Wor78] |
| Pr | 5.46 | 394.5 | $576.2^A$ | – | $N_2$ | [Wor78] |
| Nd | 5.53 | 463.4 | $435.2^A$ | – | $N_2$ | [Wor78] |
| Nd | 5.53 | 588.8 | 596.9 | $596.9^A$ | CVL | [Alk87, Zyu88] |
| Sm | 5.64 | 600.4 | 675.2 | $676.2^A$ | CVL | [Mis87b] |
| Eu | 5.67 | 576.5 | 557.3 | $555.7^A$ | CVL | [Alk83, Zhe84b] |
| Gd | 6.15 | 561.8 | 635.2 | $613.4^A$ | $N_2$ | [Bek78a] |
| Gd | 6.15 | 569.6 | 597.6 | $613.5^A$ | $N_2$ | [Mis87a] |
| Gd | 6.15 | 276.1 | $740.8^A$ | – | XeCl | [**?**] |
| Tb | 5.86 | 601.9 | 613.9 | 618.7 | CVL | [Let87] |
| Dy | 5.94 | 625.9 | 677.0 | $583.1^A$ | $N_2$ | [Wor78] |
| Ho | 6.02 | 592.1 | 572.5 | 626.8 | CVL | [Alk87] |
| Er | 6.11 | 622.1 | 645.2 | 564.9 | | [Let87] |
| Tm | 6.18 | 589.6 | 571.2 | $575.5^A$ | CVL | [Mis87b, Mis93] |
| Tm | 6.18 | 597.1 | 600.3 | 552.4 | CVL | [Bar98a] |
| Yb | 6.25 | 555.6 | 581.1 | 581.1 | CVL | [Mis93, Bar98a] |
| Yb | 6.25 | 555.6 | 680.0 | $581.3^R$ | CVL | [Bek78b, Bek81] |
| Lu | 5.43 | 452.0 | 452.0 | – | Flashl. | [Mil82] |
| Lu | 5.43 | 451.9 | $463\text{-}471^R$ | $\vec{E}$ | $N_2$ | [VA92] |
| Hf | 6.83 | ? | $?^R$ | $\vec{E}$ | Excimer | [Cal88a] |
| Ta | 7.55 | 575.2 | $\approx 230^R$ | $\vec{E}$ | | [Sim94] |
| W | 7.86 | 384.9 | $\approx 267^R$ | $\vec{E}$ | Nd-YAG | [CM96] |
| Re | 7.83 | 299.2 | 299.2 | – | Nd-YAG | [Fas83] |
| Re | 7.83 | 283.5 | 297.2 | – | Nd-YAG | [Wal86] |
| Re | 7.83 | 346.1 | $\approx 292^R$ | $\vec{E}$ | Nd-YAG | [CM96] |
| Os | 8.44 | 280.7 | 297.7 | – | Nd-YAG | [Wal86] |
| Os | 8.44 | 353.0 | $\approx 252^R$ | – | Nd-YAG | [Col97] |
| Ir | 8.97 | 307.6 | $\approx 251.5^R$ | – | Nd-YAG | [Col97] |
| Ir | 8.97 | 266.5 | 562.0 | $642^R$ | Excimer | [Mat95] |
| Ir | 8.97 | 380.0 | 402.0 | $516^R$ | Excimer | [Mat95] |

Table B.8.4.: Continuation of table B.8.1.

| El. | IP (eV) | $\lambda_1$ (nm) | $\lambda_2$ (nm) | $\lambda_3$ (nm) | Pumping laser | Reference |
|-----|---------|------------------|------------------|------------------|---------------|-----------|
| Pt | 8.96 | 266 | 451 | 532 | Nd-YAG | [Krö91] |
| Pt | 8.96 | 306.6 | 253-257$^R$ | | Nd-YAG | [Mar95] |
| Pt | 8.96 | 331.6 | 213-215$^A$ | | Nd-YAG | [Mar95] |
| Au | 9.23 | 267.6 | 407 | 532 | Nd-YAG | [Wal87, Krö91] |
| Au | 9.23 | 267.6 | 407 | 592$^A$ | Nd-YAG | [Krö87] |
| Au | 9.23 | 267.6 | 583.7 | 481$^A$ | $N_2$ | [Bek87] |
| Hg | 10.44 | 253.7 | 286 | 532 | Nd-YAG | [Dye83] |
| Hg | 10.44 | 253.7 | 286 | 696$^A$ | Nd-YAG | [Dye85] |
| Hg | 10.44 | 253.7 | 435.8 | 458-470$^R$ | $N_2$ | [Tur90] |
| Hg | 10.44 | 253.7 | 435.8 | 466.2$^R$ | Excimer | [Mat95] |
| Tl | 6.11 | 377.6 | 377.6 | − | $N_2$ | [Min86] |
| Tl | 6.11 | 377.6 | 452.1 | *coll.* | XeCl | [Lau92] |
| Pb | 7.42 | 283.3 | 414.1$^R$ | $\vec{E}$ | XeCl | [Gul95] |
| Pb | 7.42 | 283.3 | 408-411 | | Nd-YAG | [Has96] |
| Bi | 7.29 | 306.8 | 555.2 | < 1224 | | [Sal92] |
| Po | 8.42 | 255.8 | <347 | | (prop.) | [Kow91] |
| Fr | 4.07 | 718 | 536.4$^R$ | $\vec{E}$ | CVL | [And87] |
| Ra | 5.28 | 482.6 | <457 | − | prop. | [Wen87] |
| Ra | 5.28 | $\approx 214$ | − | − | prop. | [Gre91] |
| Ra | 5.28 | 235-243$^R$ | $\vec{E}$ | − | prop. | [Arm80] |
| Th | 6.31 | 580.4 | 622.9 | 568 | CVL | [Dei95] |
| U | 6.19 | 591.5 | 564.8 | 632.3$^A$ | CVL | [Rus89] |
| Np | 6.27 | 607.4 | 585.7 | 588$^R$ & $\vec{E}$ | $N_2$ | [Wor79] |
| Np | 6.27 | 587.8 | 610.9 | 575.9$^A$ | CVL | [Rie93] |
| Np | 6.27 | 311.8 | 544 | − | CVL | [Dei95] |
| Pu | 6.03 | 649.1 | 629.8 | 579 | CVL | [Dei95] |
| Pu | 6.03 | 420.8 | 847.3 | 756.3 | Nd-YAG | [Grü98] |
| Am | 5.97 | 640.5 | 654.4 | 578$^A$ | CVL | [Dei95] |
| Am | 5.97 | 468.2 | 351, 353 | − | XeF | [Bac98] |
| Cm | 5.99 | 655.6 | 640.7 | 573$^A$ | CVL | [Dei95] |
| Bk | 6.20 | 566.1 | 720.7 | 544$^A$ | CVL | [Köh96] |
| Cf | 6.28 | 572.8 | 625.2 | 581$^A$ | CVL | [Köh96] |
| Es | 6.37 | 561.7 | 661.3 | 544$^A$ | CVL | [Pet98, Erd98a] |

## B.9.   Background and selectivity

The detected event rate in a certain region of interest is typically composed from events of the isotope to study $r_x$, from events of internal background $r_{int}$ (isobars and other beam contaminations) and from external background $r_{BG}$. These detected event rates are connected to the activity of the respective sources by multiplication with the individual branching ratios and the detector response for the respective decay. It is obvious that detection methods being only sensitive to "exotic" decay modes like beta-delayed particles are intrinsically able to suppress background from activity close to stability by many orders of magnitude. For simplicity in the following the hypothetical case is discussed where all contributing sources have a proportionality factor (equal branching ratio times detector response) of unity. This case is approximately realized when using a beta detector with a flat energy response function. A generalization of the formulae, including the individual branching ratios and detector response, is straightforward.

The number of events detected during the measurement time $t_M$ in the region of interest becomes:

$$n_1 = (r_x + r_{int} + r_{BG})t_M. \tag{B.9.1}$$

The external background can be determined in a separate measurement by blocking the ion beam while keeping all other parameters similar. At a spallation facility it has to be taken into account that this background is partly related to the primary beam. A small part of the energetic spallation neutrons can pass all shieldings and enter the experimental hall. Background is then created directly in neutron sensitive detectors or by secondary reactions ($(n,\gamma)$, etc.) in the surroundings.

An additional contribution was observed with actinide targets: through the impact of the pulsed proton beam noble gases are released as a bunch and drift through the beam tubes. With detector positions close to the separator the corresponding activity can cause background rates of up to 1 kHz within some seconds after proton impact. With appropriate shielding or coincidence requirements the external background can be normally reduced to an acceptable level.

The internal background is in many cases much worse. Implanted at the same position as the desired isotope, the solid angle for detection is equal and normally no improvement is achievable with unspecific coincidence requirements (beta trigger, gamma multiplicity trigger, etc.). The application of gamma gating has a major limitation: for very exotic nuclides often no transitions are known which could be used to install a hardware gate. Thus, *all* data has to be saved in list-mode for later reconstruction. Depending on the data acquisition system the event rate cannot exceed some 0.1 to 10 kHz. For precise lifetime measurements requiring a low dead time the restrictions are even much stricter.

The decay daughters of the isotope to study reach in the worst case a comparable intensity. Accumulation of longer-lived daughters can be prevented by implanting the beam onto a tape and moving this periodically away.

In the case of laser ionization the surface ionized background can be determined in a separate measurement, where all target and ion source parameters are kept the same, but at least one of the resonant laser beams is detuned in frequency or blocked. Such a measurement of total background (i.e. external plus internal background) should be done shortly before or after the corresponding "real" measurement, since the target ion source system is subject to changes during a beam time of hours or days.

The number of events detected in the region of interest during the laser-off measurement with the time $t_{BG}$ is:

$$n_0 = (r_{int} + r_{BG})t_{BG}. \tag{B.9.2}$$

For simplification $t_{BG}$ is chosen identical to $t_M$. In reality it should be optimized for individual cases. For gamma background from isotopes with accurately known decay schemes the contribution of

low intensity lines can be scaled from more intense lines and a shorter background measurement is sufficient.

The number of events of the isotope to be studied $x$ is given by the difference of $n_1$ and $n_0$. With normal distributed event rates the error is:

$$\begin{aligned}
\Delta x &= \sqrt{\sqrt{n_1}^2 + \sqrt{n_0}^2} = \\
&= t_M \sqrt{(r_x + r_{int} + r_{BG})t_M + (r_{int} + r_{BG})t_M} = \\
&= \sqrt{t_M}\sqrt{r_x + 2r_{int} + 2r_{BG}}.
\end{aligned} \tag{B.9.3}$$

Thus, $x$ can be determined with a statistical accuracy $a$:

$$a = \frac{\Delta x}{x} = \frac{\sqrt{t_M}\sqrt{r_x + 2r_{int} + 2r_{BG}}}{r_x t_M} = \sqrt{t}\sqrt{\frac{r_x + 2r_{int} + 2r_{BG}}{r_x^2}}. \tag{B.9.4}$$

To reach a given accuracy $a$, the required measurement time $t_M$ is:

$$t_M = \frac{1}{a^2}\frac{r_x + 2r_{int} + 2r_{BG}}{r_x^2}. \tag{B.9.5}$$

Figure B.9.1 shows the relation of the required beam purity $r_x/r_{int}$ versus beam intensity $r_x$ for different background rates $r_{BG}$ and a given statistical accuracy of 10 %.
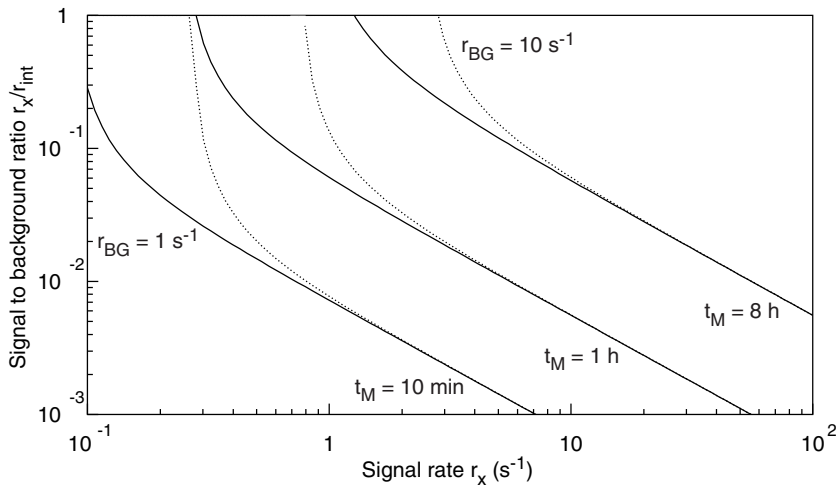


Figure B.9.1.: Required signal to background ratio for a given count rate. The continuous lines are with a background rate of $1\ \text{s}^{-1}$, the dotted ones for $10\ \text{s}^{-1}$.

It is clearly seen that a high beam purity is often equally or more important than a high beam intensity. Thus, especially in nuclear spectroscopy and nuclear solid state physics experiments a selective RILIS can outdo a hot plasma source despite an efficiency which might be lower by a factor 3 to 10.

# B.10.    Experimental resonance width

The experimental width $\delta\nu_{\text{res}}$ of a resonant laser transition $(i,f)$ is determined by several contributions.

## B.10.1.    Natural linewidth

The finite lifetimes of the levels involved in the transition will cause a finite line width described by a Lorentzian profile:

$$I(\nu) = \frac{1}{2\pi} \frac{\delta\nu_{\text{nat}}}{(\nu - \nu_0)^2 + (\delta\nu_{\text{nat}}/2)^2} \tag{B.10.1}$$

with $\nu_0$ the central frequency of the transition and the natural linewidth $\delta\nu_{\text{nat}}$ (FWHM):

$$\delta\nu_{\text{nat}} = \delta\nu_{\text{nat}}^i + \delta\nu_{\text{nat}}^f = \frac{1}{2\pi\tau_i} + \frac{1}{2\pi\tau_f}. \tag{B.10.2}$$

Typical lifetimes are in the range of some ns. Thus, the natural width is of the order of some ten to hundreds of MHz which is much smaller than the contributions discussed below.

Only in the case of autoionizing states the lifetime is much shorter ($10^{-15} - 10^{-10}$ s) and consequently the width significantly broader (GHz to THz). Therefore transitions to autoionizing states are not used for scanning the frequency in spectroscopic applications.

## B.10.2.    Doppler width

Depending on the motion of the atom relative to the photon beam, the atom will "observe" a Doppler shifted frequency. In thermal equilibrium with the hot ionizer cavity the atoms will follow a Maxwellian velocity distribution with the most probable velocity $\hat{v} = \sqrt{2kT/m}$. $m$ is the mass of the atom and $T$ the temperature of the cavity.

The Doppler broadened spectral line is described by a Gaussian:

$$I(\nu) = I_0 \exp\left(-\frac{(\nu - \nu_0)^2}{\nu_0 \hat{v}}\right) = I_0 \exp\left(-\frac{4\ln 2(\nu - \nu_0)^2}{\delta\nu_D}\right). \tag{B.10.3}$$

The full halfwidth $\delta\nu_{\text{D}}$, called Doppler width, is:

$$\delta\nu_{\text{D}} = \nu_0\sqrt{\frac{8kT\ln 2}{mc^2}} = 7.16 \cdot 10^{-7}\nu_0\sqrt{\frac{T/\text{K}}{M/(\text{g/mol})}}. \tag{B.10.4}$$

For a 2000 °C hot cavity and a transition in the visible range ($\lambda_0 = 500$ nm) the Doppler width varies between 1.3 GHz ($A = 238$) and 8.4 GHZ ($A = 6$).

## B.10.3.    Collisional broadening

At a high gas pressure the mean time between two atomic collisions can get shorter than the natural lifetime. The collisions will provoke non-radiative transitions between different levels. The level population is disturbed and the lifetime is reduced. The resonance profile remains a Lorentzian, but the effective linewidth becomes:

$$\delta\nu_{\text{eff}} = \delta\nu_{\text{nat}} + \delta\nu_{\text{coll}} \tag{B.10.5}$$

where the collisional broadening is proportional to the gas pressure $p$:

$$\delta\nu_{\text{coll}} = a_{\text{coll}}\, p. \tag{B.10.6}$$

The magnitude of $a_{\text{coll}}$ is some ten to hundred MHz per mbar gas pressure [Dem98]. It is negligible in a hot cavity RILIS but can become important in a gas cell RILIS.

## B.10.4.    Power broadening

Also a strong pumping of the atomic transition $(i, f)$ with a laser beam will disturb the level population. Due to this saturation effect the width of the natural Lorentzian profile is broadened to:

$$\delta\nu_{\text{sat}} = \delta\nu_{\text{nat}}\sqrt{1 + S} \tag{B.10.7}$$

with the saturation parameter $S$ given by:

$$S = \frac{2\sigma_{12}I(\nu)\tau_{21}}{h\nu}. \tag{B.10.8}$$

Using equation (3.2.10) as expression for $\sigma_{12}$ and assuming that the resonance width $\delta\nu_{\text{res}}$ is dominated by the Doppler broadening $\delta\nu_D$ gives:

$$S = \frac{g_2\lambda^3}{g_1hc2\delta\nu_{\text{D}}}I(\nu). \tag{B.10.9}$$

In the case of much stronger pumping even a splitting of the resonance line into two peaks can occur.

However, in the practical application of a RILIS it is more a problem that occasionally the laser power is not sufficient rather than that far too much power is available. In the latter case the dye laser power can be easily reduced. For spectroscopic applications the beam power of the scanned transition is deliberately reduced by introduction of an absorber. Some ionization efficiency is lost, but the spectral resolution is increased.

## B.10.5.    Shape of the resonance curve

The widths of all Lorentzian contributions, i.e. natural linewidth, collisional broadening and power broadening, will add directly to the resonance width $\delta\nu_{\text{res}}$. In a hot cavity RILIS normally the Doppler width will dominate the resonance width and the resonance is rather described by a Gaussian. However, if the Lorentzian width becomes larger (e.g. by significant power broadening) for a correct description of the shape Gaussian and Lorentzian have to be folded, resulting in a Voigtian curve.

## B.10.6.    Laser bandwidth

The bandwidth of the dye lasers depends on the geometry of the used resonator cavity. In normal operation the ISOLDE RILIS dye lasers have a large bandwidth of some 20 to 30 GHz. Thus, typically the experimentally observed resonance width is dominated by the laser bandwidth. This is useful since atomic physics effects (isotope shift, hyperfine splitting) should not reduce the ionization efficiency of exotic isotopes.

However, for atomic spectroscopy applications a smaller bandwidth is required. By introduction of a Fabry-Perot etalon the dye laser bandwidth can be reduced to some GHz (depending on the etalon). The actual bandwidth of a single laser pulse is much smaller, but since the dye laser is pulsed, it has to pass the laser threshold 10000 times per second. Each time one of the possible resonance modes will be randomly amplified and the frequency will "jump" from shot to shot within the quoted range. To reduce these wavelength fluctuations, one has to stabilize a single lasing mode of the multi-mode laser. This can be achieved by "seeding": i.e. the dye laser is always pumped by a cw pumping laser and amplified with the pulsed CVL or Nd-YAG beam, see e.g. [Pin77]. An $Ar^+$ laser provides 514.5 nm light which is close enough to the green line of the CVL (511 nm) or Nd-YAG (532 nm) laser to excite the same dye. Thus, it is ideal for seeding the dye laser.

## B.11.  Beta-delayed neutron emission

For very neutron-rich nuclei the $Q_\beta$ value often exceeds the neutron binding energy $S_n$ of the daughter nuclide. Thus, particle-unstable levels above the neutron separation threshold can be populated in beta-decay, leading to so-called beta-delayed neutron emission ($\beta$n). This decay mode was observed in neutron-rich fission products already in 1939 [Rob39] and was theoretically explained soon after that [Boh39]. The average number of emitted neutrons per decay is called $P_n$ value (probability of neutron emission). For extremely neutron-rich isotopes even multiple neutron emission can occur (for $Q_{\beta^-} > S_{2n}$, $S_{3n}$, etc.). The respective individual branching ratios are designated $P_{1n}$, $P_{2n}$, ... and the total $P_n$ value is given by:

$$P_n = P_{1n} + 2 \cdot P_{2n} + 3 \cdot P_{3n} + \cdots . \tag{B.11.1}$$

The neutron emission does not necessarily proceed to the ground state, but can also populate excited states in $^{A-1}(Z-1)$. The difference between the energy of the neutron unstable level $E_x(^A(Z-1))$ and the populated level $E_y(^{A-1}(Z-1))$ is distributed as kinetic energy among the emitted neutron and the recoiling rest nucleus respecting momentum conservation:

$$E_n = \frac{A-1}{A} \cdot \left( E_x(^A(Z-1)) - E_y(^{A-1}(Z-1)) \right) . \tag{B.11.2}$$

The width of the energy distribution is given by the lifetime $\tau_y$ of the neutron-emitting level:

$$\Delta E = \frac{h}{\tau} \tag{B.11.3}$$

and slightly broadened by the recoil of the decay beta.

For most of the heavier nuclides the high level density leads to an overlap of the discrete neutron-emitting levels giving a more or less continuous neutron energy spectrum $N(E)$ which can be characterized by the mean energy $\bar{E}_n$ and the width $\sigma$. $\sigma$ is the square root of the second moment of the energy distribution:

$$\sigma = \sqrt{\frac{\int (E_n - \bar{E}_n)^2 N(E) dE}{\int N(E) dE}}. \tag{B.11.4}$$

Typically the energies of beta-delayed neutrons range from some ten keV to MeV. Due to the technological importance for the control of reactors, $P_n$ values and neutron energy spectra have been studied for most beta-delayed neutron emitters in the fission product region, see e.g. [Rud91].

For very proton-rich nuclei the corresponding process is beta-delayed proton emission ($\beta$p)[33]. The detection of beta-delayed protons with $\Delta E/E$ telescopes is a good way for efficient and selective identification of nuclei close to the proton dripline.

---

[33]In rare cases also other particles can be emitted after beta-decay, giving rise to decay modes like: $\beta$d, $\beta$t and $\beta\alpha$. For an overview see e.g. [Han89].

## B.11.1. Detection of delayed neutrons

Several methods are used to detect neutrons and to determine their kinetic energy (see e.g. ref. [Kno89]):

1. Direct recoils from n-p-scattering in a hydrogen containing counter (gas or scintillator) are used in so-called "proton recoil detectors" for the detection of neutrons down to energies of some keV. In organic scintillators the neutron events are separated from gamma events by pulse shape discrimination.

2. For a time-of-flight (TOF) measurement the start signal is given by detection of a beta- or gamma-ray emitted in the decay and the stop signal by the detected neutron. With typical TOF distances $l \approx 1$ m and a timing resolution $\delta t \approx 1$ ns, the achievable energy resolution $\delta E_n$ is about 50 keV for 1 MeV neutrons.

$$\delta E_n = 2E_n \frac{\delta t}{t} = \frac{(2E)^{\frac{3}{2}}}{l\sqrt{m}}. \approx 50 \cdot (E_n/\text{MeV})^{\frac{3}{2}} \text{ keV} \tag{B.11.5}$$

An alternative way, the TOF spectroscopy of the recoil atoms, is still under development, see ref. [Der95].

3. Also direct detection with an ionization chamber filled with $^3$He can provide an energy information. For slow neutrons the energy given to the subsequently detected fragments is just the $Q$-value of the reaction:

$$^3\text{He} + \text{n} \rightarrow \text{p} + \text{t}, \ \ Q = 764 \text{ keV} \tag{B.11.6}$$

For higher energies the fragments carry additionally the kinetic energy of the incoming particle and an energy $Q + E_n$ is detected. Other contributions have to be taken into account like elastic scattering on helium or competing channels opening at higher energies, e.g. (n,d). With a typical energy resolution $\delta E \leq 20$ keV [Fra77], the energy of individual neutron peaks can be resolved with an accuracy better than about 4 keV.

In all these cases the cross-section and thus the detection efficiency decrease considerably at higher neutron energies. Only few detector arrays exist which are big enough to give a good TOF resolution and still cover a large solid angle. An example is the TONNERRE array, which was specially designed for delayed-neutron spectroscopy [Orr98, But00].

High detection efficiencies ($\gg 10\%$) which are essential for the detection of very rare beta-delayed neutron emitters are obtained by moderating the neutrons before detection. $^3$He proportional counters are embedded into a moderating matrix of low-$Z$ material, e.g. polyethylene $(CH_2)_n$. Loosing half of the kinetic energy in each collision with a hydrogen atom, the neutrons will be thermalized after about 25 collisions[34]. The time between emission and detection is thus some hundred $\mu$s, requiring a large time window for coincidences with the prompt signal from beta- or gamma detectors. With sufficient moderating material a flat response curve can be achieved which is useful to determine $P_n$ values for isotopes with an unknown neutron energy spectrum.

The direct energy information is lost through moderation, but from the mean range of the neutrons a rough energy information can be gained. An arrangement of $^3$He counters in concentric rings of different radius embedded in a cylindrical moderator allows to combine the advantage of a flat energy response while retaining some energy sensitivity. The total efficiency (obtained by summing the count rates of all rings) is approximately constant over a large energy range (up to some MeV), but the ratio of detected neutrons in outer and inner rings gives an approximate information on $\bar{E}_n$. This technique was extensively used for measurement of delayed neutron energies of fission products at TRISTAN [Ree81] and OSIRIS [Rud91].

---

[34] $x \approx \log \left( \frac{E_n}{25 \text{ meV}} \right) / \log(2)$ with $E_n$ given in eV.

## B.11.2.   Neutron long counter

We used the Mainz neutron long counter [Böh96] for all presented measurements of $\beta$-delayed neutrons. It consists of up[35] to 64 $^3$He proportional counters embedded in a polyethylene matrix. The counters are arranged in three concentric rings of 22, 20 and 22 counters. The tubes are of the type Reuter-Stokes RS-P4-0810-109, they are filled with 4000 torr of $^3$He (at 273 K) and some percent of $CO_2$ as quenching gas. The active length is 254 mm and the active volume is 113.7 cm$^3$. The complete detector is shielded against neutrons coming from outside by several layers of boron carbide, cadmium and moderating material.

Due to the long moderation time $\beta$-n, $\gamma$-n or n-n coincidences are problematic to measure at high count rates. However, with clean conditions (one or few distinguishable isotopes involved), the time spectra of the neutrons and the betas can be taken independently and after fitting the spectra individually, the $P_n$ value is calculated from the ratio of the derived amplitudes. The individual probabilities for multi-neutron emission ($P_{2n}$, etc.) cannot be obtained in this way. Either n-n-coincidences with fast neutron detectors (scintillators) or a special time-correlation technique [Ber99] has to be used.

The data were accumulated with a 8-channel multiscaling module (model 7884 from FAST ComTec [FAS]), which accepts event rates up to 1.5 MHz and has very low deadtime effects for lower event rates. This is extremely important for a reliable lifetime determination. Taking decay data of short-lived nuclei, the dead-time can change significantly during each measurement cycle and it would be very difficult to extract reliable lifetime information if a large dead-time correction has to be applied.

---

[35]In experiments where less tubes were available, the missing ones in the outer ring were replaced by polyethylene plugs and the resulting loss of detection efficiency was taken into account.

## B.12.    "Radioactive-Ion-Beam" facility or "Radioactive" Ion-Beam-facility?

Due to the high intensities of radioactive beams which can be achieved at ISOLDE, measures have to be taken for an efficient radiation protection. The target area and the separator room are well shielded and closed during proton beam operation. Depending on the target and the irradiation history they can be accessed after a certain decay period (hours to days). The targets are removed by a robot.

With the most intense ion beams (maximum some $10^{11}$ ions per s) an equilibrium activity of up to 10 Ci (including the daughter decays) can be reached at the collection point. However, such strong beams of isotopes rather close to stability are only used for off-line applications. The samples are collected in dedicated collection chambers with appropriate shielding and remote handling.

Applications in nuclear spectroscopy involve much smaller activities (a too strong beam would just saturate all detectors), and the resulting dose rate for the experimentalists is negligible. As a typical example figure B.12.1 shows the radiation level measured with a monitor close to the experimental set-up of a nuclear spectroscopy experiment where beams of heavy copper and cadmium isotopes were used [IS365].
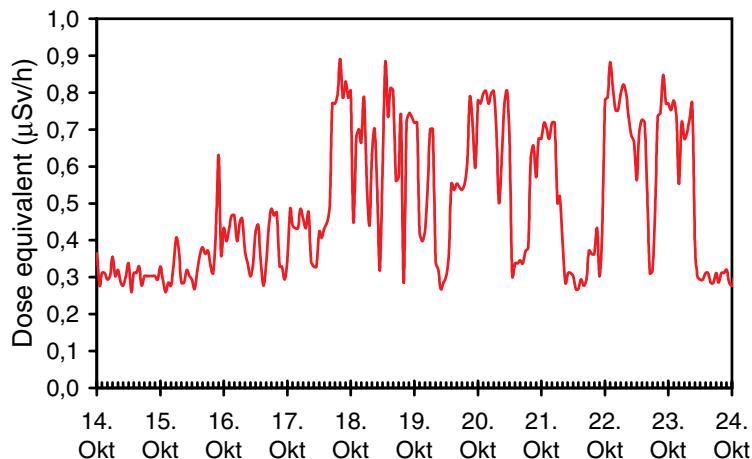


Figure B.12.1.:  Monitored dose rate close to the beam position LA1 in the ISOLDE hall. Note that the detector (a hydrogen ionization chamber) is calibrated to measure directly the dose equivalent of fast neutrons. The response to gammas will result in an overestimation of the gamma dose equivalent by a factor of about three.

An experimentalist who spends during one week 15 h daily close to this set-up would get an additional (above natural background) dose equivalent of less than 40 $\mu$Sv. This can be compared with the average annual dose equivalent of 2000 $\mu$Sv or to other sources of activity. Assume that he decides after the successful experiment to climb some high mountains of the Western Alps (e.g. the nearby Mont Blanc). Staying for one week at 4000 m altitude he will get from cosmic radiation also an additional dose equivalent of about 40 $\mu$Sv. Going to present his results on a conference in the U.S. he will be exposed to cosmic radiation and receive during a return flight Geneva-Chicago also about 40 $\mu$Sv.

## B.13.   A poor man's radioactive beam collider

Among many other applications the high beam intensity of a reactor-based RIB facility like MAFF [MAFF] will allow to produce via fusion reactions more neutron-rich isotopes of the heavy and superheavy elements, thus approaching the region of spherical superheavy nuclei where considerably longer half-lives are predicted [Smo97]. An alternative to asymmetric fusion reactions is the symmetric or near-symmetric fusion with target and projectile nuclei of comparable size. This way has not yet been explored systematically at sufficient sensitivity, since the macroscopical models requiring an extra-push and an extra-extra-push energy [Swi81, Blo86] forbid the complete fusion of massive symmetric systems at the interaction barrier. However, the synthesis of the heaviest elements (e.g. [Hof96b]) is obviously not described by a macroscopic model which does not include the importance of nuclear structure in the entrance channel (e.g. for N=82) [Qui93]. This was reconfirmed by recent results from the investigation of fusion-evaporation residues from the reaction $^{86}$Kr on $^{130}$Xe and $^{136}$Xe [Sto96]. Considering the shell structure especially nuclei around the doubly magic $^{132}$Sn would be promising projectiles for near symmetric fusion [Laz97].

While new neutron-rich isotopes of heavy elements could be produced in this way, the extremely neutron-rich heavy elements, e.g. the highly interesting isotopes towards $^{264}$Fm[(36](36) will still be out of range by fusion with any combination of stable targets and available radioactive projectiles. A way to reach the required $N/Z$ ratio is fusion of very neutron-rich projectiles with neutron-rich (radioactive) target nuclides. Due to the short lifetimes both, projectile and target nuclei, have to be produced on-line. An appropriate radioactive ion beam collider would not only be very costly, but also require a new separation mechanism as an alternative to the traditional recoil separators which use the favorable reaction kinematics of a fixed target with a strongly forward focused beam of fusion-evaporation products.

### B.13.1.   Radioactive on-line target

Alternatively a radioactive target was first proposed for the PIAFE project [Münze]. It can be prepared by implantation of a low-energy radioactive ion beam into a foil. Bombarding this "on-line-target" *simultaneously* with radioactive projectiles minimizes the losses due to radioactive decay of the target nuclei. The reachable luminosity will be determined by the equilibrium concentration of the target nuclei (equal to the cumulative isotopic yield times their lifetime), the intensity of the projectile beam and the size of the overlapping beam spots. The beam intensities are given by the RIB facility, but the size of the implantation area has to be optimized.

Table B.13.1 shows possible target nuclei which are suitable for a radioactive target. The cumulative yields have been calculated for a fission rate of $10^{14}$ s$^{-1}$ and ionization with an unselective plasma ion source. The equilibrium concentration and the respective target thickness are given after maximum 5 days of collection on a beam spot of 1 mm$^2$. A target thicker than $10^{18}$ atoms/cm$^2$ is not useful due to excessive energy loss of the projectiles (e.g. limitation for $^{132}$Te). The reachable detection limit (for 1 reaction per day) is given for a 1 pnA projectile beam. A $^{126}$Sn target could also be prepared off-line, but is given here for comparison. The average and the maximum temperatures for an accelerated beam with 10% duty cycle are given.

These detection limits have to be compared with unhindered fusion cross-sections of 10 to 100 $\mu$barn [Laz97].

It follows a brief discussion of the technical challenges and physical limitations of such a set-up to be realized at the Munich Accelerator for Fission Fragments (MAFF) [MAFF]. This discussion will concentrate on isotopes close to $^{132}$Sn, but similar considerations could be applied for fusion

---

[36]According to a longstanding prediction [Fai64] these should mainly decay by symmetric cold fission.

Table B.13.1.: Possible target nuclides for a radioactive on-line target.

| Isotope | $T_{1/2}$ | Cumulat. yield $(s^{-1})$ | Equilib. size (atoms) | Rad. target thickness $(\mu g/cm^2)$ | Detect. limit (nbarn) | 20 $\mu g/cm^2$ C | | 100 $\mu g/cm^2$ C | |
|---|---|---|---|---|---|---|---|---|---|
| | | | | | | $\theta_{mean}$ °C | $\theta_{max}$ °C | $\theta_{mean}$ °C | $\theta_{max}$ °C |
| $^{126}$Sn | $10^5$ a | $1.5 \cdot 10^{10}$ | $6 \cdot 10^{15}$ | 135 | **3** | 200 | 490 | 380 | 850 |
| $^{128}$Sn | 1 h | $7.5 \cdot 10^{10}$ | $4 \cdot 10^{14}$ | 8 | **50** | 230 | 500 | 390 | 860 |
| $^{130}$Sn | 3.7 min | $3.0 \cdot 10^{11}$ | $6 \cdot 10^{13}$ | 1.3 | **320** | 330 | 530 | 440 | 870 |
| $^{132}$Sn | 40 s | $1.7 \cdot 10^{11}$ | $1 \cdot 10^{13}$ | 0.2 | **2000** | 430 | 580 | 510 | 890 |
| $^{131}$Sb | 23 min | $6.5 \cdot 10^{11}$ | $1 \cdot 10^{15}$ | 28 | **15** | 380 | 560 | 470 | 880 |
| $^{132}$Te | 76 h | $1.1 \cdot 10^{12}$ | $1 \cdot 10^{16}$ | 300 | **1.3** | 430 | 580 | 510 | 890 |
| $^{134}$Te | 42 min | $1.7 \cdot 10^{12}$ | $6 \cdot 10^{15}$ | 135 | **3** | 530 | 640 | 590 | 910 |

reactions in other mass regions, e.g. for neutron-rich isotopes with masses 90 to 100 or even for reactions of neutron-deficient on neutron-deficient isotopes at an accelerator-based RIB facility.

## B.13.2.   Ion optics

The mass separator has to provide simultaneously two beams of different masses which are extracted from the focal plane by an electrostatic switchyard. This technique is successfully used since long time at ISOLDE [Kug92].
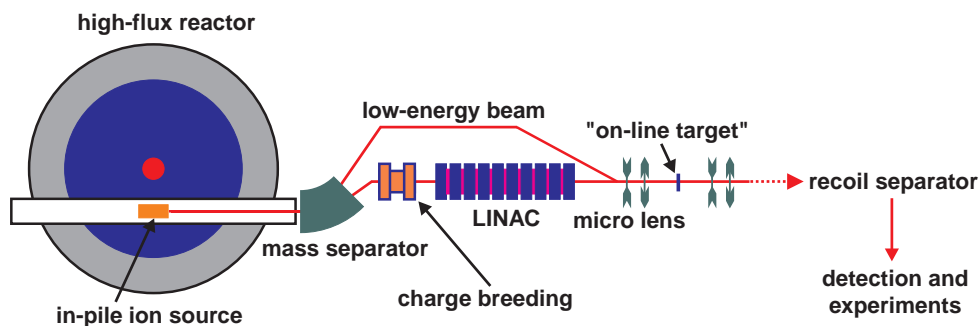


Figure B.13.1.: Implementation of a radioactive on-line target at the Munich Accelerator for Fission Fragments (MAFF).

The low-energy ion beam will be provided directly from the in-pile ion source kept at a positive potential of about 30 kV. An unselective "hot plasma source" will give the best cumulative yields. For such a source an emittance of $\varepsilon_{2\sigma} = 15\pi$ mm mrad at 15 keV is quoted (FEBIAD-F with 1.2 mm orifice) [Kir87b]. Efficient focusing of the beam can be achieved with a multiplet of electrostatic quadrupoles. For better focusing and deeper implantation the target beam can be slightly post-accelerated up to about 200 kV by putting the implantation area on a negative potential. A focal point of about 1 mm$^2$ could be realized even in case of a non-optimized emittance. Space charge effects can still be neglected for this current density.

The fusion barrier, estimated with the macroscopic Bass formula [Bas74], is around 4 A·MeV for symmetric reactions of tin on tin. For efficient post-acceleration the projectile beam will be charge-breeded to $A/q < 6.3$ in a pulsed ECR ion source [Cha98] and accelerated by a LINAC [Kes98]. This one has a design similar to the lead injector LINAC at CERN which gives an emittance of

about $\varepsilon_{4rms} = 10\pi$ mm mrad at 4.2 A·MeV output energy [Las96]. The focusing of the projectile beam will be done by a multiplet of strong magnetic quadrupoles. Such a microlens, capable to focus ion beams with up to 200 MeV·$q^2/A$ to sub-$\mu$m dimensions, has just been constructed at the Technische Universität in München [Hin97a]. For our case the requirements concerning the beam size are much less stringent than in real microbeam applications (the current density will be limited by other considerations, see below), but the design of this microlens allows to guide and focus both, target and projectile beam, from the same side onto the target.

While the magnetic rigidity varies between both beams only by a factor of two to six (for 200 keV and 30 keV target beams respectively), the electrical rigidity differs by two to three orders of magnitude. This allows to set the magnetic elements for the high-energy beam and focus the low-energy beam nearly independently by applying additional electrical multipole fields and optionally even a longitudinal acceleration voltage. The electrical multipoles inside the Munich microlens can hold a voltage of up to 4 kV [Dolli] which is largely sufficient to control the low-energy ion beam with up to 200 keV energy. Both beams will be combined with an electrostatic deflector in front of the microlens.

The fusion products will be separated from the primary beam by the MORRIS separator [Thi97]. Its first part consists of a Wien-filter type recoil separator similar to SHIP at the GSI [Mün79]. With an angular acceptance of about 50 mrad most fusion products will be transmitted even for a highly focused beam spot.

## B.13.3.    Collection foil

The key part of an on-line collected target is the collection foil. Its thickness has to be sufficient to be mechanically stable and stop the target beam, but thin enough to avoid too high energy loss of the projectile beam[37] and the fusion products. Foils of low-$Z$ materials (Be, C, ... ) with 20 to 100 $\mu$g/cm$^2$ thickness have not only a good ratio of mechanical stability to energy loss, but moreover avoid the losses of target nuclei due to backscattering.

The electrical conductivity of the foil has to be sufficient to avoid a charging-up due to the deposited charge of the low-energy beam and emitted secondary electrons. Materials with a specific electrical resistivity $< 100$ $\Omega$m will keep the potential difference small enough to prevent any deteriotation of the low-energy beam focus. Most metal and graphite foils fulfill this requirement while insulators like diamond-like graphite or pure Al$_2$O$_3$ can cause problems.

### Foil temperature

Several sources contribute to the heating of the foil:

- The low energy beam will deposit its full kinetic energy in the immediate vicinity of the impact (some nm straggling). With a non-selective ion source the mass yield may reach 600 nA (at mass 134) and thus contribute up to 18 mW heating for 30 keV implantation energy and up to 120 mW for 200 keV implantation energy respectively.

- The stopping power of 4 A·MeV Sn in carbon is about 72 MeV per mg/cm$^2$ [Bie80], i.e. for a 100 $\mu$g/cm$^2$ foil and 1 pnA of $^{132}$Sn the accelerated beam deposits about 7 mW.

- Only a small part of the energy released in the radioactive decay of the target atoms will contribute to a local heating. Most will be deposited further away by the long range beta particles.

---

[37]The fusion excitation function has a narrow width, typically about 10 MeV for asymmetric fusion [Hof95].

- Also the energy loss of the fusion products can be neglected due to their low production rate.

The deposited energy will mainly be emitted by radiation. Neglecting the thermal conduction in the thin foil an upper limit for the foil temperature can be estimated. Depending on the duty cycle of the accelerated beam, the target temperature will fluctuate more or less around the average temperature. Due to the small heat capacity the characteristic time for heating and cooling is in the millisecond range (see [Mar79] for an analytical description).

The heating of the foil has several side effects: by annealing structural damages created by the particle impact the lifetime of the foil can be considerably prolonged. On the other hand an over-heating will reduce the lifetime due to evaporation of foil material. Already before, the implanted radioactive isotopes start to migrate from the implantation region to other parts of the foil or even leave it completely. While for tin no large release is expected at the quoted temperatures, the more volatile elements antimony and tellurium start to escape much earlier. Higher target temperatures could be tolerated if the implanted nuclides form an appropriate chemical compound which hinders migration and release (e.g. very slow diffusion of Te in Si [Zhd77]). In a suitable target matrix the volatilization enthalpy can exceed the sublimation enthalpy considerably, thus keeping the implanted atoms bound even at temperatures above the boiling point.

### Foil lifetime

To run most of the time "in saturation" after buildup to the maximum concentration of target atoms, the foil lifetime should be at least of the order of days. The irradiation damage mechanisms in carbon foils were studied thoroughly [Dol89] and empirical formulae were proposed to estimate the lifetime of a carbon foil bombarded by energetic heavy ions [Fri77, Nic82, Kop87]. With a projectile beam of 1 pnA lifetimes of weeks and longer are predicted. However, for the low energy beam these formulae cannot be applied since the ions are stopped close to the surface (20 to 110 nm range depending on the implantation energy) while most of the bulk material stays unaffected of the recoil cascades. Also the structural changes due to a high concentration of implanted ions are difficult to evaluate. Therefore the foil lifetime should be tested experimentally with an appropriate stable ion beam.

## B.13.4.   Conclusion

It has been shown that a "poor man's radioactive beam collider" realized by on-line collection of radioactive ions on a target foil could attain a detection limit which is orders of magnitude below the predicted unhindered fusion cross-sections. Since the reaction rate depends on the product of the intensities of projectile and target beams, the natural place for such a radioactive on-line target is a reactor-based RIB facility providing by far the highest yields in the region around $^{132}$Sn. While carbon foils are suitable for the collection of tin beams, for very volatile elements special foil materials have to be chosen to prevent a rapid release of the radioactive nuclides.

The specific requirements of a radioactive on-line target (e.g. the parallel separation of at least two masses) can be foreseen at MAFF without big additional effort as interesting supplement to the huge physics program with stable targets.

The largest uncertainty lies however in the expected fusion cross-sections for neutron-rich systems. It is difficult to quantify how the shell stabilization affects the fusion probability and the theories differ significantly in their predictions. Also complementary reaction mechanisms like multinu-cleon transfer from neutron-rich projectiles to trans-uranium targets should be considered [Fri99]. Another possible way to produce neutron-rich superheavy isotopes is the indirect population via alpha decay chains from even heavier isotopes. Each alpha decay removes an equal number of

protons and neutrons from the nuclide and thus further increases the $N/Z$ ratio. With the very high production cross-section recently observed for the possible production of element 118 [Nin99] and an efficient trapping mechanism for the recoil nuclei (buffer gas cell) this way could become competitive for the production of very neutron-rich superheavy elements.

# Bibliography

[Afa77]   V.P. Afanas'ev, V.A. Obukhov and V.I. Raiko, 'Thermoionization efficiency in the ion source cavity', Nucl. Instr. Meth. 145 (1977) 533–536.

[Ahm83]   S.A. Ahmad et al., 'Determination of nuclear spins and moments in a series of radium isotopes', Phys. Lett. B 133 (1983) 47–52.

[Alb78]   D.E. Alburger et al., 'Core excited $T = 2$ levels in $A = 12$ from studies of $^{12}$Be', Phys. Rev. C 17 (1978) 1525–1530.

[Ale63]   J.M. Alexander, C. Baltzinger and M. Frances Gazdik, 'Cross sections and recoil studies of reactions of $U^{238}$ with protons of 0.5 to 6.2 GeV', Phys. Rev. C 129 (1963) 1826–1834.

[Ale80]   K. Aleklett, P. Hoff, E. Lund and G. Rudstam, 'Delayed neutron emission probabilities of the precursors $^{89,90,91}$Br and $^{139,140,141}$I', Z. Phys. A 295 (1980) 331–332.

[Alk83]   G.D. Alkhazov et al., 'Measurement of isotropic variations in the charge radii of europium nuclei by the method of three-stepped laser photoionization of atoms', JETP Lett. 37 (1983) 274–278.

[Alk87]   G.D. Alkhazov et al., 'Studies of the nuclear charge radii and electromagnetic moments of radioactive Nd, Sm, Eu, Ho, Tm isotopes by laser resonance atomic photoionization', Preprint 1309, Leningrad Nucl. Phys. Inst., Leningrad (1987).

[Alm57]   O. Almén and K.O. Nielsen, 'Systematic investigation of a magnetic ion source for an electromagnetic isotope separator', Nucl. Instr. Meth. 1 (1957) 302–322.

[Als70]   J. Alstad, B. Bergersen, T. Jahnsen, A.C. Pappas and T. Tunaal, 'Tellurium tetra-chloride as a target for production of tin and antimony', CERN Report 70-3, Geneva (1970).

[Alt86]   G.D. Alton, 'Semi-empirical mathematical relationships for electropositive adsorbate induced work function changes', Surf. Sci. 175 (1986) 226–240.

[Alt96]   G.D. Alton, 'Selection of targets and ion sources for radioactive ion beam generation at the Holifield radioactive ion beam facility', Rev. Sci. Instr. 67 (1996) 3831–3842.

[Ama67]   I. Amarel et al., 'On-line mass-spectrometric method for the study of short-lived Rb, Cs and Na isotopes', Ark. Fys. 36 (1967) 77–89.

[Amb71]   R.V. Ambartsumyan, V.N. Kalinin and V.S. Letokhov, 'Two-step photoionization of rubidium atoms by laser radiation', JETP Lett. 13 (1971) 217–219.

[Amb75]   R.V. Ambartsumyan, G.I. Bekov, V.S. Letokhov and V.I. Mishin, 'Excitation of high-lying state of the sodium atom by dye-laser radiation and their autoionization in an electric field', JETP Lett. 21 (1975) 279–281.

[Amb76]   R.V. Ambartsumyan et al., 'Selective two-step ionization of rubidium by laser radiation', Sov. Phys. JETP 43 (1976) 866–872.

[Ame90]   F. Ames et al., 'A high-temperature laser ion source for trace analysis and other applications', Appl. Phys. B 51 (1990) 200–206.

[Ame98]   F. Ameil et al., '$\beta$-decay half-lives of very neutron-rich isotopes of elements from Ti to Ni', Eur. Phys. J. A 1 (1998) 275–283.

[Ami76]   S. Amiel, G. Engler, Y. Nir-El and M. Shmid, 'Experiments with the surface ionization integrated target-ion source of the SOLIS', Nucl. Instr. Meth. 139 (1976) 305–309.

[Ana92]   A. Anastassov et al., 'Nuclear charge radii changes of uranium and hafnium isotopes determined by laser spectroscopy', Hyp. Int. 74 (1992) 31–40.

[And69]   V.N. Andreev, V.G. Nedopekin and V.I. Rogov, 'Long-range particles with $Z > 2$ in ternary fission of U$^{235}$ by thermal neutrons', Sov. J. Nucl. Phys. 8 (1969) 22–28.

[And86]   S.V. Andreev, V.I. Mishin and V.S. Letokhov, 'High-efficiency laser resonance photoionization of Sr atoms in a hot cavity', Opt. Comm. 57 (1986) 317–320.

[And87]   S.V. Andreev, V.S. Letokhov and V.I. Mishin, 'Laser resonance photoionization spectroscopy of Rydberg levels in Fr', Phys. Rev. Lett. 59 (1987) 1274–1276.

[And91]   H. Andreasen et al., 'Mixtures of molten metals and graphite as targets for on-line mass separators', Nucl. Instr. Meth. B 58 (1991) 247–251.

[And99]   T. Andersen, H.K. Haugen and H. Hotop, 'Binding energies in atomic negative ions: III', J. Phys. Chem. Ref. Data 28 (1999) 1511–1533.

[Ans86]   M. Anselment et al., 'The odd-even staggering of the nuclear charge radii of Pb isotopes', Nucl. Phys. A 451 (1986) 471–480.

[Aoi97]   N. Aoi et al., '$\beta$-spectroscopy of $^{11}$Li and $^{14}$Be – with a $\beta$-n-$\gamma$ triple coincidence method', Nucl. Phys. A 616 (1997) 181c–188c.

[Ärj86]   J. Ärje et al., 'The ion guide isotope separator on-line, IGISOL', Nucl. Instr. Meth. A 247 (1986) 431–437.

[Arl93]   H.F. Arlinghaus et al., 'Quantitative and sensitive profiling of dopants and impurities in semiconductors using sputter-initiated resonance ionization spectroscopy', J. Vac. Sci. Technol. A 11 (1993) 2317–2323.

[Arm76]   P. Armbruster et al., 'The recoil separator LOHENGRIN: performance and special features for experiments', Nucl. Instr. Meth. 139 (1976) 213–222.

[Arm80]   J.A. Armstrong, J.J. Wynne and F.S. Tomkins, 'Bound, $7snp\,^1P_1^o$ series in Ra I: measurements and predictions', J. Phys. B 13 (1980) L133–L137.

[Arn87]   E. Arnold et al., 'Nuclear spin and magnetic moment of $^{11}$Li', Phys. Lett. B 197 (1987) 311–314.

[Arn92]   E. Arnold et al., 'Quadrupole moment of $^{11}$Li', Phys. Lett. B 281 (1992) 16–19.

[AS87]   F. Ajzenberg-Selove, 'Energy levels of light nuclei $A = 18 - 20$', Nucl. Phys. A 475 (1987) 1–198.

[AS88]   F. Ajzenberg-Selove, 'Energy levels of light nuclei $A = 5 - 10$', Nucl. Phys. A 490 (1988) 1–225.

[AS90]   F. Ajzenberg-Selove, 'Energy levels of light nuclei $A = 11 - 12$', Nucl. Phys. A 506 (1990) 1–158.

[AS91]   F. Ajzenberg-Selove, 'Energy levels of light nuclei $A = 13 - 15$', Nucl. Phys. A 523 (1991) 1–196.

[Ase91a]   S.A. Aseyev, Yu.A. Kudryavtsev, V.S. Letokhov and V.V. Petrunin, 'Laser detection of the rare isotope $^3$He at concentrations as low as $10^{-9}$', Opt. Lett. 16 (1991) 514–516.

[Ase91b]   S.A. Aseyev, Yu.A. Kudryavtsev, V.S. Letokhov and V.V. Petrunin, 'A method of detecting the rare isotopes $^{85}$Kr and $^{81}$Kr by means of collinear laser photoionization of atoms in an accelerated beam', J. Phys. B 24 (1991) 2755–2763.

[Asg75]   M. Asghar et al., 'The $P_n$ values of the $^{235}$U(n$_{th}$,f) produced precursors in the mass chains 90, 91, 93-95, 99, 134 and 137-139', Nucl. Phys. A 247 (1975) 359–376.

[Ask70]   J. Askill, *Tracer Diffusion Data for Metals, Alloys and Simple Oxides*, IFI/Plenum, New York (1970).

[ATOS]    http://www.atos-online.de.

[Aud86]   G. Audi et al., 'Mass-spectrometric measurements of exotic Rb, Cs and Fr isotopes', Nucl. Phys. A 449 (1986) 491–518.

[Aud95]   G. Audi and A.H. Wapstra, 'The 1995 update to the atomic mass evaluation', Nucl. Phys. A 595 (1995) 409–480.

[Aud97]   G. Audi, O. Bersillon, J. Blachot and A.H. Wapstra, 'The Nubase evaluation of nuclear and decay properties', Nucl. Phys. A 624 (1997) 1–124.

[Bac97]   H. Backe et al., 'A compact apparatus for mass selective resonance ionization spectroscopy in a buffer gas cell', Nucl. Instr. Meth. B 126 (1997) 406–410.

[Bac98]   H. Backe et al., 'Isotope shift measurements for superdeformed fission isomeric states', Phys. Rev. Lett. 80 (1998) 920–923.

[Bak90]   H. Bakker et al., *Diffusion in Solid Metals and Alloys*, vol. III/26 of *Landolt-Börnstein*, Springer, Berlin (1990).

[Bal74]   S.J. Balestrini and L. Forman, 'Independent fission yields of Rb and Cs from $^{238}$U induced by fission-spectrum neutrons', Phys. Rev. C 10 (1974) 1872–1879.

[Bal94]   'Coating materials and targets, Catalogue', Balzers, Liechtenstein (1994).

[Barke]   James Barker, priv. comm.

[Bar77]   D.M. Barrus and R.L. Blake, 'Technique for producing ultrathin polypropylene films', Rev. Sci. Instr. 48 (1977) 116–117.

[Bar97]   A.E. Barzakh, V.P. Denisov, D.V. Fedorov, S.Yu. Orlov and M.D. Seliverstov, 'A mass-separator laser ion source', Nucl. Instr. Meth. B 126 (1997) 85–87.

[Bar98a]  A.E. Barzakh et al., 'Application of the laser ion source for isotope shift and hyperfine structure investigations', in [ENA98], pp. 94–97.

[Bar98b]  A.E. Barzakh et al., 'Isotope shift and hyperfine structure measurements for $^{155}$Yb by laser ion source technique', Eur. Phys. J. A 1 (1998) 3–5.

[Bar99]   E. Baron, 'High intensities for SISSI and SPIRAL in 1999', Nouvelles du GANIL 64 (1999) 10–11.

[Bar00]   A.E. Barzakh et al., 'Mean square charge radii of the neutron-deficient rare-earth isotopes in the region of the nuclear shell $N = 82$ measured by the laser ion source spectroscopy technique', Phys. Rev. C 61 (2000) 034304.

[Bas74]   R. Bass, 'Fusion of heavy nuclei in a classical model', Nucl. Phys. A 231 (1974) 45–63.

[Bas80]   R. Bass, *Lecture notes in physics: Deep-inelastic and fusion reactions with heavy ions*, vol. 117, Springer, Berlin, 1980, pp. 281–293.

[Bau87]   F. Baumgärtner, K. Krebs and B. Merté, 'Zur Emission von Spaltprodukten und Transuranen aus hochradioaktivem Abfall zwischen 200 und 1100 °C', Kerntechnik 51 (1987) 151–156.

[Bau92a]  W. Baum et al., 'Light charged particles ($Z \leq 8$) in $^{235}$U(n$_{th}$,f) and $^{241}$Am(n$_{th}$,f)', in [BKS92], pp. 477–479.

[Bau92b]  Wolf Baum, *Teilchenbegleitete Spaltung von $^{235}$U und $^{242}$Am*, Ph.D. thesis, TH Darmstadt (1992).

[Bay81]    R. Bayer, Z. Dlouhý, J. Švanda and I. Wilhelm, 'A multiparameter system for heavy nuclei fission study', Czech. J. Phys. B 31 (1981) 1273–1285.

[Bec96]    H. Becquerel, 'Sur les radiations invisibles émises par les corps phosphorescents', C. R. Acad. Sci. Paris 122 (1896) 501.

[Bec82]    F.S. Becker and K.L. Kompa, 'The practical and physical aspect of uranium isotope separation with lasers', Nucl. Techn. 58 (1982) 329–353.

[Bek78a]   G.I. Bekov, V.S. Letokhov, O.I. Matveev and V.I. Mishin, 'Observation of a long-lived autoionization state in the spectrum of the gadolinium atom', JETP Lett. 28 (1978) 283–285.

[Bek78b]   G.I. Bekov, V.S. Letokhov, O.I. Matveev and V.I. Mishin, 'Single-atom detection of ytterbium by selective laser excitation and field ionization from Rydberg states', Opt. Lett. 3 (1978) 159–161.

[Bek81]    G.I. Bekov, A.N. Zherikhin, V.S. Letokhov, V.I. Mishin and V.N. Fedoseev, 'Difference in the yields of even and odd Yb isotopes in multistep photoionization by polarized laser beams', JETP Lett. 33 (1981) 450–453.

[Bek83]    G.I. Bekov and V.S. Letokhov, 'Laser atomic photoionization spectral analysis of element traces', Appl. Phys. B 30 (1983) 161–176.

[Bek84a]   G.I. Bekov, G.A. Maksimov, D.N. Nikogosyan and V.N. Radaev, 'Enhancement of the selectivity of laser photoionization analysis in the case of two-pulse interaction of an electric field with Rydberg atoms', Sov. J. Quant. Electron. 14 (1984) 852–853.

[Bek84b]   G.I. Bekov et al., 'Ruthenium in the ocean', Nature 312 (1984) 748–750.

[Bek85]    G.I. Bekov, V.S. Letokhov and V.N. Radaev, 'Laser photoionization spectroscopy of ruthenium traces at the level of 1 part in $10^{12}$', J. Opt. Soc. Amer. B 2 (1985) 1554–1560.

[Bek87]    G.I. Bekov, A.T. Tursunov, G. Khasanov and N.B. Eshkobilov, 'Laser photoionization spectroscopy of highly excited states of gold atoms', Opt. Spectr. (USSR) 62 (1987) 163–166.

[Bel80]    B.N. Belyaev, V.D. Domkin, Yu.G. Korobulin, L.N. Andronenko and G.E. Solyakin, 'Rb and Cs isotopic distributions from 1 GeV proton fission of $^{238}$U', Nucl. Phys. A 348 (1980) 479–492.

[Benll]    Jose Benlliure, priv. comm.

[Ben96]    T. von Egidy et al., eds., 'Int. Workshop on Research with Fission Fragments, Benediktbeuern, October 1996', World Scientific, Singapore, 1997.

[Ben97]    J.R.J. Bennett, 'Targets for production of high intensity radioactive ion beams', Nucl. Instr. Meth. B 126 (1997) 105–112.

[Ben98]    J. Benlliure, A. Grewe, M. de Jong, K.H. Schmidt and S. Zhdanov, 'Calculated nuclide production yields in relativistic collisions of fissile nuclei', Nucl. Phys. A 628 (1998) 458–478.

[Ben99a]   J. Benlliure et al., 'Fission investigation in Au+p collisions at $800A$ MeV', Nucl. Phys. A A654 (1999) 833c–836c.

[Ben99b]   J. Benlliure et al., 'Possibilities for the production of non-stable isotopes', in 'Proc. of the XXXVII Int. Winter Meeting on Nuclear Physics, Bormio', 1999.

[Ben99c]   J.R.J. Bennett et al., 'Measurement of intense beams of $^{11}$Li from a tantalum foil target', Nucl. Instr. Meth. B 155 (1999) 515–517.

[Ber69]    E.Ye. Berlovich and Yu.N. Novikov, 'Delayed nuclear fission', Phys. Lett. 29B (1969) 155–156.

[Ber89]   H. Bergström, W.X. Peng and A. Persson, 'Two different types of hollow-cathode discharges used for high resolution laser spectroscopy on copper', Z. Phys. D 13 (1989) 203–206.

[Ber91]   M. Bernas et al., 'Discovery of neutron-rich Co and Fe isotopes in $^{239}$Pu($n_{th}$,f): yields and half-lives', Phys. Rev. Lett. 67 (1991) 3661–3664.

[Ber95]   Dan Berkovits, *Laser and accelerator mass spectrometry*, Ph.D. thesis, Hebrew University of Jerusalem (1995).

[Ber99]   U.C. Bergmann et al., 'New information on $\beta$-delayed neutron emission from $^{12,14}$Be', Nucl. Phys. A 658 (1999) 129–145.

[Bet66]   H.D. Betz et al., 'The average charge of stripped heavy ions', Phys. Lett. 22 (1966) 643–644.

[Bey71]   G.J. Beyer, E. Herrmann, A. Piotrowski, V.J. Raiko and H. Tyrroff, 'A new method for rare-earth isotope separation', Nucl. Instr. Meth. 96 (1971) 437–439.

[Bey77]   G.J. Beyer, W.D. Fromm and A.F. Novgorodov, 'Trace diffusion of different nuclear reaction products in polycrystalline tantalum', Nucl. Instr. Meth. 146 (1977) 419–430.

[Bey78]   G.J. Beyer, O. Knotek, M. Jachim, J. Jushkevič and A.F. Novgorodov, 'Selektive Gewinnung kurzlebiger neutronendefizierter Nuklide des Yttriums, Strontiums und Rubidiums bei Verwendung von Molybdän bzw. Zirkonium als on-line Festkörpertargetmaterial', Nucl. Instr. Meth. 148 (1978) 543–551.

[Bey81]   G.J. Beyer et al., 'Fast isobaric separation at the collector of ISOL-facilities', Nucl. Instr. Meth. 186 (1981) 401–407.

[Bey98]   G.J. Beyer, 'Medical applications of radioactive ion beams', in [PIAFE], 1998, p. 29.

[Bez97]   V.I. Beznosjuck, D.V. Fedorov, S.Yu. Orlov, M.D. Seliverstov and V.I. Tikhonov, 'Reduction of the thermoionic current in the laser ion source', Nucl. Instr. Meth. B 126 (1997) 92–94.

[Bha93]   M.R. Bhat, 'Nuclear data sheets update for $A = 70$', Nucl. Data Sheets 68 (1993) 117–63.

[Bie80]   J.P. Biersack and L.G. Haggmark, 'A Monte Carlo computer program for the transport of energetic ions in amorphous targets', Nucl. Instr. Meth. 174 (1980) 257–269.

[Bil97]   J. Billowes et al., 'First collinear laser spectroscopy measurements of radioisotopes from an IGISOL ion source', Nucl. Instr. Meth. B 126 (1997) 416–418.

[Bis85a]  W.K. Bischel and L.J. Jusinski, 'Multiphoton ionization spectroscopy of atomic fluorine', in T.W. Hänsch and Y.R. Shen, eds., 'Laser Spectroscopy VII, Proc. of Seventh Int. Conf., Hawaii', Springer, Berlin, 1985, pp. 94–95.

[Bis85b]  W.K. Bischel and L.J. Jusinski, 'Multiphoton ionization spectroscopy of atomic fluorine', J. Opt. Soc. Amer. A 2 (1985) P5.

[Bjo78]   G.C. Bjorklund, C.P. Ausschnitt, R.R. Freeman and R.H. Storz, 'Detection of atomic hydrogen and deuterium by resonant three-photon ionization', Appl. Phys. Lett. 33 (1978) 54–56.

[Bjø80]   T. Bjørnstad et al., 'Structure of the levels in the doubly magic nucleus $^{132}_{50}$Sn$_{82}$', Phys. Lett. 91B (1980) 35–37.

[Bjø81]   T. Bjørnstad et al., 'New targets for on-line mass separation of nuclei formed in 600 MeV proton and 910 MeV $^3$He reactions', Nucl. Instr. Meth. 186 (1981) 391–400.

[Bjø86]   T. Bjørnstad et al., 'Methods for production of intense beams of unstable nuclei: new developments at ISOLDE', Phys. Scr. 34 (1986) 578–590.

[Bjø87]   T. Bjørnstad et al., 'Recent developments of high-temperature metal targets for ISOLDE', Nucl. Instr. Meth. B 26 (1987) 174–182.

[BKS92]   R. Neugart and A. Wöhr, eds., '6th Int. Conf. on Nuclei far from Stability & 9th Int. Conf. on Atomic Masses and Fund. Const., Bernkastel-Kues', Inst. Phys. Conf. Ser. No. 132, IOP, Bristol, 1992.

[Bla76]   J. Blaise and L.J. Radziemski, 'Energy levels of neutral atomic uranium (U I)', J. Opt. Soc. Amer. 66 (1976) 644–659.

[Bla95]   B. Blank et al., 'New isotopes from $^{78}$Kr fragmentation and the ending point of the astrophysical rapid-proton-capture process', Phys. Rev. Lett. 74 (1995) 4611–4614.

[Bla97]   F. Le Blanc et al., 'Nuclear moments and deformation change in $^{184}$Au$^{g,m}$ from laser spectroscopy', Phys. Rev. Lett. 79 (1997) 2213–2216.

[Blo69]   J. Blocki et al., 'Li and Be nuclei emitted during the thermal neutron fission of $^{235}$U', Nucl. Phys. A 127 (1969) 495–502.

[Blo86]   J.P. Blocki, H. Feldmeier and W.J. Swiatecki, 'Dynamical hindrance to compound-nucleus formation in heavy-ion reactions', Nucl. Phys. A 459 (1986) 145–172.

[BM85]    A. Baas-May, J.V. Kratz and N. Trautmann, 'Absence of delayed fission in the $\beta^-$ decay of 2.3 min $^{238}$Pa', Z. Phys. A 322 (1985) 457–462.

[Boc70]   J.P. Bocquet, R. Brissot, J. Crancon, C. Ristori and A. Moussa, 'An isotope separator connected with a 14 MeV neutron generator for on-line fission studies', Nucl. Instr. Meth. 88 (1970) 51–59.

[Boc88]   J.P. Bocquet, R. Brissot and H.R. Faust, 'A large ionization chamber for fission fragment nuclear charge identification at the LOHENGRIN spectrometer', Nucl. Instr. Meth. A 267 (1988) 466–472.

[Bog75]   D.D. Bogdanov, A.V. Demyanov, V.A. Karnaukhov and L.A. Petrov, 'New delayed-proton emitters $^{119}$Ba, $^{121}$Ba and $^{116}$Cs', Sov. J. Nucl. Phys. 21 (1975) 123–125.

[Bog98]   D.D. Bogdanov et al., 'Cross-sections for the production of evaporation particles from compound nuclei $^{210,212}$Ra obtained in $^{35}$Cl+$^{175}$Lu and $^{31}$P+$^{181}$Ta interactions', Phys. At. Nucl. 61 (1998) 727–733.

[Boh39]   N. Bohr and J.A. Wheeler, 'The mechanism of nuclear fission', Phys. Rev. 56 (1939) 426–450.

[Boh50]   A. Bohr and V.F. Weisskopf, 'The influence of nuclear structure on the hyperfine structure of heavy elements', Phys. Rev. 77 (1950) 94–98.

[Böh78]   H.D. V. Böhm, W. Michaelis and C. Weitkamp, 'Hyperfine structure and isotope shift measurements on $^{235}$U and laser separation of uranium isotopes by two-step photoionization', Opt. Comm. 26 (1978) 177–182.

[Böh96]   Wigbert Böhmer, *Kernphysikalische Aspekte zur Erklärung der korrelierten Ca-Ti-Cr Isottopenanomalien im Einschluß EK 1-4-1 des Allende-Meteoriten*, Ph.D. thesis, Johannes-Gutenberg-Universität Mainz (1996).

[Bol92]   V.A. Bolshakov, 'The production of neutron-rich heavy nuclei of astrophysical interest at the IRIS facility', Nucl. Instr. Meth. B 70 (1992) 69–74.

[Bon85]   K.D. Bonin, T.J. McIlrath and K. Yoshino, 'High-resolution laser and classical spectroscopy of xenon autoionization', J. Opt. Soc. Amer. B 2 (1985) 1275–1283.

[Bor65]   S. Borg, U. Fägerquist, G. Holm and F. Kropff, 'Experiences of on-line isotope separation of short-lived isotopes', Nucl. Instr. Meth. 38 (1965) 296–298.

[Bor71]   S. Borg et al., 'On-line separation of isotopes at a reactor in Studsvik (OSIRIS)', Nucl. Instr. Meth. 91 (1971) 109–116.

[Bor88]   R.J. Borg and G.J. Dienes, *An Introduction to Solid State Diffusion*, Academic Press, Boston (1988).

[Bor92]   M.J.G. Borge et al., 'On the nuclear structure of $^{229}$Ra', Nucl. Phys. A 539 (1992) 249–262.

[Bör93]   Berthold Börsig, *Neutroneninduzierte Clusteremission von $^{241}Am(2n_{th},f)$*, Ph.D. thesis, Universität Tübingen (1993).

[Bos88]   U. Bosch et al., 'Beta- and gamma-decay studies of neutron-rich chromium, manganese, cobalt and nickel isotopes including the new isotopes $^{60}$Cr and $^{60g}$Mn', Nucl. Phys. A 477 (1988) 89–104.

[Bou94]   Boualem Bouzid, *Etude de l'émission de particules légères chargées dans la fission d'uranium 235 et d'américium 241 induite par des neutrons thermiques*, Ph.D. thesis, Université des sciences et de technologie Houari Boumedienne, Alger (1994).

[Bou98]   B. Bouzid, M. Asghar, M. Djebara and M. Medkour, 'The nature of dynamics of the last stages of the fission process', J. Phys. G 24 (1998) 1029–1037.

[Boy97]   L. Boy, A. Chabert, C. Ricaud and B. Laune, 'Tuning methods for the SPIRAL facility', Nucl. Instr. Meth. A 400 (1997) 1–8.

[BR81]   Y. Baudinet-Robinet, 'Equilibrium charge-state distributions of highly stripped ions in carbon foils', Nucl. Instr. Meth. 190 (1981) 197–202.

[BR82]   Y. Baudinet-Robinet, 'Equilibrium charge-state distributions for heavy ions exiting carbon foils', Phys. Rev. A 26 (1982) 62–71.

[Bro90]   U. Brosa, S. Grossmann and A. Müller, 'Nuclear Scission', Phys. Rep. 197 (1990) 167–262.

[Buc87]   F. Buchinger et al., 'The N-dependence of Cd mean square charge radii ($54 \leq N \leq 72$) and the nuclear moments of $^{103}$Cd', Nucl. Phys. A 462 (1987) 305–332.

[Bud90]   A. Budzanovski et al., Report IFI N1509/Pl, IFI, Krakow (1990).

[Burch]   Angela Burchard, priv. comm.

[Bur57]   E.M. Burbidge, G.R. Burbidge, W.A. Fowler and F. Hoyle, 'Synthesis of the elements in stars', Rev. Mod. Phys. 29 (1957) 547–650.

[Bur74]   K.H. Burkhard, W. Dumanski, R. Kirhner and E. Roeckl, 'Statusbericht der On-line-Massenseparator-Gruppe', Rep. GSI-PB-2-74, GSI, Darmstadt (1974).

[But00]   A. Buta et al., 'TONNERRE: an array for delayed-neutron decay spectroscopy', Nucl. Instr. Meth. A 455 (2000) 412–423.

[Caa98]   J.L. Duggan and I.L. Morgan, eds., 'Applications of Accelerators in Research and Industry, Proc. of the Fifteenth Int. Conf., Denton', AIP Conf. Proc. 475, Woodbury, NY, 1998.

[Caï80]   F. Caïtucoli et al., 'The thermal-neutron-induced alpha-accompanied fission of $^{235}$U, investigation of the low energy part of the alpha spectrum', Z. Phys. A 298 (1980) 219–223.

[Cal88a]   C.L. Callender, P.A. Hackett and D.M. Rayner, 'First ionization potential of hafnium by double-resonance field-ionization spectroscopy', J. Opt. Soc. Amer. B 5 (1988) 1341–1342.

[Cal88b]   C.L. Callender, P.A. Hackett and D.M. Rayner, 'First-ionization potential of ruthenium, rhodium and palladium by double-resonance ionization spectroscopy', J. Opt. Soc. Amer. B 5 (1988) 614–618.

[Cam69]   M. Cambiaghi, F. Fossati and T. Pinelli, 'Long-range alpha-particles and light charged nuclei in the neutron-induced fission of $^{233}$U', II Nuovo Cimento LIX B (1969) 236–243.

[Cam72]    M. Cambiaghi et al., 'Experimental results concerning long-range light particles and fragments in the ternary fission of $^{233}$U, $^{235}$U, $^{239}$Pu and $^{252}$Cf', Nuovo Cimento 11A (1972) 716–723.

[Câr75]    N. Cârjan, A. Săndulescu and V.V. Pashkevich, 'Shell and pairing effects in alpha-accompanied fission', Phys. Rev. C 11 (1975) 782–788.

[Câr76]    N. Cârjan, 'Sur l'origine des alphas de scission', J. Phys. (Paris) 37 (1976) 1279–1285.

[Car78]    L.C. Carraz, I.R. Haldorsen, H.L. Ravn, M. Skarestad and L. Westgaard, 'Fast release of nuclear reaction products from refractory matrices', Nucl. Instr. Meth. 148 (1978) 217–230.

[Car79]    L.C. Carraz, S. Sundell, H. Ravn, M. Skarestad and L. Westgaard, 'High-temperature carbide targets for fast on-line mass separation of alkali and noble gas elements', Nucl. Instr. Meth. 158 (1979) 69–80.

[Câr80]    N. Cârjan and B. Leroux, 'Finite-size effects in trajectory calculations for $\alpha$ particles emitted during nuclear fission', Phys. Rev. C 22 (1980) 2008–2017.

[Car97]    H.K. Carter et al., 'First on-line results for As and F beams from HRIBF target/ion sources', Nucl. Instr. Meth. B 126 (1997) 166–169.

[CAS]      http://www.casix.com.

[Cas90]    B. Castel and I.S. Towner, *Modern theories of nuclear moments*, Clarendon Press, Oxford (1990).

[Cas97]    R.F. Casten et al., 'Scientific opportunities with an advanced ISOL facility', http://www.er.doe.gov/production/henp/np/manpwr98.html (1997).

[Cas01]    E. Casarejos et al., 'Isotopic cross-sections of heavy residues from reactions of 1 GeV protons and 2 GeV deuterons with $^{238}$U measured in inverse kinematics', Nucl. Phys. A (2001) in press.

[Caz96]    J. Cazalet, 'Le procédé atomique SILVA', Revue Générale Nucléaire 2 (Mars-Avril) (1996) 20–23.

[Cha97]    C. Chandler et al., 'Evidence for a highly deformed oblate $0^+$ state in $^{74}_{36}$Kr', Phys. Rev. C 56 (1997) R2924–R2928.

[Cha98]    N. Chauvin et al., 'Electron cyclotron resonance ion trap, a multicharged ion breeder/buncher', Nucl. Instr. Meth. A 419 (1998) 185–188.

[Che60]    Francis F. Chen, *Electric Probes*, Chapman & Hall, London, 1960, pp. 113–200.

[Che72]    E. Cheifetz, B. Eylon, E. Fraenkel and A. Gavron, 'Emission of $^5$He in the spontaneous fission of $^{252}$Cf', Phys. Rev. Lett. 29 (1972) 805–808.

[Chu93]    K.T. Chung and X.W. Zhu, 'Energies, fine structures and isotope shifts of the $1s^22snl$ excited states of the beryllium atom', Phys. Rev. A 48 (1993) 1944–1954.

[Chw67]    J. Chwaszczewska et al., 'Emission of long-range charged particles in the fission of $^{235}$U induced by thermal neutrons', Phys. Lett. 24B (1967) 87–89.

[Cia97]    G. Ciavola et al., 'The ISOL exotic beam facility at LNS: the EXCYT project', Nucl. Instr. Meth. B 126 (1997) 258–261.

[CM96]     M.D. Campbell-Miller and B. Simard, 'First ionization potentials of tungsten and rhenium by mass-selected double-resonance ionization spectroscopy', J. Opt. Soc. Amer. B 13 (1996) 2115–2120.

[Coc99]    J.F.C. Cocks et al., 'Spectroscopy of Rn, Ra and Th isotopes using multi-nucleon transfer reactions', Nucl. Phys. A 645 (1999) 61–91.

[Coc00]    J.F.C. Cocks et al., 'Multi-nucleon transfer reactions as a tool for spectroscopy of heavy nuclei', J. Phys. G 26 (2000) 23–34.

[Col97]     P. Colarusso, M.A. Lebeault-Dorget and B. Simard, 'First ionization potentials of os-mium and iridium determined by mass-analyzed double-resonance field-ionization spec-troscopy', Phys. Rev. A 55 (1997) 1526–1529.

[Cos67]     S.W. Cosper, J. Cerny and R.C. Gatti, 'Long-range particles of $Z = 1$ to 4 emitted during the spontaneous fission of $^{252}$Cf', Phys. Rev. 154 (1967) 1193–1206.

[Cow58]     G.A. Cowan and C.J. Orth, 'Diffusion of fission products at high temperatures from refractory matrices', in 'Proc. 2nd Int. Conf. Peaceful Uses Atomic Energy, Geneva', vol. 7, United Nations, 1958, pp. 328–334.

[Cow99]     J.J. Cowan et al., 'R-process abundances and chronometers in metal-poor stars', As-trophys. J. 521 (1999) 194–205.

[Cra70]     J. Crank, *The mathematics of diffusion*, Clarendon Press, Oxford (1970).

[Cum81]     D.E. Cumpstey and D.G. Vass, 'The $^6$He emission accompanying the spontaneous fission of $^{252}$Cf', Nucl. Phys. A 359 (1981) 377–385.

[Cur98]     P. Curie and M. Slodowska-Curie, 'Sur une nouvelle substance radio-active contenu dans la pechblende', C. R. Acad. Sci. Paris 127 (1898) 175.

[Cur86]     M.S. Curtin et al., 'Lifetime measurements of neutron-rich light isotopes $^{14}$Be and $^{17}$C', Phys. Rev. Lett. 56 (1986) 34–37.

[D'A78]     J.M. D'Auria et al., 'Properties of the lightest known caesium isotopes $^{114-118}$Cs', Nucl. Phys. A 301 (1978) 397–410.

[Dak67]     M. Dakowski, J. Chwaszczewska, T. Krogulski, E. Piasecki and M. Sowinski, 'Energy spectra of long range particles from the thermal neutron fission of $^{235}$U', Phys. Lett. 25B (1967) 213–214.

[Dak79]     M. Dakowski, E. Piasecki and L. Nowicki, 'On the incorrect use of ternary fission data in the determination of scission configuration', Nucl. Phys. A 315 (1979) 370–380.

[Dan96]     J. Kliman and B.I. Pustylnik, eds., 'Dynamical Aspects of Nuclear Fission, Proc. of 3rd Int. Conf. held at Častá-Papiernička', JINR, Dubna, 1996.

[Dav87]     P. David et al., 'The study of prompt and delayed muon induced fission', Z. Phys. A 328 (1987) 37–47.

[Dav97]     Marco Davi, *Messung von Ausbeuten in der Spaltung von $^{250}$Cf$^*$ und $^{239}$Np$^*$ am Massenseparator LOHENGRIN*, Ph.D. thesis, Universität Mainz (1997).

[Dei95]     R. Deissenberger et al., 'First determination of the ionization potential of americium and curium', Angew. Chem. Int. 34 (1995) 814–815.

[Dem98]     Wolfgang Demtröder, *Laser Spektroscopy, Basic Concepts and Instrumentation*, Springer, Berlin, second edn. (1998).

[Dendo]     Peter Dendooven, priv. comm.

[Den86]     H.O. Denschlag, 'Independent fission yield measurements', Nucl. Sci. Eng. 94 (1986) 337–352.

[Den97]     C.J. Densham, C. Thwaites and J.R.J. Bennett, 'Critical parameters for the delay time of a RIB target', Nucl. Instr. Meth. B 126 (1997) 154–159.

[Der95]     A.G. Dernjatin et al., 'Recoil-atom time-of-flight spectrometer for delayed neutron study', in [ENA95], pp. 585–586.

[D'H80]     P. D'Hondt, C. Wagemans, A. Declercq, G. Barreau and A. Deruytter, 'Energy distri-butions and absolute yields of the charged light particles emitted during the thermal neutron induced ternary fission of $^{235}$U', Nucl. Phys. A 346 (1980) 461–472.

[Dia99]     W.T. Diamond, 'A radioactive ion beam facility using photofission', Nucl. Instr. Meth. A 432 (1999) 471–482.

[Dic81]   J.K. Dickens and J.W. McConnell, 'Yields of fission products produced by thermal-neutron fission of $^{245}$Cm', Phys. Rev. C 23 (1981) 331–350.

[Div77]   R.B. Diver and E.A. Fletchner, 'Thoria effusion membranes', Am. Ceram. Soc. Bull. 56 (1977) 1019–1020.

[Dlo92]   Z. Dlouhý, J. Švanda, R. Bayer and I. Wilhelm, 'Emission of light charged particles with $Z \geq 2$ in spontaneous fission of $^{252}$Cf', in [BKS92] 481–483.

[Doa86]   T.P. Doan et al., 'Light nuclei from the thermal neutron induced fission of $^{235}$U', Rad. Eff. 93 (1986) 61–64.

[Dob96]   J. Dobaczewski et al., 'Mean-field description of ground-state properties of drip-line nuclei: pairing and continuum effects', Phys. Rev. C 53 (1996) 2809–2840.

[Dolli]   Günther Dollinger, priv. comm.

[Dol89]   G. Dollinger and P. Maier-Komor, 'Heavy-ion irradiation damage in carbon stripper foils', Nucl. Instr. Meth. A 282 (1989) 223–235.

[Dombs]   Marik Dombsky, priv. comm.

[Dom90]   M. Dombsky et al., 'Target and ion source development at the TISOL facility at TRIUMF', Nucl. Instr. Meth. A 295 (1990) 291–298.

[Dom96]   M. Dombsky and J.M. D'Auria, 'Zeolite target development at TISOL', in J.L. Duggan and I.L. Morgan, eds., 'Applications of Accelerators in Research and Industry, Proc. of the Fourteenth Int. Conf., Denton', AIP Conf. Proc. 492, Woodbury, NY, 1996, pp. 365–368.

[Dom97]   M. Dombsky et al., 'An ion source test stand for the ISAC facility at TRIUMF', Nucl. Instr. Meth. B 126 (1997) 50–54.

[Dom98]   M. Dombsky et al., 'Evaluation of a prototype isotope separator accelerator surface ionization source', Rev. Sci. Instr. 69 (1998) 1170–1172.

[Don98]   C. Donzaud et al., 'Low-energy fission investigated in reactions of $750 A \cdot$ MeV $^{238}$U-ions on $^{208}$Pb. II: Isotopic distributions', Eur. Phys. J. A 1 (1998) 407–426.

[Dor65]   D.W. Dorn and R.W. Hoff, 'Spontaneous fission in very neutron-rich isotopes', Phys. Rev. Lett. 14 (1965) 440–441.

[Dru97]   P.V. Drumm et al., 'A comparison of RIST and ISOLDE tantalum targets and geometries used on-line at ISOLDE', Nucl. Instr. Meth. B 126 (1997) 121–124.

[Duf84]   J.P. Dufour et al., 'Beta-delayed neutron radioactivity of $^{15}$B', Z. Phys. A 319 (1984) 237–238.

[Dup92]   P. Van Duppen et al., 'A laser ion source for on-line mass separation', Hyp. Int. 74 (1992) 193–204.

[Dup97]   P. Van Duppen, 'Laser ion sources for on-line isotope separators', Nucl. Instr. Meth. B 126 (1997) 66–72.

[Dup98]   P. Van Duppen et al., 'A new pulsed release method for element selective production of neutron rich isotopes near $^{208}$Pb', Nucl. Instr. Meth. B 134 (1998) 267–270.

[Dye83]   P. Dyer, G.C. Baldwin, C. Kittrell, D.G. Imre and E. Abramson, 'Isotopically selective photoionization of mercury atoms', Appl. Phys. Lett. 42 (1983) 311–313.

[Dye85]   P. Dyer et al., 'Isomerically selective photoionization of mercury-197', J. Appl. Phys. 58 (1985) 2431–2436.

[Ebe86]   J. Eberz et al., 'Collinear laser spectroscopy on $^{108g,108m}$In using an ion source with bunched beam relase', Z. Phys. A 323 (1986) 119–123.

[Ebe87]   J. Eberz et al., 'Nuclear spins, moments and charge radii of $^{108-111}$Sn', Z. Phys. A 326 (1987) 121–129.

[Ede92]   R. Eder et al., 'The production yields of radioactive ion-beams from fluorinated targets at the ISOLDE on-line mass separator', Nucl. Instr. Meth. B 62 (1992) 535–540.

[Egi81]   T. von Egidy et al., 'The rotational structure of $^{227}$Ra', Nucl. Phys. A 365 (1981) 26–60.

[Egi93]   T. von Egidy et al., 'Antiproton induced fission', Nucl. Phys. A 558 (1993) 383c–392c.

[Ehr72]   B. Ehrenberg and S. Amiel, 'Independent yields of Krypton and Xenon isotopes in thermal-neutron induced fission of $^{235}$U. Observation of an odd-even effect in the element yield distribution', Phys. Rev. C 6 (1972) 618–628.

[Eic85a]  B. Eichler, S. Hübener and H. Roßbach, 'Adsorption flüchtiger Metalle auf metallischen Oberflächen und Möglichkeiten ihrer Anwendung in der Kernchemie - Berechnung der Adsorptionsenthalpien der Actinoide', Rep. ZfK-560, Zentralinstitut für Kernforschung, Rossendorf (1985).

[Eic85b]  B. Eichler, S. Hübener and H. Roßbach, 'Adsorption flüchtiger Metalle auf metallischen Oberflächen und Möglichkeiten ihrer Anwendung in der Kernchemie - Berechnung der Adsorptionsenthalpien der Seltenerdmetalle', Rep. ZfK-561, Zentralinstitut für Kernforschung, Rossendorf (1985).

[Eik94]   K.S.E. Eikema, W. Ubachs and W. Hogervorst, 'Isotope shift in the neon ground state by extreme-ultraviolet laser spectroscopy at 74 nm', Phys. Rev. A 49 (1994) 803–808.

[Eik96]   K.S.E. Eikema, W. Ubachs, W. Vassen and W. Hogervorst, 'Precision measurements in helium at 58 nm: ground state Lamb shift and the $1\,^1S - 2\,^1P$ transition isotope shift', Phys. Rev. Lett. 76 (1996) 1216–1219.

[Elh98]   Angelika Elhardt, *Bestimmung der Spaltausbeute von $^{60}$Fe aus der Spaltung von $^{235}$U*, Master's thesis, TU München (1998).

[Elm78]   T. Elmroth et al., 'Beta-delayed proton emission from $^{97}$Cd and $^{99}$Cd', Nucl. Phys. A 304 (1978) 493–502.

[ENA95]   M. de Saint Simon and O. Sorlin, eds., 'Exotic Nuclei and Atomic Masses, ENAM'95, Arles, June 1995', Editions Frontières, Gif-sur-Yvette, 1995.

[ENA98]   B.M. Sherill, D.J. Morrissey and C.N. Davids, eds., 'Exotic Nuclei and Atomic Masses, ENAM'98, Bellaire, Michigan June 1998', AIP Conf. Proc. 455, Woodbury, NY, 1998.

[End90]   P.M. Endt, 'Energy levels of $A = 21 - 44$ nuclei (VII)', Nucl. Phys. A 521 (1990) 1–830.

[Eng98]   Christian Otto Engelmann, *Kernspaltung relativistischer Uranprojektile und Erzeugung extrem neutronenreicher Isotope*, Ph.D. thesis, Universität Tübingen (1998).

[Enq96]   T. Enqvist et al., 'Alpha decay properties of $^{200-202}$Fr', Z. Phys. A 354 (1996) 1–2.

[Erd98a]  N. Erdmann et al., 'Determination of the first ionization potential of nine actinide elements by resonance ionization mass spectroscopy (RIMS)', J. Alloys and Compounds 271-273 (1998) 837–840.

[Erd98b]  N. Erdmann et al., 'Frequency tripling for resonance ionization spectroscopy (RIS) of Cd', Appl. Phys. B 66 (1998) 431–433.

[Erd98c]  Nicole Erdmann, *Resonanzionisationsmassenspektroskopie zur Bestimmung der Ionisationsenergien von Berkelium und Californium und zur Spurenanalytik von Plutonium*, Ph.D. thesis, Universität Mainz (1998).

[Est91]   R.C. Estler and N.S. Nogar, 'Ablation of high temperature superconductor studied by resonance ionization mass spectrometry (RIMS)', J. Appl. Phys. 69 (1991) 1654–1659.

[Eve97]   A.H.M. Evensen et al., 'Release and yields from thorium and uranium targets irradiated with a pulsed proton beam', Nucl. Instr. Meth. B 126 (1997) 160–165.

[Ewa80] G.T. Ewan, E. Hagberg, B. Jonson, S. Mattsson and P. Tidemand-Petersson, 'Alpha decay studies of new neutron-deficient francium isotopes and their daughters', Z. Phys. A 296 (1980) 223–228.

[Ewa84] G.T. Ewan et al., 'Intense mass-separated beams of halogens and beta-delayed neutron emission from heavy bromine isotopes', Z. Phys. A 318 (1984) 309–314.

[Fae84] T. Faestermann, A. Gillitzer, K. Hartel, P. Kienle and E. Nolte, 'Evidence for proton radioactivity of $^{113}$Cs and $^{109}$I', Phys. Lett. 137B (1984) 23–26.

[Fai64] H. Faissner and K. Wildermuth, 'Cluster model of nuclear fission. (I.) Aymmetric mass distributions', Nucl. Phys. A 58 (1964) 177–200.

[Fai87] W.M. Fairbank and H.K. Carter, 'A completely cold laser ion source for separators', Nucl. Instr. Meth. B 26 (1987) 357–361.

[Fai89] W.M. Fairbank, M.T. Spaar, J.E. Parks and J.M.R. Hutchinson, 'Anomalous odd- to even-mass isotope ratios in resonance ionization with broad-band lasers', Phys. Rev. A 40 (1989) 2195–2198.

[Farge] Fanny Farget, priv. comm.

[Far47] G. Farwell, E. Segrè and C. Wiegand, 'Long range alpha-particles emitted in connection with fission. Preliminary report', Phys. Rev. 71 (1947) 327–330.

[Far98] F. Farget et al., 'Spallation-reaction cross sections relevant for accelerator-driven systems', in [Sey98], pp. 11–18.

[FAS] http://www.fastcomtec.com.

[Fas83] J.D. Fassett, J.C. Travis, L.J. Moore and F.E. Lytle, 'Atomic ion formation and measurement with resonance ionization mass spectrometry', Anal. Chem. 55 (1983) 765–770.

[Fas84] J.D. Fassett, L.J. Powell and L.J. Moore, 'Determination of iron in serum and water by resonance ionization isotope dilution mass spectrometry', Anal. Chem. 56 (1984) 2228–2233.

[Fau82] H. Faust, P. Geltenbort, F. Gönnenwein and A. Oed, 'Determination of isobaric elemental yields in velocity selected fission products', Nucl. Instr. Meth. 193 (1982) 577–580.

[Fau94] H. Faust and G. Fioni, 'Estimates for far asymmetric fission yields from Lohengrin data', in [Sey94], pp. 91–96.

[Fau95a] H. Faust, 'Calculation of mass and charge distribution in nuclear fission using a Boltzmann formulation', in C. Wagemans, ed., 'Proc. Seminar on Fission, Pont d'Oye III', 1995, pp. 211–219.

[Fau95b] H. Faust and Z. Bao, 'Calculation of relative LCP yields in ternary fission by a Boltzmann distribution', in C. Wagemans, ed., 'Proc. Seminar on Fission, Pont d'Oye III', 1995, pp. 220–231.

[Fea74] N. Feather, 'Simultaneous emission of two light charged particles in fission', Proc. Royal Soc. Edinburgh 71 (1974) 323–331.

[Fedos] Valentin N. Fedoseyev, priv. comm.

[Fed95a] V.N. Fedoseyev et al., 'Study of short-lived silver isotopes with a laser ion source', Z. Phys. A 353 (1995) 9–10.

[Fed95b] V.N. Fedoseyev et al., 'Study of short-lived tin isotopes with a laser ion source', in [RIS94], 465–467.

[Fed97] V.N. Fedoseyev et al., 'Chemically selective laser ion source of manganese', Nucl. Instr. Meth. B 126 (1997) 88–91.

[Fed98] V.N. Fedoseyev, 'The use of lasers for the selective ionization of radionuclei for RIB generation', in [Caa98], pp. 296–300.

[Feh97]   P. Fehsenfeld, A. Kleinrahm and R. Kubat, 'Thin layer activation for wear measurements', in M.N.H. Comsan and Z.A. Saleh, eds., '2nd School and Workshop on Cyclotrons and Applications, 15.-19. March 1997, Cairo', Nuclear Research Center, Atomic Energy Authority, 1997.

[Fer34a]  E. Fermi, 'Possible production of elements of atomic number higher than 92', Nature 133 (1934) 898–899.

[Fer34b]  E. Fermi, 'Radioactivity induced by neutron bombardment', Nature 133 (1934) 757.

[Fio93]   G. Fioni et al., 'Reduction of energy dispersion on a parabola mass spectrometer', Nucl. Instr. Meth. A 332 (1993) 175–180.

[Fir96]   R.B. Firestone and V.S. Shirley, eds., *Table of Isotopes*, John Wiley & Sons, New York, 8th edn. (1996).

[Flü39]   S. Flügge and K.E. Zimens, 'Die Bestimmung von Korngrößen und von Diffusionskonstanten aus dem Emaniervermögen', Z. Phys. Chem. B42 (1939) 179–220.

[Fogel]   Birger Fogelberg, priv. comm.

[Fog92]   B. Fogelberg et al., 'Efficiency and delay of the integrated target-ion source of OSIRIS', Nucl. Instr. Meth. B 70 (1992) 137–141.

[Fog97]   B. Fogelberg, H. Mach and L. Jacobsson, 'The OSIRIS facility and ion source at Studsvik', in [Ben96], pp. 69–73.

[Fog98]   B. Fogelberg, H. Mach, H. Gausemel, J.P. Omtvedt and K.A. Mezilev, 'New high spin isomers obtained in thermal fission', in [Sey98], pp. 191–195.

[Fog99]   B. Fogelberg, K.A. Mezilev, H. Mach, V.I. Isakov and J. Slivova, 'Precise atomic mass values near $^{132}$Sn: the resolution of a puzzle', Phys. Rev. Lett. 82 (1999) 1823–1826.

[Fom70]   V.S. Fomenko, *Emissionnij svoijstva materialov*, Naukova Dumka, Kiev (1970).

[Fon56]   P. Fong, 'Statistical theory of nuclear fission: asymmetric fission', Phys. Rev. 102 (1956) 434–448.

[Fon70]   P. Fong, '$\alpha$-particle trajectories in ternary fission', Phys. Rev. C 2 (1970) 735–742.

[Fon71]   P. Fong, 'Mechanism and rate of long-range $\alpha$-particle emission in fission', Phys. Rev. C 3 (1971) 2025–2027.

[For98]   S. Fortier et al., 'Study of the $^{11}$Be structure via the p($^{11}$Be,$^{10}$Be)d reaction', in [ENA98], pp. 239–244.

[Fra77]   H. Franz et al., 'Delayed-neutron spectroscopy with $^{3}$He spectrometers', Nucl. Instr. Meth. 144 (1977) 253–261.

[Fra98a]  S. Franchoo et al., 'Beta-decay of $^{68-74}$Ni and level structure of neutron-rich Cu isotopes', Phys. Rev. Lett. 81 (1998) 3100–3103.

[Fra98b]  S. Franchoo et al., 'Beta decay of neutron-rich cobalt and nickel isotopes', in [ENA98], pp. 757–760.

[Fra99]   Serge Franchoo, *Evolution of nuclear structure towards $^{78}$Ni investigated by the $\beta$ decay of laser-ionized $^{68-74}$Ni*, Ph.D. thesis, K.U. Leuven (1999).

[Fre98]   M. Freer et al., 'Exotic molecular and halo states in $^{12,14}$Be', in [ENA98], pp. 314–318.

[Fri39]   O.R. Frisch, 'Physical evidence for the division of heavy nuclei under neutron bombardment', Nature 143 (1939) 276.

[Fri63]   G. Friedlander, L. Friedman, B. Gordon and L. Yaffe, 'Excitation functions and nuclear charge dispersion in the fission of uranium by 0.1 to 6.2 GeV protons', Phys. Rev. C 129 (1963) 1809–1825.

[Fri77]   G. Frick et al., 'Stripping experiments in carbon foils with heavy ions in the energy range of 0.4-0.9 MeV/A', Rev. Phys. Appl. 12 (1977) 1525.

[Fri90]   Harald Friedrich, *Theoretical Atomic Physics*, Springer, Berlin (1990).

[Fri98a]  T. Friedrichs et al., 'Investigation of mass, charge and energy of thermal neutron induced fission of $^{245}$Cm and $^{241}$Pu', in [Sey98], pp. 231–238.

[Fri98b]  Thomas Friedrichs, *Untersuchung der neutroneninduzierten Spaltung von $^{245}$Cm und $^{241}$Pu sowie Bestimmung von Kernmassen mittels $\beta\gamma$-Koinzidenzspektroskopie*, Ph.D. thesis, TU Braunschweig (1998).

[Fri99]   J. Friese, *Nucleon transfer on transuranium targets*, in [MAFF], 1999.

[Fuj81]   M. Fujioka and Y. Arai, 'Diffusion of radioisotopes from solids in the form of foils, fibers and particles', Nucl. Instr. Meth. 186 (1981) 409–412.

[Gäg86]   H. Gäggeler et al., 'Production of cold target-like fragments in the reaction of $^{48}$Ca+$^{248}$Cm', Phys. Rev. C 33 (1986) 1983–1987.

[Gäg88]   H.W. Gäggeler, 'Reaktionsmechanismen zur Synthese schwerster Elemente aus Schwerionenreaktionen', Rep. 14, Paul Scherrer Institut, Villingen, Switzerland (1988).

[Gal99]   Jean Galy, *Mesure de la distribution en masse et en charge des produits de la fission rapide de l'$^{233}$U*, Ph.D. thesis, Université d'Aix-Marseille I (1999).

[Gan78]   Yu.P. Gangrskii, G.M. Marinescu, M.B. Miller, V.N. Samosyuk and I.F. Kharisov, 'Delayed fission of neutron-rich protactinium isotopes', Sov. J. Nucl. Phys. 27 (1978) 475–478.

[Gav75]   A. Gavron, 'Scission-point parameters determined by light particle emission in fission of $^{252}$Cf', Phys. Rev. C 11 (1975) 580–586.

[Gaz70]   Y. Gazit, E. Nardi and S. Katcoff, 'Emission of particles of $3 \leq Z \leq 8$ in the fission of $^{252}$Cf', Phys. Rev. C 1 (1970) 2101–2108.

[Gei95]   H. Geissel, G. Münzenberg and K. Riisager, 'Secondary exotic nuclear beams', Annu. Rev. Nucl. Part. Sci. 45 (1995) 163–203.

[Gei99]   W. Geithner et al., 'Measurement of the magnetic moment of the one-neutron-halo nucleus $^{11}$Be', Phys. Rev. Lett. 83 (1999) 3792–3795.

[Gel89]   P. Gelin, J.L. Debrun, O. Gobert, R.L. Inglebert and B. Dubreuil, 'Resonant ionization of sputtered neutral atoms for trace analysis in high purity materials', Nucl. Instr. Meth. B 40/41 (1989) 290–292.

[Gel96a]  R. Geller, *Electron Cyclotron Resonance Ion Sources and ECR Plasmas*, IOP, Bristol (1996).

[Gel96b]  R. Geller, C. Tamburella and J.L. Belmont, 'The ISOL-MAFIOS source', Rev. Sci. Instr. 67 (1996) 1281–1285.

[Gen99]   J. Genevey et al., 'Identification of $\mu$s isomers in the fission products of $^{241}$Pu(n$_{th}$,f)', Phys. Rev. C 59 (1999) 82–89.

[Geo99]   U. Georg et al., 'Radioactive ion beams at ISOLDE/CERN, recent developments and perspectives', in B. Rubio, M. Lozano and W. Gelletly, eds., 'Experimental Nuclear Physics in Europe, ENPE'99, Sevilla, June 1999', AIP Conf. Proc. 495, Woodbury, NY, 1999, pp. 349–352.

[Ghi88]   A. Ghiorso et al., 'SASSY, a gas-filled magnetic separator for the study of fusion reaction products', Nucl. Instr. Meth. A 269 (1988) 192–201.

[Gil74]   R. Gillette, 'Uranium enrichment: rumors of Israeli progress with lasers', Science 183 (1974) 1173–1174.

[Gil85]  R.L. Gill and A. Piotrowski, 'A new FEBIAD-type ion source for use at the reactor-based ISOL facility TRISTAN', Nucl. Instr. Meth. A 234 (1985) 213–217.

[Gim92]  G. Gimond et al., 'Present status of singly charged ion ECR sources at the SARA on-line separator', Nucl. Instr. Meth. B 70 (1992) 118–124.

[Gip86]  K.L. Gippert et al., 'Decay studies of neutron-rich radium and actinium isotopes, including the new nuclides $^{232}$Ra and $^{233,234}$Ac', Nucl. Phys. A 453 (1986) 1–14.

[Glä82]  P. Glässel, D. v. Harrach, L. Grodzins and H.J. Specht, 'Direct observation of nonequilibrium effects in sequential fission', Phys. Rev. Lett. 48 (1982) 1089–1093.

[Gön91]  F. Gönnenwein and B. Börsig, 'The model of cold fission', Nucl. Phys. A 530 (1991) 27–57.

[Gön92a]  F. Gönnenwein, 'On the notion of odd-even effects in the yields of fission fragments', Nucl. Instr. Meth. A 316 (1992) 405–415.

[Gön92b]  F. Gönnenwein et al., 'Emission of clusters in nuclear fission', in [BKS92], pp. 453–458.

[Gön94]  F. Gönnenwein et al., 'Parity violation in ternary fission', Nucl. Phys. A 567 (1994) 303–316.

[Gön97]  F. Gönnenwein et al., 'Cold binary and ternary fission', Il Nuovo Cimento 110 A (1997) 1089–1095.

[Gön98]  F. Gönnenwein et al., 'Cold ternary fission', in 'Proc. Conf. Perspectives in Nuclear Physics, Paradise Island, 1998', 1998.

[Gov71]  N.B. Gove and M.J. Martin, 'Log-$f$ tables for beta decay', Nucl. Data Tables 10 (1971) 205–317.

[Gra88]  V.T. Grachëv, Yu.I. Gusev and D.M. Seliverstov, 'Angular, energy and mass distributions for spontaneous fission of $^{252}$Cf with emission of $^{3}$H, $^{4}$He and $^{6}$He nuclei', Sov. J. Nucl. Phys. 47 (1988) 395–402.

[Gre63]  A.E. Greendale and D.L. Love, 'A rapid radiochemical procedure for tin', Anal. Chem. 35 (1963) 1712–1715.

[Gre91]  C.H. Greene and M. Aymar, 'Spin-orbit effects in the heavy alkaline-earth atoms', Phys. Rev. A 44 (1991) 1773–1790.

[Gro97]  M. Groß and D. Habs, 'An adjustable neutron absorber for the fission fragment accelerator', Jahresbericht, Beschleunigerlaboratorium der Universität und Technischen Universität München (1997).

[Gro99]  J.S. Grossman et al., 'Hyperfine anomaly measurements in francium isotopes and the radial distribution of neutrons', Phys. Rev. Lett. 83 (1999) 935–938.

[Grü98]  C. Grüning et al., 'A high repetition rate solid state laser system for resonance ionisation spectrometry of actinides', in [RIS98], 1998.

[Gua84]  G. Guarino et al., 'Mass drift in reactions between a heavy and a light nucleus', Nucl. Phys. A 424 (1984) 157–183.

[Gue80]  C.R. Guet, H.A. Nifenecker, C. Signarbieux and M. Asghar, 'On the compatibility of LRA fission distributions with compact scission', in 'Conf. on Chemistry and Physics of Fission', IAEA-SM-241/F13, 1980, pp. 247–265.

[Gue87]  K.H. Guenther, 'Growth structures in a thick vapor deposited $MgF_2$ multiple layer coating', Appl. Opt. 26 (1987) 188–190.

[Gul72]  T.D. Gulden, 'Carbon thermal diffusion in the $UC_2$-C system', J. Am. Chem. Soc. 55 (1972) 14–18.

[Gul95]  V.M. Gulevich, D.Yu. Pakhomov and A.D. Zuzikov, 'Optical schemes of resonant photoionization of lead atoms', Opt. Comm. 118 (1995) 275–280.

[Gun67]    H.R. von Gunten, K.F. Flynn and L.E. Glendenin, 'Distribution of mass and charge in the fission of $^{245}$Cm', Phys. Rev. 161 (1967) 1192–1195.

[Gup79]    S.K. Gupta and K.A. Gingerich, 'Observation and atomization energies of the gaseous uranium carbides, UC, UC$_2$, UC$_3$, UC$_4$, UC$_5$ and UC$_6$ by high temperature mass spectrometry', J. Chem. Phys. 71 (1979) 3072–3080.

[Hab78]    D. Habs, H. Klewe-Nebenius, V. Metag, B. Neumann and H.J. Specht, 'Determination of the fission barrier of $^{232}$Pu from $\beta$-delayed fission and the problem of the first barrier', Z. Phys. A 285 (1978) 53–57.

[Hac86]    P.A. Hackett, M.R. Humphries, S.A. Mitchell and D.M. Rayner, 'The first ionization potential of zirconium atoms determined by two laser, field-ionization spectroscopy of high lying Rydberg series', J. Chem. Phys. 85 (1986) 3194–3197.

[Hag67]    E. Hagebø, A. Kjelberg and S. Sundell, 'ISOLDE target development at CERN', Ark. Fys. 36 (1967) 127–132.

[Hag70]    E. Hagebø, A. Kjelberg, P. Patzelt, G. Rudstam and S. Sundell, 'Performance of the ISOLDE target system', CERN Report 70-3, Geneva (1970).

[Hag92a]   E. Hagberg et al., 'Indirect measurements of beam-energy differences for various species of ions extracted from a FEBIAD source', Nucl. Instr. Meth. B 70 (1992) 546–550.

[Hag92b]   E. Hagebø et al., 'New production systems at ISOLDE', Nucl. Instr. Meth. B 70 (1992) 165–174.

[Hag94]    E. Hagberg et al., 'Tests of isospin mixing corrections in superallowed $0^+ \rightarrow 0^+$ $\beta$ decays', Phys. Rev. Lett. 73 (1994) 396–399.

[Hah39a]   O. Hahn and F. Strassmann, 'Nachweis der Entstehung aktiver Bariumisotope aus Uran und Thorium durch Neutronenbestrahlung; Nachweis weiterer aktiver Bruchstücke bei der Uranspaltung', Naturwiss. 28 (1939) 89–95.

[Hah39b]   O. Hahn and F. Strassmann, 'über den Nachweis und das Verhalten der bei der Bestrahlung des Urans mittels Neutronen entstehenden Erdalkalimetalle', Naturwiss. 28 (1939) 11–15.

[Hal71]    I. Halpern, 'Three fragment fission', Annu. Rev. Nucl. Sci. 21 (1971) 245–294.

[Hal89]    H.L. Hall et al., '$\beta$-delayed fission from $^{256}$Es$^m$ and the level scheme of $^{256}$Fm', Phys. Rev. C 39 (1989) 1866–1875.

[Hal92]    H.L. Hall and D.C. Hoffman, 'Delayed fission', Annu. Rev. Nucl. Part. Sci. 42 (1992) 147–175.

[Ham99]    J.H. Hamilton et al., 'Cold spontaneous fission processes of $^{252}$Cf and the structure of neutron rich Ba and La nuclei', Acta Phys. Slovaca 49 (1999) 31–42.

[Han69]    P.G. Hansen et al., 'Decay characteristics of short-lived radio-nuclides studied by on-line isotope separation techniques', Phys. Lett. 29B (1969) 415–419.

[Hän72]    T.W. Hänsch, 'Repetitively pulsed tunable dye laser for high resolution spectroscopy', Appl. Opt. 11 (1972) 895–898.

[Han73]    F. Hansen, A. Lindahl, O.B. Nielsen and G. Sidenius, 'The application of ceramic oxides at high temperatures as ISOL-targets', in G. Andersson and G. Holmen, eds., 'Proc. of the 8th Int. EMIS Conf. on Low Energy Ion Accelerators and Mass Separators', Chalmers University of Technology, 1973, pp. 426–431.

[Han87]    P.G. Hansen and B. Jonson, 'The neutron halo of extremely neutron-rich nuclei', Europhys. Lett. 4 (1987) 409–414.

[Han89]    P.G. Hansen and B. Jonson, *Beta-delayed particle emission from neutron-rich nuclei*, vol. III of Poenaru and Ivascu [Poe89], 1989, pp. 157–202.

[Han99a]  S. Hankonen et al., 'Exotic neutron rich $^{34}$Al and $^{35}$Al isotopes studied at CERN ISOLDE', in [Str99], pp. 191–195.

[Han99b]  M. Hannawald et al., 'Decay of neutron-rich Mn nuclides and deformation of heavy Fe isotopes', Phys. Rev. Lett. 82 (1999) 1391–1394.

[Han00]  M. Hannawald et al., 'Selective laser ionisation of very neutron-rich cadmium isotopes: decay properties of $^{131}$Cd$_{83}$ and $^{132}$Cd$_{84}$', Phys. Rev. C 62 (2000) 054301.

[Har82]  D. v. Harrach, P. Glässel, L. Grodzins, S.S. Kapoor and H.J. Specht, 'Direct observation of proximity effects in ternary heavy-ion reactions', Phys. Rev. Lett. 48 (1982) 1093–1097.

[Har00]  S. Hargrove, 'Laser technology follows in Lawrence's footsteps', Science and Technology Review (LLNL) May (2000) 13–21.

[Has96]  Sh. Hasegawa and A. Suzuki, 'Resonance ionization spectroscopy and analysis on even-parity states of Pb I', Phys. Rev. A 53 (1996) 3014–3022.

[Has98a]  H. Haseroth et al., 'Developments of the CERN laser ion source', Rev. Sci. Instr. 69 (1998) 1051–1053.

[Has98b]  M. Hass et al., 'Measurement of the $^{7}$Be(p,$\gamma$)$^{8}$B cross-section with an implanted $^{7}$Be target', in [ENA98], pp. 864–867.

[Hau76]  P.E. Haustein et al., 'New neutron-rich isotope: $^{190}$W', Phys. Rev. C 14 (1976) 645–649.

[Hau77]  P.E. Haustein, E.M. Franz, R.F. Petry and J.C Hill, 'New neutron-rich isotope: $^{196}$Os', Phys. Rev. C 16 (1977) 1559–1565.

[Hau79]  P.E. Haustein et al., 'Identification and decay of $^{242}$U and $^{242}$Np', Phys. Rev. C 19 (1979) 2332–2343.

[Hec63]  H.H. Heckman, E.L. Hubbard and W.G. Simon, 'Electronic charge distributions for heavy ions at high velocities', Phys. Rev. 129 (1963) 1240–1249.

[Hel92]  M. Hellström, B. Fogelberg, L. Jacobsson, L. Spanier and G. Rudstam, 'Some studies of molecular ions obtained from a U + C target at > 2100°C', Nucl. Instr. Meth. B 70 (1992) 142–145.

[Hel96]  M. Hellström et al., 'Beta-delayed proton emission around $N = 50$ and the rp-process', Z. Phys. A 356 (1996) 229–231.

[Her82]  G. Herrmann and N. Trautmann, 'Rapid chemical methods for identification and study of short-lived nuclides', Annu. Rev. Nucl. Part. Sci. 32 (1982) 117–147.

[Her89]  P. Herzog, U. Dämmrich, K. Freitag, C.D. Herrmann and K. Schlösser, 'The magnetic moments of $(\nu g_{9/2})$-levels in odd Zn isotopes', Z. Phys. A 332 (1989) 247–250.

[Hes93]  M. Hesse, H. Faust, G. Fioni, M. Groß and F. Gönnenwein, in H. Maerten et al., eds., 'Proc. Workshop on High Resolution Spectroscopy of Fission Fragments. Neutrons and $\gamma$ rays', report FZR-93-08, Rossendorf, 1993, pp. 31–.

[Hes97]  Michael Hesse, *Emission von schweren ternären Teilchen in der Kernspaltung*, Ph.D. thesis, Eberhard-Karls-Universität Tübingen (1997).

[Het86]  D.W. Hetherington, M.A. Lone and R.L. Graham, 'Leak rates for air and isobutane through thin polypropylene films', Nucl. Instr. Meth. A 242 (1986) 270–276.

[Hic85]  K.H. Hicks et al., 'Fission of heavy nuclei induced by energetic pions', Phys. Rev. C 31 (1985) 1323–1333.

[Hil77]  D.L. Hildenbrand, 'Thermochemistry of gaseous UF$_5$ and UF$_4$', J. Chem. Phys. 66 (1977) 4788–4794.

[Hil85]  P. Hill, N. Kaffrell, W. Kurcewicz and G. Nyman, 'The new neutron-rich nuclei $^{231}$Fr and $^{231}$Ra', Z. Phys. A 320 (1985) 531–532.

[Hil86]  J.C. Hill et al., 'Level structure of $^{148}$Ba: a test of the $N_pN_n$ scheme far off stability', Phys. Rev. C 34 (1986) 2312–2315.

[Hil88]  K. Hilpert, H. Gerads, D. Kath and D. Kobertz, 'Sorption of cesium and its vaporization from graphitic materials at high temperatures', High Temperatures-High Pressures 20 (1988) 157–164.

[Hil89]  C. Hill, K. Schindl and H. Schönauer, 'Move of ISOLDE – Implications for the PS Booster', Internal Note PS/HI 89-7, CERN, Geneva (1989).

[Hil94]  D.L. Hildenbrand and K.H. Lau, 'Thermochemistry of gaseous manganese oxides and hydroxides', J. Chem. Phys. 100 (1994) 8377–8380.

[Hil96]  C.E. Hill and K. Langbein, 'Experiments on a 14.5 GHz ECR source', in [LIN96], pp. 366–368.

[Hin97a] G. Hinderer, G. Dollinger, G. Datzmann and H.J. Körner, 'Design of the superconducting microprobe system in Munich', Nucl. Instr. Meth. B 130 (1997) 51–56.

[Hin97b] B. Hinfurtner, G. Seewald, E. Hagn, E. Zech and I.S. Towner, 'Nuclear magnetic moments of 2.0 h $^{89}$Nb and 78 h $^{89}$Zr', Nucl. Phys. A 620 (1997) 317–326.

[Hir92]  M. Hirsch, A. Staudt and H.V. Klapdor-Kleingrothaus, 'Prediction of average $\beta$ and $\gamma$ energies and probabilities of $\beta$-delayed neutron emission in the region of fission products', At. Data Nucl. Data Tables 51 (1992) 243–271.

[Hof80]  P. Hoff et al., 'Production of molecular ions in the integrated target/ion-source of an isotope-separation-on-line system', Nucl. Instr. Meth. 172 (1980) 413–418.

[Hof81]  P. Hoff et al., 'Molecular ion techniques at the OSIRIS mass separator', Nucl. Instr. Meth. 186 (1981) 381–383.

[Hof84]  P. Hoff, O.C. Jonsson, E. Kugler and H. Ravn, 'Release of nuclear reaction products from refractory compounds', Nucl. Instr. Meth. 221 (1984) 313–329.

[Hof86]  R.W. Hoff, 'Beta decay of neutron-rich transuranic nuclei', in H.V. Klapdor, ed., 'Weak and Electromagnetic Interactions in Nuclei', Springer, Berlin, 1986, pp. 207–212.

[Hof89]  D.C. Hoffman and L.P. Somerville, *Spontaneous fission*, vol. III of Poenaru and Ivascu [Poe89], 1989, pp. 1–40.

[Hof94]  P. Hofmann et al., 'Fission of heavy nuclei induced by stopped antiprotons. I. Inclusive characteristics of fission fragments', Phys. Rev. C 49 (1994) 2555–2268.

[Hof95]  S. Hofmann et al., 'Production and decay of $^{269}$110', Z. Phys. A 350 (1995) 277–280.

[Hof96a] P. Hoff et al., 'Single-neutron states in $^{133}$Sn', Phys. Rev. Lett. 77 (1996) 1020–1023.

[Hof96b] S. Hofmann et al., 'The new element 112', Z. Phys. A 354 (1996) 229–230.

[Hon69]  R.E. Honig and D.A. Kramer, 'Vapour pressure data for the solid and liquid elements', RCA Review 30 (1969) 285–305.

[Hot85]  H. Hotop and W.C. Lineberger, 'Binding energies in atomic negative ions: II', J. Phys. Chem. Ref. Data 14 (1985) 731–750.

[Huh97]  M. Huhta et al., 'Independent yields of neutron-rich nuclei in charged-particle induced fission', Nucl. Instr. Meth. B 126 (1997) 201–204.

[Huh98]  M. Huhta et al., 'New evidence for deformation in $^{73}$Zn', Phys. Rev. C 58 (1998) 3187–3194.

[Hui81]  H. Huizenga, J.A.M. Bleeker, W.H. Diemer and A.P. Huben, 'Submicron entrance windows for an ultrasoft x-ray camera', Rev. Sci. Instr. 52 (1981) 673–677.

[Hul73]  R. Hultgen et al., *Selected values of the thermodynamic properties of the elements*, American Society for Metals, Metals Park, Ohio (1973).

[Hur77]   G.S. Hurst, M.H. Nayfeh and J.P. Young, 'A demonstration of one-atom detection', Appl. Phys. Lett. 30 (1977) 229–231.

[Hur79]   G.S. Hurst, M.G. Payne, S.D. Kramer and J.P. Young, 'Resonance ionization spectroscopy and one-atom detection', Rev. Mod. Phys. 51 (1979) 767–819.

[Hur85]   G.S. Hurst et al., 'Method for counting noble gas atoms with isotopic selectivity', Rep. Prog. Phys. 48 (1985) 1333–1370.

[Hur88]   G.S. Hurst and M.G. Payne, *Principles and Applications of Resonance Ionisation Spectroscopy*, Adam Hilger, Bristol (1988).

[Huy83]   M. Huyse, 'Ionization in a hot cavity', Nucl. Instr. Meth. 215 (1983) 1–5.

[Huy92]   M. Huyse et al., 'Isomers in three doubly odd Fr-At-Bi $\alpha$-decay chains', Phys. Rev. C 46 (1992) 1209–1216.

[Ich89]   S. Ichikawa, T. Sekine, H. Iimura, M. Oshima and N. Takahashi, 'Selective mass separation of light lanthanoids by means of ionization of their monoxides', Nucl. Instr. Meth. A 274 (1989) 259–264.

[Ich98]   S. Ichikawa et al., '$\beta$-decay half-lives of new neutron-rich lanthanide isotopes', in [ENA98], pp. 540–543.

[Ike92]   N. Ikeda et al., 'Study of a thick target surface ionizer at INS', Nucl. Instr. Meth. B 70 (1992) 150–155.

[Ing69]   J.S. Ingley, 'Nuclear explosion experiments to determine nuclear properties of heavy isotopes', Nucl. Phys. A 124 (1969) 130–144.

[IS358]   'Magnetic moment of $^{67}$Ni and $^{67}$Ni$\rightarrow^{67}$Cu beta decay', ISOLDE experiment IS358, spokesperson: J. Rikovska.

[IS364]   'Beta decay study of n$\hbar\o mega$ excitations in neutron-rich (fp) nuclei. Test of the empirical nuclear interaction', ISOLDE experiment IS364, spokesperson: G. Walter.

[IS365]   'Nuclear spectroscopy with copper isotopes of extreme $N/Z$ ratios', ISOLDE experiment IS365, spokesperson: D. Habs.

[ISI20]   'Measurement of the $^{7}$Be(p,$\gamma$)$^{8}$B absolute cross section in inverse kinematics', ISOLDE Letter of Intent I20, spokespersons: C. Rolfs and U. Greife.

[ISI22]   'Test measurements of neutron-rich Cd isotopes with a chemically selective laser ion source', ISOLDE Letter of Intent I22, spokesperson: K.L. Kratz.

[ISP55]   'Towards the proton drip-line along the cadmium isotopic chain', ISOLDE Proposal P55, spokesperson: K. Rykaczewski.

[ISP95]   'Study of the $^{163}$Ho decay for a neutrino mass experiment', ISOLDE Proposal P95, spokesperson: M. Altmann.

[ISP99]   'Beta-decay study of dripline isotopes of Be', ISOLDE Proposal P99, spokesperson: G. Nyman.

[Iva96]   M.P. Ivanov et al., 'Dependence of light charged particles parameters on $Z^2/A$ in ternary fission', Z. Phys. A 355 (1996) 341–342.

[Iva97]   M.P. Ivanov, I.V. Kuznetsov, V.F. Kushniruk and Yu.G. Sobolev, 'Inclusive energy spectra and yields of light nuclei from the spontaneous fission of $^{248}$Cm', Phys. At. Nucl. 60 (1997) 329–333.

[Izo92]   I.N. Izosimov, 'Structure of the $\beta$-decay strength function and delayed fission of $^{232}$Fr', Bull. Russ. Acad. Sci. Phys. 56 (1992) 88–90.

[Jac87]   L. Jacobsson, B. Fogelberg, B. Ekström and G. Rudstam, 'An unconventional bi-mode ion source (ANUBIS) for the OSIRIS facility', Nucl. Instr. Meth. B 26 (1987) 223–226.

[Jad96a]  Y. Jading and K. Riisager, 'Systematic errors in $\chi^2$-fitting of Poisson distributions', Nucl. Instr. Meth. A 372 (1996) 289–292.

[Jad96b]  Ylva Jading, *Towards the "Waiting-Point" Nucleus* $^{129}Ag$, Ph.D. thesis, Johannes-Gutenberg-Universität Mainz (1996).

[Jad97]  Y. Jading et al., 'Production of radioactive Ag ion beams with a chemically selective laser ion source', Nucl. Instr. Meth. B 126 (1997) 76–80.

[Jan76]  G.S. Janes, I. Itzkan, C.T. Pike, R.H. Levy and L. Levin, 'Two-photon laser isotope separation of atomic uranium: spectroscopic studies, excited-state lifetimes and photoionization cross sections', IEEE J. Quant. Elec. QE-12 (1976) 111–120.

[Jay98]  K. Jayamanna et al., 'An electron cyclotron resonance source for radioactive beryllium ion beam production', Rev. Sci. Instr. 69 (1998) 756–757.

[Jes98]  P. Jesinger et al., 'Can time reversal invariance be tested in ternary fission', in [Sey98], pp. 395–404.

[Joh73]  P.G. Johnson, A. Bolson and C.M. Henderson, 'A high temperature ion source for isotope separators', Nucl. Instr. Meth. 106 (1973) 83–87.

[Joh98]  I.P. Johnstone and I.S. Towner, 'Effective magnetic dipole operators for $^{88}$Sr and $^{90}$Zr closed-shell cores', Eur. Phys. J. A 3 (1998) 237–242.

[Joh99]  G.D. Johns et al., 'High energy neutron induced fission: charge yield distributions and new isomer search and spectroscopy', in 'Second Int. Conf. on Fission and Neutron-rich Nuclei, St. Andrews, Scotland', World Scientific, Singapore, 1999.

[Jok95]  A. Jokinen et al., 'First observation of neutron single particle states in $^{133}$Sn', in [ENA95], 1995, pp. 499–504.

[Jok96]  A. Jokinen et al., 'Proton instability of $^{73}$Rb', Z. Phys. A 355 (1996) 227–230.

[Jok97]  A. Jokinen et al., 'Selective laser ionization of radioactive Ni-isotopes', Nucl. Instr. Meth. B 126 (1997) 95–99.

[Jok98]  A. Jokinen et al., 'Beta decay of the $M_T = -1$ nucleus $^{58}$Zn studied by selective laser ionization', Eur. Phys. J. A 3 (1998) 271–276.

[Jon81]  B. Jonson, O.B. Nielsen, L. Westgaard and J. Zylicz, 'The decay of $^{207}_{80}$Hg$\rightarrow^{207}_{81}$Tl', in '4th International Conference on Nuclei far from Stability, Helsingør', CERN report 81-09, Geneva, 1981, pp. 640–643.

[Jon98]  B. Jonson, 'Status of neutron drip-line nuclei', in [ENA98], pp. 166–173.

[Kal76]  V.V. Kalygin and V.M. Prokop'ev, 'Efficiency of a tubular surface ionizer', Sov. Phys. Tech. Phys. 20 (1976) 801–803.

[Kat72]  T. Kato et al., 'Thin polypropylene window proportional counters for the observation of cosmic soft X-rays', Jap. J. Appl. Phys. 11 (1972) 1351–1356.

[Kat73]  S.K. Kataria, E. Nardi and S.G. Thompson, 'Simultaneous emission of two light-charged particles in spontaneous fission of $^{252}$Cf', in 'Physics and Chemistry of Fission 1973, Proc. of an Int. Symp.', Preprint IAEA-SM-174/63, 1973, pp. 389–403.

[Kat86]  K. Kato, 'Second-harmonic generation to 2048 Å in $\beta$-BaB$_2$O$_4$', IEEE J. Quant. Elec. 22 (1986) 1013–1014.

[Kauts]  Thomas Kautzsch, priv. comm.

[Kau96]  T. Kautzsch et al., 'Laser ionization of $^{124}$Ag and its decay to levels of $^{124}$Cd', Phys. Rev. C 54 (1996) R2811–R2814.

[Kau98]  T. Kautzsch, W.B. Walters and K.L. Kratz for the ISOLDE-IS333 Collaboration, 'Laser isotope and isomer separation of neutron-rich Ag isotopes', in [Sey98] 1998, pp. 183–190.

[Kaw82]   K. Kawade et al., 'Evidence for doubly magic structure of $^{132}$Sn', Z. Phys. A 308 (1982) 33–38.

[Kaw89]   Y. Kawase and K. Okano, 'The oxidation technique for efficient ionization of lanthanides by a helium-jet loaded on-line isotope separator', Nucl. Instr. Meth. B 37/38 (1989) 116–119.

[Kaw92]   Y. Kawase, K. Okano, M. Shibata and A. Taniguchi, 'Fluorination method for the surface ionization of Sr and Ba with a helium-jet type ISOL', Nucl. Instr. Meth. B 70 (1992) 146–149.

[Kel94]   H. Keller et al., 'Search for forbidden $\beta$-decays of the drip line nucleus $^{12}$Be', Z. Phys. A 348 (1994) 61–62.

[Ker73]   A. Kerek, G.B. Holm, L.E. De Geer and S. Borg, 'The first excited state in the doubly-closed-shell nucleus $^{132}$Sn populated in the 0.12 s $\beta^-$-decay of $^{132}$In', Phys. Lett. 44B (1973) 252–254.

[Kes98]   O. Kester et al., 'The LINAC of the Munich accelerator for fission fragments (MAFF)', in 'XIV Int. Linear Accelerator Conf., LINAC'98, Chicago, August 1998', 1998.

[Key94]   U. Keyser and A. Paul, 'Aerosolgenerator for the collection and transport of radioactive isotopes', in [Sey94], 1994, pp. 161–168.

[KH51]   O. Kofoed-Hansen and K.O. Nielsen, Mat. Fys. Medd. Dan. Vid. Selsk. 26 (1951) 3–16.

[Kin84]   W.H. King, *Isotope shifts in atomic spectra*, Physics of atoms and molecules, Plenum Press, New York (1984).

[Kirch]   Reinhard Kirchner, priv. comm.

[Kir76]   R. Kirchner and E. Roeckl, 'Investigation of gaseous discharge ion sources for isotope separation on-line', Nucl. Instr. Meth. 133 (1976) 187–204.

[Kir77]   R. Kirchner et al., 'New neutron-deficient tellurium, iodine and xenon isotopes produced by reactions of 290 MeV $^{58}$Ni ions on $^{58}$Ni and $^{63}$Cu targets', Phys. Lett. 70B (1977) 150–154.

[Kir78]   R. Kirchner and A. Piotrowski, 'Thermal ionization in a hot cavity', Nucl. Instr. Meth. 153 (1978) 291–292.

[Kir81a]   R. Kirchner, 'Progress in ion source development for on-line separators', Nucl. Instr. Meth. 186 (1981) 275–293.

[Kir81b]   R. Kirchner, K.H. Burkard, W. Hüller and O. Klepper, 'The ion sources for the GSI on-line separator', Nucl. Instr. Meth. 186 (1981) 295–305.

[Kir86]   R. Kirchner, 'An ion source with storage capability for bunched beam release and controlled chemical separation', Nucl. Instr. Meth. A 247 (1986) 265–280.

[Kir87a]   R. Kirchner, 'An ion source with bunched beam release', Nucl. Instr. Meth. B 26 (1987) 204–212.

[Kir87b]   R. Kirchner, O. Klepper, D. Schardt and T. Sekine, 'Ion source development for the GSI on-line isotope separator', Nucl. Instr. Meth. B 26 (1987) 235–239.

[Kir90]   R. Kirchner, 'On the thermoionization in hot cavities', Nucl. Instr. Meth. A 292 (1990) 203–208.

[Kir92a]   R. Kirchner, 'On the release and ionization efficiency of catcher-ion-source systems in isotope separation on-line', Nucl. Instr. Meth. B 70 (1992) 186–199.

[Kir92b]   R. Kirchner, K. Burkard, W. Hüller and O. Klepper, 'Ion source development for the on-line isotope separator at GSI', Nucl. Instr. Meth. B 70 (1992) 56–61.

[Kir96]   R. Kirchner, 'Ion sources for radioactive beams and related problems (Review)', Rev. Sci. Instr. 67 (1996) 928–933.

[Kir97]    R. Kirchner, 'Release studies of elementary and metal-fluoride ions at the GSI on-line mass separator', Nucl. Instr. Meth. B 126 (1997) 135–140.

[Kla68]    R. Klapisch et al., 'Isotopic distributions of Rb and Cs produced by 10.5 MeV protons on U, Th, Ta and identification of new isotopes: $^{77}$Rb, $^{78}$Rb, $^{120}$Cs, $^{121}$Cs, $^{122}$Cs and $^{124}$Cs', Phys. Rev. Lett. 20 (1968) 743–745.

[Kla84]    H.V. Klapdor, J. Metzinger and T. Oda, 'Beta-decay half-lives of neutron-rich nuclei', At. Data Nucl. Data Tables 31 (1984) 81–111.

[Klu86]    H.J. Kluge, 'ISOLDE user's guide', Rep. 86-05, CERN, Geneva (1986).

[Knie]    Klaus Knie, priv. comm.

[Kno89]    G.F. Knoll, *Radiation detection and measurement*, John Wiley & Sons, New York (1989).

[Köh96]    S. Köhler et al., 'Die experimentelle Bestimmung der Ionisationsenergien von Berkelium und Californium', Angew. Chem. 108 (1996) 3036–3038.

[Koi97]    M. Koizumi, A. Osa, T. Sekine and M. Kubota, 'Development of a laser ion source with pulsed ion extraction', Nucl. Instr. Meth. B 126 (1997) 100–104.

[Kop87]    E.A. Koptelov, S.G. Lebedev and V.N. Panchenko, 'A model of carbon stripper target failure under ion beam bombardment', Nucl. Instr. Meth. A 256 (1987) 247–250.

[Kop94]    I.G. Koprinkov, G.A. Naylor and J.P. Pique, 'Generation of 10 mW tunable narrowband radiation around 210 nm using a 6.5 kHz repetition rate copper vapour laser pumped dye laser', Opt. Comm. 104 (1994) 363–368.

[Kör86]    H.J. Körner, 'Uranium-induced multinucleon transfer reactions', in N. Angert and P. Kienle, eds., 'Proc. of the Symp. 10 Years of Uranium Beam at the Unilac', GSI, GSI report 86-19, Darmstadt, 1986, pp. 158–178.

[Kor95]    A.A. Korsheninnikov et al., 'Spectroscopy of $^{12}$Be and $^{13}$Be using a $^{12}$Be radioactive beam', Phys. Lett. B 343 (1995) 53–58.

[Kös94]    U. Köster, 'Neutronenaktivierungsanalyse: Nachweis von metallischen Verunreinigungen auf Silizium-Wafern', Institut für Radiochemie, TU München (1994).

[Kös95]    U. Köster, *Ternäre Spaltprodukte am LOHENGRIN & PIAFE: Ausbeuten leichter Isotope und ein hochauflösender Massenseparator*, Master's thesis, TU München (1995).

[Kos97a]    V.T. Koslowsky et al., 'The half-lives of $^{42}$Sc, $^{46}$V, $^{50}$Mn and $^{54}$Co', Nucl. Instr. Meth. A 401 (1997) 289–298.

[Kös97b]    U. Köster et al., 'In-pile arrangements of reactor-based RIB facilities', Nucl. Instr. Meth. B 126 (1997) 253–257.

[Kös98a]    U. Köster, O. Kester and D. Habs, 'Ion sources for fission fragment accelerators', Rev. Sci. Instr. 69 (1998) 1316–1321.

[Kös98c]    U. Köster et al., 'Ternary fission yields of $^{241}$Pu($n_{th}$,f)', in [Sey98], 1998, pp. 315–329.

[Kös99]    U. Köster et al., 'Ternary fission yields of $^{241}$Pu($n_{th}$,f)', Nucl. Phys. A 652 (1999) 371–387.

[Kös00]    U. Köster et al., 'Isomer separation of $^{70g}$Cu and $^{70m}$Cu with a resonance ionization laser ion source', Nucl. Instr. Meth. B 160 (2000) 528–535.

[Köt98]    A. Kötzle et al., 'Parity nonconservation in nuclear fission', in [Sey98], 1998, pp. 384–394.

[Kow91]    D. Kowalewska et al., 'Isotope shifts and hyperfine structure in polonium isotopes by atomic-beam laser spectroscopy', Phys. Rev. A 44 (1991) R1442–R1445.

[Koz88]    Piotr Kozcoñ, *Mass and energy distributions of the products from the $^{245}$Cm($n_{th}$,f) reaction*, Ph.D. thesis, TH Darmstadt (1988).

[KR00]    S. Kandri-Rody et al., 'Exotic nuclei produced by fast neutrons in a liquid uranium target', Nucl. Instr. Meth. B 160 (2000) 1–6.

[Kra73]   K.L. Kratz and G. Herrmann, 'Systematics of neutron emission probabilities from delayed neutron precursors', Z. Phys. 263 (1973) 435–442.

[Kra74]   K.L. Kratz and G. Herrmann, 'Delayed-neutron emission from short-lived Br and I isotopes', Nucl. Phys. A 229 (1974) 179–188.

[Kra75]   K.L. Kratz, W. Lauppe and G. Herrmann, 'Gamma-ray emission from short-lived bromine and iodine isotopes', Inorg. Nucl. Chem. Lett. 11 (1975) 331–339.

[Kra79]   S.D. Kramer, J.P. Young, G.S. Hurst and M.G. Payne, 'Resonance ionization spectroscopy of lithium', Opt. Comm. 30 (1979) 47–50.

[Kra86]   S.D. Kramer et al., 'Analysis of $^{81}$Kr in groundwater using laser resonance ionization spectroscopy', Nucl. Instr. Meth. B 17 (1986) 395–401.

[Kra87]   K.L. Kratz et al., 'Constraints on r-process conditions from beta-decay properties far off stability and r-abundances', Rep. MPA 320, Max-Planck-Institut für Physik und Astrophysik, Garching (Oct 1987).

[Kra91]   K.L. Kratz et al., 'Neutron-rich isotopes around the $r$-process "waiting-point" nuclei $^{79}_{29}$Cu$_{50}$ and $^{80}_{30}$Zn$_{50}$', Z. Phys. A 340 (1991) 419–420.

[Kra98a]  A. Krasznahorkay et al., 'Experimental evidence for hyperdeformed states in U isotopes', Phys. Rev. Lett. 80 (1998) 2073–2076.

[Kra98b]  K.L. Kratz et al., 'Laser isotope and isomer separation of heavy Ag nuclides: half-life of the r-process waiting-point isotope $^{129}$Ag and structure of neutron-rich Cd nuclides', in J.H. Hamilton and A.V. Ramayya, eds., 'Proc. Int. Conf. on Fission and Properties of Neutron-Rich Nuclei, Sanibel Island, Nov. 1997', World Scientific, Singapore, 1998, pp. 586–595.

[Kra99]   A. Krasznahorkay et al., 'On the excitation energy of the ground state in the third minimum of $^{234}$U', Phys. Lett. B 461 (1999) 15–21.

[Kra00]   K.L. Kratz, B. Pfeiffer, F.K. Thielemann and W.B. Walters, 'Nuclear structure studies at ISOLDE and their impact on the astrophysical r-process', Hyp. Int. 129 (2000) 185–221.

[Kro69]   T. Krogulski et al., 'Emission of light nuclei in thermal neutron fission of $^{239}$Pu', Nucl. Phys. A 128 (1969) 219–223.

[Krö87]   U. Krönert, St. Becker, Th. Hilberath, H.J. Kluge and C. Schulz, 'Resonance ionization mass spectroscopy with a pulsed thermal atomic beam', Appl. Phys. A 44 (1987) 339–345.

[Krö91]   U. Krönert et al., 'On-line laser spectroscopy by resonance ionization of laser-desorbed refractory elements', Nucl. Instr. Meth. A 300 (1991) 522–537.

[Krugl]   Kirill Kruglov, priv. comm.

[Kud85]   Yu.A. Kudryavtsev, V.S. Letokhov and V.V. Petrunin, 'Laser detection of $^{40}$K by isotopically selective ionization in a beam of accelerated atoms', JETP Lett. 42 (1985) 26–30.

[Kud92]   Yu.A. Kudryavtsev, 'Detection of very rare isotopes by laser collinear resonant ionization of fast atoms', Hyp. Int. 74 (1992) 171–180.

[Kud96]   Y. Kudryavtsev et al., 'Beams of short-lived nuclei produced by selective laser ionization in a gas cell', Nucl. Instr. Meth. B 114 (1996) 350–365.

[Kug72]   G. Kugler and W.B. Clarke, 'Mass-spectrometric measurements of $^3$H, $^3$He and $^4$He produced in thermal-neutron ternary fission of $^{235}$U: evidence for short-range $^4$He', Phys. Rev. C 5 (1972) 551–560.

[Kug92]  E. Kugler et al., 'The new CERN-ISOLDE on-line mass-separator facility at the PS-booster', Nucl. Instr. Meth. B 70 (1992) 41–49.

[Kuo98]  T. Kuo et al., 'Beam characteristics using stable isotopes from a multicusp source for the TRIUMF ISAC facility', Rev. Sci. Instr. 69 (1998) 767–769.

[Kur81]  W. Kurcewicz, E. Ruchowska, N. Kaffrell, T. Bjørnstad and G. Nyman, 'Collective excitations in the transitional nuclei $^{224,226}$Ra', Nucl. Phys. A 356 (1981) 15–25.

[Kur82]  W. Kurcewicz et al., 'Investigations of very neutron-deficient isotopes below $^{100}$Sn in $^{40}$Ca-induced reactions', Z. Phys. A 308 (1982) 21–31.

[Kur87]  W. Kurcewicz et al., 'Collective states in $^{230}$Ra fed by $\beta^-$ decay of $^{230}$Fr', Nucl. Phys. A 464 (1987) 1–8.

[Kuz94]  G. Kuznetsov, 'High temperature cathodes for high current density', Nucl. Instr. Meth. A 340 (1994) 204–208.

[Kwa90]  J. Kwasny, K. Hilpert and H. Nickel, 'Cäsium-Sorptionsuntersuchungen an graphitischen Reaktorwerkstoffen', Rep. Jül-2353, Forschungszentrum Jülich (1990).

[LaCom]  Marco La Commara, priv. comm.

[Lalaz]  Georgios Lalazissis, priv. comm.

[Lal99]  G.A. Lalazissis, S. Raman and P. Ring, 'Ground-state properties of even-even nuclei in the relativistic mean-field theory', At. Data Nucl. Data Tables 71 (1999) 1–40.

[Lam87]  R.H. Lamoreaux, D.L. Hildenbrand and L. Brewer, 'High-temperature vaporization behaviour of oxides - II. oxides of Be, Mg, Ca, Sr, Ba, B, Al, Ga, In, Tl, Si, Ge, Sn, Pb, Zn, Cd and Hg', J. Phys. Chem. Ref. Data 16 (1987) 419–443.

[Lam98]  T. Lamy et al., 'Production of multicharged radioactive ion beams: New results for the 1+ → n+ method with the MINIMAFIOS and SARA-CAPRICE electron cyclotron resonance ion sources', Rev. Sci. Instr. 67 (1998) 1322–1326.

[Lan13]  I. Langmuir, Phys. Rev. 2 (1913) 329–.

[Lan25]  I. Langmuir and K.H. Kingdon, 'Thermionic effects caused by vapours of alkali metals', Proc. Roy. Soc. London 107 (1925) 61–79.

[Lan31]  I. Langmuir and K.T. Compton, 'Electrical discharges in gases. Part II. Fundamental phenomena in electrical discharges', Rev. Mod. Phys. 3 (1931) 191–257.

[Lan79]  Willi Lang, *Nuklidausbeuten bei der Reaktion $^{235}U(n_{\mathrm{th}},f)$ als Funktion der kinetischen Energie der Spaltprodukte – ein experimenteller Zugang zur Dynamik des Spaltprozesses*, Ph.D. thesis, TH Darmstadt (1979).

[Lan83]  M. Langevin et al., '$^{35}$Na: a new neutron-rich sodium isotope', Phys. Lett. B 125 (1983) 116–118.

[LAS]  http://www.las.de.

[Las96]  N. Catalan Lasheras, M. Crescenti and M. Vretenar, 'Commissioning and experience in stripping, filtering and measuring the 4.2 MeV/u lead ion beam at CERN LINAC 3', in [LIN96], 1996, pp. 363–365.

[Lat74]  A. Latuszyński, K. Zuber, J. Zuber, A. Potempa and W. Żuk, 'Method of electromagnetic separation of radioactive isotopes of rare-earth elements directly from targets', Nucl. Instr. Meth. 120 (1974) 321–328.

[Lat75]  A. Latuszynski and V.I. Raiko, 'Studies of the ion source with surface-volume ionization', Nucl. Instr. Meth. 125 (1975) 61–66.

[Lau82]  K.H. Lau and D.L. Hildenbrand, 'Thermodynamical properties of the gaseous lower valent fluorides of uranium', J. Chem. Phys. 76 (1982) 2646–2652.

[Lau90]   H.M. Lauranto, I.H. Auterinen, T.T. Kajava, K.M. Nyholm and R.R.E. Salomaa, 'Determination of hyperfine structures and Rydberg convergence limits of selected optical transitions in $^{93}$Nb using resonance ionization spectroscopy', Appl. Phys. B 50 (1990) 323–329.

[Lau92]   W. Lauth et al., 'Resonance ionization spectroscopy in a buffer gas cell with radioactive decay detection, demonstrated using $^{208}$Tl', Phys. Rev. Lett. 68 (1992) 1675–1678.

[Law65]   J.N.P. Lawrence, 'Static fission barrier calculations of a two-parameter liquid drop', Phys. Rev. 139 (1965) B1227–B1231.

[Laz87]   Yu.A. Lazarev et al., 'Observation of delayed nuclear fission in the region of $^{180}$Hg', Europhys. Lett. 4 (1987) 893–898.

[Laz97]   Yu.A. Lazarev and Yu.Ts. Oganessian, 'Nuclear fusion studies with PIAFE beams', in [Ben96], 1997, pp. 314–339.

[Leb98]   E. Lebiush et al., 'High power high repetition rate diode side-pumped Q-switched Nd:YAG rod laser', Opt. Comm. 145 (1998) 119–122.

[Lec97]   N. Lecesne et al., 'A new method for measuring the absolute efficiency of isotope separation on-line', Nucl. Instr. Meth. B 126 (1997) 141–145.

[Led98]   X. Ledoux et al., 'Formation and decay of hot nuclei in 475 MeV, 2 GeV proton- and 2 GeV $^3$He-induced reactions on Ag, Bi, Au and U', Phys. Rev. C 57 (1998) 2375–2392.

[Lee96]   Y. Lee et al., 'Production of low energy spread ion beams with multicusp sources', Nucl. Instr. Meth. A 374 (1996) 1–6.

[Leh83]   B.E. Lehmann et al., 'A pulsed laser ionization source for an ultrasensitive noble gas mass spectrometer', in H.P. Weber and W. Lüthy, eds., 'Laser Spectroscopy VI, Proc. of Sixth Int. Conf., Interlaken, Switzerland', Springer, Berlin, 1983 p. 100.

[Lei97]   M. Leino, 'In-flight separation with gas-filled systems', Nucl. Instr. Meth. B 126 (1997) 320–328.

[Ler98]   R. Leroy et al., 'Constraints due to the production of radioactive ion beams in the SPIRAL project', Rev. Sci. Instr. 69 (1998) 758–760.

[Lettr]   Jacques Lettry, priv. comm.

[Let77]   V.S. Letokhov, V.I. Mishin and A.A. Puretzky, 'Selective photoionization of atoms by laser radiation and its applications', Prog. Quant. Electr. 5 (1977) 139–203.

[Let87]   V.S. Letokhov, *Laser photoionization spectroscopy*, Academic Press, Orlando (1987).

[Let97a]  J. Lettry et al., 'Pulse shape of the ISOLDE radioactive ion beams', Nucl. Instr. Meth. B 126 (1997) 130–134.

[Let97b]  J. Lettry et al., 'Release from ISOLDE molten metal targets under pulsed proton beam conditions', Nucl. Instr. Meth. B 126 (1997) 170–175.

[Let98]   J. Lettry et al., 'Recent developments of the ISOLDE laser ion source', Rev. Sci. Instr. 69 (1998) 761–763.

[Lev99]   J.M.G. Levins et al., 'First on-line laser spectroscopy of radioisotopes of a refractory element', Phys. Rev. Lett. 82 (1999) 2476–2479.

[Lia82]   C.F. Liang et al., 'Selective on-line separation of new Ta, Zr and Sr isotopes', Z. Phys. A 309 (1982) 185–186.

[Lia96]   C.F. Liang, P. Paris, R.K. Sheline, P. Alexa and A. Gizon, '$\alpha$-decay of $^{216}$Fr and $^{212}$At', Phys. Rev. C C54 (1996) 2304–2309.

[Lia99]   C.F. Liang, P. Paris and R.K Sheline, 'Configurations and level structure of $^{215}$Po', Phys. Rev. C 59 (1999) 648–654.

[HB]     David R. Lide, ed., *Handbook of Chemistry and Physics*, CRC Press, Cleveland, 79th edn. (1998).

[LIN96]  C. Hill and M. Vretenar, eds., 'Proc. of the XVIII int. linear accelerator conference', CERN, Geneva, 1996.

[Lin97]  M. Lindroos et al., 'Measurement of the magnetic moment of $^{23}$Mg using the tilted foil polarization technique', Nucl. Instr. Meth. B 126 (1997) 423–426.

[Lun88]  E. Lund, B. Ekström, B. Fogelberg and G. Rudstam, 'Identification and half-life determination of very neutron-rich copper isotopes', in I.S. Towner, ed., 'Fifth Int. Conf. on Nuclei far from Stability, Rosseau Lake, Ontario, 1987', AIP Conf. Proc. 164, 1988, pp. 578–580.

[Lun97]  D. Lunney et al., 'Accurate mass measurements of very short-lived nuclei at ISOLDE with MISTRAL', in [Ben96], 1997, pp. 225–230.

[Lun99]  M.D. Lunney and R.B. Moore, 'Cooling of mass-separated beams using an RFQ ion guide', Int. J. Mass Spectrometry 190/191 (1999) 153–160.

[Lyu86]  Yu.S. Lyutostanskii, 'The processes which accompany $\beta$-decay of nuclei with a great excess of neutrons', Bull. Acad. Sci. USSR, Phys. Ser. 50 (1986) 1–13.

[Mac87]  H. Mach et al., 'Search for new isotopes in the mass 149-152 region', Bull. Am. Phys. Soc. 32 (1987) 1018, only abstract!

[Mac95]  H. Mach et al., 'Detailed spectroscopy of doubly-magic $^{132}$Sn and its neighbours; perspective for further studies at PIAFE', Nucl. Phys. A 588 (1995) 179c–184c.

[MAFF]   D. Habs et al., eds., *MAFF, Munich Accelerator for Fission Fragments, Physics Case and Technical Description*, Ludwig-Maximilians-Universität, München (Oct 1998).

[Maier]  Hans-Jörg Maier, priv. comm.

[Mai70]  L.I. Maissel and R. Glang, *Handbook of Thin Film Technology*, McGraw-Hill, New York (1970).

[Mam98]  A. Mamdouh, J.M. Pearson, M. Rayet and F. Tondeur, 'Large-scale fission-barrier calculations with the ETFSI method', Nucl. Phys. A 644 (1998) 389–414.

[Manti]  Paul Mantica, priv. comm.

[Man68]  C.L. Mantell, *Carbon and Graphite Handbook*, Interscience Publishers, New York (1968).

[Man72]  F. Manero and V.A. Konshin, 'Status of the energy-dependent $\bar{\nu}$-values for the heavy isotopes ($Z > 90$) from thermal to 15 MeV and of $\bar{\nu}$-values for spontaneous fission', At. Energy Rev. 10 (1972) 637–756.

[Mar79]  D. Marx, F. Nickel and W. Thalheimer, 'Rotating sandwich targets of isotopically enriched lead for high intensity heavy ion beams', Nucl. Instr. Meth. 167 (1979) 151–152.

[Mar87]  Y. Maruyama, Y. Suzuki, T. Arisawa and K. Shiba, 'Laser isotope separation of titanium by two-step photoionization', Appl. Phys. B 44 (1987) 163–166.

[Mar95]  A. Marijnissen, J.J. ter Meulen, P.A. Hackett and B. Simard, 'First ionization potential of platinum by mass-selected double-resonance field-ionization spectroscopy', Phys. Rev. A 52 (1995) 2606–2610.

[Mat73]  Hj. Matzke and C. Politis, 'Self-diffusion of uranium in uranium dicarbide $UC_2$', Solid State Comm. 12 (1973) 401–404.

[Mat80]  Hj. Matzke, 'Gas release mechanisms in $UO_2$ – a critical review', Rad. Eff. 53 (1980) 219–242.

[Mat86]  Hj. Matzke, 'Diffusion processes in nuclear fuels', J. Less-Common Metals 121 (1986) 537–564.

[Mat95]   O.I. Matveev, P. Cavalli and N. Omenetto, 'Three-step laser induced ionization of Ir and Hg atoms in an air-acetylene flame and a gas cell', in [RIS94], 1995, pp. 269–272.

[May90]   S. Mayo, J.D. Fassett, H.M. Kingston and R.J. Walker, 'Measurement of vanadium impurity in oxygen-implanted silicon by isotope dilution and resonance ionization mass spectrometry', Anal. Chem. 62 (1990) 240–244.

[Maz81]   K. Mazumdar et al., 'Performance of the on-line isotope separation facility HELIOS at the Mainz reactor', Nucl. Instr. Meth. 186 (1981) 131–134.

[McC75]   J.R. McConnell and W.L. Talbert, 'The TRISTAN on-line isotope separator facility', Nucl. Instr. Meth. 128 (1975) 227–243.

[Meh73]   G.K. Mehta, J. Poitou, M. Ribrag and C. Signarbieux, 'Detailed study of alpha emission in $^{252}$Cf fission', Phys. Rev. C 7 (1973) 373–387.

[Mei39]   L. Meitner and O.R. Frisch, 'Disintegration of uranium by neutrons: a new type of nuclear reaction', Nature 143 (1939) 239–240.

[Men97]   Mariano Menna, *Nuclear and radiochemistry at CERN-ISOLDE: target synthesis and diffusion studies*, Master's thesis, Università di Napoli "Federico II" (1997).

[Mey88]   R.J. Meyer, E.H.E. Pietsch and A. Kotowski, eds., *Thorium Supplement*, vol. A3 of *Gmelin Handbuch der Anorganischen Chemie*, Springer, Berlin, 8th edn. (1988).

[Mey89]   B.S. Meyer et al., 'Beta-delayed fission and neutron emission calculations for the actinide cosmochronometers', Phys. Rev. C 39 (1989) 1876–1882.

[Mez90]   K.A. Mezilev, Yu.N. Novikov, A.V. Popov, Yu.Ya. Sergeev and V.IU. Tikhonov, 'Search for delayed fission in neutron-rich nuclei', Z. Phys. A 337 (1990) 109.

[Mic77]   H.B. Michaelson, 'The work function of the elements and its periodicity', J. Appl. Phys. 48 (1977) 4729–4733.

[Mic97]   R. Michel and P. Nagel, 'International codes and model intercomparison for intermediate energy activation yields', Rep. NSC/DOC(97)-1, Nuclear Energy Agency, OECD, Paris (1997).

[Mil82]   C.M. Miller, N.S. Nogar, A.J. Gancarz and W.R. Shields, 'Selective laser photoionization for mass spectrometry', Anal. Chem. 54 (1982) 2377–2378.

[Min86]   T. Minowa, H. Katsuragawa, A. Kawamura and M. Shimazu, 'Highly sensitive detection of thallium atoms using resonance ionization', Opt. Comm. 60 (1986) 37–40.

[Min92]   T. Minowa, H. Katsuragawa and H. Komatsu, 'Resonance ionization spectroscopy of molybdenum and its applications to a pure ion source', Nucl. Instr. Meth. B 72 (1992) 255–260.

[Mir78]   M.Y. Mirza and W.W. Duley, 'Two photon laser spectroscopy of indium', Proc. Roy. S. Lond. A 364 (1978) 255–263.

[Mir83]   S. Mirzadeh, P.P. Parekh, S. Katcoff and Y.Y. Chu, 'Cross-section systematics for nuclide production at a medium energy spallation neutron facility', Nucl. Instr. Meth. 216 (1983) 149–154.

[Mis87a]   V.I. Mishin and V.N. Fedoseev, 'Laser resonance photoionization spectroscopy of excited and autoionizing atomic states of rare-earth elements. 2: Gadolinium', Opt. Spectr. (USSR) 63 (1987) 420–422.

[Mis87b]   V.I. Mishin et al., 'Resonance photoionization spectroscopy and laser separation of $^{141}$Sm and $^{164}$Tm nuclear isomers', Opt. Comm. 61 (1987) 383–386.

[Mis93]   V.I. Mishin et al., 'Chemically selective laser ion-source for the CERN-ISOLDE on-line mass separator facility', Nucl. Instr. Meth. B 73 (1993) 550–560.

[Miy86]    K. Miyazaki, H. Sakai and T. Sato, 'Efficient deep-ultraviolet generation by frequency doubling in $\beta$-BaB$_2$O$_4$ crystals', Opt. Lett. 11 (1986) 797–799.

[MK72]     P. Maier-Komor, 'A simple technique of producing thin carbon films', Nucl. Instr. Meth. 102 (1972) 485–486.

[Moi76]    B.L. Moiseiwitsch, *Negative ions*, North-Holland, Amsterdam (1976).

[Mol70]    E. Moll et al., 'A mass spectrometer for the investigation of fission products', in H. Wagner and W. Walcher, eds., 'Proc. of the Int. Conf. on Electromagnetic Isotope Separators and the Techniques of their Applications', Universität Marburg, Report BMBW-FB K 70-28, 1970, pp. 241–254.

[Mol77]    E. Moll et al., 'Design and working principles of the Lohengrin mass separator for fission products at the high flux reactor in Grenoble', Kerntechnik 19 (1977) 374–381.

[Möl95]    P. Möller, J.R. Nix, W.D. Myers and W.J. Swiatecki, 'Nuclear ground-state masses and deformations', At. Data Nucl. Data Tables 59 (1995) 185–381.

[Möl97]    P. Möller, J.R. Nix and K.L. Kratz, 'Nuclear properties for astrophysical and radioactive-ion-beam applications', At. Data Nucl. Data Tables 66 (1997) 131–343.

[Moo85]    L.J. Moore, J.D. Fassett, J.C. Travis, T.B. Lucatorto and C.W. Clark, 'Resonance-ionization mass spectrometry of carbon', J. Opt. Soc. Amer. B 2 (1985) 1561–1565.

[Mor72]    L.G. Moretto, 'Pairing fluctuations in excited nuclei and the absence of a second order phase transition', Phys. Lett. 40B (1972) 1–4.

[Mor94]    D.J. Morrissey, W. Benenson and W.A. Friedman, 'Measurement of temperature in nuclear reactions', Annu. Rev. Nucl. Part. Sci. 44 (1994) 27–63.

[Mor95]    K. Morita et al., 'New $\alpha$-decaying neutron deficient isotopes $^{197}$Rn and $^{200}$Fr', Z. Phys. A 352 (1995) 7–8.

[Mot97]    B. Le Motais and V. Panchout, 'Urananreicherung in Frankreich', atw 42 (1997) 626–628.

[Muc83]    M.L. Muchnik et al., 'Production of the indium ion beam with the method of selective laser photoionization', Sov. J. Quant. Electr. 10.

[Mue99]    W.F. Mueller et al., 'On the magicity of the $^{68}$Ni semi-double-magic nucleus probed by Gamow-Teller decay of the odd-$A$ neighbors', Phys. Rev. Lett. 83 (1999) 3613–3616.

[Mül98]    P. Müller et al., 'Ultratrace determination of the long-lived isotope $^{41}$Ca', in [RIS98], 1998.

[Münze]    Gottfried Münzenberg, priv. comm.

[Mün79]    G. Münzenberg et al., 'The velocity filter SHIP, a separator of unslowed heavy ion fusion products', Nucl. Instr. Meth. 161 (1979) 65–82.

[Mut96a]   M. Mutterer and J.P. Theobald, *Particle-accompanied fission*, IOP, Bristol, 1996, pp. 487–530.

[Mut96b]   M. Mutterer et al., 'Recent results on the energetics of the ternary fission process', in [Dan96], 1996, pp. 250–261.

[Mut99]    M. Mutterer et al., 'Angular correlations with $\gamma$-rays and neutrons in ternary fission of $^{252}$Cf', in C. Wagemans, O. Serot and P. D'Hondt, eds., 'Seminar on Fission, Pont d'Oye IV', World Scientific, Singapore, 1999, pp. 95–109.

[Nak97]    H. Nakata, T. Tachibana and M. Yamada, 'Semi-gross theory of nuclear $\beta$-decay', Nucl. Phys. A 625 (1997) 521–553.

[Nak98]    T. Nakamura et al., 'Coulomb dissociation of $^{19}$C', in [ENA98], pp. 215–220.

[Nar69]    E. Nardi, Y. Boneh and Z. Fraenkel, 'Trajectory calculations in light-particle fission', in 'Conf. on Physics and Chemistry of Fission', IAEA, Vienna, 1969, pp. 143–152.

[Nesvi]   Valery Nesvishevsky, priv. comm.

[Nes63]   A.N. Nesmeyanov, *Vapor pressure of the chemical elements*, Elsevier, Amsterdam (1963).

[Neu62]   S. Neumann and H. Ewald, 'Fokussierende Parabelspektrographen', Z. Phys. 169 (1962) 224–238.

[Neu92]   Sigurd Neumaier, *Energieverteilungen und Häufigkeiten der leichten Teilchen* $5 \leq Z \leq 8$ *bei der teilchenbegleiteten Spaltung von* $^{242}Am(n_{th},f)$, Master's thesis, TH Darmstadt (1992).

[Ney97]   G. Neyens, G. S'heeren and R. Coussement, 'Nuclear orientation in a two-step laser ionization process', Nucl. Instr. Meth. B 122 (1997) 121–126.

[Nic82]   F. Nickel, 'The influence of temperature on stripper foil lifetimes', Nucl. Instr. Meth. 195 (1982) 457–460.

[Nie57]   K.O. Nielsen, 'The development of magnetic ion sources for an electromagnetic isotope separator', Nucl. Instr. Meth. 1 (1957) 289–301.

[Nik68]   V.S. Nikolaev and I.S. Dmitriev, 'On the equilibrium charge distribution in heavy element ion beams', Phys. Lett. 28A (1968) 277–278.

[Nin99]   V. Ninov et al., 'Observation of superheavy nuclei produced in the reaction of $^{86}$Kr with $^{208}$Pb', Phys. Rev. Lett. 83 (1999) 1104–1107.

[NISTA]   'NIST Atomic Spectra Database', http://physics.nist.gov/cgi-bin/AtData/display.ksh.

[Nis73]   K. Nishizawa, K. Narisada, H. Teranatsu, M. Soya and M. Shinagawa, 'Charge distribution for $^{133}$Xe-$^{133}$Cs decay process', Mass Spectrometry (Japan) 21 (1973) 45–51.

[Nit85]   J.M. Nitschke, 'An electron-beam-generated-plasma ion source for on-line isotope separation', Nucl. Instr. Meth. A 236 (1985) 1–16.

[NL92]   Ute Nast-Linke, *Die relativen Häufigkeiten der leichten geladenen Teilchen der teilchenbegleiteten Spaltung*, Master's thesis, TH Darmstadt (1992).

[Nod34]   I. Noddack, 'über das Element 93', Angew. Chem. 47 (1934) 653–655.

[Nolen]   Jerry Nolen, priv. comm.

[Nor51]   L.W. Nordheim, 'Nuclear shell structure and beta-decay. II. Even $A$ nuclei', Rev. Mod. Phys. 23 (1951) 322–327.

[Nor63]   L.C. Northcliffe, 'Passage of heavy ions through matter', Annu. Rev. Nucl. Sci. 13 (1963) 67–102.

[Num01]   S. Nummela et al., 'Spectroscopy of $^{34,35}$Si by $\beta$ decay: sd-fp shell gap and single-particle states', Phys. Rev. C (2001) in press.

[Obe92]   S. Oberstedt and N. Cârjan, 'Information on nuclear shapes near the scission point from internal trajectory calculations', Z. Phys. A 344 (1992) 59–66.

[Oinon]   Markku Oinonen, priv. comm.

[Oin99]   M. Oinonen et al., 'Beta decay of $^{61}$Ga', Eur. Phys. J. A 5 (1999) 151–156.

[Oin01]   M. Oinonen et al., 'Ground-state spin of $^{59}$Mn', Eur. Phys. J. A (2001) in press.

[Orr98]   N. Orr et al., 'TONNERRE: an array for delayed-neutron spectroscopy', Nouvelles du GANIL 63 (1998) 4–7.

[Ort61]   C.J. Orth, 'Diffusion of lanthanides and actinides from graphite at high temperatures', Nucl. Sci. Eng. 9 (1961) 417–420.

[Ott89]   E.W. Otten, *Nuclear Radii and Moments of Unstable Isotopes*, vol. 8 of *Treatise on Heavy-Ion Science*, Plenum Press, New York (1989).

[Oya98]     M. Oyaizu et al., 'Beam bunching of the radioactive nuclear beam in a 6.4 GHz electron cyclotron resonance ion source', Rev. Sci. Instr. 69 (1998) 770–772.

[Pag94]     R.D. Page et al., 'Decays of odd-odd $N - Z = 2$ nuclei above $^{100}$Sn: the observation of proton radioactivity from $^{112}$Cs', Phys. Rev. Lett. 72 (1994) 1798–1801.

[Par76]     P. Paris et al., 'Development of the Orsay high current on-line separator ISOCELE', Nucl. Instr. Meth. 139 (1976) 251–256.

[Pat70]     P. Patzelt, 'The hydroxides of titanium, zirconium, cerium (IV) and thorium for on-line production of noble gases', Rep. 70-3, CERN, Geneva (1970).

[Pen95]     Yu.E. Penionzhkevich, 'Investigation of very neutron-rich isotopes of the lightest elements', in [ENA95], 1995, pp. 269–274.

[Pet98]     J.R. Peterson et al., 'Determination of the first ionization potential of einsteinium by resonance ionization mass spectroscopy (RIMS)', J. Alloys and Compounds 271-273 (1998) 876–878.

[Pfe99]     B. Pfeiffer, K.L. Kratz and P. Möller, 'Predictions of $T_{1/2}$- and $P_n$-values', rep., Institut für Kernchemie, Johannes-Gutenberg Universität Mainz (1999).

[Pfü98]     M. Pfützner et al., 'New isotopes and isomers produced by the fragmentation of $^{238}$U at 1000 MeV/nucleon', Phys. Lett. B 444 (1998) 32–37.

[PIAFE]     U. Köster and J.A. Pinston, eds., *PIAFE (Production, Ionisation et Accélération des Faisceaux Exotiques), Project Report*, Institut des Sciences Nucléaires, Grenoble (Mar 1998).

[Pia80]     E. Piasecki and L. Nowicki, 'Polar emission in fission', in 'Physics and Chemistry of Fission 1979, Proc. of an Int. Symp., Jülich', IAEA, Vienna, 1980, pp. 193–221.

[Pil87]     E.H. Pilzer and G. Engler, 'A new ion source for fission-yield measurements of rare-earth isotopes', Nucl. Instr. Meth. B 26 (1987) 218–222.

[Pin77]     J. Pinard and S. Liberman, 'A frequency locked, single mode pulsed dye laser. Application to single frequency tunable UV generation', Opt. Comm. 20 (1977) 344–346.

[Pio97]     A. Piotrowski, T. Kozlowski and M. Laskus, 'Study of negative ion emission from the tubular ionizer', Nucl. Instr. Meth. 129 (1997) 410–413.

[Plo92]     A. Plochoki et al., 'Gamow-Teller beta decay of the very neutron-deficient $N = 50$ nuclide $^{98}$Cd', Z. Phys. A 342 (1992) 43–51.

[Poe89]     D.N. Poenaru and M.S. Ivascu, eds., *Particle emission from nuclei*, CRC Press, Boca Raton (1989).

[Pol89]     S. Polikanov, 'Meson, hyperon and antiproton induced fission', Nucl. Phys. A 502 (1989) 195c–212c.

[Pos65]     A.M. Poskanzer, P.L. Reeder and I. Dostrovsky, 'New delayed-neutron-emitting isotope: $^{12}$Be', Phys. Rev. 138 (1965) B18–B20.

[Pou87]     F. Pougheon et al., 'Direct observation of new proton rich nuclei in the region $23 \leq Z \leq 29$ using a $55A$ MeV $^{58}$Ni beam', Z. Phys. A 327 (1987) 17–24.

[PP84]      G.A. Pik-Pichak, 'Ternary fission with emission of $\alpha$ particles', Sov. J. Nucl. Phys. 40 (1984) 215–222.

[PP94]      G.A. Pik-Pichak, 'On the mechanism of ternary fission with emission of light charged particles', Phys. At. Nucl. 57 (1994) 906–913.

[Pre41]     R.D. Present, 'Possibility of ternary fission', Phys. Rev. 59 (1941) 466.

[PSyie]     ISOLDE PSB yield databank, unpublished.

[Put81]     J.C. Putaux et al., 'Target ion source systems at the Orsay ISOCELE 2 separator', Nucl. Instr. Meth. 186 (1981) 321–328.

[Put87]   J.C. Putaux, J. Obert, G. Boissier and P. Paris, 'Comparison between Nier-Bernas and Nielsen type ion sources for extracted ion-beam intensities in the mA range', Nucl. Instr. Meth. B 26 (1987) 213–217.

[Put97]   J.C. Putaux et al., 'Graphite target for the SPIRAL project', Nucl. Instr. Meth. B 126 (1997) 113–116.

[Qui93]   B. Quint et al., 'Investigation of the fusion of heavy nearly symmetric systems', Z. Phys. A 346 (1993) 119–131.

[Rab87]   V. Rabbel et al., 'A negative surface-ionization ion source for the on-line mass separator OSTIS', Nucl. Instr. Meth. B 26 (1987) 246–248.

[Rad75]   L.J. Radziemski, S. Gerstenkorn and P. Luc, 'Uranium transitions and energy levels which may be useful in atomic-photoionization schemes for separating $^{238}$U and $^{235}$U', Opt. Comm. 15 (1975) 273–276.

[Rad85]   A.A. Radzig and B.M. Smirnov, *Reference Data on Atoms, Molecules and Ions*, Springer, Berlin (1985).

[Rai68]   G.M. Raisbeck and T.D. Thomas, 'Light nuclei emitted in the fission of $^{252}$Cf', Phys. Rev. 172 (1968) 1272–1282.

[Ram96]   A.V. Ramayya et al., 'Cold fragmentation in the spontaneous fission of $^{252}$Cf', in [Dan96], 1996, pp. 307–321.

[Ram97]   A.V. Ramayya et al., 'Cold binary and ternary fragmentations in spontaneous fission of $^{252}$Cf', Il Nuovo Cimento 110 A (1997) 1073–1078.

[Ram98a]  A.V. Ramayya et al., 'Cold (neutronless) $\alpha$ ternary fission of $^{252}$Cf', Phys. Rev. C 57 (1998) 2370–2374.

[Ram98b]  A.V. Ramayya et al., 'Observation of $^{10}$Be emission in the cold ternary spontaneous fission of $^{252}$Cf', Phys. Rev. Lett. 81 (1998) 947–950.

[Rao97]   R. Rao and O. Kultashev, 'Ir-Ce cathodes as high-density emitters in electron beam ion sources', Meas. Sci. Technol. 8 (1997) 184–188.

[Rav75a]  H.L. Ravn, S. Sundell, L. Westgaard and E. Roeckl, 'Short-lived isotopes of alkali and alkaline-earth elements studied by on-line isotope separator techniques', J. Inorg. Nucl. Chem. 37 (1975) 383–393.

[Rav75b]  H.L. Ravn, S. Sundell, L. Westgaard and the ISOLDE Collaboration, 'Target techniques for the ISOLDE on-line isotope separator', Nucl. Instr. Meth. 123 (1975) 131–144.

[Rav76]   H.L. Ravn, 'Progress in targets and ion sources for on-line separators', Nucl. Instr. Meth. 139 (1976) 281–290.

[Rav79]   H.L. Ravn, 'Experiments with intense secondary beams of radioactive ions', Phys. Rep. 54 (1979) 201–259.

[Rav87]   H.L. Ravn et al., 'Use of refractory oxides, carbides and borides as targets for on-line mass separation', Nucl. Instr. Meth. B 26 (1987) 183–189.

[Rav89]   H.L. Ravn and B.W. Allardyce, *On-line mass separators*, vol. 8 of *Treatise on Heavy-Ion Science*, Plenum Press, New York (1989).

[Rav94]   H.L. Ravn et al., 'Comparison of radioactive ion-beam intensities produced by means of thick targets bombarded with neutrons, protons and heavy ions', Nucl. Instr. Meth. B 88 (1994) 441–461.

[Rav97a]  H.L. Ravn, 'ISOLDE ion sources and targets with relevance to PIAFE', in [Ben96], 1997, pp. 62–68.

[Rav97b]  H.L. Ravn et al., 'Bunched release of gases from oxide targets', Nucl. Instr. Meth. B 126 (1997) 176–181.

[Rav98]   H.L. Ravn, 'Radioactive ion-beam projects based on the two-accelerator or ISOL principle', Phil. Trans. R. Soc. Lond. A 356 (1998) 1955–1984.

[Ray99]   A. Ray et al., 'Observation of large change of $^7$Be decay rate in Au and $Al_2O_3$ and its implications', Phys. Lett. B 455 (1999) 69–76.

[Ree76]   P.L. Reeder, L.J. Alquist and J.F. Wright, 'Separation of alkaline earth from alkali metal fission products in the SOLAR on-line mass spectrometer', Nucl. Instr. Meth. 133 (1976) 501–502.

[Ree77]   T. Reetz, B. Eichler, H. Gäggeler and I. Zvara, 'Verflüchtigung der Schwerionenreaktionsprodukte Hg, Tl, Pb und Bi aus den Catchermaterialien Cu, Au, Ni und Graphit', Radiochim. Acta 24 (1977) 69–72.

[Ree81]   P.L. Reeder and R.A. Warner, 'Measurement of average neutron energies by a counting rate ratio technique', Nucl. Instr. Meth. 180 (1981) 173–183.

[Ree85]   P.L. Reeder, R.A. Warner, G.P. Ford and H. Willmes, 'Independent isomer yield ratio of $^{90}$Rb from thermal neutron fission of $^{235}$U', Phys. Rev. C 32 (1985) 1327–1334.

[Ree91]   P.L. Reeder, R.A. Warner, W.K. Hensley, D.J. Vieira and J.M. Wouters, 'Half-lives and delayed neutron emission probabilities of neutron-rich Li-Al nuclides', Phys. Rev. C 44 (1991) 1435–1453.

[Rei75]   W.L. Reiter, W.H. Breunlich and P. Hille, 'Short-lived activities produced in $^{70}$Zn with 14 MeV neutrons', Nucl. Phys. A 249 (1975) 166–172.

[Rei80]   L. von Reisky et al., 'An on-line mass separator for fission-produced alkali isotopes', Nucl. Instr. Meth. 172 (1980) 423–430.

[Ren97]   Sh. Rencheng et al., 'Laser ion source via direct ionization at the outlet of a helium jet', Rev. Sci. Instr. 68 (1997) 3027–3030.

[Reu99]   I. Reusen et al., '$\beta$-decay study of $^{54,55}$Ni produced by an element-selective laser ion source', Phys. Rev. C 59 (1999) 2416–2421.

[Richa]   Jean-Paul Richaud, priv. comm.

[Ric99]   M.V. Ricciardi et al., 'Dependence of exotic nuclides production on target and beam features', Ann. Nucl. En. 26 (1999) 1643–1656.

[Ric01]   M.V. Ricciardi et al., 'Experimental study on the production of light nuclei in spallation-fission reactions and projectile fragmentation of $^{238}$U', Nucl. Phys. A (2001) in press.

[Rie93]   J. Riegel et al., 'Resonance ionization mass spectroscopy for trace analysis of neptunium', Appl. Phys. B 56 (1993) 275–280.

[Rii92]   K. Riisager, A.S. Jensen and P. Möller, 'Two-body halos', Nucl. Phys. A 548 (1992) 393–413.

[Rikov]   Jirina Rikovska, priv. comm.

[RIS94]   H.J. Kluge, J.E. Parks and K. Wendt, eds., '7th Int. Symp. on Resonance Ionization Spectroscopy, RIS'94, Bernkastel-Kues', AIP Conf. Proc. 329, Woodbury, 1995.

[RIS98]   J.C. Vickerman, I. Lyon, N.P. Lockyer and J.E. Parks, eds., 'Proc. of the 9th Int. Symp. on Resonance Ionisation Spectroscopy, Manchester', AIP Conf. Proc. 454, Woodbury, NY, 1998.

[Rob39]   R.B. Roberts, R.C. Meyer and P. Wang, 'Further observations on the splitting of uranium and thorium', Phys. Rev. 55 (1939) 510–511.

[Roe74]   E. Roeckl et al., 'Decay properties of the neutron-rich isotopes $^{11}$Li and $^{27-31}$Na', Phys. Rev. C 10 (1974) 1181–1188.

[Roe80]   E. Roeckl et al., 'The decay of 0.57 s $^{114}$Cs', Z. Phys. A 294 (1980) 221–232.

[Roosb]   Jan Van Roosbroeck, priv. comm.

[Rös86]   F. Rösch and B. Eichler, 'Adsorption von Metallen auf metallische Oberflächen und Möglichkeiten ihrer Nutzung in der Kernchemie - Modellberechnungen zur Trennung von Radionukliden durch thermische Desorption von festen Metalloberflächen', Rep. ZfK-575, Zentralinstitut für Kernforschung, Rossendorf (1986).

[Ros94]   A.S. Roshchin, V.A. Rubchenya and S.G. Yavshits, 'Trajectory calculations of ternary fission of nuclei', Phys. At. Nucl. 57 (1994) 974–983.

[Roß84]   H. Roßbach and B. Eichler, 'Adsorption von Metallen auf metallische Oberflächen und Möglichkeiten ihrer Nutzung in der Kernchemie - Ermittlung von Adsorptionsenthalpien mit dem Rechenprogramm APO', Rep. ZfK-527, Zentralinstitut für Kernforschung, Rossendorf (1984).

[Rot89]   I. Rotter, 'Particle decay and fission', J. Phys. G 15 (1989) 251–263.

[Roy92]   G. Royer, F. Haddad and J. Mignen, 'On nuclear ternary fission', J. Phys. G 18 (1992) 2015–2026.

[Rubch]   Valery Rubchenya, priv. comm.

[Rub88]   V.A. Rubchenya and S.G. Yavshits, 'Dynamic treatment of ternary fission', Z. Phys. A 329 (1988) 217–228.

[Rub94]   V.A. Rubchenya, A.S. Roschin and S.G. Yavshits, 'Fission dynamics and ternary fission', in [Sey94], 1994, pp. 26–36.

[Ruc82]   E. Ruchowska, W. Kurcewicz, N. Kaffrell, T. Bjørnstad and G. Nyman, 'The decay scheme of $^{228}$Fr and $K = 0$ bands in $^{228}$Ra', Nucl. Phys. A 383 (1982) 1–10.

[Rud76]   G. Rudstam, 'The on-line mass separator OSIRIS and the study of short-lived fission products', Nucl. Instr. Meth. 139 (1976) 239–249.

[Rud81]   G. Rudstam, P. Aagaard, P. Hoff, B. Johansson and H.U. Zwicky, 'Chemical separation combined with an ISOL-system', Nucl. Instr. Meth. 186 (1981) 365–379.

[Rud90]   G. Rudstam et al., 'Yields of products from thermal neutron-induced fission of $^{235}$U', Radiochim. Acta 49 (1990) 155–191.

[Rud91]   G. Rudstam, K. Aleklett and L. Sihver, 'Delayed-neutron branching ratios and average kinetic energies', Research report NFL-69, Univ. of Uppsala, The Studsvik Neutron Research Laboratory, S-61182 Nyköping (1991).

[Rud93]   G. Rudstam, K. Aleklett and L. Sihver, 'Delayed-neutron branching ratios of precursors in the fission product region', At. Data Nucl. Data Tables 53 (1993) 1–22.

[Rud94]   G. Rudstam, P.I. Johansson, K. Aleklett and J. Eriksen, 'Fast fission of $^{238}$U', in J.K. Dickens, ed., 'Proc. of the Int. Conf. on Nuclear Data for Science and Technology', American Nuclear Society, La Grange Park, Il, 1994, pp. 977–980.

[Rud96]   G. Rudstam, P.I. Johansson and J. Eriksen, 'Summary of yield values from thermal fission of $^{233}$U', Research report nfl-78, University of Uppsala (1996).

[Run83]   E. Runte et al., 'Decay studies of neutron-rich products from $^{76}$Ge induced multinucleon transfer reactions including the new isotopes $^{62}$Mn, $^{63}$Fe and $^{71,72,73}$Cu', Nucl. Phys. A 399 (1983) 163–180.

[Run85]   E. Runte et al., 'Decay studies of neutron-rich isotopes of manganese, iron, cobalt, nickel, copper and zinc', Nucl. Phys. A 441 (1985) 237–260.

[Rus89]   W. Ruster et al., 'A resonance ionization mass spectrometer as an analytical instrument for trace analysis', Nucl. Instr. Meth. A 281 (1989) 547–558.

[Ryk89]   K. Rykaczewski et al., 'Investigation of neutron-rich rare-earth nuclei including the new isotopes $^{177}$Tm and $^{184}$Lu', Nucl. Phys. A 499 (1989) 529–545.

[Ryk95]    K. Rykaczewski et al., 'Identification of new nuclei at and beyond the proton drip line near the doubly magic nucleus $^{100}$Sn', Phys. Rev. C 52 (1995) R2310–R2313.

[Sah20]    M.N. Saha, 'Ionization in the solar chromosphere', Phil. Mag. 40 (1920) 472.

[Sal90]    E.B. Saloman, 'A resonance ionization spectroscopy/resonance ionization mass spectrometry data service. I. Data sheets for As, B, Cd, C, Ge, Au, Fe, Pb, Si and Zn', Spectrochim. Acta 45B (1990) 37–83.

[Sal91]    E.B. Saloman, 'A resonance ionization spectroscopy/resonance ionization mass spectrometry data service. II. Data sheets for Al, Ca, Cs, Cr, Co, Cu, Kr, Mg, Hg and Ni', Spectrochim. Acta 46B (1991) 319–378.

[Sal92]    E.B. Saloman, 'A resonance ionization spectroscopy/resonance ionization mass spectrometry data service. III. Data sheets for Sb, Bi, P, Na and Sn', Spectrochim. Acta 47B (1992) 517–543.

[Sal93]    E.B. Saloman, 'A resonance ionization spectroscopy/resonance ionization mass spectrometry data service. IV. Data sheets for Be, In, Li, K, Rb, Ag, Ti and V and an update of the data sheet for Ni', Spectrochim. Acta B 48B (1993) 1139–1203.

[Sal95]    E.B. Saloman, 'A resonance ionization spectroscopy/resonance ionization mass spectrometry data service. V. Data sheets for Ga, Mn, Sc and Ti', Spectrochim. Acta B 49B (1995) 251–281.

[Sam71]    G.V. Samsonov, V.Ya. Naumenko and L.N. Okhremchuk, 'Herstellung und Eigenschaften von Karbiden der Übergangsmetalle in ihren Homogenitätsbereichen', Phys. Stat. Sol. (a) 6 (1971) 201–211.

[San97]    A. Sandulescu et al., 'Binary and ternary cold fission of $^{252}$Cf', Il Nuovo Cimento 110 A (1997) 1079–1087.

[San98b]   A. Sandulescu et al., 'Cold (neutronless) alpha ternary fission of $^{252}$Cf: theory and comparison with experiment', Int. J. Mod. Phys. E 7 (1998) 625–638.

[Sau84]    J. Sauvage et al., 'The ISOCELE II separator: a general description, recent results and future developments', in J. Crawford and J.M. D'Auria, eds., 'Proceedings of the TRIUMF-ISOL Workshop, Mont Gabriel, Québec', TRIUMF, report TRI-84-1, 1984, pp. 161–178.

[Sav62]    E.M. Savitzkii and M.A. Tylkina, *Physical Properties of Re and its Alloys*, Elsevier, Amsterdam, 1962, pp. 36–66.

[Sav01]    G. Savard, 'ISOL beams from fragmentation: the best of both worlds', Nucl. Phys. A (2001) in press.

[Schin]    Karlheinz Schindl, priv. comm.

[Sch91]    Arndt Schubert, *Emissionsmechanismen leichter geladener Teilchen bei der Spontanspaltung von $^{252}$Cf*, Ph.D. thesis, TU Dresden (1991).

[Sch92]    P. Schillebeeckx, C. Wagemans, A.J. Deruytter and R. Barthélémy, 'Comparative study of the fragments' mass and energy characteristics in the spontaneous fission of $^{238}$Pu, $^{240}$Pu and $^{242}$Pu and in the thermal-neutron-induced fission of $^{239}$Pu', Nucl. Phys. A 545 (1992) 623–645.

[Sch93]    Franz Scheerer, *Eine chemisch selektive Laserionenquelle zur on-line Isotopenseparation*, Ph.D. thesis, Johannes-Gutenberg Universität, Mainz (1993).

[Sch94]    P. Schillebeeckx, C. Wagemans, P. Geltenbort, F. Gönnenwein and A. Oed, 'Investigation of mass, charge and energy of $^{241}$Pu(n$_{th}$,f) fragments with the Cosi-Fan-Tutte spectrometer', Nucl. Phys. A 580 (1994) 15–32.

[Sch95]    R. Schäfer and T. Fliessbach, 'Quantum mechanical treatment of alpha-particle emission during fission', J. Phys. G 21 (1995) 861–878.

[Sch96]　A. Schüttauf et al., 'Universality of spectator fragmentation at relativistic bombarding energies', Nucl. Phys. A 607 (1996) 457–486.

[Sch97]　K. Schmidt et al., 'Decay properties of very neutron-deficient isotopes of silver and cadmium', Nucl. Phys. A 624 (1997) 185–209.

[Sch98a]　K.H. Schmidt et al., 'Influence of shell effects on fission probabilities and on fission-fragment properties of $^{238}$U projectile fragments', Nucl. Phys. A 630 (1998) 208c–214c.

[Sch98b]　W. Schwab et al., 'Fission of highly excited fragments from collisions of $750A\cdot$ MeV $^{238}$U-ions on $^{208}$Pb', Eur. Phys. J. A 2 (1998) 179–191.

[Sch01]　J. Schönfelder et al., 'SHIPTRAP - a capture and storage facility for heavy radionuclides at GSI', Nucl. Phys. A (2001) in press.

[Scriv]　Richard Scrivens, priv. comm.

[SCyie]　http://www.cern.ch/ISOLDE/normal/isoprodsc.html.

[Sea90]　Glenn T. Seaborg and Walter D. Loveland, *The Elements beyond Uranium*, John Wiley & Sons, New York (1990).

[Seb97]　V. Sebastian, T. Budiman and G. Huber, 'Laser preparation of bunched ion beams', Nucl. Instr. Meth. B 126 (1997) 73–75.

[Seb98]　V. Sebastian et al., 'Spectroscopic applications of the ISOLDE laser ion source', in [ENA98] pp. 126–129.

[Seb99]　Volker Sebastian, *Laserionisation und Laserionenquelle an ISOLDE/CERN*, Ph.D. thesis, Johannes-Gutenberg-Universität, Mainz (1999).

[Sem96]　D.R. Semon et al., '$l$-forbidden Gamow-Teller $\beta$-decay of $^{57}$Cu', Phys. Rev. C 53 (1996) 96–105.

[Sey94]　H. Faust and G. Fioni, eds., 'Proc. of the Workshop on Nuclear Fission and Fission-Product Spectroscopy, Seyssins', Institut Laue Langevin, ILL report 94FA05T, 1994.

[Sey98]　G. Fioni, H. Faust, S. Oberstedt and F.J. Hambsch, eds., 'Nuclear Fission and Fission-Product Spectroscopy, Second Int. Workshop, Seyssins, France', AIP Conf. Proc. 447, Woodbury, NY, 1998.

[Sha74]　S. Shalev and G. Rudstam, 'Energy spectra of delayed neutrons from separated fission products. (I). The precursors $^{85}$As, $^{87}$Br, $^{134}$Sn, $^{135}$Sb, $^{136}$Te and $^{137}$I', Nucl. Phys. A 230 (1974) 153–172.

[She96]　R. Sherr, 'Simple model of neutron "halo nuclei"', Phys. Rev. C 54 (1996) 1177–1181.

[Shi82]　K. Shima, T. Ishihara and T. Mikumo, 'Empirical formula for the average equilibrium charge-state of heavy ions behind various foils', Nucl. Instr. Meth. 200 (1982) 605–608.

[Shi92]　K. Shima, N. Kuno, M. Yamanouchi and H. Tawara, 'Equilibrium charge fractions of ions of $Z = 4 - 92$ emerging from a carbon foil', At. Data Nucl. Data Tables 51 (1992) 173–241.

[Shm81]　M. Shmid, G. Engler, I. Yoresh and E. Skurnik, 'A negative surface ionization integrated target-ion source for an on-line isotope separator', Nucl. Instr. Meth. 186 (1981) 349–351.

[Shm83]　M. Shmid, R.L. Gill and C. Chung, 'Comparison between solid graphite and graphite cloth as a target backing material for an ISOL system', Nucl. Instr. Meth. 211 (1983) 287–291.

[Shu93a]　Y. Shuanggui et al., 'New neutron-rich nuclide $^{185}$Hf', Z. Phys. A 344.

[Shu93b]　Y. Shuanggui et al., 'The synthesis and identification of new heavy neutron-rich nuclide $^{237}$Th', Z. Phys. A 346.

[Sic89]   A. Sicre et al., 'Emission of Be, C and O isotopes in $^{235}$U(n$_{th}$,f)', preprint CENBG 8926, CENBG, Bordeaux-Gradignan (1989).

[Sid89]   J.L. Sida et al., 'Mass, charge and energy distributions in very asymmetric thermal fission of $^{235}$U', Nucl. Phys. A 502 (1989) 233c–242c.

[Sil73]   R. Silberberg and C.H. Tsao, 'Cross Sections of Proton-Nucleus Interactions at High Energies', NRL Report 7593, Naval Research Laboratory, Washington, D.C. (1973).

[Sil90]   R. Silberberg and C.H. Tsao, 'Spallation processes and nuclear interaction products of cosmic rays', Phys. Rep. 191 (1990) 351–408.

[Simon]   Haik Simon, priv. comm.

[Sim62]   C.T. Sims, *Properties of Rhenium*, Elsevier, Amsterdam, 1962, pp. 23–35.

[Sim94]   B. Simard, P. Kowalczyk and A.M. James, 'First ionization potential of tantalum by mass-selected double-resonance field-ionization spectroscopy', Phys. Rev. A 50 (1994) 846–849.

[Sin83]   A.K. Sinha and G.K. Mehta, 'Model for deriving scission configuration', Phys. Rev. C 28 (1983) 271–275.

[Sin89]   A.K. Sinha, D.M. Nadkarni and G.K. Mehta, 'Light-charge particle emission in fission', Pramāna J. Phys. 33 (1989) 85–107.

[Sin96]   P. Singer et al., 'New results on $\gamma$ emission in binary and ternary fission of $^{252}$Cf', in [Dan96], 1996, pp. 262–269.

[Sin97]   Peter Singer, *Kinematik und Abregungsprozeß der Fragmente und des ternären Teilchens bei der teilchenbegleiteten Spontanspaltung von $^{252}$Cf*, Ph.D. thesis, TH Darmstadt (1997).

[Skl98]   M. Sklodowska Curie, 'Rayons émis par les composés de l'uranium et du thorium', C. R. Acad. Sci. Paris 126 (1898) 1101–1103.

[Sko72]   N.K. Skobelev, 'Delayed fission of some neutron-deficient nuclei', Sov. J. Nucl. Phys. 15 (1972) 249–250.

[Smi92]   C.J. Smithells, *Smithells metals reference book*, Butterworth-Heinemann, Oxford, 7th edn. (1992).

[Smo97]   R. Smolanczuk, 'Properties of the hypothetical spherical superheavy nuclei', Phys. Rev. C 56 (1997) 812–824.

[SO87]   W.D. Schmidt-Ott et al., 'Search for light fragments in the $^{50}$Ti+$^{238}$U reaction', GSI scientific report 1987, p. 18, Darmstadt (1987).

[SO89]   W.D. Schmidt-Ott et al., 'Isotope production in fast fission of $^{20}$Ne and $^{238}$U', GSI scientific report 1989, p. 29, Darmstadt (1989).

[SO91]   W.D. Schmidt-Ott, 'Neutron-rich isotope production in reactions of $^{50}$Ti with $^{nat}$W and $^{238}$U in fission of $^{238}$U with 13 MeV/u $^{20}$Ne', Nucl. Phys. A 522 (1991) 610–620.

[SO92]   W.D. Schmidt-Ott et al., 'Conversion measurements in the odd-odd isotopes $^{58}$Mn and $^{60}$Mn', in [BKS92], 1992, pp. 627–629.

[Sol69]   Z.I. Solov'eva, 'Energy distribution of $\alpha$ particles formed in thermal-neutron fission of Pu$^{241}$ and Am$^{241}$', Sov. J. Nucl. Phys. 8 (1969) 264–266.

[Sorta]   Pascal Sortais, priv. comm.

[Sou88]   R.T. de Souza et al., 'Evolution of mass and charge asymmetry in damped heavy-ion reactions', Phys. Rev. C 37 (1988) 1783–1786.

[Spe72]   H.J. Specht, J. Weber, E. Konecny and D. Heunemann, 'Identification of a rotational band in the $^{240}$Pu fission isomer', Phys. Lett. 41B (1972) 43–46.

[Spr97]  G.D. Sprouse, L.A. Orozco, J.E. Simsarian, W. Shi and W.Z. Zhao, 'Laser trapping of radioactive francium atoms', Nucl. Instr. Meth. B 126 (1997) 370–373.

[SS82]  M. de Saint-Simon et al., 'Independent cross sections of Na, K, Rb, Cs and Fr isotopes produced in Ta and U targets bombarded by $^{12}$C ions up to 77 MeV/nucleon', Phys. Rev. C 26 (1982) 2447–2457.

[ST46]  T. San-Tsiang, R. Chastel, H. Zah-Wei and L. Vigneron, 'Sur la tripartition de l'uranium provoquée par la capture d'un neutron', C. R. Acad. Sci. Paris 223 (1946) 986–987.

[ST47]  T. San-Tsiang, H. Zah-Wei, R. Chastel and L. Vigneron, 'On the new fission processes of uranium nuclei', Phys. Rev. 71 (1947) 382–383.

[Sta92]  A. Staudt and H.V. Klapdor-Kleingrothaus, 'Calculation of $\beta$-delayed fission rates of neutron-rich nuclei far off stability', Nucl. Phys. A 549 (1992) 254–264.

[Ste71]  C.A. Stearns and F.J. Kohl, 'Vaporization thermodynamics of the lanthanum carbon system. Mass spectrometric determination of the dissociation energy of $LaC_2$, $LaC_3$ and $LaC_4$', J. Chem. Phys. 54 (1971) 5180–5187.

[Stolz]  Andreas Stolz, priv. comm.

[Stone]  N.J. Stone, 'Table of new nuclear moments (preprint)', http://www.nndc.bnl.gov/nndc/stone_moments/moments.html.

[Sto66]  R.W. Stoenner and M. Hillman, 'Search for radiochemical evidence for ternary fission of $^{235}$U by thermal neutrons', Phys. Rev. 142 (1966) 716–719.

[Sto96]  C. Stodel et al., 'Evaporation residue cross sections for the reaction $^{86}$Kr + $^{130,136}$Xe', GSI annual report, Darmstadt (1996).

[Sto97]  N.J. Stone et al., 'Magnetic moments of odd-$A$ Sb isotopes to $^{133}$Sb: significant evidence for mesonic exchange current contributions and on core collective $g$ factors', Phys. Rev. Lett. 78 (1997) 820–823.

[Str67]  V.M. Strutinsky, 'Shell effects in nuclear masses and deformation energies', Nucl. Phys. A 95 (1967) 420–442.

[Str99]  Ph. Dessagne, A. Michalon and Ch. Miehé, eds., 'The beta decay, from weak interaction to nuclear structure, Proc. of the workshop, March 1999, Strasbourg', Institut de Recherches Subatomiques, IRES, Strasbourg, 1999.

[Sun92]  S. Sundell, H. Ravn and the ISOLDE Collaboration, 'Ion source with combined cathode and transfer line heating', Nucl. Instr. Meth. B 70 (1992) 160–164.

[Suz97]  T. Suzuki and T. Otsuka, 'Gamov-Teller transitions from $^{11}$Li and $^{12}$Be', Phys. Rev. C 56 (1997) 847–856.

[Suz98]  T. Suzuki, 'Gamow-Teller and magnetic dipole transitions for $^{11}$Li, $^{12}$Be and $^{11}$Be', J. Phys. G 24 (1998) 1455–1460.

[Swa70]  K. Swars, ed., *Tantal*, vol. B1 of *Gmelin Handbuch der Anorganischen Chemie*, Verlag Chemie, Weinheim, 8th edn. (1970).

[Swi81]  W.J. Swiatecki, 'The dynamics of nuclear coalescence or reseparation', Phys. Scr. 24 (1981) 113–122.

[Sze95]  J. Szerypo et al., 'Beta decay of neutron-deficient even-mass indium isotopes: evidence for population of highly-excited states in the cadmium-daughter nuclei', Nucl. Phys. A 584 (1995) 221–240.

[Sze97]  J. Szerypo et al., 'Decay properties of the ground-state and isomer of $^{103}$In', Z. Phys. A 359 (1997) 117–126.

[Tac90]  T. Tachibana, M. Yamada and Y. Yoshida, 'Improvement of the gross theory of $\beta$-decay. II', Prof. Theo. Phys. 84 (1990) 641–657.

[Taf71]   L.M. Taff, B.K.S. Koene and J. Van Klinken, 'The decays of $^{70a}$Cu, $^{70b}$Cu and $^{67}$Ni', Nucl. Phys. A 164 (1971) 565–575.

[Tag99]   Y. Tagaya et al., 'The $\alpha$-decay energies and halflives of $^{195g,m}$At and $^{199}$Fr', Eur. Phys. J. A 5 (1999) 123–125.

[Tal76]   W.L. Talbert et al., 'Target developments at TRISTAN', Nucl. Instr. Meth. 139 (1976) 257–266.

[Tam96]   Claire Tamburella, *Projet PIAFE: production d'états de charges élevées pour des ions radioactifs*, Ph.D. thesis, Université Denis Diderot Paris VII (1996).

[Tam97]   C. Tamburella et al., 'Production of multicharged radioactive ion beams: the $1^+$ to n$^+$ charge state transformation for the Production, Ionisation, Accélération de Fasiceaux Exotiques project', Rev. Sci. Instr. 68 (1997) 2319–2321.

[Tan85]   I. Tanihata et al., 'Measurements of interaction cross sections and radii of He isotopes', Phys. Lett. 160B (1985) 380–384.

[Tan87]   O. Tanimura and T. Fliessbach, 'Dynamic model for alpha particle emission during fission', Z. Phys. A 328 (1987) 475–486.

[Tem98]   J.P. Temirov, O. Tuhlibaev and A.T.Tursunov, 'Measurement of the ultra-low partial pressure of cesium by the method of laser spectroscop', Opt. Spectr. (USSR) 85 (1998) 709–710.

[TFP83]   Ernst Hoinkis, ed., 'Transport of Fission Products in Matrix and Graphite, Proc. of Coll. held at the HMI, Nov. 1981', HMI-B372, Berlin, 1983.

[Thi83]   F.K. Thielemann, J. Metzinger and H.V. Klapdor, 'Beta-delayed fission and neutron emission: consequences for the astrophysical $r$-process and the age of the galaxy', Z. Phys. A 309 (1983) 301–317.

[Thi97]   P. Thirolf et al., 'Concept of a high-resolution online mass separator for the Munich fission fragment accelerator', Nucl. Instr. Meth. B 126 (1997) 242–245.

[Til93]   D.R. Tilley, H.R. Weller and C.M. Cheves, 'Energy levels of light nuclei $A = 16 - 17$', Nucl. Phys. A 564 (1993) 1–184.

[To79]   K.X. To and R. Drouin, 'Détermination semi-empirique des états de charges d'un faisceau d'ions rapides ($Z \leq 18$)', Nucl. Instr. Meth. 160 (1979) 461–463.

[Tōk85]   J. Tōke et al., 'Quasi-fission – the mass-drift mode in heavy-ion reactions', Nucl. Phys. A 440 (1985) 327–365.

[Ton96]   W. Tongqing, F. Hongmei, G. Bing, Zh. Jinghua and G. Yingxiang, 'FEBIAD target-ion-source for on-line isotope separator in Lanzhou', Annual report IMP & NLHIAL, Institute of Modern Physics, Lanzhou, China (1996), p. 151.

[Tow87]   I.S. Towner, 'Quenching of spin matrix elements in nuclei', Phys. Rep. 155 (1987) 263–377.

[TP71]   Catherine Thibault-Philippe, *Etude par spectromètre de masse en ligne de noyaux légers exotiques produits dans les reactions à haute énergie*, Ph.D. thesis, Université de Paris (1971).

[Tra72]   B.L. Tracy et al., 'Rb and Cs isotopic cross sections from 40-60 MeV-proton-induced fission of $^{238}$U, $^{232}$Th and $^{235}$U', Phys. Rev. C 5 (1972) 222–234.

[Tur90]   A.T. Tursunov, N.B. Eshkobilov and A.T. Khalmanov, 'Laser spectroscopy of atomic mercury Rydberg states', Opt. Spectr. (USSR) 68 (1990) 294–297.

[Tür98]   A. Türler et al., 'Decay properties of $^{265}$Sg ($Z = 106$) and $^{266}$Sg ($Z = 106$)', Phys. Rev. C 57 (1998) 1648–1655.

[Urb97]   W. Urban et al., 'Octupole correlations in neutron-rich, even-even barium isotopes', Nucl. Phys. A 613 (1997) 107–131.

[VA92]   E.P. Vidolova-Angelova, D.A. Angelov, T.B. Krustev and S.T. Mincheva, 'Investigation of lutetium Rydberg states by laser multistep resonance ionization spectroscopy', Z. Phys. D 23 (1992) 215–218.

[Val76]   G.V. Val'skiĭ, 'Yields of light nuclei in ternary fission', Sov. J. Nucl. Phys. 24 (1976) 140–144.

[Var97]   V.E. Varlamov et al., 'Observation of the penetration of subbarrier ultracold neutrons through beryllium foils and coatings', JETP Lett. 66 (1997) 336–343.

[Var98]   R.L. Varner et al., 'Measurement of the E1 strength function of $^{11}$Be', in [ENA98] pp. 245–251.

[Ven70]   A. Venezia and S. Amiel, 'Separation of fission produced iodine by surface ionization', Nucl. Instr. Meth. 87 (1970) 307–309.

[Ver81]   J. Verplancke et al., 'Present status and expected evolution of LISOL, the Leuven isotope separator on-line', Nucl. Instr. Meth. 186 (1981) 99–103.

[Ver84]   J. Verplancke et al., 'Decay study of $^{103}$In and $^{105}$In', Z. Phys. A 315 (1984) 307–317.

[Ver99]   S. Versyck, 'Meson exchange currents in first forbidden beta decays in the lead region', in [Str99], 1999, pp. 22–29.

[Ves92]   S.P. Vesnovskii, V.N. Polynov and L.D. Danilin, 'Highly enriched isotope samples of uranium and transuranium elements for scientific investigation', Nucl. Instr. Meth. A 312 (1992) 1–4.

[Vil97]   A.C.C. Villari, 'ECR development for accelerated radioactive ion beams', Nucl. Instr. Meth. B 126 (1997) 35–44.

[Vor69]   A.A. Vorobiev et al., 'Light nuclei from $^{233}$U neutron fission', Phys. Lett. 30B (1969) 332–334.

[Vor72]   A.A. Vorobyov et al., 'Light nuclei from $^{235}$U neutron fission', Phys. Lett. 40B (1972) 102–104.

[Vor75]   A.A. Vorob'ev et al., 'Ternary fission of $^{239}$Pu and $^{242m}$Am by neutrons', Sov. J. Nucl. Phys. 20 (1975) 248–250.

[Vos81]   B. Vosicki, T. Bjørnstad, L.C. Carraz, J. Heinemeier and H.L. Ravn, 'Intense beams of radioactive halogens produced by means of surface ionization', Nucl. Instr. Meth. 186 (1981) 307–313.

[Wag86]   C. Wagemans, P. D'hondt, P. Schillebeeckx and R. Brissot, 'Triton and alpha emission in the thermal-neutron-induced ternary fission of $^{233}$U, $^{235}$U, $^{239}$Pu and $^{241}$Pu', Phys. Rev. C 33 (1986) 943–953.

[Wag89]   C. Wagemans, *Light particle-accompanied fission*, vol. III of Poenaru and Ivascu [Poe89], 1989, pp. 63–98.

[Wag91a]   C. Wagemans, ed., CRC Press, Boca Raton (1991).

[Wag91b]   C. Wagemans, *Charged-particle-induced fission*, in [Wag91a], 1991, pp. 199–226.

[Wag92]   C. Wagemans, in J. Kristiak and B.I. Pustylnik, eds., 'Proc. Int. Workshop on Dynamical Aspects of Nuclear Fission, Smolenice, Slovakia, 1991', Dubna, pp. 139–.

[Wah62]   A.C. Wahl et al., 'Nuclear-charge distribution in low-energy fission', Phys. Rev. 126 (1962) 1112–1127.

[Wah88]   A.C. Wahl, 'Nuclear-charge distribution and delayed-neutron yields for thermal-neutron-induced fission of $^{235}$U, $^{233}$U and $^{239}$Pu and for spontaneous fission of $^{252}$Cf', At. Data Nucl. Data Tables 39 (1988) 1–156.

[Wal85]    P.M. Walker, 'First experiments and future prospects at the Daresbury on-line isotope separator', Hyp. Int. 22 (1985) 475–482.

[Wal86]    R.J. Walker and J.D. Fassett, 'Isotopic measurement of subnanogram quantities of rhenium and osmium by resonance ionization mass spectrometry', Anal. Chem. 58 (1986) 2923–2927.

[Wal87]    K. Wallmeroth et al., 'Sudden change in the nuclear charge distribution of very light gold isotopes', Phys. Rev. Lett. 58 (1987) 1516–1519.

[Wal90]    Jearl Walker, 'A homemade copper chloride laser emits powerful bursts of green and yellow light', Scientific American 262 (1990) 88–91.

[Wan99]    J.C. Wang et al., '$\beta$-delayed neutron decay of $^{104}$Y, $^{112}$Tc, $^{113}$Tc and $^{114}$Tc: test of half-life predictions for neutron-rich isotopes of refractory elements', Phys. Lett. B 454 (1999) 1–7.

[Web92]    M. Weber et al., 'New neutron-rich isotopes in the scandium-to-nickel region, produced by fragmentation of a 500 MeV/u $^{86}$Kr beam', Z. Phys. A 343 (1992) 67–71.

[Wefer]    Elmar Wefers, priv. comm.

[Weg61]    H.E. Wegner, 'Additional long-range particles from the spontaneous fission of Cf$^{252}$', Bull. Am. Phys. Soc. 6 (1961) 307.

[Weiss]    Leo Weissman, priv. comm.

[Wei91]    H. Weigmann, *Fission barriers*, in [Wag91a], 1991, pp. 7–33.

[Wei99]    L. Weissman et al., 'A detector setup to study the decay properties of exotic nuclei', Nucl. Instr. Meth. A 423 (1999) 328–336.

[Wel98]    R. Welton, G.D. Alton, B. Cui and S.N. Murray, 'Experimental methods in radioactive ion-beam target/ion source development and characterization', Rev. Sci. Instr. 69 (1998) 2892–2896.

[Wen87]    K. Wendt et al., 'On the hyperfine structure and isotope shift of radium', Z. Phys. D 4 (1987) 227–241.

[Weyer]    Gerd Weyer, priv. comm.

[Whe67]    S.L. Whetstone and T.D. Thomas, 'Light charged particles from spontaneous fission of Cf$^{252}$', Phys. Rev. 154 (1967) 1174–1181.

[Wid95]    W. Widdra et al., '$\beta$-NMR on single-crystal surfaces: method', Rev. Sci. Instr. 66 (1995) 2465–2475.

[Wil76]    B.D. Wilkens, E.P. Steinberg and R.R. Chasman, 'Scission-point model of nuclear fission based on deformed-shell effects', Phys. Rev. C 14 (1976) 1832–1863.

[Wil84]    M.W. Williams, D.W. Beekman, J.B. Swan and E.T. Arakawa, 'Detection of trace elements with resonance ionization and time-of-flight mass spectrometry', Anal. Chem. 56 (1984) 1348–1350.

[Wil85]    J.F. Wild et al., 'Light-charged-particle emission in the spontaneous fission of $^{250}$Cf, $^{256}$Fm and $^{257}$Fm', Phys. Rev. C 32 (1985) 488–495.

[Win89]    J.A. Winger et al., 'Structure of neutron-rich $^{74}$Zn from $^{74}$Cu decay and shell-model calculations for even-$A$ Zn nuclei', Phys. Rev. C 39 (1989) 1976–1984.

[Win90]    J.A. Winger et al., 'Structure of $^{76}$Zn from $^{76}$Cu decay and systematics of neutron-rich Zn nuclei', Phys. Rev. C 42 (1990) 954–960.

[Win93]    J.A. Winger et al., 'Half-life measurements for $^{61}$Ga, $^{63}$Ge and $^{65}$As and their importance in the $rp$ process', Phys. Rev. C 48 (1993) 3097–3105.

[Wla00]    W. Wlazlo et al., 'Cross-sections of spallation residues produced in $1A$ GeV $^{208}$Pb on proton reactions', Phys. Rev. Lett. 84 (2000) 5736–5739.

[Wor78]   E.F. Worden, R.W. Solarz, J.A. Paisner and J.G. Conway, 'First ionization potentials of lanthanides by laser spectroscopy', J. Opt. Soc. Amer. 68 (1978) 52–61.

[Wor79]   E.F. Worden and J.G. Conway, 'Laser spectroscopy of neptunium: first ionization potential, lifetimes and new high-lying energy levels of Np I', J. Opt. Soc. Amer. 69 (1979) 733–738.

[Wös96]   M. Wöstheinrich, M. Hesse and F. Gönnenwein, 'Yields of ternary particles from fission in an extended Halpern model', in [Dan96], 1996, pp. 231–237.

[Wös98]   M. Wöstheinrich et al., 'Ternary particles from the reactions $^{229}$Th($n_{th}$,f), $^{233}$U($n_{th}$,f) and $^{239}$Pu($n_{th}$,f)', in [Sey98], 1998, pp. 330–337.

[Wös99a]   M. Wöstheinrich et al., 'Yields of ternary particles from the reactions $^{229}$Th($n_{th}$,f), $^{233}$U($n_{th}$,f) and $^{239}$Pu($n_{th}$,f)', Acta Phys. Slovaca 49 (1999) 117–124.

[Wös99b]   Marcus Wöstheinrich, *Emission von ternären Teilchen aus den Reaktionen $^{229}$Th($n_{th}$,f), $^{233}$U($n_{th}$,f) und $^{239}$Pu($n_{th}$,f)*, Ph.D. thesis, Uni Tübingen (1999).

[Wün78]   K.D. Wünsch, 'An on-line mass-separator for thermally ionisable fission products: OSTIS', Nucl. Instr. Meth. 155 (1978) 347–351.

[Wut98]   D. Wutte et al., 'Development of an rf driven multicusp ion source for nuclear science experiments', Nucl. Instr. Meth. B 142 (1998) 409–416.

[Xie98]   Z.Q. Xie, 'Techniques for enhancing the performances of high charge state ECR ion sources', in [Caa98], 1998, pp. 48–51.

[Xu90]   X.Y. Xu, J.Z. Tang, W. Huang, W.Z. Zhao and D.Y. Chen, 'Rydberg energy levels and their structure in the ruthenium atom', JPB 23 (1990) 3315–3323.

[Xu93]   C.B. Xu et al., 'The study of autoionizing states of lutetium atoms by resonance ionization spectroscopy', JPB 26 (1993) 2827–2835.

[Xu95]   X.Y. Xu, D.Y. Chen, K.L. Wen, S.L. Wang and Q. Hui, 'RIMS efforts in China', in [RIS94], 1995, pp. 227–232.

[Yer94]   A.V. Yeremin et al., 'The kinematic separator VASSILISSA. Performance and experimental results', Nucl. Instr. Meth. A 350 (1994) 608–617.

[Yos87]   M. Yoshii et al., 'The ion-guide isotope separator on-line at the Tohoku university cyclotron', Nucl. Instr. Meth. B 26 (1987) 410–418.

[Zah93]   M. Zahar et al., 'Momentum distributions for $^{12,14}$Be fragmentation', Phys. Rev. C 48 (1993) R1484–R1487.

[Zan71]   E.Ya. Zandberg and N.I. Ionov, *Surface ionization*, Israel Program for Scientific Translations, Jerusalem (1971).

[Zha98a]   L. Zhang et al., 'Identification of $^{209}$Hg', Eur. Phys. J. A 2 (1998) 5–7.

[Zha98b]   L. Zhang et al., 'Neutron-rich heavy residues and exotic multinucleon transfer', Phys. Rev. C 58 (1998) 156–163.

[Zhd77]   N.S. Zhdanovich and Yu.I. Kozlov, Nauka, Moscow, 1977, pp. 115–.

[Zhe83]   A.N. Zherikhin, V.S. Letokhov, V.I. Mishin, M.E. Muchnik and V.N. Fedoseyev, 'Production of photoionic gallium beams through stepwise ionization of atoms by laser radiation', Appl. Phys. B 30 (1983) 47–52.

[Zhe84a]   A.N. Zherikhin, V.I. Mishin and V.N. Fedoseev, 'Determining the absolute $nf^2F^0$ energy levels of the Al I Rydberg series via laser step excitation and photoionization', Opt. Spectr. (USSR) 57 (1984) 476–479.

[Zhe84b]   A.N. Zherikhin et al., 'High-resolution laser photoionization spectroscopy of radioactive europium isotopes', Sov. Phys. JETP 59 (1984) 729–736.

[Zhi96]   Zh. Zhizheng et al., 'Chemical selectivity of a laser ion source for on-line mass separator of IMP', Annual report IMP & NLHIAL, Institute of Modern Physics, Lanzhou, China (1996), p. 150.

[Zhu94]   M.V. Zhukov, A.A. Korsheninnikov and M.H. Smedberg, 'Simplified $\alpha + 4n$ model for the $^8$He nucleus', Phys. Rev. C 50 (1994) R1–R4.

[Zir74]   J.P. Zirnheld, 'On-line fission fragment separator using a helium jet ion source', Nucl. Instr. Meth. 114 (1974) 517–520.

[Zöl95a]   Christoph M. Zöller, *Untersuchung der neutroneninduzierten Spaltung von $^{238}$U im Energiebereich von 1 MeV bis 500 MeV*, Ph.D. thesis, TH Darmstadt (1995).

[Zöl95b]   C.M. Zöller et al., 'Fission fragment properties in the $^{238}$U(n,f) reaction at incident neutron energies from 1 MeV to 500 MeV', Rep. IKDA 95/25, Institute for Nuclear Physics, TH Darmstadt (1995).

[Zyu88]   A.D. Zyuzikov, V.I. Mishin and V.N. Fedoseev, 'Laser resonance photoionization spectroscopy of excited and autoionizing atomic states of rare-earth elements. 3: Neodymium', Opt. Spectr. (USSR) 64 (1988) 287–288.

# Acknowledgements